
Electronic Thesis and Dissertation Repository

6-19-2017 12:00 AM

Structural Modification, Polymerization and Applications of Boron Difluoride Formazanates

Stephanie M. Barbon
The University of Western Ontario

Supervisor
Prof. Joe Gilroy
The University of Western Ontario

Graduate Program in Chemistry
A thesis submitted in partial fulfillment of the requirements for the degree in Doctor of Philosophy
© Stephanie M. Barbon 2017

Follow this and additional works at: <https://ir.lib.uwo.ca/etd>

 Part of the [Materials Chemistry Commons](#)

Recommended Citation

Barbon, Stephanie M., "Structural Modification, Polymerization and Applications of Boron Difluoride Formazanates" (2017). *Electronic Thesis and Dissertation Repository*. 4611.
<https://ir.lib.uwo.ca/etd/4611>

This Dissertation/Thesis is brought to you for free and open access by Scholarship@Western. It has been accepted for inclusion in Electronic Thesis and Dissertation Repository by an authorized administrator of Scholarship@Western. For more information, please contact wlsadmin@uwo.ca.

Abstract

This thesis describes the synthesis and characterization of a new family of fluorescent and redox-active BF_2 complexes of formazanate $[\text{R}^1\text{-N-N}=\text{C}(\text{R}^3)\text{-N}=\text{N-R}^5]^-$ ligands. The complexes were easily synthesized in two high-yielding steps, from inexpensive starting materials and readily purified by conventional methods. The properties of the resulting complexes can be tuned through structural variation – for example, appending electron donating or withdrawing substituents, or extending π conjugation. These methods of structural variation can bathochromically or hypsochromically shift the maximum absorption and emission wavelengths, vary the quantum yields, and allow for tuning of the reduction potentials. Using these methods, the properties of these complexes were optimized for use as fluorescence cell-imaging agents, and efficient electrochemiluminescence emitters.

In order to expand the scope of this chemistry, copper-assisted azide-alkyne cycloaddition (CuAAC) chemistry was used to further modify the BF_2 formazanate scaffold. Using this method, benzyl groups were appended to the BF_2 complexes, which showed that the reaction proceeded cleanly, and that the resulting products had red-shifted wavelengths of maximum absorption and emission, and increased fluorescence quantum yields. Using the same strategy, a tetraethylene glycol based azide imparted water solubility, and the resulting complex was used in fluorescence cell-imaging experiments. Additionally, ferrocene moieties could be appended, which quenched the fluorescence of the resulting complex. Upon oxidation of the ferrocene groups, the fluorescence was regenerated allowing for these compounds to be used as redox sensors. Finally, CuAAC was used to synthesize copolymers of BF_2 formazanate complexes and 9,9-dihexylfluorene. The resulting polymers had low band gaps ($E_g = 1.67$ eV) and good film-forming properties, paving the way for their use in organic photovoltaics.

Finally, reaction of an *o*-phenol-substituted formazan with $\text{BF}_3 \cdot \text{OEt}_2$ and NEt_3 resulted in a complex reaction mixture, which contained 5 BN heterocycles with unprecedented connectivity and interesting optical and electronic properties. Two of the most unique

complexes were selected, and their chemical reduction products – a stable anion, radical anion and diradical dianion were studied in detail.

Combined, this work has opened up an entirely new area of molecular materials with application in a variety of fields. This thesis describes the details of the work described above.

Keywords

Formazanate Ligands, Boron Difluoride, BN Heterocycles, Multifunctional Polymers, Electrochemistry, Absorption and Emission Spectroscopy, Redox Chemistry, Fluorescence, Copper-Assisted Alkyne-Azide Cycloaddition, Cell Imaging, Electrochemiluminescence.

Co-Authorship Statement

The work described in this thesis contains contributions from the authors as well as co-workers Dr. Jacquelyn T. Price, Pauline A. Reinkeluers, Prof. Viktor Staroverov, Umesh Yogarajah, Ryan Maar, Neha Sharma, Dr. Mahdi Hesari, Prof. Zhifeng Ding, Samantha Novoa, Desiree Bender, Hillary Groom, Prof. Leonard G. Luyt and Prof. Joe B. Gilroy. The contributions of each are described below.

Chapter 1 was written by the author and edited by Prof. Joe Gilroy

Chapter 2 describes a series of compounds which were synthesized and characterized, for the most part, by the author. Dr. Price was responsible for the synthesis of two BF_2 complexes and Pauline Reinkeluers was responsible for the optimization of the BF_2 complex synthesis. Crystallography experiments were done by Dr. Price, and the computational work was completed by Prof. Viktor Staroverov. Cell-imaging studies were facilitated by Ryan Maar, and completed by Neha Sharma and Hilary Groom in the lab of Prof. Leonard Luyt. Electrochemiluminescence studies were done by Dr. Hesari in the lab of Prof. Zhifeng Ding. The chapter was written by the author and edited by Prof. Gilroy.

Chapter 3 describes the synthesis and characterization of a set of BF_2 formazanate complexes that were synthesized by the author. Dr. Price and Umesh Yogarajah were responsible for initial efforts toward the synthesis of the dimers. Prof. Staroverov was responsible for computational studies. The chapter was written by the author and edited by Prof. Gilroy.

Chapter 4 details a project involving a series of complexes and polymers synthesized by copper-assisted alkyne azide cycloaddition reactions. Initial work towards the synthesis of the tetraethylene glycol substituted complex was done by Desiree Bender, and the synthesis and characterization of the asymmetric 3-cyanoformazanate BF_2 complexes was done by Samantha Novoa. The remainder of the synthesis and characterization was done by the author. Cell imaging studies were done by Hillary Groom in the lab of Prof. Leonard Luyt. The chapter was written by the author and edited by Prof. Gilroy.

Chapter 5 describes a project in which all the synthesis and characterization was completed by the author. The computational studies were done by Prof. Viktor Staroverov. The chapter was written by the author and edited by Prof. Gilroy.

Chapter 6 was written by the author and edited by Prof. Gilroy.

Acknowledgments

First and foremost I have to give a big thank you to my supervisor, Joe. You have been so incredibly helpful these four years, I have learned so much (though still not how to use a ratchet-action screwdriver), and really appreciate you always pushing me to pursue extra-curricular professional development activities. I would not have become the chemist that I am without your guidance!!

Secondly to my labmates – everyone always says they have the best labmates ever, but that can't be true, because I know that I do. Joe and Amir, who were there from the beginning, Sam and Ryan who have been part of team formazan for the last bunch of years, and those who have been part of the Gilroy lab throughout the years (Kit, Jackie, Alex, Ana). I've learned a lot from each and every one of you, and you have always made it fun to come into work, even when the chemistry wasn't going so well. I can safely say I couldn't have made it through grad school *for the life of me* without you all, so 'thank goodness' you were there! ☺

To the rest of the department, a huge thank you – over my 8 years at Western, I've had the opportunity to be taught by, or collaborate with most of the faculty, and I am very thankful for the opportunities to learn from everyone. The support staff also deserves a huge thanks – Mat, Doug, Aneta and Paul, for always being willing to go above and beyond to help me get the data I needed. Finally to the grad students I have spent so much time with over the last 4 years – you are all awesome, and I am so grateful to each of you for being willing to chat about chemistry, and making the time outside the lab so great as well!

A big thank you to my committee – Prof. Mike Kerr, Prof. Johanna Blacquiere, Prof. Takashi Kuboki and Prof. Frieder Jäkle – for taking the time to read this document.

Finally, I have to give a big thank you to my family. Mom and Dad, and my siblings Jen, Andrew and Elizabeth. You have all been so supportive of me – always encouraging me, cheering me up when lab-work was tiring me out, and acting interested when I talk about nic-nacs and glowing things. You guys are awesome, and I love you all so much!

Table of Contents

Abstract.....	ii
Co-Authorship Statement.....	iv
Acknowledgments.....	vi
Table of Contents.....	vii
List of Tables.....	xii
List of Figures.....	xiv
List of Schemes.....	xxi
List of Appendices.....	xxii
List of Abbreviations.....	xxiii
Chapter 1.....	1
1 BF ₂ Complexes of <i>N</i> -donor Ligands.....	1
1.1 Boron Difluoride Complexes of <i>N</i> -donor Ligands.....	3
1.2 Polymers.....	7
1.3 Applications.....	9
1.3.1 Photovoltaics.....	9
1.3.2 Organic Thin-Film Transistors, Light Emitting Diodes, and Batteries.....	10
1.3.3 Sensing.....	12
1.3.4 Biomedical Applications.....	13
1.3.5 ECL Devices.....	18
1.3.6 Self-Assembled Micelles.....	19
1.4 Formazans.....	20
1.5 Scope of Thesis.....	25
1.6 References.....	26

Chapter 2.....	36
2 Structural Modification of BF ₂ Formazanate Dyes.....	36
2.1 Introduction.....	36
2.2 Results.....	39
2.2.1 Synthesis.....	39
2.2.2 X-ray Crystallography.....	40
2.2.3 Absorption and Emission Spectroscopy.....	43
2.2.4 Cyclic Voltammetry.....	47
2.3 Discussion.....	49
2.4 Applications.....	51
2.4.1 Electrochemiluminescence.....	51
2.4.2 Cell Imaging.....	51
2.5 Conclusions.....	52
2.6 Experimental.....	53
2.6.1 General Considerations.....	53
2.6.2 Electrochemical Methods.....	54
2.6.3 X-ray Crystallography Details.....	54
2.7 References.....	63
Chapter 3.....	68
3 The Effect of Extended π Conjugation on the Properties of BF ₂ Formazanate Dyes..	68
3.1 Introduction.....	68
3.2 Results and Discussion.....	71
3.2.1 Synthesis.....	71
3.2.2 Naphthyl-Substituted BF ₂ Formazanate Complexes.....	72

3.2.3 3-Phenyl-, 3-Cyano-, and 3-Nitro-Substituted BF ₂ Formazanate Complexes.....	77
3.2.4 Electronic Structure Calculations.....	82
3.2.5 Benzene-Bridged BF ₂ Formazanate Complexes.....	84
3.3 Conclusion	89
3.4 Experimental Section.....	90
3.4.1 General Considerations	90
3.4.2 Electrochemical Methods.....	90
3.4.3 X-ray Crystallography Details	91
3.5 References.....	100
Chapter 4.....	106
4 BF ₂ Formazanate Complexes Modified by Copper-Assisted Alkyne Azide Cycloaddition – Molecular Materials and Polymers.....	106
4.1 Introduction.....	106
4.2 Synthesis and Characterization of Molecular Materials	108
4.2.1 Benzyl-Functionalized BF ₂ Complexes of 3-Cyanoformazanates.....	108
4.2.2 Ferrocene-Functionalized BF ₂ Complexes of 3-Cyanoformazanates	114
4.2.3 Tetraethylene Glycol-Functionalized BF ₂ Complexes of 3-Cyanoformazanates.....	116
4.3 π -Conjugated Polymers of BF ₂ Formazanates.....	119
4.4 Conclusions.....	128
4.5 Experimental Section.....	129
4.5.1 General Considerations	129
4.5.2 Electrochemical Methods.....	130
4.5.3 Gel Permeation Chromatography (GPC)	130
4.5.4 Thermal Analysis	130

4.5.5 Scanning Electron Microscopy	131
4.5.6 X-ray Crystallography Details	131
4.5.7 Cell Imaging Studies	132
4.6 References.....	146
Chapter 5.....	152
5 Structurally Diverse Boron-Nitrogen Heterocycles from an $N_2O_2^{3-}$ Formazanate Ligand	152
5.1 Introduction.....	152
5.2 Results and Discussion	153
5.3 Conclusions.....	163
5.4 Experimental Section	164
5.4.1 General Considerations	164
5.4.2 Purity of New Compounds.....	164
5.4.3 Electrochemical Methods.....	165
5.4.4 X-ray Crystallography Details	165
5.5 References.....	173
Chapter 6.....	177
6 Conclusions and Future Work.....	177
6.1 Conclusions.....	177
6.2 Future Work	181
6.2.1 Molecular Materials: Three-Coordinate Boron Complexes.....	181
6.2.2 Polymeric Materials: BF_2 Formazanate Platinum Polyynes	182
6.2.3 Device Fabrication	182
6.3 References.....	183
Appendices	186

Appendix A1 – Permission to Reuse Copyrighted Material	186
Appendix A2 – Supporting Information for Chapter 2	194
Appendix A3 – Supporting Information for Chapter 3	225
Appendix A4 – Supporting Information for Chapter 4	255
Appendix A5 – Supporting Information for Chapter 5	280
Curriculum Vitae	306

List of Tables

Table 1.1.: Properties of photovoltaic complexes 1.21–1.23	10
Table 1.2.: Optical and Electrochemiluminescence properties of complexes 1.37–1.40 .	18
Table 2.1.: List of substituents for formazans 2.8a–l and BF ₂ formazanate complexes 2.13a–l	39
Table 2.2.: Selected bond lengths (Å) and angles (degrees) for BF ₂ formazanate complexes 2.13d–f and 2.13j–l , determined by X-ray diffraction.	42
Table 2.3.: Optical properties of BF ₂ formazanate complexes 2.13a–l	46
Table 2.4.: Electrochemical data (mV vs. Fc/Fc ⁺) for BF ₂ formazanate complexes 2.13a–l	49
Table 2.5.: X-ray diffraction data collection and refinement details for complexes 2.13d–f and 2.13j–l	55
Table 3.1.: Substituents for formazans 3.11a–k and BF ₂ formazanate complexes 3.10a–k	71
Table 3.2.: Solution characterization data for BF ₂ complexes 3.10a–h, j and k	76
Table 3.3.: Selected bond lengths (Å) and angles (°) for 3.10e, 3.10g, 3.10i, 3.10j and 3.10k	78
Table 3.4.: HOMO/LUMO energies for BF ₂ complexes 3.10a (Ar ¹ = Ar ⁵ = R ³ = Ph), 3.10e (Ar ¹ = Ar ⁵ = Ph, R ³ = CN) and 3.10g (Ar ¹ = Ar ⁵ = Ph, R ³ = NO ₂) in vacuum and toluene solution calculated at the M06/6-311+G* level of theory using the SCRF method.....	83
Table 3.5.: X-ray diffraction data collection and refinement details for BF ₂ complexes 3.10g, 3.10j and 3.10k	92

Table 4.1.: Optical and electronic properties of BF ₂ formazanate complexes 4.9–4.11 and 4.13–4.16	113
Table 4.2.: Absorption and emission properties of complex 4.16 in different solvents. 117	
Table 4.3.: Summary of absorption/emission and electrochemical properties of 4.21–4.26 in DMF and as thin films.	126
Table 4.4.: Optical and electrochemical band gaps and HOMO/LUMO energies of 4.21, 4.23–4.26	127
Table 4.5.: X-ray diffraction data collection and refinement details for mono-alkyne-substituted complex 4.9	132
Table 5.1.: Varied conditions and the resulting distribution (as a percent of the total reaction mixture) of the different products..	156
Table 5.2.: Optical and electronic properties of complexes 5.9–5.13 and their reduction products.....	162
Table 5.3.: Selected bond lengths (Å) and angles (°) for solid-state structures of various products.....	163
Table 5.4.: X-ray diffraction data collection and refinement details for compounds 5.9, 5.10, 5.12, 5.13, 5.15, 5.10⁻, 5.10^{•2-}, and 5.16⁻	167

List of Figures

Figure 1.1.: a) Head of wild-type budgerigars (*Melopsittacus undulatus*) under white light (top) and UV illumination (bottom). b) Jellyfish *Periphylla periphylla* under white light (left) and UV illumination (right). c) Fluorescence of the head and anterior region of the loggerhead sea turtle *Caretta caretta*. d) Adult male tree frog *Hypsiboas punctatus* fluorescence. e) Luminescence from the false stonefish *Scorpaenopsis diabolus*. Images reproduced with permission from Refs. [1], [12], [8], [6], [10] respectively.1

Figure 1.2.: Polymeric redox-flow battery schematic. Anode and cathode are separated by a size-exclusion membrane. Anolyte and catholyte are polymers **1.24** and **1.25** respectively.12

Figure 1.3.: Confocal microscopic images of HeLa cells treated with a) **1.32**, b) **1.33** and c) **1.34**. Confocal microscopy images were obtained by using laser excitation at $\lambda =$ a) 514 nm, b) 543 nm and c) 643 nm. Scale bar is 47.62 μm long. Image reproduced with permission from Ref. [115].14

Figure 1.4.: *A. fumigatus* incubated with cell membrane counterstain Syto82 (red) and BODIPY-peptide (green) for (i) 0 min, (ii) 1 min, (iii) 3 min, and (iv) 10 min. Scale bar = 2.5 μm . Image reproduced with permission from Ref. [117].16

Figure 1.5.: (a) In vivo NIR fluorescence images of 4T1 tumor-bearing mice after being injected with 150 μL of a 50 $\mu\text{g}/\text{mL}$ solution of targeted-BODIPY nanoparticles (top row), and non-targeting BODIPY nanoparticles (bottom row). The arrow indicates the tumor site. (b) Average weights of tumors 10 days after treatment. Treatment varied based on group number. Group 1 – control group; 2 – light irradiation only; 3 – targeted-BODIPY nanoparticle injection only; 4 – non-targeted BODIPY nanoparticle injection and irradiation; and 5 – targeted BODIPY nanoparticle injection and irradiation. Image reproduced with permission from Ref. [123].17

Figure 1.6.: Selection of colours of micelles which can be produced mixing red, green and blue fluorescent block copolymers. Raw images of solutions of these fluorescent micelles

under UV irradiation, and corresponding laser scanning confocal microscopy (LCSM) images. Scale bar = 3 μm . Image reproduced with permission from Ref. [128]......19

Figure 1.7.: 96-well plate containing (a) blank control wells, (b) untreated cell control wells, and (c-e) cell lines with various concentrations of drugs. Image reproduced with permission from Ref. [136]......22

Figure 2.1.: ^1H NMR spectrum of formazan **2.8d** (black) and BF_2 complex **2.13d** (red) in CDCl_3 . The NH signal for **2.8d** is inset.40

Figure 2.2.: Solid-state structures – top view (left) and side view (right). Thermal ellipsoids are shown at 50% probability and hydrogen atoms are removed for clarity.42

Figure 2.3.: UV-vis absorption spectra (a) and emission spectra (b) of **2.13a** (black), **2.13b** (red) and **2.13c** (blue) and absorption (c) and emission (d) spectra of **2.13j** (purple), **2.13k** (green) and **2.13l** (grey) recorded for 10^{-5} M degassed toluene solutions.....44

Figure 2.4.: Cyclic voltammograms of **2.13j** (purple), **2.13k** (green), and **2.13l** (grey) recorded at 100 mV s^{-1} in 1 mM acetonitrile solutions containing 0.1 M $[\text{nBu}_4\text{N}][\text{PF}_6]$ as supporting electrolyte.....49

Figure 2.5.: Spooling ECL spectra of **2.13l** in the presence of TPrA acquired over a time interval of 1s. The blue and red spectra represent the forward scan and the black spectra represent the reverse scan.51

Figure 2.6.: Confocal fluorescent micrographs of mouse fibroblast cells stained with BF_2 formazanate complex **2.13l** and DAPI. Images (a) and (b) were visualized with excitation at 559 nm and emission collected between 625–725 nm. Images (c) and (d) are an overlay of images (a) and (b) with those obtained from excitation at 405 nm and emission collected between 425–475 nm.....52

Figure 3.1.: ^1H NMR spectra of **3.10j** (left) and **3.10k** (right) in CDCl_3 . ^{19}F and ^{11}B NMR spectra are shown as insets.72

Figure 3.2.: UV-vis absorption spectra (a) and emission spectra (b) of **3.10a** (black, Ar¹ = Ar⁵ = R³ = Ph), **3.10b** (blue, Ar¹ = Ar⁵ = Ph, R³ = Np), **3.10c** (red, Ar¹ = R³ = Ph, Ar⁵ = Np) and **3.10d** (green, Ar¹ = Ar⁵ = Np, R³ = Ph). UV-vis absorption and emission spectra were recorded for 10⁻⁵ M degassed toluene solutions.74

Figure 3.3.: Cyclic voltammograms of **3.10a** (black), **3.10b** (blue), **3.10c** (red) and **3.10d** (green), recorded at 100 mV s⁻¹ in 1 mM MeCN solutions containing 0.1 M [nBu₄N][PF₆] as supporting electrolyte. L = redox-active formazanate ligand.75

Figure 3.4.: a) Top view and b) side view of the solid-state structure of BF₂ formazanate complex **3.10g**. Thermal displacement ellipsoids are shown at 50% probability and hydrogen atoms have been omitted for clarity.78

Figure 3.5.: UV-vis absorption spectra (a) and emission spectra (b) of **3.10a** (black, Ar¹ = Ar⁵ = R³ = Ph), **3.10e** (red, Ar¹ = Ar⁵ = Ph, R³ = CN) and **3.10g** (blue, Ar¹ = Ar⁵ = Ph, R³ = NO₂). UV-vis absorption spectra (c) and emission spectra (d) of **3.10d** (green, Ar¹ = Ar⁵ = Np, R³ = Ph), **3.10f** (purple, Ar¹ = Ar⁵ = Np, R³ = CN) and **3.10h** (orange, Ar¹ = Ar⁵ = Np, R³ = NO₂). All UV-vis absorption and emission spectra were recorded for 10⁻⁵ M degassed toluene solutions.81

Figure 3.6.: Cyclic voltammograms of **3.10d** (green), **3.10f** (purple) and **3.10h** (orange) recorded at 100 mV s⁻¹ in 1 mM acetonitrile solutions containing 0.1 M [nBu₄N][PF₆] as supporting electrolyte.82

Figure 3.7.: HOMOs and LUMOs for BF₂ complexes **3.10a** (Ar¹ = Ar⁵ = R³ = Ph), **3.10e** (Ar¹ = Ar⁵ = Ph, R³ = CN) and **3.10g** (Ar¹ = Ar⁵ = Ph, R³ = NO₂) calculated in toluene solution.83

Figure 3.8.: a,c) Top view and b,d) side view of the solid-state structure of BF₂ formazanate dimers **3.10j** and **3.10k**. Thermal displacement ellipsoids are shown at 50% probability and hydrogen atoms have been omitted for clarity. Only one of two very similar molecules in the asymmetric unit for **3.10j** is shown.85

Figure 3.9.: UV-vis absorption spectra (dashed) and emission spectra (solid) of a) **3.10j** and b) **3.10k**, recorded in 10^{-5} M degassed toluene solutions.86

Figure 3.10.: Cyclic voltammograms of **3.10j** (grey), **3.10k** (pink) and **3.10a** (black) recorded at 100 mV s^{-1} in 1 mM CH_2Cl_2 solutions containing 0.1 M $[\text{nBu}_4\text{N}][\text{PF}_6]$ as supporting electrolyte.....88

Figure 4.1.: Solid-state structure of **4.9**. Anisotropic displacement ellipsoids are shown at 50% probability and hydrogen atoms have been omitted for clarity. Selected bond lengths (Å): B1–N1 1.5759(15), N1–N2 1.3023(15), N2–C1 1.3351(13), O1–C11 1.418(5), C9–C10 1.191(7). Selected bond angles (°): B1–N1–N2 124.57(10), N1–N2–C1 117.24(11).....109

Figure 4.2.: ^1H NMR spectra of a) benzyl azide (blue), mono-alkyne substituted complex **4.9** (red) and mono-benzyl-functionalized complex **4.10** (black) and b) benzyl azide (blue), bis-alkyne-substituted complex **4.13** (red) and bis-benzyl-functionalized complex **4.14** (black) in CDCl_3 . The asterisks denote residual solvent signals.110

Figure 4.3.: Cyclic voltammograms of (a) mono-alkyne-substituted complex **4.9** (black) and mono-benzyl-functionalized complex **4.10** (blue) and (b) bis-alkyne-substituted complex **4.13** (red) and bis-benzyl-functionalized complex **4.14** (purple), recorded at 100 mV s^{-1} in 1 mM THF solutions containing 0.1 M $[\text{nBu}_4\text{N}][\text{PF}_6]$ as supporting electrolyte.....111

Figure 4.4.: UV-vis absorption spectra (solid line) and emission spectra (dashed line) of (a) **4.9**, (b) **4.10**, (c) **4.13** and (d) **4.14**, recorded for 10^{-5} M toluene solutions.112

Figure 4.5.: Cyclic voltammograms of mono-ferrocene-substituted BF_2 complex **4.11** (red) and bis-ferrocene-substituted complex **4.15** (black) recorded at 100 mV s^{-1} in 1 mM THF solutions containing 0.1 M $[\text{nBu}_4\text{N}][\text{PF}_6]$ as supporting electrolyte.115

Figure 4.6.: Emission spectra of solutions of ferrocene-substituted complexes (a) **4.11** and (b) **4.15** treated with 0 equiv. (black), 0.5 equiv. (blue), 1.0 equiv. (red), 1.5 equiv. (green)

and 2.0 equiv. (purple) of NOBF_4 , recorded in degassed CH_2Cl_2 at a concentration of 10^{-5} M. The arrows indicate the trends upon addition of NOBF_4116

Figure 4.7.: UV-vis absorption (solid line) and emission (dashed line) spectra of TEG-functionalized complex **4.16** in CH_2Cl_2 (black) and H_2O (red), recorded for degassed solutions at a concentration of 10^{-5} M.117

Figure 4.8.: Confocal fluorescence micrographs of mouse fibroblast cells stained with TEG-functionalized complex **4.16** and DAPI. Images (a) and (c) were visualized with excitation at 579 nm and emission collected between 620–720 nm. Images (b) and (d) are an overlay of images (a) and (c) with those obtained from excitation at 405 nm and emission collected between 425–475 nm.118

Figure 4.9.: Number average molecular weight of **4.21** as a function of time. The black line has been added as a guide for the eye.121

Figure 4.10.: ^1H NMR spectra of bis alkyne BF_2 complex **4.18** (red), bis azide fluorene **4.20** (blue) and polymer **4.21** (black) in CDCl_3 . The asterisks denote residual solvent signals.122

Figure 4.11.: a) UV-vis absorption spectra of **4.21** (purple), **4.23** (black), **4.24** (green) and **4.25** (red), recorded for 10^{-5} M DMF solutions. b) Normalized UV-vis absorption spectra from 400–750 nm for comparison.124

Figure 4.12.: a) UV-vis absorption spectra of **4.21** (purple), **4.22** (grey), **4.25** (red) and **4.26** (blue), recorded for 10^{-5} M DMF solutions. b) Normalized UV-vis absorption spectra for 280–400 nm region for comparison.125

Figure 4.13.: Cyclic voltammogram of polymer **4.21** recorded at 250 mV s^{-1} in a 1 mM DMF solution containing 0.1 M $[\text{nBu}_4\text{N}][\text{PF}_6]$ as supporting electrolyte.128

Figure 5.1.: Solid-state structures of (a) **5.9** and (b) **5.10**. Thermal displacement ellipsoids are shown at the 50% probability level, and phenyl substituents have been made wireframe

for clarity. Hydrogen atoms have also been removed for clarity. Insets in panels show only the atoms in the respective ten-membered rings.....	157
Figure 5.2.: Cyclic voltammograms of 5.9 (black) and 5.10 (blue) recorded at 100 mV s ⁻¹ in 1 mM CH ₂ Cl ₂ solutions containing 0.1 M [nBu ₄ N][PF ₆] as supporting electrolyte....	158
Figure 5.3.: Solid-state structures of (a) 10^{•-} and (b) 10^{••2-} . Thermal ellipsoids are shown at the 50% probability level, and phenyl substituents have been made wireframe for clarity. Hydrogen atoms have also been removed for clarity.....	159
Figure 5.4.: UV-vis absorption spectra of complexes 5.10 (blue), 5.10^{•-} (red) and 10^{••2-} (black) in CH ₃ CN.....	160
Figure 5.5.: Solid-state structures of (a) 5.12 and (b) 5.13 with thermal displacement ellipsoids shown at the 50% probability level. Hydrogens, aside from the hydrogens on N5 in both 5.12 and 5.13 and on O1 in 5.12 have been removed for clarity.....	161
Figure 5.6.: Solid-state structure of 5.16⁻ with thermal displacement ellipsoids shown at the 50% probability level. Hydrogen atoms and the nBu ₄ N cation have been removed for clarity.	162
Figure 5.7.: HOMOs and LUMOs for 5.13 and 5.16⁻ calculated at the PBE1PBE/6-311+G(d,p) level.	163
Figure 6.1.: Substituent-driven optical and electronic properties of BF ₂ complexes of formazanate ligands.	177
Figure 6.2.: Extended conjugation through naphthyl substituents and benzene-bridged dimers, and the effect on the optical properties.	178
Figure 6.3.: Copper-assisted alkyne-azide cycloaddition as a useful tool for the synthesis of polymeric and molecular materials.....	179
Figure 6.4.: Synthesis of five new BN heterocycles from a single reaction.	180

Figure 6.5.: Proposed inverted bulk-heterojunction solar cell architecture comprised of an active layer containing BF₂ formazanate complexes.183

List of Schemes

Scheme 1.1.: Synthesis of formazans based on active methylene species	21
Scheme 1.2.: Synthesis of formazans by phase-transfer conditions.....	21
Scheme 2.1.: Otten's synthesis of homoleptic zinc formazanate complex 2.12 and boron difluoride formazanate complex 2.13a	38
Scheme 2.2.: Synthesis of BF ₂ formazanate complexes 2.13a–l	39
Scheme 2.3.: Stepwise reduction of triarylformazanate BF ₂ complexes.....	47
Scheme 3.1.: Synthesis of BF ₂ formazanate complexes 3.10a–k	71
Scheme 3.2.: Electrochemical/chemical reactions for 3.10j and 3.10k	88
Scheme 4.1.: Synthesis of (a) mono- and (b) bis-CuAAC-functionalized BF ₂ complexes.	110
Scheme 4.2.: Synthesis of polymer 4.21 by copper-catalyzed alkyne-azide cycloaddition chemistry.....	120
Scheme 5.1.: Products formed from the reaction of formazan 5.7 with BF ₃ •OEt ₂ and NEt ₃ . The Gibbs free energies (ΔG°) were computed for the formation of each compound under conditions simulating those employed in the actual synthesis, and are expressed in kJ mol ⁻¹ of the corresponding formazan. The dashed arrow indicates interconversion in solution.	154
Scheme 5.2.: Products formed from the reaction of formazan 5.14 with BF ₃ •OEt ₂ and NEt ₃ . The Gibbs free energy (ΔG°) was computed for the formation of 5.15 under conditions simulating those employed, and are expressed in kJ mol ⁻¹ of formazan 5.14	155
Scheme 5.3.: Chemical reduction of 13 to 16⁻ with cobaltocene.....	162

List of Appendices

Appendix A1: Permission to Reuse Copyrighted Material.....	186
Appendix A2: Supporting Information for Chapter 2.....	194
Appendix A3: Supporting Information for Chapter 3.....	225
Appendix A4: Supporting Information for Chapter 4.....	255
Appendix A5: Supporting Information for Chapter 5.....	280

List of Abbreviations

°C	Degrees Celsius
μ	Experimental Absorption Coefficient
μA	Microamps
^{13}C	Carbon 13
^1H	Proton
a	Crystallography Lattice Constant – Unit Cell Length
a.u.	Arbitrary Units
AIE	Aggregation Induced Emission
Alq3	Tris-(8-hydroxyquinoline)aluminum
Ar	Aryl
ATR	Attenuated Total Reflectance
b	Crystallography Lattice Constant – Unit Cell Length
BODIPY	4,4-difluoro-4-bora-3a,4a-diaza-s-indacene
bpy	Bipyridine
br	Broad
c	Crystallography Lattice Constant – Unit Cell Length
CAD	Canadian Dollars
CCDC	Cambridge Crystallographic Data Centre
cm	Centimeter
cm^{-1}	Wavenumber
CoCp ₂	Cobaltocene
CuAAC	Copper-Assisted Azide-Alkyne Cycloaddition
CV	Cyclic Voltammogram
d	Doublet
\mathcal{D}	Dispersity
DAPI	4,6-Diamidino-2-phenylindole
DFT	Density Functional Theory
dipp	2,5-diisopropylphenyl
DMEM	Dulbecco's Modified Eagle Medium

DMF	Dimethyl Formamide
DMSO	Dimethyl Sulfoxide
DNA	Deoxyribonucleic Acid
DSC	Differential Scanning Calorimetry
e^-	Electron
ECL	Electrochemiluminescence
E_g	Band Gap
EI	Electron Impact
E_{ox1}	First Oxidation Potential
E_{pa}	Anodic Peak Potential
E_{pc}	Cathodic Peak Potential
EPR	Electron Paramagnetic Resonance
E_{red1}	First Reduction Potential
E_{red2}	Second Reduction Potential
E_{red3}	Third Reduction Potential
ESI	Electrospray Ionization
Et	Ethyl
EtOAc	Ethyl Acetate
eV	Electron Volt
FBS	Fetal Bovine Serum
Fc	Ferrocene
Fc^+	Ferrocenium
FF	Fill Factor
FT-IR	Fourier Transform Infrared
FW	Formula Weight
g	Gram
GOF	Goodness of Fit
GPC	Gel Permeation Chromatography
h	Hour
HOMO	Highest Occupied Molecular Orbital
Hz	Hertz

ⁱ Pr	Isopropyl
IR	Infrared
ITO	Indium Tin Oxide
K	Degrees Kelvin
kJ	Kilojoule
LCT	Liquid Chromatography Time of Flight
LED	Light Emitting Diode
LUMO	Lowest Unoccupied Molecular Orbital
m	Multiplet
M	Molar
Me	Methyl
Mes	Mesityl
mg	Milligram
MHz	Megahertz
min	Minutes
mL	Millilitre
mM	Millimolar
mmol	Millimole
M _n	Number Average Molecular Weight
mol	Mole
Mp	Melting Point
mT	Millitesla
MTT	3-(4,5-dimethylthiazol-2-yl)-2,5-diphenyltetrazolium bromide
mV	Millivolt
M _w	Weight Average Molecular Weight
<i>n</i> -Bu	<i>n</i> -Butyl
NIR	Near-Infrared
nm	Nanometer
NMR	Nuclear Magnetic Resonance
Np	Naphthyl
OLED	Organic Light-Emitting Diode

PBS	Phosphate Buffer Saline
PCBM	Phenyl-C61-Butyric Acid Methyl Ester
PCM	Polarizable Continuum Model
PET	Photoinduced Electron Transfer
Ph	Phenyl
PMDETA	<i>N,N,N',N'',N'''</i> -Pentamethyldiethylenetriamine
ppm	Parts Per Million
PS	Polystyrene
<i>p</i> -tol	<i>Para</i> -tolyl
py	Pyridine
q	Quartet
R ₁	Confidence Factor Observed Data
RAFT	Reversible Addition-Fragmentation Chain-Transfer
R _f	Retention Factor
RI	Refractive Index
s	Singlet
s	Second
S/N	Signal to Noise
SCRF	Self-Consistent Reaction Field
SEM	Scanning Electron Microscopy
SOMO	Singly Occupied Molecular Orbital
t	Triplet
T	Temperature
TEG	Tetraethylene Glycol
TEM	Transmission Electron Microscopy
TEMPO	(2,2,6,6-Tetramethylpiperidin-1-yl)oxyl
TGA	Thermal Gravimetric Analysis
THF	Tetrahydrofuran
TLC	Thin Layer Chromatography
TPrA	Tripropyl Amine
UV-vis	UV-visible

V	Volts
V	Volume
W	Watts
Z	Formula Unit
α	Crystallography Lattice Constant – Unit Cell Angle
β	Crystallography Lattice Constant – Unit Cell Angle
γ	Crystallography Lattice Constant – Unit Cell Angle
ΔE_e	Change in Electronic Energy
ΔG°	Change in Gibbs Free Energy
ΔH°	Change in Enthalpy
ε	Molar Absorptivity
λ	Wavelength
λ_{em}	Wavelength of Maximum Emission
λ_{ex}	Wavelength of Excitation
λ_{max}	Wavelength of Maximum Absorption
ν_{ST}	Stokes Shift
ρ	Density
Φ_F	Fluorescence Quantum Yield
ωR_2	Confidence Factor All Data

Chapter 1

1 Introduction - BF₂ Complexes of N-donor Ligands

For many centuries, scientists and non-scientists alike have been fascinated by naturally occurring luminophores. Many examples of both land and sea animals display fluorescent or phosphorescent markings including birds (Figure 1.1a),^[1-2] spiders and bugs,^[3-5] frogs (Figure 1.1c),^[6] and a multitude of sea creatures, including coral,^[7] turtles (Figure 1.1d),^[8] shrimp,^[9] fish (Figure 1.1e)^[10] and jellyfish (Figure 1.1b).^[11-12]

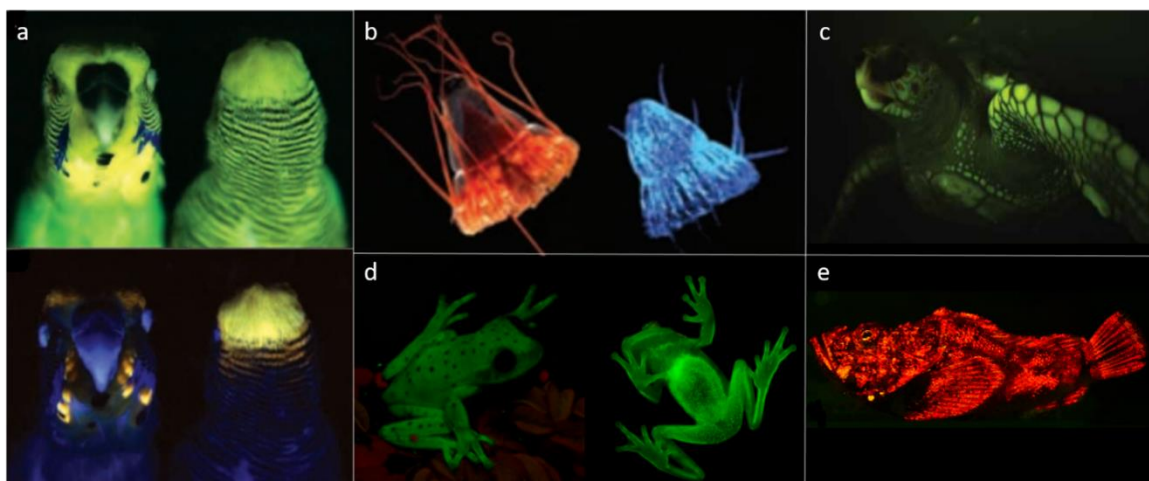
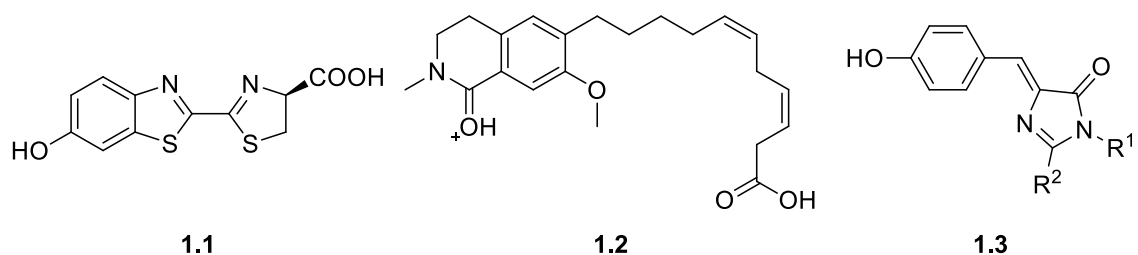


Figure 1.1. a) Head of wild-type budgerigars (*Melopsittacus undulatus*) under white light (top) and UV illumination (bottom). b) Jellyfish *Periphylla periphylla* under white light (left) and UV illumination (right). c) Fluorescence of the head and anterior region of the loggerhead sea turtle *Caretta caretta*. d) Adult male tree frog *Hypsiboas punctatus* fluorescence. e) Luminescence from the false stonefish *Scorpaenopsis diabolus*. Images reproduced with permission from Refs. [1], [12], [8], [6], [10], respectively.

There are many different purposes for this luminescence in animals, including photoprotective reasons,^[7] signalling,^[1-3,9] as antioxidants,^[13] for camouflage^[14] or defense,^[15] and for attracting prey.^[16] The identity of the emissive compound varies from species to species, though many animals utilize the same or similar compounds. One of the most common examples is luciferin. Luciferase, an enzyme, oxidizes luciferin and generates an excited state of the oxyluciferin molecule. This emits light as it relaxes to the ground state. There are many different forms of luciferases and luciferins (*e.g.* **1.1**, found in fireflies), though all act by the same general mechanism.^[17] The Faivovich group

identified a new fluorophore **1.2** produced in the glands of a tree frog (Figure 1.1c), that has not been attributed to the luminescence of any other living species to date. The pigment, which fluoresces blue, gives the tree-frogs their green fluorescence when filtered through the skin.^[6] Perhaps the most famous contributor to bioluminescence is the green fluorescent protein. The chromophore present (**1.3**, $R^{1,2} = \text{amino acids}$), is not fluorescent alone, but when contained in the cylindrical tertiary structure of the remainder of the protein, is fluorescent.^[18-20] This protein is most famously expressed in jellyfish, but has been used for a multitude of other applications, and ultimately resulted in the Nobel Prize in Chemistry in 2008.^[11]

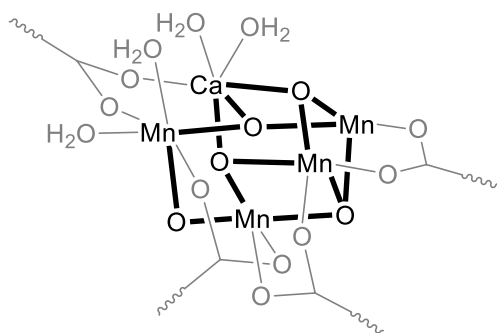


The scientific community is similarly interested in naturally occurring redox processes. These processes are central to life as we know it. Perhaps the most well-known biological redox process is photosynthesis. In photosynthesis, a photon sets in motion a series of electron transfer events which ultimately result in the conversion of carbon dioxide and water to glucose and oxygen. One of the key parts of this reaction is the $\text{Mn}_4\text{O}_5\text{Ca}$ cluster (**1.4**) which is part of the photosystem II enzyme. Here, water is oxidized to oxygen, releasing two electrons and two protons which can be used to form glucose.^[21]

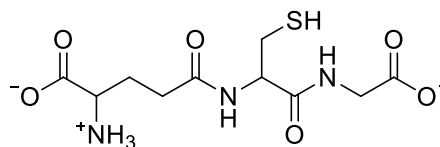
Glutathione (**1.5**) is observed in high concentrations in animal cells, and it has important function in many different cellular processes. One of the most important of these functions is as an antioxidant. Reactive oxygen species will preferentially oxidize glutathione to prevent oxidation of cellular components that cause adverse effects.^[22] Glutathione also is responsible for keeping vitamins C and E in their active, reduced forms.^[23]

Another process which is vital to life is DNA replication. The Barton and Chazin groups recently discovered that the redox chemistry of a small Fe_4S_4 cluster (**1.6**)^[24] present in DNA primase and DNA polymerase, two enzymes that are essential to the DNA replication process, plays an important role. They found that when the cluster is in its oxidized (3+)

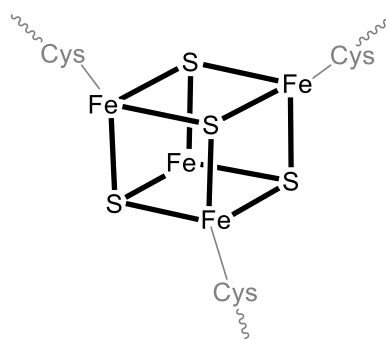
state, DNA is bound tightly to the enzyme, and replication can occur. However, when the cluster is in its reduced (2+) state, DNA is more loosely bound, and replication does not occur.^[25]



1.4



1.5



1.6

Chemists have long been interested in replicating the work of nature, and producing both luminescent and redox-active materials. There are many structural motifs often employed in the synthesis of materials with one of these properties, however less that offer both traits. One such recurring theme is that of boron difluoride (BF_2) chelated by *N*-donor ligands.

1.1 Boron Difluoride Complexes of *N*-donor Ligands

Much of the research involving BF_2 complexes of *N*-donor ligands has focused on dipyrromethenes as the *N*-donor ligand, which, when complexed with BF_2 , are known as boron-dipyrromethenes (BODIPYs, *e.g.* **1.7**).^[26] The first example of a BODIPY was synthesized in 1968,^[27] and similar complexes have since been the focus of hundreds of papers.^[28-29] The reasons for this research intensity are the desirable properties that most

BODIPYs exhibit, including high molar absorptivities, narrow absorption and emission bands and typically high fluorescence quantum yields. BODIPYs also are electrochemically active, with interesting redox properties in both the ground and excited states.^[26]

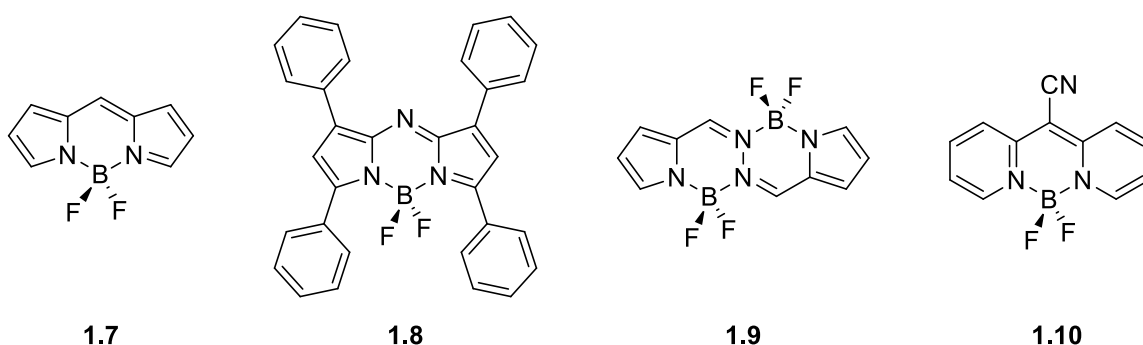
Though many of the properties of BODIPYs are desirable, there are a few drawbacks associated with them, including their often difficult and low-yielding syntheses. Most BODIPYs are not water soluble and emit at wavelengths below 600 nm, which limits their application, especially in biological settings. In these applications, the primary medium is water and red emission is desirable, as it penetrates further through tissue.^[26] Additionally, the photostability of BODIPYs has been shown to be quite low, though this has been improved by replacing the fluorine substituents on the boron with substituted alkynes.^[30] Finally, due to the planar structure of BODIPYs, molecules tend to pack tightly together in the solid state leading to quenched fluorescence, which limits the use of BODIPYs in optoelectronics.^[26]

Due to some of these drawbacks, other fluorophores based on BF_2 chelates of *N*-donor ligands which address the abovementioned issues have been sought. The first class of these molecules take structural inspiration from BODIPYs, and have conjugated planar cores consisting of multiple fused heterocycles. Aza-BODIPYs (*e.g.* **1.8**) are structurally very similar, with only the replacement of a nitrogen for the carbon in the meso position.^[31] The synthetic routes to these molecules are also different, which allows for most aza-BODIPYs to be decorated with aryl substituents. As a result of these modifications, aza-BODIPYs tend to emit at wavelengths of much lower energy, while maintaining high molar absorptivities and quantum yields, though they are still produced in low synthetic yields from time-consuming syntheses.^[31]

A relatively new and exciting fluorophore of this class is the bis(difluoroboron)-1,2-bis((1*H*-pyrrol-2-yl)methylene)hydrazine (BOPHY, *e.g.* **1.9**), which were first reported in 2014.^[32] These complexes have a fused ring structure, reminiscent of a shortened BODIPY dimer. They have high molar absorptivities, as well as outstanding quantum yields. The Stokes shifts are typically larger than BODIPYs, which limits reabsorption of emitted photons, especially in concentrated solutions. BOPHYs are still relatively

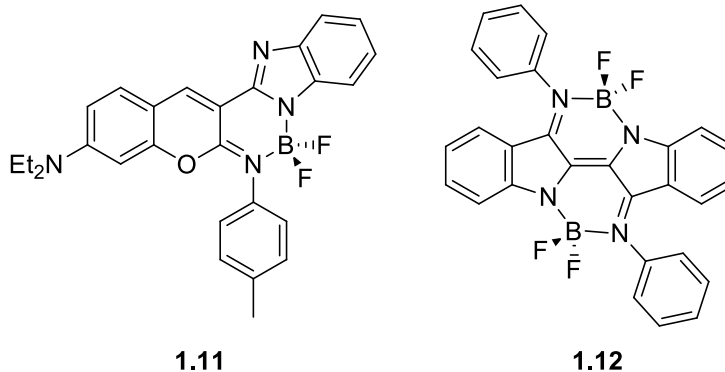
understudied,^[33-34] though most reported complexes exhibit many of the same drawbacks as BODIPYs, including low yielding syntheses and emission at *ca.* 500 nm.

BF₂ complexes of pyridomethene ligands (*e.g.* **1.10**) are also structurally similar to BODIPYs, but differ by the two aromatic rings flanking the central six-membered ring – two six membered rings, as opposed to the five membered rings of BODIPYs. Though the molar absorptivities of these complexes are on-par with many other fluorophores in this class, the lower quantum yields, and low synthetic yields, limit the widespread use of these dyes.^[35]

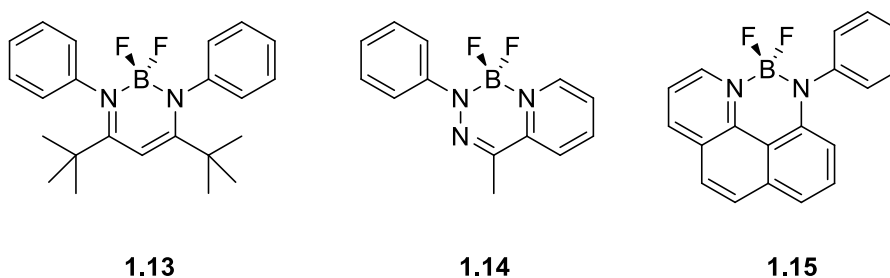


A second strategy for the design of functional BF₂ complexes of chelating *N*-donor ligands is to modify existing fluorophores to have a bidentate *N*-donating ligand available for chelation of boron. This method has been used with two different commonly known fluorophores – coumarin and indigo. Coumarin was first isolated from the Tonka bean in the 1820s,^[36] and has many different uses, some of which take advantage of its fluorescence (*e.g.* laser dyes^[37-38] and LED's^[39]), and many which do not (*e.g.* use in perfumes and cosmetics,^[40] as anti-HIV agents,^[41] and as a commercially available anti-coagulant, warfarin^[42-43]). Indigo is a blue dye that has been used in Egypt since *ca.* 2000 B.C., and is used mainly today for the production of ~1 billion pairs of blue jeans annually,^[44] though it has also been used for a variety of organic electronic applications.^[45-46] Both dyes were modified to include a chelating, bidentate nitrogen pocket, and complexed with BF₂.^[47-49] In both cases, the whole synthesis was accomplished in >70% overall yield, which is a significant improvement over BODIPYs and related systems. The emission of the BF₂ complexes of the coumarin-based ligand (BORICO's, *e.g.* **1.11**) is quite strong, with

quantum yields often >80%. However, the emission still falls outside of the ideal red region.^[49] On the other hand, BF₂ complexes of ‘Nindigo’ ligands (*e.g.* **1.12**), emit at *ca.* 800 nm, though the emission is described only as weak.^[48]



The final strategy commonly used in the design of fluorescent BF₂ based dyes is the use of commonly studied, easily synthesized *N*-donor ligands, with non-rigid *N*-aryl substituents. Three common families of ligands that have been used for this purpose are β-diketiminates,^[50] anilido imines^[51] and hydrazones.^[52] β-diketiminates are generally straightforward to synthesize, and so BF₂ complexes of these ligands (*e.g.* **1.13**) are produced in high yields. The resulting complexes tend to be highly absorbing, with large Stokes shifts, but generally low quantum yields.^[53] BF₂ complexes of hydrazones (BODIHYs, *e.g.* **1.14**) also have large Stokes shifts, and generally low quantum yields in solution, however they have been shown to have increased quantum yields in the solid state.^[54] Finally, anilido-imines and the related anilido pyridines have been complexed to BF₂ (*e.g.* **1.15**), in high yields. These complexes typically have large Stokes shifts, moderate quantum yields, and emission approaching red light. The one drawback to these systems are their low molar absorptivities (<10,000 M⁻¹ cm⁻¹).^[55-57]

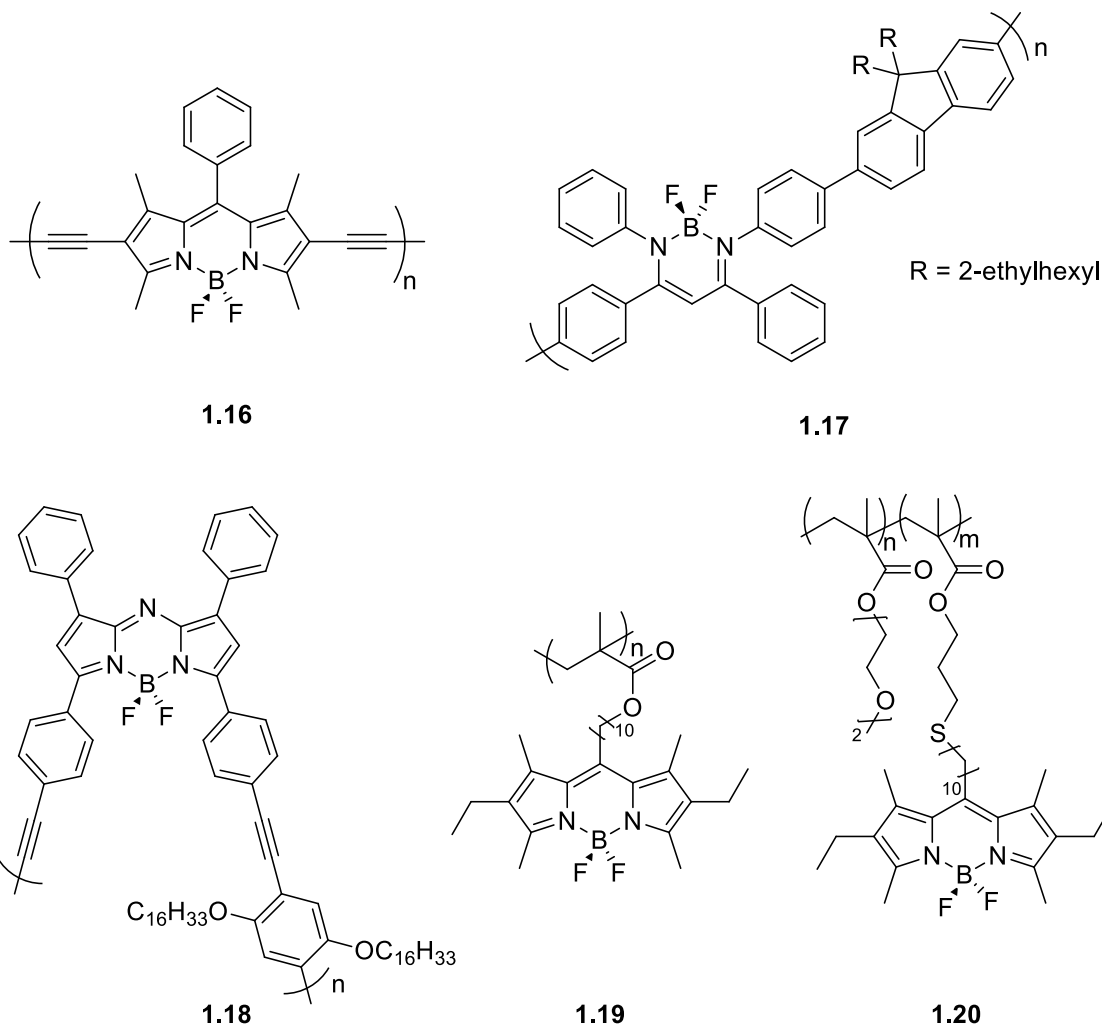


1.2 Polymers

Many classes of BF_2 complexes of *N*-donor ligands have been incorporated into polymer frameworks, specifically BODIPYs, aza-BODIPYs and BF_2 complexes of β -diketiminates. All three of these types of complexes have been incorporated into the main-chain of π -conjugated polymers. The first example was shown by the Li group in 2008, where iodo- and alkyne- substituted BODIPYs were subjected to Sonogashira coupling to produce polymer **1.16**.^[58] The absorption and emission maxima of this polymer were red-shifted significantly when compared to the less-conjugated monomer (**1.16**: $\lambda_{\text{max}} = 640$ nm, monomer: $\lambda_{\text{max}} = 535$ nm), and also had a good quantum yield of 24%.^[58] A similar method was used to prepare co-polymers of BF_2 β -diketimate complexes. The Chujo group used Suzuki coupling to combine iodo-substituted BF_2 complexes and boronic acid-substituted fluorene to make conjugated polymer **1.17**.^[59] These polymers were essentially non-emissive in solution, though all derivatives exhibited both aggregation-induced emission and crystallization-induced emission enhancement. The authors also demonstrated the pH-responsiveness of these materials. The colour of a thin-film of the polymer could be reversibly switched by introduction of acidic or basic vapors.^[59] Aza-BODIPY conjugated copolymer **1.18** was also synthesized by Sonogashira coupling.^[60] This polymer emitted in a narrow emission band at 753 nm, in the near-IR region, and also had a quantum yield of 24%.^[60]

To date, side-chain polymers of BF_2 complexes of *N*-donor ligands have most commonly been prepared with BODIPYs. The Chujo group polymerized a methyl-methacrylate monomer appended with a BODIPY moiety by RAFT polymerization to produce side-chain BODIPY polymer **1.19**.^[61] Nanoparticles of these polymers were observed, due to the π -stacking of the BODIPY dyes, which quenched the luminescence. Nanoparticles were also synthesized from block copolymers made with the same monomer as **1.20** and polystyrene had a quantum yield of fluorescence over 70%, due to the styrene breaking up the π -stacking of the BODIPYs.^[61] Another method for the synthesis of block-copolymers containing BODIPY units in the side-chain was employed by the París group, who first synthesized a block copolymer where one of the blocks contained an alkene moiety. After polymerization, thiol-ene click chemistry could be used to append the BODIPY units to

the polymer backbone.^[62] The authors found that the optical properties of the resulting polymer were very similar to that of the small-molecule BODIPY starting material, and was also unchanged with varying degrees of BODIPY functionalization of the polymer backbone.^[62]



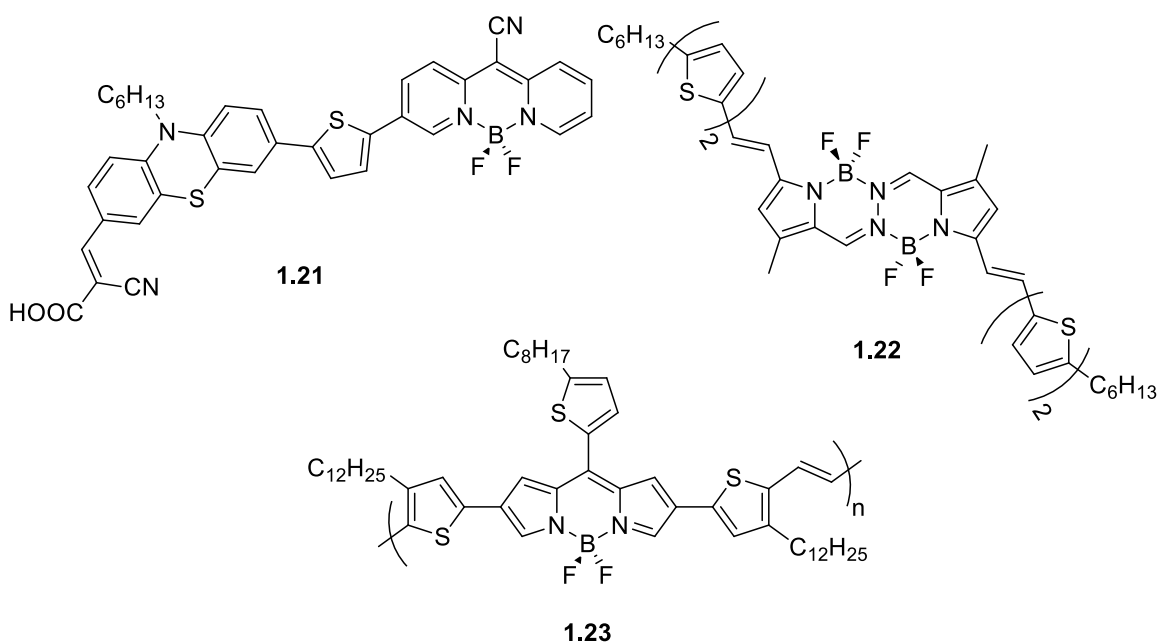
Polymers with BODIPYs, aza-BODIPYs and BF_2 complexes of β -diketiminates have found many different applications, in a variety of fields, including in a variety of biomedical imaging applications,^[63-68] organic electronics,^[69-74] sensing applications,^[59,75-81] re-writable data storage,^[82] photocatalysis,^[83-84] as laser dyes,^[85-86] electrochemiluminescence devices,^[87] and plastic scintillators.^[88] Some of these applications will be discussed in more detail below.

1.3 Applications

The above mentioned families of fluorescent dyes based on BF_2 complexes of chelating N -donor ligands have different strengths, as well as drawbacks, which renders some examples better suited for certain applications than others. Because of the many classes of these complexes, there are many different fields which these molecular and polymeric materials find applications, including photovoltaics, organic electronics, sensing, biomedical applications, electrochemiluminescence, and materials science.

1.3.1 Photovoltaics

The typically high molar absorptivities, broad absorption range, and redox properties of BF_2 complexes of N -donor ligands has led to their study in photovoltaics.^[70,89-93] Phenothiazine modified pyridomethene BF_2 complex **1.21**^[94] was incorporated into a dye-sensitized solar cell and bulk-heterojunction solar cells were fabricated using thiophene-BOPHY complex **1.22**^[95] and thiophene-BODIPY copolymer **1.23**^[72].



All three complexes were chosen because they absorb strongly through much of the visible region, and some into the near-IR. The electronic conjugation of the parent BF_2 complexes was extended by appending π -conjugated groups such as thiophene and phenothiazine in

order to maximize absorption. For example, thin-films of BODIPY polymer **1.23** have a wavelength of maximum absorption (λ_{max}) of 848 nm (see Table 1). The extended conjugation of these complexes also serves to minimize the band gaps of the complexes, with band gaps ranging from 2.41 eV in **1.21** to 1.15 eV in **1.23**. The photovoltaic devices built containing **1.21–1.23** were successful in solar energy conversion. All three devices had comparable fill factors (FF), at around 60%. The efficiency of BODIPY-polymer **1.23** based bulk heterojunction solar cell reached a maximum of 1.1%, despite having the largest absorption window.^[72] BOPHY **1.22** based bulk heterojunction solar cell has provided an excellent starting point for BOPHY-based photovoltaics. This first example of an organic electronic device using BOPHY's had a good efficiency, at 4.3%.^[95] Finally, the dye sensitized solar cell containing pyridomethene BF₂ complex **1.21** had the highest efficiency of 6.6%. This was in part due to the phenothiazine substituent, but the combination of the two dyes results in devices with higher efficiencies and better photostabilities.^[94]

Table 1.1. Properties of photovoltaic complexes **1.21–1.23**.

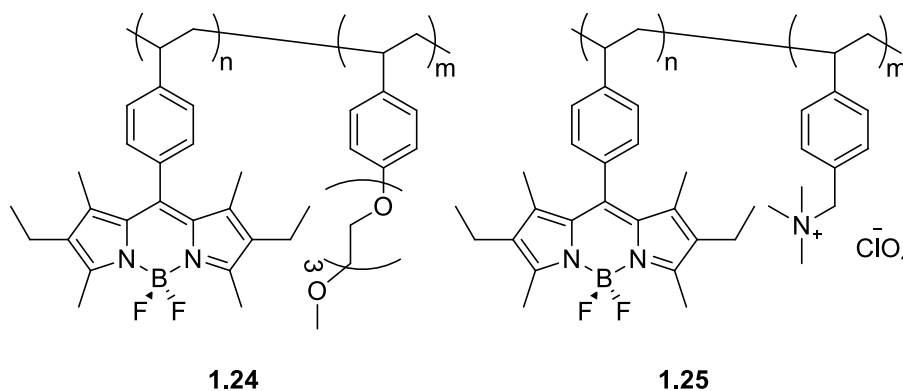
Compound	Type of Solar Cell	$\lambda_{\text{max, film}}$ (nm)	Band gap (eV)	FF (%)	Power Conversion Efficiency (%)
1.21	Dye-Sensitized	478	2.41	62	6.6
1.22	Bulk Heterojunction	656	1.62	57	4.3
1.23	Bulk Heterojunction	848	1.15	56	1.1

1.3.2 Organic Thin-Film Transistors, Light Emitting Diodes, and Batteries

Similar to their use in photovoltaics, the inherent properties of BF₂ complexes of *N*-donor ligands make them well suited for many other types of organic electronics. Both aza-BODIPYs and BODIPYs exhibit strong π - π stacking interactions, which, combined with their excellent ability to accept electrons makes them ideal candidates for electron-only devices.^[96] The small band-gap, flexibility and solvent processability of conjugated BODIPY polymers are properties which make organic thin-film transistors of these materials as effective and attractive as they are.^[69,74] The typically intense emission of BODIPY dyes also makes them useful materials for organic light emitting diodes. OLED's

were fabricated either with thin films of BODIPYs,^[97] films of poly(methyl methacrylate) doped with BODIPYs,^[98] or BODIPY coatings on blue inorganic LED's to produce white-light emitting devices.^[99]

The Schubert group has studied redox flow batteries made up of BODIPY polymers.^[73] Here, it is the reversible and tunable oxidation and reduction properties of BODIPYs which make polymers **1.24** and **1.25** excellent materials for this application. The BODIPY core was completely substituted to prevent any side reactivity, and co-monomers were selected to enhance solubility. Polymer **1.24** was synthesized with an M_n of 17 000 g mol^{-1} , and $D = 2.3$. Polymer **1.25** had an M_n of 4000 g mol^{-1} and $D = 1.5$. Two different batteries were fabricated – one with **1.24** as the anolyte, and a TEMPO based polymer as the catholyte, and the second with **1.24** as the anolyte and **1.25** as the catholyte (Figure 1.2). The first battery had a high average discharge voltage of 1.82 V, as well as good reversibility, with 99% coulombic efficiency after 100 cycles. The second battery, made up of both **1.24** and **1.25** had a slightly worse performance, with an average discharge voltage of 1.28 V, and 89% coulombic efficiency retained after 10 cycles.^[73]



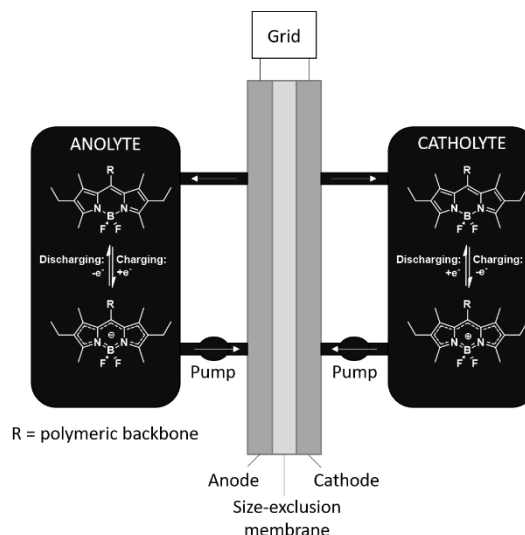


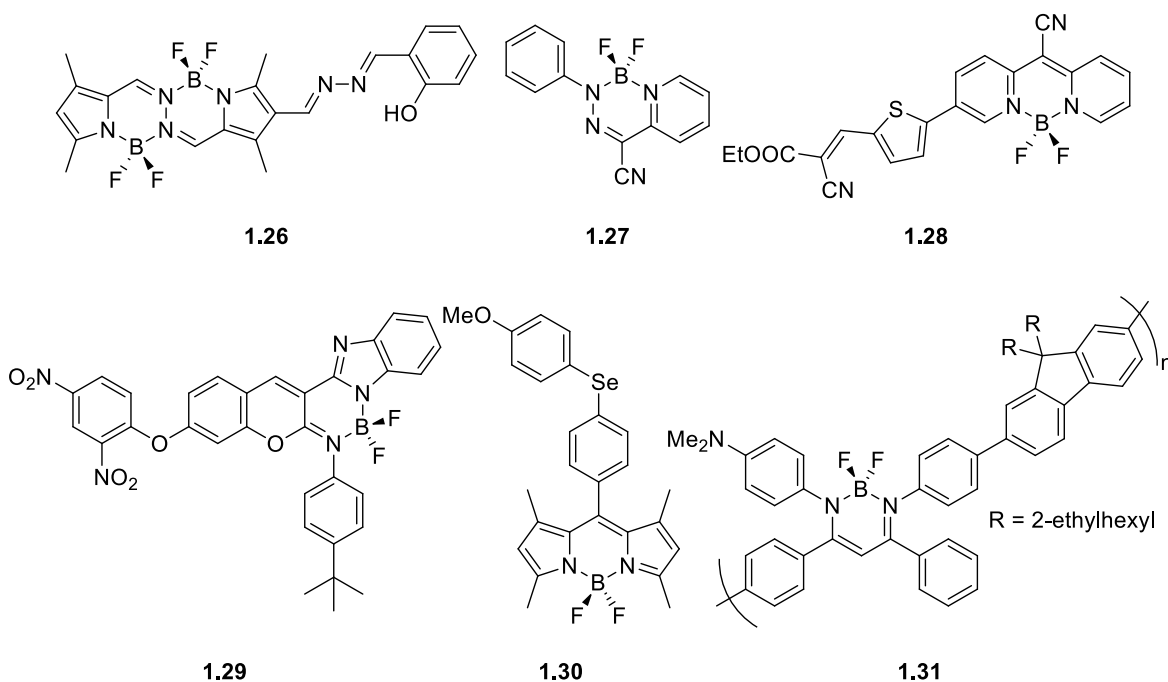
Figure 1.2. Polymeric redox-flow battery schematic. Anode and cathode are separated by a size-exclusion membrane. Anolyte and catholyte are polymers **1.24** and **1.25**, respectively.^[73]

1.3.3 Sensing

Due to their often intense colours and emission properties, as well as sites for structural modification, BF₂ complexes of *N*-donor ligands are tailor-made for sensing applications. A wide variety of these BF₂ complexes have been employed as sensors for many different things.^[54,100-103] For example, BOPHY **1.26** is modified with a functionality which quenches its fluorescence. In the presence of copper (II) ions, which bind to the pocket appended to the BOPHY, fluorescence is regenerated. This sensor was quite selective for copper, and able to detect Cu²⁺ ions at concentrations as low as 50 nM.^[104] BODIHY dye **1.27** is highly sensitive to changes in viscosity – as the viscosity of the solvent increases, so does the fluorescence of the BODIHY dye, which is an aggregation-induced emission (AIE) emitter.^[105] Pyridomethene BF₂ complex **1.28** reacts in the presence of hydrazine, and as a result the colour of the emission is drastically altered. Upon reaction, the emission at *ca.* 650 nm is quenched, and a new emission band at *ca.* 500 nm appears. This reaction is selective for hydrazine, the same response is not observed for a variety of different tested ions (*e.g.* F⁻, NO₃⁻, Ca²⁺ and Na⁺).^[94] BORICO dye **1.29** will react with thiols, including the biologically relevant L-cysteine and thiophosphate anion, to produce a complex with

increased fluorescence intensity. The detection limit of this system for L-cysteine was determined to be $1.76 \mu\text{M}$.^[106]

The presence of the selenium ion in complex **1.30** quenches the fluorescence of the BODIPY moiety. However, upon exposure to hypochlorous acid (HClO), the selenium is oxidized, and the complex becomes strongly fluorescent. Compound **1.30** was used to image HClO in cells, which is important, as HClO is a reactive oxygen species.^[107] Finally, the Chujo group incorporated BF_2 complex of β -diketiminato into polymer **1.31** with 9,9-(2-ethylhexyl)fluorene. This polymer, which is AIE active, is responsive to changes in pH. A thin-film of this polymer emits bright yellow light upon exposure to a vapour of trifluoroacetic acid, due to the protonation of the dimethylamino group. The introduction of a vapour of triethylamine can reverse this protonation, and return the emission of the polymer film to a dark-red colour.^[59]



1.3.4 Biomedical Applications

In the biomedical field, two major applications for fluorophores arise – first is visualization – whether this is detection of a disease or enabling the visualization of a process or part of

an organism. The second is treatment, and in terms of fluorophores, most applications revolve around photodynamic therapy.

BF₂ complexes of *N*-donor ligands have been used for many different imaging applications, including imaging biological membranes with BF₂ complexes of anilido pyridines,^[55] using BODIPYs to image DNA,^[108-109] and the detection of reactive oxygen species,^[110] and using BODIPY polymeric nanoparticles to specifically label breast cancer cells.^[66,68]

BODIPY dyes are ideally suited for fluorescence cell imaging because of their high quantum yields and small size, which does not disrupt the function of the cells.^[111] The dyes can be tailored to localize themselves in a particular region of the cell, for example, the cytoplasm,^[112] to target specific types of cells, for example, cancerous cells,^[113] or to act as a sensor in cells, for example, as a sensor for mercury.^[114]

The ability to tune the colour of the emission of BODIPY dyes is also quite useful. The Prasad group was able to show that by reaction of green-emissive dye **1.32** with 4-dimethylamino benzaldehyde, they were able to produce dyes **1.33** and **1.34**, which emitted in the yellow and red regions respectively (see Figure 1.3).^[115]

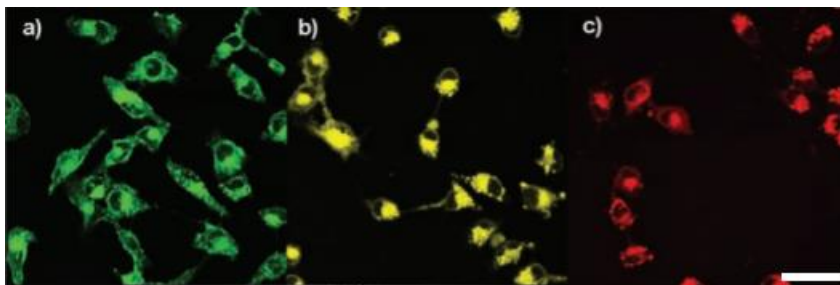
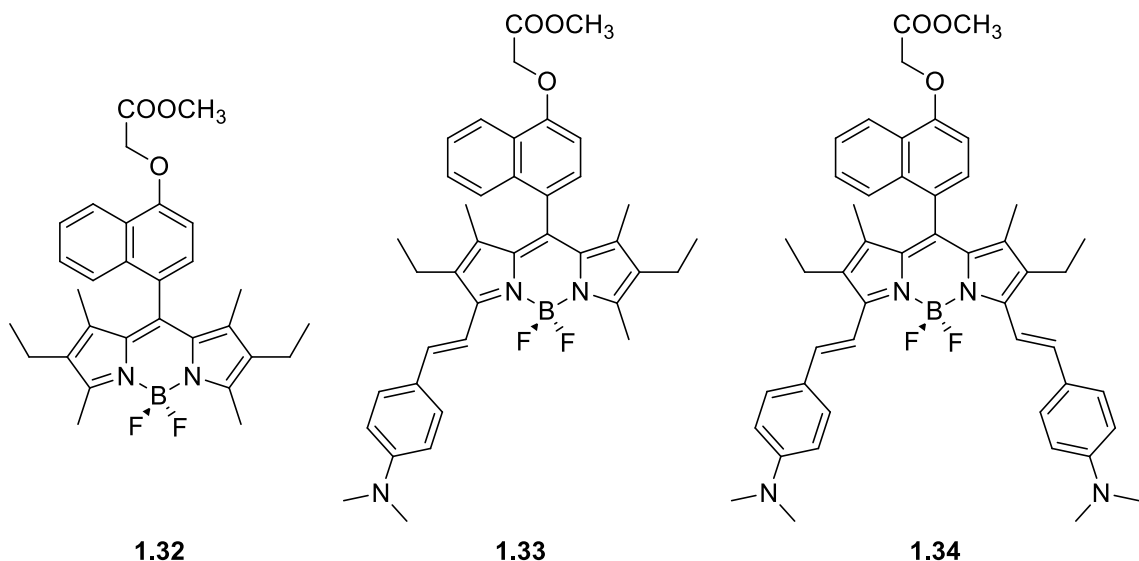
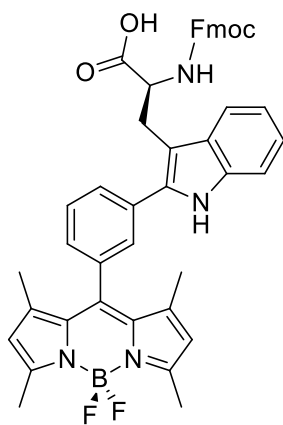


Figure 1.3 Confocal microscopic images of HeLa cells treated with a) **1.32**, b) **1.33** and c) **1.34**. Confocal microscopy images were obtained by using laser excitation at $\lambda =$ a) 514 nm, b) 543 nm and c) 643 nm. Scale bar is 47.62 μm long. Image reproduced with permission from Ref. [115].



Because of their usefulness as cell imaging agents, many BODIPYs are commercially available for this purpose. They are available for purchase in a wide range of colours, and for a variety of functions, but can be quite expensive (on average, 420 CAD per 5 mg at Thermo Fisher Scientific).^[116]

The Lavilla and Vendrell groups developed an imaging agent based on a BODIPY-amino acid conjugate **1.35**. The approach taken to modify the amino-acid sequence is unique, as it does not entail a post-synthetic conjugation reaction, which requires the removal of unreacted fluorophores, and does not rely on reaction of polar groups present in the peptide (*e.g.* alcohols, carboxylic acids) which often disrupt the hydrogen bonding of the peptide, changing the biological properties. This amino acid was incorporated into a 6-amino acid peptide anti-fungal agent.^[117] This BODIPY-containing anti-fungal agent was found to

**1.35**

have similar anti-fungal activity as the parent peptide, and was effective at imaging several different fungal pathogens, including *Aspergillus fumigatus*, which causes Invasive Pulmonary Aspergillosis (IPA), a fungal pneumonia with mortality rates up to 40%.^[117] Interestingly, the BODIPY based agent was also found to have significantly longer stability than commercially available membrane dye Syto82, a red dye. Incubation of *A. fumigatus* with both the BODIPY-peptide and Syto82 led to primarily red confocal microscopy images initially, due to the Syto82, though

after 3 min, degradation of Syto82 led to an image with almost entirely the green fluorescence of the BODIPY (Figure 1.4). The authors found that the BODIPY-peptide retained 95% of its fluorescence intensity after 24 h of incubation.^[117] Because of its long fluorescence lifetime, and minimally-disruptive structure, BODIPY-amino acid **1.35** is likely to find application in many imaging probes.

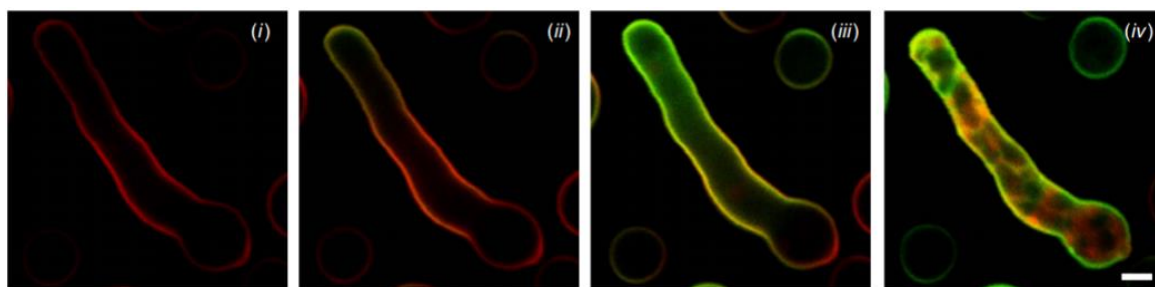
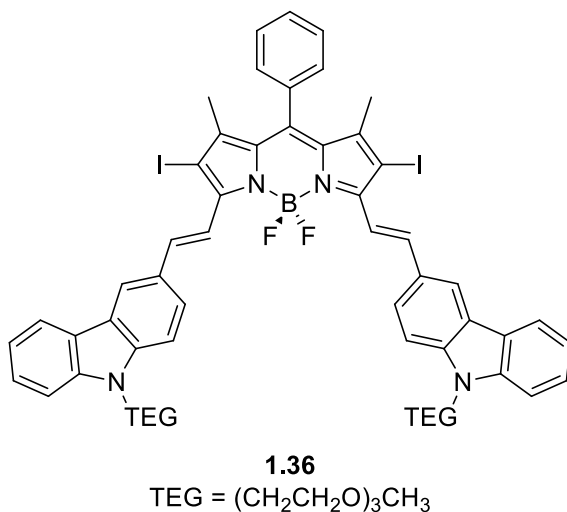


Figure 1.4. *A. fumigatus* incubated with cell membrane counterstain Syto82 (red) and BODIPY-peptide (green) for (i) 0 min, (ii) 1 min, (iii) 3 min, and (iv) 10 min. Scale bar = 2.5 μm . Image reproduced with permission from Ref. [117].

The second common biologically-relevant application of BF₂ based fluorophores is photodynamic therapy, which involves the use of a photosensitizer to destroy tumor cells. Upon irradiation with light, the photosensitizer will act as a catalyst, to convert oxygen into a variety of reactive oxygen species. These species have been shown to destroy tumors in many ways, including necrosis or apoptosis and starvation through the shutdown of blood vessels.^[118] Due to their typically near-IR absorption and emission, aza-BODIPYs have proven quite useful for this application.^[119-121] BODIPYs have also been studied extensively for their use in photodynamic therapy as well.^[122]

The Han group synthesized a BODIPY based photosensitizer **1.36**, which emits in the near-IR region, and has a high singlet-oxygen yield (67%).^[123] These molecules were incorporated into cancer-targeting micelles, based on poly(lactic acid)-*b*-poly(ethylene glycol) copolymers, with appended folic acid groups. As a control, similar block copolymers were synthesized without the appended cancer-targeting folic acid groups. Both of these particles were injected into mice containing breast cancer cells, and the near-IR fluorescence of the BODIPY dye was measured (Figure 1.5a). It was found that the targeting nanoparticles were much more localized in the area of the tumor than the non-targeting nanoparticles, and maximum imaging intensity occurred *ca.* 24 h after injection.



The photodynamic therapy potential of the dyes were then tested, with mice being divided into 5 groups. The first group was a control, group 2 was irradiated with 670-800 nm light, group 3 were only injected with the targeted BODIPY micelles, group 4 were injected with the non-targeted BODIPY micelles and irradiated with light, and group 5 were injected with the targeted BODIPY micelles and irradiated with light

(Figure 1.5b). It was found that significant tumor reduction over the control group was only observed after injection with the targeted BODIPY micelles, and irradiation with 670-800 nm light.^[123]

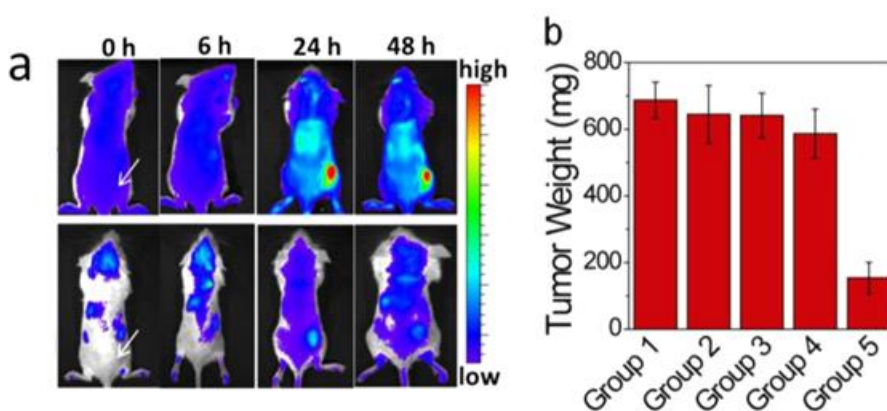


Figure 1.5. (a) In vivo NIR fluorescence images of 4T1 tumor-bearing mice after being injected with 150 μ L of a 50 μ g/mL solution of targeted-BODIPY nanoparticles (top row), and non-targeting BODIPY nanoparticles (bottom row). The arrow indicates the tumor site. (b) Average weights of tumors 10 days after treatment. Treatment varied based on group number. Group 1 - control group; 2 - light irradiation only; 3 - targeted-BODIPY nanoparticle injection only; 4 - non-targeted BODIPY nanoparticle injection and irradiation; and 5 - targeted BODIPY nanoparticle injection and irradiation. Image reproduced with permission from Ref. [123].

1.3.5 ECL Devices

Electrochemiluminescence (ECL) is the generation of luminescence through an electrochemically generated excited state. Redox-active fluorescent dyes such as BODIPYs and aza-BODIPYs are often highly ECL active.^[124] Bard *et al.* have extensively studied a wide range of aza-BODIPY and BODIPY monomers, dimers and polymers (including **1.37–1.40**) for their ECL properties (Table 2).^[87,125] All four complexes are emissive at wavelengths greater than 500 nm, with BODIPY monomer **1.37** emitting at the lowest wavelength of 513 nm, and aza-BODIPY **1.39** emitting at the highest wavelength of 682 nm. BODIPY polymer **1.38** has a fluorescence quantum yield of 35%. In most cases, the electrochemically generated luminescence occurs at a similar wavelength to that of the fluorescence, except for dimer **1.40**, where the ECL emission is red shifted by almost 200 nm, with respect to the fluorescence (Table 2), indicating the ECL emission occurs from a different excited state to that of the fluorescence.^[125] In all cases, the efficiency of ECL was relatively weak (<1%), compared to that of the $[\text{Ru}(\text{bpy})_3]^{2+}$ standard, for which $\Phi_{\text{ECL}} = 5\%$.^[87,125]

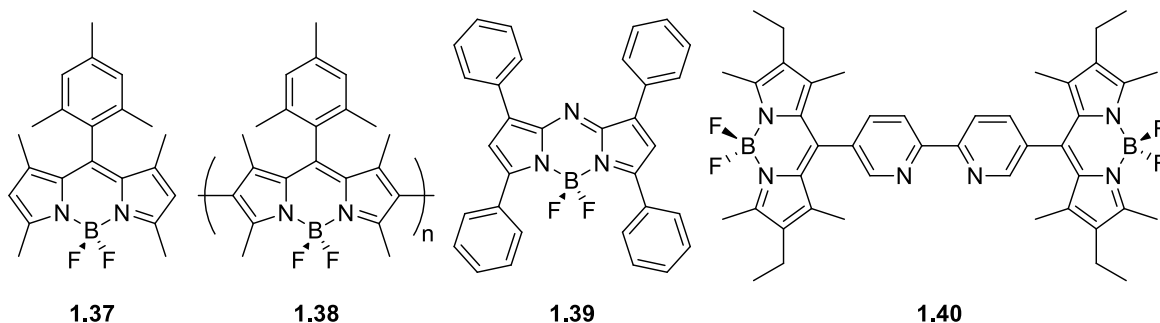


Table 1.2. Optical and electrochemiluminescence properties of complexes **1.37–1.40**.^[87,125]

	λ_{abs} (nm)	λ_{em} (nm)	Φ_{F} (%)	λ_{max} (ECL)	Φ_{ECL} (%)
1.37	501	513	97	538	0.7
1.38	590	614	35	620	<0.1
1.39	647	682	30	695	<0.1
1.40	528	545	39	740	0.6

1.3.6 Self-Assembled Micelles

Self-assembly of polymers appended with fluorescent dyes expands the scope of applications of the resulting micelles. For example, the Ambade group synthesized a block copolymer of poly(ethylene glycol) and polystyrene, with a BODIPY moiety at the junction of the two polymers, with the polystyrene attached directly to the BODIPY *via* a B-O bond. The resulting block copolymer self-assembled into micelles. The B-O bond could be cleaved photolytically, resulting in two homopolymers and the degradation of the micelle, potentially releasing a payload.^[126] Similarly, the Zhu group appended aza-BODIPYs into the poly(methacrylic acid) block of a block copolymer consisting of poly(methacrylic acid) and poly(methyl ether methacrylate-graft-poly(ethylene glycol)), which self-assembled into pH responsive micelles. The aza-BODIPY, which emits in the near-IR allowed the authors to image the localization and integrity of their micelles.^[127]

The Manners group appended red, green and blue fluorescent BODIPYs onto poly(ferrocenyldimethylsilane)-*b*-poly(dimethylsiloxane) copolymers, which self-assemble into cylindrical micelles.^[128] By carefully tuning the ratio of the three coloured block copolymers, they were able to design micelles which emitted in a variety of different colours (both in solid-state and solution), including white light (see Figure 1.6). Additionally, the authors showed they could make multiblock micelles, with each block a different colour, with the colours only visible under a laser scanning confocal microscope, in contrast to the TEM image, where the micelles appear uniform.^[128]

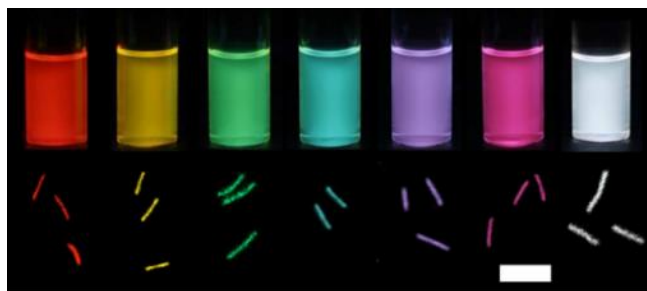
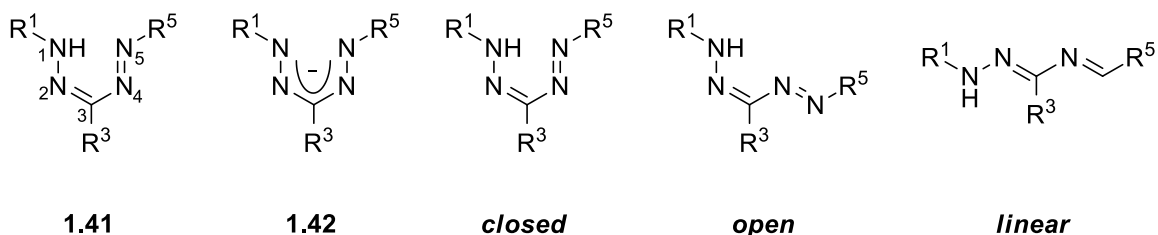


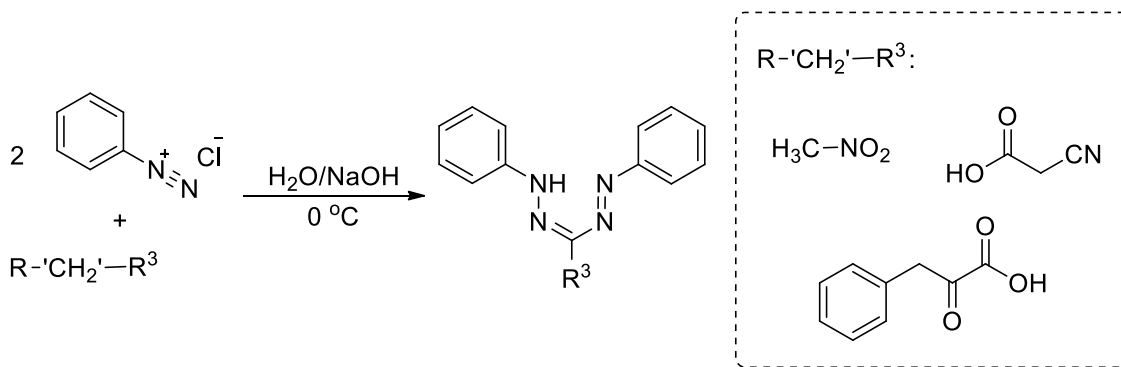
Figure 1.6. Selection of colours of micelles which can be produced mixing red, green and blue fluorescent block copolymers. Raw images of solutions of these fluorescent micelles under UV irradiation, and corresponding laser scanning confocal microscopy (LCSM) images. Scale bar = 3 μm . Image reproduced with permission from Ref. [128].

1.4 Formazans

One class of chelating *N*-donor ligands which had not been studied as ligands for BF₂ complexes were the formazanate ligands, which are based on formazans. Formazans were first reported in the late 1800's, and have been studied ever since for a variety of different applications. Formazans (**1.41**) possess a R¹-NH-N=C(R³)-N=N-R⁵ backbone, typically with aromatic substituents on N¹ and N⁵, and a variety of different substituents on C³, including aromatics, alkyls, heterocycles, and cyano and nitro groups. Deprotonation of the formazan NH results in a monoanionic formazanate (**1.42**). Formazans can exist in three different isomeric forms – *closed*, *open*, or *linear*. When R³ is a non-linear substituent, such as aromatic or nitro, only the *closed* form is observed. When R³ is less bulky or linear (e.g. cyano), free rotation around the C-N bonds of the formazan backbone is possible, resulting in the *open* or *linear* forms typically being observed. The ratio between the three forms are dependent on the *N*-aryl substituents.

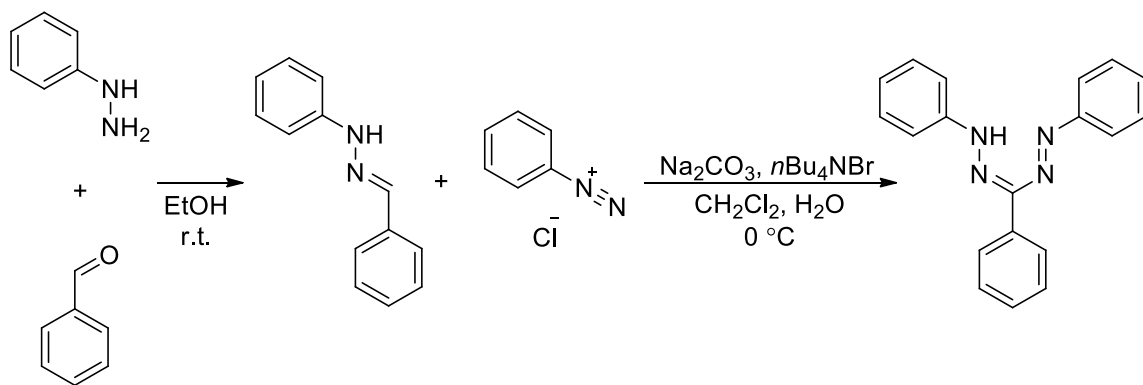


Formazans are typically synthesized *via* one of two routes. The first route (see Scheme 1) involves the deprotonation of a species with two activated CH bonds (e.g. phenylpyruvic acid, cyanoacetic acid, nitromethane), and the subsequent reaction with two equivalents of a diazonium salt. This method is straightforward, high yielding and inexpensive, and amenable to a variety of R³ substituents with the major limitation to the synthesis being the route does not allow for the clean production of asymmetric formazans.^[129-130]



Scheme 1.1. Synthesis of formazans from active methylene species.

The second common method for the synthesis of formazans enables the facile production of both symmetric and asymmetric formazans, but has only been demonstrated for aromatic substituents in the R^3 position. This route involves the condensation reaction of an aryl hydrazine and benzaldehyde to form a hydrazone. In the same pot, CH_2Cl_2 and water are added to form a biphasic reaction mixture, as well as base and a phase-transfer catalyst ($[\text{nBu}_4\text{N}][\text{PF}_6]$). An aryl diazonium salt can then be added, and the formazan is produced, generally in high yields.^[131]



Scheme 1.2. Synthesis of formazans under phase-transfer conditions.

Formazans have been used for a variety of applications, including tetrazolium assays, in the textile industry as dyes, and for metal sequestration and identification. In tetrazolium assays, tetrazolium salts (e.g. 3-(4,5-dimethylthiazol-2-yl)-2,5-diphenyl tetrazolium bromide, MTT, **1.43**) are introduced into cell cultures. If the cells are viable, the cellular reductase enzymes present will reduce the colourless tetrazolium salt to the darkly coloured formazan (Figure 1.7).^[132] Tetrazolium assays have been used to study superoxide

production,^[133] the antibacterial properties of fungal extracts,^[134] and to quantify microbials in different water sources,^[135] among others.^[132]

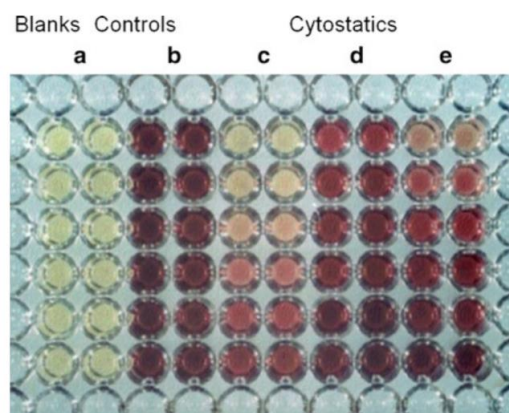
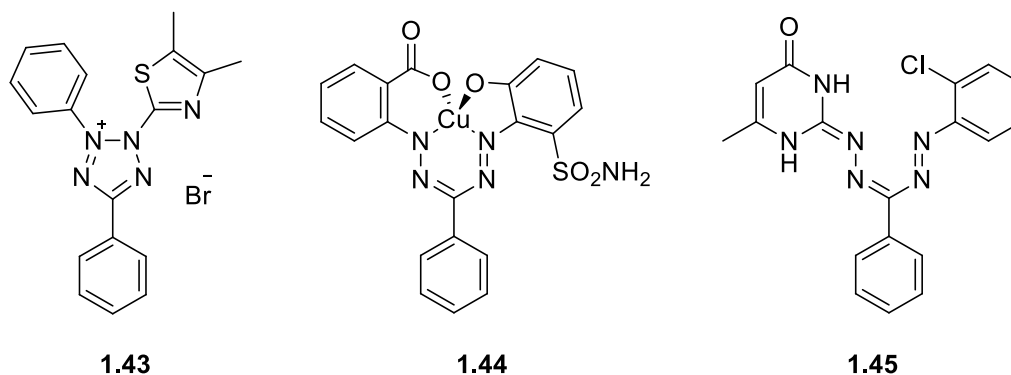


Figure 1.7. 96-well plate containing (a) blank control wells, (b) untreated cell control wells, and (c-e) cell lines with various concentrations of drugs. Image reproduced with permission from Ref. [136].

The first patent for the use of formazans as a dye for wool was granted in 1949,^[137] and since, many patents and publications have reported the use of formazans, and metal complexes of formazans for dyeing wool, protein fibres, and plastics.^[138-139] For example, blue-coloured copper complex **1.44** was demonstrated to be an excellent dye for cellulose fibers and wool.^[140]

The ability of formazans to chelate to metal centres has been exploited in their use as selective metal extraction and detection agents. Formazan **1.45** was incorporated into an electrode, with which lead, copper, cadmium and zinc could accurately be detected.^[141-142] Using other formazans, manganese in natural water has been detected.^[143] Finally, the Kettrup group has shown that silica or polystyrene beads with appended formazans were active as ion-exchange materials.^[144]

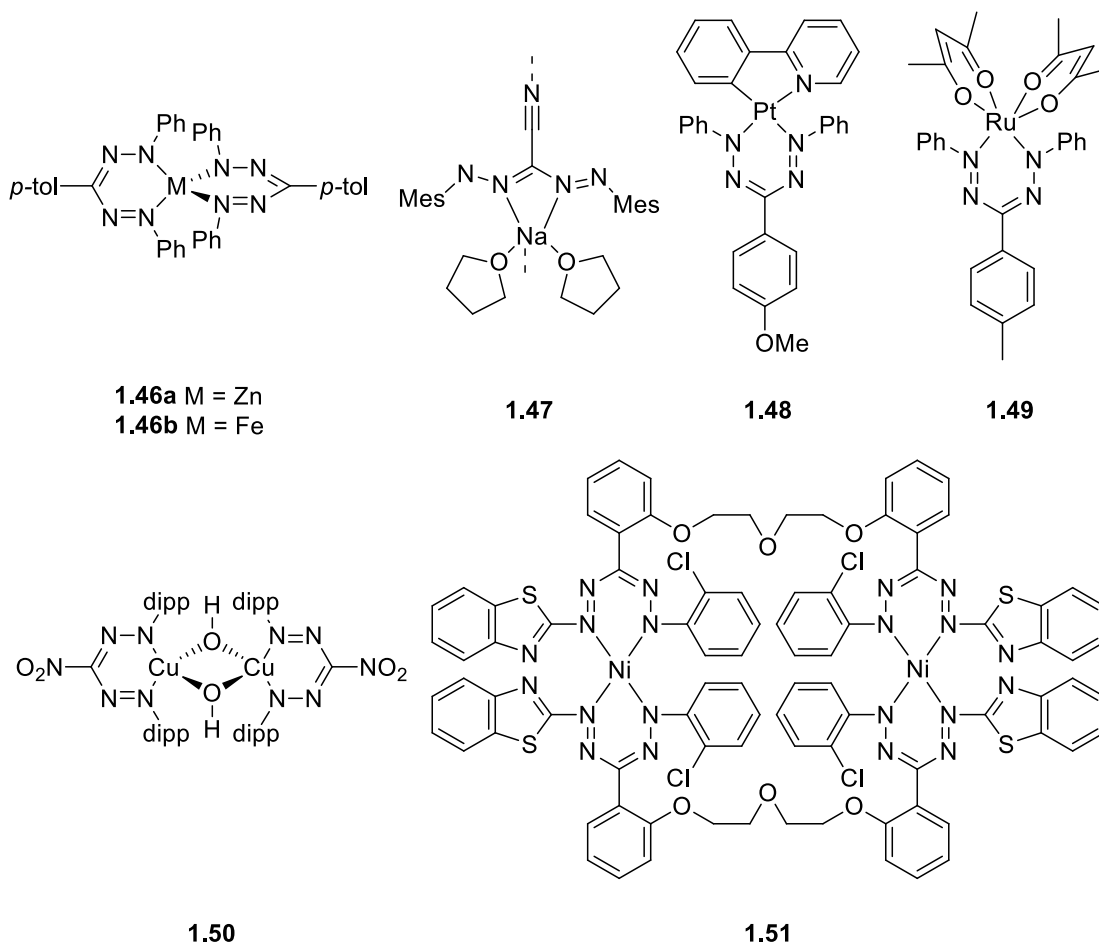


Formazans have also been sporadically studied for their use as ligands. Much of this work was done in the middle of the twentieth century,^[145-148] and so a lot of the metal complexes were not structurally characterized. However, there has been a renaissance in the use of formazans as ligands in the last ten years. The Otten group reported homoleptic zinc complex **1.46a** in 2014, and demonstrated the reversible reduction of each of the formazanate ligands individually.^[149] The same group found that by making the same complex with iron (**1.46b**) they were able to demonstrate spin crossover, a phenomenon that is rare in four-coordinate iron complexes.^[150] Unique bonding modes were observed when coordination of alkali metals to formazans was attempted.^[151] Sodium preferred to coordinate to the formazan through the N² and N⁴ nitrogen's, where the formazan exists in the *open* form. The cyano substituent acted as a ligand for the sodium as well, forming a coordination polymer (**1.47**). Similar bonding modes were observed for potassium as well.^[151]

The coordination of heavier transition metals with formazans has also been studied recently. Heteroleptic platinum complex **1.48** was synthesized by the Teets group.^[152] They demonstrated that coordination to the platinum center resulted in a red-shifted λ_{\max} by over 100 nm from the formazan.^[152] Ruthenium complex of formazanate ligand **1.49** was used to probe the non-innocent behavior of the formazanate ligand. The authors used EPR spectroscopy, UV-vis-NIR spectroelectrochemistry and computational calculations in order to assign the location of the various redox processes which were occurring.^[153]

Due to the redox-activity of formazanate ligands, they have the potential to be useful in catalysis. The Tolman and Hicks group synthesized copper complexes of formazanates to study their activation of dioxygen, which is a pivotal step in many copper-based catalytic

systems. Upon reaction of the copper-formazan complexes with oxygen, dimeric species **1.50** was formed, and this same species was not observed for copper complexes of other ligands, indicating the unusual reactivity of formazanate complexes.^[154] Finally, bis nickel complex **1.51** was studied as a catalyst towards the polymerization of ethylene by the Lipunov group. They demonstrated that with a co-catalyst (AlEtCl_2), ethylene oligomerization was possible – after reaction, analysis of the reaction mixture contained α - and β -olefins (up to octene).^[155]



Given these examples, formazans are an attractive class of molecules due to their facile and inexpensive synthesis, and many available modification sites.^[156] Their application in tetrazolium assays and as dyes has been quite widely examined. However, their use as ligands, and the applications of the resulting complexes is relatively understudied and has significant potential to impact many different fields of research.

1.5 Scope of Thesis

BF_2 complexes of *N*-donor ligands are an interesting class of materials, studied for their spectroscopic and redox properties. A yet-unstudied ligand for these types of complexes are formazanate ligands, which despite being known for over a century, have very little known about their coordination to main-group elements. Due to their ease of synthesis, formazanate ligands and their complexes have the potential to impact a variety of different applications, though this is a significantly underdeveloped field as well.

This thesis focuses on the coordination of the BF_2 moiety by formazanate ligands, and the resulting optical and electronic properties of the complexes. It discusses the incorporation of these BF_2 complexes into polymers, their use as molecular materials, and unprecedented boron complexes observed when a specific bis-hydroxy-substituted trianionic, potentially tetradentate formazanates were employed.

Chapter 2 focuses on the effect of substituent variation on the formazanate ligand on the resulting BF_2 complexes. This includes the effects of electron donating and withdrawing substituents on the aryl substituents, and a study of how these substituents affected the resulting optical and electrochemical properties of the complex.

Chapter 3 describes studies of the effect of extending the conjugation of BF_2 complexes of formazanate ligands. The difference between the 3 R^3 substituents (Ph, NO_2 and CN) was explored. A set of dimers were also synthesized – one being conjugated and one cross conjugated, and the properties of these dimers were contrasted with that of a monomeric model complex.

Chapter 4 highlights the use of copper-assisted alkyne-azide cycloaddition (CuAAC) to synthesize molecular materials and polymers that would not be possible by other means. This includes both a water soluble BF_2 formazanate complex, which was used for cell-imaging applications, and a ferrocene-substituted complex which was employed as a redox sensor. Finally, the same methods were used to synthesize a π -conjugated copolymer with 9,9-dihexylfluorene. Model complexes were synthesized in order to rationalize the observed spectroscopic properties of the polymer.

Chapter 5 explores the unique reactivity of a 1,5-(2-phenol)-3-cyanoformazan with boron trifluoride diethyl etherate. The resulting reaction mixture contained multiple unprecedented boron heterocycles. The spectroscopic and electronic properties of these complexes was studied in detail. Finally, the chemical reduction of two of the products was studied, and the characterization of these reduced species described.

Chapter 6 summarizes the results and key conclusions of the previous chapters, and suggests future directions for the project.

1.6 References

- (1) Arnold, K. E.; Owens, I. P. F.; Marshall, N. J. *Science* **2002**, *295*, 92–92.
- (2) Hausmann, F.; Arnold, K. E.; Marshall, N. J.; Owens, I. P. F. *Proc. R. Soc. Lond. B, Biol. Sci.* **2003**, *270*, 61–67.
- (3) Lim, M. L. M.; Land, M. F.; Li, D. *Science* **2007**, *315*, 481.
- (4) Vukusic, P.; Hooper, I. *Science* **2005**, *310*, 1151–1151.
- (5) Green, A. A.; McElroy, W. D. *Biochim. Biophys. Acta* **1956**, *20*, 170–176.
- (6) Taboada, C.; Brunetti, A. E.; Pedron, F. N.; Carnevale Neto, F.; Estrin, D. A.; Bari, S. E.; Chemes, L. B.; Peporine Lopes, N.; Lagorio, M. G.; Faivovich, J. *Proc. Natl. Acad. Sci. USA* **2017**, *114*, 3672–3677.
- (7) Salih, A.; Larkum, A.; Cox, G.; Kuhl, M.; Hoegh-Guldberg, O. *Nature* **2000**, *408*, 850–853.
- (8) Gruber, D. F.; Sparks, J. S. *Am. Mus. Novit.* **2015**, *3845*, 1–7.
- (9) Mazel, C. H.; Cronin, T. W.; Caldwell, R. L.; Marshall, N. J. *Science* **2004**, *303*, 51–51.
- (10) Sparks, J. S.; Schelly, R. C.; Smith, W. L.; Davis, M. P.; Tchernov, D.; Pieribone, V. A.; Gruber, D. F. *PLOS ONE* **2014**, *9*, e83259.
- (11) Zimmer, M. *Chem. Soc. Rev.* **2009**, *38*, 2823–2832.
- (12) Widder, E. A. *Science* **2010**, *328*, 704–708.
- (13) Bou-Abdallah, F.; Chasteen, N. D.; Lesser, M. P. *Biochim. Biophys. Acta* **2006**, *1760*, 1690–1695.
- (14) Young, R.; Roper, C. *Science* **1976**, *191*, 1046–1048.

- (15) Marek, P.; Papaj, D.; Yeager, J.; Molina, S.; Moore, W. *Curr. Biol.* **2011**, *21*, R680–R681.
- (16) Young, R. E. *Bull. Marine Sci.* **1983**, *33*, 829–845.
- (17) Kaskova, Z. M.; Tsarkova, A. S.; Yampolsky, I. V. *Chem. Soc. Rev.* **2016**, *45*, 6048–6077.
- (18) Cody, C. W.; Prasher, D. C.; Westler, W. M.; Prendergast, F. G.; Ward, W. W. *Biochemistry* **1993**, *32*, 1212–1218.
- (19) Ormö, M.; Cubitt, A. B.; Kallio, K.; Gross, L. A.; Tsien, R. Y.; Remington, S. J. *Science* **1996**, *273*, 1392–1395.
- (20) Yang, F.; Moss, L. G.; Phillips, G. N. *Nat. Biotech.* **1996**, *14*, 1246–1251.
- (21) Umena, Y.; Kawakami, K.; Shen, J.-R.; Kamiya, N. *Nature* **2011**, *473*, 55–60.
- (22) Noctor, G.; Mhamdi, A.; Chaouch, S.; Han, Y. I.; Neukermans, J.; Marquez-Garcia, B.; Queval, G.; Foyer, C. H. *Plant Cell Environ.* **2012**, *35*, 454–484.
- (23) Scholz, R. W.; Graham, K. S.; Gumprich, E.; Reddy, C. C. *Ann. N. Y. Acad. Sci.* **1989**, *570*, 514–517.
- (24) Hirano, Y.; Takeda, K.; Miki, K. *Nature* **2016**, *534*, 281–284.
- (25) O'Brien, E.; Holt, M. E.; Thompson, M. K.; Salay, L. E.; Ehlinger, A. C.; Chazin, W. J.; Barton, J. K. *Science* **2017**, *355*.
- (26) Loudet, A.; Burgess, K. *Chem. Rev.* **2007**, *107*, 4891–4932.
- (27) Treibs, A.; Kreuzer, F.-H. *Justus Liebigs Ann. Chem.* **1968**, *718*, 208–223.
- (28) Ulrich, G.; Ziessel, R.; Harriman, A. *Angew. Chem. Int. Ed.* **2008**, *47*, 1184–1201.
- (29) Ziessel, R.; Ulrich, G.; Harriman, A. *New J. Chem.* **2007**, *31*, 496–501.
- (30) Goze, C.; Ulrich, G.; Ziessel, R. *J. Org. Chem.* **2007**, *72*, 313–322.
- (31) Ge, Y.; O'Shea, D. F. *Chem. Soc. Rev.* **2016**, *45*, 3846–3864.
- (32) Tamgho, I.-S.; Hasheminasab, A.; Engle, J. T.; Nemykin, V. N.; Ziegler, C. J. *J. Am. Chem. Soc.* **2014**, *136*, 5623–5626.
- (33) Zhou, L.; Xu, D.; Gao, H.; Zhang, C.; Ni, F.; Zhao, W.; Cheng, D.; Liu, X.; Han, A. *J. Org. Chem.* **2016**, *81*, 7439–7447.
- (34) Wang, L.; Tamgho, I. S.; Crandall, L. A.; Rack, J. J.; Ziegler, C. J. *Phys. Chem. Chem. Phys.* **2015**, *17*, 2349–2351.

- (35) Kubota, Y.; Tsuzuki, T.; Funabiki, K.; Ebihara, M.; Matsui, M. *Org. Lett.* **2010**, *12*, 4010–4013.
- (36) Harborne, J. B., *The Natural Coumarins: Occurrence, Chemistry and Biochemistry*. Blackwell Publishing: 1982; Vol. 5, p 435–436.
- (37) Jones, G.; Rahman, M. A. *J. Phys. Chem.* **1994**, *98*, 13028–13037.
- (38) Stathatos, E.; Lianos, P.; Stangar, U. L.; Orel, B. *Chem. Phys. Lett.* **2001**, *345*, 381–385.
- (39) Chen, J.-X.; Liu, W.; Zheng, C.-J.; Wang, K.; Liang, K.; Shi, Y.-Z.; Ou, X.-M.; Zhang, X.-H. *ACS Appl. Mater. Interfaces* **2017**, *9*, 8848–8854.
- (40) *Coumarins: Biology, Applications, and Mode of Action*. John Wiley & Sons: New York, 1997.
- (41) Yu, D.; Suzuki, M.; Xie, L.; Morris-Natschke, S. L.; Lee, K.-H. *Med. Res. Rev.* **2003**, *23*, 322–345.
- (42) Hirsh, J.; Fuster, V.; Ansell, J.; Halperin, J. L. *J. Am. Coll. Cardiol.* **2003**, *41*, 1633–1652.
- (43) Pisklak, M.; Maciejewska, D.; Herold, F.; Wawer, I. *J. Mol. Struct.* **2003**, *649*, 169–176.
- (44) Steingruber, E., Indigo and Indigo Colorants. In *Ullmann's Encyclopedia of Industrial Chemistry*, Wiley-VCH Verlag GmbH & Co. KGaA: 2000.
- (45) Głowacki, E. D.; Voss, G.; Sariciftci, N. S. *Adv. Mater.* **2013**, *25*, 6783–6800.
- (46) Robb, M. J.; Ku, S.-Y.; Brunetti, F. G.; Hawker, C. J. *J. Polym. Sci., Part A: Polym. Chem.* **2013**, *51*, 1263–1271.
- (47) Nawn, G.; McDonald, R.; Hicks, R. G. *Inorg. Chem.* **2013**, *52*, 10912–10919.
- (48) Nawn, G.; Oakley, S. R.; Majewski, M. B.; McDonald, R.; Patrick, B. O.; Hicks, R. G. *Chem. Sci.* **2013**, *4*, 612–621.
- (49) Frath, D.; Poirel, A.; Ulrich, G.; De Nicola, A.; Ziessel, R. *Chem. Commun.* **2013**, *49*, 4908–4910.
- (50) Bourget-Merle, L.; Lappert, M. F.; Severn, J. R. *Chem. Rev.* **2002**, *102*, 3031–3066.
- (51) Hayes, P. G.; Welch, G. C.; Emslie, D. J. H.; Noack, C. L.; Piers, W. E.; Parvez, M. *Organometallics* **2003**, *22*, 1577–1579.
- (52) Stadler, A.-M.; Harrowfield, J. *Inorg. Chim. Acta* **2009**, *362*, 4298–4314.

- (53) Macedo, F. P.; Gwengo, C.; Lindeman, S. V.; Smith, M. D.; Gardinier, J. R. *Eur. J. Inorg. Chem.* **2008**, 2008, 3200–3211.
- (54) Yang, Y.; Su, X.; Carroll, C. N.; Aprahamian, I. *Chem. Sci.* **2012**, 3, 610–613.
- (55) Araneda, J. F.; Piers, W. E.; Heyne, B.; Parvez, M.; McDonald, R. *Angew. Chem. Int. Ed.* **2011**, 50, 12214–12217.
- (56) Liu, X.; Ren, Y.; Xia, H.; Fan, X.; Mu, Y. *Inorg. Chim. Acta* **2010**, 363, 1441–1447.
- (57) Ren, Y.; Liu, X.; Gao, W.; Xia, H.; Ye, L.; Mu, Y. *Eur. J. Inorg. Chem.* **2007**, 1808–1814.
- (58) Zhu, M.; Jiang, L.; Yuan, M.; Liu, X.; Ouyang, C.; Zheng, H.; Yin, X.; Zuo, Z.; Liu, H.; Li, Y. *J. Polym. Sci., Part A: Polym. Chem.* **2008**, 46, 7401–7410.
- (59) Yoshii, R.; Hirose, A.; Tanaka, K.; Chujo, Y. *J. Am. Chem. Soc.* **2014**, 136, 18131–18139.
- (60) Yoshii, R.; Nagai, A.; Chujo, Y. *J. Polym. Sci., Part A: Polym. Chem.* **2010**, 48, 5348–5356.
- (61) Nagai, A.; Kokado, K.; Miyake, J.; Chujo, Y. *Macromolecules* **2009**, 42, 5446–5452.
- (62) Liras, M.; García-García, J. M.; Quijada-Garrido, I.; Gallardo, A.; París, R. *Macromolecules* **2011**, 44, 3739–3745.
- (63) Miki, K.; Enomoto, A.; Inoue, T.; Nabeshima, T.; Saino, S.; Shimizu, S.; Matsuoka, H.; Ohe, K. *Biomacromolecules* **2017**, 18, 249–256.
- (64) Yang, D.; Zhang, S.; Hu, Y.; Chen, J.; Bao, B.; Yuwen, L.; Weng, L.; Cheng, Y.; Wang, L. *RSC Adv.* **2016**, 6, 114580–114586.
- (65) Thivierge, C.; Loudet, A.; Burgess, K. *Macromolecules* **2011**, 44, 4012–4015.
- (66) Rong, Y.; Wu, C.; Yu, J.; Zhang, X.; Ye, F.; Zeigler, M.; Gallina, M. E.; Wu, I. C.; Zhang, Y.; Chan, Y.-H.; Sun, W.; Uvdal, K.; Chiu, D. T. *ACS Nano* **2013**, 7, 376–384.
- (67) Rong, Y.; Yu, J.; Zhang, X.; Sun, W.; Ye, F.; Wu, I. C.; Zhang, Y.; Hayden, S.; Zhang, Y.; Wu, C.; Chiu, D. T. *ACS Macro Lett.* **2014**, 3, 1051–1054.
- (68) Mosaiab, T.; In, I.; Park, S. Y. *Macromol. Rapid Commun.* **2013**, 34, 1408–1415.
- (69) Usta, H.; Yilmaz, M. D.; Avestro, A.-J.; Boudinet, D.; Denti, M.; Zhao, W.; Stoddart, J. F.; Facchetti, A. *Adv. Mater.* **2013**, 25, 4327–4334.

- (70) He, W.; Jiang, Y.; Qin, Y. *Polym. Chem.* **2014**, *5*, 1298–1304.
- (71) Debnath, S.; Singh, S.; Bedi, A.; Krishnamoorthy, K.; Zade, S. S. *J. Phys. Chem. C* **2015**, *119*, 15859–15867.
- (72) Squeo, B. M.; Gasparini, N.; Ameri, T.; Palma-Cando, A.; Allard, S.; Gregoriou, V. G.; Brabec, C. J.; Scherf, U.; Chochos, C. L. *J. Mater. Chem. A* **2015**, *3*, 16279–16286.
- (73) Winsberg, J.; Hagemann, T.; Muench, S.; Friebe, C.; Häupler, B.; Janoschka, T.; Morgenstern, S.; Hager, M. D.; Schubert, U. S. *Chem. Mater.* **2016**, *28*, 3401–3405.
- (74) Singh, S.; Chithiravel, S.; Krishnamoorthy, K. *J. Phys. Chem. C* **2016**, *120*, 26199–26205.
- (75) Wang, L.; Fang, G.; Cao, D. *Sens. Actuators, B* **2015**, *221*, 63–74.
- (76) Sen, C. P.; Devendar Goud, V.; Shrestha, R. G.; Shrestha, L. K.; Ariga, K.; Valiyaveetil, S. *Polym. Chem.* **2016**, *7*, 4213–4225.
- (77) Khoerunnisa; Mazrad, Z. A. I.; In, I.; Park, S. Y. *Biosens. Bioelec.* **2017**, *90*, 394–402.
- (78) Wang, D.; Miyamoto, R.; Shiraishi, Y.; Hirai, T. *Langmuir* **2009**, *25*, 13176–13182.
- (79) París, R.; Quijada-Garrido, I.; García, O.; Liras, M. *Macromolecules* **2011**, *44*, 80–86.
- (80) Meng, G.; Velayudham, S.; Smith, A.; Luck, R.; Liu, H. *Macromolecules* **2009**, *42*, 1995–2001.
- (81) Hirose, A.; Tanaka, K.; Yoshii, R.; Chujo, Y. *Polym. Chem.* **2015**, *6*, 5590–5595.
- (82) Chen, J.; Zhong, W.; Tang, Y.; Wu, Z.; Li, Y.; Yi, P.; Jiang, J. *Macromolecules* **2015**, *48*, 3500–3508.
- (83) Liras, M.; Iglesias, M.; Sánchez, F. *Macromolecules* **2016**, *49*, 1666–1673.
- (84) Bandyopadhyay, S.; Anil, A. G.; James, A.; Patra, A. *ACS Appl. Mater. Interfaces* **2016**, *8*, 27669–27678.
- (85) Costela, A.; García-Moreno, I.; Gómez, C.; Amat-Guerri, F.; Liras, M.; Sastre, R. *Appl. Phys. B* **2003**, *76*, 365–369.

- (86) López Arbeloa, F.; Bañuelos Prieto, J.; López Arbeloa, I.; Costela, A.; García-Moreno, I.; Gómez, C.; Amat-Guerri, F.; Liras, M.; Sastre, R. *Photochem. Photobiol.* **2003**, *78*, 30–36.
- (87) Nepomnyashchii, A. B.; Bröring, M.; Ahrens, J.; Bard, A. J. *J. Am. Chem. Soc.* **2011**, *133*, 8633–8645.
- (88) Tanaka, K.; Yanagida, T.; Hirose, A.; Yamane, H.; Yoshii, R.; Chujo, Y. *RSC Adv.* **2015**, *5*, 96653–96659.
- (89) Poe, A. M.; Della Pelle, A. M.; Subrahmanyam, A. V.; White, W.; Wantz, G.; Thayumanavan, S. *Chem. Commun.* **2014**, *50*, 2913–2915.
- (90) Mao, Z.; Senevirathna, W.; Liao, J.-Y.; Gu, J.; Kesava, S. V.; Guo, C.; Gomez, E. D.; Sauvé, G. *Adv. Mater.* **2014**, *26*, 6290–6294.
- (91) Leblebici, S. Y.; Catane, L.; Barclay, D. E.; Olson, T.; Chen, T. L.; Ma, B. *ACS Appl. Mater. Interfaces* **2011**, *3*, 4469–4474.
- (92) Leblebici, S. Y.; Chen, T. L.; Olalde-Velasco, P.; Yang, W.; Ma, B. *ACS Appl. Mater. Interfaces* **2013**, *5*, 10105–10110.
- (93) Senevirathna, W.; Liao, J.-y.; Mao, Z.; Gu, J.; Porter, M.; Wang, C.; Fernando, R.; Sauve, G. *J. Mater. Chem. A* **2015**, *3*, 4203–4214.
- (94) Lin, Y.-D.; Ke, B.-Y.; Chang, Y. J.; Chou, P.-T.; Liao, K.-L.; Liu, C.-Y.; Chow, T. *J. Mater. Chem. A* **2015**, *3*, 16831–16842.
- (95) Mirloup, A.; Hualme, Q.; Leclerc, N.; Leveque, P.; Heiser, T.; Retailleau, P.; Ziessel, R. *Chem. Commun.* **2015**, *51*, 14742–14745.
- (96) Yoshii, R.; Yamane, H.; Nagai, A.; Tanaka, K.; Taka, H.; Kita, H.; Chujo, Y. *Macromolecules* **2014**, *47*, 2316–2323.
- (97) Chapran, M.; Angioni, E.; Findlay, N. J.; Breig, B.; Cherpak, V.; Stakhira, P.; Tuttle, T.; Volyniuk, D.; Grazulevicius, J. V.; Nastishin, Y. A.; Lavrentovich, O. D.; Skabara, P. J. *ACS Appl. Mater. Interfaces* **2017**, *9*, 4750–4757.
- (98) Liu, C.-L.; Chen, Y.; Shelar, D. P.; Li, C.; Cheng, G.; Fu, W.-F. *J. Mater. Chem. C* **2014**, *2*, 5471–5478.
- (99) Findlay, N. J.; Bruckbauer, J.; Inigo, A. R.; Breig, B.; Arumugam, S.; Wallis, D. J.; Martin, R. W.; Skabara, P. J. *Adv. Mater.* **2014**, *26*, 7290–7294.

- (100) Grossi, M.; Morgunova, M.; Cheung, S.; Scholz, D.; Conroy, E.; Terrile, M.; Panarella, A.; Simpson, J. C.; Gallagher, W. M.; O'Shea, D. F. *Nat. Commun.* **2016**, *7*, 10855–10868.
- (101) Ashokkumar, P.; Weißhoff, H.; Kraus, W.; Rurack, K. *Angew. Chem. Int. Ed.* **2014**, *53*, 2225–2229.
- (102) Karakus, E.; Ucuncu, M.; Emrullahoglu, M. *Chem. Commun.* **2014**, *50*, 1119–1121.
- (103) Islamy Mazrad, Z. A.; In, I.; Lee, K.-D.; Park, S. Y. *Biosens. Bioelectron.* **2017**, *89*, 1026–1033.
- (104) Li, Y.; Zhou, H.; Yin, S.; Jiang, H.; Niu, N.; Huang, H.; Shahzad, S. A.; Yu, C. *Sens. Actuators, B* **2016**, *235*, 33–38.
- (105) Qian, H.; Cousins, M. E.; Horak, E. H.; Wakefield, A.; Liptak, M. D.; Aprahamian, I. *Nat. Chem.* **2017**, *9*, 83–87.
- (106) Roubinet, B.; Massif, C.; Moreau, M.; Boschetti, F.; Ulrich, G.; Ziessel, R.; Renard, P.-Y.; Romieu, A. *Chem. Eur. J.* **2015**, *21*, 14589–14601.
- (107) Wang, B.; Li, P.; Yu, F.; Song, P.; Sun, X.; Yang, S.; Lou, Z.; Han, K. *Chem. Commun.* **2013**, *49*, 1014–1016.
- (108) Dziuba, D.; Jurkiewicz, P.; Cebecauer, M.; Hof, M.; Hocek, M. *Angew. Chem. Int. Ed.* **2016**, *55*, 174–178.
- (109) Yang, S. K.; Shi, X.; Park, S.; Ha, T.; Zimmerman, S. C. *Nat. Chem.* **2013**, *5*, 692–697.
- (110) Zhu, H.; Fan, J.; Wang, J.; Mu, H.; Peng, X. *J. Am. Chem. Soc.* **2014**, *136*, 12820–12823.
- (111) Kowada, T.; Maeda, H.; Kikuchi, K. *Chem. Soc. Rev.* **2015**, *44*, 4953–4972.
- (112) Hu, R.; Gomez-Duran, C. F. A.; Lam, J. W. Y.; Belmonte-Vazquez, J. L.; Deng, C.; Chen, S.; Ye, R.; Pena-Cabrera, E.; Zhong, Y.; Wong, K. S.; Tang, B. Z. *Chem. Commun.* **2012**, *48*, 10099–10101.
- (113) Hama, Y.; Urano, Y.; Koyama, Y.; Choyke, P. L.; Kobayashi, H. *Biochem. Biophys. Res. Commun.* **2006**, *348*, 807–813.
- (114) Zhang, X.; Xiao, Y.; Qian, X. *Angew. Chem. Int. Ed.* **2008**, *47*, 8025–8029.
- (115) Zheng, Q.; Xu, G.; Prasad, P. N. *Chem. Eur. J.* **2008**, *14*, 5812–5819.

- (116) BODIPY Dye Series. <https://www.thermofisher.com/ca/en/home/references/molecular-probes-the-handbook/fluorophores-and-their-amine-reactive-derivatives/bodipy-dye-series.html> (accessed April 7 2017).
- (117) Mendive-Tapia, L.; Zhao, C.; Akram, A. R.; Preciado, S.; Albericio, F.; Lee, M.; Serrels, A.; Kielland, N.; Read, N. D.; Lavilla, R.; Vendrell, M. *Nat. Commun.* **2016**, *7*, 10940–10948.
- (118) Castano, A. P.; Mroz, P.; Hamblin, M. R. *Nat. Rev. Cancer* **2006**, *6*, 535–545.
- (119) Gorman, A.; Killoran, J.; O'Shea, C.; Kenna, T.; Gallagher, W. M.; O'Shea, D. F. *J. Am. Chem. Soc.* **2004**, *126*, 10619–10631.
- (120) Momeni, M. R.; Brown, A. *J. Phys. Chem. A* **2016**, *120*, 2550–2560.
- (121) Tang, Q.; Si, W.; Huang, C.; Ding, K.; Huang, W.; Chen, P.; Zhang, Q.; Dong, X. *J. Mater. Chem. B* **2017**, *5*, 1566–1573.
- (122) Kamkaew, A.; Lim, S. H.; Lee, H. B.; Kiew, L. V.; Chung, L. Y.; Burgess, K. *Chem. Soc. Rev.* **2013**, *42*, 77–88.
- (123) Huang, L.; Li, Z.; Zhao, Y.; Zhang, Y.; Wu, S.; Zhao, J.; Han, G. *J. Am. Chem. Soc.* **2016**, *138*, 14586–14591.
- (124) Hesari, M.; Lu, J.-s.; Wang, S.; Ding, Z. *Chem. Commun.* **2015**, *51*, 1081–1084.
- (125) Qi, H.; Teesdale, J. J.; Pupillo, R. C.; Rosenthal, J.; Bard, A. J. *J. Am. Chem. Soc.* **2013**, *135*, 13558–13566.
- (126) Patil, N. G.; Basutkar, N. B.; Ambade, A. V. *Chem. Commun.* **2015**, *51*, 17708–17711.
- (127) Liu, X.; Chen, B.; Li, X.; Zhang, L.; Xu, Y.; Liu, Z.; Cheng, Z.; Zhu, X. *Nanoscale* **2015**, *7*, 16399–16416.
- (128) Hudson, Z. M.; Lunn, D. J.; Winnik, M. A.; Manners, I. *Nat. Commun.* **2014**, *5*, 3372–3379.
- (129) Gök, Y.; Şentürk, H. B. *Dyes Pigments* **1991**, *15*, 279–287.
- (130) Gilroy, J. B.; Ferguson, M. J.; McDonald, R.; Patrick, B. O.; Hicks, R. G. *Chem. Commun.* **2007**, 126–128.
- (131) Katritzky, A. A.; Belyakov, S. A.; Cheng, D.; Durst, H. D. *Synthesis* **1995**, *1995*, 577–581.

- (132) Berridge, M. V.; Herst, P. M.; Tan, A. S., Tetrazolium dyes as tools in cell biology: New insights into their cellular reduction. In *Biotechnology Annual Review*, Elsevier: 2005; Vol. Volume 11, pp 127–152.
- (133) Zhao, J.; Zhang, B.; Li, J.; Liu, Y.; Wang, W. *Chem. Commun.* **2016**, 52, 11595–11598.
- (134) Corrado, M.; Rodrigues, K. F. *J. Basic Microbiol.* **2004**, 44, 157–160.
- (135) Rodriguez, G. G.; Phipps, D.; Ishiguro, K.; Ridgway, H. F. *Appl. Environ. Microbiol.* **1992**, 58, 1801–1808.
- (136) van Meerloo, J.; Kaspers, G. J. L.; Cloos, J., Cell Sensitivity Assays: The MTT Assay. In *Cancer Cell Culture: Methods and Protocols*, Cree, I. A., Ed. Humana Press: Totowa, NJ, 2011, 237–245.
- (137) Mayer, H.; Widmer, W. Disazo dye from dihydroxy benzidine and process therefor. US2476259 A, 1949.
- (138) Sokolowska-Gajda, J.; Freeman, H. S.; Reife, A. *Dyes Pigments* **1996**, 30, 1–20.
- (139) Edwards, L. C.; Freeman, H. S. *Color. Tech.* **2005**, 121, 271–274.
- (140) Zhang, Y.; Liu, D. *Dyes Pigments* **1995**, 29, 57–63.
- (141) Brainina, K. Z.; Stozhko, N. Y.; Aleshina, L. V.; Lipunova, G. N. *J. Analyt. Chem.* **2003**, 58, 965–971.
- (142) Stozhko, N. Y.; Lipunova, G. N.; Maslakova, T. I.; Aleshina, L. V.; Brainina, K. Z. *J. Analyt. Chem.* **2004**, 59, 179–184.
- (143) Stozhko, N. Y.; Inzhevatova, O. V.; Kolyadina, L. I.; Lipunova, G. N. *J. Analyt. Chem.* **2005**, 60, 163–168.
- (144) Grote, M.; Schwalk, A.; Kettrup, A. *Analyt. Chem.* **1982**, 313, 297–303.
- (145) Hirsch, B. *Justus Liebigs Ann. Chem.* **1960**, 637, 167–172.
- (146) Beffa, F.; Lienhard, P.; Steiner, E.; Schetty, G. *Helv. Chim. Acta* **1963**, 46, 1369–1376.
- (147) Dale, D. *J. Chem. Soc. A* **1967**, 278–287.
- (148) Siedle, A. R.; Pignolet, L. H. *Inorg. Chem.* **1980**, 19, 2052–2056.
- (149) Chang, M.-C.; Dann, T.; Day, D. P.; Lutz, M.; Wildgoose, G. G.; Otten, E. *Angew. Chem. Int. Ed.* **2014**, 53, 4118–4122.

- (150) Travieso-Puente, R.; Broekman, J. O. P.; Chang, M.-C.; Demeshko, S.; Meyer, F.; Otten, E. *J. Am. Chem. Soc.* **2016**, *138*, 5503–5506.
- (151) Travieso-Puente, R.; Chang, M.-C.; Otten, E. *Dalton Trans.* **2014**, *43*, 18035–18041.
- (152) Kabir, E.; Wu, C.-H.; Wu, J. I.-C.; Teets, T. S. *Inorg. Chem.* **2016**, *55*, 956–963.
- (153) Mandal, A.; Schwederski, B.; Fiedler, J.; Kaim, W.; Lahiri, G. K. *Inorg. Chem.* **2015**, *54*, 8126–8135.
- (154) Hong, S.; Hill, L. M. R.; Gupta, A. K.; Naab, B. D.; Gilroy, J. B.; Hicks, R. G.; Cramer, C. J.; Tolman, W. B. *Inorg. Chem.* **2009**, *48*, 4514–4523.
- (155) Zaidman, A. V.; Pervova, I. G.; Vilms, A. I.; Belov, G. P.; Kayumov, R. R.; Slepukhin, P. A.; Lipunov, I. N. *Inorg. Chim. Acta* **2011**, *367*, 29–34.
- (156) Nineham, A. W. *Chem. Rev.* **1955**, *55*, 355–483.

Chapter 2

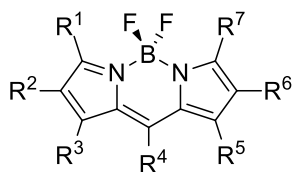
2 Structural Modification of BF₂ Formazanate Dyes

Adapted from:

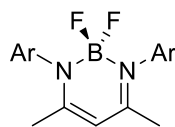
1. Barbon, S. M.; Price, J. T.; Reinkeluers, P. A.; Gilroy, J. B. *Inorg. Chem.* **2014**, *53*, 10585-10593.
2. Barbon, S. M.; Reinkeluers, P. A.; Price, J. T.; Staroverov, V. N.; Gilroy, J. B. *Chem. Eur. J.* **2014**, *20*, 1340-11344.

2.1 Introduction

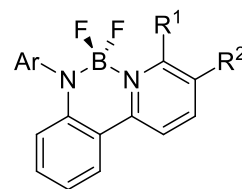
Boron difluoride (BF₂) complexes of chelating *N*-donor ligands have been extensively studied over the past 20 years^[1-10] as functional materials with useful properties that are tunable through structural modification, including high molar absorptivities and fluorescence quantum yields and unusual redox properties. A wide range of chelating *N*-donor ligands have been studied as the backbone of these BF₂ complexes, including dipyrrens,^[11-13] β-diketiminates,^[14-16] anilido-pyridines,^[17] anilido-imines,^[18-19] pyridomethenes^[20] and indigo-*N,N'*-diarylamines,^[21-22] resulting in complexes **2.1–2.6**. Complexes derived from dipyrren ligands **2.1**, commonly known as BODIPYs have been widely used in a large number of applications due to their high quantum yields, although their syntheses can be challenging.^{[11-13],[23-28]} BF₂ complexes of β-diketiminates **2.2** are redox-active and exhibit high extinction coefficients, but have been shown to have low fluorescence quantum yields.^[14-16] Piers' anilido-pyridine BF₂ complexes, **2.3**, have high quantum yields and exhibit large Stokes shifts,^[17] as do related complexes based on anilido-imines **2.4**.^[18-19] The large Stokes shifts are a key requirement for the potential use of BF₂ complexes as optical imaging agents. Pyridomethane BF₂ complexes **2.5** exhibit moderate quantum yields in solution and the solid-state,^[20] while those derived from indigo-*N,N'*-diarylamines, **2.6**, have rich redox chemistry and are emissive in the near-IR.^[21-22]



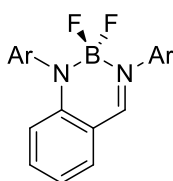
2.1



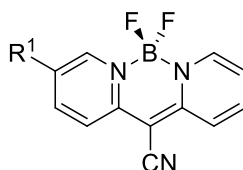
2.2



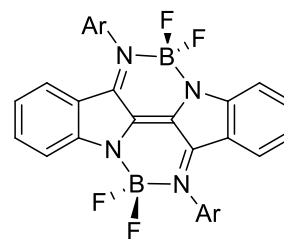
2.3



2.4

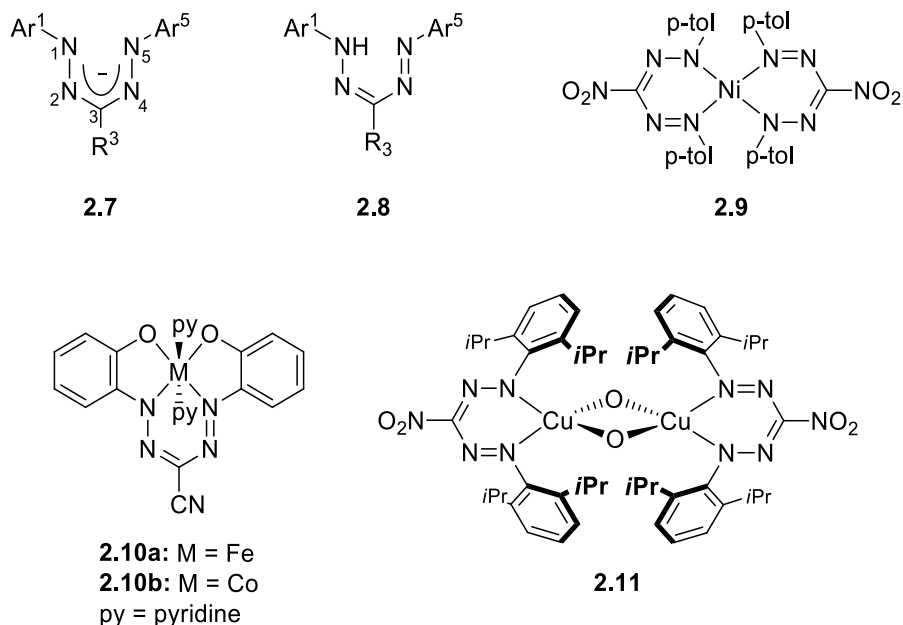


2.5

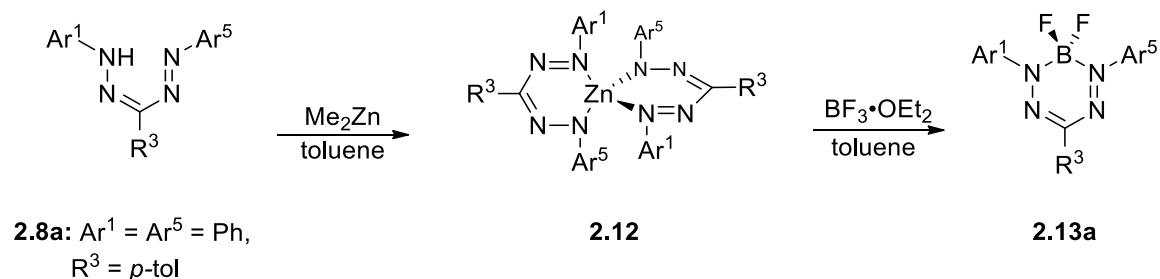


2.6

One family of chelating *N*-donor ligands that has not been widely studied in this context are formazanate ligands **2.7**,^[29-30] which are derived from formazans **2.8**. Formazans have been used widely within the textile industry as dyes,^[31-34] and as colorimetric indicators of cell activity in biology.^[35-39] However, their behavior as ligands has only been explored intermittently over the past 75 years.^[40-49] In the last decade, the Hicks group has reported a series of transition metal complexes of 3-cyanoformazanates and 3-nitroformazanates, including heteroleptic nickel complex **2.9** and iron and cobalt complexes **2.10a,b** derived from a tetradentate, trianionic 3-cyanoformazanate ligand.^[47] Tolman and co-workers have studied copper (II) complexes of 3-nitroformazanates **2.11** during studies designed to model oxygen activation processes prevalent in biological systems.^[45,49]



More recently, while this work was being completed, the Otten group has employed triarylformazans, e.g. **2.8a**, for the synthesis of homoleptic zinc complexes, e.g. **2.12**, and demonstrated the utility of formazanate ligands as electron reservoirs.^[50] In 2014, a report describing the use of these zinc complexes as starting materials for the production of formazanate BF₂ complexes, e.g. **2.13a**, via a transmetallation reaction was published (Scheme 2.1).^[51] Herein, we report the synthesis and characterization of BF₂ complexes of 3-cyanoformazanate and 3-arylformazanate ligands by a straightforward route to produce a series of formazanate BF₂ complexes,^[52-53] to afford a series of triarylformazanate BF₂ complexes. Through judicious structural modification, we studied the effect of substituents on their optical and electronic properties.

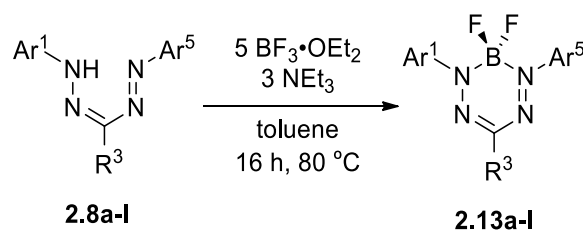


Scheme 2.1. Otten's synthesis of homoleptic zinc formazanate complex **2.12** and boron difluoride formazanate complex **2.13a**.^[50-51]

2.2 Results

2.2.1 Synthesis

Triarylformazans **2.8a–i** were prepared according to a previously published procedure^[54-55] and exhibited a characteristic NH shift between 14–16 ppm in their ¹H NMR spectra (Figures A2.1–A2.8). Similarly, 3-cyanoformazans **2.8j–l**, prepared according to a previously published procedure^[47] exhibited NH shifts between 10–12 ppm. Formazanate BF₂ complexes **2.13a–l** were synthesized from their parent formazans by refluxing them in a toluene solution containing excess boron trifluoride diethyl etherate and triethylamine for 16 h (Scheme 2.2, Table 2.1). Purified yields ranged from 55–92%, with the exception of **2.13b**, which was isolated in 16% yield due to difficulties encountered during purification.



Scheme 2.2. Synthesis of BF₂ formazanate complexes **2.13a–l**.

Table 2.1. List of substituents for formazans **2.8a–l** and BF₂ formazanate complexes **2.13a–l**.^a

	Ar ¹	Ar ⁵	R ³
a	C ₆ H ₅	C ₆ H ₅	<i>p</i> -C ₆ H ₄ -CH ₃
b	<i>p</i> -C ₆ H ₄ -CN	<i>p</i> -C ₆ H ₄ -CN	<i>p</i> -C ₆ H ₄ -CH ₃
c	<i>p</i> -C ₆ H ₄ -OMe	<i>p</i> -C ₆ H ₄ -OMe	<i>p</i> -C ₆ H ₄ -CH ₃
d	<i>p</i> -C ₆ H ₄ -CH ₃	<i>p</i> -C ₆ H ₄ -CH ₃	C ₆ H ₅
e	<i>p</i> -C ₆ H ₄ -CH ₃	<i>p</i> -C ₆ H ₄ -CH ₃	<i>p</i> -C ₆ H ₄ -CN
f	<i>p</i> -C ₆ H ₄ -CH ₃	<i>p</i> -C ₆ H ₄ -CH ₃	<i>p</i> -C ₆ H ₄ -OMe
g	<i>p</i> -C ₆ H ₄ -CN	<i>p</i> -C ₆ H ₄ -OMe	<i>p</i> -C ₆ H ₄ -CH ₃
h	<i>p</i> -C ₆ H ₄ -CH ₃	<i>p</i> -C ₆ H ₄ -CN	<i>p</i> -C ₆ H ₄ -OMe
i	<i>p</i> -C ₆ H ₄ -OMe	<i>p</i> -C ₆ H ₄ -CH ₃	<i>p</i> -C ₆ H ₄ -CN
j	C ₆ H ₅	C ₆ H ₅	CN
k	<i>p</i> -C ₆ H ₄ -CN	<i>p</i> -C ₆ H ₄ -CN	CN
l	<i>p</i> -C ₆ H ₄ -OMe	<i>p</i> -C ₆ H ₄ -OMe	CN

^a*p*-C₆H₄-CH₃ substituents were chosen as ‘placeholders’ throughout this study, as their presence simplified NMR spectra and facilitated purification by crystallization.

The incorporation of the $[\text{BF}_2]^+$ fragment into the formazanate framework was accompanied by a color change from dark red to purple in triarylformazanate BF_2 complexes, and orange to dark red or purple in 3-cyanoformazanate BF_2 complexes. The reaction could also be monitored by ^1H NMR spectroscopy, as the NH signals disappeared in the spectra of **2.13a–l** (Figures 2.1, A2.9–A2.30). The BF_2 formazanate complexes were characterized by ^{11}B and ^{19}F NMR spectroscopy, where diagnostic 1:2:1 triplets in the ^{11}B NMR spectra between -0.5 and -0.9 ppm, and 1:1:1:1 quartets in the ^{19}F NMR spectra between -129.6 and -145.8 ppm were observed. Further analysis by ^{13}C NMR spectroscopy, mass spectrometry, IR spectroscopy and elemental analysis confirmed the proposed structures of complexes **2.13a–l**.

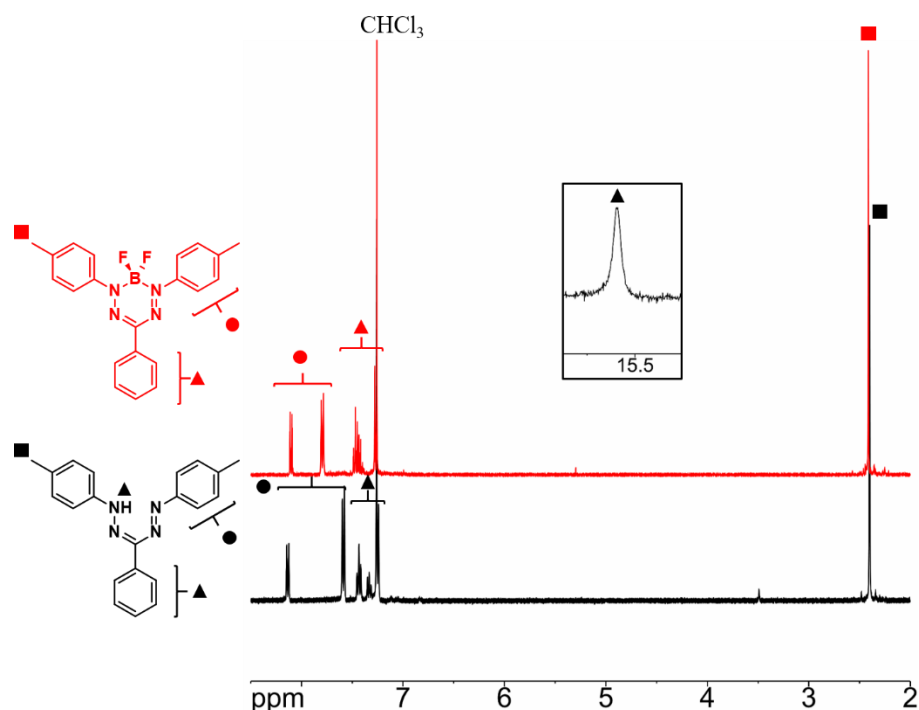


Figure 2.1. ^1H NMR spectrum of formazan **2.8d** (black) and BF_2 complex **2.13d** (red) in CDCl_3 . The NH signal for **2.8d** is inset.

2.2.2 X-ray Crystallography

Slow evaporation of concentrated CH_2Cl_2 solutions of **2.13d–f** and **2.13j–l** yielded single crystals suitable for X-ray diffraction analysis. The solid-state structures show that the boron atoms in complexes **2.13d–f** and **2.13j–l** are four-coordinate and adopt a slightly distorted tetrahedral geometry. Each complex has a delocalized formazanate backbone,

with all C-N and N-N bond lengths approximately half way between the standard single and double bonds for the respective atoms involved.^[56]

The boron atoms are displaced slightly from the N₄ plane (plane defined by N1, N2, N3 and N4) of the formazanate backbone, by 0.192 Å in **2.13j** and by 0.025 Å in **2.13k**. The unit cell of the crystalline structure of **2.13l** contains two molecular units in distinct conformations (Figure 2.2, A2.31). Conformer A is almost flat and has a geometry very similar to **2.13j** and **2.13k**, with the boron atom displaced from the N₄ plane by 0.143 Å. The second conformer, conformer B, is shaped like a dragonfly and has the boron atom displaced from the N₄ plane by 0.376 Å. The structures of the triarylformazanate BF₂ complexes were very similar, as complexes **2.13d** and **2.13e** were relatively planar, with the boron atom displaced by 0.022 Å in **2.13d** and 0.290 Å in **2.13e**. The solid-state structure of **2.13f** is similar to the dragonfly shaped conformer of **2.13l**, with the boron atom displaced from the N₄ plane by 0.538 Å in a boat-like conformation.

The 1,5-aryl substituents of BF₂ complexes **2.13d**, **2.13e**, **2.13j**, **2.13k**, and **2.13l** (conformer A) are moderately twisted with respect to the formazanate backbone, with the angle between the N₄ plane and the plane defined by the *N*-aryl substituents ranging from 4.7 to 25.4°. For comparison, the same angles in conformer B of **2.13l** are 36.6–37.6°, and in **2.13f** are 43–50°. Similar BF₂ complexes of other monoanionic, bidentate *N*-donor ligands exhibit significantly larger angles between the *N*-aryl substituents and the ligand backbones involved. For example, the aryl substituent in anilido-pyridine BF₂ complex **2.3** (Ar = phenyl) is twisted by 77°,^[17] while the aryl substituents in β-diketimate BF₂ complexes are almost perpendicular to the ligand backbone, with twisting of 76–88°. ^[14-15] These structures are similar to the structure of complex **2.13a** reported previously.^[51] Subtle changes between structures are likely due to crystal packing interactions.

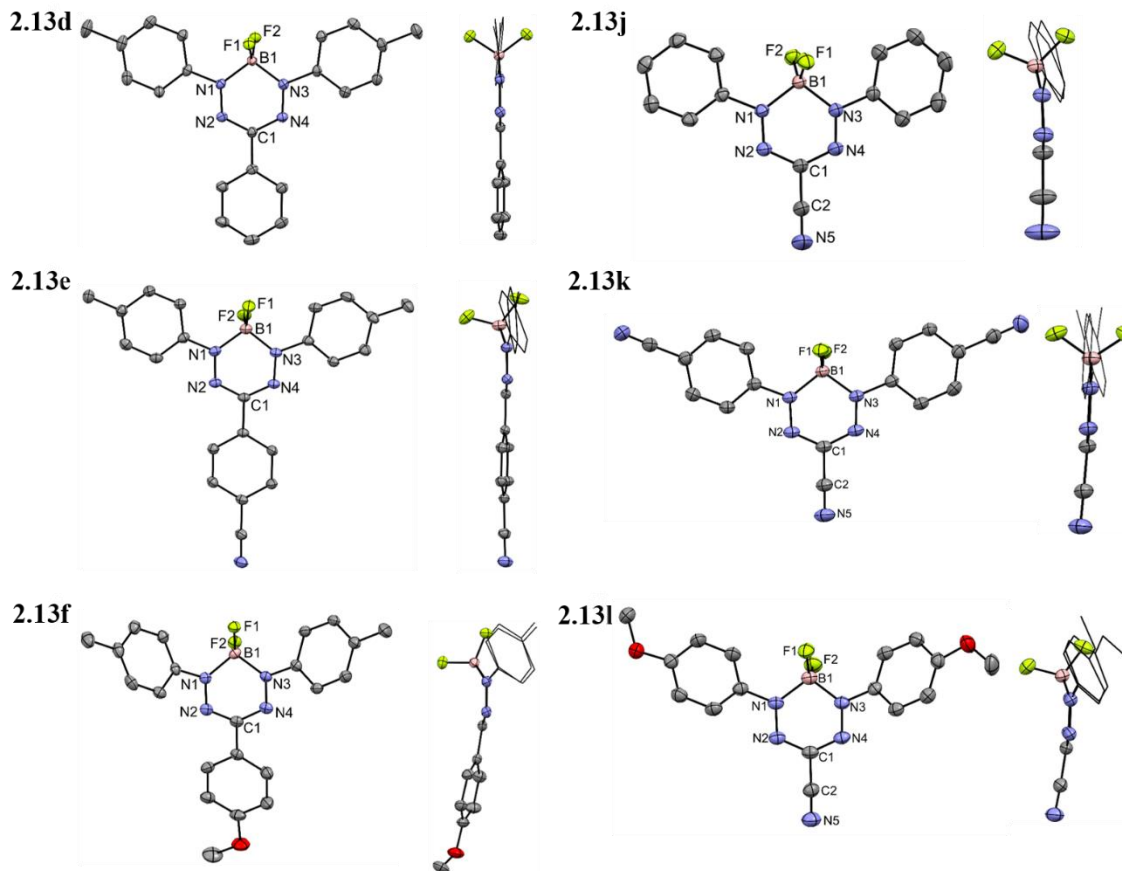


Figure 2.2. Solid-state structures - top view (left) and side view (right). Thermal ellipsoids are shown at 50% probability and hydrogen atoms are removed for clarity.

Table 2.2. Selected bond lengths (Å) and angles (degrees) for BF₂ formazanate complexes **2.13d–f** and **2.13j–l**, determined by X-ray diffraction.

	2.13d	2.13e	2.13f	2.13j	2.13k	2.13lA	2.13lB
N1–N2,	1.3117(18),	1.3012(17),	1.315(3),	1.2900(15),	1.3017(15),	1.307(2),	1.306(2),
N3–N4	1.3094(18)	1.3085(17)	1.315(3)	1.2948(15)	1.2945(15)	1.304(2)	1.302(2)
C1–N2,	1.339(2),	1.3431(19),	1.344(3),	1.3408(17),	1.3289(17),	1.340(3),	1.335(3),
C1–N4	1.346(2)	1.340(2)	1.338(3)	1.3379(17)	1.3382(17)	1.335(3)	1.340(3)
N1–B1,	1.561(2),	1.560(2),	1.551(4),	1.5748(18),	1.5714(18),	1.558(3),	1.563(3),
N3–B1	1.561(2)	1.576(2)	1.556(4)	1.5771(17)	1.5817(18)	1.567(3)	1.563(3)
N1–N2–C1,	118.84(13),	118.24(12),	117.2(2),	117.14(11),	117.28(11),	116.75(18),	116.21(17),
N3–N4–C1	118.78(13)	118.57(12)	117.3(2)	117.30(11)	117.76(11)	116.90(18)	116.21(17)
N2–C1–N4	126.66(14)	126.83(13)	124.6(2)	129.33(12)	129.41(11)	130.0(2)	129.32(18)
N1–B1–N3	106.28(12)	105.17(12)	101.68(19)	105.55(10)	105.65(10)	106.85(17)	104.75(16)
Boron displacement ^a	0.022	0.290	0.538	0.192	0.025	0.143	0.376
Dihedral angles ^b	7.20, 5.48,	25.52, 7.78	50.26,	18.10,	16.86, 4.71	15.28,	37.63,
	6.38	6.22	43.08, 17.20	25.41		21.37	36.62

^aDistance between B1 and N₄ plane. ^bAngles between the plane defined by the N1, N3 and C1 aryl substituents and the N₄ plane.

2.2.3 Absorption and Emission Spectroscopy

The optical properties of BF₂ complexes were explored in three different solvents using UV-vis absorption and emission spectroscopy (Table 2.3). Firstly we will discuss the spectral trends observed upon variation of the 1,5-substituents (phenyl, *p*-benzonitrile, *p*-anisole) in 3-aryl complexes **2.13a–c** (Figures 2.3, A2.32–A2.34). Each complex was highly absorbing between 450 and 600 nm, with wavelengths of maximum absorption (λ_{max}) in toluene of 523 nm ($\epsilon = 22,400 \text{ M}^{-1} \text{ cm}^{-1}$) for **2.13a**, 550 nm ($\epsilon = 20,500 \text{ M}^{-1} \text{ cm}^{-1}$) for **2.13b**, and 552 nm ($\epsilon = 28,200 \text{ M}^{-1} \text{ cm}^{-1}$) for **2.13c**. With the electron donating 1,5-(*p*-anisole) substituents in **2.13c**, the λ_{max} of **2.13c** was red shifted by *ca.* 25 nm with respect to the phenyl-substituted analog **2.13a**. The λ_{max} of the *p*-benzonitrile-substituted derivative, **2.13b**, was also red shifted relative to **2.13a**. Although this observation may seem counter intuitive, the same trend was observed for monosubstituted benzenes (Figure A2.35), and is likely caused by the extended conjugation of the cyano substituent. Each complex in the series **2.13a–c** was shown to be emissive, with wavelengths of maximum emission (λ_{em}) of 639 nm, 674 nm and 686 nm, respectively in toluene. The trends observed for the emission spectra mirrored those observed for the absorption spectra. The observed Stokes shifts (ν_{ST}) were high, $\nu_{\text{ST}} = 116 \text{ nm}$ (**2.13a**), 124 nm (**2.13b**), and 134 nm (**2.13c**) in toluene, and quantum yields (Φ_{F}) were calculated to be between 0.5% and 5.0% and were highest in electron-donating *p*-anisole-substituted **2.13c**.

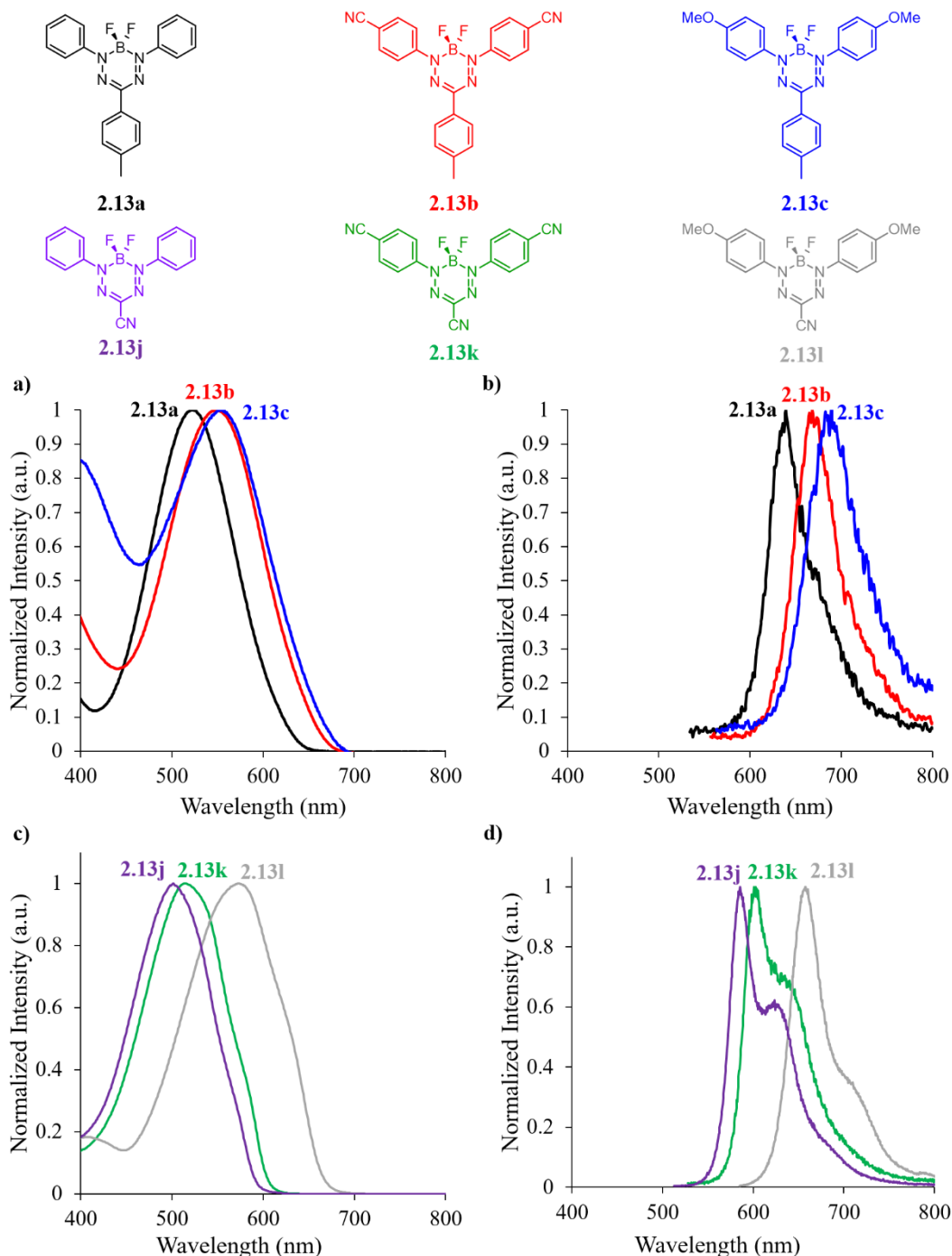


Figure 2.3. UV-vis absorption spectra (a) and emission spectra (b) of **2.13a** (black), **2.13b** (red) and **2.13c** (blue) and absorption (c) and emission (d) spectra of **2.13j** (purple), **2.13k** (green) and **2.13l** (grey) recorded for 10^{-5} M degassed toluene solutions.

Complexes **2.13d–f** were studied in order to assess the influence of the same series of aryl substituents at the 3-position of the formazanate framework (Figures A2.36–A2.38, Table

2.3). Similar to compounds **2.13a–c**, all three complexes were highly absorbing between 450 and 600 nm, with high molar absorptivities at their respective λ_{\max} in toluene [**2.13d**: $\lambda_{\max} = 524$ nm ($\epsilon = 30,300$ M⁻¹ cm⁻¹); **2.13e**: $\lambda_{\max} = 525$ nm ($\epsilon = 25,300$ M⁻¹ cm⁻¹); **2.13f**: $\lambda_{\max} = 544$ nm ($\epsilon = 25,800$ M⁻¹ cm⁻¹)]. Again, the λ_{\max} for the 3-(*p*-anisole)-substituted derivative (**2.13f**), was significantly red shifted with respect to the phenyl-substituted complex (**2.13d**), but unlike the **2.13a–c** series, a red shift in λ_{\max} was not observed for complex **2.13e** (Ar³ = *p*-C₆H₄-CN). The observed trend was similar for the emission spectra of complexes **2.13d–f**, where the λ_{em} for **2.13f** (Ar³ = *p*-C₆H₄-OMe, $\lambda_{\text{em}} = 669$ nm) was red shifted relative to the λ_{em} for **2.13d** (Ar³ = C₆H₅, $\lambda_{\text{em}} = 640$ nm). However, a blue shift in λ_{em} for the electron withdrawing *p*-benzointrile-substituted complex **2.13e** ($\lambda_{\text{em}} = 634$ nm) was observed relative to **2.13d**. The Stokes shifts for complexes **2.13d–f** were again substantial (110–135 nm), and the calculated quantum yields ranged from 0.5 to 2.0%, with the 3-(*p*-benzointrile)-substituted BF₂ complex (**2.13e**) exhibiting the highest quantum yield in toluene.

Thirdly, we studied the optical properties of asymmetrically-substituted 3-aryl substituted complexes **2.13g–i**, which contain *p*-anisole, *p*-benzointrile and *p*-tolyl substituents in three different arrangements (Figures A2.39–A2.41, Table 2.3). All three absorbed visible light between 450 and 650 nm, and had λ_{\max} values of 561 nm ($\epsilon = 24,400$ M⁻¹ cm⁻¹), 560 nm ($\epsilon = 21,500$ M⁻¹ cm⁻¹) and 541 nm ($\epsilon = 25,100$ M⁻¹ cm⁻¹), respectively. In toluene, their λ_{em} values were 666 nm (**2.13g**), 672 nm (**2.13h**) and 651 nm (**2.13i**). These complexes also exhibited high Stokes shifts between 105 and 128 nm and calculated quantum yields of 8.7% for **2.13g**, 5.3% for **2.13h** and 9.8% for **2.13i**.

Finally, we studied the effect of changing the 3-aryl substituent to a withdrawing 3-cyano substituent in complexes **2.13j–l**. Each complex shows strong, substituent-dependent absorption with λ_{\max} values increasing from 502 nm (**2.13j**) to 515 nm (**2.13k**) to 572 nm (**2.13l**) in toluene (Figures 2.3, A2.42–A2.44). We note that similarly to complexes **2.13a** and **2.13b** the UV-vis and emission spectra of **2.13k** (R = CN) are red-shifted relative to **2.13j** (R = H) and is likely caused by the extended conjugation of the cyano substituent, which is observed in the DFT calculated HOMO (Figure A2.52). The 3-cyanoformazan ligands **2.13j–l** are non-emissive across a broad concentration range in THF, CH₂Cl₂ and toluene. Under similar conditions, BF₂ complexes **2.13j–l** are highly emissive in the visible

region, with λ_{em} of 586 nm ($\Phi_F = 15\%$, $v_{ST} = 84$ nm), 598 nm ($\Phi_F = 14\%$, $v_{ST} = 83$ nm) and 656 nm ($\Phi_F = 77\%$, $v_{ST} = 84$ nm) observed in toluene for **2.13j–l**, respectively. The 3-cyano substituted BF₂ formazanate complexes exhibit significantly higher tunability based on the 1,5 substituents, and also exhibit higher quantum yields than the 3-aryl analogs, however they exhibit smaller Stokes shifts.

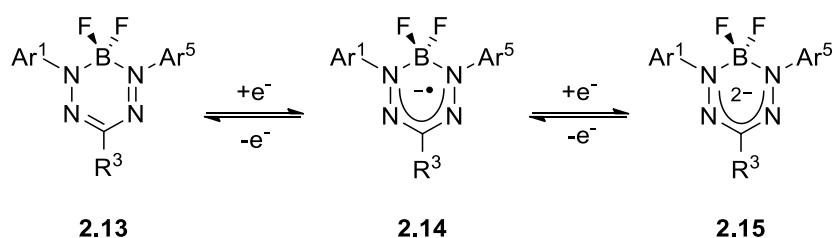
Table 2.3. Optical properties of BF₂ formazanate complexes **2.13a–l**.

Compound	Solvent	λ_{max} (nm)	ϵ (M ⁻¹ cm ⁻¹)	λ_{em} (nm)	Φ_F (%) ^a	v_{ST} (cm ⁻¹)	v_{ST} (nm)
2.13a	THF	517	21,700	641	0.5	3,740	124
	CH ₂ Cl ₂	518	24,700	641	0.8	3,705	123
	Toluene	523	22,400	639	0.7	3,470	116
2.13b	THF	541	22,800	673	1.5	3,625	132
	CH ₂ Cl ₂	545	24,500	678	0.9	3,600	133
	Toluene	550	20,500	674	2.1	3,345	124
2.13c	THF	545	22,300	692	1.5	3,900	147
	CH ₂ Cl ₂	544	29,300	690	2.4	3,890	146
	Toluene	552	28,200	686	5.0	3,540	134
2.13d	THF	520	29,300	641	0.6	3,630	121
	CH ₂ Cl ₂	520	36,600	640	0.5	3,610	120
	Toluene	524	30,300	640	0.9	3,460	116
2.13e	THF	521	33,800	631	0.9	3,350	110
	CH ₂ Cl ₂	521	36,600	631	0.7	3,350	110
	Toluene	525	25,300	634	2.0	3,275	109
2.13f	THF	539	24,600	674	1.1	3,715	135
	CH ₂ Cl ₂	539	25,200	673	1.1	3,695	134
	Toluene	544	25,800	669	1.4	3,435	125
2.13g	THF	552	30,100	667	5.4	3,125	115
	CH ₂ Cl ₂	553	27,500	666	6.2	3,070	113
	Toluene	561	24,400	666	8.7	2,810	105
2.13h	THF	553	22,500	674	4.1	3,245	121
	CH ₂ Cl ₂	553	24,500	676	3.8	3,290	123
	Toluene	560	21,500	672	5.3	2,975	112
2.13i	THF	535	32,500	651	6.4	3,330	116
	CH ₂ Cl ₂	534	33,900	651	5.8	3,365	117
	Toluene	541	25,100	651	9.8	3,125	110
2.13j	THF	489	25,400	585	5.1	3,356	96
	CH ₂ Cl ₂	491	34,600	584	9.2	3,243	93
	Toluene	502	30,400	586	15.0	2,855	84
2.13k	THF	497	22,600	590	12.2	3,172	93
	CH ₂ Cl ₂	499	22,400	589	16.7	3,062	90
	Toluene	515	35,000	598	14.3	2,695	84
2.13l	THF	556	33,400	662	45.7	2,880	106
	CH ₂ Cl ₂	558	35,300	661	65.3	2,793	103
	Toluene	572	42,700	656	77.0	2,239	84

^aQuantum yields were estimated according to published protocols using ruthenium tris(bipyridine) hexafluorophosphate as a relative standard and corrected for wavelength-dependent detector sensitivity (Figure A2.45).^[57,58]

2.2.4 Cyclic Voltammetry

The substituent effects for complexes **2.13a–l** were studied by cyclic voltammetry (CV), referenced to the ferrocene/ferrocenium redox couple. Each complex exhibited two ligand-centred reversible (or quasi-reversible) one-electron reduction waves corresponding to the production of their radical anion (**2.14**) and dianion (**2.15**) forms (Scheme 2.3, Figures 2.4, A2.46–A2.48, Table 2.4). Most of the complexes studied also exhibited irreversible oxidation events in their CVs within the electrochemical window of acetonitrile (Figures A2.49–A2.52).



Scheme 2.3. Stepwise reduction of triarylformazanate BF₂ complexes.

Again we begin by discussing the 1,5-substituted complexes **2.13a–c** (Figure A2.48). Phenyl-substituted complex **2.13a** was reversibly reduced at $E_{\text{red1}} = -830$ mV and $E_{\text{red2}} = -1870$ mV. The introduction of electron withdrawing *p*-benzonitrile substituents in complex **2.13b** substantially decreased the potential required for reduction to $E_{\text{red1}} = -500$ mV and $E_{\text{red2}} = -1470$ mV. Electron rich, *p*-anisole-substituted complex **2.13c** was more difficult to reduce than **2.13a,b**, with reduction waves observed at $E_{\text{red1}} = -970$ mV and $E_{\text{red2}} = -1940$ mV. All 3 complexes have a difference in reduction potentials (ΔE) of approximately 1000 mV.

The trends observed for the 3-substituted formazanate complexes **2.13d–f** were not obvious. The phenyl-substituted derivative was reduced at potentials of $E_{\text{red1}} = -920$ mV and $E_{\text{red2}} = -1930$ mV, while *p*-benzonitrile-substituted complex **2.13e** was easier to reduce ($E_{\text{red1}} = -830$ mV and $E_{\text{red2}} = -1920$ mV). Unexpectedly, *p*-anisole-substituted complex **2.13f** was also slightly easier to reduce than **2.13d** at $E_{\text{red1}} = -900$ mV and $E_{\text{red2}} = -1890$ mV. Similar to complexes **2.13a–c**, the ΔE of **2.13d–f** were approximately 1000 mV.

Interestingly, **2.13e** also exhibits a third reversible reduction wave within the solvent window, perhaps due to the formation of a radical trianion (Figure A2.49).

For the series of asymmetrically-substituted BF₂ complexes **2.13g–i**, the 1,5-substituents had the most significant effect on their electrochemical reduction. Complex **2.13g**, bearing *p*-anisole and *p*-benzotrile substituents at the 1,5-positions, was reversibly reduced at $E_{\text{red1}} = -720$ mV and $E_{\text{red2}} = -1740$ mV. Interchanging the electron donating *p*-anisole substituent with a weakly donating *p*-tolyl group in complex **2.13h** decreased the reduction potentials by *ca.* 30 mV to $E_{\text{red1}} = -690$ mV and $E_{\text{red2}} = -1720$ mV. Complex **2.13i** has two donating *N*-substituents (*p*-anisole and *p*-tolyl), and thus was the most difficult to reduce, at $E_{\text{red1}} = -860$ mV and $E_{\text{red2}} = -1940$ mV. The ΔE for these complexes were 1020 mV for **2.13g**, 1030 mV for **2.13h**, and 1080 mV for **2.13i**.

All of the expected trends were observed in the electrochemical studies of the 3-cyanoformazante BF₂ complexes **2.13j–l**. Each complex exhibited two fully reversible reduction waves (Figure 2.4) but only **2.13l** gave rise to an irreversible oxidation event within the electrochemical window of acetonitrile (Figure A2.52). As with **2.13a–c**, the reduction potentials followed the expected trend based on the *para*-substituent introduced at the aryl rings. BF₂ complex **2.13j** (R = H) is reduced to a radical anion and then a dianion at -0.53 V and -1.68 V against the ferrocene/ferrocenium redox couple, while **2.13k** (R = CN) was reduced at -0.21 V and -1.25 V and **2.13l** (R = OMe) was reduced at -0.68 V and -1.82 V. Due to the electron withdrawing nature of the 3-cyano substituent, all three complexes were significantly easier to reduce (*ca.* 300 mV) than their 3-aryl substituted analogs.

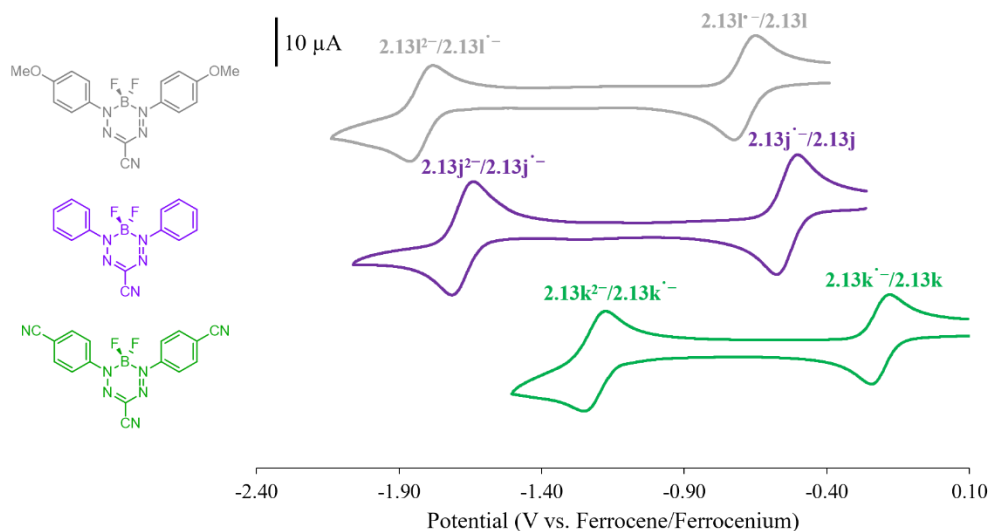


Figure 2.4. Cyclic voltammograms of **2.13j** (purple), **2.13k** (green), and **2.13l** (grey) recorded at 100 mV s^{-1} in 1 mM acetonitrile solutions containing 0.1 M $[n\text{Bu}_4\text{N}][\text{PF}_6]$ as supporting electrolyte.

Table 2.4. Electrochemical data (mV vs. Fc/Fc^+) for BF_2 formazanate complexes **2.13a–l**.

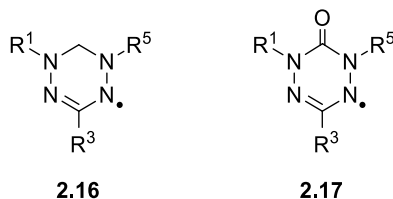
	E_{red1}^a (mV)	E_{red2}^a (mV)	ΔE^b (mV)
2.13a	−840	−1870	1030
2.13b	−500	−1470	970
2.13c	−970	−1940	970
2.13d	−920	−1930	1010
2.13e	−830	−1920	1090
2.13f	−900	−1890	990
2.13g	−720	−1740	1020
2.13h	−690	−1720	1030
2.13i	−860	−1940	1080
2.13j	−530	−1680	1150
2.13k	−210	−1250	1040
2.13l	−680	−1820	1140

^aCyclic voltammetry experiments were conducted in CH_3CN containing 1 mM analyte and 0.1 M $[n\text{Bu}_4\text{N}][\text{PF}_6]$ as supporting electrolyte at a scan rate of 250 mV s^{-1} . Voltammograms were referenced internally against the ferrocene/ferrocenium redox couple. ^bDefined as the difference between E_{red1} and E_{red2} .

2.3 Discussion

Through inspection of the electrochemical and optical spectroscopy data collected for complexes **2.13a–f**, it is clear that the 1,5-substituents have a more pronounced effect on the properties observed in triaryl formazanate BF_2 complexes. For the series **2.13a–c**,

predictable trends in reduction potentials based on the electron donating/withdrawing character of the *N*-aryl substituents were observed, including a shift of *ca.* 500 mV in the reduction potentials (E_{red1} and E_{red2}) upon switching from *p*-benzonitrile to *p*-anisole 1,5-substituents. For **2.13d–f**, the observed trend is not easily rationalized, as the electron-rich 3-(*p*-anisole) derivative was easier to reduce than the 3-phenyl analog. Similarly, the absorption and emission properties of **2.13a–f** were much more sensitive to the 1,5-substituents than the 3-substituents. These trends are similar to those observed for Kuhn-type verdazyls **2.16** and 6-oxoverdazyls **2.17**, where the singly occupied molecular orbital (π -SOMO) is centered on the four nitrogen atoms, and contains very little electron density at the 3-position of the heterocyclic ring due to the presence of a nodal plane.^{[55],[59]} The LUMOs of the 3-cyanoformazanate BF₂ complexes **2.13j–l** were shown to possess very similar features,^[52] and so similarly, the LUMOs of the triarylformazanate BF₂ complexes described are not expected to differ significantly from each other.



Breaking the symmetry in derivatives **2.13g–i** did not result in significant changes in electrochemical or absorption properties relative to symmetrically-substituted analogs **2.13a–f**. However, a modest enhancement in quantum yields was observed for all three substituent configurations. This enhancement of emission intensity is consistent with trends observed for asymmetrically substituted BODIPYs^[60–65] and other BF₂ complexes of *N*-donor ligands.^[66–69]

While varying the *para*-substituent on the 3-aryl ring had little effect on the properties of the resulting complexes, directly changing the 3-aryl substituent to an electron withdrawing cyano group had a significant effect on the properties. The more electron poor derivatives **2.13j–l** were much easier to reduce and had significantly higher fluorescence quantum yields.

For all of the complexes studied (**2.13a–i**), the fluorescence intensities, and thus quantum yields, were higher in toluene than THF or CH₂Cl₂. This effect may arise due to the

stabilization of polar excited states, by polar solvents, potentially allowing for competing deactivation pathways to operate.^[70]

2.4 Applications

2.4.1 Electrochemiluminescence

Electrochemiluminescence (ECL) involves the generation of light from an electrochemically excited species. Boron difluoride complexes of formazanate ligands provide an attractive choice as an electrochemiluminescent material due to their inexpensive and straightforward synthesis. The BF₂ complex of *p*-aniso substituted 3-cyanoformazanate **2.131** was chosen due to its high fluorescence quantum yield, and well-behaved electrochemical properties. It was found that in the presence of a tripropyl amine (TPrA) coreactant, electrochemiluminescence was obtained at 724 nm (Figure 2.5). At a scan rate of 200 mV s⁻¹, the ECL efficiency was found to be 4.5 times higher than the benchmark Ru(bpy)₃/TPrA system.^[71]

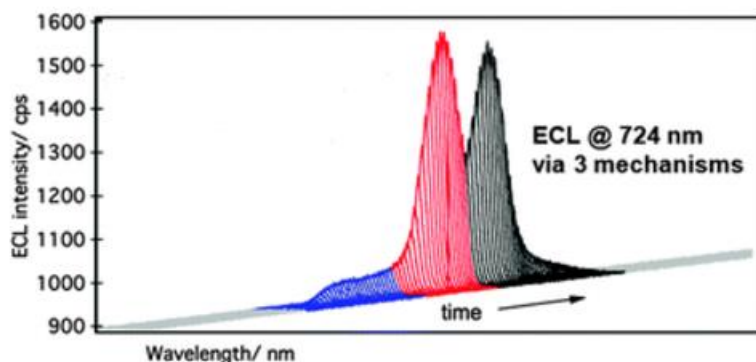


Figure 2.5. Spooling ECL spectra of **2.131** in the presence of TPrA acquired over a time interval of 1s. The blue and red spectra represent the forward scan and the black spectra represent the reverse scan.

2.4.2 Cell Imaging

The same *p*-aniso substituted BF₂ complex **2.131** proved to be an excellent candidate for use in cell-imaging studies, due to its high quantum yield and emission approaching the near-IR. It was found that dye **2.131** localized within the cytoplasm of mouse fibroblast cells. Due to the low energy of the emission, **2.131** is ideally suited for orthogonal imaging applications. This was achieved by using 4'6-diamidino-2-phenylindole (DAPI), which is a nuclear stain that emits in the blue region. Using this combination, the cytoplasm and nucleus of the mouse fibroblast cells could be imaged simultaneously and orthogonally.^[72]

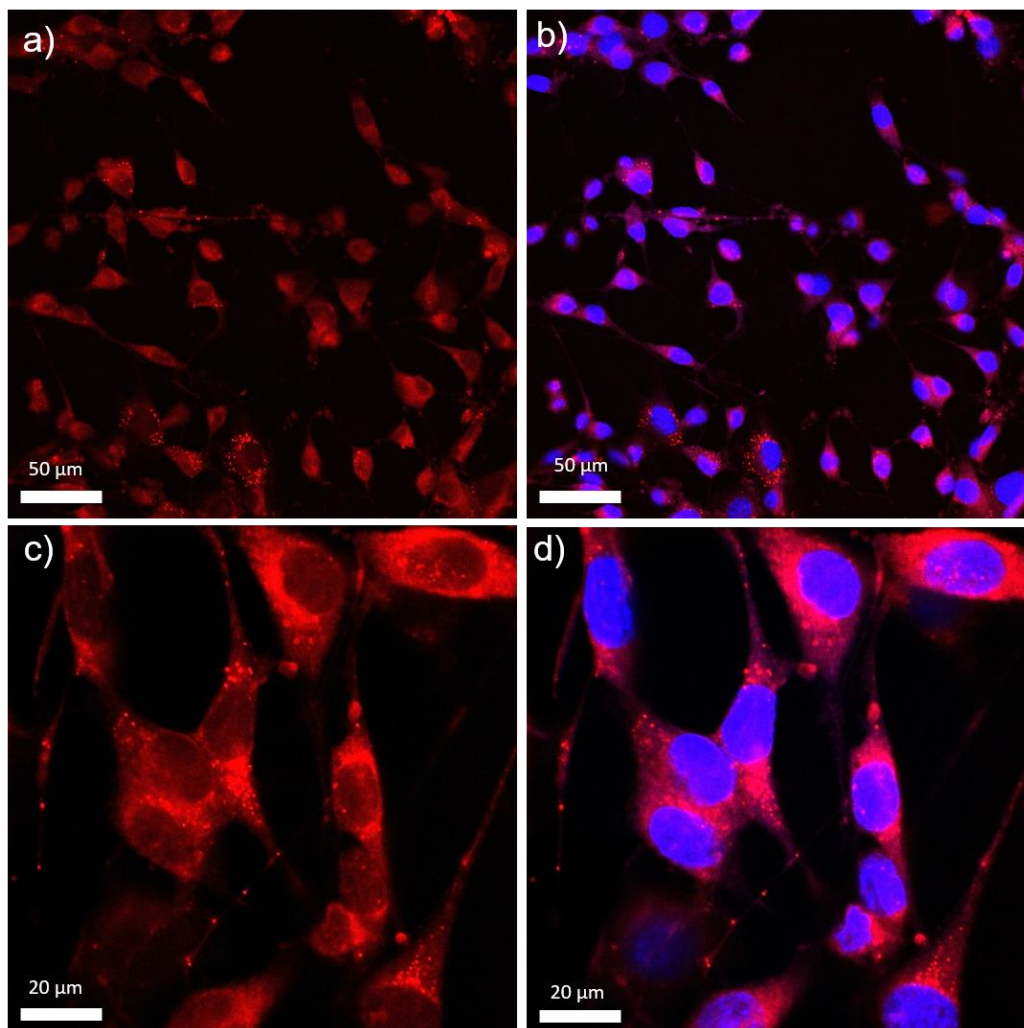


Figure 2.6. Confocal fluorescent micrographs of mouse fibroblast cells stained with BF₂ formazanate complex **2.131** and DAPI. Images (a) and (b) were visualized with excitation at 559 nm and emission collected between 625–725 nm. Images (c) and (d) are an overlay of images (a) and (b) with those obtained from excitation at 405 nm and emission collected between 425–475 nm.

2.5 Conclusions

In conclusion, we have demonstrated a straightforward synthetic route to a series of twelve formazanate boron difluoride complexes allowing for studies of their substituent-dependent properties to be conducted. We have shown that the properties of these complexes, including their wavelengths of maximum absorption and emission, quantum yields, and electrochemical properties can be tuned by the introduction of electron-donating (*p*-anisole) or electron-withdrawing (*p*-benzotrile) aryl substituents at the formazanate ligand backbone. Changes in the properties of BF₂ complexes of triaryl

formazanates were more dramatic when 1,5-substituents were varied compared to similar structural variations at the 3-position of the formazanate backbone, and were most dramatic when varying the 1,5-substituent on the 3-cyanoformazanate derivatives. Modest enhancements in emission intensity of triarylformazanate BF₂ complexes were observed for asymmetrically-substituted complexes, which exhibited quantum yields close to 10%. 3-cyanoformazanate BF₂ complexes exhibited significantly higher quantum yields, reaching up to 77%. Finally, it was demonstrated that the 3-cyanoformazanate BF₂ complex with *p*-anisole *N*-aryl substituents was effective for use both as an electrochemiluminescent emitter, and for orthogonal cell imaging applications.

2.6 Experimental

2.6.1 General Considerations

Reactions and manipulations were carried out under a nitrogen atmosphere using standard Schlenk techniques unless otherwise stated. Solvents were obtained from Caledon Laboratories, dried using an Innovative Technologies Inc. solvent purification system, collected under vacuum, and stored under a nitrogen atmosphere over 4 Å molecular sieves. Reagents were purchased from Sigma-Aldrich or Alfa Aesar and used as received. Formazans **2.8a–l** were synthesized according to previously published procedures, and the characterization data for **2.8a–f**, **2.8j** and **2.8l** were consistent with the same reports.^[47,55] NMR Spectra were recorded on a 400 MHz (¹H: 399.8 MHz, ¹¹B: 128.3 MHz, ¹⁹F: 376.1 MHz) or 600 MHz (¹H: 599.5 MHz, ¹³C: 150.8 MHz) Varian INOVA instrument or a 400 MHz (¹³C: 100.6 MHz) Varian Mercury Instrument. ¹H NMR spectra were referenced to residual CHCl₃ (7.27 ppm) and ¹³C NMR spectra were referenced to CDCl₃ (77.2 ppm). ¹¹B spectra were referenced to BF₃·OEt₂ at 0 ppm, and ¹⁹F spectra were referenced to CFCl₃ at 0 ppm. Mass spectrometry data was recorded in positive-ion mode using a high resolution Finnigan MAT 8400 spectrometer using electron impact ionization. UV-vis spectra were recorded using a Cary 300 Scan instrument. Four separate concentrations were run for each sample, and molar extinction coefficients were determined from the slope of a plot of absorbance against concentration. Infrared spectra were recorded on a KBr disk using a Bruker Vector 33 FT-IR spectrometer. Emission spectra were obtained using a Photon Technology International QM-4 SE spectrofluorometer. Excitation wavelengths

were chosen based on λ_{\max} from the respective UV-vis absorption spectrum in the same solvent. Quantum yields were estimated relative to ruthenium tris(bipyridine) hexafluorophosphate by previously described methods and corrected for wavelength dependent detector sensitivity (Figure A2.33).^[57-58] Elemental analyses (C, H, N) were carried out by Laboratoire d'Analyse Élémentaire de l'Université de Montréal, Montréal, QC, Canada.

2.6.2 Electrochemical Methods

Cyclic voltammetry experiments were performed with a Bioanalytical Systems Inc. (BASi) Epsilon potentiostat and analyzed using BASi Epsilon software. Electrochemical cells consisted of a three-electrode setup including a glassy carbon working electrode, platinum wire counter electrode, and silver wire *pseudo* reference electrode. Experiments were run at scan rates of 250 mV s⁻¹ in degassed acetonitrile solutions of the analyte (~1 mM) and supporting electrolyte (0.1 M [*n*Bu₄N][PF₆]). Cyclic voltammograms were referenced against an internal standard (~1 mM ferrocene) and corrected for internal cell resistance using the BASi Epsilon software.

2.6.3 X-ray Crystallography Details

Single crystals of complexes **2.13d–f** and **2.13j–l** suitable for X-ray diffraction studies were grown by slow evaporation of a concentrated solution of each compound in CH₂Cl₂. The samples were mounted on a MiTeGen polyimide micromount with a small amount of Paratone *N* oil. All X-ray measurements were made on a Bruker Kappa Axis Apex2 diffractometer at a temperature of 110 K. The data collection strategy included a number of ω and ϕ scans which collected data over a range of angles, 2θ . The frame integration was performed using SAINT.^[73] The resulting raw data was scaled and absorption corrected using a multi-scan averaging of symmetry equivalent data using SADABS.^[74] The structures were solved by direct methods using the XS program.^[75] All non-hydrogen atoms were obtained from the initial solution. The hydrogen atoms were introduced at idealized positions and were allowed to refine isotropically. The structural model was fit to the data using full matrix least-squares based on F^2 . The calculated structure factors included corrections for anomalous dispersion from the usual tabulation. The structure was refined using the SHELXL-2014 program from SHELXTL.^[76] For complex **2.13f**, a fractional dichloromethane solvent was present which could not be modelled reliably, so it

was treated with the squeeze procedure in Platon.^[77] See Table 2.5 for additional crystallographic data.

Table 2.5. X-ray diffraction data collection and refinement details for complexes **2.13d–f** and **2.13j–l**.

	2.13d	2.13e	2.13f	2.13j	2.13k	2.13l
Chemical Formula	C ₂₁ H ₁₉ BF ₂ N ₄	C ₂₂ H ₁₈ BF ₂ N ₅	C ₂₂ H ₂₁ BF ₂ N ₄ O	C ₁₄ H ₁₀ BF ₂ N ₅	C ₁₆ H ₉ BF ₂ N ₇	C ₁₆ H ₁₄ BF ₂ N ₅ O ₂
FW (g mol ⁻¹)	376.21	401.22	406.24	297.08	348.11	357.13
Crystal Habit	Red plate	Green rectangular	Red needle	Red plate	Red plate	Purple needle
Crystal System	Monoclinic	Monoclinic	Triclinic	Triclinic	Monoclinic	Orthorhombic
Space Group	<i>P</i> 2 ₁ / <i>n</i>	<i>P</i> 2 ₁ / <i>c</i>	<i>P</i> $\bar{1}$	<i>P</i> $\bar{1}$	<i>P</i> 2 ₁ / <i>c</i>	<i>P</i> 2 ₁ 2 ₁ 2 ₁
T (K)	113(2)	110	110	200	200	200
λ (Å)	0.71073	0.71073	0.71073	0.71073	0.71073	0.71073
<i>a</i> (Å)	9.7298(10)	16.818(7)	10.362(6)	9.1735(14)	17.220(9)	7.897(5)
<i>b</i> (Å)	18.713(2)	16.188(5)	28.120(17)	9.573(2)	6.729(4)	19.905(9)
<i>c</i> (Å)	10.3804(12)	7.257(3)	28.16(2)	16.289(4)	14.760(7)	20.920(10)
α (deg)	90	90	117.075(13)	96.419(11)	90	90
β (deg)	97.825(6)	99.220(18)	96.626(17)	93.695(10)	114.342(13)	90
γ (deg)	90	90	98.667(16)	105.880(13)	90	90
<i>V</i> (Å ³)	1872.4(4)	1950.0(13)	7062(8)	1360.5(5)	1558.2(14)	3288(3)
<i>Z</i>	4	4	12	2	4	8
ρ (g/cm ³)	1.335	1.367	1.146	1.450	1.484	1.443
μ (cm ⁻¹)	0.094	0.097	0.083	0.0	0.112	0.113
<i>R</i> ₁ , ^a <i>wR</i> ₂ ^b	0.0711,	0.0599,	0.0669,	0.0416,	0.0421,	0.0447,
[<i>I</i> > 2 σ]	0.1511	0.1676	0.1625	0.1062	0.1072	0.0747
<i>R</i> ₁ , <i>wR</i> ₂	0.2110,	0.0826,	0.1407,	0.0699,	0.0623,	0.0971,
(all data)	0.2048	0.1835	0.1849	0.1231	0.1200	0.0885
GOF ^c	0.977	1.035	1.122	1.029	0.969	1.008

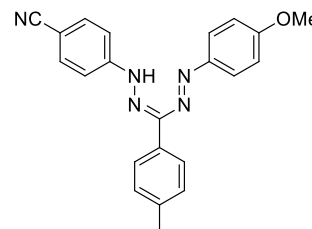
^a*R*₁ = $\Sigma(|F_o| - |F_c|) / \Sigma F_o$, ^b*wR*₂ = $[\Sigma(w(F_o^2 - F_c^2)^2) / \Sigma(wF_o^4)]^{1/2}$, ^cGOF = $[\Sigma(w(F_o^2 - F_c^2)^2) / (\text{No. of reflns.} - \text{No. of params.})]^{1/2}$

Representative procedure: triarylformazan **2.8g**

In air, 4-cyanophenyl hydrazine hydrochloride (1.50 g, 8.80 mmol) was dissolved in EtOH (15 mL) containing NEt₃ (1.60 g, 2.21 mL, 15.8 mmol). *p*-Tolualdehyde (1.06 g, 1.04 mL, 8.80 mmol) was then added and the solution was stirred for 10 min.

After this time, a light yellow precipitate had formed. CH₂Cl₂

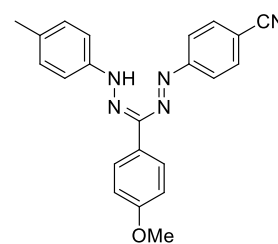
(50 mL) and water (50 mL) were added to form a biphasic reaction mixture. Sodium carbonate (3.17 g, 29.9 mmol) and [*n*Bu₄N][Br] (0.28 g, 0.88 mmol) were added, and the mixture was cooled in an ice bath to 0 °C. In a separate flask, *p*-anisidine (1.11 g, 9.00



mmol) and concentrated HCl (3.6 mL, 43.2 mmol) were mixed in water (20 mL), and cooled in an ice bath. A cooled solution of sodium nitrite (0.69 g, 10 mmol) was added slowly to the aniline solution. This mixture was stirred at 0 °C for 30 min, after which time it was added dropwise to the biphasic reaction mixture described above over 10 min. The resulting solution was stirred for 18 h, gradually turned dark red over this time. The dark red organic fraction was then washed with deionized water (3 x 50 mL), dried over MgSO₄, gravity filtered and concentrated *in vacuo*. The resulting residue was purified by flash chromatography (dichloromethane, neutral alumina) to yield formazan **2.8g** as a dark red microcrystalline solid. Yield = 2.40 g, 74%. Melting point = 154–156 °C. ¹H NMR (599.5 MHz, CDCl₃) δ 14.26 (s, 1H, NH), 7.96 (d, ³J_{HH} = 8 Hz, 2H, aryl CH), 7.93 (d, ³J_{HH} = 9 Hz, 2H, aryl CH), 7.60 (d, ³J_{HH} = 8 Hz, 2H, aryl CH), 7.40 (d, ³J_{HH} = 8 Hz, 2H, aryl CH), 7.26 (d, ³J_{HH} = 8 Hz, 2H, aryl CH), 7.06 (d, ³J_{HH} = 9 Hz, 2H, aryl CH), 3.93 (s, 3H, OCH₃), 2.42 (s, 3H, CH₃). ¹³C{¹H} NMR (100.6 MHz, CDCl₃): δ 163.4, 147.5, 146.9, 143.0, 138.6, 133.8, 133.7, 129.3, 126.7, 124.8, 119.7, 114.9, 114.7, 104.7, 55.9, 21.5. FT-IR (KBr): 3420 (s), 3067 (m), 2918 (m), 2841 (m), 2219 (m), 1603 (s), 1509 (s), 1257 (s), 1231 (m), 1143 (m) cm⁻¹. UV-vis (toluene): λ_{max} = 489 nm (ε = 28,300 M⁻¹ cm⁻¹). Mass Spec. (EI, +ve mode): exact mass calculated for [C₂₂H₁₉N₅O]⁺: 369.1590; exact mass found: 369.1598; difference: +2.3 ppm. Anal. Calcd. (%) for C₂₂H₁₉N₅O: C, 71.53; H, 5.18; N, 18.96. Found: C, 71.43; H, 5.00; N, 18.76.

Formazan 2.8h

From 12.6 mmol of *p*-tolyl hydrazine hydrochloride/aldehyde: Yield = 3.74 g, 80%. Melting point = 156–158 °C. ¹H NMR (599.5 MHz, CDCl₃) δ 14.37 (s, 1H, NH), 8.02 (d, ³J_{HH} = 9 Hz, 2H, aryl CH), 7.82 (d, ³J_{HH} = 8 Hz, 2H, aryl CH), 7.60 (d, ³J_{HH} = 9 Hz, 2H, aryl CH), 7.38 (d, ³J_{HH} = 9 Hz, 2H, aryl CH), 7.35 (d, ³J_{HH} = 8 Hz, 2H, aryl CH), 6.98 (d, ³J_{HH} = 8 Hz, 2H, aryl CH), 3.88 (s, 3H, OCH₃), 2.47 (s, 3H, CH₃). ¹³C{¹H} NMR (100.6 MHz, CDCl₃): δ 160.2, 150.4, 147.5, 143.3, 142.6, 133.7, 130.3, 129.1, 128.1, 122.6, 119.7, 114.9, 114.0, 104.9, 55.5, 21.8. FT-IR (KBr): 3421 (s), 3003 (m), 2935 (m), 2840 (m), 2219 (s), 1603 (s), 1508 (s), 1248 (s), 1228 (s), 1170 (s) cm⁻¹. UV-vis (toluene): λ_{max} = 501 nm (ε = 16,800 M⁻¹ cm⁻¹). Mass Spec. (EI, +ve mode): exact mass calculated for [C₂₂H₁₉N₅O]⁺: 369.1590; exact mass found: 369.1592; difference: +0.7



ppm. Anal. Calcd. (%) for $C_{22}H_{19}N_5O$: C, 71.53; H, 5.18; N, 18.96. Found: C, 71.95; H, 5.17; N, 18.23.

Formazan 2.8i

From 12.6 mmol of *p*-tolyl hydrazine hydrochloride/aldehyde:

Yield = 3.34 g, 72%. Melting point = 179–181 °C. 1H NMR (599.5

MHz, $CDCl_3$) δ 15.61 (s, 1H, NH), 8.19 (d, $^3J_{HH} = 8$ Hz, 2H, aryl

CH), 7.76 (d, $^3J_{HH} = 9$ Hz, 2H, aryl CH), 7.66 (d, $^3J_{HH} = 8$ Hz, 2H,

aryl CH), 7.38 (d, $^3J_{HH} = 8$ Hz, 2H, aryl CH), 7.20 (d, $^3J_{HH} = 8$ Hz,

2H, aryl CH), 7.01 (d, $^3J_{HH} = 9$ Hz, 2H, aryl CH), 3.90 (s, 3H, OCH_3), 2.37 (s, 3H, CH_3).

$^{13}C\{^1H\}$ NMR (100.6 MHz, $CDCl_3$): δ 161.4, 144.6, 142.2, 142.2, 138.7, 135.6, 132.1,

130.1, 125.6, 122.6, 119.5, 116.6, 114.7, 110.0, 55.7, 21.1. FT-IR (KBr): 3411 (s), 3003

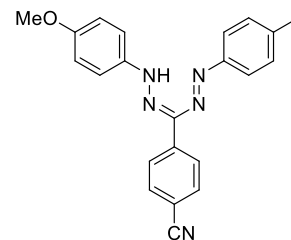
(m), 2918 (m) 2841 (m), 2222 (s), 1603 (s), 1499 (s), 1248 (s), 1189 (m), 1145 (m) cm^{-1} .

UV-vis (toluene): $\lambda_{max} = 506$ nm ($\epsilon = 22,400$ $M^{-1} cm^{-1}$). Mass Spec. (EI, +ve mode): exact

mass calculated for $[C_{22}H_{19}N_5O]^+$: 369.1590; exact mass found: 369.1602; difference: +3.3

ppm. Anal. Calcd. (%) for $C_{22}H_{19}N_5O$: C, 71.53; H, 5.18; N, 18.96. Found: C, 71.63; H,

5.14; N, 18.78.



Representative procedure: 3-cyanoformazan 2.8k

In air, cyanoacetic acid (0.85 g, 0.010 mol) was dissolved in deionized water (75 mL) containing NaOH (4.00 g, 0.100 mol).

This colourless solution was stirred for 45 min in an ice bath.

Meanwhile, 4-aminobenzonitrile (2.36 g, 0.020 mol) was mixed with concentrated HCl (5 mL, 0.060 mol) in deionized water (30 mL). This solution was cooled in an ice bath for 10

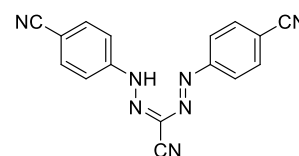
min before a solution of sodium nitrite (1.48 g, 0.021 mmol) in deionized water (15 mL) was cooled in an ice bath, and then added slowly to the 4-aminobenzonitrile solution over

a ten min period. This mixture was stirred in an ice bath for 30 min, and then added slowly to the basic cyanoacetic acid solution. A dark red/orange colour persisted almost

immediately and a dark red/orange precipitate formed after a few min. The mixture was stirred in an ice bath for an additional 6 h before ethyl acetate (250 mL) was added and the

organic layer was isolated, then washed with deionized water (3×100 mL) and dried over $MgSO_4$, gravity filtered and concentrated *in vacuo*. The resulting residue was purified by

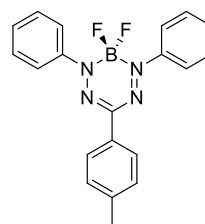
flash chromatography (CH_2Cl_2 , neutral alumina) to yield 3-cyanoformazan **2.8k** as a dark



orange solid. Yield = 2.63 g, 88%. Melting point = 230–240 °C (dec.). ^1H NMR (599.5 MHz, d_6 -DMSO) δ 13.19 (s, 1H, NH), 8.01 (m, 4H, AB spin system aryl CH) 7.87 (m, 4H, AB spin system, aryl CH). ^{13}C NMR (100.6 MHz, d_6 -DMSO): δ 149.5, 133.8, 120.7, 118.6, 112.0, 110.4, 96.0. FT-IR (KBr): 3461 (s), 2224 (m), 2112 (m), 1653 (s), 1540 (m), 1256 (s), 1169 (s) cm^{-1} . UV-vis (toluene): λ_{max} 423 nm ($\epsilon = 25,300 \text{ M}^{-1} \text{ cm}^{-1}$). Mass Spec. (EI, +ve mode): exact mass calculated for $\text{C}_{16}\text{H}_9\text{N}_7$: 299.0919; exact mass found: 299.0929; difference: +3.2 ppm. Anal. Calcd. (%) for $\text{C}_{16}\text{H}_9\text{N}_7$: C, 64.21; H, 3.03; N, 32.76. Found: C, 63.98; H, 2.79; N, 31.74.

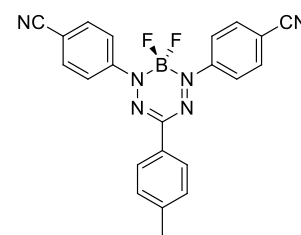
Representative procedure: formazanate BF_2 complex 2.13a

In air, formazan **2.8a** (1.00 g, 2.76 mmol) was dissolved in dry toluene (100 mL). NEt_3 (0.84 g, 1.2 mL, 8.3 mmol) was then added slowly and the solution was stirred for 10 min. $\text{BF}_3 \cdot \text{OEt}_2$ (1.96 g, 1.73 mL, 13.8 mmol) was then added by syringe, and the solution was heated at 80 °C for 18 h. The solution gradually turned from dark red to dark purple during this time. After cooling to 20 °C, deionized water (10 mL) was added to quench any excess reactive boron-containing compounds. The purple toluene solution was then washed with deionized water (3 x 50 mL), dried over MgSO_4 , gravity filtered and concentrated *in vacuo*. The resulting residue was purified by flash chromatography (CH_2Cl_2 , neutral alumina) to yield the BF_2 complex as a dark purple microcrystalline solid. Yield = 0.69 g, 60%. ^1H NMR (599.5 MHz, CDCl_3) δ 8.01 (d, $^3J_{\text{HH}} = 8 \text{ Hz}$, 2H, aryl CH), 7.91 (d, $^3J_{\text{HH}} = 7 \text{ Hz}$, 4H, aryl CH), 7.47 (m, 6H, aryl CH), 7.30 (d, $^3J_{\text{HH}} = 8 \text{ Hz}$, 2H, aryl CH), 2.44 (s, 3H, CH_3). These data were consistent with those reported by Otten and coworkers.¹⁴



Formazanate BF_2 complex 2.13b

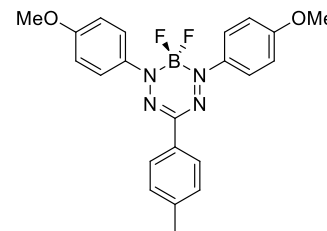
From 2.83 mmol of formazan: Yield = 0.18 g, 16%. Melting point = 169–171 °C. ^1H NMR (599.5 MHz, CDCl_3) δ 8.06 (d, $^3J_{\text{HH}} = 9 \text{ Hz}$, 4H, aryl CH), 7.96 (d, $^3J_{\text{HH}} = 8 \text{ Hz}$, 2H, aryl CH), 7.80 (d, $^3J_{\text{HH}} = 9 \text{ Hz}$, 4H, aryl CH), 7.32 (d, $^3J_{\text{HH}} = 8 \text{ Hz}$, 2H, aryl CH), 2.45 (s, 3H, CH_3). $^{13}\text{C}\{^1\text{H}\}$ NMR (100.6 MHz, CDCl_3): δ 146.7, 140.7, 133.3, 129.9, 129.7, 125.8, 123.9 (t, $^4J_{\text{CF}} = 3 \text{ Hz}$), 118.0, 113.5, 110.2, 21.6. ^{11}B NMR (128.3 MHz, CDCl_3): δ -0.7 (t, $^1J_{\text{BF}} = 29 \text{ Hz}$). ^{19}F NMR (376.1 Hz, CDCl_3): δ -141.8 (q, $^1J_{\text{FB}} = 29 \text{ Hz}$). FT-IR (KBr): 2949 (m), 2916 (m), 2847 (m), 2218 (s), 1650 (s), 1559



(m), 1507 (m), 1458 (m) cm^{-1} . UV-vis (toluene): $\lambda_{\text{max}} = 548 \text{ nm}$ ($\epsilon = 20,500 \text{ M}^{-1} \text{ cm}^{-1}$). Mass Spec. (EI, +ve mode): exact mass calculated for $[\text{C}_{22}\text{H}_{15}\text{N}_6\text{BF}_2]^+$: 412.1419; exact mass found: 412.1408; difference: -2.7 ppm . Anal. Calcd. (%) for $\text{C}_{22}\text{H}_{15}\text{N}_6\text{BF}_2$: C, 64.10; H, 3.67; N, 20.39. Found: C, 64.38; H, 3.50; N, 20.08.

Formazanate BF_2 complex 2.13c

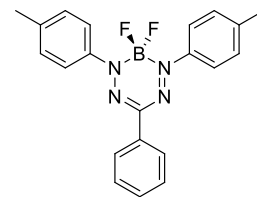
From 2.67 mmol of formazan: Yield = 0.83 g, 74%. Melting point = 186–188 $^\circ\text{C}$. ^1H NMR (599.5 MHz, CDCl_3) δ 7.98 (d, $^3J_{\text{HH}} = 8 \text{ Hz}$, 2H, aryl CH), 7.86 (d, $^3J_{\text{HH}} = 9 \text{ Hz}$, 4H, aryl CH), 7.26 (d, $^3J_{\text{HH}} = 8 \text{ Hz}$, 2H, aryl CH), 6.96 (d, $^3J_{\text{HH}} = 9 \text{ Hz}$, 4H, aryl CH), 3.87 (s, 6H, OCH_3), 2.42 (s, 3H, CH_3). $^{13}\text{C}\{^1\text{H}\}$ NMR



(100.6 MHz, CDCl_3): δ 160.8, 139.1, 137.8, 137.7, 131.4, 129.5, 125.5, 125.0 (t, $^4J_{\text{CF}} = 3 \text{ Hz}$), 114.4, 55.8, 21.5. ^{11}B NMR (128.3 MHz, CDCl_3): δ -0.7 (t, $^1J_{\text{BF}} = 29 \text{ Hz}$). ^{19}F NMR (376.1 Hz, CDCl_3): δ -145.7 (q, $^1J_{\text{FB}} = 29 \text{ Hz}$). FT-IR (KBr): 3025 (m), 2918 (m), 2794 (m), 1653 (s), 1559 (m), 1508 (s), 1458 (m) cm^{-1} . UV-vis (toluene): $\lambda_{\text{max}} = 552 \text{ nm}$ ($\epsilon = 28,200 \text{ M}^{-1} \text{ cm}^{-1}$). Mass Spec. (EI, +ve mode): exact mass calculated for $[\text{C}_{22}\text{H}_{21}\text{N}_4\text{O}_2\text{BF}_2]^+$: 422.1726; exact mass found: 422.1745; difference: $+4.6 \text{ ppm}$. Anal. Calcd. (%) for $\text{C}_{22}\text{H}_{21}\text{N}_4\text{O}_2\text{BF}_2$: C, 62.58; H, 5.01; N, 13.27. Found: C, 62.52; H, 5.10; N, 12.56.

Formazanate BF_2 complex 2.13d

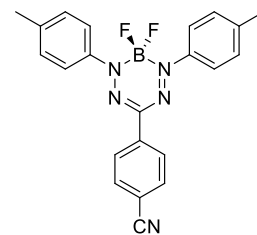
From 3.04 mmol of formazan: Yield = 0.98 g, 84%. Melting point = 154–156 $^\circ\text{C}$. ^1H NMR (599.5 MHz, CDCl_3) δ 8.10 (d, $^3J_{\text{HH}} = 7 \text{ Hz}$, 2H, aryl CH), 7.80 (d, $^3J_{\text{HH}} = 8 \text{ Hz}$, 4H, aryl CH), 7.46 (m, 2H, aryl CH), 7.27 (d, $^3J_{\text{HH}} = 8 \text{ Hz}$, 4H, aryl CH), 2.42 (s, 6H, CH_3). $^{13}\text{C}\{^1\text{H}\}$



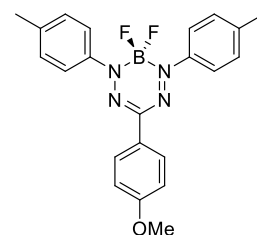
NMR (100.6 MHz, CDCl_3): δ 141.9, 140.3, 134.0, 130.4, 129.8, 129.2, 128.8, 125.6, 123.4 (t, $^4J_{\text{CF}} = 3 \text{ Hz}$), 21.5. ^{11}B NMR (128.3 MHz, CDCl_3): δ -0.5 (t, $^1J_{\text{BF}} = 29 \text{ Hz}$). ^{19}F NMR (376.1 Hz, CDCl_3): δ -144.6 (q, $^1J_{\text{FB}} = 29 \text{ Hz}$). FT-IR (KBr): 2961 (m), 2873 (m), 1580 (s), 1500 (m), 1458 (m), 1267 (m) cm^{-1} . UV-vis (toluene): $\lambda_{\text{max}} = 524 \text{ nm}$ ($\epsilon = 30,300 \text{ M}^{-1} \text{ cm}^{-1}$). Mass Spec. (EI, +ve mode): exact mass calculated for $[\text{C}_{21}\text{H}_{19}\text{N}_4\text{BF}_2]^+$: 376.1671; exact mass found: 376.1671; difference: -0.3 ppm . Anal. Calcd. (%) for $\text{C}_{21}\text{H}_{19}\text{N}_4\text{BF}_2$: C, 67.04; H, 5.09; N, 14.89. Found: C, 67.85; H, 5.35; N, 14.87.

Formazanate BF₂ complex 2.13e

From 2.83 mmol of formazan: Yield = 0.80 g, 70%. Melting point = 190–192 °C. ¹H NMR (599.5 MHz, CDCl₃) δ 8.23 (d, ³J_{HH} = 8 Hz, 2H, aryl CH), 7.69 (d, ³J_{HH} = 8 Hz, 2H, aryl CH), 7.58 (d, ³J_{HH} = 8 Hz, 4H, aryl CH), 7.27 (d, ³J_{HH} = 8 Hz, 4H, aryl CH), 2.41 (s, 6H, CH₃). ¹³C{¹H} NMR (100.6 MHz, CDCl₃): δ 141.6, 140.9, 138.3, 132.6, 130.2, 129.9, 125.6, 123.3 (t, ⁴J_{CF} = 2 Hz), 118.9, 112.2, 21.4. ¹¹B NMR (128.3 MHz, CDCl₃): δ 3.8 (t, ¹J_{BF} = 29 Hz). ¹⁹F NMR (376.1 Hz, CDCl₃): δ -143.1 (q, ¹J_{FB} = 29 Hz). FT-IR (KBr): 3026 (m), 2914 (m), 2870 (m), 2222 (m), 1654 (s), 1559 (m), 1507 (s), 1458 (m) cm⁻¹. UV-vis (toluene): λ_{max} = 525 nm (ε = 25,300 M⁻¹ cm⁻¹). Mass Spec. (EI, +ve mode): exact mass calculated for [C₂₂H₁₈N₅BF₂]⁺: 401.1623; exact mass found: 401.1610; difference: -3.2 ppm. Anal. Calcd. (%) for C₂₂H₁₈N₅BF₂: C, 65.86; H, 4.52; N, 17.46. Found: C, 66.42; H, 4.63; N, 17.61.

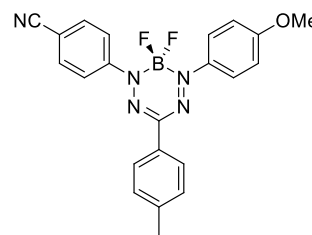
**Formazanate BF₂ complex 2.13f**

From 2.78 mmol of formazan: Yield = 0.81 g, 72%. Melting point = 166–168 °C. ¹H NMR (599.5 MHz, CDCl₃) δ 8.03 (d, ³J_{HH} = 9 Hz, 2H, aryl CH), 7.78 (d, ³J_{HH} = 9 Hz, 4H, aryl CH), 7.26 (d, ³J_{HH} = 9 Hz, 4H, aryl CH), 6.99 (d, ³J_{HH} = 9 Hz, 2H, aryl CH), 3.88 (s, 3H, OCH₃), 2.41 (s, 6H, CH₃). ¹³C{¹H} NMR (100.6 MHz, CDCl₃): δ 160.6, 141.7, 141.7, 140.0, 129.7, 126.9, 126.5, 123.3 (t, ⁴J_{CF} = 3 Hz), 114.1, 55.4, 21.4. ¹¹B NMR (128.3 MHz, CDCl₃): δ -0.6 (t, ¹J_{BF} = 29 Hz). ¹⁹F NMR (376.1 Hz, CDCl₃): δ -145.8 (q, ¹J_{FB} = 29 Hz). FT-IR (KBr): 3035 (m), 3027 (m), 2997 (m), 2951 (m), 2916 (m), 2831 (m), 1605 (s), 1504 (m), 1455 (m) cm⁻¹. UV-vis (toluene): λ_{max} = 544 nm (ε = 25,800 M⁻¹ cm⁻¹). Mass Spec. (EI, +ve mode): exact mass calculated for [C₂₂H₂₁N₄OBF₂]⁺: 406.1776; exact mass found: 406.1788; difference: +2.9 ppm. Anal. Calcd. (%) for C₂₂H₂₁N₄OBF₂: C, 65.04; H, 5.21; N, 13.79. Found: C, 64.79; H, 5.22; N, 13.58.

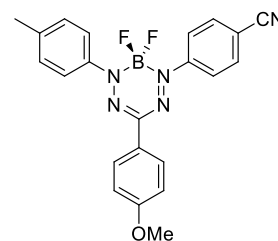


Formazanate BF₂ complex 2.13g

From 2.70 mmol of formazan: Yield = 0.82 g, 73%. Melting point = 151–153 °C. ¹H NMR (599.5 MHz, CDCl₃) δ 7.98 (m, 6H, aryl CH), 7.72 (d, ³J_{HH} = 9 Hz, 2H, aryl CH), 7.29 (d, ³J_{HH} = 8 Hz, 2H, aryl CH), 7.01 (d, ³J_{HH} = 9 Hz, 2H, aryl CH), 3.90 (s, 3H, OCH₃), 2.43 (s, 3H, CH₃). ¹³C{¹H} NMR (100.6 MHz, CDCl₃): δ 162.3, 147.4, 139.9, 137.7, 133.1, 130.7, 129.7, 125.7 (t, ⁴J_{CF} = 3 Hz), 125.7, 123.1 (t, ⁴J_{CF} = 3 Hz), 118.6, 114.9, 114.8, 111.3, 55.9, 21.5. ¹¹B NMR (128.3 MHz, CDCl₃): δ -0.6 (t, ¹J_{BF} = 29 Hz). ¹⁹F NMR (376.1 Hz, CDCl₃): δ -142.9 (q, ¹J_{FB} = 29 Hz). FT-IR (KBr): 3004 (m), 2985 (m), 2910 (m), 2834 (m), 2222 (s), 1596 (s), 1505 (s), 1295 (m), 1254 (s), 1170 (m) cm⁻¹. UV-vis (toluene): λ_{max} = 561 nm (ε = 24,400 M⁻¹ cm⁻¹). Mass Spec. (EI, +ve mode): exact mass calculated for [C₂₂H₁₈N₅OBF₂]⁺: 417.1572; exact mass found: 417.1609; difference: +8.7 ppm. Anal. Calcd. (%) for C₂₂H₁₈N₅OBF₂: C, 63.33; H, 4.35; N, 16.79 Found: C, 63.40; H, 4.43; N, 15.99.

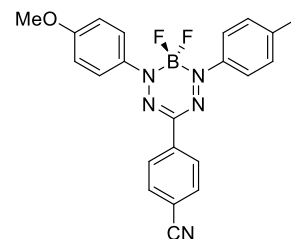
**Formazanate BF₂ complex 2.13h**

From 2.70 mmol of formazan: Yield = 1.03 g, 92%. Melting point = 154–156 °C. ¹H NMR (599.5 MHz, CDCl₃) δ 8.02 (d, ³J_{HH} = 9 Hz, 2H, aryl CH), 7.99 (d, ³J_{HH} = 8 Hz, 2H, aryl CH), 7.84 (d, ³J_{HH} = 8 Hz, 2H, aryl CH), 7.74 (d, ³J_{HH} = 9 Hz, 2H, aryl CH), 7.31 (d, ³J_{HH} = 8 Hz, 2H, aryl CH), 7.01 (d, ³J_{HH} = 9 Hz, 2H, aryl CH), 3.89 (s, 3H, OCH₃), 2.44 (s, 3H, CH₃). ¹³C{¹H} NMR (100.6 MHz, CDCl₃): δ 161.2, 147.4, 142.2, 141.9, 133.2, 130.2, 127.3, 125.9, 123.9 (t, ⁴J_{CF} = 2 Hz), 123.4 (t, ⁴J_{CF} = 3 Hz), 118.6, 114.5, 111.8, 111.1, 55.7, 21.7. ¹¹B NMR (128.3 MHz, CDCl₃): δ -0.7 (t, ¹J_{BF} = 29 Hz). ¹⁹F NMR (376.1 Hz, CDCl₃): δ -145.7 (q, ¹J_{FB} = 29 Hz). FT-IR (KBr): 3035 (m), 3026 (m), 2998 (m), 2931 (m), 2835 (m), 2227 (s), 1603 (s), 1509 (s), 130 (m), 1248 (s), 1170 (m) cm⁻¹. UV-vis (toluene): λ_{max} = 554 nm (ε = 21,500 M⁻¹ cm⁻¹). Mass Spec. (EI, +ve mode): exact mass calculated for [C₂₂H₁₈N₅OBF₂]⁺: 417.1572; exact mass found: 417.1579; difference: +1.5 ppm. Anal. Calcd. (%) for C₂₂H₁₈N₅OBF₂: C, 63.33; H, 4.35; N, 16.79. Found: C, 63.35; H, 4.47; N, 15.98.

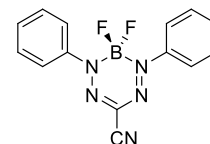


Formazanate BF₂ complex 2.13i

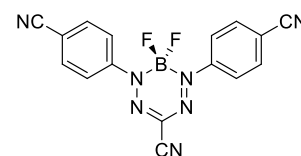
From 2.70 mmol of formazan, Yield = 0.62 g, 55%. Melting point = 172–174 °C. ¹H NMR (599.5 MHz, CDCl₃) δ 8.21 (d, ³J_{HH} = 8 Hz, 2H, aryl CH), 7.89 (d, ³J_{HH} = 9 Hz, 2H, aryl CH), 7.78 (d, ³J_{HH} = 8 Hz, 2H, aryl CH), 7.74 (d, ³J_{HH} = 8 Hz, 2H, aryl CH), 7.28 (d, ³J_{HH} = 8 Hz, 2H, aryl CH), 6.99 (d, ³J_{HH} = 9 Hz, 2H, aryl CH), 3.89 (s, 3H, OCH₃), 2.43 (s, 3H, CH₃). ¹³C{¹H} NMR (100.6 MHz, CDCl₃): δ 161.5, 140.7, 140.6, 138.5, 137.5, 132.7, 130.0, 125.7, 125.3 (t, ⁴J_{CF} = 3 Hz), 125.3, 123.3 (t, ⁴J_{CF} = 3 Hz), 119.0, 114.7, 112.3, 55.9, 21.5. ¹¹B NMR (128.3 MHz, CDCl₃): δ -0.6 (t, ¹J_{BF} = 29 Hz). ¹⁹F NMR (376.1 Hz, CDCl₃): δ -143.4 (q, ¹J_{FB} = 29 Hz). FT-IR (KBr): 3035 (m), 3001 (m), 2997 (m), 2911 (m), 2835 (m), 2227 (m), 1599 (s), 1507 (s), 1318 (m), 1256 (s), 1168 (s) cm⁻¹. UV-vis (toluene): λ_{max} = 541 nm (ε = 25,100 M⁻¹ cm⁻¹). Mass Spec. (EI, +ve mode): exact mass calculated for [C₂₂H₁₈N₅OBF₂]⁺: 417.1572; exact mass found: 417.1583; difference: +2.5 ppm. Anal. Calcd. (%) for C₂₂H₁₈N₅OBF₂: C, 63.33; H, 4.35; N, 16.79. Found: C, 64.33; H, 4.43; N, 16.76.

**Formazanate BF₂ complex 2.13j**

From 4.00 mmol of formazan. Yield = 1.03 g, 87%. Melting point = 107–109 °C. ¹H NMR (599.5 MHz, CDCl₃) δ 7.91–7.88 (m, 4H, aryl CH), 7.50–7.48 (m, 6H, aryl CH). ¹³C{¹H} NMR (100.6 MHz, CDCl₃): δ 143.1, 131.6, 129.6, 123.2 (t, ⁴J_{CF} = 3 Hz), 119.6, 114.1. ¹¹B NMR (128.3 MHz, CDCl₃): δ -0.8 (t, ¹J_{BF} = 30 Hz). ¹⁹F NMR (376.1 Hz, CDCl₃): δ -133.6 (q, ¹J_{FB} = 30 Hz). FT-IR (KBr): 3267 (s), 3116 (m), 3074 (m), 2962 (m), 2928 (m), 2236 (s), 1587 (m), 1381 (s), 1348 (s), 1148 (s), 1037 (s) cm⁻¹. UV-vis (toluene): λ_{max} 502 nm (ε = 30,400 M⁻¹ cm⁻¹). Mass Spec. (EI, +ve mode): exact mass calculated for C₁₄H₁₀N₅BF₂: 297.0997; exact mass found: 297.1003; difference: +1.0 ppm. Anal. Calcd. (%) for C₁₄H₁₀N₅BF₂: C, 56.60; H, 3.39; N, 23.57. Found: C, 56.63; H, 3.39; N, 23.46.

**Formazanate BF₂ complex 2.13k**

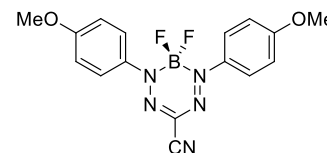
From 1.85 mmol of formazan. Yield = 0.55 g, 85%. Melting point = 212 – 214 °C. ¹H NMR (399.8 MHz, CDCl₃) δ 8.09 (d, 4H, ³J_{HH} = 9 Hz, aryl CH), 7.85 (d, 4H, ³J_{HH} = 9 Hz, aryl CH). ¹³C{¹H} NMR (100.6 MHz, CD₂Cl₂): δ 145.5, 133.7, 123.8, 123.7 (t, ⁴J_{CF} = 3 Hz), 117.4,



115.5, 113.1. ^{11}B NMR (128.3 MHz, CDCl_3): δ -0.9 (t, $^1J_{\text{BF}} = 31$ Hz). ^{19}F NMR (376.1 MHz, CDCl_3): δ -129.6 (q, $^1J_{\text{FB}} = 31$ Hz). FT-IR (KBr): 3245 (s), 2958 (m), 2914 (m), 2849 (m), 2254 (m), 2228 (m), 1559 (m), 1332 (s), 1261 (m), 1154 (m) cm^{-1} . UV-vis (toluene): λ_{max} 515 nm ($\epsilon = 35,500 \text{ M}^{-1} \text{ cm}^{-1}$). Mass Spec. (EI, +ve mode): exact mass calculated for $\text{C}_{16}\text{H}_8\text{N}_7\text{BF}_2$: 347.0902; exact mass found: 347.0906; difference: +0.9 ppm. Anal. Calcd. (%) for $\text{C}_{16}\text{H}_8\text{N}_7\text{BF}_2$: C, 55.37; H, 2.32; N, 28.25. Found: C, 55.66; H, 2.45; N, 27.60.

Formazanate BF_2 complex 2.13l

From 3.20 mmol of formazan. Yield = 1.04 g, 91%. Melting point = 113–115 °C. ^1H NMR (599.5 MHz, CDCl_3) δ 7.87 (d, 4H, $^3J_{\text{HH}} = 9$ Hz, aryl CH), 6.98 (d, 4H, $^3J_{\text{HH}} = 9$ Hz, aryl CH), 3.89 (s, 6H, OCH_3). $^{13}\text{C}\{^1\text{H}\}$ NMR (100.6 MHz, CDCl_3): δ 162.3, 137.1, 137.1, 125.1 (t, $^4J_{\text{CF}} = 3$ Hz), 115.0, 114.7, 56.0. ^{11}B NMR (128.3 MHz, CDCl_3): δ -0.7 (t, $^1J_{\text{BF}} = 31$ Hz). ^{19}F NMR (376.1 MHz, CDCl_3): δ -135.4 (q, $^1J_{\text{FB}} = 31$ Hz). FT-IR (KBr): 3397 (s), 3267 (s), 2954 (m), 2926 (m), 2856 (m), 2240 (m), 1599 (s), 1506 (m), 1260 (s), 1165 (s) cm^{-1} . UV-vis (toluene): λ_{max} 572 nm ($\epsilon = 42,700 \text{ M}^{-1} \text{ cm}^{-1}$). Mass Spec. (EI, +ve mode): exact mass calculated for $\text{C}_{16}\text{H}_{14}\text{N}_5\text{O}_2\text{BF}_2$: 357.1209; exact mass found: 357.1205; difference: -1.0 ppm. Anal. Calcd. (%) for $\text{C}_{16}\text{H}_{14}\text{N}_5\text{O}_2\text{BF}_2$: C, 53.81; H, 3.95; N, 19.61. Found: C, 54.31; H, 3.98; N, 19.03.



2.7 References

- (1) Frath, D.; Massue, J.; Ulrich, G.; Ziessel, R. *Angew. Chem. Int. Ed.* **2014**, *53*, 2290–2310.
- (2) Roacho, R. I.; Metta-Magaña, A.; Portillo, M. M.; Peña-Cabrera, E.; Pannell, K. H. *J. Org. Chem.* **2013**, *78*, 4245–4250.
- (3) Bonnier, C.; Machin, D. D.; Abdi, O.; Koivisto, B. D. *Org. Biomol. Chem.* **2013**, *11*, 3756–3760.
- (4) Frath, D.; Poirel, A.; Ulrich, G.; De Nicola, A.; Ziessel, R. *Chem. Commun.* **2013**, *49*, 4908–4910.
- (5) Lu, J.-S.; Ko, S.-B.; Walters, N. R.; Kang, Y.; Sauriol, F.; Wang, S. *Angew. Chem. Int. Ed.* **2013**, *52*, 4544–4548.

- (6) Firinci, E.; Bates, J. I.; Riddlestone, I. M.; Phillips, N.; Aldridge, S. *Chem. Commun.* **2013**, *49*, 1509–1511.
- (7) Vogels, C. M.; Westcott, S. A. *Chem. Soc. Rev.* **2011**, *40*, 1446–1458.
- (8) Fischer, G. M.; Daltrozzo, E.; Zumbusch, A. *Angew. Chem. Int. Ed.* **2011**, *50*, 1406–1409.
- (9) Belcher, W. J.; Hodgson, M. C.; Sumida, K.; Torvisco, A.; Ruhlandt-Senge, K.; Ware, D. C.; Boyd, P. D. W.; Brothers, P. J. *Dalton Trans.* **2008**, 1602–1614.
- (10) Cheng, F.; Jäkle, F. *Chem. Commun.* **2010**, *46*, 3717–3719.
- (11) Loudet, A.; Burgess, K. *Chem. Rev.* **2007**, *107*, 4891–4932.
- (12) Ulrich, G.; Ziesel, R.; Harriman, A. *Angew. Chem. Int. Ed.* **2008**, *47*, 1184–1201.
- (13) Boens, N.; Leen, V.; Dehaen, W. *Chem. Soc. Rev.* **2012**, *41*, 1130–1172.
- (14) Barbon, S. M.; Staroverov, V. N.; Boyle, P. D.; Gilroy, J. B. *Dalton Trans.* **2014**, *43*, 240–250.
- (15) Macedo, F. P.; Gwengo, C.; Lindeman, S. V.; Smith, M. D.; Gardinier, J. R. *Eur. J. Inorg. Chem.* **2008**, 3200–3211.
- (16) Qian, B.; Baek, S. W.; Smith III, M. R. *Polyhedron* **1999**, *18*, 2405–2414.
- (17) Araneda, J. F.; Piers, W. E.; Heyne, B.; Parvez, M.; McDonald, R. *Angew. Chem. Int. Ed.* **2011**, *50*, 12214–12217.
- (18) Ren, Y.; Liu, X.; Gao, W.; Xia, H.; Ye, L.; Mu, Y. *Eur. J. Inorg. Chem.* **2007**, 1808–1814.
- (19) Liu, X.; Ren, Y.; Xia, H.; Fan, X.; Mu, Y. *Inorg. Chim. Acta* **2010**, *363*, 1441–1447.
- (20) Kubota, Y.; Tsuzuki, T.; Funabiki, K.; Ebihara, M.; Matsui, M. *Org. Lett.* **2010**, *12*, 4010–4013.
- (21) Nawn, G.; Oakley, S. R.; Majewski, M. B.; McDonald, R.; Patrick, B. O.; Hicks, R. G. *Chem. Sci.* **2013**, *4*, 612–621.
- (22) Nawn, G.; Waldie, K. M.; Oakley, S. R.; Peters, B. D.; Mandel, D.; Patrick, B. O.; McDonad, R.; Hicks, R. G. *Inorg. Chem.* **2011**, *50*, 9826–9837.
- (23) Manjare, S. T.; Kim, J.; Lee, Y.; Churchill, D. G. *Org. Lett.* **2013**, *16*, 520–523.
- (24) Carlson, J. C. T.; Meimetis, L. G.; Hilderbrand, S. A.; Weissleder, R. *Angew. Chem. Int. Ed.* **2013**, *52*, 6917–6920.

- (25) Zhang, C.; Zhao, J.; Wu, S.; Wang, Z.; Wu, W.; Ma, J.; Guo, S.; Huang, L. *J. Am. Chem. Soc.* **2013**, *135*, 10566–10578.
- (26) Bozdemir, O. A.; Erbas-Cakmak, S.; Ekiz, O. O.; Dana, A.; Akkaya, E. U. *Angew. Chem. Int. Ed.* **2011**, *50*, 10907–10912.
- (27) Lazarides, T.; McCormick, T. M.; Wilson, K. C.; Lee, S.; McCamant, D. W.; Eisenberg, R. *J. Am. Chem. Soc.* **2010**, *133*, 350–364.
- (28) Hudnall, T. W.; Gabbai, F. P. *Chem. Commun.* **2008**, 4596–4597.
- (29) Nineham, A. W. *Chem. Rev.* **1955**, *55*, 355–483.
- (30) Sigeiken, G. I.; Lipunova, G. N.; Pervova, I. G. *Russ. Chem. Rev.* **2006**, *75*, 885–900.
- (31) Gök, Y. *Dyes Pigments* **1989**, *11*, 101–107.
- (32) Gök, Y.; Şentürk, H. B. *Dyes Pigments* **1991**, *15*, 279–287.
- (33) Zhang, Y.; Liu, D. *Dyes Pigments* **1995**, *29*, 57–63.
- (34) Szymczyk, M.; El-Shafei, A.; Freeman, H. S. *Dyes Pigments* **2007**, *72*, 8–15.
- (35) Weislow, O. S.; Kiser, R.; Fine, D. L.; Bader, J.; Shoemaker, R. H.; Boyd, M. R. *J. Natl. Cancer Inst.* **1989**, *81*, 577–586.
- (36) Abou-Elenien, G. M. *J. Electroanal. Chem.* **1994**, *375*, 301–305.
- (37) Goodwin, C. J.; Holt, S. J.; Downes, S.; Marshall, N. J. *J. Immunol. Methods* **1995**, *179*, 95–103.
- (38) Gruden, C. L.; Fevig, S.; Abu-Dalo, M.; Hernandez, M. *J. Microbiol. Methods* **2003**, *52*, 59–68.
- (39) Frederiks, W. M.; van Marle, J.; van Oven, C.; Comin-Anduix, B.; Cascante, M. *J. Histochem. Cytochem.* **2006**, *54*, 47–52.
- (40) Hunter, L.; Roberts, C. B. *J. Chem. Soc.* **1941**, 823–826.
- (41) Irving, H.; Gill, J. B.; Cross, W. R. *J. Chem. Soc.* **1960**, 2087–2095.
- (42) Siedle, A. R.; Pignolet, L. H. *Inorg. Chem.* **1980**, *19*, 2052–2056.
- (43) Jameson, G. B.; Muster, A.; Robinson, S. D.; Wingfield, J. N.; Ibers, J. A. *Inorg. Chem.* **1981**, *20*, 2448–2456.
- (44) Brown, D. A.; Bögge, H.; Lipunova, G. N.; Müller, A.; Plass, W.; Walsh, K. G. *Inorg. Chim. Acta* **1998**, *280*, 30–38.

- (45) Hong, S.; Hill, L. M. R.; Gupta, A. K.; Naab, B. D.; Gilroy, J. B.; Hicks, R. G.; Cramer, C. J.; Tolman, W. B. *Inorg. Chem.* **2009**, *48*, 4514–4523.
- (46) Gilroy, J. B.; Patrick, B. O.; McDonald, R.; Hicks, R. G. *Inorg. Chem.* **2008**, *47*, 1287–1294.
- (47) Gilroy, J. B.; Otieno, P. O.; Ferguson, M. J.; McDonald, R.; Hicks, R. G. *Inorg. Chem.* **2008**, *47*, 1279–1286.
- (48) Gilroy, J. B.; Ferguson, M. J.; McDonald, R.; Patrick, B. O.; Hicks, R. G. *Chem. Commun.* **2007**, 126–128.
- (49) Hong, S.; Gupta, A. K.; Tolman, W. B. *Inorg. Chem.* **2009**, *48*, 6323–6325.
- (50) Chang, M.-C.; Dann, T.; Day, D. P.; Lutz, M.; Wildgoose, G. G.; Otten, E. *Angew. Chem. Int. Ed.* **2014**, *53*, 4118–4122.
- (51) Chang, M.-C.; Otten, E. *Chem. Commun.* **2014**, *50*, 7431–7433.
- (52) Barbon, S. M.; Reinkeluers, P. A.; Price, J. T.; Staroverov, V. N.; Gilroy, J. B. *Chem. Eur. J.* **2014**, *20*, 11340–11344.
- (53) Barbon, S. M.; Price, J. T.; Reinkeluers, P. A.; Gilroy, J. B. *Inorg. Chem.* **2014**, *53*, 10585–10593.
- (54) Katritzky, A. A.; Belyakov, S. A.; Cheng, D.; Durst, H. D. *Synthesis* **1995**, *1995*, 577–581.
- (55) Gilroy, J. B.; McKinnon, S. D. J.; Koivisto, B. D.; Hicks, R. G. *Org. Lett.* **2007**, *9*, 4837–4840.
- (56) *CRC Handbook of Chemistry and Physics*. CRC Press: Boca Raton, FL, 2012.
- (57) Fery-Forgues, S.; Lavabre, D. *J. Chem. Educ.* **1999**, *76*, 1260–1264.
- (58) Suzuki, K.; Kobayashi, A.; Kaneko, S.; Takehira, K.; Yoshihara, T.; Ishida, H.; Shiina, Y.; Oishi, S.; Tobita, S. *Phys. Chem. Chem. Phys.* **2009**, *11*, 9850–9860.
- (59) Gilroy, J. B.; McKinnon, S. D. J.; Kennepohl, P.; Zsombor, M. S.; Ferguson, M. J.; Thompson, L. K.; Hicks, R. G. *J. Org. Chem.* **2007**, *72*, 8062–8069.
- (60) Ziesel, R.; Retailleau, P.; Elliott, K. J.; Harriman, A. *Chem. Eur. J.* **2009**, *15*, 10369–10374.
- (61) Didier, P.; Ulrich, G.; Mély, Y.; Ziesel, R. *Org. Biomol. Chem.* **2009**, *7*, 3639–3642.

- (62) Collado, D.; Casado, J.; Rodríguez González, S.; López Navarrete, J. T.; Suau, R.; Perez-Inestrosa, E.; Pappenfus, T. M.; Raposo, M. M. M. *Chem. Eur. J.* **2011**, *17*, 498–507.
- (63) Niu, S.; Ulrich, G.; Retailleau, P.; Ziessele, R. *Tetrahedron Lett.* **2011**, *52*, 4848–4853.
- (64) Shi, W.-J.; Lo, P.-C.; Singh, A.; Ledoux-Rak, I.; Ng, D. K. P. *Tetrahedron* **2012**, *68*, 8712–8718.
- (65) Ulrich, G.; Barsella, A.; Boeglin, A.; Niu, S.; Ziessele, R. *Chem. Phys. Chem.* **2014**, *15*, 2693–2700.
- (66) Zhou, Y.; Xiao, Y.; Chi, S.; Qian, X. *Org. Lett.* **2008**, *10*, 633–636.
- (67) Wu, Y.-Y.; Chen, Y.; Gou, G.-Z.; Mu, W.-H.; Lv, X.-J.; Du, M.-L.; Fu, W.-F. *Org. Lett.* **2012**, *14*, 5226–5229.
- (68) D'Aléo, A.; Gachet, D.; Heresanu, V.; Giorgi, M.; Fages, F. *Chem. Eur. J.* **2012**, *18*, 12764–12772.
- (69) D'Aleo, A.; Fages, F. *Photochem. Photobiol. Sci.* **2013**, *12*, 500–510.
- (70) Lakowicz, J. R. *Principles of Fluorescence Spectroscopy*, 3rd ed.; Springer: New York, 2006.
- (71) Hesari, M.; Barbon, S. M.; Staroverov, V. N.; Ding, Z.; Gilroy, J. B. *Chem. Commun.* **2015**, *51*, 3766–3769.
- (72) Maar, R. R.; Barbon, S. M.; Sharma, N.; Groom, H.; Luyt, L. G.; Gilroy, J. B. *Chem. Eur. J.* **2015**, *21*, 15589–15599.
- (73) Bruker-Nonius, SAINT version 2013.8, 2013, Bruker-AXS, Madison, WI 53711, USA.
- (74) Bruker-Nonius, SADABS version 2012.1, 2012, Bruker-AXS, Madison, WI 53711, USA.
- (75) *XS program, beta version*, Sheldrick, G. M. **2014**, *University of Gottingen*.
- (76) Sheldrick, G. M. *Acta Cryst.* **2008**, *A64*, 112–122.
- (77) Spek, A. L. *Acta Cryst.* **1990**, *A46*, 194–201.

Chapter 3

3 The Effect of Extended π Conjugation on the Properties of BF_2 Formazanate Dyes

Adapted from:

1. **Barbon, S. M.**; Price, J. T.; Yogarajah, U.; Gilroy, J. B. *RSC Adv.* **2015**, *5*, 56316–56324.
2. **Barbon, S. M.**; Staroverov, V. N.; Gilroy J. B. *J. Org. Chem.* **2015**, *80*, 5226–5235.

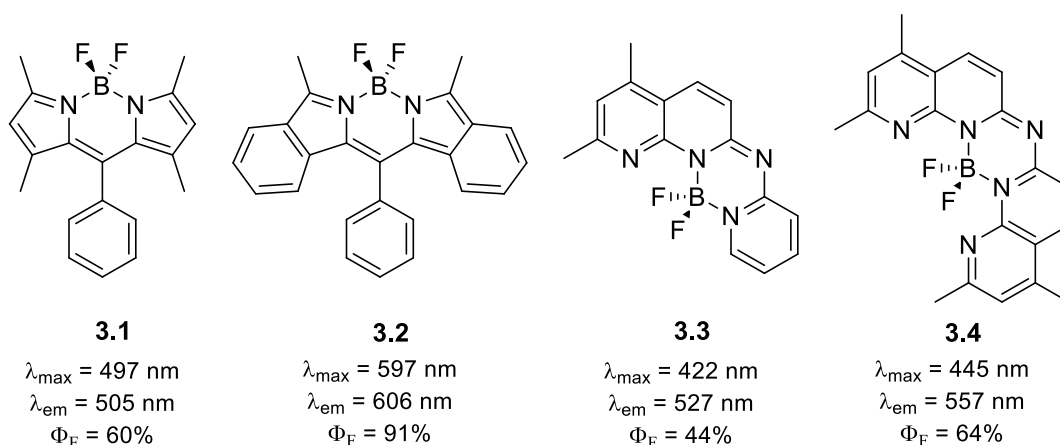
3.1 Introduction

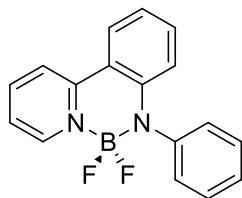
It has long been known that extended π conjugation has a drastic effect on the electronic properties and spectroscopic features of molecules containing aromatic π -systems. Perhaps the simplest molecules that demonstrate this behavior are benzene, naphthalene, and anthracene. In this series, as the extent of π conjugation increases, so does the wavelength of maximum absorption, going from ~ 260 nm for benzene, to ~ 310 nm for naphthalene and ~ 375 nm for anthracene.^[1] The emission quantum yields of these compounds follow the same trend, increasing from 5% in benzene to 19% and 27% in naphthalene and anthracene, respectively.^[1] As the structures of π -conjugated molecules become increasingly complex, so do their electronic properties and utility in a variety of applications. π -Conjugated molecules are frequently employed in photovoltaic cells,^[2] as luminescent materials,^[3] in field-effect transistors,^[4] and as materials exhibiting aggregation-induced emission.^[5] For many of these applications, materials with maximum absorption/emission wavelengths in the far-red/near-IR regions of the electromagnetic spectrum are required.

Amongst the most common hybrid conjugated molecular materials are boron difluoride (BF_2) complexes of *N,N*-, *O,O*- and *N,O*-chelating ligands.^[3,6-18] Boron dipyrromethenes (BODIPYs) are by far the most common of this class of complexes.^{[19-21],[22-35]} BODIPY **3.1**, which was first reported by Daub and co-workers in 1998, showed absorption and emission maxima around 500 nm, with an emission quantum yield of 60%.^[36] Ono *et al.*

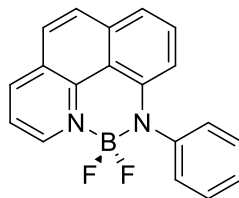
synthesized compound **3.2**, which is structurally very similar to **3.1**, but includes a greater degree of π -conjugation. The addition of two fused phenyl rings increased the wavelength of maximum absorption and emission by close to 100 nm, and the quantum yield to 91%.^[37] Similarly, Fu's group has applied this strategy to their naphthyridine BF₂ complexes **3.3** and **3.4**, and observed that by extending the conjugation of the naphthyridine ligand by a pyridine moiety, the solid-state fluorescence quantum yield increased by 20%, and the wavelength of maximum absorption and emission was red-shifted by more than 20 nm.^[38] Piers *et al.* have modified the structure of anilido-pyridine ligands to study the properties of the BF₂ complexes of both the parent anilido-pyridine complex **3.5** and the modified BF₂ complex **3.6**, which has a higher degree of π -conjugation. This modification nearly doubled the emission quantum yield from 33% to 60% and red-shifted the absorption and emission maxima by *ca.* 50 nm.^[39]

Another common strategy involves combining two or more BF₂ dye moieties into a single molecule.^[15,40] By fusing together two BODIPY units with benzene rings and effectively extending π conjugation, for example, in dimers **3.7** and **3.8**, λ_{em} red-shifts significantly to 940 nm (**7**)^[41] and 712 nm (**3.8**).^[42] BODIPY units have also been linked via *para*-benzene spacers, *e.g.* **3.9**, whereby the wavelength of maximum emission was red-shifted relative to unlinked BODIPYs.^[43]

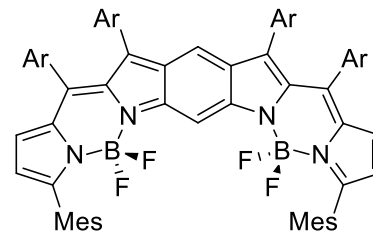


**3.5**

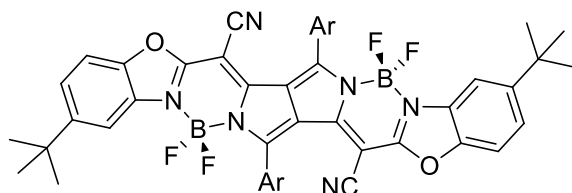
$\lambda_{\max} = 417 \text{ nm}$
 $\lambda_{\text{em}} = 531 \text{ nm}$
 $\Phi_{\text{F}} = 33\%$

**3.6**

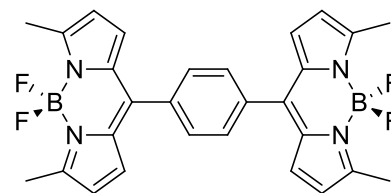
$\lambda_{\max} = 465 \text{ nm}$
 $\lambda_{\text{em}} = 584 \text{ nm}$
 $\Phi_{\text{F}} = 60\%$

**3.7**

$\lambda_{\max} = 629 \text{ nm}$
 $\lambda_{\text{em}} = 940 \text{ nm}$
 $\Phi_{\text{F}} < 1\%$

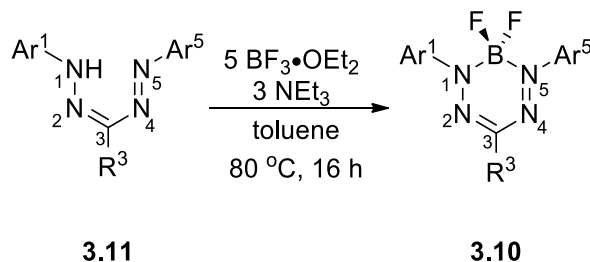
**3.8**

$\lambda_{\max} = 690 \text{ nm}$
 $\lambda_{\text{em}} = 712 \text{ nm}$
 $\Phi_{\text{F}} = 57\%$

**3.9**

$\lambda_{\max} = 513 \text{ nm}$
 $\lambda_{\text{em}} = 538 \text{ nm}$
 $\Phi_{\text{F}} = 5\%$

In an effort to assess the effect of extended π -conjugation on the properties of BF_2 formazanate dyes, and taking advantage of the ease of structural variation of the formazanate backbone, we have synthesized a series of formazans **3.11a–k** and BF_2 complexes **3.10a–k** (Scheme 3.1, Table 3.1). We have systematically introduced naphthyl (Np) substituents at the 1, 3, and 5 positions of the formazanate backbone, as well as synthesized the first examples of boron difluoride formazanate dimers exhibiting conjugated and cross-conjugated electronic structures, as we work towards functional molecular materials based on formazanate ligands with optical properties in the far-red/near-IR.



Scheme 3.1. Synthesis of BF₂ formazanate complexes **3.10a–k**.

Table 3.1. Substituents for formazans **3.11a–k** and BF₂ formazanate complexes **3.10a–k**.

	Ar ¹	Ar ⁵	R ³
a	Ph	Ph	Ph
b	Ph	Ph	Np
c	Ph	Np	Ph
d	Np	Np	Ph
e ^[44]	Ph	Ph	CN
f	Np	Np	CN
g	Ph	Ph	NO ₂
h	Np	Np	NO ₂
i ^[45]	Ph	Ph	<i>p</i> -tolyl
j	Ph	Ph	<i>p</i> -BF ₂ complex of 1,3,5-phenyl formazanate
k	Ph	Ph	<i>m</i> -BF ₂ complex of 1,3,5-phenyl formazanate

3.2 Results and Discussion

3.2.1 Synthesis

Triarylformazans **3.11a–d**, 3-cyanoformazans **3.11e–f**, 3-nitroformazans **3.11g–h**, and *meta*- and *para*-substituted benzene bridged bisformazans **3.11j–k**, were synthesized by adapting previously published protocols.^[46–50] Formazanate BF₂ complexes **3.10a–k** were prepared by refluxing the parent formazans in toluene in the presence of excess NEt₃ and BF₃·OEt₂ (Scheme 3.1).^[44,51] Analysis by ¹H, ¹¹B, ¹³C, and ¹⁹F NMR spectroscopy (Figures 3.1, A3.1–A3.30), mass spectrometry and IR spectroscopy confirmed the proposed structures of formazans **3.11a–k** and BF₂ complexes **3.10a–k**. The BF₂ complexes showed characteristic 1:2:1 triplets in the ¹¹B NMR spectra (*e.g.* **3.10j**: –0.5 ppm; **3.10k**: –0.5 ppm) and 1:1:1:1 quartets in the ¹⁹F NMR spectra (*e.g.* **3.10j**: –144.1 ppm; **3.10k**: –143.8 ppm)

(Figure 3.1, insets). The aryl regions of the ^1H NMR spectra differ slightly from that of the respective formazans and the disappearance of the resonances above 15 ppm indicate the loss of the NH protons. The bidentate coordination mode observed for the formazanate ligands was consistent with other complexes of boron^[44-45,51-52] and transition metals.^[53-61]

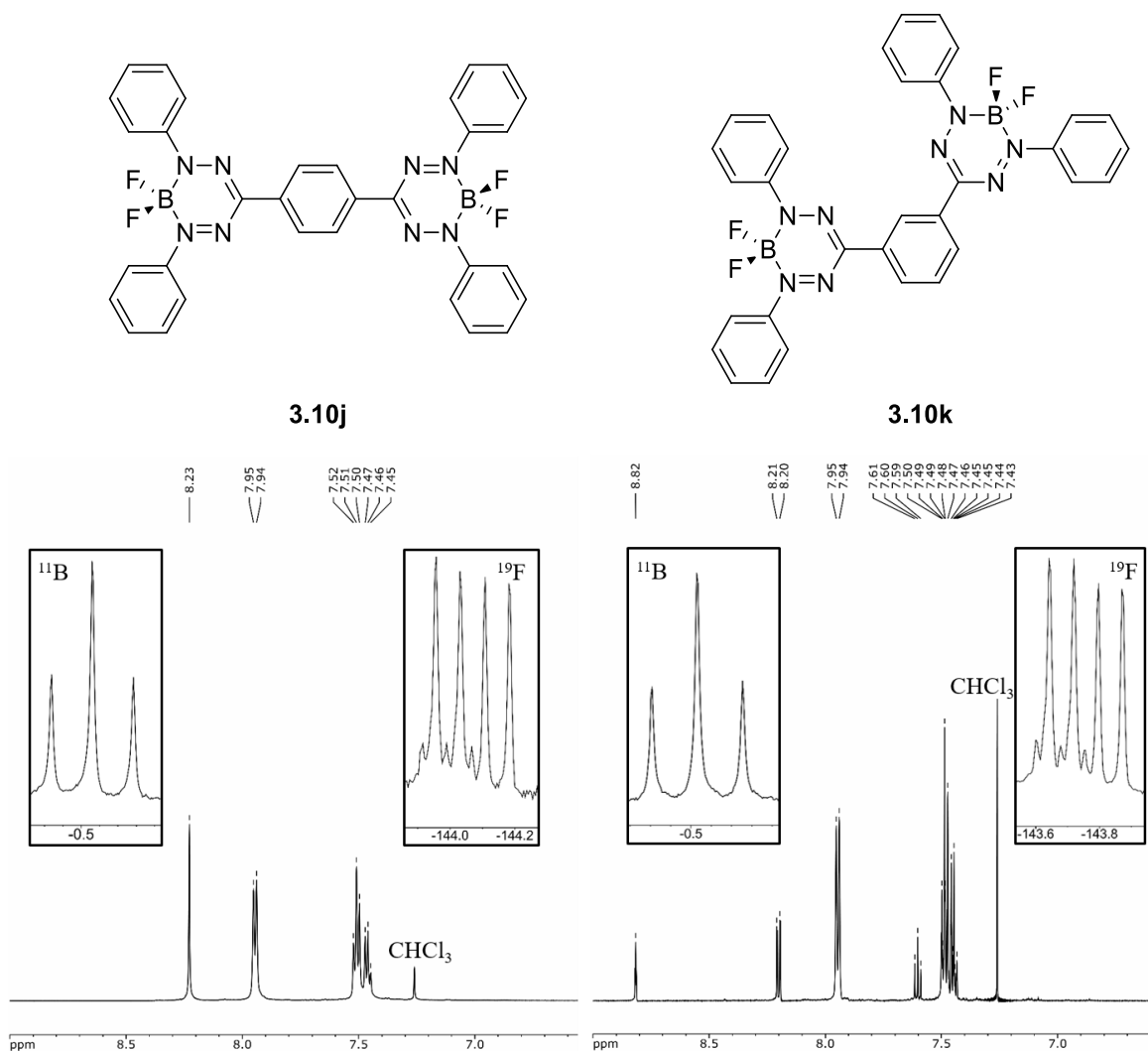


Figure 3.1. ^1H NMR spectra of **3.10j** (left) and **3.10k** (right) in CDCl_3 . ^{19}F and ^{11}B NMR spectra are shown as insets.

3.2.2 Naphthyl-Substituted BF_2 Formazanate Complexes

By comparing 1,3,5-triphenyl-substituted BF_2 complex **3.10a** with naphthyl-substituted complexes **3.10b–d**, the effect of π -conjugation on the properties of BF_2 triarylformazanate complexes was explored. Molar absorptivities associated with $\pi \rightarrow \pi^*$ transitions in

3.10a–d ranged from 20,900–26,800 $M^{-1} \text{ cm}^{-1}$ in toluene. The replacement of one phenyl substituent for a naphthyl substituent in **3.10b** ($Ar^1 = Ar^5 = \text{Ph}$, $R^3 = \text{Np}$) and **3.10c** ($Ar^1 = R^3 = \text{Ph}$, $Ar^5 = \text{Np}$) caused a red-shift of maximum absorption (λ_{max}) in toluene, from 517 nm for **3.10a** to 529 nm for **3.10b** and 535 nm for **3.10c**. The replacement of a second phenyl substituent in **3.10d** ($Ar^1 = Ar^5 = \text{Np}$, $R^3 = \text{Ph}$) resulted in a further red shift in λ_{max} to 556 nm (Figure 3.2a, Table 3.2). In order to verify that the observed absorption properties were not simply due to the presence of a naphthyl group, the UV-vis absorption spectrum of 2-naphthylamine was recorded ($\lambda_{\text{max}} = 345$ nm, Figure A3.31). Interestingly, when comparing compound **3.10b** and **3.10c**, which both have one naphthyl and two phenyl substituents (**3.10b**: $R^3 = \text{Np}$, **3.10c**: $R^5 = \text{Np}$), **3.10c** has a slightly longer wavelength of maximum absorption (529 vs. 535 nm).

All four compounds are weakly emissive, with maximum emission (λ_{em}) observed between 626 and 681 nm (Figures 3.2b, A3.32, A3.33, Table 3.2). The trend observed for the wavelengths of maximum absorption is mirrored here, with the λ_{em} of **3.10b–d** red-shifted with respect to **3.10a**. Quantum yields for all four complexes are below 5%. However, the observed Stokes shifts (ν_{ST}) were large (**3.10a**, $\nu_{\text{ST}} = 109$ nm, 3368 cm^{-1} ; **3.10b**, $\nu_{\text{ST}} = 124$ nm, 3590 cm^{-1} ; **3.10c**, $\nu_{\text{ST}} = 124$ nm, 3517 cm^{-1} ; **3.10d**, $\nu_{\text{ST}} = 125$ nm, 3301 cm^{-1}).

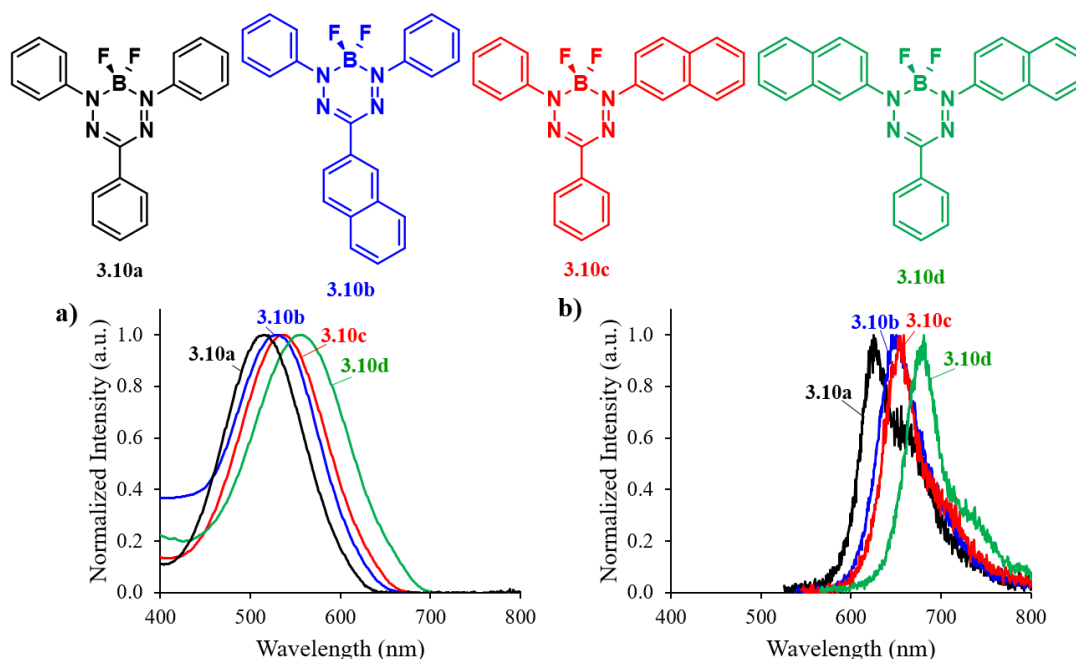


Figure 3.2. UV-vis absorption (a) and emission spectra (b) of **3.10a** (black, $\text{Ar}^1 = \text{Ar}^5 = \text{R}^3 = \text{Ph}$), **3.10b** (blue, $\text{Ar}^1 = \text{Ar}^5 = \text{Ph}$, $\text{R}^3 = \text{Np}$), **3.10c** (red, $\text{Ar}^1 = \text{R}^3 = \text{Ph}$, $\text{Ar}^5 = \text{Np}$) and **3.10d** (green, $\text{Ar}^1 = \text{Ar}^5 = \text{Np}$, $\text{R}^3 = \text{Ph}$). UV-vis absorption and emission spectra were recorded for 10^{-5} M degassed toluene solutions.

Complexes **3.10a–d** are electrochemically active, exhibiting two reversible one-electron reduction waves corresponding to the reversible formation of ligand-centered radical anions and dianions, (Figure 3.3, Table 3.2) and irreversible oxidation waves (Figure A3.34). The reduction potentials observed for **3.10a–d**, become less negative (easier to reduce) as naphthyl substituents are introduced (**3.10a**, -0.82 and -1.89 V; **3.10b**, -0.81 and -1.88 V; **3.10c**, -0.80 and -1.85 V; and **3.10d**, -0.78 and -1.78 V). This trend is consistent with naphthyl substituents having stabilized LUMOs due to enhanced π -conjugation when compared to phenyl substituents. A single naphthyl substituent at the 1,5-position has a more drastic effect than the same substituent at the 3 position, as **3.10c** is easier to reduce than **3.10b** by approximately 13 mV.

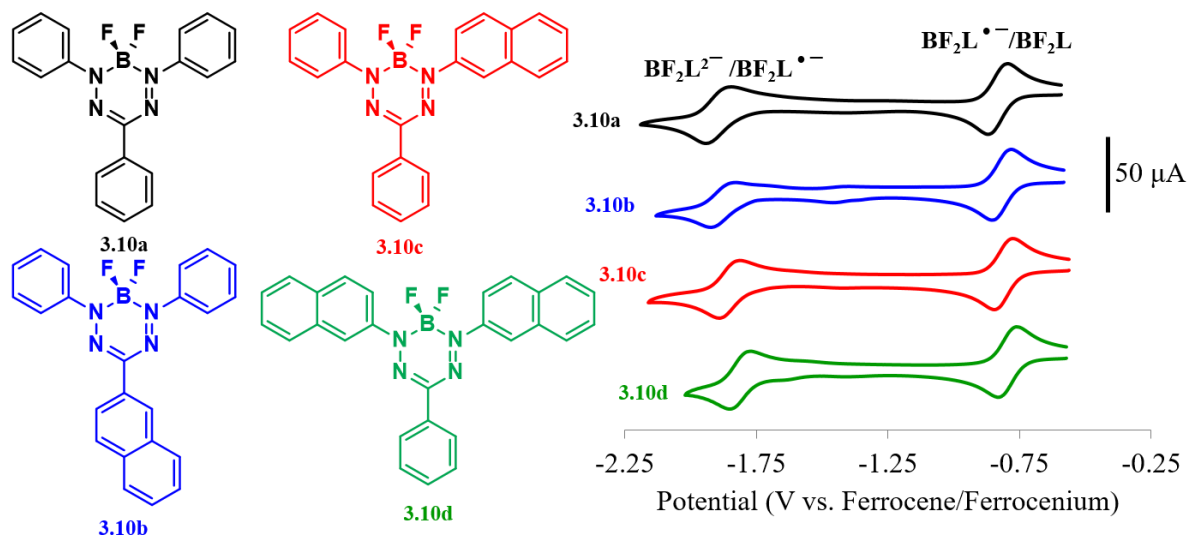


Figure 3.3. Cyclic voltammograms of **3.10a** (black), **3.10b** (blue), **3.10c** (red) and **3.10d** (green), recorded at 100 mV s⁻¹ in 1 mM MeCN solutions containing 0.1 M [*n*Bu₄N][PF₆] as supporting electrolyte. L = redox-active formazanate ligand.

The data collected for compounds **3.10a–d** allows for the conclusion that extended π-conjugation has an effect on the properties of BF₂ formazanate complexes. Systematically extending π-conjugation increases the emission quantum yields, red-shifts the wavelengths of maximum absorption and emission, and raises the reduction potentials of the resulting compounds. It is noteworthy that these data also demonstrate that extending the π-conjugation at the 3 position of the formazanate backbone has a less pronounced effect than similar structural modification at the 1,5-positions, which is consistent with the absorption data (see Section 3.2.4 below).

Table 3.2. Solution characterization data for BF₂ complexes **3.10a–h, j** and **k**.

	Solvent	λ_{\max} (nm)	ϵ (M ⁻¹ cm ⁻¹)	λ_{em} (nm)	Φ_{F}^a (%)	v_{ST} (nm)	v_{ST} (cm ⁻¹)	E_{red1}^b (V)	E_{red2}^b (V)
3.10a	THF	509	22,500	627	1	118	3697		
	toluene	517	23,800	626	< 1	109	3368	-0.82	-1.89
	CH ₂ Cl ₂	509	23,400	630	1	121	3773		
3.10b	THF	522	22,000	658	1	136	3960		
	toluene	529	20,900	653	< 1	124	3590	-0.81	-1.88
	CH ₂ Cl ₂	524	20,300	656	9	132	3840		
3.10c	THF	529	25,000	655	< 1	126	3636		
	toluene	535	26,800	659	2	124	3517	-0.80	-1.85
	CH ₂ Cl ₂	530	27,500	656	3	126	3624		
3.10d	THF	550	22,900	680	2	130	3476		
	toluene	556	25,200	681	5	125	3301	-0.78	-1.78
	CH ₂ Cl ₂	551	23,600	682	< 1	131	3486		
3.10e ^[44]	THF	489	25,400	585	5	96	3356		
	toluene	502	30,400	586	15	84	2855	-0.53	-1.68
	CH ₂ Cl ₂	491	34,600	584	9	93	3243		
3.10f	THF	551	27,700	676	25	125	3356		
	toluene	581	25,700	670	39	89	2286	-0.49	-1.54
	CH ₂ Cl ₂	558	23,900	669	32	111	2973		
3.10g	THF	487	21,000	585	3	98	3440		
	toluene	505	26,000	590	5	85	2853	-0.48	-1.61
	CH ₂ Cl ₂	488	29,200	587	3	99	3456		
3.10h	THF	561	27,500	679	23	118	3098		
	toluene	583	24,100	671	48	88	2250	-0.45	-1.49
	CH ₂ Cl ₂	563	26,700	677	28	114	2991		
3.10j	THF	523	26,700	650	3	127	3736		
	toluene	534	28,800	649	4	115	3318	-0.90	-1.78 ^c
	CH ₂ Cl ₂	523	30,900	654	8	131	3830		
3.10k	THF	509	35,800	625	< 1	116	3646		
	toluene	518	30,200	628	1	110	3381	-0.92	-1.82 ^c
	CH ₂ Cl ₂	507	39,600	627	3	120	3775		

^aQuantum yields were measured according to a published method using [Ru(bpy)₃][PF₆]₂ as a relative standard, and corrected for detector non-linearity (Figure A3.35).^[62,63] ^bCyclic voltammetry experiments were conducted in MeCN (complexes **3.10a–3.10h**) and CH₂Cl₂ (**3.10j, 3.10k**) containing 1 mM analyte and 0.1 M [*n*Bu₄N][PF₆] at a scan rate of 100 mV s⁻¹. All voltammograms were referenced internally against the ferrocene/ferrocenium redox couple. ^cIrreversible reduction, cathodic peak potential reported.

3.2.3 3-Phenyl-, 3-Cyano-, and 3-Nitro-Substituted BF₂ Formazanate Complexes

The influence of cyano-, nitro-, and phenyl-substituents at the R³ position of the formazanate backbone on the properties of BF₂ formazanate dyes was assessed through comparison of 1,5-diphenyl-substituted compounds **3.10a** (R³ = Ph), **3.10e** (R³ = CN), and **3.10g** (R³ = NO₂). Single crystals of complex **3.10g** were grown by slow evaporation of a concentrated CH₂Cl₂ solution (Figure 3.4). The solid-state structure of complex **3.10e** has previously been published.^[44] Attempts to crystallize complex **3.10a** under a variety of conditions consistently resulted in weakly diffracting, multiply twinned crystals (likely due to the *pseudo* three-fold symmetry of **3.10a**) unsuitable for X-ray diffraction studies. Therefore, complex **3.10i** (Ar¹ = Ar⁵ = Ph, R³ = *p*-tolyl), previously reported by the Otten group,^[45] has been included for comparison as the structural metrics associated with the presence of a single *p*-tolyl substituent are not expected to differ significantly from those expected for complex **3.10a**. All three BF₂ complexes contain a four-coordinate boron centre in a distorted tetrahedron, which is slightly displaced from the plane of the formazanate backbone. It is also noteworthy that the formazanate backbone is delocalized in all three examples (Table 3.3) with CN and NN bonds in between typical single and double bonds for the respective atoms involved. Each complex possesses moderate degrees of twisting between the *N*-aryl substituents and the formazanate backbone (**3.10e**, 22.0° and 24.4°, **3.10g**, 36.4° and 38.2° and **3.10i**, 48.0° and 42.0°). Overall we can conclude that structurally, all three complexes are very similar, and the nature of the R³ substituent has little influence over the bond lengths and angles of the BF₂ formazanate heterocycle (Table 3.3).

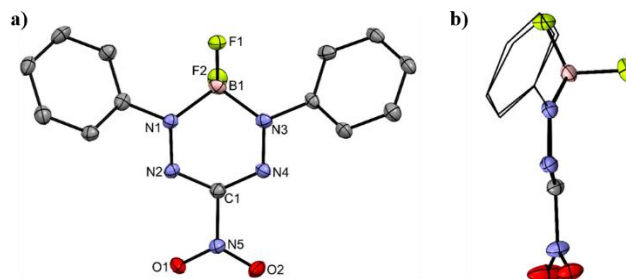


Figure 3.4. a) Top view and b) side view of the solid-state structure of BF_2 formazanate complex **3.10g**. Thermal displacement ellipsoids are shown at 50% probability and hydrogen atoms have been omitted for clarity.

Table 3.3. Selected bond lengths (\AA) and angles ($^\circ$) for **3.10e**, **3.10g**, **3.10i**,^[45] **3.10j** and **3.10k**

	3.10e	3.10g^a	3.10i^{b,[45]}	3.10j	3.10k
N1-N2, N3-N4	1.2900(15), 1.2948(15)	1.302(5), 1.304(5)	1.308(1), 1.308(1)	1.297(2), 1.303(2)	1.3026(18), 1.3077(18)
N5-N6, N7-N8	—	—	—	1.305(2), 1.302(2)	1.3078(19), 1.3130(19)
C1-N2, C1-N4	1.3408(17), 1.3379(17)	1.330(5), 1.318(5)	1.346(1), 1.343(1)	1.346(3), 1.336(2)	1.343(2), 1.340(2)
C20-N6, C20-N8	—	—	—	1.337(3), 1.344(2)	1.341(2), 1.339(2)
N1-B1, N3-B1	1.5748(18), 1.5771(17)	1.576(6), 1.563(6)	1.559(2), 1.552(2)	1.562(3), 1.556(3)	1.559(2), 1.553(2)
N5-B2, N7-B2	—	—	—	1.563(3), 1.546(3)	1.556(2), 1.556(2)
N2-C1-N4	129.33(12)	130.0(4)	124.2(1)	126.29(17)	126.24(15)
N6-C20-N8	—	—	—	124.78(17)	124.37(15)
C1-N2-N1, C1-N4-N3	117.14(11), 117.30(11)	115.6(3), 115.5(3)	117.68(9), 117.72(9)	118.56(15), 118.61(16)	117.15(14), 119.12(14)
C20-N6-N5, C20-N8-N7	—	—	—	118.74(15), 116.89(16)	118.14(13), 117.02(14)
Boron displacement ^c	0.192	0.456	0.500	0.159, 0.503	0.307, 0.577
Dihedral angles ^d	18.7, 26.2	36.4, 38.2	48.0, 42.0	25.05, 31.59, 27.46, 49.88	18.77, 38.96, 40.44, 37.20
Benzene bridge dihedral angles ^e	—	—	—	10.46, 17.48	8.79, 12.04

^aThe second molecule in the unit cell of **3.10g** has very similar structural metrics and is not reported here. ^bThe numbering convention for the structure previously reported by Otten and co-workers^[45] has been modified for ease of comparison. ^cDistance between B1 and N₄ plane. ^dAngles between the plane defined by the N1 and N3 aryl substituents and the N₄ plane. ^eAngles between the benzene bridge and the N₄ plane.

As both cyano and nitro groups are strongly electron-withdrawing, complexes **3.10e** ($R^3 = \text{CN}$) and **3.10g** ($R^3 = \text{NO}_2$) have similar spectroscopic and electrochemical properties, though they differ significantly when compared to complex **3.10a** ($R^3 = \text{Ar}$). All three complexes are strongly absorbing between 400 and 600 nm ($\pi \rightarrow \pi^*$), though their λ_{max} range from 502 nm (**3.10e**) to 505 nm (**3.10g**) and 517 nm (**3.10a**) (Figures 3.5a, A3.36, A3.37, Table 3.2). Similarly, while all three phenyl-substituted complexes are fluorescent (Figure 3.5b, Table 3.2), the emission quantum yields vary dramatically (**3.10a**: $\lambda_{\text{em}} = 626$ nm, $\Phi_{\text{F}} = <1\%$, **3.10e**: $\lambda_{\text{em}} = 586$ nm, $\Phi_{\text{F}} = 15\%$, **3.10g**: $\lambda_{\text{em}} = 590$ nm, $\Phi_{\text{F}} = 5\%$). We assume that the difference in quantum yields is likely due to non-radiative decay pathways associated with the 3-phenyl substituent. While complex **3.10a** has the lowest quantum yield, it has the highest Stokes shift ($v_{\text{ST}} = 109$ nm, or 3368 cm^{-1} in toluene), significantly higher than complexes **3.10e** ($v_{\text{ST}} = 84$ nm, 2855 cm^{-1}) and **3.10g** ($v_{\text{ST}} = 85$ nm, 2853 cm^{-1}).

The electron-withdrawing nature of the R^3 substituent has a significant effect on the electrochemical properties of BF_2 formazanate complexes. Complex **3.10g** ($R^3 = \text{NO}_2$) is the easiest to reduce, with the first and second one-electron reductions occurring at -0.48 V and -1.61 V vs. ferrocene/ferrocenium. Complex **3.10e** ($R^3 = \text{CN}$) is slightly more difficult to reduce at potentials of -0.53 V and -1.68 V. Finally, complex **3.10a** ($R^3 = \text{Ph}$), is substantially more difficult to reduce, with two one-electron reductions occurring at -0.82 V and -1.89 V (Figure A3.38, Table 3.2). As mentioned earlier, the properties of complexes bearing phenyl and naphthyl substituents at the 3-position of the formazanate backbone did not differ dramatically. We have also previously shown that the substitution of electron-donating and withdrawing groups introduced on aryl rings at the 3-position of the formazanate backbone did not significantly alter the properties of the resulting BF_2 complexes.^[51] However, complexes **3.10a**, **3.10e**, and **3.10g** clearly demonstrate that the same trend is not true for all substituents at the 3 position, as the properties of **3.10e** ($R^3 = \text{CN}$) and **3.10g** ($R^3 = \text{NO}_2$) are drastically different than those of **3.10a** ($R^3 = \text{Ph}$). This is likely due to the strong electron-withdrawing characteristics of the cyano and nitro substituents, and less related to the extent of π -conjugation in these complexes.

By comparing naphthyl-substituted complexes **3.10d**, **3.10f** and **3.10h** with phenyl-substituted complexes **3.10a**, **3.10e**, and **3.10g**, the effect of π -conjugation on the properties

of BF₂ 3-phenyl-, 3-cyano- and 3-nitro-formazanate complexes was studied. The wavelength of maximum absorption of naphthyl substituted complexes **3.10d** (R³ = Ph), **3.10f** (R³ = CN) and **3.10h** (R³ = NO₂) were red-shifted (relative to the phenyl-substituted analogs **3.10a** [R³ = Ph], **3.10e** [R³ = CN] and **3.10g** [R³ = NO₂]), from 502 to 581 nm for complex **3.10f** (R³ = CN), from 505 to 583 nm for complex **3.10h** (R³ = NO₂), and from 517 to 556 nm for complex **3.10d** (R³ = Ph) (Figure 3.5c, Table 3.2). While in all three cases the observed trend was the same, the magnitude of the red-shift upon replacement of two phenyl substituents with two naphthyl substituents was much greater for complexes with strongly electron withdrawing R³ substituents [$\Delta\lambda_{\max} = 79$ nm, 2709 cm⁻¹ (R³ = CN); $\Delta\lambda_{\max} = 78$ nm, 2649 cm⁻¹ (R³ = NO₂); $\Delta\lambda_{\max} = 39$ nm, 1357 cm⁻¹ (R³ = Ph)].

The emission spectra of complexes **3.10d**, **3.10f** and **3.10h** (Figure 3.5d, Table 3.2) were also red-shifted with respect to the phenyl-substituted analogs, with λ_{em} of 681 nm (**3.10d**), 670 nm (**3.10f**) and 671 nm (**3.10g**) in toluene. The emission quantum yields of these three complexes were significantly higher than the quantum yields of the phenyl-substituted complexes. The addition of the naphthyl substituent increases the emission quantum yield for **3.10d** to 5% (from < 1% in complex **3.10a**), for **3.10f** to 39% (from 15% in complex **3.10e**) and for **3.10h** to 48% (from 5% in complex **3.10g**). The Stokes shifts observed for the 3-cyano- and 3-nitro-substituted complexes were smaller than those of 3-phenyl substituted complexes. All complexes with R³ = cyano or nitro have Stokes shifts ranging from 84–89 nm in toluene (2250–2855 cm⁻¹), while those with R³ = Ph, have generally larger Stokes shifts, from 109–125 nm in toluene (3368–3590 cm⁻¹).

The cyclic voltammograms of complexes **3.10d**, **3.10f** and **3.10h** demonstrate that the more electron-deficient complexes **3.10f** and **3.10h** are significantly easier to reduce (by almost 300 mV) than complex **3.10d** (Figure 3.6, Table 3.2). In all three examples, the reduction potential of the naphthyl-substituted complexes was 30–45 mV higher than the phenyl-substituted analogs. Complexes **3.10f**, **3.10g** and **3.10h** also underwent irreversible oxidation within the electrochemical window of the solvent (CH₃CN) (Figure A3.39).

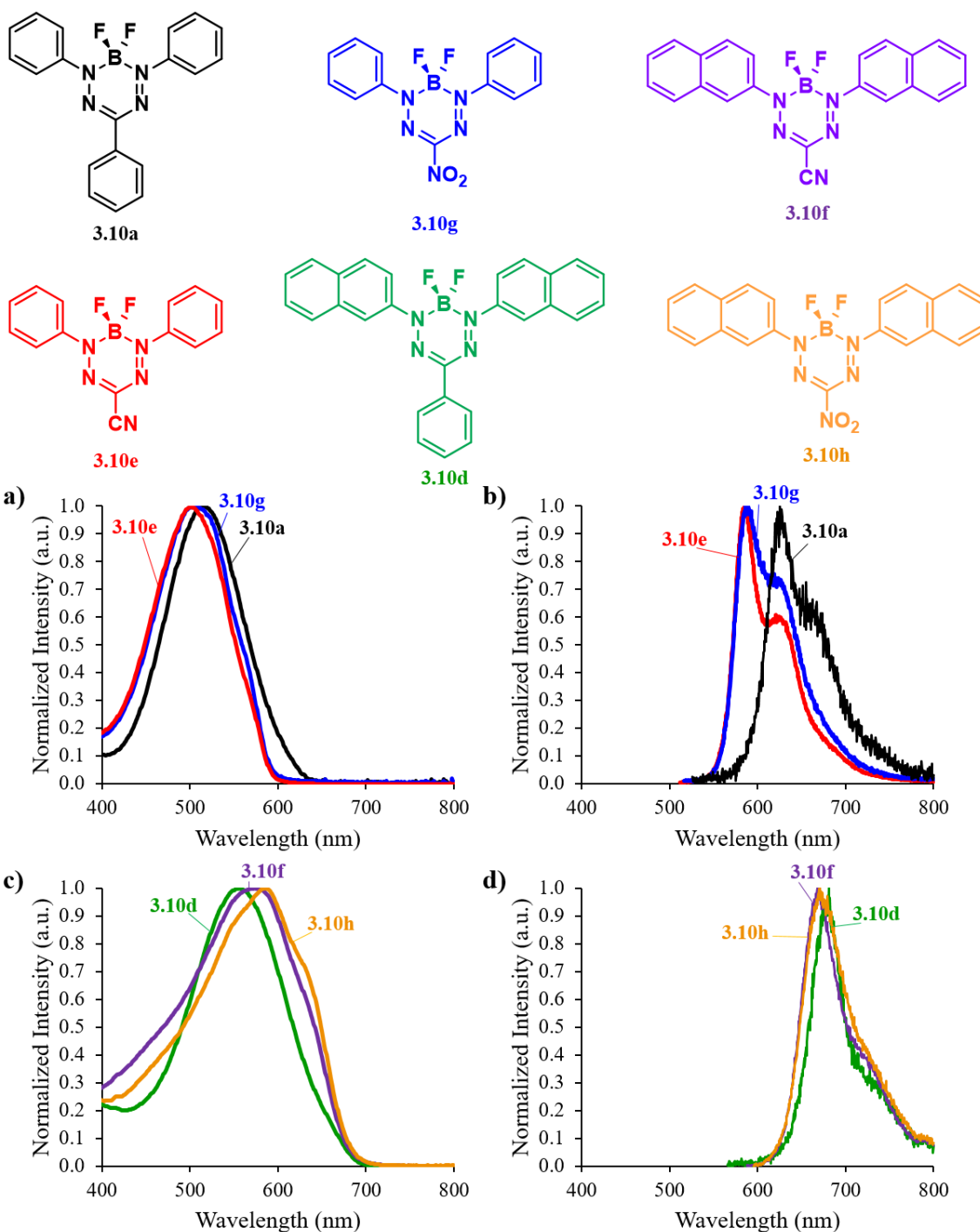


Figure 3.5. UV-vis absorption spectra (a) and emission spectra (b) of **3.10a** (black, Ar¹ = Ar⁵ = R³ = Ph), **3.10e** (red, Ar¹ = Ar⁵ = Ph, R³ = CN) and **3.10g** (blue, Ar¹ = Ar⁵ = Ph, R³ = NO₂). UV-vis absorption spectra (c) and emission spectra (d) of **3.10d** (green, Ar¹ = Ar⁵ = Np, R³ = Ph), **3.10f** (purple, Ar¹ = Ar⁵ = Np, R³ = CN) and **3.10h** (orange, Ar¹ = Ar⁵ = Np, R³ = NO₂). All UV-vis absorption and emission spectra were recorded for 10⁻⁵ M degassed toluene solutions.

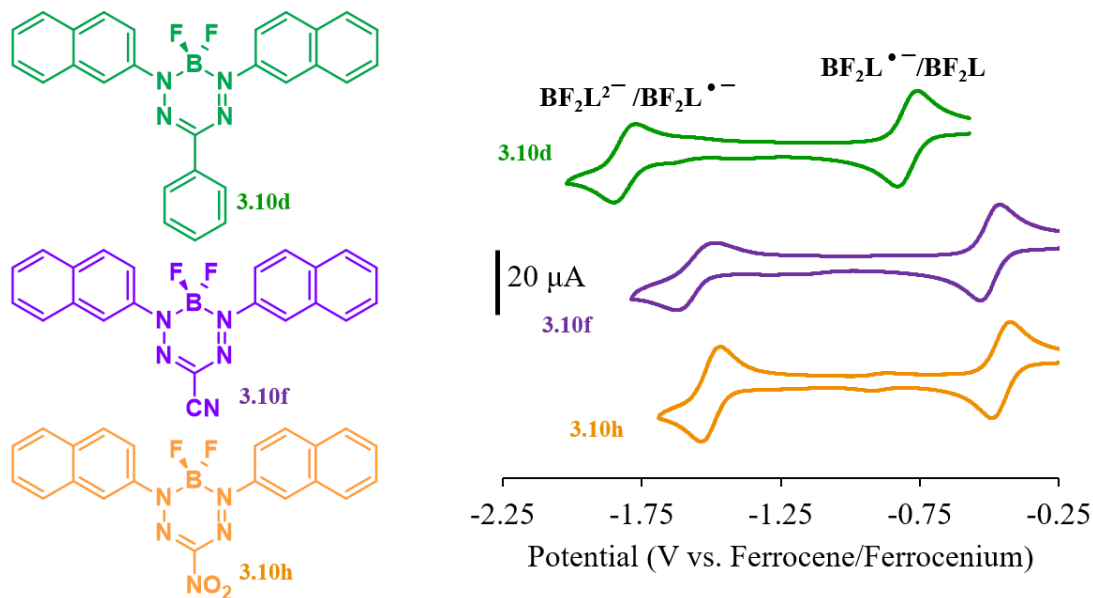


Figure 3.6. Cyclic voltammograms of **3.10d** (green), **3.10f** (purple) and **3.10h** (orange) recorded at 100 mV s^{-1} in 1 mM acetonitrile solutions containing 0.1 M $[n\text{Bu}_4\text{N}][\text{PF}_6]$ as supporting electrolyte.

3.2.4 Electronic Structure Calculations

In an attempt to rationalize the trends observed, we calculated the highest occupied and lowest unoccupied molecular orbitals (HOMOs and LUMOs) of **3.10a**, **3.10e**, and **3.10g** (Figure 3.7 and Table 3.4) with the *Gaussian 09* program^[64] using the M06 density functional^[65] and the 6-311+G* basis set, in vacuum and in toluene solution. The Kohn–Sham molecular orbitals of **3.10a**, **3.10e** and **3.10g** were computed for the corresponding optimized molecular structures. The UltraFine integration grid was employed in all calculations. Solvation effects were treated implicitly using the polarizable continuum model (SCRF=PCM). All optimized structures of **3.10a**, **3.10e** and **3.10g** have C_s symmetry and were confirmed by vibrational analysis to be minima on the potential energy surface, both in vacuum and in toluene solution (see Appendix A3 for further details).

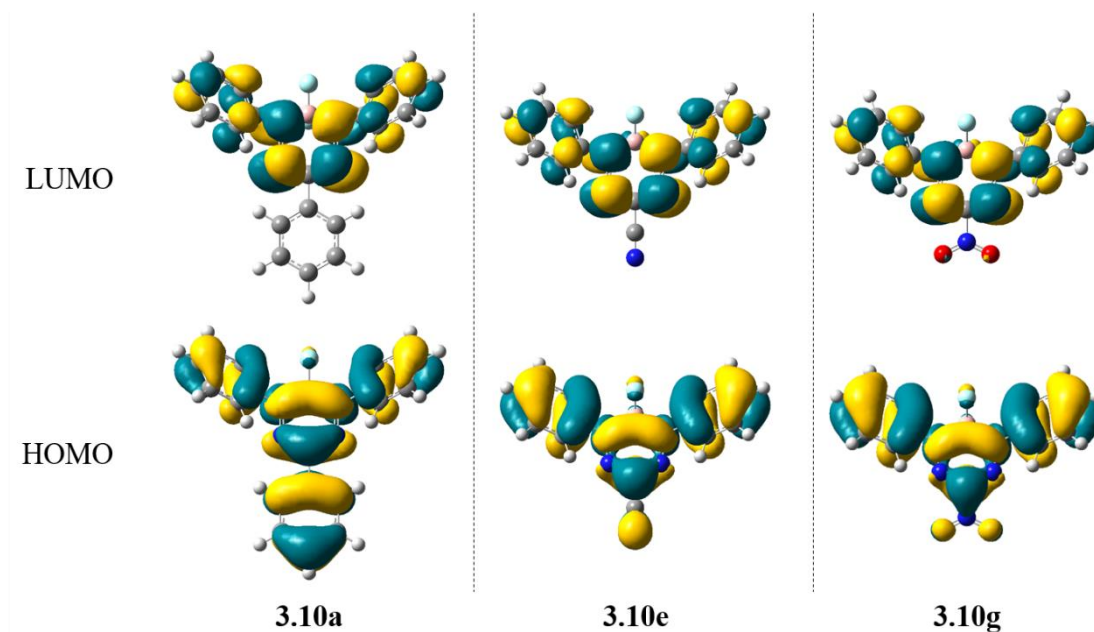


Figure 3.7. HOMOs and LUMOs for BF₂ complexes **3.10a** (Ar¹ = Ar⁵ = R³ = Ph), **3.10e** (Ar¹ = Ar⁵ = Ph, R³ = CN) and **3.10g** (Ar¹ = Ar⁵ = Ph, R³ = NO₂) calculated in toluene solution.

Table 3.4. HOMO/LUMO energies for BF₂ complexes **3.10a** (Ar¹ = Ar⁵ = R³ = Ph), **3.10e** (Ar¹ = Ar⁵ = Ph, R³ = CN) and **3.10g** (Ar¹ = Ar⁵ = Ph, R³ = NO₂) in vacuum and toluene solution calculated at the M06/6–311+G* level of theory using the SCRF method.

Compound	ϵ_{HOMO} (eV)	ϵ_{LUMO} (eV)	HOMO-LUMO Gap (eV)	HOMO-LUMO Gap (nm)
Vacuum				
3.10a	-6.38	-3.25	3.13	397
3.10e	-7.12	-3.79	3.34	372
3.10g	-7.24	-3.85	3.39	366
Toluene Solution				
3.10a	-6.45	-3.30	3.15	393
3.10e	-7.12	-3.76	3.36	369
3.10g	-7.23	-3.83	3.40	365

The calculated LUMOs for complexes **3.10a**, **3.10e** and **3.10g** are highly delocalized over the formazanate backbone and *N*-aryl substituents, but do not extend over the 3-substituents. By contrast, the HOMOs are delocalized over both the *N*-aryl and 3-substituents (Ph, CN and NO₂). The electrochemical reduction of complexes **3.10a**, **3.10e**,

and **3.10g** should primarily involve the LUMOs of each complex. Based solely on the shape of the calculated frontier orbitals, the reduction potentials for each compound should be similar. However, due to the differing electron-withdrawing characteristics of the 3-substituents, the experimentally determined reduction potentials varied significantly. The observed trend in the first and second reduction potentials (E_{red1} and E_{red2}), which involve stepwise population of the LUMO, was consistent with the trend in computed LUMO energies (ϵ_{LUMO}) in toluene solution: **3.10g** (-3.83 eV) < **3.10e** (-3.76 eV) < **3.10a** (-3.30 eV). The finding that the LUMOs do not extend over the 3-substituent is also consistent with the fact that the reduction potentials observed for 1,5-diphenyl-substituted complexes **3.10a** ($R^3 = \text{Ph}$) and **3.10b** ($R^3 = \text{Np}$) are similar. The small difference in these potentials may be attributed to the subtle difference in the electron-withdrawing nature of phenyl and naphthyl substituents.

The absorption and emission properties of BF_2 formazanate complexes **3.10a**, **3.10e** and **3.10g** varied significantly and involve both the HOMO and LUMO orbitals. The HOMO/LUMO for **3.10a** ($R^3 = \text{Ph}$) were significantly higher in energy than those found for complexes **3.10e** and **3.10g** ($R^3 = \text{CN}$ and NO_2 , respectively). This is a result of destabilization of the HOMO, due to the extended π -conjugation associated with the 3-phenyl substituent, which leads to a decrease in the HOMO/LUMO gap, red-shifting of its absorption and emission spectra relative to **3.10e** and **3.10g**. Although one cannot expect quantitative agreement between HOMO-LUMO gaps and lowest electronic excitation energies, we note that the observed trends in λ_{max} and λ_{em} are consistent with the trends in calculated HOMO-LUMO gaps in toluene [**3.10a** (393 nm) > **3.10e** (369 nm) \approx **3.10g** (365 nm)].

3.2.5 Benzene-Bridged BF_2 Formazanate Complexes

Single crystals of dimers **3.10j** and **3.10k** suitable for X-ray diffraction studies were grown by slow evaporation of concentrated CH_2Cl_2 solution (Figure 3.8, Table 3.3). In both solid-state structures, the formazanate-benzene-formazanate π frameworks are relatively planar with angles between the benzene bridge and formazanate planes of 10.46° and 17.48° in **3.10j** and 8.79° and 12.04° in **3.10k**. This planarity renders these compounds the perfect platform for probing electronic communication through *meta*- and *para*- benzene spacers.

The *N*-phenyl substituents are moderately twisted in each structure with dihedral angles of 25.05–49.88° (**3.10j**) and 18.77–40.44° (**3.10k**) relative to the nearest formazanate moiety. The twisting is most likely the result of crystal packing effects. We also note that the formazanate backbones are delocalized with all N-N, C-N and C-C bonds falling between the typical single and double bond lengths for the respective atoms involved. The C-C bond lengths in the benzene bridges of **3.10j** and **3.10k** are between 1.375(3) Å and 1.397(3) Å, and are similar to other aromatic C-C bonds. For both dimers **3.10j** and **3.10k**, one of the two BF₂ formazanate moieties exists in a relatively planar conformation and the other in a ‘dragonfly’ conformation where the boron atom is displaced from the formazanate plane by more than 0.5 Å. We have previously reported that these two conformations differ in energy by only a few kcal/mol.^[44]

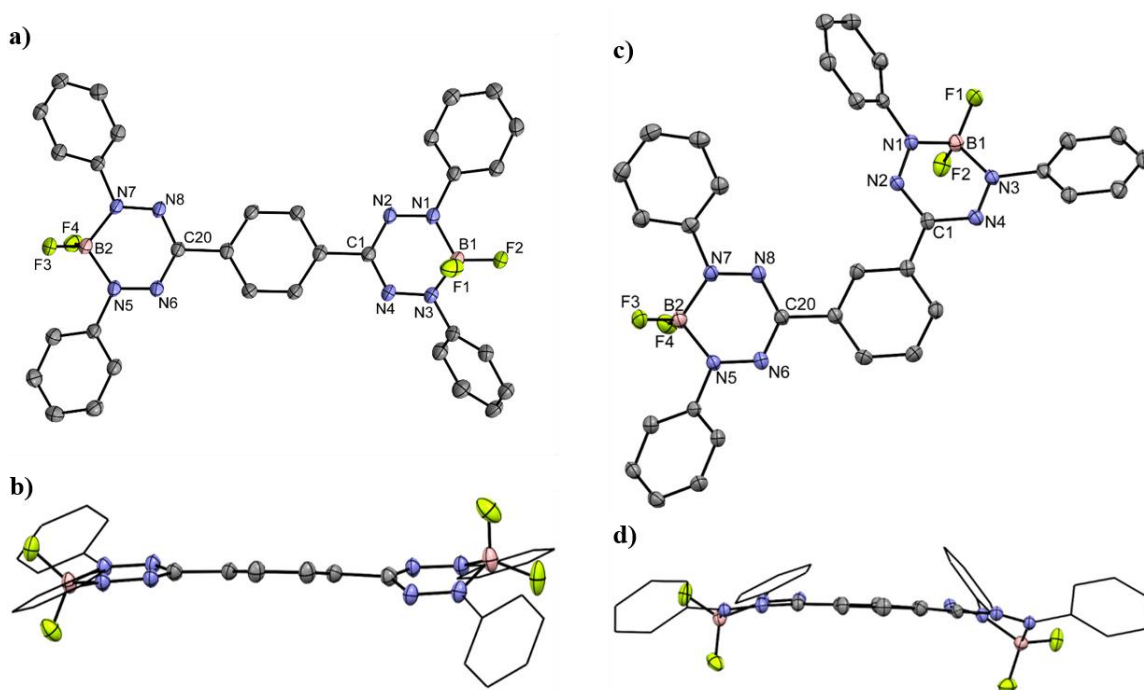


Figure 3.8. a,c) Top view and b,d) side view of the solid-state structure of BF₂ formazanate dimers **3.10j** and **3.10k**. Thermal displacement ellipsoids are shown at 50% probability and hydrogen atoms have been omitted for clarity. Only one of two very similar molecules in the asymmetric unit for **3.10j** is shown.

Qualitatively, *meta*-substituted bridged dimer **3.10k** and triphenyl BF₂ complex **3.10a** have very similar absorption and emission spectra. In CH₂Cl₂, **3.10k** has a wavelength of maximum absorption of 507 nm, which is very similar to that of **3.10a** (Ar¹ = R³ = Ar⁵ =

Ph, $\lambda_{\max} = 509$ nm). **3.10a** is highly absorbing, with a molar absorptivity (ϵ) of $23,400 \text{ M}^{-1} \text{ cm}^{-1}$, while **3.10k** has molar absorptivity of nearly double that, at $39,600 \text{ M}^{-1} \text{ cm}^{-1}$ due to the presence of two boron difluoride formazanate moieties. In comparison, *para*-substituted bridged complex **3.10j** has a higher wavelength of maximum absorption of 523 nm in CH_2Cl_2 and is strongly absorbing ($\epsilon = 30,900 \text{ M}^{-1} \text{ cm}^{-1}$) (Figure 3.9, Table 3.2). BF_2 complexes **3.10j** and **3.10k** are weakly emissive, with wavelengths of maximum emission of 654 and 627 nm and modest emission quantum yields of 8% and 3%, respectively. Each compound exhibits a large Stokes shift, ranging from 120 to 131 nm ($3773\text{--}3830 \text{ cm}^{-1}$). It is noteworthy that the emission quantum yields increase for the dimers, relative to triphenyl ‘monomer’ **3.10a**. It has been shown that the emission quantum yield of *para*-benzene bridged BODIPY dimers **3.9** is significantly reduced relative to phenyl-substituted monomer **3.7**.^[66] A major factor contributing to the decreased emission intensity in BODIPY dimer **3.9** is the small Stokes shifts observed for the monomeric units ($\nu_{\text{ST}} = 25$ nm, 906 cm^{-1}), which leads to reabsorption of emitted photons by the fluorophore in close proximity within the dimer framework. In the case of dimers **3.10j** and **3.10k**, the large Stokes shifts result in minimal overlap between absorption and emission bands and limit reabsorption of emitted photons by the dimer pairs.

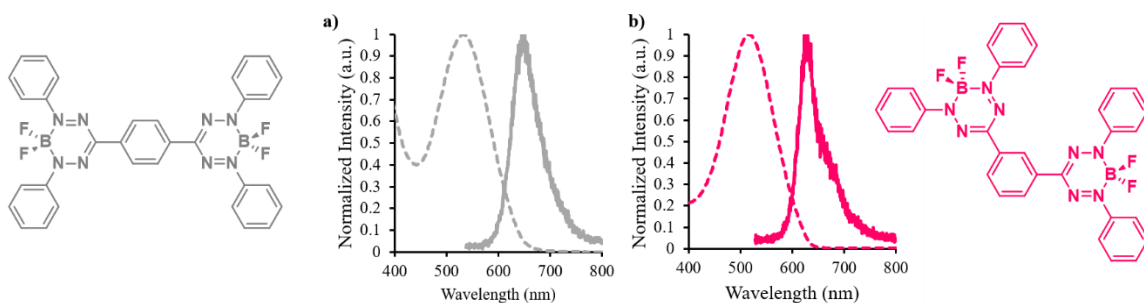


Figure 3.9. UV-vis absorption spectra (dashed) and emission spectra (solid) of a) **3.10j** and b) **3.10k**, recorded in 10^{-5} M degassed toluene solutions.

Due to the poor solubility of compounds **3.10j** and **3.10k** in CH_3CN , CH_2Cl_2 was used for the cyclic voltammetry studies. The cyclic voltammograms of compounds **3.10a**, **3.10j** and **3.10k** in CH_2Cl_2 are shown in Figure 3.10. BF_2 formazanate dimers **3.10j** and **3.10k** each undergo reversible electrochemical reduction at $E_{\text{red1}} = -0.90$ V (**3.10j**) and -0.92 V (**3.10k**) corresponding to the transfer of two electrons (Figure 3.10, Table 3.2). Both dimers undergo a second irreversible electrochemical reduction at a cathodic peak potential (E_{pc}),

$E_{pc,red2} = -1.78$ V (**3.10j**) and -1.89 V (**3.10k**) also consistent with a two-electron transfer. The first reversible reduction of dimers **3.10j** and **3.10k** corresponds to the formation of the bis-radical anion form of the dimer, as depicted in Scheme 3.2. The second reduction of compounds **3.10j** and **3.10k** corresponds to the bis-radical anions being transformed into bis-dianions. Monomer **3.10a** displayed similar electrochemical properties ($E_{red1} = -0.93$ V and $E_{pc, red2} = -1.84$ V in CH_2Cl_2), with each reduction corresponding to transfer of a single electron. We have previously shown that the electrochemical properties of monomeric BF_2 formazanate complexes are sensitive to the presence of electron-withdrawing and electron-donating carbon substituents.^[44,51] We therefore attribute the relative ease of reduction (less negative potentials) associated with **3.10j** to the electron withdrawing nature of the BF_2 formazanate moieties, which is enhanced in the *para*-substituted dimer.

The second reduction waves for **3.10j**, **3.10k** and **3.10a** were not reversible in CH_2Cl_2 , despite the second reduction of monomer **3.10a** being fully reversible in CH_3CN . The anodic peak current associated with the second reduction wave increased as the scan rate increased (Figures A3.40–A3.42), indicating that the irreversibility may arise due to a competing chemical reaction, which oxidizes the bis-dianions to bis-radical anions. Initially, we considered the possibility that the electrogenerated bis-dianions could undergo a comproportionation (*e.g.*, $LBF_2^{2-} + LBF_2 \rightarrow 2 LBF_2^{\bullet-}$) reaction with neutral BF_2 complexes to generate two equivalents of bis-radical anions. However, based on the symmetry of the anodic and cathodic peak currents associated with the first reduction, we do not feel that this is the case. We conclude that the electrogenerated dianions are oxidized back to their radical anion forms within the electrochemical cell, although the identity of the oxidant remains elusive.

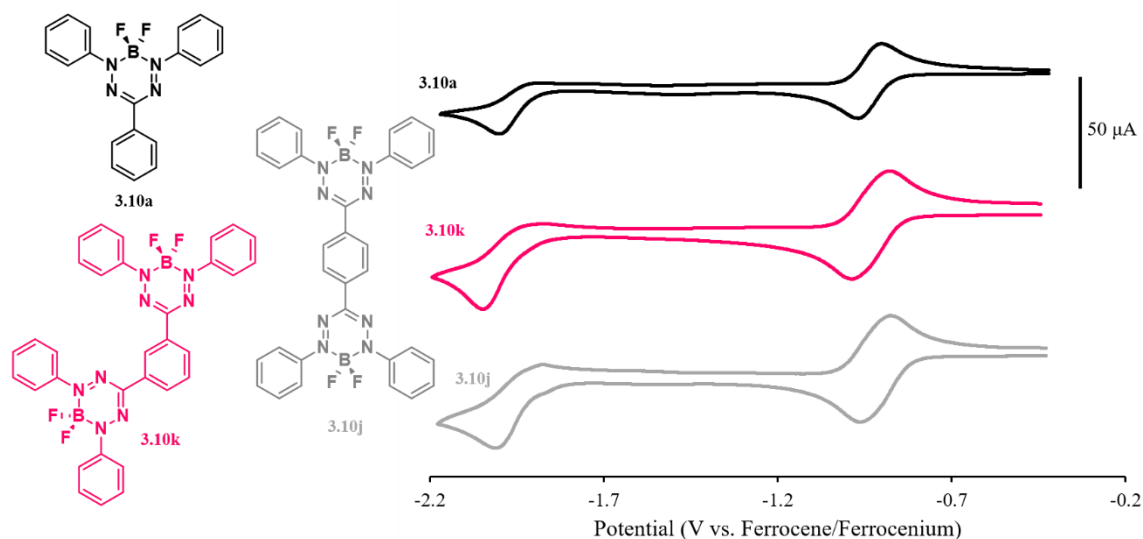
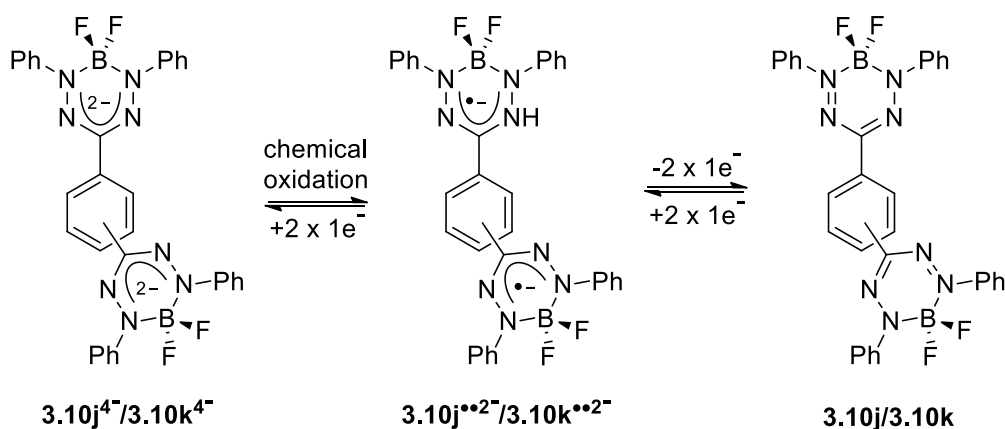


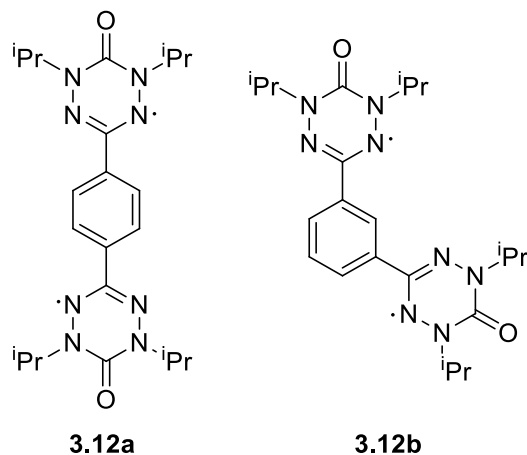
Figure 3.10. Cyclic voltammograms of **3.10j** (grey), **3.10k** (pink) and **3.10a** (black) recorded at 100 mV s^{-1} in $1 \text{ mM CH}_2\text{Cl}_2$ solutions containing $0.1 \text{ M } [n\text{Bu}_4\text{N}][\text{PF}_6]$ as supporting electrolyte.

Due to the broad appearance of the reduction peaks in the cyclic voltammograms of dimers **3.10j** and **3.10k** relative to monomer **3.10a** we believe each process involves two distinct one-electron reductions (one electron for each of the BF_2 formazanate moieties). However, we were unable to resolve each wave, even when square wave or differential pulse voltammetry techniques were employed. All three complexes also undergo irreversible electrochemical oxidation within the solvent window (Figure A3.43).



Scheme 3.2. Electrochemical/chemical reactions for **3.10j** and **3.10k**.

Closely related benzene-bridged diradicals **3.12a** and **3.12b** have been shown to undergo reversible electrochemical oxidation and reduction to their closed shell bis-cation and bis-anion forms. In these systems, electrochemical reduction occurred in two well-resolved steps, which supports the interpretation of our results.



3.3 Conclusion

In conclusion, we have described the synthesis and characterization of eight BF_2 formazanate complexes and two BF_2 formazanate dimers allowing us to systematically assess the effect of extended π -conjugation on the spectroscopic and electrochemical properties of BF_2 formazanate complexes. In general, extending the π -conjugation of complexes by replacing phenyl substituents with naphthyl substituents increased fluorescence quantum yields, increased (less negative) reduction potentials and red-shifted the wavelengths of maximum absorption and emission. We have also demonstrated that the differences in properties between BF_2 complexes of 3-aryl-, cyano- and nitro-formazans relate primarily to the electron-withdrawing nature of the 3-substituents ($\text{NO}_2 > \text{CN} \gg \text{Ph}$). The complexes of 3-cyano and 3-nitro formazans have significantly increased emission quantum yields, and their properties are very sensitive to extension of their π -systems. The electrochemical properties of the dimers were closely related to those of the triphenyl monomer. In contrast, the *para*-substituted dimer exhibited optical properties consistent with extended π conjugation, including a red-shift in the wavelength of maximum absorption and emission, and an increase in emission quantum yield. The *meta*-substituted dimer displayed characteristics consistent with a cross-conjugated electronic structure and essentially behaved as two independent BF_2 formazanate moieties.

3.4 Experimental Section

3.4.1 General Considerations

Reactions and manipulations were carried out under a nitrogen atmosphere using standard Schlenk techniques unless otherwise stated. Solvents were obtained from Caledon Laboratories, dried using an Innovative Technologies Inc. solvent purification system, collected under vacuum, and stored under a nitrogen atmosphere over 4 Å molecular sieves. The synthesis and characterization of formazans **3.11a**,^[48] **3.11e**, **3.11g**,^[49] **3.11j** and **3.11k**^[50] and BF₂ complex **3.10e**^[44] have been reported previously. The details of the synthesis and characterization of formazans **3.11j** and **3.11k** were limited, and so we have therefore included full experimental details for these compounds.

NMR Spectra were recorded on a 400 MHz (¹H: 399.8 MHz, ¹¹B: 128.3 MHz, ¹⁹F: 376.1 MHz) or 600 MHz (¹H: 599.5 MHz, ¹³C: 150.8 MHz) instrument. ¹H NMR spectra were referenced to residual CHCl₃ (7.26 ppm) or DMSO-*d*₅ (2.50 ppm) and ¹³C NMR spectra were referenced to CDCl₃ (77.2 ppm), CD₂Cl₂ (53.8 ppm) or DMSO-*d*₆ (39.5 ppm). ¹¹B spectra were referenced to BF₃·OEt₂ at 0 ppm, and ¹⁹F spectra were referenced to CFC₃ at 0 ppm. Mass spectrometry data were recorded in positive-ion mode using electron impact ionization and electrospray ionization. UV-vis absorption data were recorded using a Cary 300 Scan instrument. Four separate concentrations were run for each sample and molar extinction coefficients were determined from the slope of a plot of absorbance against concentration. Infrared spectra were recorded on a KBr disk using a Bruker Vector 33 FT-IR spectrometer. Emission spectra were obtained using a Photon Technology International QM-4 SE spectrofluorometer. Excitation wavelengths for the emission spectra were chosen based on λ_{max} from the respective UV-vis absorption spectrum in the same solvent. Emission quantum yields were estimated relative to ruthenium tris(bipyridine) hexafluorophosphate by previously described methods and corrected for wavelength dependent detector sensitivity (Figure A3.35).^[62-63]

3.4.2 Electrochemical Methods

Cyclic voltammetry experiments were performed with a Bioanalytical Systems Inc. (BASi) Epsilon potentiostat and analyzed using BASi Epsilon software. Electrochemical cells consisted of a three-electrode setup including a glassy carbon working electrode, platinum wire counter electrode, and silver wire *pseudo* reference electrode. Experiments were run

at various scan rates (100–2000 mV s⁻¹) in degassed CH₃CN or CH₂Cl₂ solutions of the analyte (~1 mM) and supporting electrolyte (0.1 M [*n*Bu₄N][PF₆]). Cyclic voltammograms were referenced against an internal standard (~1 mM ferrocene) and corrected for internal cell resistance using the software.

3.4.3 X-ray Crystallography Details

Single crystals of complex **3.10g**, **3.10j** and **3.10k** suitable for X-ray diffraction studies were grown by slow evaporation of a concentrated CH₂Cl₂ solutions. The samples were mounted on MiTeGen polyimide micromounts with a small amount of Paratone *N* oil. X-ray measurements were made on a Nonius KappaCCD Apex2 (**3.10j**) or Bruker Kappa Axis Apex2 (**3.10g**, **3.10k**) at a temperature of 110 K. The data collection strategy included a number of ω and φ scans which collected data over a range of angles, 2θ . The frame integration was performed using SAINT.^[67] The resulting raw data was scaled and absorption corrected using a multi-scan averaging of symmetry equivalent data using SADABS.^[68] The structures were solved by direct methods using the XS program (**3.10g**)^[69] or dual space methodology using the SHELXT program (**3.10j**, **3.10k**).^[70] Non-hydrogen atoms were obtained from the initial solution. The hydrogen atoms were introduced at idealized positions and were allowed to refine isotropically. The structural model was fit to the data using full matrix least-squares based on F^2 . The calculated structure factors included corrections for anomalous dispersion from the usual tabulation. The structure was refined using the SHELXL-2014 program from the SHELX suite of crystallographic software.^[71] See Table 3.5 for additional crystallographic data.

Table 3.5. X-ray diffraction data collection and refinement details for BF₂ complexes **3.10g**, **3.10j** and **3.10k**.

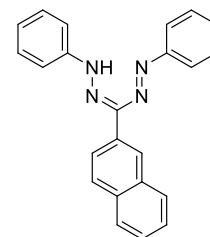
	3.10g	3.10j	3.10k
Chemical Formula	C _{13.50} H ₁₁ BClF ₂ N ₅ O ₂	C ₂₄ H ₁₈ B _{1.50} F ₃ N ₆	C ₃₂ H ₂₄ B ₂ F ₄ N ₈
FW (g mol ⁻¹)	359.53	463.66	618.21
Crystal Habit	Red Prism	Red Prism	Red Plate
Crystal System	Monoclinic	Triclinic	Monoclinic
Space Group	<i>P</i> 2 ₁ / <i>n</i>	<i>P</i> $\bar{1}$	<i>C</i> 2/ <i>c</i>
T (K)	110	110	110
λ (Å)	0.71073	1.54178	0.71073
<i>a</i> (Å)	9.555(8)	11.492(2)	18.424(7)
<i>b</i> (Å)	17.226(11)	14.163(3)	17.935(7)
<i>c</i> (Å)	18.840(14)	15.253(3)	18.574(6)
α (deg)	90	65.150(6)	90
β (deg)	98.070(13)	69.157(9)	110.646(10)
γ (deg)	90	82.705(8)	90
<i>V</i> (Å ³)	3070(4)	2104.6(7)	5743(4)
<i>Z</i>	8	4	8
ρ (g/cm ³)	1.556	1.463	1.430
μ (cm ⁻¹)	0.290	0.905	0.106
R ₁ , ^a wR ₂ ^b [<i>I</i> > 2 σ]	0.0588, 0.1730	0.0427, 0.1064	0.0460, 0.0912
R ₁ , wR ₂ (all data)	0.0811, 0.1901	0.0604, 0.1181	0.0932, 0.1079
GOF ^c	1.025	1.020	1.018

^aR₁ = $\Sigma(|F_o| - |F_c|) / \Sigma F_o$, ^bwR₂ = $[\Sigma(w(F_o^2 - F_c^2)^2) / \Sigma(wF_o^4)]^{1/2}$, ^cGOF = $[\Sigma(w(F_o^2 - F_c^2)^2) / (\text{No. of reflns.} - \text{No. of params.})]^{1/2}$

Representative procedure for the preparation of formazans **3.11b** and **3.11c**:

Formazan **3.11b**

In air, phenyl hydrazine (0.69 g, 0.63 mL, 6.4 mmol) was dissolved in EtOH (15 mL). 2-Naphthylaldehyde (1.00 g, 6.40 mmol) was then added and the solution was stirred for 10 min. After this time, a light yellow precipitate had formed. CH₂Cl₂ (50 mL) and water (50 mL) were added to form a biphasic reaction mixture. Na₂CO₃ (2.17 g, 20.5 mmol) and [nBu₄N][Br] (0.21 g, 0.64 mmol) were added, and the mixture was cooled in an ice bath to 0 °C. In a separate flask, aniline (0.60 g, 6.4 mmol) and concentrated HCl (1.6 mL) were mixed in water (15 mL), and cooled in an ice bath. A cooled solution of sodium nitrite (0.51 g, 7.4 mmol) in water (5 mL) was added slowly to the amine solution. This mixture was stirred at 0 °C for 30 min, after which time it was added dropwise to the biphasic reaction mixture described above over 10 min. The resulting solution was stirred for 18 h,

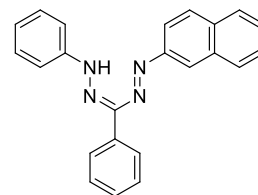


which gradually turned dark red over this time. The dark red organic fraction was then washed with deionized water (3 x 50 mL), dried over MgSO₄, gravity filtered and concentrated *in vacuo*. The resulting residue was purified by flash chromatography (CH₂Cl₂, neutral alumina) to afford formazan **3.11b** as a dark red microcrystalline solid. Yield = 1.11 g, 50%. Melting point = 124–126 °C. ¹H NMR (599.5 MHz, CDCl₃) δ 15.49 (s, 1H, NH), 8.62 (s, 1H, aryl CH), 8.29–8.28 (m, 1H, aryl CH), 7.95–7.87 (m, 3H, aryl CH), 7.74 (d, ³J_{HH} = 8 Hz, 4H, aryl CH), 7.52–7.48 (m, 6H, aryl CH), 7.33–7.30 (m, 2H, aryl CH). ¹³C{¹H} NMR (100.6 MHz, CDCl₃): δ 148.0, 141.1, 135.0, 133.7, 133.1, 129.5, 128.6, 128.0, 127.7, 127.6, 126.1, 125.9, 124.7, 124.1, 118.9. FT-IR (KBr): 3267 (br, s), 3055 (s), 026 (m), 2915 (m), 2846 (m), 1598 (s), 1501 (s), 1453 (m), 1348 (m), 1253 (s), 1226 (s) cm⁻¹. UV-vis (toluene): λ_{max} = 498 nm (ε = 10, 100 M⁻¹ cm⁻¹). Mass Spec. (EI, +ve mode): exact mass calculated for [C₂₃H₁₈N₄]⁺: 350.1532; exact mass found: 350.1537; difference: +1.6 ppm.

Formazan 3.11c

In air, from 6.98 mmol of hydrazine/aldehyde: Yield = 2.24 g, 92%.

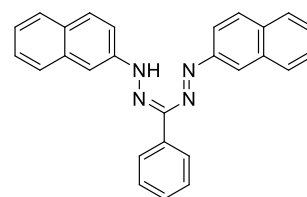
Melting point = 140–142 °C. ¹H NMR (400.1 MHz, CDCl₃) δ 15.56 (s, 1H, NH), 8.21 (d, ³J_{HH} = 7 Hz, 2H, aryl CH), 8.04 (s, 1H, aryl CH), 7.93–7.88 (m, 3H, aryl CH), 7.85–7.83 (m, 1H, aryl CH), 7.69



(d, ³J_{HH} = 8 Hz, 2H, aryl CH), 7.56–7.47 (m, 6H, aryl CH), 7.43–7.40 (m, 1H, aryl CH), 7.31–7.28 (m, 1H, aryl CH). ¹³C{¹H} NMR (100.6 MHz, CDCl₃): δ 147.4, 146.4, 141.4, 137.6, 134.0, 133.3, 129.6, 129.5, 128.5, 128.5, 128.1, 127.8, 127.1, 127.0, 126.5, 126.0, 120.1, 118.5, 116.5. FT-IR (KBr): 3242 (br, s), 3050 (m), 3021 (m), 2915 (m), 2847 (m), 1597 (m), 1515 (m), 1494 (s), 1445 (m), 1348 (m), 1227 (s) cm⁻¹. UV-vis (toluene): λ_{max} = 508 nm (ε = 16, 500 M⁻¹ cm⁻¹). Mass Spec. (EI, +ve mode): exact mass calculated for [C₂₃H₁₈N₄]⁺: 350.1532; exact mass found: 350.1537; difference: +1.6 ppm.

Formazan 3.11d

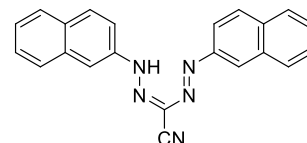
In air, phenylpyruvic acid (0.51 g, 3.1 mmol) was dissolved in 150 mL deionized water with NaOH (0.94 g, 23 mmol), and cooled in an ice bath for 30 min. In a separate flask, 2-naphthylamine (1.00 g, 6.98 mmol) and concentrated HCl (1.7 mL) were mixed in water (15 mL), and cooled in an ice bath for 10 min. A cooled solution



of sodium nitrite (0.55 g, 8.0 mmol) in water (5 mL) was added slowly to the amine solution. This mixture was stirred at 0 °C for 30 min, after which time it was added dropwise to the phenylpyruvic acid reaction mixture described above over a 10 min period. The resulting solution was stirred for 18 h, during which time a dark purple precipitate was formed. The dark purple solid was filtered off and purified by flash chromatography (CH₂Cl₂, neutral alumina) to afford formazan **3.11d** as a dark purple microcrystalline solid. Yield = 1.03 g, 82%. Melting point = 152–154 °C. ¹H NMR (599.5 MHz, CDCl₃) δ 15.72 (s, 1H, NH), 8.24 (d, ³J_{HH} = 7 Hz, 2H, aryl CH), 8.12 (s, 2H, aryl CH), 7.97–7.91 (m, 6H, aryl CH), 7.87 (d, ³J_{HH} = 8 Hz, 2H, aryl CH), 7.56–7.47 (m, 6H, aryl CH), 7.42–7.38 (m, 1H, aryl CH). ¹³C{¹H} NMR (100.6 MHz, CDCl₃): δ 145.8, 141.8, 137.6, 134.1, 133.1, 129.7, 128.6, 128.4, 128.2, 127.9, 127.1, 126.3, 126.2, 119.1, 116.5. FT-IR (KBr): 3267 (br, s), 3050 (s), 3034 (m), 2914 (m), 2847 (m), 1629 (m), 1596 (s), 1499 (s), 1438 (m), 1358 (m), 1226 (s) cm⁻¹. UV-vis (toluene): λ_{max} = 532 nm (ε = 10, 300 M⁻¹ cm⁻¹). Mass Spec. (EI, +ve mode): exact mass calculated for [C₂₇H₂₀N₄]⁺: 400.1688; exact mass found: 400.1695; difference: +1.8 ppm.

Formazan 3.11f

In air, cyanoacetic acid (0.30 g, 3.5 mmol) was dissolved in 150 mL deionized water with NaOH (1.40 g, 34.9 mmol), and cooled in an ice bath. In a separate flask, 2-naphthylamine (1.00 g, 6.98

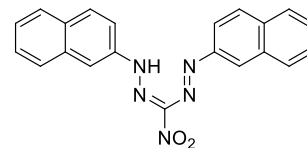


mmol) and concentrated HCl (1.7 mL) were mixed in water (15 mL), and cooled in an ice bath. A cooled solution of sodium nitrite (0.55 g, 8.0 mmol) in water (5 mL) was added slowly to the amine solution. This mixture was stirred at 0 °C for 30 min, after which time it was added dropwise to the cyanoacetic acid solution described above over a 10 min period. The resulting solution was stirred for 18 h, during which time a dark red precipitate was formed. The dark red solid was filtered off and purified by flash chromatography (CH₂Cl₂, neutral alumina) to afford formazan **3.11f** as a dark red microcrystalline solid. Yield = 1.06 g, 86%. Melting point = 187–189 °C. ¹H NMR (599.5 MHz, DMSO-*d*₆) δ 12.90 (s, 1H), 8.39 (s, 2H), 8.18–7.88 (m, 8H), 7.62–7.51 (m, 4H). ¹³C{¹H} NMR (100.6 MHz, DMSO-*d*₆): δ 144.9, 133.3, 132.7, 129.5, 128.6, 127.9, 127.8, 127.2, 127.0, 126.7, 116.5, 112.9. FT-IR (KBr): 3276 (br, m), 3053 (m), 2970 (m), 2219 (s), 1604 (s), 1531 (s), 1367 (m), 1346 (m), 1267 (m) cm⁻¹. UV-vis (toluene): λ_{max} = 472 nm (ε = 12, 900 M⁻¹

cm⁻¹). Mass Spec. (EI, +ve mode): exact mass calculated for [C₂₂H₁₅N₅]⁺: 349.1327; exact mass found: 349.1330; difference: +0.7 ppm.

Formazan 3.11h

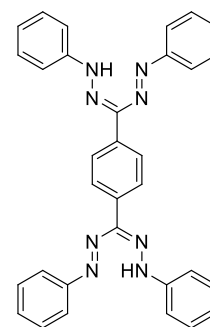
In air, nitromethane (0.21 g, 0.19 mL, 3.5 mmol) was dissolved in 100 mL deionized water with NaOH (0.31 g, 7.7 mmol), and cooled in an ice bath. In a separate flask, 2-naphthylamine (1.00 g, 6.98 mmol) and concentrated HCl (1.7 mL) were mixed in water (15 mL), and cooled in an ice bath. A cooled solution of sodium nitrite (0.55 g, 8.0 mmol) in water (5 mL) was added slowly to the amine solution. This mixture was stirred at 0 °C for 30 min, after which time it was added dropwise to the nitromethane solution described above over a 10 min period. The resulting solution was stirred for 18 h, during which time a dark red precipitate was formed. The dark red solid was filtered off and purified by flash chromatography (CH₂Cl₂, neutral alumina) to afford formazan **3.11h** as a dark red microcrystalline solid. Yield = 0.35 g, 27%. Melting point = 179–181 °C. ¹H NMR (599.5 MHz, CDCl₃) δ 15.63 (s, 1H), 8.18 (s, 2H), 8.00–7.96 (m, 6H), 7.90 (d, ³J_{HH} = 7 Hz, 2H), 7.60–7.56 (m, 4H). ¹³C{¹H} NMR (100.6 MHz, CD₂Cl₂): δ 144.5, 134.3, 133.9, 130.6, 129.1, 128.5, 127.9, 125.8, 122.0, 116.3, 110.4. FT-IR (KBr): 3242 (br, s), 3035 (m), 2915 (m), 2857 (m), 1589 (m), 1547 (s), 1502 (m), 1342 (s), 1277 (s) cm⁻¹. UV-vis (toluene): λ_{max} = 488 nm (ε = 12, 500 M⁻¹ cm⁻¹). Mass Spec. (EI, +ve mode): exact mass calculated for [C₂₁H₁₅N₅O₂]⁺: 369.1226; exact mass found: 369.1220; difference: -1.6 ppm. This compound decomposes over several hours in halogenated solvents.



Representative procedure for the preparation of formazans 3.11j and 3.11k:

Formazan Dimer 3.11j

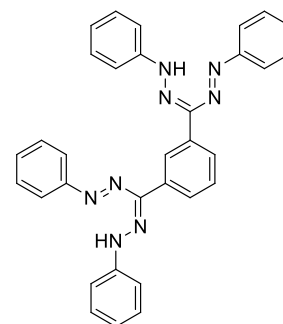
In air, phenyl hydrazine (5.08 g, 4.62 mL, 47.0 mmol) was dissolved in EtOH (30 mL), before terephthalaldehyde (1.50 g, 22.0 mmol) was added and the solution was stirred for 10 min. At this time, a light yellow precipitate had formed. DMF (100 mL) and pyridine (100 mL) were added and the mixture was cooled in an ice bath to 0 °C. In a separate flask, aniline (5.12 g, 5.02 mL, 55.0 mmol) and concentrated HCl (11.8 mL) were mixed in water (30 mL) and cooled in an ice bath. A cooled solution of sodium nitrite (4.00 g, 58.0 mmol) in water (10 mL) was added slowly to the



amine solution. This mixture was stirred at 0 °C for 30 min, at which time it was added dropwise to the DMF/pyridine mixture described above over a 10 min period. The resulting solution was stirred for 18 h, during which time a dark red/brown precipitate formed. The dark red/brown solid was isolated by vacuum filtration, washed with water and MeOH and purified by flash chromatography (CH₂Cl₂, neutral alumina) to afford formazan **3.11j** as a dark red/brown microcrystalline solid. Yield = 2.60 g, 23%. Melting point = 196–198 °C. ¹H NMR (599.5 MHz, CDCl₃) δ 15.45 (s, 2H, NH), 8.24 (s, 4H, aryl CH), 7.73 (d, ³J_{HH} = 7 Hz, 8H, aryl CH), 7.48 (t, ³J_{HH} = 7 Hz, 8H, aryl CH), 7.30 (t, ³J_{HH} = 7 Hz, 4H, aryl CH). ¹³C{¹H} NMR (100.6 MHz, CDCl₃): δ 148.2, 136.9, 129.7, 127.7, 126.1, 119.1. After 10,000 scans on a 600 MHz NMR spectrometer, only 6 signals were observed due to the poor solubility of **3.11j** in common organic solvents. FT-IR (KBr): 3267 (br, s), 3035 (m), 3006 (m), 1598 (s), 1509 (s), 1455 (m), 1405 (m), 1351 (s), 1311 (w), 1221 (s) cm⁻¹. UV-vis (toluene): λ_{max} = 500 nm (ε = 28,900 M⁻¹ cm⁻¹). Mass Spec. (EI, +ve mode): exact mass calculated for [C₃₂H₂₆N₈]⁺: 522.2280; exact mass found: 522.2280; difference: -0.2 ppm.

Formazan Dimer 3.11k

In air, from 11.2 mmol aldehyde and 28.0 mmol hydrazine: Yield = 1.68 g, 36%. Melting point = 175–177 °C. ¹H NMR (599.5 MHz, CDCl₃) δ 15.44 (s, 2H, NH), 9.03 (s, 1H, aryl CH), 8.14 (d, ³J_{HH} = 8 Hz, 2H, aryl CH), 7.76 (d, ³J_{HH} = 8 Hz, 8H, aryl CH), 7.52 (t, ³J_{HH} = 8 Hz, 1H, aryl CH), 7.50–7.47 (m, 8H, aryl CH), 7.31 (t, ³J_{HH} = 7 Hz, 4H, aryl CH). ¹³C{¹H} NMR (100.6 MHz, CDCl₃): δ

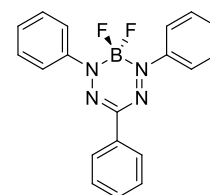


148.2, 141.1, 137.6, 129.6, 128.8, 127.6, 125.1, 123.6, 119.0. FT-IR (KBr): 3272 (br, s), 3026 (m), 3019 (m), 1598 (s), 1510 (s), 1455 (m), 1451 (m), 1343 (m), 1217 (s) cm⁻¹. UV-vis (toluene): λ_{max} = 496 nm (ε = 39,200 M⁻¹ cm⁻¹). Mass Spec. (EI, +ve mode): exact mass calculated for [C₃₂H₂₆N₈]⁺: 522.2280; exact mass found: 522.2285; difference: +0.8 ppm.

Representative procedure for the preparation of BF₂ complexes 3.10a-h:

Formazanate BF₂ Complex 3.10a

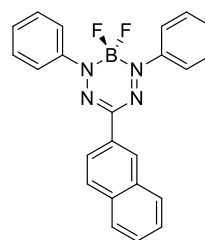
Formazan **3.11a** (0.50 g, 1.6 mmol) was dissolved in dry toluene (50 mL). NEt₃ (0.50 g, 0.68 mL, 4.9 mmol) was then added slowly, and the solution was stirred for 10 min. BF₃•OEt₂ (1.16 g, 1.01 mL, 8.15 mmol) was then added, and the solution was heated at 80 °C for 18 h. The



solution gradually turned from dark red to dark purple during this time. The reaction was then cooled to 20 °C, and deionized water (10 mL) was added to quench any excess reactive boron-containing compounds. The red/purple toluene solution was then washed with deionized water (3 x 50 mL), dried over MgSO₄, gravity filtered, and concentrated *in vacuo*. The resulting residue was purified by flash chromatography (CH₂Cl₂, neutral alumina) to afford BF₂ complex **3.10a** as a dark purple microcrystalline solid. Yield = 0.38 g, 67%. Melting point = 129–131 °C. ¹H NMR (599.5 MHz, CDCl₃) δ 8.12 (d, ³J_{HH} = 7 Hz, 2H), 7.92 (d, ³J_{HH} = 7 Hz, 4H), 7.50–7.43 (m, 9H). ¹³C{¹H} NMR (100.6 MHz, CDCl₃) δ 143.9, 133.6, 129.7, 129.3, 129.1, 128.8, 125.5, 123.5 (t, ⁴J_{CF} = 3 Hz). ¹¹B NMR (128.3 MHz, CDCl₃): δ -0.6 (t, ¹J_{BF} = 29 Hz). ¹⁹F NMR (376.1 Hz, CDCl₃): δ -144.6 (q, ¹J_{FB} = 29 Hz). FT-IR (KBr): 3263 (m), 3035 (m), 2900 (m), 2889 (m), 1310 (m), 1290 (s), 1265 (s), 1218 (m), 1168 (m), 1113 (s) cm⁻¹. UV-vis (toluene): λ_{max} = 517 nm (ε = 23, 800 M⁻¹ cm⁻¹). Mass Spec. (EI, +ve mode): exact mass calculated for [C₁₉H₁₅N₄BF₂]⁺: 348.1358; exact mass found: 348.1374; difference: +4.7 ppm.

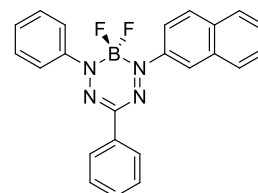
Formazanate BF₂ Complex 3.10b

From 1.70 mmol of formazan **3.11b**: Yield = 0.31 g, 46%. Melting point = 127–129 °C. ¹H NMR (599.5 MHz, CDCl₃) δ 8.56 (s, 1H), 8.27–8.25 (m, 1H), 7.96–7.93 (m, 6H), 7.90–7.88 (m, 1H), 7.54–7.50 (m, 6H), 7.48–7.45 (m, 2H). ¹³C{¹H} NMR (100.6 MHz, CDCl₃): δ 144.0, 134.0, 133.6, 131.1, 129.9, 129.3, 128.8, 128.7, 128.0, 126.8, 126.7, 125.1, 123.7 (t, ⁴J_{CF} = 4 Hz), 123.1, 110.2. ¹¹B NMR (128.3 MHz, CDCl₃): δ -0.5 (t, ¹J_{BF} = 29 Hz). ¹⁹F NMR (376.1 Hz, CDCl₃): δ -144.8 (q, ¹J_{FB} = 29 Hz). FT-IR (KBr): 3236 (m), 3055 (m), 2915 (m), 2860 (m), 1313 (s), 1279 (s), 1220 (m), 1172 (m), 1106 (m), 1105 (m) cm⁻¹. UV-vis (toluene): λ_{max} = 529 nm (ε = 20, 900 M⁻¹ cm⁻¹). Mass Spec. (EI, +ve mode): exact mass calculated for [C₂₃H₁₇N₄BF₂]⁺: 398.1514; exact mass found: 398.1513; difference: -0.3 ppm.



Formazanate BF₂ Complex 3.10c

From 1.50 mmol of formazan **3.11c**: Yield = 0.44 g, 73%. Melting point = 106–108 °C. ¹H NMR (599.5 MHz, CDCl₃) δ 8.46 (s, 1H), 8.18–8.16 (m, 2H), 8.07–8.05 (m, 1H), 7.97–7.92 (m, 4H), 7.88–7.86 (m, 1H), 7.57–7.43 (m, 8H). ¹³C{¹H} NMR (100.6 MHz,

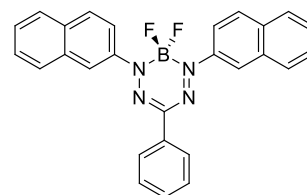


CDCl₃): δ 149.4, 144.1, 141.6, 133.8, 133.6, 133.2, 129.8, 129.5, 129.3, 129.3, 129.2, 128.9, 127.9, 127.8, 127.2, 125.7, 123.6 (t, $^4J_{CF} = 2$ Hz), 123.4 (t, $^4J_{CF} = 4$ Hz), 120.7. ¹¹B NMR (128.3 MHz, CDCl₃): δ -0.4 (t, $^1J_{BF} = 29$ Hz). ¹⁹F NMR (376.1 Hz, CDCl₃): δ -143.9 (q, $^1J_{FB} = 29$ Hz). FT-IR (KBr): 3236 (m), 3059 (s), 2915 (m), 2845 (m), 1347 (m), 1341 (m), 1294 (s), 1266 (s), 1218 (m), 1174 (m) cm⁻¹. UV-vis (toluene): $\lambda_{max} = 535$ nm ($\epsilon = 26, 800$ M⁻¹ cm⁻¹). Mass Spec. (EI, +ve mode): exact mass calculated for [C₂₃H₁₇N₄BF₂]⁺: 398.1514; exact mass found: 398.1512; difference: -0.6 ppm.

Formazanate BF₂ Complex 3.10d

From 2.70 mmol of formazan **3.11d**: Yield = 0.95 g, 78%.

Melting point = 140–142 °C. ¹H NMR (599.5 MHz, CDCl₃) δ 8.49 (s, 2H), 8.21 (d, $^3J_{HH} = 7$ Hz, 2H), 8.10–8.08 (m, 2H), 7.97–7.93 (m, 4H), 7.89–7.86 (m, 2H), 7.57–7.48 (m, 7H). ¹³C{¹H}

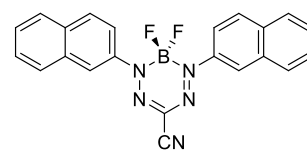


NMR (100.6 MHz, CDCl₃): δ 141.6, 133.9, 133.5, 133.1, 129.4, 129.3, 129.3, 128.9, 127.9, 127.7, 127.1, 125.7, 123.3 (t, $^4J_{CF} = 4$ Hz), 120.6, 119.1. ¹¹B NMR (128.3 MHz, CDCl₃): δ -0.2 (t, $^1J_{BF} = 29$ Hz). ¹⁹F NMR (376.1 Hz, CDCl₃): δ -143.3 (q, $^1J_{FB} = 29$ Hz). FT-IR (KBr): 3276 (m), 3050 (s), 2915 (m), 2846 (m), 1626 (m), 1592 (m), 1507 (s), 1344 (s), 1298 (s), 1265 (m) cm⁻¹. UV-vis (toluene): $\lambda_{max} = 556$ nm ($\epsilon = 25, 200$ M⁻¹ cm⁻¹). Mass Spec. (ESI, +ve mode): exact mass calculated for [C₂₇H₁₉N₄BF₂Na]⁺: 471.1568; exact mass found: 471.1569; difference: +0.1 ppm.

Formazanate BF₂ Complex 3.10f

From 2.30 mmol of formazan **3.11f**: Yield = 0.74 g, 81%.

Melting point = 118–120 °C. ¹H NMR (599.5 MHz, CDCl₃) δ 8.51 (s, 2H), 8.03–8.01 (m, 2H), 7.98–7.93 (m, 4H), 7.89–7.87



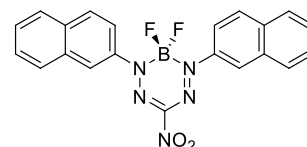
(m, 2H), 7.62–7.56 (m, 4H). ¹³C{¹H} NMR (100.6 MHz, CDCl₃): δ 141.0, 134.4, 133.1, 130.1, 129.9, 129.0, 128.2, 127.8, 126.4, 124.2, 119.5 (t, $^4J_{CF} = 3$ Hz), 114.5. ¹¹B NMR (128.3 MHz, CDCl₃): δ -0.4 (t, $^1J_{BF} = 31$ Hz). ¹⁹F NMR (376.1 Hz, CDCl₃): δ -132.7 (q, $^1J_{FB} = 31$ Hz). FT-IR (KBr): 3235 (m), 3035 (m), 2895 (m), 2240 (s), 1350 (s), 1146 (m), 1124 (m), 1028 (m) cm⁻¹. UV-vis (toluene): $\lambda_{max} = 581$ nm ($\epsilon = 25, 700$ M⁻¹ cm⁻¹). Mass Spec. (EI, +ve mode): exact mass calculated for [C₂₂H₁₄N₅BF₂]⁺: 397.1310; exact mass found: 397.1311; difference: +0.2 ppm.

Formazanate BF₂ Complex 3.10g

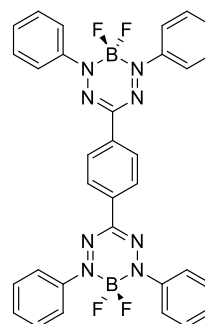
From 2.90 mmol of formazan **3.11g**: Yield = 0.27 g, 29%. Melting point = 108–110 °C. ¹H NMR (399.8 MHz, CDCl₃) δ 8.01–7.99 (m, 4H), 7.56–7.52 (m, 6H). ¹³C{¹H}NMR (100.6 MHz, CDCl₃): δ 143.4, 132.2, 129.9, 123.7 (t, ⁴J_{CF} = 2 Hz). ¹¹B NMR (128.3 MHz, CDCl₃): δ -0.7 (t, ¹J_{BF} = 30 Hz). ¹⁹F NMR (376.1 Hz, CDCl₃): δ -135.4 (q, ¹J_{FB} = 29 Hz). FT-IR (KBr): 3257 (m), 3062 (m), 2915 (m), 2912 (m), 2844 (m), 1557 (s), 1417 (s), 1333 (s), 1327 (s), 1271 (m), 1175 (m), 1151 (m) cm⁻¹. UV-vis (toluene): λ_{max} = 505 nm (ε = 26, 000 M⁻¹ cm⁻¹). Mass Spec. (EI, +ve mode): exact mass calculated for [C₁₃H₁₀N₅O₂BF₂]⁺: 317.0896; exact mass found: 317.0901; difference: +1.7 ppm.

**Formazanate BF₂ Complex 3.10h**

From 0.54 mmol of formazan **3.11h**: Yield = 0.22 g, 99%. Melting point = 199–201 °C. ¹H NMR (599.5 MHz, CDCl₃) δ 8.61 (s, 2H), 8.14 (d, ³J_{HH} = 9 Hz, 2H), 8.01–7.97 (m, 4H), 7.90 (d, ³J_{HH} = 8 Hz, 2H), 7.65–7.58 (m, 4H). ¹³C{¹H} NMR (100.6 MHz, CDCl₃): δ 141.1, 134.6, 133.1, 130.4, 130.3, 129.9, 129.2, 128.2, 127.8, 124.6 (t, ⁴J_{CF} = 4 Hz), 119.5. ¹¹B NMR (128.3 MHz, CDCl₃): δ -0.3 (t, ¹J_{BF} = 29 Hz). ¹⁹F NMR (376.1 Hz, CDCl₃): δ -134.3 (q, ¹J_{FB} = 29 Hz). FT-IR (KBr): 3270 (s), 3036 (m), 2888 (m), 1554 (s), 1538 (m), 1425 (m), 1377 (m), 1317 (s), 1269 (w) cm⁻¹. UV-vis (toluene): λ_{max} = 583 nm (ε = 24, 100 M⁻¹ cm⁻¹). Mass Spec. (EI, +ve mode): exact mass calculated for [C₂₁H₁₄N₅O₂BF₂]⁺: 417.1209; exact mass found: 417.1208; difference: -0.2 ppm.

**Representative procedure for the preparation of formazanate BF₂ complexes 3.10j and 3.10k:****Formazanate BF₂ Dimer 3.10j**

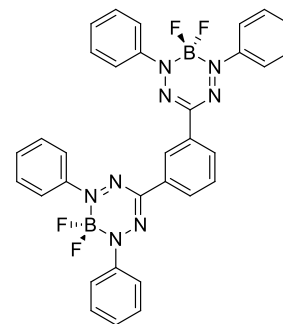
Formazan **3.11j** (1.00 g, 1.91 mmol) was dissolved in dry toluene (100 mL) and NEt₃ (1.16 g, 1.60 mL, 11.4 mmol) was added slowly, before the solution was stirred for 10 min. BF₃•OEt₂ (2.72 g, 2.36 mL, 19.1 mmol) was then added and the solution heated at 80 °C for 18 h. The solution gradually changed colour from dark red to dark purple during this time. The reaction was then cooled to 20 °C and deionized water (10 mL) was added to quench any excess reactive boron-containing



compounds. The red/purple toluene fraction was then washed with deionized water (3 x 50 mL), dried over MgSO_4 , gravity filtered and concentrated *in vacuo*. The resulting residue was purified by flash chromatography (CH_2Cl_2 , neutral alumina) to afford BF_2 complex **3.10j** as a dark purple microcrystalline solid. Yield = 0.94 g, 80%. Melting point = 192–194 °C. ^1H NMR (599.5 MHz, CDCl_3) δ 8.23 (s, 4H, aryl CH), 7.94 (d, $^3J_{\text{HH}} = 7$ Hz, 8H, aryl CH), 7.52–7.45 (m, 12H, aryl CH). $^{13}\text{C}\{^1\text{H}\}$ NMR (100.6 MHz, CDCl_3): δ 148.7, 143.9, 134.4, 129.9, 129.2, 125.8, 123.5. ^{11}B NMR (128.3 MHz, CDCl_3): δ -0.5 (t, $^1J_{\text{BF}} = 29$ Hz). ^{19}F NMR (376.1 Hz, CDCl_3): δ -144.1 (q, $^1J_{\text{FB}} = 29$ Hz). FT-IR (KBr): 3035 (m), 3004 (m), 1582 (m), 1487 (m), 1429 (m), 1322 (s), 1309 (s), 1260 (s), 1216 (m), 1153 (m), 1116 (s) cm^{-1} . UV-vis (toluene): $\lambda_{\text{max}} = 521$ nm ($\epsilon = 28,800$ $\text{M}^{-1} \text{cm}^{-1}$). Mass Spec. (EI, +ve mode): exact mass calculated for $[\text{C}_{32}\text{H}_{24}\text{N}_8\text{B}_2\text{F}_4]^+$: 618.2246; exact mass found: 618.2257; difference: +1.8 ppm.

Formazanate BF_2 Dimer **3.10k**

From 1.91 mmol of formazan **3.11k**: Yield = 0.88 g, 75%. Melting point = 208–210 °C. ^1H NMR (599.5 MHz, CDCl_3) δ 8.82 (s, 1H, aryl CH), 8.20 (d, $^3J_{\text{HH}} = 8$ Hz, 2H, aryl CH), 7.94 (d, $^3J_{\text{HH}} = 8$ Hz, 8H, aryl CH), 7.60 (t, $^3J_{\text{HH}} = 8$ Hz, 1H, aryl CH), 7.50–7.43 (m, 12H, aryl CH). $^{13}\text{C}\{^1\text{H}\}$ NMR (100.6 MHz, CDCl_3): δ 144.0, 134.5, 130.0, 129.4, 129.3, 129.2, 126.3, 123.6, 122.8. ^{11}B NMR (128.3 MHz, CDCl_3): δ -0.5 (t, $^1J_{\text{BF}} = 29$ Hz). ^{19}F NMR (376.1 Hz, CDCl_3): δ -143.8 (q, $^1J_{\text{FB}} = 29$ Hz). FT-IR (KBr): 3034 (m), 3007 (w), 1581 (m), 1457 (m), 1454 (m), 1341 (m), 1301 (s), 1281 (s), 1216 (m), 1179 (m), 1106 (s) cm^{-1} . UV-vis (toluene): $\lambda_{\text{max}} = 518$ nm ($\epsilon = 20,200$ $\text{M}^{-1} \text{cm}^{-1}$). Mass Spec. (EI, +ve mode): exact mass calculated for $[\text{C}_{32}\text{H}_{24}\text{N}_8\text{B}_2\text{F}_4]^+$: 618.2246; exact mass found: 618.2228; difference: -2.9 ppm.



3.5 References

- (1) Murov, S. L., *Handbook of Photochemistry*. Marcel Dekker, Inc.: New York, 1973.
- (2) Roncali, J.; Leriche, P.; Blanchard, P. *Adv. Mater.* **2014**, *26*, 3821–3838.

- (3) Frath, D.; Massue, J.; Ulrich, G.; Ziesel, R. *Angew. Chem. Int. Ed.* **2014**, *53*, 2290–2310.
- (4) Wu, W.; Liu, Y.; Zhu, D. *Chem. Soc. Rev.* **2010**, *39*, 1489–1502.
- (5) Mei, J.; Hong, Y.; Lam, J. W. Y.; Qin, A.; Tang, Y.; Tang, B. Z. *Adv. Mater.* **2014**, *26*, 5429–5479.
- (6) Qian, B.; Baek, S. W.; Smith III, M. R. *Polyhedron* **1999**, *18*, 2405–2414.
- (7) Norman, D. W.; Edwards, J. P.; Vogels, C. M.; Decken, A.; Westcott, S. A. *Can. J. Chem.* **2002**, *80*, 31–40.
- (8) Liddle, B. J.; Silva, R. M.; Morin, T. J.; Macedo, F. P.; Shukla, R.; Lindeman, S. V.; Gardinier, J. R. *J. Org. Chem.* **2007**, *72*, 5637–5646.
- (9) Kubota, Y.; Tsuzuki, T.; Funabiki, K.; Ebihara, M.; Matsui, M. *Org. Lett.* **2010**, *12*, 4010–4013.
- (10) Oakley, S. R.; Nawn, G.; Waldie, K. M.; MacInnis, T. D.; Patrick, B. O.; Hicks, R. G. *Chem. Commun.* **2010**, *46*, 6753–6755.
- (11) Cheng, F.; Jäkle, F. *Chem. Commun.* **2010**, *46*, 3717–3719.
- (12) Kersey, F. R.; Zhang, G.; Palmer, G. M.; Dewhurst, M. W.; Fraser, C. L. *ACS Nano* **2010**, *4*, 4989–4996.
- (13) Bonnier, C.; Machin, D. D.; Abdi, O.; Koivisto, B. D. *Org. Biomol. Chem.* **2013**, *11*, 3756–3760.
- (14) Kubota, Y.; Ozaki, Y.; Funabiki, K.; Matsui, M. *J. Org. Chem.* **2013**, *78*, 7058–7067.
- (15) Albrett, A. M.; Thomas, K. E.; Maslek, S.; Młodzianowska, A.; Conradie, J.; Beavers, C. M.; Ghosh, A.; Brothers, P. J. *Inorg. Chem.* **2014**, *53*, 5486–5493.
- (16) Barbon, S. M.; Staroverov, V. N.; Boyle, P. D.; Gilroy, J. B. *Dalton Trans.* **2014**, *43*, 240–250.
- (17) Liao, C.-W.; Rao M, R.; Sun, S.-S. *Chem. Commun.* **2015**, *51*, 2656–2659.
- (18) Kubota, Y.; Kasatani, K.; Takai, H.; Funabiki, K.; Matsui, M. *Dalton Trans.* **2015**, *44*, 3326–3341.
- (19) Loudet, A.; Burgess, K. *Chem. Rev.* **2007**, *107*, 4891–4932.
- (20) Ulrich, G.; Ziesel, R.; Harriman, A. *Angew. Chem. Int. Ed.* **2008**, *47*, 1184–1201.
- (21) Boens, N.; Leen, V.; Dehaen, W. *Chem. Soc. Rev.* **2012**, *41*, 1130–1172.

- (22) Chen, J.; Burghart, A.; Derecskei-Kovacs, A.; Burgess, K. *J. Org. Chem.* **2000**, *65*, 2900–2906.
- (23) Ueno, Y.; Jose, J.; Loudet, A.; Pérez-Bolívar, C.; Anzenbacher, P.; Burgess, K. *J. Am. Chem. Soc.* **2010**, *133*, 51–55.
- (24) Niu, S.; Ulrich, G.; Retailleau, P.; Ziesel, R. *Tetrahedron Lett.* **2011**, *52*, 4848–4853.
- (25) Nepomnyashchii, A. B.; Bröring, M.; Ahrens, J.; Bard, A. J. *J. Am. Chem. Soc.* **2011**, *133*, 8633–8645.
- (26) Lu, J.-s.; Ko, S.-B.; Walters, N. R.; Wang, S. *Org. Lett.* **2012**, *14*, 5660–5663.
- (27) Zhang, X.; Yu, H.; Xiao, Y. *J. Org. Chem.* **2011**, *77*, 669–673.
- (28) Jameson, L. P.; Dzyuba, S. V. *Bioorg. Med. Chem. Lett.* **2013**, *23*, 1732–1735.
- (29) Manjare, S. T.; Kim, J.; Lee, Y.; Churchill, D. G. *Org. Lett.* **2013**, *16*, 520–523.
- (30) Frenette, M.; Hatamimoslehabadi, M.; Bellinger-Buckley, S.; Laoui, S.; La, J.; Bag, S.; Mallidi, S.; Hasan, T.; Bouma, B.; Yelleswarapu, C.; Rochford, J. *J. Am. Chem. Soc.* **2014**, *136*, 15853–15856.
- (31) Shie, J.-J.; Liu, Y.-C.; Lee, Y.-M.; Lim, C.; Fang, J.-M.; Wong, C.-H. *J. Am. Chem. Soc.* **2014**, *136*, 9953–9961.
- (32) Bandi, V.; Das, S. K.; Awuah, S. G.; You, Y.; D'Souza, F. *J. Am. Chem. Soc.* **2014**, *136*, 7571–7574.
- (33) Bruhn, T.; Pescitelli, G.; Jurinovich, S.; Schaumlöffel, A.; Witterauf, F.; Ahrens, J.; Bröring, M.; Bringmann, G. *Angew. Chem. Int. Ed.* **2014**, *53*, 14592–14595.
- (34) Raut, S.; Kimball, J.; Fudala, R.; Doan, H.; Maliwal, B.; Sabnis, N.; Lacko, A.; Gryczynski, I.; Dzyuba, S. V.; Gryczynski, Z. *Phys. Chem. Chem. Phys.* **2014**, *16*, 27037–27042.
- (35) Lakshmi, V.; Ravikanth, M. *RSC Adv.* **2014**, *4*, 44327–44336.
- (36) Kollmannsberger, M.; Rurack, K.; Resch-Genger, U.; Daub, J. *J. Phys. Chem. A* **1998**, *102*, 10211–10220.
- (37) Shen, Z.; Röhr, H.; Rurack, K.; Uno, H.; Spieles, M.; Schulz, B.; Reck, G.; Ono, N. *Chem. Eur. J.* **2004**, *10*, 4853–4871.
- (38) Quan, L.; Chen, Y.; Lv, X.-J.; Fu, W.-F. *Chem. Eur. J.* **2012**, *18*, 14599–14604.

- (39) Araneda, J. F.; Piers, W. E.; Heyne, B.; Parvez, M.; McDonald, R. *Angew. Chem. Int. Ed.* **2011**, *50*, 12214–12217.
- (40) Manjare, S. T.; Kim, J.; Lee, Y.; Churchill, D. G. *Org. Lett.* **2014**, *16*, 520–523.
- (41) Wakamiya, A.; Murakami, T.; Yamaguchi, S. *Chem. Sci.* **2013**, *4*, 1002–1007.
- (42) Fischer, G. M.; Isomäki-Kron Dahl, M.; Göttker-Schnetmann, I.; Daltrozzi, E.; Zumbusch, A. *Chem. Eur. J.* **2009**, *15*, 4857–4864.
- (43) Zhu, M.; Jiang, L.; Yuan, M.; Liu, X.; Ouyang, C.; Zheng, H.; Yin, X.; Zuo, Z.; Liu, H.; Li, Y. *J. Polym. Sci., Part A: Polym. Chem.* **2008**, *46*, 7401–7410.
- (44) Barbon, S. M.; Reinkeluers, P. A.; Price, J. T.; Staroverov, V. N.; Gilroy, J. B. *Chem. Eur. J.* **2014**, *20*, 11340–11344.
- (45) Chang, M.-C.; Otten, E. *Chem. Commun.* **2014**, *50*, 7431–7433.
- (46) A. Ibrahim, Y.; H.M. Elwahy, A.; A. Abbas, A. *Tetrahedron* **1994**, *50*, 11489–11498.
- (47) Katritzky, A. A.; Belyakov, S. A.; Cheng, D.; Durst, H. D. *Synthesis* **1995**, *1995*, 577–581.
- (48) Gilroy, J. B.; McKinnon, S. D. J.; Koivisto, B. D.; Hicks, R. G. *Org. Lett.* **2007**, *9*, 4837–4840.
- (49) Gilroy, J. B.; Otieno, P. O.; Ferguson, M. J.; McDonald, R.; Hicks, R. G. *Inorg. Chem.* **2008**, *47*, 1279–1286.
- (50) Kuhn, R.; Neugebauer, F. A.; Trischmann, H. *Monatsh. Chem.* **1966**, *97*, 525–553.
- (51) Barbon, S. M.; Price, J. T.; Reinkeluers, P. A.; Gilroy, J. B. *Inorg. Chem.* **2014**, *53*, 10585–10593.
- (52) Gilroy, J. B.; Ferguson, M. J.; McDonald, R.; Patrick, B. O.; Hicks, R. G. *Chem. Commun.* **2007**, 126–128.
- (53) Gilroy, J. B.; Ferguson, M. J.; McDonald, R.; Hicks, R. G. *Inorg. Chim. Acta* **2008**, *361*, 3388–3393.
- (54) Gilroy, J. B.; Patrick, B. O.; McDonald, R.; Hicks, R. G. *Inorg. Chem.* **2008**, *47*, 1287–1294.
- (55) Hong, S.; Gupta, A. K.; Tolman, W. B. *Inorg. Chem.* **2009**, *48*, 6323–6325.
- (56) Hong, S.; Hill, L. M. R.; Gupta, A. K.; Naab, B. D.; Gilroy, J. B.; Hicks, R. G.; Cramer, C. J.; Tolman, W. B. *Inorg. Chem.* **2009**, *48*, 4514–4523.

- (57) Lipunova, G. N.; Rezinskikh, Z. G.; Maslakova, T. I.; Slepukhin, P. A.; Pervova, I. G.; Lipunov, I. N.; Sigeikin, G. I. *Russ. J. Coord. Chem.* **2009**, *35*, 215–221.
- (58) Zaidman, A. V.; Pervova, I. G.; Vilms, A. I.; Belov, G. P.; Kayumov, R. R.; Slepukhin, P. A.; Lipunov, I. N. *Inorg. Chim. Acta* **2011**, *367*, 29–34.
- (59) Chang, M.-C.; Dann, T.; Day, D. P.; Lutz, M.; Wildgoose, G. G.; Otten, E. *Angew. Chem. Int. Ed.* **2014**, *53*, 4118–4122.
- (60) Travieso-Puente, R.; Chang, M.-C.; Otten, E. *Dalton Trans.* **2014**, *43*, 18035–18041.
- (61) Chang, M.-C.; Roewen, P.; Travieso-Puente, R.; Lutz, M.; Otten, E. *Inorg. Chem.* **2015**, *54*, 379–388.
- (62) Fery-Forgues, S.; Lavabre, D. *J. Chem. Educ.* **1999**, *76*, 1260–1264.
- (63) Suzuki, K.; Kobayashi, A.; Kaneko, S.; Takehira, K.; Yoshihara, T.; Ishida, H.; Shiina, Y.; Oishi, S.; Tobita, S. *Phys. Chem. Chem. Phys.* **2009**, *11*, 9850–9860.
- (64) Gaussian 09, Revision B.01, Frisch, M. J.; Trucks, G. W.; Schlegel, H. B.; Scuseria, G. E.; Robb, M. A.; Cheeseman, J. R.; Scalmani, G.; Barone, V.; Mennucci, B.; Petersson, G. A.; Nakatsuji, H.; Caricato, M.; Li, X.; Hratchian, H. P.; Izmaylov, A. F.; Bloino, J.; Zheng, G.; Sonnenberg, J. L.; Hada, M.; Ehara, M.; Toyota, K.; Fukuda, R.; Hasegawa, J.; Ishida, M.; Nakajima, T.; Honda, Y.; Kitao, O.; Nakai, H.; Vreven, T.; Montgomery, Jr., J. A.; Peralta, J. E.; Ogliaro, F.; Bearpark, M.; Heyd, J. J.; Brothers, E.; Kudin, K. N.; Staroverov, V. N.; Kobayashi, R.; Normand, J.; Raghavachari, K.; Rendell, A.; Burant, J. C.; Iyengar, S. S.; Tomasi, J.; Cossi, M.; Rega, N.; Millam, J. M.; Klene, M.; Knox, J. E.; Cross, J. B.; Bakken, V.; Adamo, C.; Jaramillo, J.; Gomperts, R.; Stratmann, R. E.; Yazyev, O.; Austin, A. J.; Cammi, R.; Pomelli, C.; Ochterski, J. W.; Martin, R. L.; Morokuma, K.; Zakrzewski, V. G.; Voth, G. A.; Salvador, P.; Dannenberg, J. J.; Dapprich, S.; Daniels, A. D.; Farkas, Ö.; Foresman, J. B.; Ortiz, J. V.; Cioslowski, J.; Fox, D. J. Gaussian, Inc., Wallingford CT, 2009.
- (65) Zhao, Y.; Truhlar, D. G. *Theor. Chem. Acc.* **2008**, *120*, 215–241.
- (66) Qin, Y.; Pagba, C.; Piotrowiak, P.; Jäkle, F. *J. Am. Chem. Soc.* **2004**, *126*, 7015–7018.
- (67) Bruker-Nonius, SAINT version 2013.8, 2013, Bruker-AXS, Madison, WI 53711, USA.

- (68) Bruker-Nonius, SADABS version 2012.1, 2012, Bruker-AXS, Madison, WI 53711, USA.
- (69) *XS program, beta version*, Sheldrick, G. M. **2014**, *University of Gottingen*.
- (70) Sheldrick, G. M. *Acta Cryst.* **2015**, *A71*, 3–8.
- (71) Sheldrick, G. M. *Acta Cryst.* **2008**, *A64*, 112–122.

Chapter 4

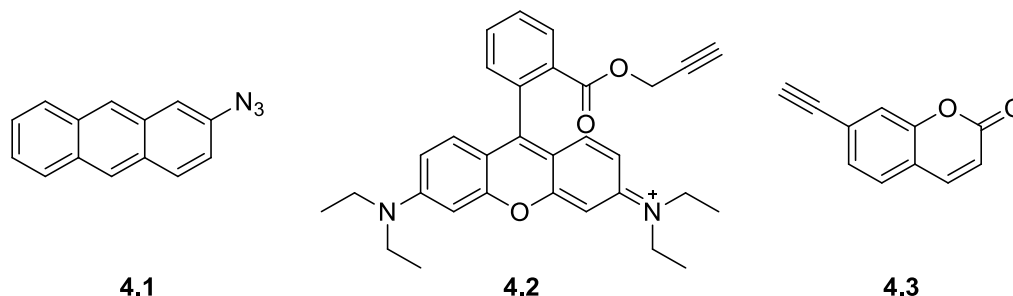
4 BF₂ Formazanate Complexes Modified by Copper-Assisted Alkyne-Azide Cycloaddition – Molecular Materials and Polymers

Adapted from:

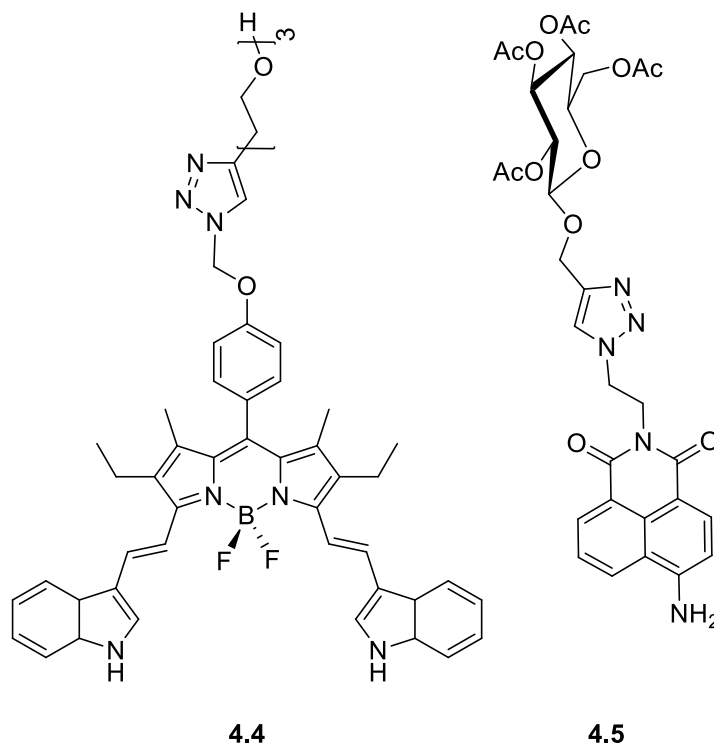
1. **Barbon, S. M.;** Gilroy, J. B.* *Polym. Chem.* **2016**, 7, 3589–3598.
2. **Barbon, S. M.;** Novoa, S.; Bender, D.; Groom, H.; Luyt, L. G.*; Gilroy, J. B.* *Org. Chem. Front.* **2017**, 4, 178–190.

4.1 Introduction

Fluorophores are a very useful class of molecules as they provide a handle with which to visualize chemical phenomena at the molecular, macromolecular and bulk size regimes.^[1-6] For this reason, the development of new classes of fluorophores has been the focus of a significant amount of research.^[7-8] One of the major hurdles to be overcome in the field was the facile synthetic modification of fluorophores in order to utilize them for an expanded range of applications.^[9-11] Significant impact was made in this area with the development of copper-assisted alkyne-azide cycloaddition (CuAAC) chemistry.^[12-13] Since the original reports appeared, the number of alkyne and azide modified fluorophores such as those based on anthracene,^[14-15] pyrene,^[16-17] boron dipyrromethenes (BODIPYs),^[18-20] rhodamine^[21-22] and coumarin^[23-24] has expanded dramatically (*e.g.*, **4.1–4.3**). The onward CuAAC chemistry of these and other fluorophores has led to their use, for example, as protein labels,^[25] in photosensitizers,^[26] as molecular switches,^[27] as probes of DNA hybridization,^[28] in radiolabeling,^[29] and in polymer synthesis.^[30-31] CuAAC chemistry has been used to create a variety of fluorescence sensors for anions,^[32] acids and bases,^[33-34] nitroxide radicals,^[35] hydroxyl radicals,^[36] and various metal ions including mercury^[37-38] and zinc.^[39-40]

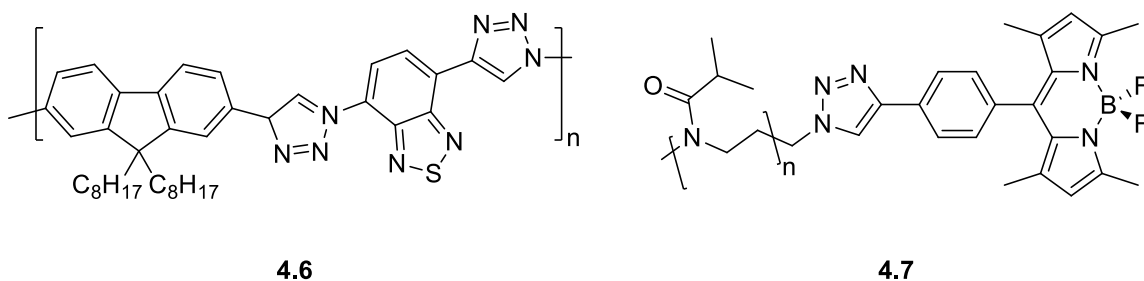


In addition to the production of sensors, CuAAC chemistry has also been utilized to modify fluorophores for biological imaging applications. This strategy has been used both to impart water solubility (*e.g.*, **4.4**),^[41] and functionalities which interact with specific biological targets (*e.g.*, **4.5**).^[42-45] More recently, this strategy has been extended to include copper-free, strain-promoted alkyne-azide cycloaddition chemistry with specific utility in biological systems.^[46-47]



CuAAC chemistry has also been used to incorporate fluorophores into polymers and dendrimers, imparting the solution processability and film-forming properties often associated with these materials.^[48-52] The Jin group used CuAAC chemistry to synthesize an alternating copolymer of 9,9-dioctyl-fluorene and benzothiadiazole **4.6**. This polymer

had interesting thin-film optical properties, including emission from both the fluorene and benzothiadiazole, and was also incorporated into dye-sensitized solar cells, with efficiencies of up to 2.8%.^[53] Similarly, the Jang group showed that 2-isopropyl-2-oxazoline was polymerized, and terminated with sodium azide, which could be reacted with an alkyne-terminated BODIPY to form Polymer **4.7**. While it only contains one BODIPY unit, **4.7** was still strongly emissive at *ca.* 525 nm, and could be combined with other polymers appended with primary-coloured dyes to produce temperature-dependent emissive materials.^[31]



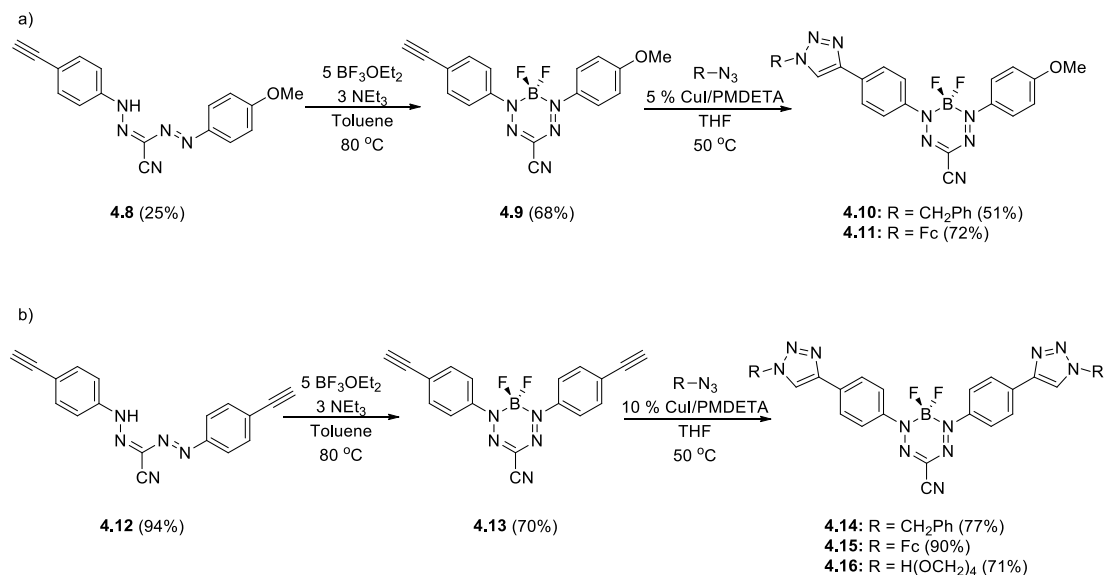
Herein we expand the scope of BF_2 formazanate chemistry further by producing a variety of functional molecular and polymeric materials through the use of CuAAC chemistry that cannot be synthesized directly by other methods.

4.2 Synthesis and Characterization of Molecular Materials

4.2.1 Benzyl-Functionalized BF_2 Complexes of 3-Cyanoformazanates

In order to study the effect of triazole formation on the photophysical properties of BF_2 complexes of 3-cyanoformazanate ligands, mono- and bis-alkyne substituted formazans **4.8** and **4.12** were converted to mono-alkyne-substituted complex **4.9** and bis-alkyne-substituted complex **4.13** by adapting previously reported protocols (Scheme 4.1).^[54] Mono-alkyne-substituted BF_2 complex **4.9** is the first example of a BF_2 complex derived from an asymmetric 3-cyanoformazan, which was isolated from a reaction mixture containing equimolar quantities of the parent aryldiazonium salts. Complex **4.9** was first characterized by single crystal X-ray diffraction (Figure 4.1), and happened to crystallize on a two-fold rotation axis. As a result, the alkyne and methoxy substituents were

disordered. However, the structure does confirm the expected connectivity and planarity throughout the molecule (torsion angle between N_4 plane and aryl substituents: 7.2°). All other structural metrics were consistent with the solid-state structures of previously reported BF_2 adducts of 3-cyanoformazanate ligands.^[54]



Scheme 4.1 Synthesis of (a) mono- and (b) bis-CuAAC-functionalized BF_2 complexes.

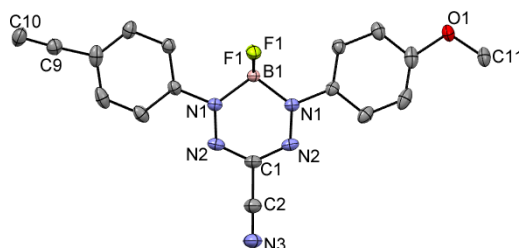


Figure 4.1 Solid-state structure of **4.9**. Anisotropic displacement ellipsoids are shown at 50% probability and hydrogen atoms have been omitted for clarity. Selected bond lengths (\AA): B1–N1 1.5759(15), N1–N2 1.3023(15), N2–C1 1.3351(13), O1–C11 1.418(5), C9–C10 1.191(7). Selected bond angles ($^\circ$): B1–N1–N2 124.57(10), N1–N2–C1 117.24(11).

The alkyne-substituted complexes **4.9** and **4.13** underwent CuAAC with benzyl azide when combined in the presence of copper (I) iodide and N,N,N',N'',N''' -pentamethyldiethylenetriamine (PMDTA) in THF to form mono- and bis-benzyl-

functionalized compounds **4.10** and **4.14** (Scheme 4.1). The successful conversion of alkyne-substituted complexes **4.9** and **4.13** to benzyl-functionalized complexes **4.10** and **4.14** was confirmed by ^1H , ^{11}B , ^{13}C and ^{19}F NMR spectroscopy (Figures 4.2, A4.1–A4.17), UV-vis absorption/emission and IR spectroscopy, and high resolution mass spectrometry. In order to further expand the scope of the BF_2 formazanate complexes, CuAAC chemistry was used to synthesize BF_2 formazanate complexes with appended ferrocene substituents (**4.11**, **4.15**) and water-solubilizing tetraethylene glycol substituents (**4.16**). Initial attempts to synthesize the water-soluble complex **4.16** were unsuccessful, likely due to the TEG chains outcompeting PMDETA for the ligation of copper(I) when all of the reagents were combined simultaneously. We circumvented this issue by stirring CuI and PMDETA in THF for 30 min before the TEG azide was added.

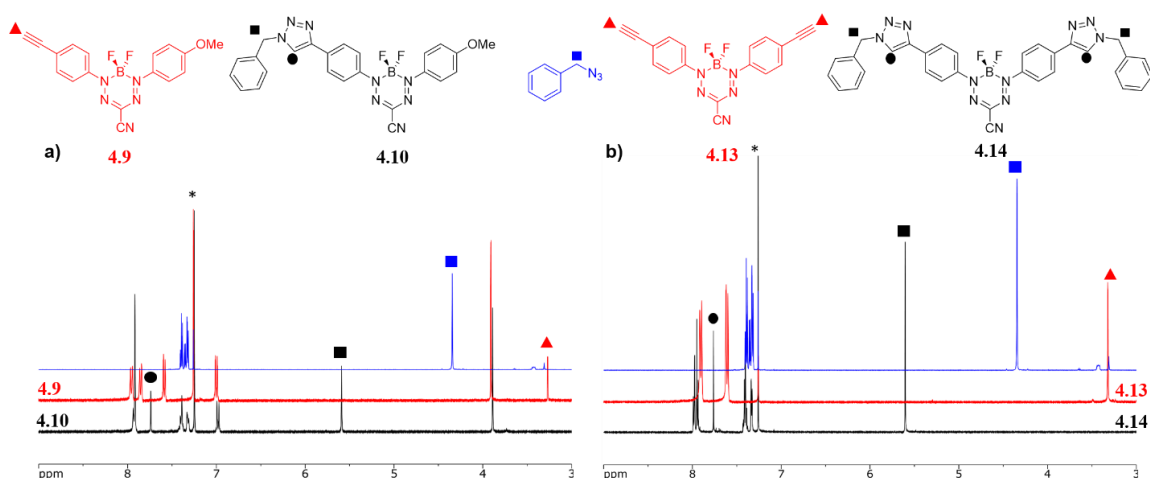


Figure 4.2 ^1H NMR spectra of a) benzyl azide (blue), mono-alkyne-substituted complex **4.9** (red) and mono-benzyl-functionalized complex **4.10** (black) and b) benzyl azide (blue), bis-alkyne-substituted complex **4.13** (red) and bis-benzyl-functionalized complex **4.14** (black) in CDCl_3 . The asterisks denote residual solvent signals.

The electrochemical properties of complexes **4.9**, **4.10**, **4.13** and **4.14** were studied using cyclic voltammetry in THF. Each voltammogram showed two reversible, one-electron reduction waves within the electrochemical window of the solvent. Considering the first reduction wave, which corresponds to the formation of a ligand-centered radical anion, bis-alkyne-substituted complex **4.13** is significantly easier to reduce than mono-alkyne-substituted complex **4.9** (-0.50 V and -0.67 V relative to the ferrocene/ferrocenium redox

couple, respectively) due to the presence of the electron donating methoxy substituent in **4.9**. The benzyl-functionalized complexes were more difficult to reduce than their alkyne-substituted precursors [(**4.10**: -0.68 V; **4.14**: -0.62 V), Figure 4.3, Table 4.1]. We have previously demonstrated that extending electronic conjugation in BF_2 complexes of 3-cyanoformazanate ligands results in complexes that are easier to reduce due to a lowering of the LUMO energy.^[55] However, in the case of complexes **4.10** and **4.14**, the more negative reduction potentials observed are likely due to the electron donating nature of the benzyl-substituted triazoles, which appear to be better electron donors than alkyne substituents. The second reduction waves, which correspond to the formation of ligand-centered dianions, followed the same trend.

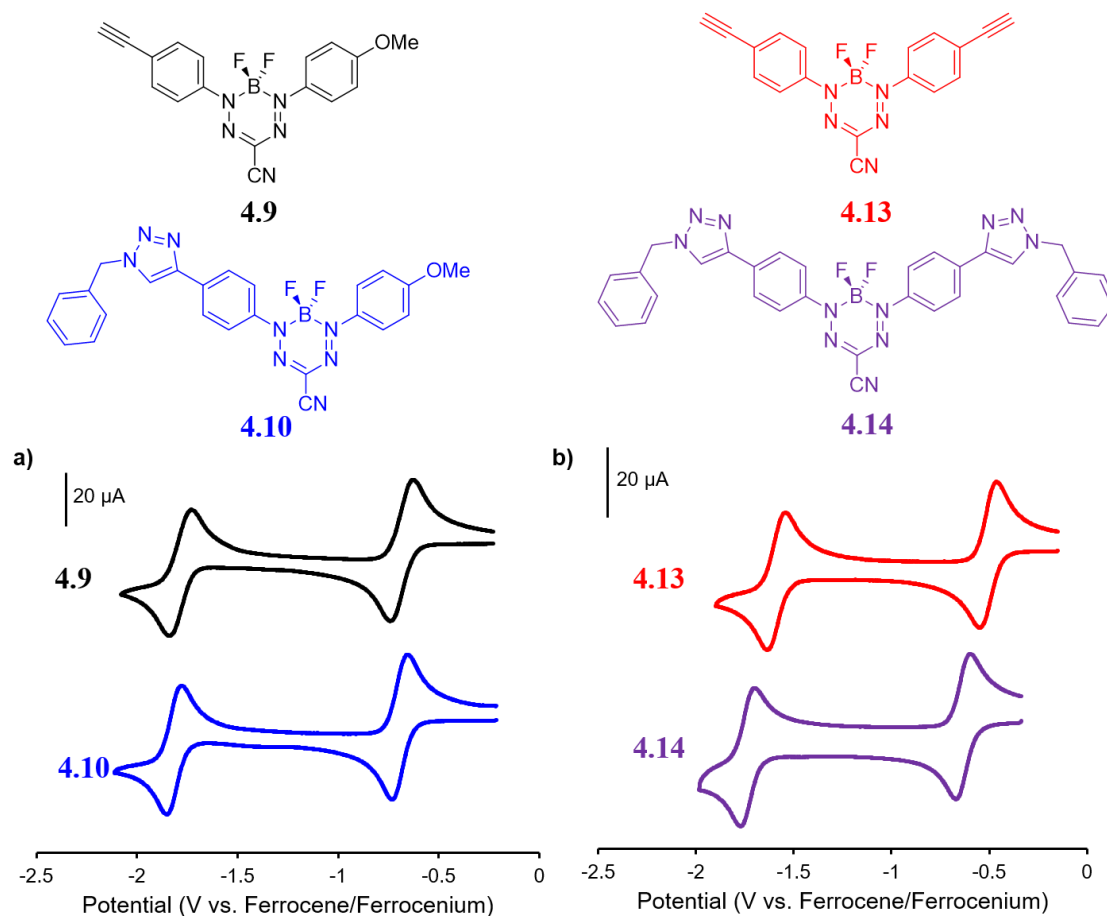


Figure 4.3 Cyclic voltammograms of (a) mono-alkyne-substituted complex **4.9** (black) and mono-benzyl-functionalized complex **4.10** (blue) and (b) bis-alkyne-substituted complex **4.13** (red) and bis-benzyl-functionalized complex **4.14** (purple), recorded at 100 mV s^{-1} in 1 mM THF solutions containing 0.1 M $[\text{nBu}_4\text{N}][\text{PF}_6]$ as supporting electrolyte.

In both the UV-vis absorption and emission spectra, the wavelength of maximum absorption (λ_{max}) and emission (λ_{em}) red-shift by approximately 10 nm when comparing mono-benzyl-functionalized complex **4.10** and mono-alkyne-substituted complex **4.9**. As may be expected, a more drastic red-shift was observed when the spectra of bis-benzyl-functionalized complex **4.14** and bis-alkyne-substituted complex **4.13** were compared. In this case, red-shifts of approximately 30 nm (absorption) and 40 nm (emission) were observed (Figure 4.4), due to a destabilization of the HOMO.

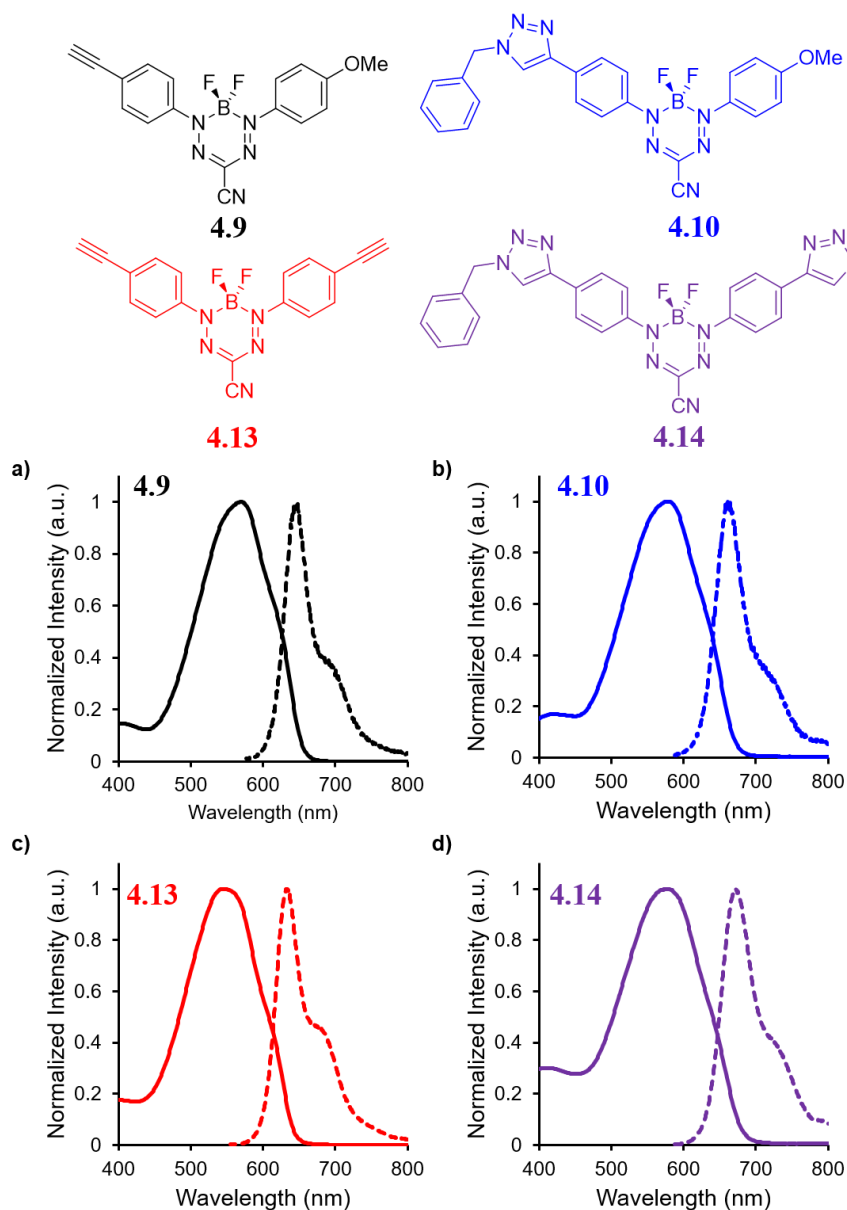


Figure 4.4 UV-vis absorption spectra (solid line) and emission spectra (dashed line) of (a) **4.9**, (b) **4.10**, (c) **4.13** and (d) **4.14**, recorded for 10^{-5} M toluene solutions.

Complexes **4.9**, **4.10**, **4.13** and **4.14** exhibit moderate fluorescence quantum yields in THF, CH₂Cl₂, and toluene (Table 4.1). Mono-alkyne-substituted complex **4.9** has a quantum yield of 30% in CH₂Cl₂, which is almost double that of bis-alkyne-substituted complex **4.13** ($\Phi_F = 18\%$ in CH₂Cl₂), likely due to its asymmetric structure.^[56] Mono-benzyl-functionalized complex **4.10** has the same quantum yield as complex **4.9**, while bis-benzyl-functionalized complex **4.14** showed the most intense emission at a quantum yield of 46%. The Stokes shifts observed (79–133 nm; 2,143–3,394 cm⁻¹) for these complexes were typical of other BF₂ complexes of 3-cyanoformazanates.^[54]

Table 4.1. Optical and electronic properties of BF₂ formazanate complexes **4.9–4.11** and **4.13–4.16**.

	Solvent	λ_{\max} (nm)	ϵ (M ⁻¹ cm ⁻¹)	λ_{em} (nm)	Φ_F (%) ^a	ν_{ST} (nm)	ν_{ST} (cm ⁻¹)	E_{ox1} (V) ^b	E_{red1} (V) ^b	E_{red2} (V) ^b
4.9	CH ₂ Cl ₂	552	30,400	647	30	95	2,660	–	–	–
	THF	550	32,500	650	27	100	2,797	–	-0.67	-1.78
	Toluene	569	26,800	648	36	79	2,143	–	–	–
4.10	CH ₂ Cl ₂	560	31,000	660	30	100	2,706	–	–	–
	THF	560	33,700	672	25	112	2,976	–	-0.68	-1.81
	Toluene	579	37,400	661	37	82	2,143	–	–	–
4.11^c	CH ₂ Cl ₂	562	28,600	–	–	–	–	–	–	–
	THF	562	31,700	–	–	–	–	0.20	-0.67	-1.80
	Toluene	578	23,900	–	–	–	–	–	–	–
4.13	CH ₂ Cl ₂	530	32,700	635	18	105	3,120	–	–	–
	THF	529	29,600	638	19	109	3,230	–	-0.50	-1.58
	Toluene	547	41,700	637	36	90	2,583	–	–	–
4.14	CH ₂ Cl ₂	558	39,600	679	46	121	3,194	–	–	–
	THF	563	34,100	696	34	133	3,394	–	-0.62	-1.72
	Toluene	577	33,700	680	72	103	2,625	–	–	–
4.15^c	CH ₂ Cl ₂	569	30,900	–	–	–	–	–	–	–
	THF	569	26,100	–	–	–	–	0.21	-0.56	-1.67
	Toluene	582	30,700	–	–	–	–	–	–	–
4.16	CH ₂ Cl ₂	542	16,500	680	53	138	3,744	–	–	–
	THF	563	11,900	697	20	134	3,415	–	-0.58	-1.68
	Toluene	–	–	–	–	–	–	–	–	–

^aQuantum yields were measured according to published protocols using [Ru(bpy)₃][PF₆]₂ as a relative standard and corrected for wavelength-dependent detector sensitivity (Figure A4.18).^[57–58] ^bCyclic voltammetry experiments were conducted in THF containing 1 mM analyte and 0.1 M [*n*Bu₄N][PF₆] as supporting electrolyte at a scan rate of 100 mV s⁻¹. All voltammograms were referenced internally against the ferrocene/ferrocenium redox couple. ^cComplexes **4.11** and **4.15** were non-emissive in the range of organic solvents employed.

4.2.2 Ferrocene-Functionalized BF_2 Complexes of 3-Cyanoformazanates

BF_2 complexes of formazanate ligands generally exhibit very well-behaved reduction chemistry.^[54-55,59-62] However, their oxidation is rarely observed within the electrochemical window of most organic solvents. Ferrocene can be reversibly oxidized, and so the electrochemical properties of compounds that contain both ferrocene and formazanate moieties may have unusual properties, including charge-transfer characteristics. Similar compounds based on different fluorophores have been previously used as viscosity probes,^[63] redox-active fluorescent switches,^[64-65] and ion pair recognition receptors.^[66] The resulting complexes were dark purple/blue in colour (Figures A4.19, A4.20) and were non-emissive in solution, likely due to excited-state electron transfer from the BF_2 formazanate moiety to the ferrocene.^[65,67-69]

Cyclic voltammetry studies of complex **4.15** revealed two characteristic BF_2 formazanate reduction waves (each corresponding to one electron) at potentials of -0.56 V and -1.67 V, respectively. This complex was more difficult to reduce than symmetric complexes **4.13** and **4.14**, due to the electron-rich nature of ferrocene. An oxidation wave corresponding to two electrons was observed at a potential of 0.21 V, which corresponds to the one-electron oxidation of both ferrocene groups (Figure 4.5). The coincident appearance of the ferrocene waves in the cyclic voltammogram of **4.15** confirmed that there was little to no electronic communication between the ferrocene units via the BF_2 formazanate spacer.

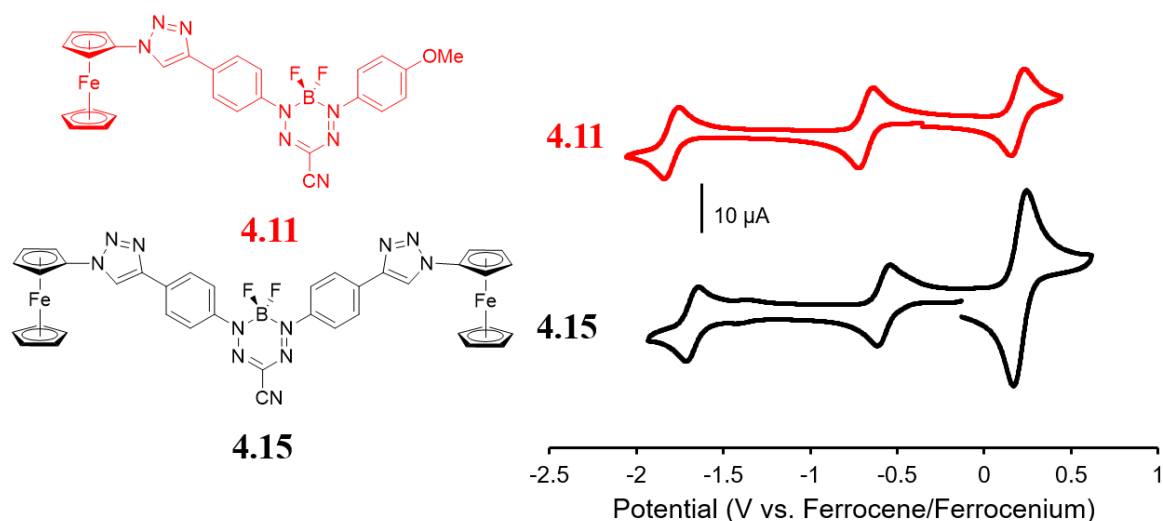


Figure 4.5 Cyclic voltammograms of mono-ferrocene-substituted BF₂ complex **4.11** (red) and bis-ferrocene-substituted complex **4.15** (black) recorded at 100 mV s⁻¹ in 1 mM THF solutions containing 0.1 M [*n*Bu₄N][PF₆] as supporting electrolyte.

In order to further explore the apparent fluorescence quenching associated with the presence of ferrocene in complexes **4.11** and **4.15**, we systematically oxidized the ferrocene units and studied their absorption and emission properties in CH₂Cl₂ (Figure 4.6). NOBF₄ was chosen as an oxidant as the gaseous byproducts were assumed not to contribute to the spectra collected upon oxidation and the oxidation potential of *ca.* 1.0 V^[70] relative to ferrocene/ferrocenium was not in a range that would oxidize the 3-cyanoformazanate ligand backbone. In CH₂Cl₂, the absorption maxima associated with the π→π* transition of the BF₂ formazanate backbone of complexes **4.11** and **4.15** underwent a blue-shift upon subsequent addition of NOBF₄, spanning a range from 563 nm (0 equiv.) to 561 nm (1 equiv.) in mono-ferrocene substituted complex **4.11**, and 569 nm (0 equiv.) to 549 nm (2 equiv.) in bis-ferrocene substituted complex **4.15**. The blue-shift appears to arise due to the removal of electron density from the ferrocene moieties, rendering the complexes less electron rich overall. This effect has been observed previously for similar complexes, whereby the introduction of electron withdrawing groups blue-shifted absorption maxima.^[54] Perhaps more significant, was the observation that upon conversion of ferrocene to ferrocenium, the solutions of **4.11** and **4.15** that had been treated with NOBF₄

became emissive. The emission intensity gradually increased with the subsequent addition of oxidizing agent until a maximum intensity ($\Phi_F = 7\%$ for complex **4.11** and 14% for complex **4.15**) was reached when 1 or 2 equiv. of NOBF_4 had been added, while λ_{em} was unchanged. These observations corroborate our hypothesis that the emission of these complexes was quenched as a result of excited-state electron transfer from the formazanate backbone to ferrocene.

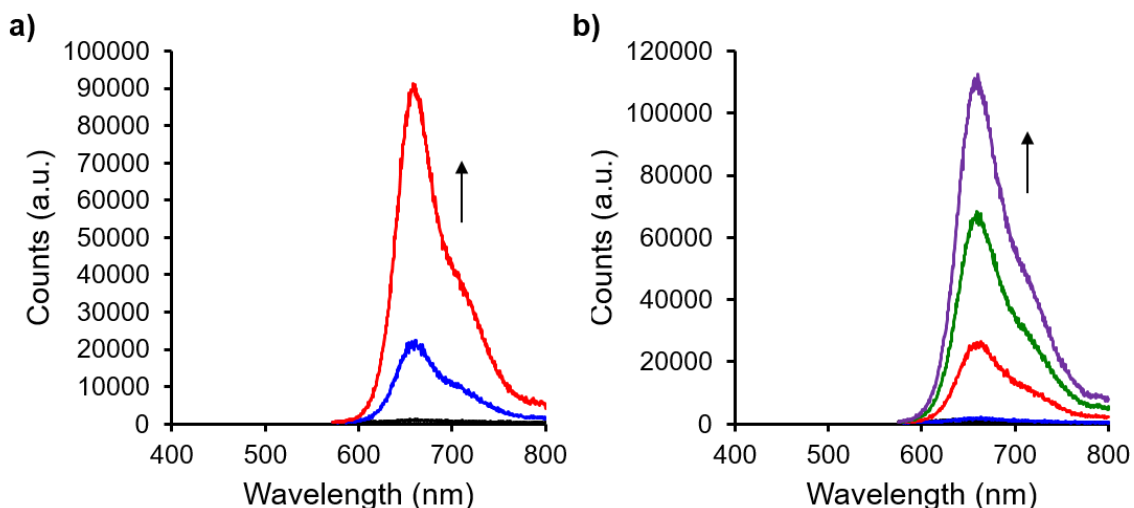


Figure 4.6 Emission spectra of solutions of ferrocene-substituted complexes (a) **4.11** and (b) **4.15** treated with 0 equiv. (black), 0.5 equiv. (blue), 1.0 equiv. (red), 1.5 equiv. (green) and 2.0 equiv. (purple) of NOBF_4 , recorded in degassed CH_2Cl_2 at a concentration of 10^{-5} M. The arrows indicate the trends upon addition of NOBF_4 .

4.2.3 Tetraethylene Glycol-Functionalized BF_2 Complexes of 3-Cyanoformazanates

Complex **4.16**, which was targeted over a mono-tetraethylene glycol substituted complex, in an effort to maximize hydrophilicity, is soluble in both polar organic solvents and water. Interestingly, the optical properties were highly dependent on the polarity of the solvent used. In relatively non-polar solvents such as CH_2Cl_2 and THF, **4.16** was moderately fluorescent (Φ_F : 53% and 20%, respectively). However, the fluorescence intensity dropped off significantly in more polar solvents (Φ_F : 5% in H_2O), and there was also a blue-shift in

the wavelength of maximum emission (Table 4.2, Figure 4.7), which is often observed for fluorescent dyes in highly polar solvents.^[71-75]

Table 4.2. Absorption and emission properties of complex **4.16** in different solvents.

Solvent	λ_{max} (nm)	ϵ ($\text{M}^{-1} \text{cm}^{-1}$)	λ_{em} (nm)	Φ_{F} (%)	ν_{ST} (nm)	ν_{ST} (cm^{-1})
CH_2Cl_2	542	16,500	680	53	138	3,744
THF	563	11,900	697	20	134	3,415
MeOH	521	19,900	681	6	160	4,510
MeCN	524	18,200	697	10	173	4,737
DMSO	526	17,600	716	<1	190	5,045
H_2O	527	15,100	698	5	171	4,649

^aQuantum yields were measured according to published protocols using $[\text{Ru}(\text{bpy})_3][\text{PF}_6]_2$ as a relative standard and corrected for wavelength-dependent detector sensitivity (Figure A4.18).^[57-58]

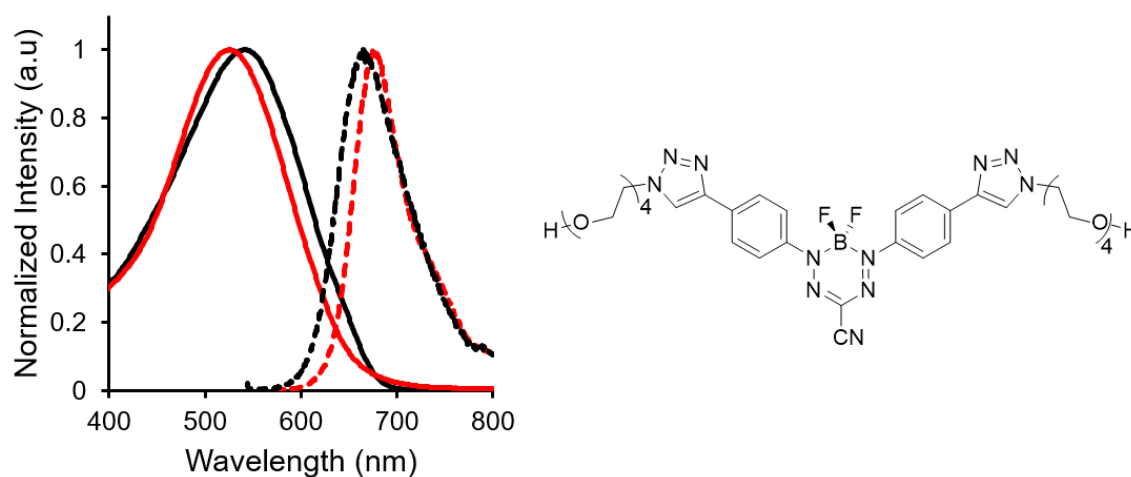


Figure 4.7 UV-vis absorption (solid line) and emission (dashed line) spectra of TEG-functionalized complex **4.16** in CH_2Cl_2 (black) and H_2O (red), recorded for degassed solutions at a concentration of 10^{-5} M.

While the emission intensity of **4.16** was relatively low in water, many other fluorophores with low quantum yields have shown promise as cell-imaging agents, especially dyes which emit in the red to near-IR region.^[76-80] With these factors in mind, complex **4.16** was introduced into mouse fibroblast cells and its utility as an imaging agent studied using fluorescence confocal microscopy.

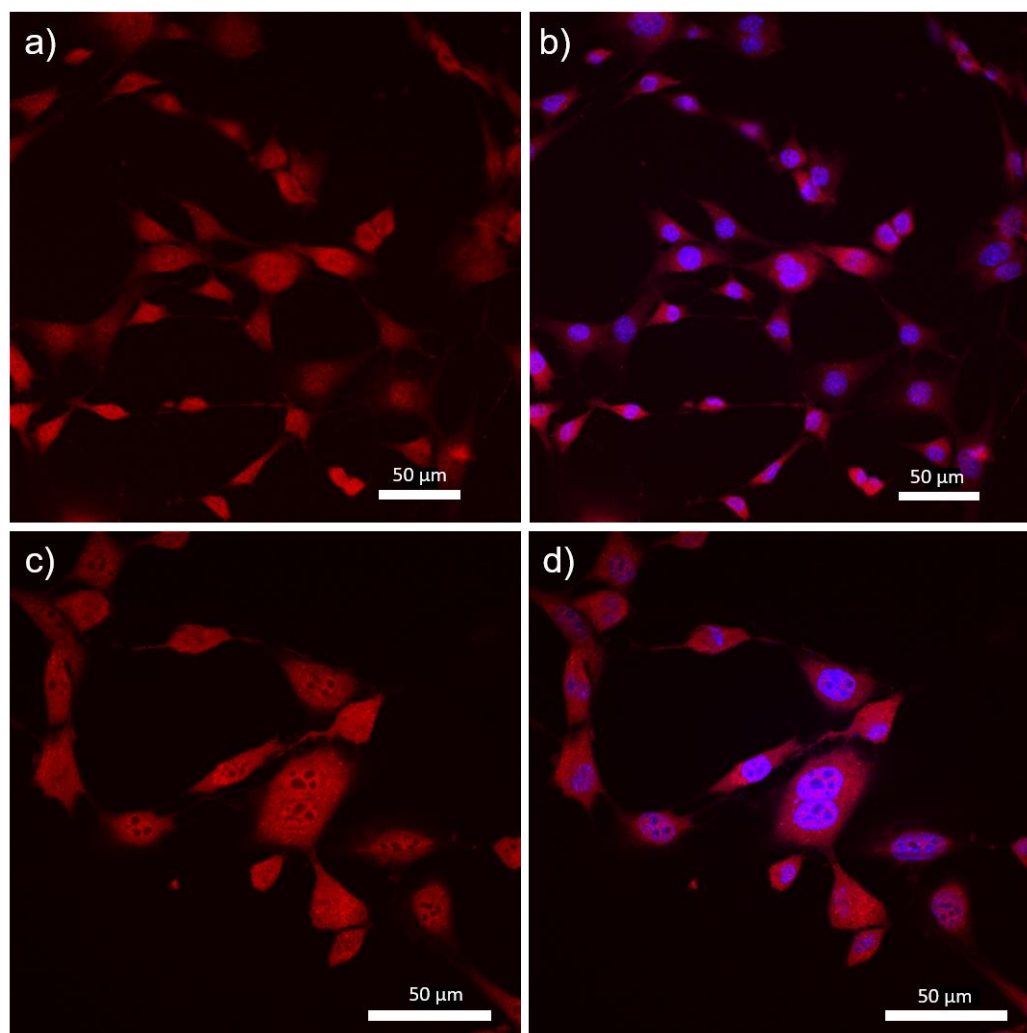


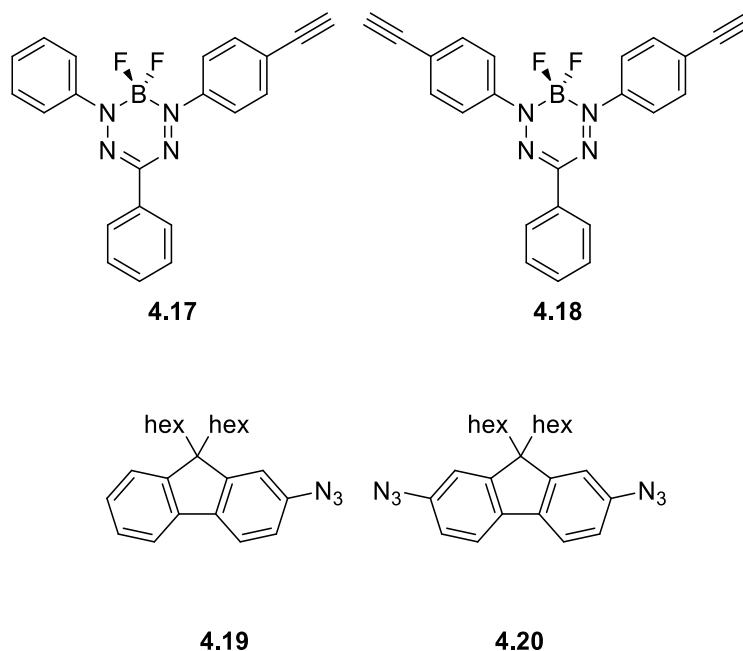
Figure 4.8 Confocal fluorescence micrographs of mouse fibroblast cells stained with TEG-functionalized complex **4.16** and DAPI. Images (a) and (c) were visualized with excitation at 579 nm and emission collected between 620–720 nm. Images (b) and (d) are an overlay of images (a) and (c) with those obtained from excitation at 405 nm and emission collected between 425–475 nm.

Complex **4.16** was successfully incorporated into the cells, as evidenced by the fluorescence micrographs shown in Figure 4.8. Specifically, complex **4.16** was distributed throughout the cell structure and clearly penetrated the cell nucleus. The dark spots visualized in Figure 4.8c are believed to be DNA-free nucleoli, and appear to be the only features of the cells that were not stained by **4.16**. Despite the widespread incorporation of complex **4.16** throughout the cell, Figures 4.8b and 4.8d demonstrate our ability to differentiate between cytoplasm and nucleus when 4',6-diamidino-2-phenylindole (DAPI),

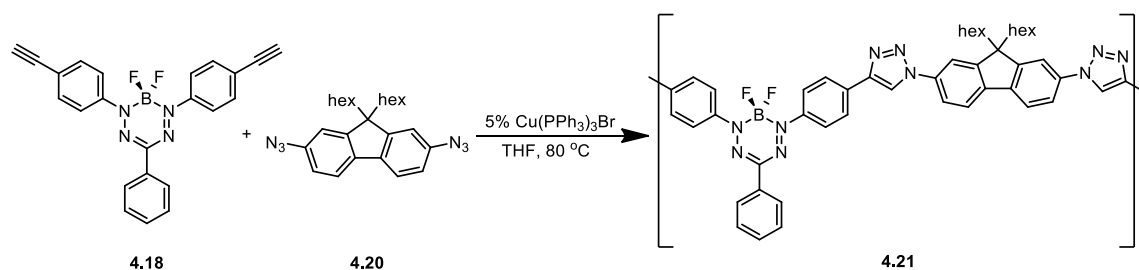
a selective nuclear stain, was employed concurrently. These results differed significantly when compared to previous studies involving BF_2 complexes of 3-cyanoformazanates bearing *p*-anisole substituents.^[60] The hydrophobic nature of the anisole-based dye resulted in selective staining of the cell cytoplasm and required the use of DMSO to achieve cellular uptake.^[60] While we have not produced a site-specific imaging agent as part of this study, we have demonstrated our ability to create hydrophilic analogs of the parent complexes and shown that, in doing so, we can drastically alter their cellular uptake. This work sets the stage for future iterations whereby site-specific staining will be achieved through the introduction of hydrophilic, tailor-made peptide chains.

4.3 π -Conjugated Polymers of BF_2 Formazanates

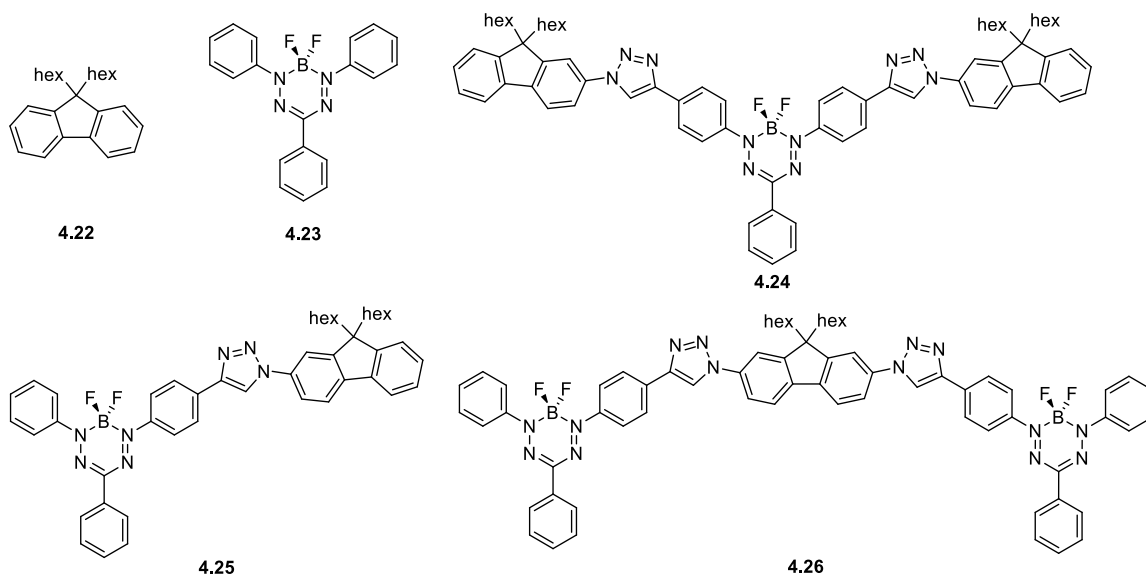
The use of CuAAC chemistry to incorporate BF_2 formazanate complexes into π -conjugated polymers was also intriguing, as we demonstrated that extending the π conjugation of BF_2 formazanates (*e.g.*, by replacing phenyl with naphthyl substituents), results in red-shifted wavelengths of maximum absorption and emission and increased emission quantum yields. Due to the limited solubility of BF_2 formazanate complexes with 3-cyano substituents, BF_2 complexes **4.9** and **4.13** were not ideally suited for the envisioned polymer studies. To circumvent this issue, similar mono-alkyne **4.17** and bis alkyne **4.18** complexes with 3-phenyl substituents were synthesized. These complexes can react with mono-azide **4.19** and bis-azide **4.20** fluorene compounds to create π -conjugated polymers and model complexes.



Bis-alkyne substituted BF₂ complex **4.18** and bis-azide substituted fluorene **4.20** were used to synthesize polymer **4.21** through copper-catalyzed alkyne-azide cycloaddition chemistry (see Scheme 4.2), and the same methods were used to synthesize model complexes **4.24–4.26**. The model compounds and polymer were fully characterized by ¹H, ¹¹B, ¹³C{¹H} and ¹⁹F NMR spectroscopy, UV-vis absorption and emission and IR spectroscopy (Figures A4.21–A4.36).



Scheme 4.2 Synthesis of polymer **4.21** by copper-catalyzed alkyne-azide cycloaddition chemistry.



Polymerization reactions (Scheme 4.2) were monitored for 7 days by removing an aliquot after 24, 48, 72 and 168 h, and it was determined by gel permeation chromatography (GPC) that the molecular weight reached a maximum after 2 days (Figures 4.9, A4.37). Decreasing the catalyst loading from 5% to 2% resulted in a decreased number average molecular weight (M_n) from $17,000 \text{ g mol}^{-1}$ [Dispersity ($D = 2.14$)] to $6,000 \text{ g mol}^{-1}$ ($D = 2.13$). Optimized conditions were chosen to maximize polymer molecular weight, while minimizing reaction time, and thus a catalyst loading of 5% and reaction time of 48 h was selected as the conditions to be used for all further polymerizations.

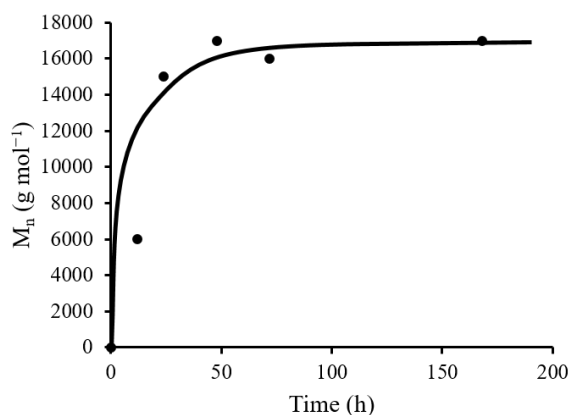


Figure 4.9 Number average molecular weight of **4.21** as a function of time. The black line has been added as a guide for the eye.

In the case of the polymer, the successful incorporation of both the BF₂ formazanate and dihexyl fluorene repeating units was confirmed using NMR spectroscopy. We noted the disappearance of the terminal alkyne proton resonance (3.25 ppm), as well as the appearance of a singlet at 8.38 ppm, consistent with the presence of the triazole ring (Figure 4.10). The boron and fluorine signals in the ¹¹B and ¹⁹F NMR spectra were retained (¹¹B NMR δ = -0.5 ppm, ¹⁹F NMR δ = -143.4 ppm), indicating that the structure of the BF₂ formazanate complex had been maintained throughout the polymerization process. The molecular weight distribution of a representative sample of **4.21** after 2 days was determined by gel permeation chromatography (GPC), yielding a polymer with M_n = 17,000 g mol⁻¹ and Đ = 2.14.

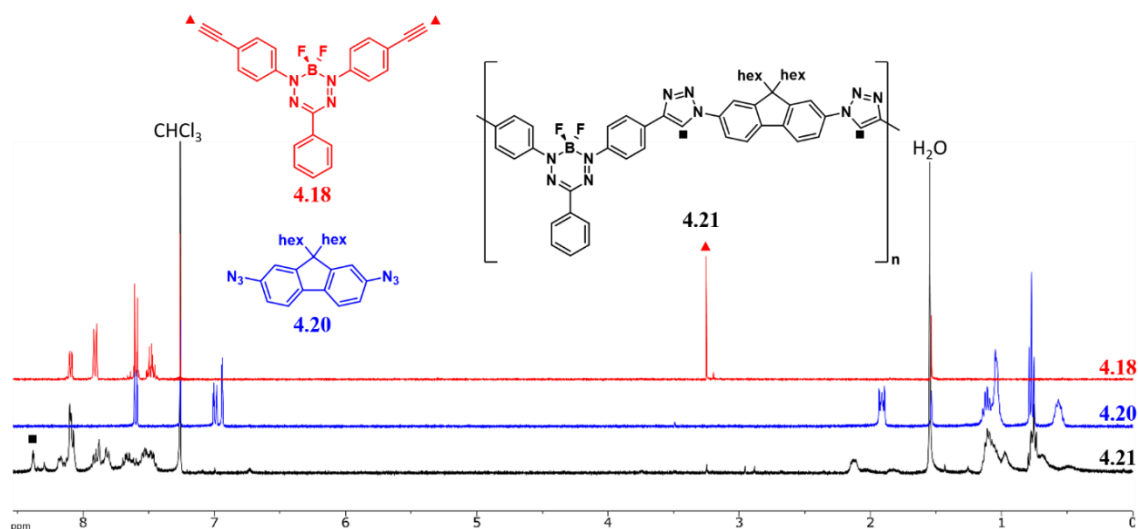


Figure 4.10 ¹H NMR spectra of bis alkyne BF₂ complex **4.18** (red), bis azide fluorene **4.20** (blue) and polymer **4.21** (black) in CDCl₃. The asterisks denote residual solvent signals.

Thermal gravimetric analysis (TGA) showed that **4.21** degraded gradually up to a temperature of 255 °C, at which time it had lost 3% of its mass. Above 255 °C, the polymer degraded quickly to 55% of its original mass at 505 °C. Above 505 °C, slower degradation occurs to a final 43% of the initial mass at 1,000 °C (Figure A4.38). There was no observable glass transition (T_g) within the stability window (0 to 200 °C) determined for **4.21** (Figure A4.39). Furthermore, there was also no observable melt transition in the differential scanning calorimetry (DSC) trace and powder X-ray diffraction studies and

scanning electron microscopy of a thin film of the polymer were consistent with the amorphous character of the polymer (Figures A4.40, A4.41).

The polymer and each of the model compounds showed strong absorbance in the 200–350 nm and the 500–600 nm regions of the electromagnetic spectrum in DMF (Table 4.3). First, we consider the low-energy wavelength of maximum absorption (λ_{max}), which has been previously attributed to a BF_2 formazanate $\pi \rightarrow \pi^*$ transition with HOMO \rightarrow LUMO character (Figure 4.11).^[55] This transition in the polymer ($\lambda_{\text{max}} = 557$ nm) is red-shifted by approximately 50 nm when compared to BF_2 formazanate model compound **4.23** ($\lambda_{\text{max}} = 505$ nm). Furthermore, when we studied the same transition in fluorene- BF_2 -fluorene model compound **4.24** ($\lambda_{\text{max}} = 557$ nm), it matched well with that of the polymer. In both polymer **4.21** and fluorene- BF_2 -fluorene model **4.24**, each BF_2 unit is bound to two triazole rings, potentially extending the degree of π conjugation. We also note that the same absorption in fluorene- BF_2 model **4.25** ($\lambda_{\text{max}} = 533$ nm), which has just one triazole bound to the BF_2 moiety, was red-shifted by just 28 nm. Based on these results, we concluded that the introduction of each triazole ring shifted the formazanate λ_{max} by approximately 30 nm. The similarity between polymer **4.21** and the model compounds also suggested that the properties of the polymer are not dictated by long range π conjugation along the polymer backbone.

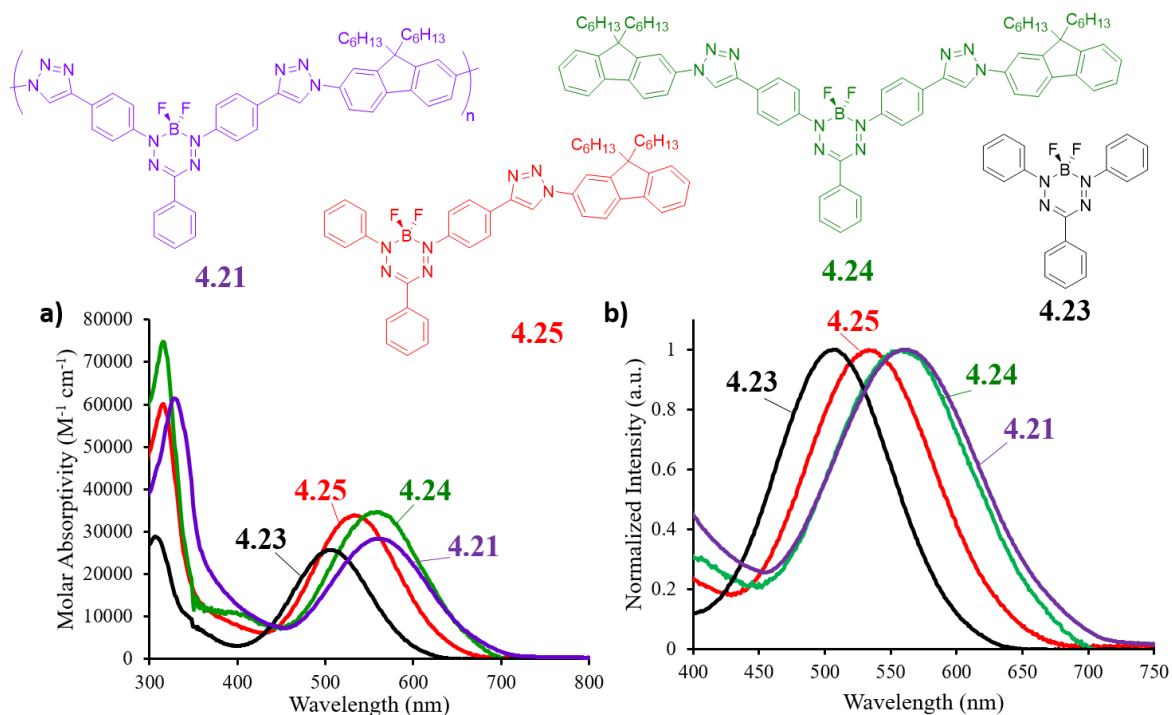


Figure 4.11 a) UV-vis absorption spectra of **4.21** (purple), **4.23** (black), **4.24** (green) and **4.25** (red), recorded for 10^{-5} M DMF solutions. b) Normalized UV-vis absorption spectra from 400–750 nm for comparison.

Next, we considered the high-energy absorption maxima for these compounds (Figure 4.12). This region is complex, as both hexyl fluorene (**4.22**) and the BF₂ formazanate complex (**4.23**) absorb between 200–350 nm. When considering the 9,9-di-*n*-hexylfluorene contributions, we observed a similar trend to that of the absorption of the BF₂ formazanate unit. The high-energy absorption band of polymer **4.21** ($\lambda_{\text{max}} = 327$ nm) was red-shifted by 23 nm, when compared to **4.22** ($\lambda_{\text{max}} = 304$ nm). Again, we attributed the red-shift to extended π conjugation relating to the presence of the triazole rings bound to 9,9-di-*n*-hexylfluorene. BF₂-fluorene model compound **4.25** has a high energy wavelength of maximum absorption ($\lambda_{\text{max}} = 317$ nm) which falls almost exactly half way between the wavelength of maximum absorption of **4.22** and polymer **4.21**, further corroborating our conclusion that the observed trends in electronic properties arise due to the presence of the triazole rings and not extended π conjugation of the polymer backbone. The observed trends are consistent with similar compounds synthesized by alkyne-azide cycloaddition

chemistry.^[25,48,81] We also note that the absorption profile is unchanged with variation in the molecular weight of polymer **4.21** (Figure A4.42). The thin-film absorption spectra of **4.21** and all model compounds were red-shifted with respect to the solution-based spectra by *ca.* 20 nm, but were qualitatively similar, indicating the formation of J-aggregates (Figure A4.43). The estimated band gap (E_g) of 1.67 eV (Table 4.4), indicates that, despite the lack of long range π conjugation in polymer **4.21**, it may find use as a light harvesting material in organic electronics.

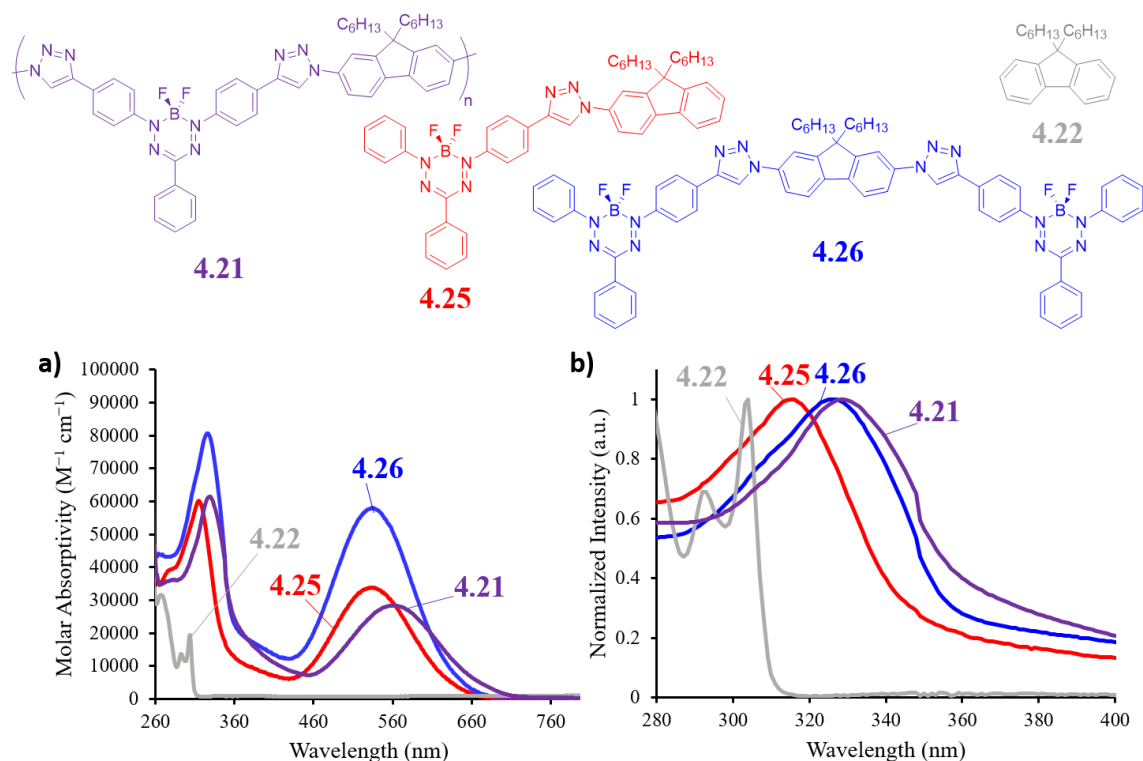


Figure 4.12 a) UV-vis absorption spectra of **4.21** (purple), **4.22** (grey), **4.25** (red) and **4.26** (blue), recorded for 10^{-5} M DMF solutions. b) Normalized UV-vis absorption spectra for 280–400 nm region for comparison.

Each of the model compounds are weakly emissive in solution, with fluorescence quantum yields (Φ_F) of < 3% in DMF (Table 4.3) and Stokes shifts (ν_{ST}) ranging from 123–143 nm (3590 – 3880 cm^{-1}). Polymer **4.21** exhibits two emission maxima when excited at 327 nm. The first is a broad, bimodal signal, with a wavelength of maximum emission (λ_{em}) at 352 nm. The second maxima at 669 nm was consistent with the emissive behavior of BF_2 formazanates (Figure A4.44).^[56] The fact that the intense emission normally associated with hexyl fluorene has been quenched leads us to believe that either a photoinduced

electron transfer (PET) mechanism or Förster resonance energy transfer (FRET) mechanism may be implicated for these systems. However, as the high energy absorption/emission bands for hexyl fluorene and the BF₂ formazanate complexes overlap, we were unable to probe this behavior in detail. The emission profile of the polymer was also unchanged with variation in the molecular weight of the polymer. The emission spectra for the model compounds were qualitatively similar to the polymer, with the high energy emission maxima generally decreasing in intensity when the ratio of BF₂ formazanate to hexyl fluorene units was increased (Table 1). All of the compounds reported in this study were non-emissive in the solid state.

Table 4.3 Summary of absorption/emission and electrochemical properties of **4.21–4.26** in DMF and as thin films.

	$\lambda_{\max, \text{DMF}}$ (nm)	$\lambda_{\max, \text{film}}$ (nm)	$\lambda_{\text{em, DMF}}$ (nm)	$\Phi_{\text{F, DMF}}$ (%) ^a	VST, DMF (nm)	VST, DMF (cm ⁻¹)	E _{red1} ^c (V)	E _{red2} ^c (V)
4.21	327	-	352	1.2	55	4400	-0.73	-1.76 ^b
	557	586	696		139	3590		
4.22	304	-	317	41.5	13	1350	-	-
	306	-	338		32	3090		
4.23	505	525	628	0.2	123	3880	-0.80	-2.00
	314	-	382		68	5670		
4.24	557	583	700	2.2	143	3670	-0.75	-1.86
	317	-	352		35	3140		
4.25	533	554	669	2.3	136	3810	-0.77	-1.84
	326	-	383		57	4560		
4.26	533	559	670	2.0	137	3840	-0.78	-1.93

^aQuantum yields were measured using ruthenium tris(bipyridine) hexafluorophosphate as a relative standard and corrected for wavelength-dependent detector sensitivity (Figure A4.18).^[57-58] ^bOnset of irreversible reduction, cathodic peak potential quoted. ^cCyclic voltammetry experiments were conducted in DMF containing 1 mM analyte and 0.1 M [*n*Bu₄N][PF₆] as supporting electrolyte at a scan rate of 250 mV s⁻¹. All voltammograms were referenced internally against the ferrocene/ferrocenium redox couple.

The electrochemical properties of polymer **4.21** and each of the model compounds are dominated by the BF₂ formazanate fragments, as 9,9-di-*n*-hexylfluorene is not redox-active within the electrochemical window of DMF (Figure A4.45). Model compounds gave rise to two reversible one-electron reduction waves per BF₂ unit in their cyclic voltammograms (Figures A4.45–4.49). As stated earlier, the first reduction corresponds to the formation of a ligand-centered radical anion, and the second to a ligand-centered dianion.^[54,82-83]

Polymer **4.21** displayed broadened electrochemical features, including a chemically-reversible one-electron reduction at $E_{\text{red1}} = -0.73$ V vs. the ferrocene/ferrocenium redox couple, and a second one-electron irreversible reduction at an onset potential, $E_{\text{pc}} = -1.76$ V (Figure 4.13). We also consistently observed the presence of a small irreversible oxidation event over multiple experiments at an onset of $E_{\text{pa}} = 0.35$ V. The first reduction potentials (E_{red1}) of the compounds and polymer follow a logical trend with the number of triazoles present in the compound (Table 4.3). The model compound with no triazoles present (**4.23**) is the most difficult to reduce, at $E_{\text{red1}} = -0.80$ V. Adding one triazole, in model compounds **4.25** and **4.26** makes the BF₂ formazanate slightly easier to reduce ($E_{\text{red1}} = -0.77$ V and -0.78 V, respectively). Finally, compound **4.24** with two triazoles is the easiest model compound to reduce, with a first reduction potential of -0.75 V, very similar to that of polymer **4.21** ($E_{\text{red1}} = -0.73$ V). The energies of the lowest occupied molecular orbital (E_{LUMO}) for each species were estimated from the onset of the first reduction, and ranged from -4.79 to -4.81 eV (Table 4.4).

Table 4.4 Optical and electrochemical band gaps and HOMO/LUMO energies of **4.21**, **4.23–4.26**.

	E_g (nm) ^a	E_g (eV) ^a	E_{LUMO} (eV) ^b	E_{HOMO} (eV) ^c
4.21	744	1.67	-4.81	-6.48
4.23	660	1.88	-4.74	-6.62
4.24	736	1.68	-4.77	-6.45
4.25	703	1.76	-4.75	-6.51
4.26	700	1.77	-4.76	-6.53

^aEstimated from the onset of absorption in the thin-film UV-vis spectra. ^bEstimated from the onset of the first electrochemical reduction, with the ferrocene/ferrocenium oxidation set at a potential of 5.39 eV.^[84] ^cEstimated from the E_{LUMO} level and the optical band gap.

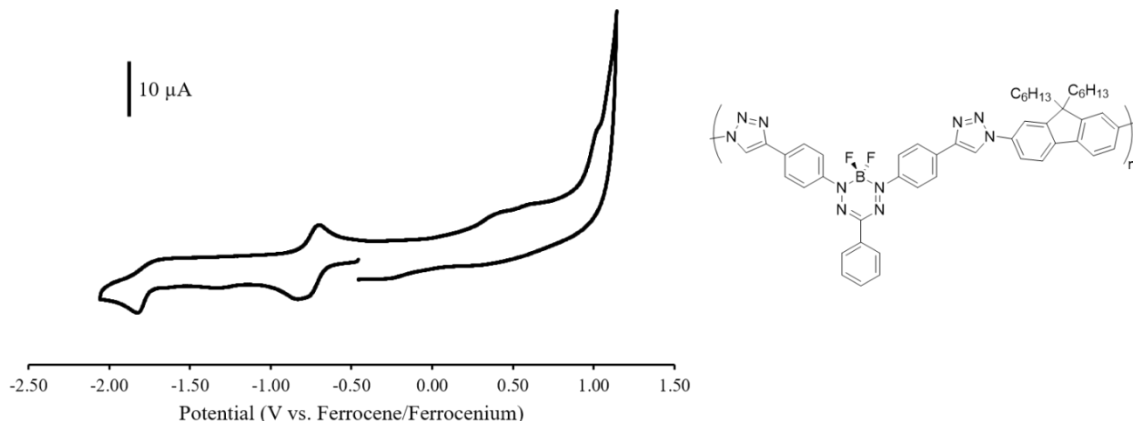


Figure 4.13 Cyclic voltammogram of polymer **4.21** recorded at 250 mV s^{-1} in a 1 mM DMF solution containing 0.1 M $[n\text{Bu}_4\text{N}][\text{PF}_6]$ as supporting electrolyte.

4.4 Conclusions

As a result of this work, we have demonstrated the effect of triazole formation on the spectroscopic and electrochemical properties of BF_2 complexes of formazanate ligands. Complexes functionalized with benzyl groups showed that the formation of triazole rings resulted in red-shifted wavelengths of maximum absorption and emission, as well as increased fluorescence quantum yields. Triazole formation also resulted in BF_2 complexes that were more difficult to reduce electrochemically. We also demonstrated how CuAAC chemistry could be used to expand the scope of BF_2 formazanate chemistry. The attachment of ferrocene into the BF_2 formazanate scaffold via CuAAC resulted in the formation of a non-emissive complex with rich electrochemistry. Specifically, an oxidation wave corresponding to one electron per ferrocene group, and two reduction waves (one electron each) originating from the formazanate backbone were observed by cyclic voltammetry. Furthermore we showed that the stepwise conversion of ferrocene to ferrocenium was accompanied by an increase in emission intensity, confirming our hypothesis that quenching arose due to excited-state electron transfer from the formazanate backbone to ferrocene. Additionally, CuAAC chemistry was used to append water-solubilizing TEG chains to a BF_2 formazanate complex. The resulting complex was used

to image mouse fibroblast cells, and demonstrated our ability to control cellular uptake via the modification of hydrophobicity/hydrophilicity. Finally, we successfully synthesized the first π -conjugated polymer based on BF_2 formazanate complexes. Comparison of model complexes with that of the polymer indicated that π conjugation does not extend beyond the triazole groups formed by alkyne-azide cycloaddition. Based on the thin-film UV-vis absorption spectra we estimate an optical band gap of 1.67 eV for the polymer, highlighting the potential application of this material in organic light-harvesting devices.

4.5 Experimental section

4.5.1 General Considerations

Reactions and manipulations were carried out under a nitrogen atmosphere using standard Schlenk techniques unless otherwise stated. Solvents were obtained from Caledon Laboratories, dried using an Innovative Technologies Inc. solvent purification system, collected under vacuum and stored under a nitrogen atmosphere over 4 Å molecular sieves. Reagents were purchased from Sigma-Aldrich or Alfa Aesar and used as received. TEG-N_3 ,^[85] Fc-N_3 ,^[86] **4.20**,^[51] **4.22**,^[87] and **4.23**^[55] were prepared according to literature procedures.

NMR spectra were recorded on 400 MHz (^1H : 399.8 MHz, ^{11}B : 128.3 MHz, ^{19}F : 376.1 MHz) or 600 MHz (^1H : 599.5 MHz, ^{13}C : 150.8 MHz) Varian INOVA instruments. ^1H NMR spectra were referenced to residual CHCl_3 (7.26 ppm) or $\text{DMSO-}d_6$ (2.50 ppm) and ^{13}C NMR spectra were referenced to CDCl_3 (77.2 ppm) or $\text{DMSO-}d_6$ (39.5 ppm). ^{11}B spectra were referenced to $\text{BF}_3 \cdot \text{OEt}_2$ at 0 ppm and ^{19}F spectra were referenced to CFCl_3 at 0 ppm. Mass spectrometry data were recorded in positive-ion mode using a high-resolution Finnigan MAT 8400 spectrometer using electron impact ionization or a Micromass LCT electrospray time-of-flight mass spectrometer. UV-vis absorption spectra were recorded using Cary 300 or Cary 5000 instruments. Four separate concentrations were run for each sample and molar extinction coefficients were determined from the slope of a plot of absorbance against concentration. Thin-film absorption spectra were recorded for films prepared by spin coating onto glass from a 15 mg mL^{-1} solution in chlorobenzene at room temperature. FT-IR spectra were recorded on a KBr disk or using an attenuated total reflectance (ATR) attachment using a Bruker Vector 33 FT-IR spectrometer. Emission

spectra were obtained using a Photon Technology International QM-4 SE spectrofluorometer. Excitation wavelengths were chosen based on λ_{\max} from the respective UV-vis absorption spectrum in the same solvent. Emission quantum yields were estimated relative to $[\text{Ru}(\text{bpy})_3][\text{PF}_6]_2$ and corrected for wavelength dependent detector sensitivity (Figure A4.18).^[57] Powder samples of **4.21** were analyzed using an Inel CPS powder diffractometer with a Cu K α source of $\lambda = 1.5406 \text{ \AA}$.

4.5.2 Electrochemical Methods

Cyclic voltammetry experiments were performed with a Bioanalytical Systems Inc. (BASi) Epsilon potentiostat and analyzed using BASi Epsilon software. Electrochemical cells consisted of a three-electrode setup including a glassy carbon working electrode, platinum wire counter electrode and silver wire *pseudo* reference electrode. Experiments were run at scan rates of 100 or 250 mV s^{-1} in degassed THF or DMF solutions of the analyte ($\sim 1 \text{ mM}$) and supporting electrolyte (0.1 M $[\text{nBu}_4\text{N}][\text{PF}_6]$). Cyclic voltammograms were referenced against an internal standard ($\sim 1 \text{ mM}$ ferrocene) and corrected for internal cell resistance using the BASi Epsilon software.

4.5.3 Gel Permeation Chromatography (GPC)

GPC experiments were conducted in chromatography-grade DMF at concentrations of 5 mg mL^{-1} using a Waters 2695 separations module equipped with a Waters 2414 differential refractometer and two PLgel 5 m mixed-D ($300 \times 7.5 \text{ mm}$) columns from Polymer Laboratories connected in series. The calibration was performed using polystyrene standards.

4.5.4 Thermal Analysis

Thermal degradation studies were performed using a TA Instruments Q50 TGA. A sample of polymer **4.21** was placed in a platinum pan and heated at a rate of $10 \text{ }^\circ\text{C min}^{-1}$ from room temperature to $1,000 \text{ }^\circ\text{C}$ under a flow of nitrogen (100 mL min^{-1}). Differential Scanning Calorimetry studies were performed on a TA Instruments DSC Q2000. A sample of polymer **4.21** was placed in an aluminum Tzero pan and heated from $20 \text{ }^\circ\text{C}$ to $200 \text{ }^\circ\text{C}$ at $10 \text{ }^\circ\text{C min}^{-1}$ under a flow of nitrogen (50 mL min^{-1}) and cooled down to $20 \text{ }^\circ\text{C}$ at $10 \text{ }^\circ\text{C min}^{-1}$, before the sample underwent two additional heating/cooling cycles.

4.5.5 Scanning Electron Microscopy

Thin films of polymer **4.21** were prepared by spin coating (150 rpm, 10 s, then 2000 rpm, 30 s) a 15 mg mL⁻¹ solution of **4.21** in chlorobenzene at room temperature onto silicon wafers. The surface morphology was assessed directly by scanning electron microscopy (SEM) at 2 keV beam energy using the LEO/Zeiss 1530 instrument at the Western Nanofabrication Facility.

4.5.6 X-ray Crystallography Details

Single crystals of mono-alkyne-substituted complex **4.9** suitable for X-ray diffraction studies were grown by slow evaporation of a concentrated CH₂Cl₂ solution. The sample was mounted on a MiTeGen polyimide micromount with a small amount of Paratone *N* oil. X-ray measurements were made on a Bruker Kappa Axis Apex2 diffractometer at a temperature of 110 K. The data collection strategy included a number of ω and ϕ scans which collected data over a range of angles, 2θ . The frame integration was performed using SAINT.^[88] The resulting raw data was scaled and absorption corrected using a multi-scan averaging of symmetry equivalent data using SADABS.^[89] The structure was solved by using a dual space methodology using the SHELXT program.^[90] All non-hydrogen atoms were obtained from the initial solution. The hydrogen atoms were introduced at idealized positions and were allowed to refine isotropically. The structural model was fit to the data using full matrix least-squares based on F^2 . The calculated structure factors included corrections for anomalous dispersion from the usual tabulation. The structure was refined using the SHELXL-2014 program from the SHELXT suite of crystallographic software.^[91] See Table 4.5 for additional crystallographic data.

Table 4.5 X-ray diffraction data collection and refinement details for mono-alkyne-substituted complex **4.9**.

4.9	
Chemical Formula	C ₁₇ H ₁₂ BF ₂ N ₅ O
FW (g mol ⁻¹)	351.13
Crystal Habit	Purple Prism
Crystal System	monoclinic
Space Group	C2/c
T (K)	110
λ (Å)	0.71073
a (Å)	10.248(6)
b (Å)	14.634(7)
c (Å)	11.146(5)
α (deg)	90
β (deg)	107.352(18)
γ (deg)	90
V (Å ³)	1595.5(14)
Z	4
ρ (g/cm ³)	1.462
μ (cm ⁻¹)	0.111
R ₁ , ^a wR ₂ ^b [I > 2σ]	0.0428, 0.0963
R ₁ , wR ₂ (all data)	0.0770, 0.1107
GOF ^c	1.038

^aR₁ = Σ(|F_o| - |F_c|) / ΣF_o, ^bwR₂ = [Σ(w(F_o² - F_c²)²) / Σ(wF_o⁴)]^{1/2}, ^cGOF = [Σ(w(F_o² - F_c²)²) / (No. of reflns. - No. of params.)]^{1/2}

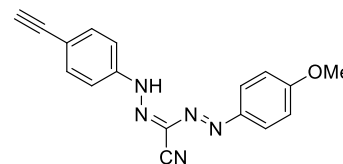
4.5.7 Cell Imaging Studies

Mouse fibroblast C3H/10T1/2 cells (ATCC) were released from the tissue culture flask and seeded onto cover slips in a 12-well tissue culture plate at approximately 50 000 cells per well. The cells were incubated overnight in Dulbecco's modified Eagle's medium (DMEM, Sigma-Aldrich) containing 10% fetal bovine serum (FBS, Sigma-Aldrich) with penicillin streptomycin at 37 °C in a 5% CO₂ atmosphere. Cell media was aspirated and the cells were washed once with serum free media and twice with phosphate buffer saline (PBS, Sigma-Aldrich). Water-soluble complex **4.16** (8 mg) was dissolved into 5 mL DMEM (serum free), filter sterilized with a 0.2 μm filter and diluted to 100 μM with serum free DMEM. The dye stock was incubated at 37 °C for 1 h with the cells. The cells were washed twice with PBS, fixed with 4% paraformaldehyde and mounted onto slides containing Pro-Long Antifade mounting medium with DAPI (ThermoFisher Scientific). Fluorescence microscopy images were obtained using an Olympus FluoView FV 1000

confocal microscope. Images based on the fluorescence of DAPI were obtained using 2% laser strength, with excitation at 405 nm and emission collected between 425 and 475 nm. Images based on the fluorescence of complex **4.16** were obtained using 10% laser strength, with excitation at 579 nm and emission collected between 620 and 720 nm.

Formazan **4.8**

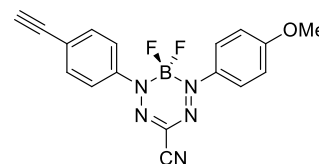
In air, cyanoacetic acid (1.00 g, 11.7 mmol) and NaOH (4.70 g, 117 mmol) were mixed with deionized H₂O (60 mL) and the solution was stirred in an ice bath for 20 min. Meanwhile, in a separate flask, 4-ethynylaniline (1.10 g, 9.36 mmol) was mixed with 12 M HCl (2.3 mL, 28 mmol) in deionized H₂O (2.3 mL). The solution was cooled in an ice bath for 15 min before a cooled solution of sodium nitrite (0.75 g, 10 mmol) in deionized H₂O (7 mL) was added dropwise. The resulting reaction mixture, which contained the corresponding diazonium salt, was stirred in an ice bath for an additional 20 min. In the meantime, in a separate flask, *p*-anisidine (1.4 g, 12 mmol) was mixed with 12 M HCl (2.9 mL, 35 mmol) in deionized H₂O (2.9 mL). The solution was cooled in an ice bath for 15 min before a cooled solution of sodium nitrite (0.93 g, 13 mmol) in deionized H₂O (8 mL) was added dropwise. The resulting reaction mixture, which contained diazonium salt, was stirred in an ice bath for an additional 20 min. The diazonium salt solutions were then mixed together and stirred in an ice bath for 10 min. The diazonium-containing solution was then added dropwise to the cyanoacetic acid solution. The solution turned dark red after approximately 2 min. After complete addition, the mixture was stirred in an ice bath for an additional 60 min before it was neutralized with 1M HCl. The resulting red-brown solid was filtered off and purified by flash chromatography using a gradient strategy (starting at 1:1 *n*-hexanes:CH₂Cl₂ and ending with 2:8 *n*-hexanes:CH₂Cl₂) where the second coloured fraction contained the desired product. Removal of the solvent *in vacuo* afforded mono-alkyne-substituted formazan **4.8** as a dark red microcrystalline solid. Yield = 0.89 g, 25%. M.p 212–213 °C. ¹H NMR (400.1 MHz, DMSO-*d*₆): δ 12.49 (br s, 1H, NH), 8.08 (d, ³J_{HH} = 9 Hz, 2H, aryl CH), 7.54 (d, 4H, aryl CH), 7.18 (d, ³J_{HH} = 9 Hz, 2H, aryl CH), 4.19 (s, 1H, alkyne CH), 3.91 (s, 3H, OCH₃). ¹³C{¹H} NMR (100.6 MHz, DMSO-*d*₆): δ 163.2, 145.9, 142.5, 132.8, 126.9, 126.2, 116.6, 115.5, 114.8, 112.6, 83.3, 80.5, 55.7. FT-IR(ATR): 3308 (m), 3230 (m), 2942 (s),



2837 (s), 2224 (m), 2099 (m), 1605 (m), 1579 (m), 1514 (s), 1249 (s), 1183 (s), 1164 (s), 1140 (s), 1110 (m), 1028 (m) cm^{-1} . UV-Vis (CH_2Cl_2): λ_{max} 444 nm ($\epsilon = 26,400 \text{ M}^{-1} \text{ cm}^{-1}$). Mass Spec. (EI, +ve mode): exact mass calculated for $[\text{C}_{17}\text{H}_{13}\text{N}_5\text{O}]^+$: 303.1120; exact mass found: 303.1111; difference: -3.0 ppm.

Formazanate BF_2 complex **4.9**

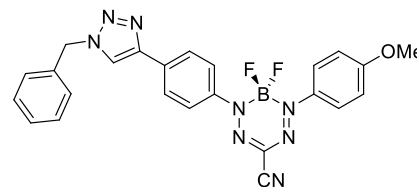
Formazan **4.8** (0.40 g, 1.3 mmol) was dissolved in dry toluene (75 mL). NEt_3 (0.40 g, 0.55 mL, 3.9 mmol) was then added slowly, and the solution was stirred for 10 min before $\text{BF}_3 \cdot \text{OEt}_2$ (0.94 g, 0.81 mL, 6.6 mmol) was added and the solution was



heated to $80 \text{ }^\circ\text{C}$ with stirring for 16 h. The solution became dark purple during this time and after cooling to $22 \text{ }^\circ\text{C}$, deionized H_2O (10 mL) was added to quench any excess boron-containing compounds. The toluene solution was then washed with deionized H_2O (3×20 mL), dried over MgSO_4 , gravity filtered, and concentrated *in vacuo*. The resulting compound was purified by flash chromatography (THF, neutral alumina) to afford mono-alkyne-substituted complex **4.9** as a dark-purple solid. Yield = 0.31 g, 68%. M.p $199\text{--}201 \text{ }^\circ\text{C}$. ^1H NMR (399.8 MHz, CDCl_3): δ 7.96 (d, $^3J_{\text{HH}} = 9$ Hz, 2H, aryl CH), 7.85 (d, $^3J_{\text{HH}} = 9$ Hz, 2H, aryl CH), 7.59 (d, $^3J_{\text{HH}} = 9$ Hz, 2H, aryl CH), 7.00 (d, $^3J_{\text{HH}} = 9$ Hz, 2H, aryl CH), 3.91 (s, 3H, OCH_3), 3.27 (s, 1H, alkyne CH). $^{13}\text{C}\{^1\text{H}\}$ NMR (150.7 MHz, CDCl_3): δ 163.0, 142.9, 136.8, 133.0, 125.3, 124.5, 122.5, 115.0, 114.0, 82.5, 80.7, 55.8. ^{11}B NMR (128.3 MHz, CDCl_3): δ -0.7 (t, $^1J_{\text{BF}} = 31$ Hz). ^{19}F NMR (376.1 MHz, CDCl_3): δ -133.7 (q, $^1J_{\text{FB}} = 31$ Hz). FT-IR (ATR): 3282 (m), 2928 (s), 2840 (s), 2240 (m), 1593 (s), 1505 (m), 1407 (s), 1343 (s), 1328 (s), 1307 (s), 1262 (s), 1166 (s), 1138 (s) cm^{-1} . UV-Vis (CH_2Cl_2): λ_{max} 552 nm ($\epsilon = 30,400 \text{ M}^{-1} \text{ cm}^{-1}$). Mass Spec. (EI, +ve mode): exact mass calculated for $[\text{C}_{17}\text{H}_{12}\text{BF}_2\text{N}_5\text{O}]^+$: 351.1103; exact mass found: 351.1108; difference: $+1.4$ ppm.

Complex **4.10**

A solution of PMDETA (0.002 g, 0.003 mL, 0.01 mmol) in dry THF (2 mL) was degassed via 3 freeze-pump-thaw cycles before CuI (0.003 g, 0.014 mmol) was added and the resulting mixture was stirred for 15

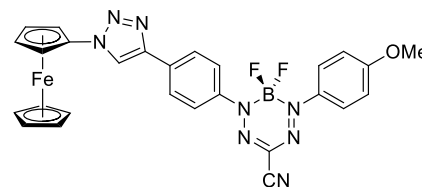


min at $22 \text{ }^\circ\text{C}$. Benzyl azide (0.04 g, 0.04 mL, 0.3 mmol) and mono-alkyne-substituted complex **7** (0.1 g, 0.3 mmol) were then added and the reaction mixture was stirred at $22 \text{ }^\circ\text{C}$

for 16 h. Upon cooling, the THF solution was then purified by flash chromatography (THF, neutral alumina) and recrystallized from MeOH to afford mono-benzyl-functionalized complex **4.10** as a dark-purple microcrystalline solid. Yield = 0.14 g, 51%. M.p 188–189 °C. ^1H NMR (400.1 MHz, CDCl_3): δ 7.95–7.93 (m, 6H, aryl CH), 7.75 (s, 1H, =CH), 7.42–7.40 (m, 3H, aryl CH), 7.34–7.32 (m, 2H, aryl CH), 7.00 (d, $^3J_{\text{HH}} = 9$ Hz, 2H, aryl CH) 5.60 (s, 2H, CH_2), 3.90 (s, 3H, CH_2). $^{13}\text{C}\{^1\text{H}\}$ NMR (150.7 MHz, CDCl_3): δ 162.7, 146.6, 142.6, 136.8, 134.4, 132.9, 129.2, 128.9, 128.1, 126.4, 125.2, 123.3, 120.5, 114.9, 114.3, 55.8, 54.3. ^{11}B NMR (128.3 MHz, CDCl_3): δ -0.7 (t, $^1J_{\text{BF}} = 29$ Hz). ^{19}F NMR (376.1 MHz, CDCl_3): δ -134.2 (q, $^1J_{\text{FB}} = 29$ Hz). FT-IR(ATR): 3123 (m), 2849 (m), 2250 (m), 1603 (s), 1509 (m), 1460 (m), 1375 (s), 1344 (s), 1326 (s), 1308 (s) cm^{-1} . UV-Vis (CH_2Cl_2): λ_{max} 560 nm ($\epsilon = 31,000 \text{ M}^{-1} \text{ cm}^{-1}$). Mass Spec. (EI, +ve mode): exact mass calculated for $[\text{C}_{24}\text{H}_{19}\text{BF}_2\text{N}_8\text{O}]^+$: 484.1743; exact mass found: 484.1759; difference: +3.3 ppm.

Complex 4.11

A solution of PMDETA (0.0018 g, 0.0022 mL, 0.011 mmol) in THF (3 mL) was degassed via 3 freeze-pump-thaw cycles before CuI (0.0020 g, 0.011 mmol) was added and the resulting mixture was stirred for 30 min.



Ferrocenyl azide (0.024 g, 0.11 mmol) and mono-alkyne-substituted complex **4.9** (0.037 g, 0.11 mmol) were then added and the reaction mixture was stirred at 50 °C for 18 h. The resulting dark purple solution was filtered through a plug of celite and purified by flash chromatography (CH_2Cl_2 , silica gel) to afford ferrocene-functionalized complex **4.11** as a dark purple powder. Yield = 0.044 g, 72%. Melting point not observed (Melting point > 250 °C). ^1H NMR (400.1 MHz, CDCl_3): δ 8.06 (s, 1H, triazole CH), 8.02–7.95 (m, 6H, aryl CH), 7.01–7.00 (m, 2H, aryl CH), 4.90 (s, 2H, ferrocene CH), 4.32 (s, 2H, ferrocene CH), 4.26 (s, 6H, ferrocene CH), 3.91 (s, 3H, OCH_3). $^{13}\text{C}\{^1\text{H}\}$ NMR (150.7 MHz, CDCl_3): δ 162.9, 146.3, 142.9, 137.0, 132.9, 126.7, 125.4, 123.6, 120.0, 115.1, 114.4, 93.6, 70.4, 67.1, 62.4, 62.3, 56.0. ^{11}B NMR (128.3 MHz, CDCl_3): δ -0.7 (t, $^1J_{\text{BF}} = 30$ Hz). ^{19}F NMR (376.1 MHz, CDCl_3): δ -134.1 (q, $^1J_{\text{FB}} = 30$ Hz). FT-IR(ATR): 3092 (w), 2926 (m), 2842 (m), 2241 (m), 1597 (s), 1505 (m), 1342 (m), 1261 (s), 1167 (s), 1029 (m), 965 (m), 832 (m), 733 (s) cm^{-1} . UV-Vis (CH_2Cl_2): λ_{max} 562 nm ($\epsilon = 28,600 \text{ M}^{-1} \text{ cm}^{-1}$). Mass Spec. (EI, +ve

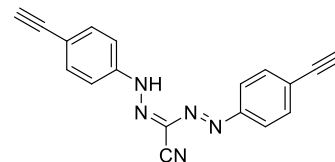
mode): exact mass calculated for $[C_{27}H_{21}BF_2FeN_8O]^+$: 578.1249; exact mass found: 578.1261; difference: +2.1 ppm.

Formazan 4.12

In air, cyanoacetic acid (0.47 g, 5.5 mmol) was dissolved in deionized H_2O (75 mL) containing NaOH (2.20 g, 55 mmol).

This colourless solution was stirred for 45 min in an ice bath.

Meanwhile, 4-ethynylaniline (1.30 g, 12 mmol) was mixed



with concentrated HCl (2.85 mL) in deionized H_2O (30 mL). This solution was cooled in an ice bath for 10 min before a solution of sodium nitrite (1.01 g, 15 mmol) in deionized H_2O (15 mL) was cooled in an ice bath, and then added slowly to the 4-ethynylaniline solution over a 10 min period. This mixture was stirred in an ice bath for 30 min, and then added slowly to the basic cyanoacetic acid solution. A dark red/orange colour persisted almost immediately, and a dark red/orange precipitate formed after a few min. The mixture was stirred in an ice bath for an additional 16 h before ethyl acetate (250 mL) was added and the organic layer was isolated, washed with deionized H_2O (3×100 mL), dried over $MgSO_4$, gravity filtered and concentrated *in vacuo*. The resulting residue was purified by flash chromatography (CH_2Cl_2 , neutral alumina) to afford bis-alkyne-substituted formazan **4.12** as a dark red solid. Yield = 1.55 g, 94%. Melting point not observed (>250 °C). 1H NMR (599.5 MHz, $CDCl_3$) δ 12.60 (s, 1H, NH), 7.60 (s, 8H, aryl CH), 3.24 (s, 2H, alkyne CH). $^{13}C\{^1H\}$ NMR (100.6 MHz, DMSO-*d*₆): δ 146.8, 133.0, 126.9, 121.7, 120.2, 112.5, 83.2, 82.8. FT-IR (KBr): 3397 (br, s), 3261 (m), 2915 (m), 2850 (m), 2221 (s), 1653 (s), 1540 (m), 1268 (m), 1193 (m), 1142 (m) cm^{-1} . UV-vis (CH_2Cl_2): $\lambda_{max} = 434$ nm ($\epsilon = 22,800$ $M^{-1} cm^{-1}$). Mass Spec. (EI, +ve mode): exact mass calculated for $[C_{18}H_{11}N_5]^+$: 297.1014; exact mass found: 297.1018; difference: +1.3 ppm.

Formazanate BF_2 complex 4.13

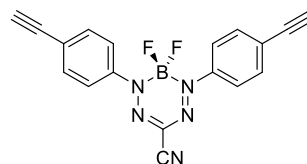
Formazan **4.12** (1.00 g, 3.40 mmol) was dissolved in dry toluene

(100 mL). NEt_3 (1.03 g, 1.42 mL, 10.2 mmol) was then added

slowly and the solution was stirred for 10 min before $BF_3 \cdot OEt_2$

(2.39 g, 2.08 mL, 16.8 mmol) was added and the solution was

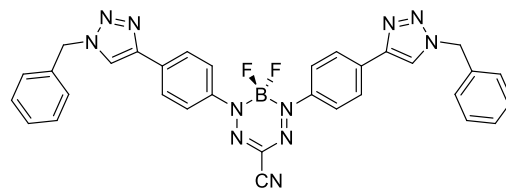
heated with stirring at 80 °C for 18 h. The solution gradually turned from dark red to dark purple during this time. After cooling to 22 °C, deionized H_2O (10 mL) was added to



quench any excess reactive boron-containing compounds. The purple toluene solution was then washed with deionized H₂O (3 × 50 mL), dried over MgSO₄, gravity filtered and concentrated *in vacuo*. The resulting residue was purified by flash chromatography (CH₂Cl₂, neutral alumina) to afford bis-alkyne-substituted complex **4.13** as a dark purple microcrystalline solid. Yield = 0.82 g, 70%. Melting point = 218 °C (decomp.). ¹H NMR (599.5 MHz, CDCl₃) δ 7.91 (d, ³J_{HH} = 9 Hz, 4H, aryl CH), 7.61 (d, ³J_{HH} = 9 Hz, 4H, aryl CH), 3.32 (s, 2H, alkyne CH). ¹³C{¹H} NMR (100.6 MHz, CDCl₃): δ 143.0, 133.4, 126.0, 123.2, 113.8, 82.6, 81.8. ¹¹B NMR (128.3 MHz, CDCl₃): δ -0.8 (t, ¹J_{BF} = 31 Hz). ¹⁹F NMR (376.1 Hz, CDCl₃): δ -132.0 (q, ¹J_{FB} = 31 Hz). FT-IR (KBr): 3290 (s), 3189 (m), 3108 (m), 3092 (m), 2244 (s), 1589 (s), 1391 (m), 1331 (s), 1187 (m), 1147 (s), 1033 (m), 958 (m), 838 (s) cm⁻¹. UV-vis (CH₂Cl₂): λ_{max} = 530 nm (ε = 32,700 M⁻¹ cm⁻¹). Mass Spec. (EI, +ve mode): exact mass calculated for [C₁₈H₁₀N₅BF₂]⁺: 345.0997; exact mass found: 345.0999; difference: +0.6 ppm.

Complex 4.14

A solution PMDETA (0.0075 g, 0.0091 mL, 0.044 mmol) in THF (3 mL) was degassed via 3 freeze-pump-thaw cycles before CuI (0.0083 g, 0.044 mmol) was added and the resulting

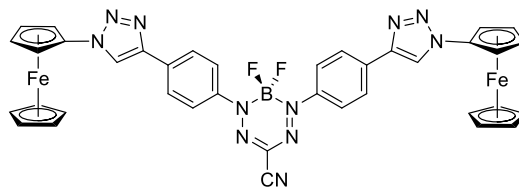


mixture was stirred for 30 min. Benzyl azide (0.174 g, 1.30 mmol) and bis-alkyne-substituted complex **4.13** (0.150 g, 0.44 mmol) were then added and the reaction mixture was stirred at 50 °C for 18 h. Upon cooling, the resulting dark purple solution was filtered through a plug of celite and purified by flash chromatography (CH₂Cl₂, silica gel) to afford bis-benzyl-functionalized complex **4.14** as a dark-purple solid. Yield = 0.21 g, 77%. Melting point not observed (>250 °C). ¹H NMR (599.5 MHz, CDCl₃) δ 7.99–7.94 (m, 8H, aryl CH), 7.76 (s, 2H, triazole CH), 7.43–7.38 (m, 6H, aryl CH), 7.34–7.33 (m, 4H, aryl CH), 5.60 (s, 4H, benzyl CH₂). ¹³C{¹H} NMR (150.7 MHz, CDCl₃): δ 146.7, 142.8, 134.4, 133.8, 129.4, 129.2, 128.3, 126.7, 123.8, 120.7, 114.2, 54.6. ¹¹B NMR (128.3 MHz, CDCl₃): δ -0.7 (t, ¹J_{BF} = 29 Hz). ¹⁹F NMR (376.1 Hz, CDCl₃): δ -133.1 (q, ¹J_{FB} = 29 Hz). FT-IR (KBr): 3109 (m), 3100 (s), 3035 (m), 2915 (m), 2246 (s), 1608 (s), 1497 (m), 1456 (s), 1326 (s), 1226 (m), 1074 (s), 1027 (s), 976 (m), 826 (m) cm⁻¹. UV-vis (CH₂Cl₂): λ_{max}

= 558 nm ($\epsilon = 39,600 \text{ M}^{-1} \text{ cm}^{-1}$). Mass Spec. (EI, +ve mode): exact mass calculated for $[\text{C}_{32}\text{H}_{25}\text{N}_{11}\text{BF}_2]^+$: 612.2356; exact mass found: 612.2362; difference: +1.0 ppm.

Complex 4.15

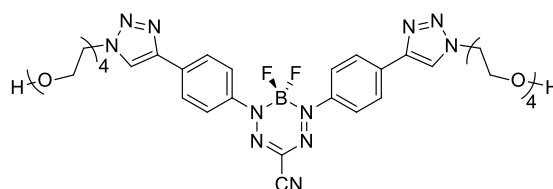
A solution of PMDETA (0.0019 g, 0.0023 mL, 0.011 mmol) in THF (4 mL) was degassed via 3 freeze-pump-thaw cycles before CuI (0.0021 g, 0.011 mmol) was added and the resulting



mixture was stirred for 30 min. Ferrocenyl azide (0.050 g, 0.22 mmol) and bis-alkyne-substituted complex **4.13** (0.038 g, 0.11 mmol) were then added and the reaction mixture was stirred at 50 °C for 18 h. The resulting dark purple solution was filtered through a plug of celite and purified by flash chromatography (CH_2Cl_2 , silica gel) to afford ferrocene-functionalized complex **4.15** as a dark purple powder. Yield = 0.08 g, 90%. Melting point not observed (>250 °C). ^1H NMR (599.5 MHz, CDCl_3) δ 8.08 (s, 2H, triazole CH), 8.05 (s, 8H, aryl CH), 4.91 (m, 4H, ferrocene CH), 4.34–4.33 (m, 4H, ferrocene CH), 4.28–4.26 (m, 10H, ferrocene CH). Due to the poor solubility of **4.15**, and despite a saturated solution in $\text{THF-}d_8$ being subjected to 10,000 scans (8 h) on a 600 MHz spectrometer, a publication quality $^{13}\text{C}\{^1\text{H}\}$ NMR spectrum was not obtained. ^{11}B NMR (128.3 MHz, CDCl_3): δ -0.6 (t, $^1J_{\text{BF}} = 28 \text{ Hz}$). ^{19}F NMR (376.1 Hz, CDCl_3): δ -132.8 (q, $^1J_{\text{FB}} = 28 \text{ Hz}$). FT-IR (KBr): 3131 (w), 3092 (m), 2929 (m), 2246 (m), 1605 (s), 1381 (m), 1341 (s), 1226 (m), 1181 (s), 1027 (m), 966 (s), 816 (s) cm^{-1} . UV-vis (CH_2Cl_2): $\lambda_{\text{max}} = 569 \text{ nm}$ ($\epsilon = 30,900 \text{ M}^{-1} \text{ cm}^{-1}$). Mass Spec. (ESI, +ve mode): exact mass calculated for $[\text{C}_{38}\text{H}_{29}\text{N}_{11}\text{BF}_2\text{Fe}_2]^+$: 800.1367; exact mass found: 800.1380; difference: +1.6 ppm.

Complex 4.16

A solution of PMDETA (0.0075 g, 0.0091 mL, 0.044 mmol) in THF (3 mL) was degassed via 3 freeze-pump-thaw cycles before CuI (0.0083 g, 0.044 mmol) was

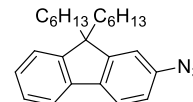


added and the resulting solution was stirred for 30 min. TEG-azide (0.29 g, 1.30 mmol) and bis-alkyne-substituted complex **4.13** (0.15 g, 0.44 mmol) were then added and the reaction mixture was stirred at 50 °C for 18 h. The resulting dark purple solution was filtered through a plug of celite and purified by precipitation of a concentrated THF

solution into *n*-hexanes thrice to yield a dark purple solid. Yield = 0.24 g, 71%. ^1H NMR (599.5 MHz, CDCl_3) δ 8.20 (s, 2H, triazole CH), 8.00 (s, 8H, aryl CH), 4.63–4.61 (m, 4H, ethylene glycol CH_2), 3.93–3.90 (m, 4H, ethylene glycol CH_2), 3.71–3.57 (m, 24H, ethylene glycol CH_2). $^{13}\text{C}\{^1\text{H}\}$ NMR (150.7 MHz, CDCl_3): 145.9, 142.4, 134.0, 126.5, 123.6, 122.6, 114.1, 72.4, 70.5, 70.4, 70.3, 70.1, 69.4, 61.5, 50.5 ppm. ^{11}B NMR (128.3 MHz, CDCl_3): δ -0.7 (t, $^1J_{\text{BF}} = 29$ Hz). ^{19}F NMR (376.1 Hz, CDCl_3): δ -133.1 (q, $^1J_{\text{FB}} = 29$ Hz). FT-IR (KBr): 3132 (br), 3317 (w), 2915 (m), 2868 (m), 2242 (w), 1604 (s), 1527 (w), 1461 (m), 1360 (m), 1333 (s), 1227 (m), 1179 (s), 1121 (s), 1069 (s), 1029 (s), 967 (s), 845 (m), 765 (w) cm^{-1} . UV-vis (CH_2Cl_2): $\lambda_{\text{max}} = 542$ nm ($\epsilon = 16,500$ $\text{M}^{-1} \text{cm}^{-1}$). UV-vis (H_2O): $\lambda_{\text{max}} = 527$ nm ($\epsilon = 15,100$ $\text{M}^{-1} \text{cm}^{-1}$). Mass Spec. (ESI, +ve mode): exact mass calculated for $[\text{C}_{34}\text{H}_{45}\text{N}_{11}\text{O}_8\text{BF}_2]^+$: 784.3514; exact mass found: 784.3540; difference: +3.3 ppm.

2-Azido-9,9-dihexyl fluorene 4.19

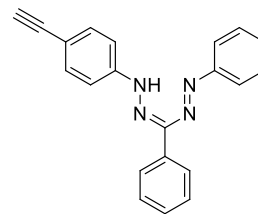
2-Bromo-9,9-di-*n*-hexylfluorene (2.50 g, 6.05 mmol) was dissolved in dry THF (125 mL) and cooled to -78 °C. *n*-BuLi (5.5 mL of a 2.5 M solution in hexanes, 14 mmol) was added slowly via a dropping funnel over a 20 min period. Upon addition, the solution turned a bright yellow color, and was stirred for 90 min at -78 °C. Tosyl azide (2.72 g, 13.8 mmol) was dissolved in 25 mL dry THF and added slowly to the 9,9-di-*n*-hexylfluorene solution, causing it to change to a dark orange/brown color. The reaction was warmed to room temperature and stirred for an additional 18 h. Deionized H_2O (10 mL) was then added to quench any excess *n*-BuLi, and the organics were extracted into CH_2Cl_2 , dried over MgSO_4 , gravity filtered and concentrated *in vacuo*. The resulting residue was purified by flash chromatography (petroleum ether, silica) to yield a light yellow oil. Yield = 0.58 g, 26%. ^1H NMR (599.5 MHz, CDCl_3) δ 7.67–7.64 (m, 2H, aryl CH), 7.33–7.27 (m, 3H, aryl CH), 7.01–6.98 (m, 2H, aryl CH), 1.99–1.89 (m, 4H, alkyl CH), 1.14–1.03 (m, 12H, alkyl CH), 0.77 (t, $^3J_{\text{HH}} = 7$ Hz, 6H, alkyl CH), 0.62–0.57 (m, 4H, alkyl CH). $^{13}\text{C}\{^1\text{H}\}$ NMR (100.6 MHz, CDCl_3): δ 153.1, 150.6, 140.5, 138.9, 138.6, 127.2, 127.1, 123.0, 120.9, 119.6, 117.9, 113.8, 55.4, 40.6, 31.7, 29.9, 23.9, 22.8, 14.2. FT-IR (KBr): 2938 (m), 2926 (s), 2856 (m), 2102 (s), 1559 (m), 1456 (m), 1375 (w), 1291 (m), 1123 (w), 1084 (w), 817 (m), 736 (m) cm^{-1} . UV-vis (CH_2Cl_2): $\lambda_{\text{max}} = 276$



nm ($\epsilon = 23,800 \text{ M}^{-1} \text{ cm}^{-1}$). Mass Spec. (EI, +ve mode): exact mass calculated for $[\text{C}_{25}\text{H}_{33}\text{N}_3]^+$: 375.2674; exact mass found: 375.2669; difference: -1.3 ppm .

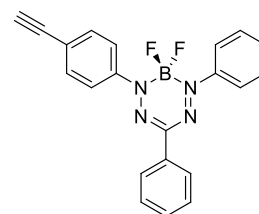
1-*p*-ethynylphenyl-3-5-phenyl formazan

In air, phenylhydrazine (0.9 g, 0.8 mL, 9 mmol) was dissolved in ethanol (10 mL) before benzaldehyde (0.9 g, 0.9 mL, 9 mmol) was added and the solution stirred for 10 min. After this time, a light yellow precipitate had formed and CH_2Cl_2 (75 mL) and deionized H_2O (75 mL) were added to form a biphasic reaction mixture. Na_2CO_3 (2.88 g, 27.2 mmol) and $[\text{nBu}_4\text{N}][\text{Br}]$ (0.27 g, 0.85 mmol) were added, and the mixture was cooled with stirring for 30 min in an ice bath to 0°C . In a separate flask, 4-ethynylaniline (1.00 g, 8.50 mmol) and concentrated HCl (2.2 mL, 26 mmol) were mixed in deionized H_2O (15 mL) and cooled in an ice bath. A cooled solution of sodium nitrite (0.67 g, 9.7 mmol) in deionized H_2O (5 mL) was added slowly to the amine solution over a 5 min period. This mixture was then stirred at 0°C for 30 min, after which time it was added dropwise to the biphasic reaction mixture described above over a 10 min period. The resulting solution was stirred for 18 h, gradually turning dark red over this time. The dark red organic fraction was then washed with deionized H_2O ($3 \times 50 \text{ mL}$), dried over MgSO_4 , gravity filtered and concentrated *in vacuo*. The resulting residue was purified by flash chromatography (CH_2Cl_2 , neutral alumina) to afford a dark red microcrystalline solid. Yield = 1.56 g, 57%. Melting point = $181\text{--}183^\circ\text{C}$. ^1H NMR (599.5 MHz, CDCl_3) δ 15.34 (s, 1H, NH), 8.13 (d, $^3J_{\text{HH}} = 7 \text{ Hz}$, 2H, aryl CH), 7.79 (d, $^3J_{\text{HH}} = 8 \text{ Hz}$, 2H, aryl CH), 7.55 (s, 4H, aryl CH), 7.52–7.46 (m, 8H, aryl CH), 7.43–7.35 (m, 2H, aryl CH), 3.15 (s, 1H, alkyne CH). $^{13}\text{C}\{^1\text{H}\}$ NMR (100.6 MHz, CDCl_3): δ 149.6, 146.5, 141.7, 137.3, 133.6, 129.6, 129.4, 128.6, 128.0, 126.1, 120.3, 119.4, 117.4, 83.8, 78.1. FT-IR (KBr): 3280 (s), 3064 (m), 3033 (w), 2915 (m), 2849 (w), 1506 (s), 1436 (m), 1348 (m), 1313 (m), 1227 (m), 1162 (m), 1017 (m), 826 (m), 762 (s) cm^{-1} . UV-vis (CH_2Cl_2): $\lambda_{\text{max}} = 306 \text{ nm}$ ($\epsilon = 39,400 \text{ M}^{-1} \text{ cm}^{-1}$), 491 nm ($\epsilon = 24,000 \text{ M}^{-1} \text{ cm}^{-1}$). Mass Spec. (EI, +ve mode): exact mass calculated for $[\text{C}_{21}\text{H}_{16}\text{N}_4]^+$: 324.1375; exact mass found: 324.1373; difference: -0.6 ppm .



1-*p*-ethynylphenyl-3,5-phenyl formazanate BF₂ complex 4.17

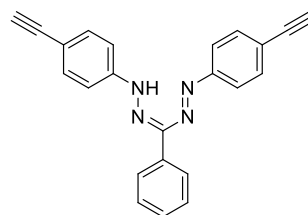
Mono-alkyne substituted formazan (2.00 g, 6.17 mmol) was dissolved in dry toluene (200 mL). NEt₃ (1.9 g, 2.6 mL, 18 mmol) was then added slowly and the solution was stirred for 10 min. BF₃·OEt₂ (4.3 g, 3.8 mL, 30 mmol) was then added, and the solution



was heated at 80 °C for 18 h. The solution gradually turned from dark red to dark purple during this time. After cooling to 20 °C, deionized H₂O (10 mL) was added to quench any excess reactive boron-containing compounds. The purple toluene solution was then washed with deionized H₂O (3 × 50 mL), dried over MgSO₄, gravity filtered and concentrated *in vacuo*. The resulting residue was purified by flash chromatography (CH₂Cl₂, neutral alumina) to yield a dark purple microcrystalline solid. Yield = 1.87 g, 83%. Melting point = 166–168 °C. ¹H NMR (399.8 MHz, CDCl₃) δ 8.12 (d, ³J_{HH} = 7 Hz, 2H, aryl CH), 7.94–7.89 (m, 4H, aryl CH), 7.60 (d, ³J_{HH} = 8 Hz, 2H, aryl CH), 7.53–7.43 (m, 6H, aryl CH), 3.24 (s, 1H, alkyne CH) ppm. ¹³C NMR (100.6 MHz, CDCl₃): δ 144.0, 133.5, 133.0, 130.2, 129.6, 129.3, 128.9, 125.7, 123.6, 123.5, 123.2, 83.0, 80.1 ppm. ¹¹B NMR (128.3 MHz, CDCl₃): δ -0.6 (t, ¹J_{BF} = 29 Hz) ppm. ¹⁹F NMR (376.1 MHz, CDCl₃) δ -143.6 (q, ¹J_{BF} = 29 Hz) ppm. FT-IR (KBr): 3066 (w), 3033 (w), 2917 (m), 2848 (m), 1507 (m), 1456 (m), 1348 (m), 1232 (s), 1148 (m), 1042 (m), 1017 (m), 764 (m) cm⁻¹. UV-vis (CH₂Cl₂): λ_{max} = 312 nm (ε = 27,400 M⁻¹ cm⁻¹), 526 nm (ε = 28,300 M⁻¹ cm⁻¹). Mass Spec. (EI, +ve mode): exact mass calculated for [C₂₁H₁₅N₄BF₂]⁺: 372.1358; exact mass found: 372.1355; difference: -0.8 ppm.

1,5-*p*-ethynylphenyl-3-phenyl formazan

In air, phenyl pyruvic acid (1.40 g, 8.53 mmol) was dissolved in 100 mL deionized H₂O containing NaOH (2.55 g, 6.38 mmol), and cooled in an ice bath. In a separate flask, 4-ethynyl aniline (2.00 g, 17.0 mmol) and concentrated hydrochloric acid (4.3

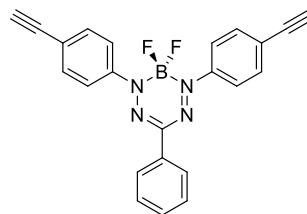


mL) were mixed in deionized H₂O (15 mL) and cooled in an ice bath to 0 °C. A cooled solution of sodium nitrite (1.35 g, 20.0 mmol) in H₂O (5 mL) was then added slowly to the amine solution over a 5 min period. This mixture was stirred at 0 °C for 30 min, after which time it was added dropwise to the biphasic reaction mixture described above over a 10 min period. A dark red/purple precipitate formed almost immediately. The resulting mixture

was stirred for an additional 18 h. The dark red/purple precipitate was then collected by filtration and washed with deionized H₂O (3 × 50 mL). The resulting residue was purified by flash chromatography (CH₂Cl₂, neutral alumina) to afford a dark red microcrystalline solid. Yield = 1.70 g, 57%. Melting point = 157–159 °C. ¹H NMR (599.5 MHz, CDCl₃) δ 15.28 (s, 1H, NH), 8.07–8.06 (m, 2H, aryl CH), 7.58–7.54 (m, 8H, aryl CH), 7.44–7.42 (m, 2H, aryl CH), 7.37–7.35 (m, 1H, aryl CH), 3.20 (s, 2H, alkyne CH). ¹³C{¹H} NMR (100.6 MHz, CDCl₃): δ 147.8, 141.8, 137.0, 133.4, 128.5, 128.1, 126.1, 121.2, 118.8, 83.6, 78.8. FT-IR (KBr): 3276 (s), 3056 (w), 3033 (m), 2921 (m), 2852 (m), 1506 (s), 1345 (m), 1310 (w), 1224 (s), 1188 (m), 1162 (m), 1042 (m), 1018 (m), 832 (m), 768 (m) cm⁻¹. UV-vis (CH₂Cl₂): λ_{max} = 276 nm (ε = 51,200 M⁻¹ cm⁻¹), 511 nm (ε = 20,500 M⁻¹ cm⁻¹). Mass Spec. (EI, +ve mode): exact mass calculated for [C₂₃H₁₆N₄]⁺: 348.1375; exact mass found: 348.1380; difference: +1.4 ppm.

1,5-*p*-ethynylphenyl-3-phenyl formazanate BF₂ complex

Bis-alkyne substituted formazan (0.70 g, 2.0 mmol) was dissolved in dry toluene (70 mL). NEt₃ (0.61 g, 0.84 mL, 6.0 mmol) was then added slowly and the solution was stirred for 10 min. BF₃·OEt₂ (1.4 g, 1.2 mL, 10. mmol) was then added, and

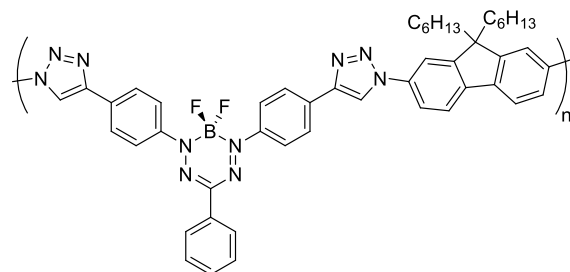


the solution was heated at 80 °C for 18 h. The solution gradually turned from dark red to dark purple during this time. After cooling to 20 °C, deionized H₂O (10 mL) was added to quench any excess reactive boron-containing compounds. The purple toluene solution was then washed with deionized H₂O (3 × 50 mL), dried over MgSO₄, gravity filtered and concentrated *in vacuo*. The resulting residue was purified by flash chromatography (CH₂Cl₂, neutral alumina) to yield a dark purple microcrystalline solid. Yield = 0.51 g, 65%. Melting point = 162–164 °C. ¹H NMR (399.8 MHz, CDCl₃) δ 8.11–8.09 (m, 2H, aryl CH), 7.91 (d, ³J_{HH} = 8 Hz, 4H, aryl CH), 7.61–7.58 (m, 4H, aryl CH), 7.52–7.45 (m, 3H, aryl CH), 3.25 (s, 2H, alkyne CH) ppm. ¹³C NMR (100.6 MHz, CDCl₃): δ 143.9, 133.4, 133.1, 129.7, 129.0, 125.7, 123.9, 123.3, 118.8, 83.0, 80.4 ppm. ¹¹B NMR (128.3 MHz, CDCl₃): δ -0.6 (t, ¹J_{BF} = 29 Hz) ppm. ¹⁹F NMR (376.1 MHz, CDCl₃) δ -142.9 (q, ¹J_{BF} = 29 Hz) ppm. FT-IR (KBr): 3065 (w), 3035 (w), 2938 (m), 2922 (m), 2857 (m), 1508 (s), 1456 (m), 1347 (m), 1301 (s), 1267 (s), 1222 (m), 1175 (m), 1119 (m), 1025 (m), 967 (s) cm⁻¹. UV-vis (CH₂Cl₂): λ_{max} = 317 nm (ε = 24,000 M⁻¹ cm⁻¹), 541 nm (ε = 27,700 M⁻¹

cm^{-1}). Mass Spec. (EI, +ve mode): exact mass calculated for $[\text{C}_{23}\text{H}_{15}\text{N}_4\text{BF}_2]^+$: 396.1358; exact mass found: 396.1360; difference: +0.5 ppm.

Polymer 4.21

In a typical procedure, **4.18** (0.13 g, 0.34 mmol) was mixed with **4.20** (0.14 g, 0.34 mmol) in dry THF (3 mL). $\text{Cu}(\text{PPh}_3)_3\text{Br}$ (0.02 g, 0.02 mmol) was then added and the mixture was purged with N_2 for 15 min. The



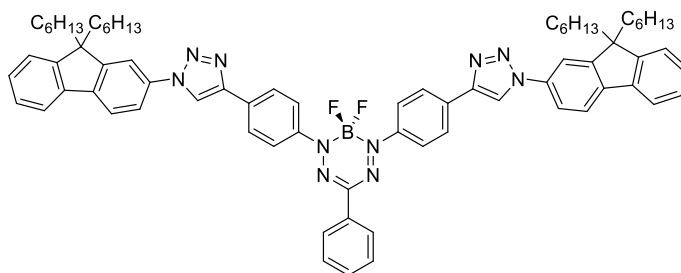
reaction mixture was heated with stirring at $60\text{ }^\circ\text{C}$ for 48 h before it was cooled to room temperature and filtered through a pad of neutral alumina. The resulting solution was added to cold hexanes to precipitate **4.21** as a dark purple solid. The precipitation was repeated two additional times before the solid was isolated by centrifugation and dried *in vacuo*. Yield = 0.26 g, 94%. ^1H NMR (399.8 MHz, CDCl_3) δ 8.38–8.30 (m, 2H, triazole CH), 8.18–8.07 (m, 5H, aryl CH), 7.94–7.80 (m, 5H, aryl CH), 7.70–7.47 (m, 9H, aryl CH), 2.13–1.82 (m, 6H, alkyl CH), 1.13–0.97 (m, 10H, alkyl CH), 0.80–0.69 (m, 8H, alkyl CH), 0.49 (br s, 2H, alkyl CH) ppm. ^{11}B NMR (128.3 MHz, CDCl_3): δ -0.5 (br s) ppm. ^{19}F NMR (376.1 MHz, CDCl_3) δ -143.4 (br s) ppm. FT-IR (KBr): 3057 (m), 2936 (m), 2924 (s), 2852 (s), 1473 (m), 1436 (m), 1346 (m), 1299 (m), 1268 (m), 1222 (m), 1176 (m), 1119 (m), 1007 (m), 963 (m), 842 (m), 720 (m) cm^{-1} . UV-vis (DMF): λ_{max} 330 nm ($\epsilon = 45, 700\text{ M}^{-1}\text{ cm}^{-1}$), 559 nm ($\epsilon = 25, 700\text{ M}^{-1}\text{ cm}^{-1}$). GPC (DMF, conventional calibration vs. PS standards): $M_n = 17,000\text{ g mol}^{-1}$, $M_w = 32,750\text{ g mol}^{-1}$, $D = 2.14$.

Study of Change in Molecular Weight vs. Time for 4.21

In a typical procedure, **4.18** (0.119 g, 0.30 mmol) was mixed with **4.20** (0.125 g, 0.30 mmol) in dry THF (3 mL). $\text{Cu}(\text{PPh}_3)_3\text{Br}$ (0.014 g, 0.015 mmol) was then added, and the mixture was purged with N_2 for 15 min. The reaction mixture was heated with stirring at $60\text{ }^\circ\text{C}$. Aliquots (0.5 mL) were removed from the reactions at 12, 24, 48, 72 and 168 h. Each aliquot was filtered through a pad of neutral alumina. The resulting solution was added to cold hexanes to precipitate **4.21** as a dark purple solid. The precipitation was repeated two additional times. The degree of polymerization was determined by GPC analysis in DMF (conventional calibration vs. polystyrene).

Complex 4.24

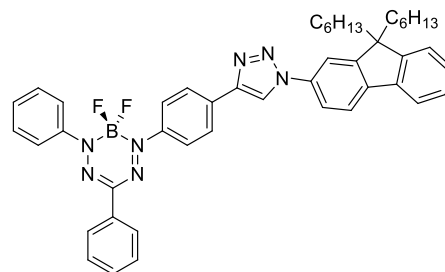
4.18 (0.10 g, 0.25 mmol) was mixed with **4.19** (0.19 g, 0.50 mmol) in dry THF (4 mL). $\text{Cu}(\text{PPh}_3)_3\text{Br}$ (0.02 g, 0.03 mmol) was then added and the mixture was purged with N_2 gas for 15



min. The reaction mixture was heated with stirring at 60 °C for 18 h before it was cooled to room temperature and filtered through a pad of neutral alumina. The resulting purple solution was concentrated *in vacuo* and the residue was purified by flash chromatography (CH_2Cl_2 , silica gel) to afford **4.24** as a dark purple solid. Yield = 0.21 g, 71%. Melting point = 77–79 °C. ^1H NMR (399.8 MHz, CDCl_3) δ 8.36 (s, 2H, triazole CH), 8.18 (d, $^3J_{\text{HH}} = 8$ Hz, 2H, aryl CH), 8.11–8.07 (m, 8H, aryl CH), 7.85–7.82 (m, 4H, aryl CH), 7.76–7.73 (m, 4H, aryl CH), 7.54–7.46 (m, 3H, aryl CH), 7.40–7.37 (m, 6H, aryl CH), 2.06–2.03 (m, 8H, alkyl CH), 1.13–1.02 (m, 24H, alkyl CH), 0.76 (t, $^3J_{\text{HH}} = 7$ Hz, 12H, alkyl CH), 0.68–0.63 (m, 8H, alkyl CH) ppm. ^{13}C NMR (100.6 MHz, CDCl_3): δ 152.8, 151.0, 147.2, 143.8, 142.1, 139.7, 135.9, 133.6, 131.8, 129.5, 129.5, 128.9, 128.0, 127.2, 126.5, 125.6, 124.0, 123.1, 120.7, 120.2, 119.4, 118.5, 115.4, 55.7, 40.4, 31.5, 29.7, 23.8, 22.6, 14.0 ppm. ^{11}B NMR (128.3 MHz, CDCl_3): δ -0.5 (t, $^1J_{\text{BF}} = 29$ Hz) ppm. ^{19}F NMR (376.1 MHz, CDCl_3) δ -143.6 (q, $^1J_{\text{BF}} = 29$ Hz) ppm. FT-IR (KBr): 3141 (m), 3035 (m), 2938 (m), 2924 (s), 2852 (m), 1457 (s), 1299 (s), 1268 (s), 1227 (m), 1180 (m), 1122 (w), 1028 (m), 963 (s), 843 (m), 737 (m) cm^{-1} . UV-vis (CH_2Cl_2): λ_{max} 315 nm ($\epsilon = 61,600 \text{ M}^{-1} \text{ cm}^{-1}$), 556 nm ($\epsilon = 31,100 \text{ M}^{-1} \text{ cm}^{-1}$). Mass Spec. (ESI, +ve mode): exact mass calculated for $[\text{C}_{73}\text{H}_{81}\text{N}_{10}\text{BF}_2 \cdot \text{Na}]^+$: 1169.6604; exact mass found: 1169.6616; difference: -1.0 ppm.

Complex 4.25

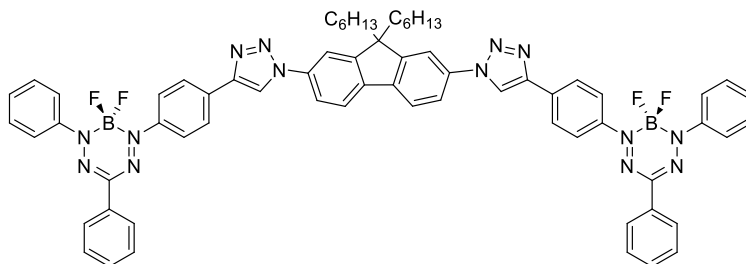
4.17 (0.20 g, 0.54 mmol) was mixed with **4.19** (0.20 g, 0.54 mmol) in dry THF (6 mL). $\text{Cu}(\text{PPh}_3)_3\text{Br}$ (0.02 g, 0.03 mmol) was then added and the mixture was purged with N_2 gas for 15 min. The reaction mixture was heated with stirring at 60 °C for 18 h before it was cooled to room temperature and filtered through



a small pad of neutral alumina. The resulting purple solution was concentrated *in vacuo* and the residue was purified by flash chromatography (2:1 CH₂Cl₂:hexanes, neutral alumina) to afford **4.25** as a dark purple solid. Yield = 0.35 g, 87%. Melting point = 63–65 °C. ¹H NMR (399.8 MHz, CDCl₃) δ 8.33 (s, 1H, triazole CH), 8.16–8.14 (m, 2H, aryl CH), 8.09–8.04 (m, 4H, aryl CH), 7.95–7.93 (m, 2H, aryl CH), 7.85–7.74 (m, 4H, aryl CH), 7.52–7.45 (m, 6H, aryl CH), 7.38–7.37 (m, 3H, aryl CH), 2.06–2.01 (m, 4H, alkyl CH), 1.13–1.02 (m, 12H, alkyl CH), 0.77–0.74 (m, 6H, alkyl CH), 0.66–0.61 (m, 4H, alkyl CH) ppm. ¹³C NMR (100.6 MHz, CDCl₃): δ 152.9, 151.1, 149.3, 147.2, 144.0, 143.8, 142.1, 139.7, 135.9, 133.7, 131.8, 129.9, 129.5, 129.2, 128.9, 128.0, 127.2, 126.5, 125.6, 124.0, 123.6, 123.1, 120.7, 120.2, 119.4, 118.6, 115.4, 55.8, 40.5, 31.6, 29.7, 23.9, 22.7, 14.1 ppm. ¹¹B NMR (128.3 MHz, CDCl₃): δ -0.5 (t, ¹J_{BF} = 29 Hz) ppm. ¹⁹F NMR (376.1 MHz, CDCl₃) δ -144.1 (q, ¹J_{BF} = 29 Hz) ppm. FT-IR (KBr): 3062 (m), 2935 (m), 2924 (m), 2851 (m), 1456 (m), 1348 (w), 1296 (m), 1268 (m), 1222 (w), 1119 (m), 964 (m), 764 (m) cm⁻¹. UV-vis (CH₂Cl₂): λ_{max} 315 nm (ε = 54,900 M⁻¹ cm⁻¹), 532 nm (ε = 31,100 M⁻¹ cm⁻¹). Mass Spec. (EI, +ve mode): exact mass calculated for [C₄₆H₄₈N₇BF₂]⁺: 747.4032; exact mass found: 747.4027; difference: -0.7 ppm.

Complex 4.26

4.17 (0.15 g, 0.40 mmol) was mixed with **4.20** (0.08 g, 0.2 mmol) in dry THF (3 mL). Cu(PPh₃)₃Br (0.02 g, 0.02 mmol) was then added and



the mixture was purged with N₂ gas for 15 min. The reaction mixture was heated with stirring at 60 °C for 18 h before it was cooled to room temperature and filtered through a pad of neutral alumina. The resulting purple solution was concentrated *in vacuo* and the residue was purified by flash chromatography (2:1 CH₂Cl₂:hexanes, neutral alumina) to afford **4.26** as a dark purple solid. Yield = 0.20 g, 86%. Melting point = 118–120 °C. ¹H NMR (399.8 MHz, CDCl₃) δ 8.36 (s, 2H, triazole CH), 8.16–8.14 (m, 4H, aryl CH), 8.10–8.05 (m, 8H, aryl CH), 7.96–7.87 (m, 8H, aryl CH), 7.82–7.80 (m, 2H, aryl CH), 7.53–7.44 (m, 12H, aryl CH), 2.15–2.10 (m, 4H, alkyl CH), 1.14–1.03 (m, 12H, alkyl CH), 0.77–0.74 (m, 6H, alkyl CH), 0.70–0.66 (m, 4H, alkyl CH) ppm. ¹³C NMR (100.6 MHz,

CDCl₃): δ 153.2, 149.2, 147.4, 144.0, 143.9, 140.6, 136.6, 133.7, 131.6, 130.0, 129.5, 129.3, 128.9, 126.6, 125.7, 124.1, 123.6, 121.3, 119.7, 118.5, 115.4, 56.4, 40.5, 31.6, 29.7, 24.0, 22.7, 14.1 ppm. ¹¹B NMR (128.3 MHz, CDCl₃): δ -0.5 (t, ¹J_{BF} = 28 Hz) ppm. ¹⁹F NMR (376.1 MHz, CDCl₃) δ -143.7 (q, ¹J_{BF} = 28 Hz) ppm. FT-IR (KBr): 3065 (m), 3048 (m), 2951 (m), 2925 (s), 2852 (m), 1477 (m), 1419 (m), 1350 (m), 1296 (s), 1267 (s), 1222 (m), 1119 (m), 1007 (m), 964 (s), 845 (m), 763 (s) cm⁻¹. UV-vis (CH₂Cl₂): λ_{\max} 325 nm (ϵ = 73, 200 M⁻¹ cm⁻¹) 535 nm (ϵ = 51,200 M⁻¹ cm⁻¹). Mass Spec. (ESI, +ve mode): exact mass calculated for [C₆₇H₆₂N₁₄BF₂·Na]⁺: 1183.5302; exact mass found: 1183.5309; difference: -0.6 ppm.

4.6 References

- (1) Eid, J.; Fehr, A.; Gray, J.; Luong, K.; Lyle, J.; Otto, G.; Peluso, P.; Rank, D.; Baybayan, P.; Bettman, B.; Bibillo, A.; Bjornson, K.; Chaudhuri, B.; Christians, F.; Cicero, R.; Clark, S.; Dalal, R.; deWinter, A.; Dixon, J.; Foquet, M.; Gaertner, A.; Hardenbol, P.; Heiner, C.; Hester, K.; Holden, D.; Kearns, G.; Kong, X.; Kuse, R.; Lacroix, Y.; Lin, S.; Lundquist, P.; Ma, C.; Marks, P.; Maxham, M.; Murphy, D.; Park, I.; Pham, T.; Phillips, M.; Roy, J.; Sebra, R.; Shen, G.; Sorenson, J.; Tomaney, A.; Travers, K.; Trulson, M.; Vieceli, J.; Wegener, J.; Wu, D.; Yang, A.; Zaccarin, D.; Zhao, P.; Zhong, F.; Korlach, J.; Turner, S. *Science* **2009**, *323*, 133–138.
- (2) Weiss, S. *Science* **1999**, *283*, 1676–1683.
- (3) Huang, B.; Wang, W.; Bates, M.; Zhuang, X. *Science* **2008**, *319*, 810–813.
- (4) Lavis, L. D.; Raines, R. T. *ACS Chem. Biol.* **2008**, *3*, 142–155.
- (5) Kim, E.; Lee, Y.; Lee, S.; Park, S. B. *Acc. Chem. Res.* **2015**, *48*, 538–547.
- (6) Laughlin, S. T.; Baskin, J. M.; Amacher, S. L.; Bertozzi, C. R. *Science* **2008**, *320*, 664–667.
- (7) Resch-Genger, U.; Grabolle, M.; Cavaliere-Jaricot, S.; Nitschke, R.; Nann, T. *Nat. Methods* **2008**, *5*, 763–775.
- (8) Ding, D.; Li, K.; Liu, B.; Tang, B. Z. *Acc. Chem. Res.* **2013**, *46*, 2441–2453.
- (9) Yang, Z.; Sharma, A.; Qi, J.; Peng, X.; Lee, D. Y.; Hu, R.; Lin, D.; Qu, J.; Kim, J. S. *Chem. Soc. Rev.* **2016**, *45*, 4651–4667.

- (10) Kobayashi, H.; Ogawa, M.; Alford, R.; Choyke, P. L.; Urano, Y. *Chem. Rev.* **2010**, *110*, 2620–2640.
- (11) Lavis, L. D.; Raines, R. T. *ACS Chem. Biol.* **2014**, *9*, 855–866.
- (12) Rostovtsev, V. V.; Green, L. G.; Fokin, V. V.; Sharpless, K. B. *Angew. Chem. Int. Ed.* **2002**, *41*, 2596–2599.
- (13) Tornøe, C. W.; Christensen, C.; Meldal, M. *J. Org. Chem.* **2002**, *67*, 3057–3064.
- (14) Liu, Q.; Tor, Y. *Org. Lett.* **2003**, *5*, 2571–2572.
- (15) Khanna, B.; Parkin, S. R.; Revell, K. D. *Tetrahedron Lett.* **2012**, *53*, 6383–6387.
- (16) Karagollu, O.; Gorur, M.; Gode, F.; Sennik, B.; Yilmaz, F. *Macromol. Chem. Phys.* **2015**, *216*, 939–949.
- (17) Chopra, R.; Kaur, P.; Singh, K. *Anal. Chim. Acta* **2015**, *864*, 55–63.
- (18) Brizet, B.; Goncalves, V.; Bernhard, C.; Harvey, P. D.; Denat, F.; Goze, C. *Chem. Eur. J.* **2014**, *20*, 12933–12944.
- (19) Dhokale, B.; Jadhav, T.; Mobin, S. M.; Misra, R. *Dalton Trans.* **2015**, *44*, 15803–15812.
- (20) Golf, H. R. A.; Reissig, H.-U.; Wiehe, A. *Org. Lett.* **2015**, *17*, 982–985.
- (21) Chen, X.; Wu, Q.; Henschke, L.; Weber, G.; Weil, T. *Dyes Pigments* **2012**, *94*, 296–303.
- (22) Gobbo, P.; Gunawardene, P.; Luo, W.; Workentin, M. S. *Synlett* **2015**, *26*, 1169–1174.
- (23) Su, Y.; Li, L.; Wang, H.; Wang, X.; Zhang, Z. *Chem. Commun.* **2016**, *52*, 2185–2188.
- (24) Evans, V.; Duncanson, P.; Motevalli, M.; Watkinson, M. *Dyes Pigments* **2016**, *135*, 36–40.
- (25) Albrecht, M.; Lippach, A.; Exner, M. P.; Jerbi, J.; Springborg, M.; Budisa, N.; Wenz, G. *Org. Biomol. Chem.* **2015**, *13*, 6728–6736.
- (26) Guo, S.; Ma, L.; Zhao, J.; Küçüköz, B.; Karatay, A.; Hayvali, M.; Yaglioglu, H. G.; Elmali, A. *Chem. Sci.* **2014**, *5*, 489–500.
- (27) Beyer, C.; Wagenknecht, H.-A. *J. Org. Chem.* **2010**, *75*, 2752–2755.
- (28) Sau, S. P.; Hrdlicka, P. J. *J. Org. Chem.* **2012**, *77*, 5–16.

- (29) Liu, Z.; Li, Y.; Lozada, J.; Schaffer, P.; Adam, M. J.; Ruth, T. J.; Perrin, D. M. *Angew. Chem. Int. Ed.* **2013**, *52*, 2303–2307.
- (30) Daugaard, A. E.; Hvilsted, S.; Hansen, T. S.; Larsen, N. B. *Macromolecules* **2008**, *41*, 4321–4327.
- (31) Kim, J.-H.; Jung, Y.; Lee, D.; Jang, W.-D. *Adv. Mater.* **2016**, *28*, 3499–3503.
- (32) Martí-Centelles, V.; Beer, P. D. *Chem. Eur. J.* **2015**, *21*, 9397–9404.
- (33) Arumugaperumal, R.; Srinivasadesikan, V.; Ramakrishnam Raju, M. V.; Lin, M.-C.; Shukla, T.; Singh, R.; Lin, H.-C. *ACS Appl. Mater. Inter.* **2015**, *7*, 26491–26503.
- (34) Ma, X.; Zhang, J.; Cao, J.; Yao, X.; Cao, T.; Gong, Y.; Zhao, C.; Tian, H. *Chem. Sci.* **2016**, *7*, 4582–4588.
- (35) Rosenthal, J.; Lippard, S. J. *J. Am. Chem. Soc.* **2010**, *132*, 5536–5537.
- (36) Yapici, N. B.; Jockusch, S.; Moscatelli, A.; Mandalapu, S. R.; Itagaki, Y.; Bates, D. K.; Wiseman, S.; Gibson, K. M.; Turro, N. J.; Bi, L. *Org. Lett.* **2012**, *14*, 50–53.
- (37) Li, K.-B.; Wang, H.; Zang, Y.; He, X.-P.; Li, J.; Chen, G.-R.; Tian, H. *ACS Appl. Mater. Inter.* **2014**, *6*, 19600–19605.
- (38) Singh, R. S.; Gupta, R. K.; Paitandi, R. P.; Misra, A.; Pandey, D. S. *New J. Chem.* **2015**, *39*, 2233–2239.
- (39) Manandhar, E.; Broome, J. H.; Myrick, J.; Lagrone, W.; Cragg, P. J.; Wallace, K. *J. Chem. Commun.* **2011**, *47*, 8796–8798.
- (40) Ingale, S. A.; Seela, F. *J. Org. Chem.* **2012**, *77*, 9352–9356.
- (41) Uppal, T.; Bhupathiraju, N. V. S. D. K.; Vicente, M. G. H. *Tetrahedron* **2013**, *69*, 4687–4693.
- (42) Kele, P.; Li, X.; Link, M.; Nagy, K.; Herner, A.; Lőrincz, K.; Béni, S.; Wolfbeis, O. S. *Org. Biomol. Chem.* **2009**, *7*, 3486–3490.
- (43) Zhou, M.; Zhang, X.; Bai, M.; Shen, D.; Xu, B.; Kao, J.; Ge, X.; Achilefu, S. *RSC Adv.* **2013**, *3*, 6756–6758.
- (44) Kwak, J. H.; He, Y.; Yoon, B.; Koo, S.; Yang, Z.; Kang, E. J.; Lee, B. H.; Han, S.-Y.; Yoo, Y. C.; Lee, K. B.; Kim, J. S. *Chem. Commun.* **2014**, *50*, 13045–13048.
- (45) Zhang, X.-t.; Gu, Z.-y.; Liu, L.; Wang, S.; Xing, G.-w. *Chem. Commun.* **2015**, *51*, 8606–8609.

- (46) Sletten, E. M.; Bertozzi, C. R. *Acc. Chem. Res.* **2011**, *44*, 666–676.
- (47) Jewett, J. C.; Bertozzi, C. R. *Chem. Soc. Rev.* **2010**, *39*, 1272–1279.
- (48) Qin, A.; Lam, J. W. Y.; Jim, C. K. W.; Zhang, L.; Yan, J.; Häussler, M.; Liu, J.; Dong, Y.; Liang, D.; Chen, E.; Jia, G.; Tang, B. Z. *Macromolecules* **2008**, *41*, 3808–3822.
- (49) Kaga, S.; Yapar, S.; Gecici, E. M.; Sanyal, R. *Macromolecules* **2015**, *48*, 5106–5115.
- (50) Wu, B.; Xu, L.; Wang, S.; Wang, Y.; Zhang, W. *Polym. Chem.* **2015**, *6*, 4279–4289.
- (51) van Steenis, D. J. V. C.; David, O. R. P.; van Strijdonck, G. P. F.; van Maarseveen, J. H.; Reek, J. N. H. *Chem. Commun.* **2005**, 4333–4335.
- (52) Bakbak, S.; Leech, P. J.; Carson, B. E.; Saxena, S.; King, W. P.; Bunz, U. H. F. *Macromolecules* **2006**, *39*, 6793–6795.
- (53) Karim, M. A.; Cho, Y.-R.; Park, J. S.; Kim, S. C.; Kim, H. J.; Lee, J. W.; Gal, Y.-S.; Jin, S.-H. *Chem. Commun.* **2008**, 1929–1931.
- (54) Barbon, S. M.; Reinkeluers, P. A.; Price, J. T.; Staroverov, V. N.; Gilroy, J. B. *Chem. Eur. J.* **2014**, *20*, 11340–11344.
- (55) Barbon, S. M.; Staroverov, V. N.; Gilroy, J. B. *J. Org. Chem.* **2015**, *80*, 5226–5235.
- (56) Barbon, S. M.; Price, J. T.; Reinkeluers, P. A.; Gilroy, J. B. *Inorg. Chem.* **2014**, *53*, 10585–10593.
- (57) Fery-Forgues, S.; Lavabre, D. *J. Chem. Educ.* **1999**, *76*, 1260–1264.
- (58) Suzuki, K.; Kobayashi, A.; Kaneko, S.; Takehira, K.; Yoshihara, T.; Ishida, H.; Shiina, Y.; Oishi, S.; Tobita, S. *Phys. Chem. Chem. Phys.* **2009**, *11*, 9850–9860.
- (59) Chang, M.-C.; Otten, E. *Chem. Commun.* **2014**, *50*, 7431–7433.
- (60) Maar, R. R.; Barbon, S. M.; Sharma, N.; Groom, H.; Luyt, L. G.; Gilroy, J. B. *Chem. Eur. J.* **2015**, *21*, 15589–15599.
- (61) Chang, M.-C.; Otten, E. *Inorg. Chem.* **2015**, *54*, 8656–8664.
- (62) Chang, M.-C.; Chantzis, A.; Jacquemin, D.; Otten, E. *Dalton Trans.* **2016**, *45*, 9477–9484.
- (63) Yin, X.; Li, Y.; Zhu, Y.; Jing, X.; Li, Y.; Zhu, D. *Dalton Trans.* **2010**, *39*, 9929–9935.
- (64) Rochford, J.; Rooney, A. D.; Pryce, M. T. *Inorg. Chem.* **2007**, *46*, 7247–7249.

- (65) Li, M.; Guo, Z.; Zhu, W.; Marken, F.; James, T. D. *Chem. Commun.* **2015**, *51*, 1293–1296.
- (66) Otón, F.; González, M. d. C.; Espinosa, A.; Ramírez de Arellano, C.; Tárraga, A.; Molina, P. *J. Org. Chem.* **2012**, *77*, 10083–10092.
- (67) Rao, M. R.; Kumar, K. V. P.; Ravikanth, M. *J. Organomet. Chem.* **2010**, *695*, 863–869.
- (68) Dhokale, B.; Gautam, P.; Mobin, S. M.; Misra, R. *Dalton Trans.* **2013**, *42*, 1512–1518.
- (69) Misra, R.; Dhokale, B.; Jadhav, T.; Mobin, S. M. *Dalton Trans.* **2013**, *42*, 13658–13666.
- (70) Connelly, N. G.; Geiger, W. E. *Chem. Rev.* **1996**, *96*, 877–910.
- (71) Tobita, S.; Ida, K.; Shiobara, S. *Res. Chem. Intermed.* **2001**, *27*, 205–218.
- (72) Sadkowski, P. J.; Fleming, G. R. *Chem. Phys.* **1980**, *54*, 79–89.
- (73) Nakamura, H.; Tanaka, J. *Chem. Phys. Lett.* **1981**, *78*, 57–60.
- (74) Quan, L.; Chen, Y.; Lv, X.-J.; Fu, W.-F. *Chem. Eur. J.* **2012**, *18*, 14599–14604.
- (75) Oshima, J.; Yoshihara, T.; Tobita, S. *Chem. Phys. Lett.* **2006**, *423*, 306–311.
- (76) Patra, C.; Bhanja, A. K.; Mahapatra, A.; Mishra, S.; Saha, K. D.; Sinha, C. *RSC Adv.* **2016**, *6*, 76505–76513.
- (77) Zhou, B.; Liu, W.; Zhang, H.; Wu, J.; Liu, S.; Xu, H.; Wang, P. *Biosens. Bioelectron.* **2015**, *68*, 189–196.
- (78) Liu, W.; Zhou, B.; Niu, G.; Ge, J.; Wu, J.; Zhang, H.; Xu, H.; Wang, P. *ACS Appl. Mater. Interfaces* **2015**, *7*, 7421–7427.
- (79) Werrett, M. V.; Wright, P. J.; Simpson, P. V.; Raiteri, P.; Skelton, B. W.; Stagni, S.; Buckley, A. G.; Rigby, P. J.; Massi, M. *Dalton Trans.* **2015**, *44*, 20636–20647.
- (80) Yang, Z.; Yan, C.; Chen, Y.; Zhu, C.; Zhang, C.; Dong, X.; Yang, W.; Guo, Z.; Lu, Y.; He, W. *Dalton Trans.* **2011**, *40*, 2173–2176.
- (81) Westlund, R.; Glimsdal, E.; Lindgren, M.; Vestberg, R.; Hawker, C.; Lopes, C.; Malmström, E. *J. Mater. Chem.* **2008**, *18*, 166–175.
- (82) Gilroy, J. B.; Ferguson, M. J.; McDonald, R.; Patrick, B. O.; Hicks, R. G. *Chem. Commun.* **2007**, 126–128.

- (83) Chang, M.-C.; Dann, T.; Day, D. P.; Lutz, M.; Wildgoose, G. G.; Otten, E. *Angew. Chem. Int. Ed.* **2014**, *53*, 4118–4122.
- (84) Cardona, C. M.; Li, W.; Kaifer, A. E.; Stockdale, D.; Bazan, G. C. *Adv. Mater.* **2011**, *23*, 2367–2371.
- (85) Gobbo, P.; Luo, W.; Cho, S. J.; Wang, X.; Biesinger, M. C.; Hudson, R. H. E.; Workentin, M. S. *Org. Biomol. Chem.* **2015**, *13*, 4605–4612.
- (86) Pauly, A. C.; Varnado, C. D.; Bielawski, C. W.; Theato, P. *Macromol. Rapid Commun.* **2014**, *35*, 210–213.
- (87) Barik, S.; Friedland, S.; Skene, W. G. *Can. J. Chem.* **2010**, *88*, 945–953.
- (88) Bruker-Nonius, SAINT version 2013.8, 2013, Bruker-AXS, Madison, WI 53711, USA.
- (89) Bruker-Nonius, SADABS version 2012.1, 2012, Bruker-AXS, Madison, WI 53711, USA.
- (90) Sheldrick, G. M. *Acta Cryst.* **2015**, *A71*, 3–8.
- (91) Sheldrick, G. M. *Acta Cryst.* **2015**, *C71*, 3–8.

Chapter 5

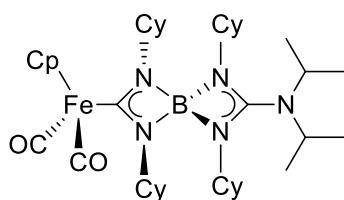
5 Structurally Diverse Boron-Nitrogen Heterocycles from an $N_2O_2^{3-}$ Formazanate Ligand

Adapted from:

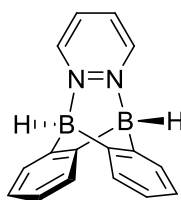
1. **Barbon, S. M.**; Staroverov, V. N.; Gilroy, J. B.* *Angew. Chem. Int. Ed.*, **2017**, DOI: 10.1002/anie.201704285.

5.1 Introduction

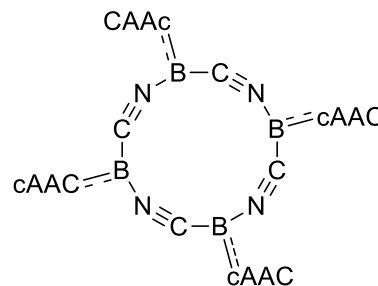
Boron-nitrogen heterocycles are of significant interest to a wide range of disciplines on account of their unusual structure, bonding, and properties.^[1-3] The most common compounds with such heterocycles, azaborines, find applications in organic electronics and chemical hydrogen storage.^[4-6] Other boron-nitrogen heterocycles, exemplified by compounds **5.1**–**5.6**, are noted for their unexpected reactivity and, in many cases, unique redox properties.^[7-18]



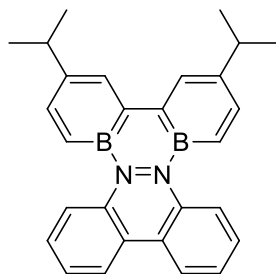
5.1



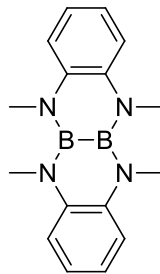
5.2



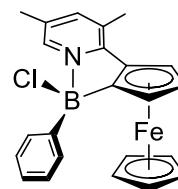
5.3



5.4



5.5



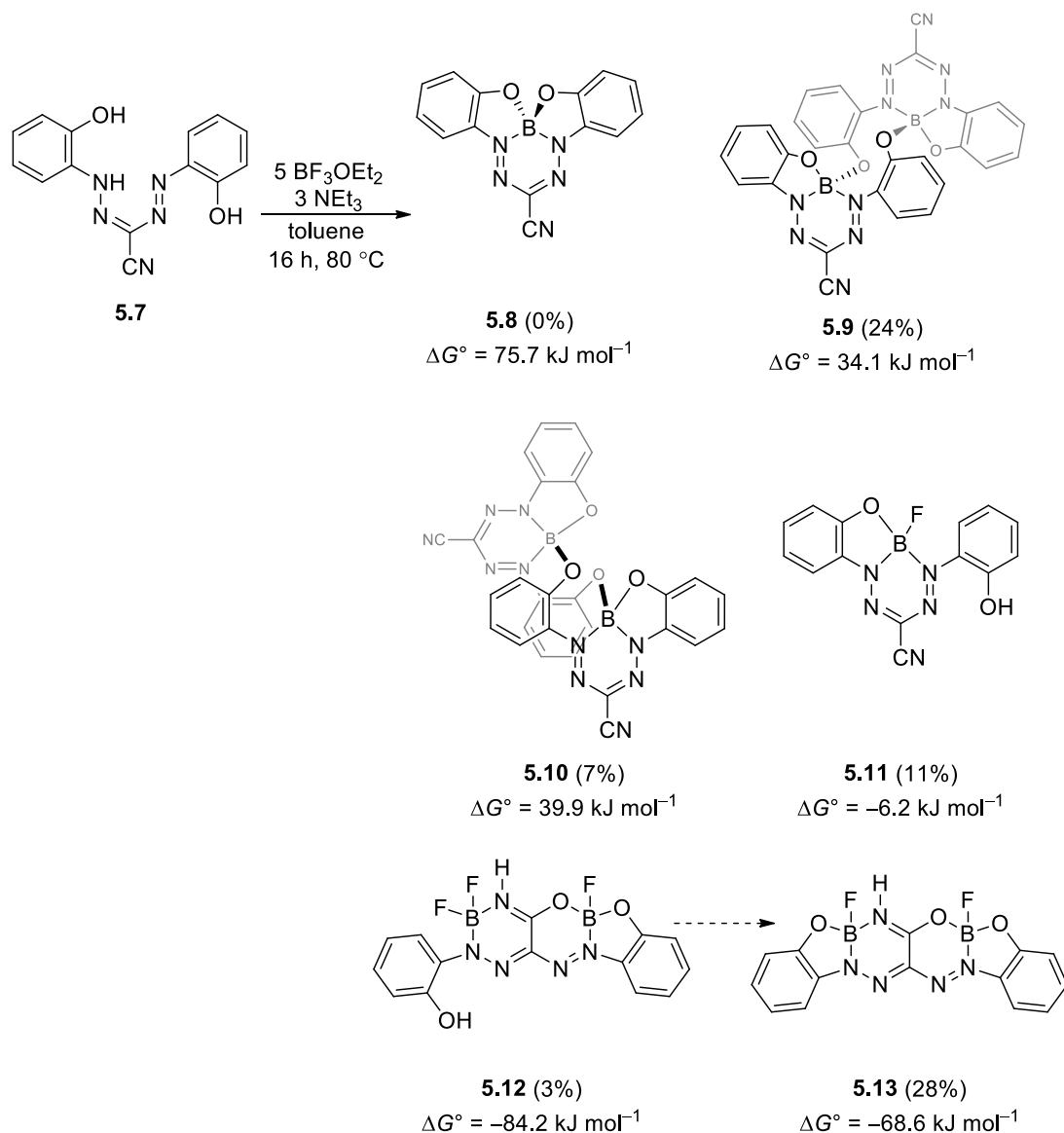
5.6

Each of compounds **5.1–5.3** contains boron-nitrogen bonds in unusual heterocyclic frameworks that were formed in an unanticipated reaction from the corresponding boron-containing precursor.^[19-21] Piers' B₂N₂ triphenylene analogue **5.4** can be reduced by one electron to form a stable radical anion,^[22] and Russell's polycyclic borazine **5.5** undergoes one-electron oxidation to form a stable radical cation.^[23] The Jäkle group has demonstrated that ferrocene boron complex **5.6** can be converted to the planar borenium cation via abstraction of the chloride.^[24]

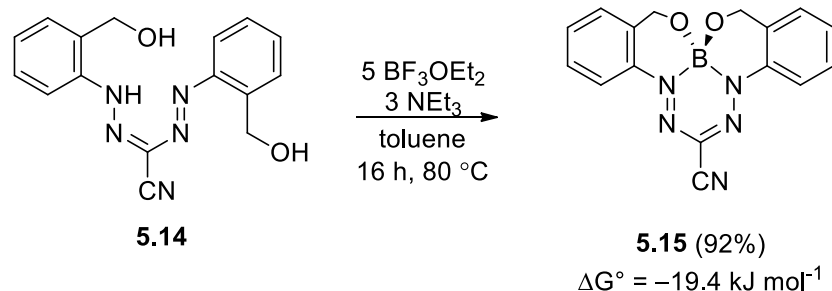
Boron difluoride complexes of formazanate ligands have many interesting and useful properties, including high molar absorptivities and a capacity for reversible stepwise reduction. In this work, we set out to study the properties of similar complexes derived from trianionic, potentially tetradentate formazanate ligands.

5.2 Results and Discussion

The parent formazan **5.7** was synthesized according to a published method.^[25] Upon reaction of **5.7** with BF₃•OEt₂ in the presence of NEt₃, the expected product **5.8** was not detected; instead, the reaction mixture was found to contain five new compounds (**5.9–5.13**) along with formazan **5.7**, which could be separated by column chromatography in 60–70% yield (Figure A5.1). Careful analysis of the ¹H, ¹¹B, ¹³C and ¹⁹F NMR spectra, as well as single-crystal X-ray diffraction analysis enabled us to identify all six compounds present (Scheme 5.1, Figures A5.2–A5.11). The complex reaction mixture obtained was in striking contrast to the clean conversion of formazan **5.14** to boron complex **5.15** in 92% yield under identical conditions (Scheme 5.2, Figures A5.12–A5.16).



Scheme 5.1. Products formed from the reaction of formazan **5.7** with $\text{BF}_3 \cdot \text{OEt}_2$ and NEt_3 . The Gibbs free energies (ΔG°) were computed for the formation of each compound under conditions simulating those employed in the actual synthesis, and are expressed in kJ mol^{-1} of the corresponding formazan. The dashed arrow indicates interconversion in solution.



Scheme 5.2. Products formed from the reaction of formazan **5.14** with $\text{BF}_3 \cdot \text{OEt}_2$ and NEt_3 . The Gibbs free energy (ΔG°) was computed for the formation of **5.15** under conditions simulating those employed, and are expressed in kJ mol^{-1} of formazan **5.14**.

To rationalize these observations, we used density-functional methods to calculate the changes in standard thermodynamic state functions for the reaction pathways leading from **5.7** to **5.8–5.13** and from **5.14** to **5.15** under the experimental reaction conditions ($80 \text{ } ^\circ\text{C}$, 1 atm, toluene solution). The calculations were performed with the *Gaussian 09* program^[26] using the hybrid version of the Perdew-Burke-Ernzerhof density functional^[27] (PBE1PBE), the 6-311+G(d,p) basis set, and implicit solvation methods. According to this level of theory (Table A5.1), the formation of tetradentate boron complex **5.8** from **5.7** is thermodynamically unfavourable ($\Delta G^\circ = 75.7 \text{ kJ mol}^{-1}$), whereas the formation of tetradentate complex **5.15** from **5.14** is favourable ($\Delta G^\circ = -19.4 \text{ kJ mol}^{-1}$). It appears that the 5-membered chelates of **5.8** are too strained to form, so less strained compounds are produced instead. Compound **5.13**, which appears to form *via* **5.12**, was predicted to be the most favoured product of this reaction ($\Delta G^\circ = -68.6 \text{ kJ mol}^{-1}$), in agreement with experiment.

Through variation of reaction conditions, we were able to optimize the yields of each of the five new compounds produced (Table 5.1). When elevated temperatures or longer reaction times were employed, the ratio of **5.13** (the thermodynamic product) to **5.9** and **5.10** was increased. When greater excess amounts of $\text{BF}_3 \cdot \text{OEt}_2$ and NEt_3 were used, products **5.9** and **5.10** were observed in higher yields.

Table 5.1. Varied conditions and the resulting distribution (as a percent of the total reaction mixture) of the different products.

Equiv. NEt ₃	Equiv. BF ₃ •OEt ₂	Reaction Time (h)	Temp. (°C)	Conc. of 7 (mg mL ⁻¹)	Distribution of Products ^a					
					9	10	11	7	12	13
3	5	16	80	10	24	7	11	27	3	28
1	1	16	80	10	–	–	8	92	–	–
6	10	16	80	10	3	29	2	63	–	3
3	5	8	80	10	6	1	22	68	1	2
3	5	32	80	10	6	2	17	6	1	68
3	5	16	50	10	4	3	21	66	–	6
3	5	16	110	10	21	11	7	15	–	46
3	5	16	80	5	1	2	21	28	3	45
3	5	16	80	20	4	11	26	18	4	37

^aOverall isolated yields were typically 60–70%.

The six compounds present in the reaction mixture were separated by column chromatography (CH₂Cl₂, silica gel). The first two that eluted ($R_f = 0.82, 0.76$) yielded very similar NMR spectra without ¹⁹F NMR resonances. We were able to identify these two compounds using X-ray crystallography as dimers **5.9** and **5.10** (Figure 5.1a, b). Both structures contain a ten-membered ring (-B-O-C-C-N-B-O-C-C-N-), where B–O bonds bridge the monomeric units. The difference between the two structures is the orientation of the ten-membered ring. The ten-membered ring exists in a *pseudo*-chair conformation in compound **5.9**, and in a *pseudo*-boat conformation in compound **5.10** (see insets, Figure 5.1a, b). We did not observe interconversion between these two products in solution, even upon prolonged heating.

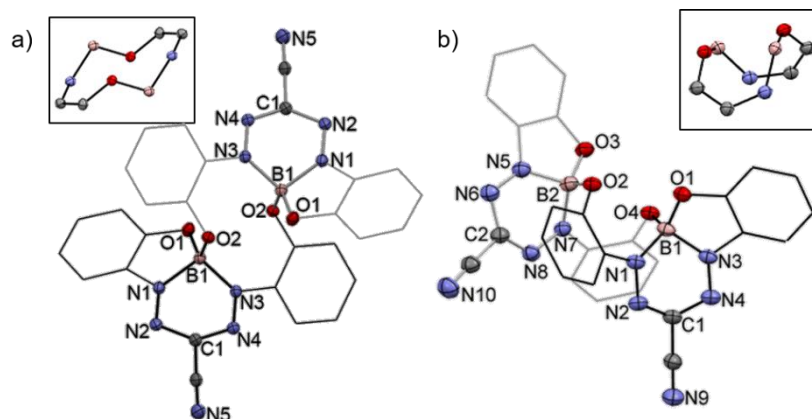


Figure 5.1. Solid-state structures of (a) **5.9** and (b) **5.10**. Thermal displacement ellipsoids are shown at the 50% probability level, and phenyl substituents have been made wireframe for clarity. Hydrogen atoms have also been removed for clarity. Insets in panels show only the atoms in the respective ten-membered rings.

The *pseudo*-boat ring conformation leads to a π -stacking interaction between aryl substituents and the formazanate backbone in the solid-state phase of **5.10**, which is not observed in **5.9**. In solution, it causes broadening of the low-energy absorption of **5.10** and the appearance of a shoulder at 597 nm that is not present in the absorption profile of **5.9** (Figures 5.4, A5.17, Table 5.2). The cyclic voltammograms of compounds **5.9** and **5.10** included three reduction waves (Figure 5.2, Table 5.2). Both compounds exhibit two reversible one-electron reduction waves (**5.9**: $E_{\text{red1}} = -760$ mV, $E_{\text{red2}} = -1010$ mV; **5.10**: $E_{\text{red1}} = -720$ mV, $E_{\text{red2}} = -1020$ mV), and a third irreversible two-electron reduction (**5.9**: $E_{\text{pc}} = -1730$ mV; **5.10**: $E_{\text{pc}} = -1770$ mV). The reversible waves correspond to the stepwise reduction of the formazanate backbones to mono- and bis-radical anions and the irreversible wave to the formation of bis-dianions. The difference between the reversible reduction potentials (ΔE_{red}) was 250 mV for **5.9** and 290 mV for **5.10**.

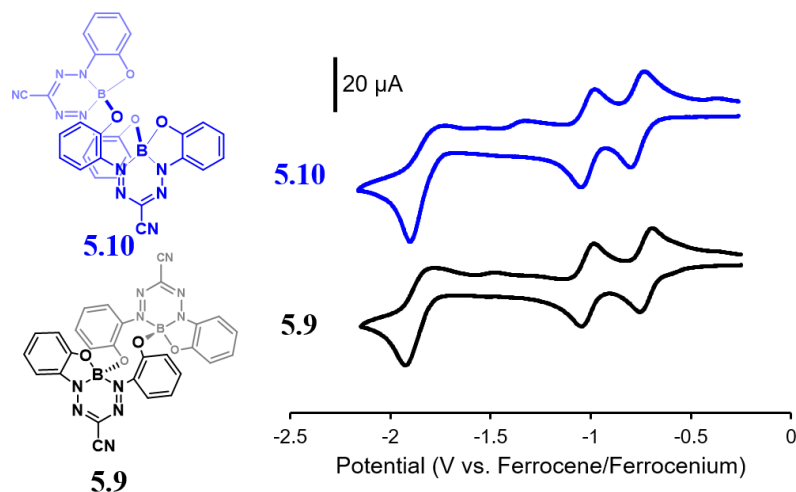


Figure 5.2. Cyclic voltammograms of **5.9** (black) and **5.10** (blue) recorded at 100 mV s^{-1} in $1 \text{ mM CH}_2\text{Cl}_2$ solutions containing $0.1 \text{ M } [n\text{Bu}_4\text{N}][\text{PF}_6]$ as supporting electrolyte.

Compound **5.10** proved easier to isolate than its structural isomer **5.9**, so it was chosen for further reactivity studies. Reduction with one and two equivalents of cobaltocene yielded compounds **5.10 $^{\bullet-}$** and **5.10 $^{2-}$** , both of which produced broad isotropic signals in their EPR spectra at $g = 2.0038$, confirming their paramagnetic nature (Figure A5.18). Both reduced species were characterized by single-crystal X-ray analysis (Figure 5.3, Table 5.3). The average N–N bond length in the neutral dimer **5.10** was $1.314(3) \text{ \AA}$, which is typical of an N–N bond with a bond order of ~ 1.5 . In compound **5.10 $^{\bullet-}$** , the average N–N bond length for N1 to N4 is $1.360(3) \text{ \AA}$, suggesting the presence of a borataverdazyl radical in which the additional electron occupies an orbital with antibonding N–N character.^[28-30] The average N–N bond length for N5 to N8 is $1.315(3) \text{ \AA}$, typical of a formazanate adduct.^[28] These metrics confirm that chemical reduction occurs in a stepwise fashion, and that the radical anion is localized on one formazanate ligand. In the doubly reduced species **5.10 $^{2-}$** , the average N–N bond length was $1.366(3) \text{ \AA}$, which corresponds to N–N single bonds as expected for borataverdazyl radicals.^[30]

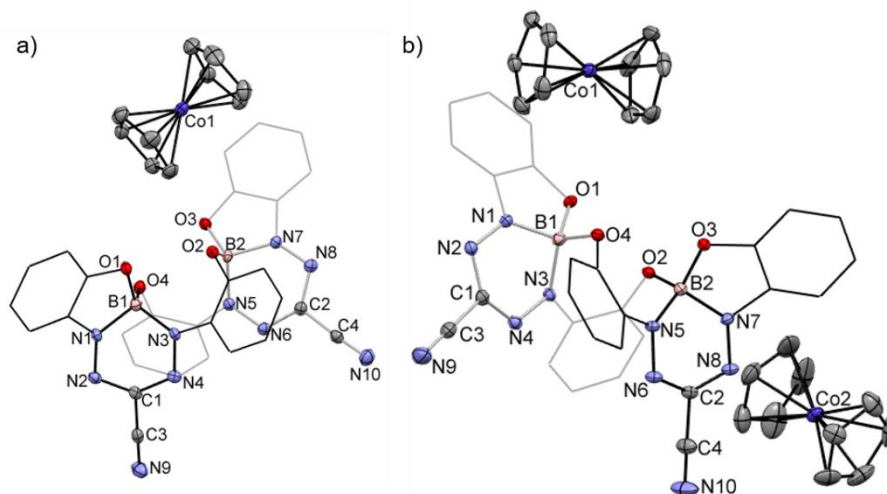


Figure 5.3. Solid-state structures of (a) $10^{\bullet-}$ and (b) $10^{\bullet 2-}$. Thermal ellipsoids are shown at the 50% probability level, and phenyl substituents have been made wireframe for clarity. Hydrogen atoms have also been removed for clarity.

These conclusions were corroborated by UV-vis absorption spectroscopy in acetonitrile (Figure 5.4, Table 5.2). Neutral dimer **5.10** has a λ_{max} at 569 nm, and a molar absorptivity of $20\,500\text{ M}^{-1}\text{ cm}^{-1}$. Singly reduced $5.10^{\bullet-}$ absorbs strongly at 568 nm, as well as 687 and 477 nm, which is typical of verdazyl species,^[30] and shows that $5.10^{\bullet-}$ is made up of independent borataverdazyl and formazanate units. Doubly reduced species $5.10^{\bullet 2-}$ absorbs minimally at 568 nm, but exhibits two absorption peaks typical of verdazyl species with λ_{max} of 687 nm ($\epsilon = 8\,200\text{ M}^{-1}\text{ cm}^{-1}$) and 477 nm ($\epsilon = 39\,200\text{ M}^{-1}\text{ cm}^{-1}$).^[31]

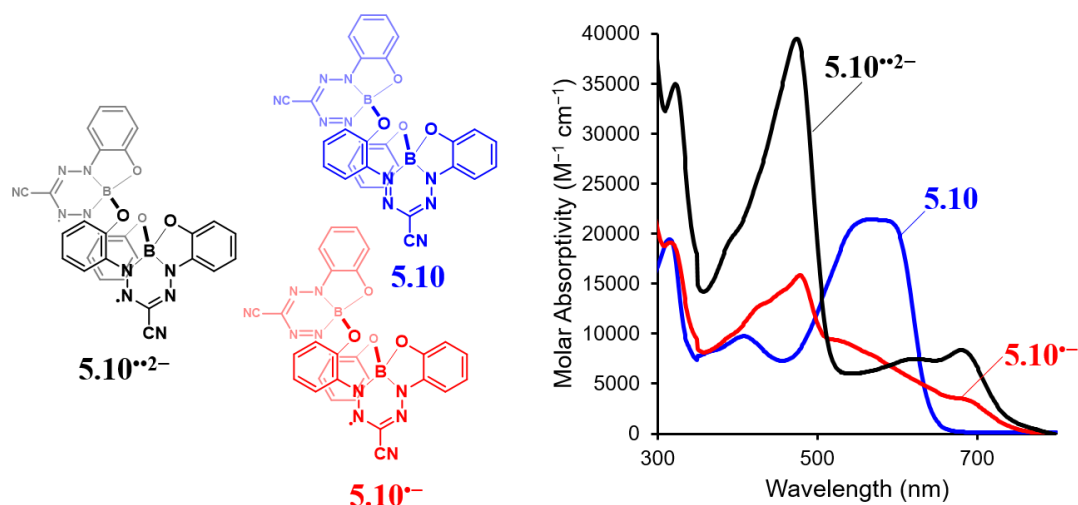


Figure 5.4. UV-vis absorption spectra of complexes **5.10** (blue), **5.10⁻** (red) and **10²⁻** (black) in CH₃CN.

We were unable to grow single crystals of the third compound to elute ($R_f = 0.61$). However, using ¹H, ¹¹B, ¹³C and ¹⁹F NMR spectroscopy and mass spectrometry, we were able to identify this product as **5.11**. This product is dark blue, can be reversibly reduced twice (Figures A5.19, A5.20, Table 5.2), and slowly converts to formazan **5.7** in solution. The fourth compound that eluted from the column ($R_f = 0.39$) was formazan **5.7**. This compound is present due to incomplete reactivity, or the hydrolysis of unstable, unidentified species formed during the reaction.

The final two compounds that eluted from the column ($R_f = 0.31, 0.22$) were identified as compounds **5.12** and **5.13**. Interestingly, **5.13** showed two doublets in its ¹¹B NMR spectrum due to the coupling of each boron atom with a single fluorine atom ($^1J_{BF} = 33, 42$ Hz). Single-crystal X-ray analysis showed that compound **5.13** was not a dimer, but contained two boron atoms bonded to one formazanate ligand, where the cyano group had been hydrolyzed.^[32] Complex **5.12** is similar to **5.13**, aside from a free OH group, and a BF₂ unit (Figure 5.5). In solution, compound **5.12** converts to **5.13** over the course of a few hours.

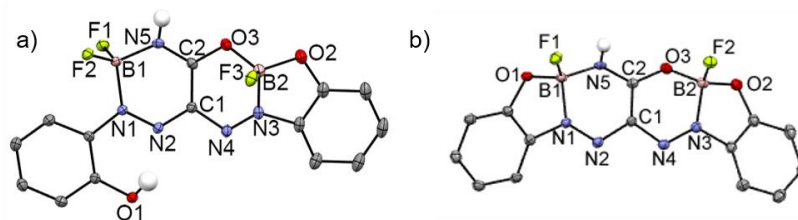
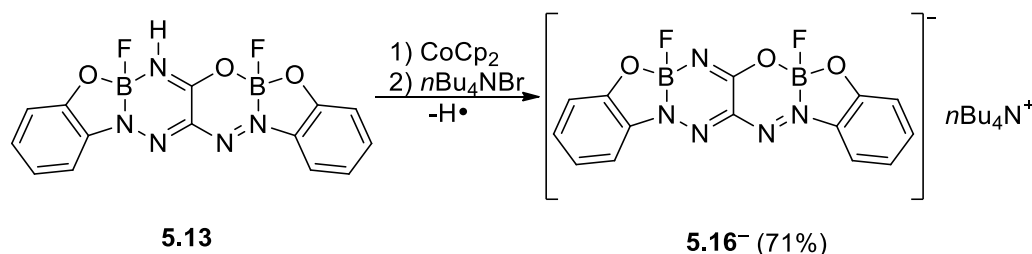


Figure 5.5. Solid-state structures of (a) **5.12** and (b) **5.13** with thermal displacement ellipsoids shown at the 50% probability level. Hydrogens, aside from the hydrogens on N5 in both **5.12** and **5.13** and on O1 in **5.12** have been removed for clarity.

The λ_{\max} of **5.12** is blue-shifted by 17 nm in CH_2Cl_2 with respect to **5.13** (Figure A5.21, A5.22). Compound **5.13** yielded a single reversible one-electron reduction in its cyclic voltammogram (Figure A5.23), prompting us to perform chemical reduction using one equivalent of cobaltocene. The solution changed from pink-purple to dark blue-purple (Scheme 3). Attempts to crystallize the resulting compounds were unsuccessful, so a salt metathesis reaction was performed with $[\text{nBu}_4\text{N}][\text{Br}]$ in order to exchange the cobaltocenium cation for the more solubilizing tetra-*n*-butyl ammonium cation. The colour of the solution was unchanged throughout this process. Single-crystal X-ray diffraction revealed the resulting product to be anion **5.16⁻**. Upon reduction, the NH bond in **5.13** appears to cleave homolytically, resulting in the formation of **5.16⁻** and H_2 (Figure 5.6). The proposed structure was confirmed by ^1H , ^{13}C NMR spectroscopy, mass spectrometry and IR spectroscopy (see Figure A5.24, A5.25). Aside from the loss of the *N*-bonded proton, the connectivity in **5.16⁻** is identical to that of **5.13**. The B1-N5 bond has shortened (**5.13**: 1.516(3) Å; **5.16⁻**: 1.442(5) Å) and the C2-N5 bond has lengthened (**5.13**: 1.304(3) Å; **5.16⁻**: 1.327(4) Å, Table 5.3). The angles around B1 and N5 change with the presence of the lone pair. For example, the N1-B1-N5 angle widens by $\sim 3.5^\circ$, while the B1-N5-C2 angle contracts by $\sim 3.6^\circ$. The same angles around B2 change less drastically (N3-B2-O2 angle contracts by 1.1° , and the B2-O3-C2 angle contracts by 2.0°). **5.16⁻** is highly absorbing ($\epsilon = 18\,000\ \text{M}^{-1}\ \text{cm}^{-1}$), with a low-energy λ_{\max} of 589 nm that was red-shifted by 12 nm with respect to neutral **5.13** (Figures A5.22, A5.26).



Scheme 5.3. Chemical reduction of **5.13** to **5.16⁻** with cobaltocene.

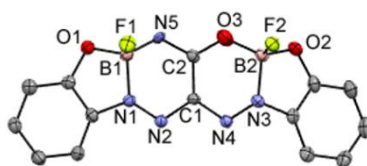


Figure 5.6. Solid-state structure of **5.16⁻** with thermal displacement ellipsoids shown at the 50% probability level. Hydrogens and the $n\text{Bu}_4\text{N}$ cation have been removed for clarity.

The calculated highest occupied molecular orbitals (HOMO) of **5.13** and **5.16⁻** are delocalized over the entire molecules (Figure 5.7). The lowest unoccupied molecular orbitals (LUMO) were delocalized over the formazanate nitrogen atoms and the *N*-aryl substituents. Time-dependent PBE1PBE/6-311+G(d,p) calculations of **5.13** and **5.16⁻** in CH_2Cl_2 solution showed the HOMO and LUMO to be the dominant orbital pair involved in the lowest energy transition in both molecules, and approximately reproduced the shift in λ_{max} from **5.13** to **5.16⁻** ($\Delta\lambda_{\text{calc}} = 8 \text{ nm}$, $\Delta\lambda_{\text{obs}} = 12 \text{ nm}$, Table A5.2).

Table 5.2. Optical and electronic properties of complexes **5.9–5.13** and their reduction products.

Compound	Solvent	λ_{max} (nm)	ϵ ($\text{M}^{-1} \text{cm}^{-1}$)	E_{red1} (mV)	E_{red2} (mV)	E_{red3} (mV)	E_{ox1} (mV)
5.9	CH_2Cl_2	535	28 100	-760	-1010	-1730 ^a	1060 ^a
5.10	CH_2Cl_2	569	20 500	-720	-1020	-1770 ^a	1020 ^a
5.11	CH_2Cl_2	577	13 500	-720	-1630	–	606 ^a
5.12	CH_2Cl_2	560	27 600	–	–	–	–
5.13	CH_2Cl_2	577	35 900	-770	-1130 ^a	–	839 ^a
5.10⁻	CH_3CN	477	15 500	–	–	–	–
5.10^{•2-}	CH_3CN	477	39 200	–	–	–	–
5.16⁻	CH_2Cl_2	589	18 000	–	–	–	–

^aOnset of irreversible reduction or oxidation.

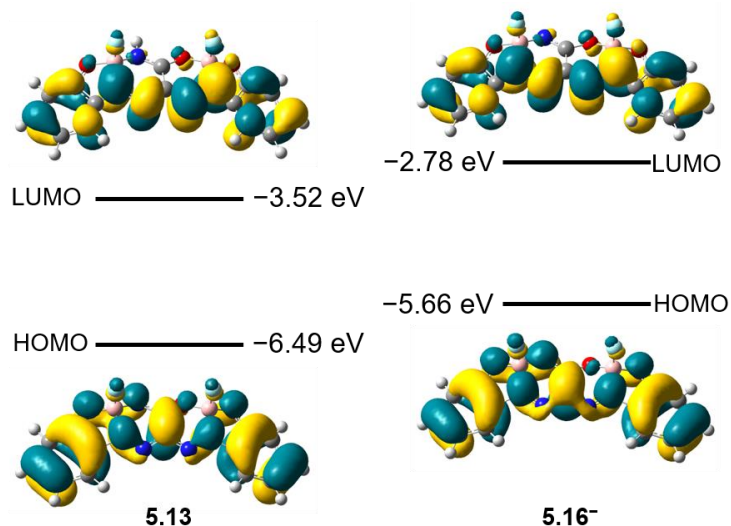


Figure 5.7. HOMOs and LUMOs for **5.13** and **5.16⁻** calculated at the PBE1PBE/6-311+G(d,p) level.

Table 5.3. Selected bond lengths (Å) and angles (°) for solid-state structures of various products.

	5.9	5.10	5.10⁻	5.10²⁻	5.12	5.13	5.16⁻
N1-N2	1.2896(16)	1.297(3)	1.353(3)	1.357(3)	1.2997(19)	1.288(2)	1.297(4)
N3-N4	1.3206(16)	1.330(3)	1.366(3)	1.375(3)	1.280(2)	1.284(2)	1.287(4)
N5-N6	–	1.299(3)	1.329(3)	1.371(3)	–	–	–
N7-N8	–	1.332(3)	1.301(3)	1.359(3)	–	–	–
B1-N1	1.5743(19)	1.572(4)	1.541(4)	1.540(3)	1.596(2)	1.573(3)	1.583(5)
B1-N5	–	–	–	–	1.532(2)	1.516(3)	1.442(5)
C2-N5	–	–	–	–	1.295(2)	1.304(3)	1.327(4)
N1-B1-N5	–	–	–	–	107.37(13)	104.45(17)	107.9(3)
B1-N5-C2	–	–	–	–	126.62(14)	120.36(18)	116.8(3)
N3-B2-O2	–	–	–	–	101.53(14)	101.62(17)	100.5(3)
B2-O3-C2	–	–	–	–	116.48(14)	118.97(17)	117.0(3)

5.3 Conclusions

In conclusion, we have reported the synthesis of five new boron-nitrogen heterocycles **5.9–5.13** by one straightforward reaction, starting from an $\text{N}_2\text{O}_2^{3-}$ formazanate ligand. The observed product distribution appears to be strain-driven as evidenced by the fact that similar heterocycles were not formed when the reactant **5.7** was replaced by a homologous compound **5.14**. Each of compounds **5.9–5.13** exhibited interesting optical and electrochemical properties. In particular, compound **5.10** was reduced to stable mono- and bis- radical anions, with electronically-isolated formazanate units. Compound **5.13**,

containing an unprecedented boron-nitrogen core, was reduced to a radical anion which rapidly lost one equivalent of H• to form a stable anion.

5.4 Experimental Section

5.4.1 General Considerations

Reactions and manipulations were carried out under a nitrogen atmosphere using standard Schlenk techniques unless otherwise stated. Solvents were obtained from Caledon Laboratories, dried using an Innovative Technologies Inc. solvent purification system, collected under vacuum and stored under a nitrogen atmosphere over 4 Å molecular sieves. Reagents were purchased from Sigma-Aldrich or Alfa Aesar and used as received. Formazan **5.7** was prepared according to a literature procedure.^[25]

NMR spectra were recorded on 400 MHz (¹H: 399.8 MHz, ¹¹B: 128.3 MHz, ¹⁹F: 376.1 MHz) or 600 MHz (¹H: 599.5 MHz, ¹³C: 150.8 MHz) Varian INOVA instruments. ¹H NMR spectra were referenced to residual CHCl₃ (7.26 ppm), CHDCl₂ (5.32 ppm) or DMSO-*d*₅ (2.50 ppm) and ¹³C{¹H} NMR spectra were referenced to CDCl₃ (77.2 ppm), CD₂Cl₂ (53.8 ppm), or DMSO-*d*₆ (39.5 ppm). ¹¹B spectra were referenced to BF₃·OEt₂ at 0 ppm and ¹⁹F spectra were referenced to CFCI₃ at 0 ppm. Mass spectrometry data were recorded in positive-ion mode using a high-resolution Finnigan MAT 8200 spectrometer using electron impact ionization. UV-vis absorption spectra were recorded using a Cary 5000 instrument. Four separate concentrations were run for each sample and molar extinction coefficients were determined from the slope of a plot of absorbance against concentration. FT-IR spectra were recorded using an attenuated total reflectance (ATR) attachment using a Bruker Vector 33 FT-IR spectrometer. Elemental analyses (C, H, N) were carried out by Laboratoire d'Analyse Élémentaire de l'Université de Montréal, Montréal, QC, Canada or Canadian Microanalytical Services Ltd., Delta, BC, Canada.

5.4.2 Purity of New Compounds

The purity of diamagnetic compounds described in this study was demonstrated by providing very clean ¹H, ¹¹B, ¹³C{¹H}, and ¹⁹F NMR spectra and high resolution mass spectrometry data. For paramagnetic compounds **5.10^{•-}** and **5.10^{••2-}**, carbon analysis was consistently low, while H and N analysis matched well across several independent batches.

This is likely due to the presence of boron, which often hampers C analysis.^[33-34] However, these data are provided to illustrate the best values obtained to date.

5.4.3 Electrochemical Methods

Cyclic voltammetry experiments were performed with a Bioanalytical Systems Inc. (BASi) Epsilon potentiostat and analyzed using BASi Epsilon software. Electrochemical cells consisted of a three-electrode setup including a glassy carbon working electrode, platinum wire counter electrode and silver wire *pseudo* reference electrode. Experiments were run at scan rates of 100 mV s⁻¹ in degassed THF solutions of the analyte (~1 mM) and supporting electrolyte (0.1 M [*n*Bu₄N][PF₆]). Cyclic voltammograms were referenced against an internal standard (~1 mM ferrocene) and corrected for internal cell resistance using the BASi Epsilon software.

5.4.4 X-ray Crystallography Details

Single crystals suitable for X-ray diffraction were grown from slow evaporation of CH₂Cl₂ (**5.10**, **5.12**, **5.13**, **5.15**, **5.10⁻**), or CHCl₃ (**5.9**), or diffusion of hexanes into a concentrated THF solution (**5.10²⁻**). To grow single crystals of **5.16⁻**, the compound was first stirred for 30 min with [*n*Bu₄N][Br] in CH₂Cl₂. The resulting solution was then filtered and concentrated *in vacuo*. Finally, crystals appeared upon diffusion of hexanes into a concentrated THF solution. Samples were mounted on a MiTeGen polyimide micromount with a small amount of Paratone *N* oil. X-ray measurements were made on a Bruker Kappa Axis Apex2 diffractometer (**5.9**, **5.12**, **5.13**, **5.15**, **5.10⁻**, **5.10²⁻** and **5.16⁻**) or Nonius KappaCCD Apex2 diffractometer (**5.10**) at a temperature of 110 K. Initial indexing indicated that the sample crystal for **5.12** was non-merohedrally twinned. The twin law was determined to be:

$$\begin{array}{ccc} -1.00038 & -0.00037 & -0.00061 \\ 0.00057 & -0.99976 & 0.00063 \\ 0.92946 & 0.44676 & 1.00014 \end{array}$$

which represents a -179.9° rotation about [0 0 -1]. The twin fraction was included in the refinement as an adjustable parameter (*vide infra*).

The data collection strategy included a number of ω and ϕ scans which collected data over a range of angles, 2θ . The frame integration was performed using SAINT.^[35] The resulting raw data were scaled and absorption corrected using a multi-scan averaging of symmetry

equivalent data using SADABS (5.9, 5.10, 5.13, 5.15, 5.10⁻, 5.10²⁻, 5.16⁻),^[36] or TWINABS (5.12)^[37]. The structures were solved by using a dual space methodology using the SHELXT program.^[38] All non-hydrogen atoms were obtained from the initial solution. The hydrogen atoms were introduced at idealized positions and were allowed to refine isotropically (5.9, 5.10, 5.12, 5.13, 5.15), or allowed to ride on the parent atom (5.10⁻, 5.10²⁻), or treated in a mixed fashion (5.16⁻). The twin fraction of 5.12 refined to a value of 0.07489. The structural model was fit to the data using full matrix least-squares based on F^2 . The calculated structure factors included corrections for anomalous dispersion from the usual tabulation. The difference map of 5.10²⁻ showed regions of electron density that could not be accurately modeled to something that makes chemical sense. Thus the PLATON SQUEEZE program^[39] was used, and analysis was continued on this data. The structure was refined using the SHELXL-2014 program from the SHELXT suite of crystallographic software.^[40] See Table 5.4 for additional crystallographic data.

Table 5.4. X-ray diffraction data collection and refinement details for compounds **5.9**, **5.10**, **5.12**, **5.13**, **5.15**, **5.10⁻**, **5.10²⁻**, and **5.16⁻**.

	5.9	5.10	5.12	5.13	5.15	5.10⁻	5.10²⁻	5.16⁻
Chemical Formula	C ₂₁ H ₈ BCl ₃ N ₅ O ₂	C ₂₀ H ₁₀ B ₂ N ₁₀ O ₄	C ₁₄ H ₁₀ B ₂ F ₃ N ₆ O ₂	C ₁₃ H ₁₀ B ₂ Cl ₂ F ₂ N ₅ O ₂	C ₁₀ H ₁₀ BN ₅ O ₂	C ₃₉ S ₁₀ H ₁₀ B ₂ Cl ₂ CON ₁₀ O ₄	C ₄₈ H ₁₀ B ₂ Co ₂ N ₁₀ O ₄	C ₂₄ H ₁₀ B ₂ F ₂ N ₆ O ₄
FW (g mol ⁻¹)	408.43	578.13	374.89	438.80	317.12	894.63	956.35	665.41
Crystal Habit	Red Prism	Red Plate	Red Plate	Purple Plate	Red Plate	Red Prism	Green Plate	Blue Prism
Crystal System	Monoclinic	Monoclinic	Triclinic	Triclinic	Triclinic	Triclinic	Monoclinic	orthorhombic
Space Group	<i>P</i> ₂ / <i>n</i>	<i>P</i> ₂ / <i>c</i>	<i>P</i> $\bar{1}$	<i>P</i> $\bar{1}$	<i>P</i> $\bar{1}$	<i>P</i> $\bar{1}$	<i>C</i> ₂ / <i>c</i>	<i>P</i> <i>n</i> a2 ₁
<i>T</i> (K)	110	110	110	110	110	110	110	110
λ (Å)	0.71073	1.54178	0.71073	0.71073	0.71073	0.71073	0.71073	0.71073
<i>a</i> (Å)	9.998(5)	12.881(3)	7.200(3)	7.26(3)	10.470(4)	9.674(4)	38.958(14)	27.391(12)
<i>b</i> (Å)	10.986(6)	22.431(6)	7.899(3)	11.186(5)	11.193(4)	13.911(6)	9.286(3)	14.196(7)
<i>c</i> (Å)	16.990(10)	9.388(2)	15.294(8)	12.213(4)	13.763(4)	15.088(6)	26.485(10)	9.375(3)
α (deg)	90	90	91.890(12)	115.101(13)	91.150(9)	71.773(13)	90	90
β (deg)	104.739(14)	91.295(9)	100.25(2)	97.410(17)	91.444(8)	86.992(9)	96.663(13)	90
γ (deg)	90	90	112.364(10)	96.153(13)	115.938(8)	87.645(7)	90	90
<i>V</i> (Å ³)	1804.8(17)	2711.8(12)	786.7(6)	876.7(6)	1449.0(8)	1925.4(13)	951.6(6)	3645(3)
<i>Z</i>	4	4	2	2	4	2	8	4
ρ (g/cm ³)	1.503	1.416	1.583	1.662	1.454	1.543	1.335	1.212
μ (cm ⁻¹)	0.528	0.820	0.135	0.421	0.100	0.712	0.751	0.086
R_1^a, wR_2^b [<i>I</i> > 2 σ]	0.0465, 0.1013	0.0483, 0.1001	0.0483, 0.1001	0.0507, 0.1049	0.0382, 0.1009	0.0563, 0.1134	0.0385, 0.0760	0.0486, 0.1159
R_1, wR_2 (all data)	0.0759, 0.1157	0.0967, 0.1194	0.0590, 0.1462	0.0877, 0.1232	0.0491, 0.1083	0.1072, 0.1334	0.0685, 0.0828	0.0707, 0.1289
GOF ^c	1.032	1.025	1.120	1.028	1.045	1.031	0.904	1.043

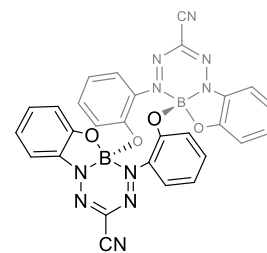
^a $R_1 = \sum(|F_o| - |F_c|) / \sum F_o$, ^b $wR_2 = [\sum(w(F_o^2 - F_c^2)^2) / \sum(wF_o^4)]^{1/2}$, ^cGOF = $[\sum(w(F_o^2 - F_c^2)^2) / (\text{No. of reflns.} - \text{No. of params.})]^{1/2}$

General Experimental for Complexes 5.9-5.13

Formazan **5.7** (0.33 g, 1.2 mmol) was dissolved in dry toluene (40 mL). NEt_3 (0.36 g, 0.49 mL, 3.5 mmol) was then added slowly and the solution stirred for 10 min before $\text{BF}_3 \cdot \text{OEt}_2$ (0.83 g, 0.72 mL, 5.8 mmol) was added and the solution was heated with stirring at 80°C for 18 h. The solution immediately turned dark blue/purple. After cooling to 22°C , the reaction mixture was poured into a separatory funnel containing deionized H_2O (100 mL). The purple toluene solution was then washed with deionized H_2O (3×100 mL), dried over MgSO_4 , gravity filtered and concentrated *in vacuo*. The resulting residue contained a mixture of compounds **5.7** and **5.9–5.13**. These compounds were separated (**5.9**: $R_f = 0.82$; **5.10**: $R_f = 0.76$; **5.11**: $R_f = 0.61$; **5.7**: $R_f = 0.39$; **5.12**: $R_f = 0.31$; **5.13**: $R_f = 0.22$) by column chromatography (CH_2Cl_2 , silica). Additional column chromatography (10:1 Toluene:EtOAc, silica) was required to separate compounds **5.9** and **5.10**, and **5.12** and **5.13**. See Table S3 for compound distributions under a variety of experimental conditions.

Dimer 5.9

Melting point = $244\text{--}246^\circ\text{C}$. ^1H NMR (400.1 MHz, CDCl_3): δ 7.80 (d, $^3J_{\text{HH}} = 9$ Hz, 2H, aryl CH), 7.39–7.34 (m, 4H, aryl CH), 7.13–7.11 (m, 2H, aryl CH), 7.05–7.00 (m, 4H, aryl CH), 6.94 (d, $^3J_{\text{HH}} = 8$ Hz, 2H, aryl CH) 6.60–6.58 (m, 2H, aryl CH). $^{13}\text{C}\{^1\text{H}\}$ NMR (150.7 MHz, CDCl_3): δ 155.7, 148.0, 138.1, 135.9, 132.6, 131.9, 130.3, 129.2, 128.4, 125.0, 124.1, 122.7, 115.7, 114.6. ^{11}B NMR (128.3 MHz, CDCl_3): δ 1.0 (s). FT-IR (ATR): 2235 (m), 1590 (m), 1483 (m), 1382 (m), 1309 (s), 1252 (s), 1079 (s), 1046 (s), 988 (m), 960 (m) cm^{-1} . UV-vis (CH_2Cl_2): λ_{max} 535 nm ($\epsilon = 28,100 \text{ M}^{-1} \text{ cm}^{-1}$), 440 nm ($\epsilon = 12,600 \text{ M}^{-1} \text{ cm}^{-1}$), 296 nm ($\epsilon = 21,500 \text{ M}^{-1} \text{ cm}^{-1}$). Mass Spec. (EI, +ve mode): exact mass calculated for $[\text{C}_{28}\text{H}_{16}\text{B}_2\text{N}_{10}\text{O}_4]^+$: 578.1542; exact mass found: 578.1531; difference: -1.9 ppm.

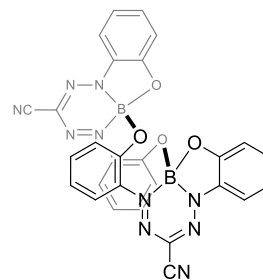


Dimer 5.10

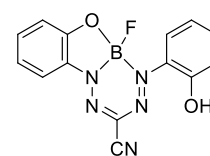
Melting point not observed (>250 °C). ^1H NMR (400.1 MHz, CDCl_3): δ 7.88–7.85. (m, 2H, aryl CH), 7.56–7.52 (m, 2H, aryl CH), 7.36–7.32 (m, 2H, aryl CH), 7.23 (d, $^3J_{\text{HH}} = 8$ Hz, 2H, aryl CH), 7.17–7.12 (m, 6H, aryl CH), 6.84–6.81 (m, 2H, aryl CH).

$^{13}\text{C}\{^1\text{H}\}$ NMR (150.7 MHz, CDCl_3): δ 156.6, 147.5, 136.4, 136.3,

132.6, 132.1, 131.0, 126.4, 125.1, 122.9, 122.3, 117.1, 116.4, 112.9. ^{11}B NMR (128.3 MHz, CDCl_3): δ 1.1 (s). FT-IR (ATR): 2923 (m), 2853 (w), 2243 (m), 1592 (m), 1481 (m), 1323 (s), 1247 (s), 1148 (m), 1084 (s), 995 (m), 971 (m) cm^{-1} . UV-vis (CH_2Cl_2): λ_{max} 605 nm ($\epsilon = 19,400 \text{ M}^{-1} \text{ cm}^{-1}$), 569 nm ($\epsilon = 20,500 \text{ M}^{-1} \text{ cm}^{-1}$), 415 nm ($8,800 \text{ M}^{-1} \text{ cm}^{-1}$), 319 nm ($19,700 \text{ M}^{-1} \text{ cm}^{-1}$). Mass Spec. (EI, +ve mode): exact mass calculated for $[\text{C}_{28}\text{H}_{16}\text{B}_2\text{N}_{10}\text{O}_4]^+$: 578.1542; exact mass found: 578.1547; difference: +0.9 ppm.

**Compound 5.11**

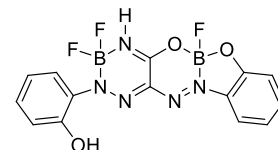
Melting point = 165–166 °C. ^1H NMR (400.1 MHz, CDCl_3): δ 9.56 (s, 1H, OH), 8.14 (d, $^3J_{\text{HH}} = 9$ Hz, 1H, aryl CH), 7.82 (d, $^3J_{\text{HH}} = 9$ Hz, 1H, aryl CH), 7.53 (m, 1H, aryl CH), 7.35–7.34 (m, 1H, aryl CH), 7.20–7.16



(m, 2H, aryl CH), 7.08–7.06 (m, 2H, aryl CH). $^{13}\text{C}\{^1\text{H}\}$ NMR (150.7 MHz, CDCl_3): δ 157.6, 153.4, 135.9, 135.8, 133.1, 133.0, 125.3, 123.3, 121.5, 120.3, 117.0, 115.6, 115.3, 113.3. ^{11}B NMR (128.3 MHz, CDCl_3): δ 0.0 (d, $^1J_{\text{BF}} = 37$ Hz). ^{19}F NMR (376.1 MHz, CDCl_3): δ -151.1 (q, $^1J_{\text{FB}} = 37$ Hz). FT-IR (ATR): 3351 (br, m), 2924 (m), 2853 (w), 2244 (m), 1594 (s), 1378 (s), 1310 (s), 1148 (m), 1102 (m), 995 (s) cm^{-1} . UV-vis (CH_2Cl_2): λ_{max} 619 nm ($\epsilon = 11,700 \text{ M}^{-1} \text{ cm}^{-1}$), 577 nm ($\epsilon = 13,500 \text{ M}^{-1} \text{ cm}^{-1}$), 445 nm ($\epsilon = 5,800 \text{ M}^{-1} \text{ cm}^{-1}$), 318 nm ($\epsilon = 11,300 \text{ M}^{-1} \text{ cm}^{-1}$). Mass Spec. (EI, -ve mode): exact mass calculated for $[\text{C}_{14}\text{H}_9\text{BFN}_5\text{O}_2]^+$: 309.0833; exact mass found: 309.0843; difference: +3.2 ppm.

Compound 5.12

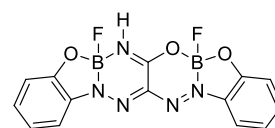
Melting point = 217–219 °C. ^1H NMR (400.1 MHz, CDCl_3): δ 10.50 (s, 1H, OH), 8.05–8.04 (m, 1H, aryl CH), 7.71–7.70 (m, 1H, aryl CH), 7.51–7.48 (m, 1H, aryl CH), 7.45 (br s, 1H, NH), 7.35–7.33 (m, 1H, aryl CH), 7.15–7.10 (m, 3H, aryl CH), 7.02–6.99 (m, 1H, aryl CH). $^{13}\text{C}\{^1\text{H}\}$ NMR (150.7 MHz, CDCl_3): δ 159.3, 152.7, 152.4, 136.0, 134.5, 132.3, 129.6,



124.6, 122.7, 120.9, 120.1, 116.1, 115.9. ^{11}B NMR (128.3 MHz, CDCl_3): δ 1.6 (d, $^1J_{\text{BF}} = 30$ Hz), 0.4 (t, $^1J_{\text{BF}} = 28$ Hz). ^{19}F NMR (376.1 MHz, CDCl_3): δ (-125.0)–(-124.7) (m), -149.8 (q, $^1J_{\text{FB}} = 28$ Hz). FT-IR (ATR): 3314 (m), 3302 (m), 2924 (m), 2854 (w), 1646 (m), 1600 (m), 1458 (m), 1406 (s), 1306 (s), 1099 (m), 1116 (m), 1002 (s), 905 (m) cm^{-1} . UV-vis (CH_2Cl_2): λ_{max} 560 nm ($\epsilon = 27,600 \text{ M}^{-1} \text{ cm}^{-1}$), 412 nm ($\epsilon = 7,600 \text{ M}^{-1} \text{ cm}^{-1}$), 348 nm ($\epsilon = 4,100 \text{ M}^{-1} \text{ cm}^{-1}$), 260 nm ($\epsilon = 4,600 \text{ M}^{-1} \text{ cm}^{-1}$). Mass Spec. (EI, +ve mode): exact mass calculated for $[\text{C}_{14}\text{H}_{10}\text{B}_2\text{F}_3\text{N}_5\text{O}_3]^+$: 374.0844; exact mass found: 374.0833; difference: -2.9 ppm.

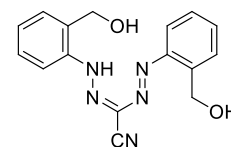
Compound 5.13

Melting point = 207–209 °C. ^1H NMR (400.1 MHz, CDCl_3): δ 7.82–7.76 (m, 2H, aryl CH), 7.69 (s, 1H, NH), 7.48–7.44 (m, 2H, aryl CH), 7.16–7.09 (m, 4H, aryl CH). $^{13}\text{C}\{^1\text{H}\}$ NMR (150.7 MHz, CDCl_3): δ 134.9, 134.1, 122.3, 122.1, 115.9, 115.8, 115.6, 115.5. ^{11}B NMR (128.3 MHz, CDCl_3): δ 1.6 (d, $^1J_{\text{BF}} = 33$ Hz), 0.9 (d, $^1J_{\text{BF}} = 42$ Hz). ^{19}F NMR (376.1 MHz, CDCl_3): δ -137.6 (q, $^1J_{\text{FB}} = 42$ Hz), -149.8 (q, $^1J_{\text{FB}} = 33$ Hz). FT-IR (ATR): 3169 (m), 1594 (m), 1431 (m), 1317 (s), 1286 (s), 1065 (s), 998 (m), 902 (m) cm^{-1} . UV-vis (CH_2Cl_2): λ_{max} 577 nm ($\epsilon = 35,900 \text{ M}^{-1} \text{ cm}^{-1}$), 407 nm ($\epsilon = 6,800 \text{ M}^{-1} \text{ cm}^{-1}$), 269 nm ($\epsilon = 14,600 \text{ M}^{-1} \text{ cm}^{-1}$). Mass Spec. (EI, +ve mode): exact mass calculated for $[\text{C}_{14}\text{H}_9\text{B}_2\text{F}_2\text{N}_5\text{O}_3]^+$: 355.0860; exact mass found: 355.0861; difference: +0.3 ppm.



Formazan 5.14

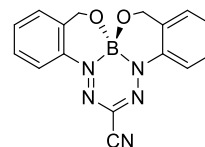
In air, cyanoacetic acid (0.21 g, 2.4 mmol) was dissolved in deionized H_2O (50 mL) containing NaOH (0.96 g, 24 mmol). This colourless solution was stirred for 45 min in an ice bath. Meanwhile, 2-aminobenzyl alcohol (0.59 g, 4.8 mmol) was mixed with concentrated HCl (1.2 mL) in deionized H_2O (15 mL). This solution was cooled in an ice bath for 10 min before a solution of sodium nitrite (0.38 g, 5.5 mmol) in deionized H_2O (10 mL) was cooled in an ice bath, and then added slowly to the 2-aminobenzyl alcohol solution over a 10 min period. This mixture was stirred in an ice bath for 30 min and then added slowly to the basic cyanoacetic acid solution. A dark red/orange colour persisted almost immediately, and a dark red/orange precipitate formed after a few min. The mixture was stirred in an ice bath for an additional 16 h before ethyl acetate (250 mL) was added and the organic layer was



isolated, washed with deionized H₂O (3 × 100 mL), dried over MgSO₄, gravity filtered and concentrated *in vacuo*. The resulting residue was purified by flash chromatography (CH₂Cl₂, neutral alumina) to afford formazan **5.14** as a dark red solid. Yield = 0.66 g, 87%. Melting point = 185–187 °C. ¹H NMR (400.1 MHz, DMSO-*d*₆): δ major isomer: 12.88 (s, 1H, NH), 7.66 (d, ³J_{HH} = 9 Hz, 2H, aryl CH), 7.52 (d, ³J_{HH} = 9 Hz, 2H, aryl CH), 7.40–7.35 (m, 4H, aryl CH), 5.81 (s, 2H, OH), 4.94 (s, 4H, CH₂). δ minor isomer: 11.72 (s, 1H, NH), 7.73–7.63 (m, 2H, aryl CH), 7.57–7.54 (m, 2H, aryl CH), 7.31–7.30 (m, 2H, aryl CH), 7.14–7.12 (m, 2H, aryl CH), 6.33 (s, 2H, OH), 5.02 (s, 2H, CH₂), 4.84 (s, 2H, CH₂). ¹³C{¹H} NMR (150.7 MHz, DMSO-*d*₆), both isomers: δ 147.7, 144.3, 141.5, 140.6, 135.6, 130.9, 128.6, 128.2, 127.2, 124.4, 115.1, 112.6, 108.2, 62.7, 60.5, 58.3. FT-IR (ATR): 3535 (w), 3399 (m), 3215 (m), 2218 (m), 1587 (w), 1522 (m), 1461 (m), 1399 (m), 1265 (m), 1206 (m), 1014 (s), 758 (s), 722 (s) cm⁻¹. UV-vis (CH₂Cl₂): λ_{max} 438 nm (ε = 20,900 M⁻¹ cm⁻¹), 294 nm (ε = 11,400 M⁻¹ cm⁻¹), 267 nm (11,100 M⁻¹ cm⁻¹). Mass Spec. (EI, +ve mode): exact mass calculated for [C₁₆H₁₅N₅O₂]⁺: 309.1226; exact mass found: 309.1230; difference: +1.3 ppm.

Compound 5.15

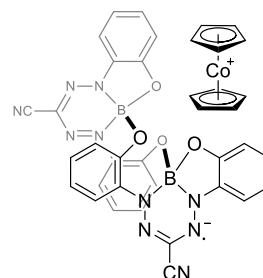
Formazan **5.14** (0.66 g, 2.1 mmol) was dissolved in dry toluene (70 mL). NEt₃ (0.65 g, 0.90 mL, 6.4 mmol) was then added slowly and the solution was stirred for 10 min before BF₃•OEt₂ (1.49 g, 1.30 mL, 10.5 mmol) was added and the solution was heated with stirring at 80 °C for 18 h. The solution gradually turned from dark red to dark purple during this time. After cooling to 22 °C, deionized H₂O (10 mL) was added to quench any excess reactive boron-containing compounds. The purple toluene solution was then washed with deionized H₂O (3 × 50 mL), dried over MgSO₄, gravity filtered and concentrated *in vacuo*. The resulting residue was purified by flash chromatography (CH₂Cl₂, neutral alumina) to afford bis-methylene-hydroxy-substituted complex **5.15** as a dark purple microcrystalline solid. Yield = 0.61 g, 92%. Melting point = 235–237 °C. ¹H NMR (400.1 MHz, CDCl₃): δ 7.78–7.76 (m, 2H, aryl CH), 7.41–7.35 (m, 4H, aryl CH), 7.09–7.08 (m, 2H, aryl CH), 5.30–5.28 (m, 2H, CH₂) 5.15–5.12 (m, 2H, CH₂). ¹³C{¹H} NMR (150.7 MHz, CDCl₃): δ 140.3, 134.3, 130.9, 128.2, 125.9, 125.7, 119.4, 114.9, 65.0. ¹¹B NMR (128.3 MHz, CDCl₃): δ -0.1 (s). FT-IR (ATR): 2986 (m), 2854 (m), 2235 (m), 1342 (s), 1299 (m), 1084 (s), 1008 (m), 988 (m), 761 (s), 707 (s) cm⁻¹.



¹. UV-vis (CH₂Cl₂): λ_{max} 596 nm (ε = 17,400 M⁻¹ cm⁻¹), 558 nm (ε = 18,800 M⁻¹ cm⁻¹), 395 nm (ε = 5,600 M⁻¹ cm⁻¹), 292 nm (ε = 12,300 M⁻¹ cm⁻¹). Mass Spec. (EI, +ve mode): exact mass calculated for [C₁₆H₁₂BN₅O₂]⁺: 317.1084; exact mass found: 317.1082; difference: -0.6 ppm.

Singly reduced dimer 5.10⁻

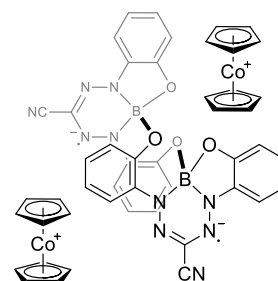
In a nitrogen-filled glovebox, **5.10** (0.034 g, 0.059 mmol) was dissolved in dry and degassed CH₂Cl₂ (5 mL). In a separate flask, cobaltocene (0.011 g, 0.059 mmol) was dissolved in dry and degassed CH₂Cl₂ (2 mL). The cobaltocene solution was added dropwise to a stirred solution of **5.10**. This mixture was stirred for an additional 30 min before it was filtered and the filtrate was



collected. The solvent was removed *in vacuo* to yield a brown microcrystalline powder. Yield = 0.031 g, 68%. Melting point = 226–228 °C. FT-IR (ATR): 3367 (m), 3109 (m), 2235 (m), 1667 (s), 1468 (m), 1415 (m), 1321 (s), 1232 (m), 1147 (m), 751 (m) cm⁻¹. UV-vis (CH₃CN): λ_{max} 520 nm (ε = 13,000 M⁻¹ cm⁻¹), 477 nm (ε = 15,500 M⁻¹ cm⁻¹), 262 nm (ε = 35,700 M⁻¹ cm⁻¹). Mass Spec. (EI, -ve mode): exact mass calculated for [C₂₈H₁₆B₂N₁₀O₄]⁻: 578.1542; exact mass found: 578.1538; difference: -0.7 ppm. Anal. Calcd. (%) for C₂₂H₁₉N₅O: C, 59.49; H, 3.42; N, 18.26. Found: C, 57.66; H, 3.31; N, 18.25.

Doubly reduced dimer 5.10²⁻

In a nitrogen-filled glovebox, **5.10** (0.025 g, 0.043 mmol) was dissolved in dry CH₂Cl₂ (5 mL). In a separate flask, cobaltocene (0.016 g, 0.086 mmol) was dissolved in dry CH₂Cl₂ (3 mL). The cobaltocene solution was added dropwise to a stirred solution of **5.10**. This mixture was stirred for an additional 30 min before it was filtered and the precipitate was collected. The precipitate was

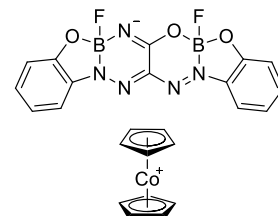


collected by dissolving in CH₃CN before the solvent was removed *in vacuo* to yield a green microcrystalline powder. Yield = 0.034 g, 82%. Melting point not observed (>250 °C). FT-IR (ATR): 3359 (m), 3098 (m), 2234 (m), 1661 (s), 1467 (m), 1393 (m), 1321 (m), 1146 (m), 749 (m) cm⁻¹. UV-vis (CH₃CN): λ_{max} 694 nm (ε = 6,500 M⁻¹ cm⁻¹), 477 nm (ε = 39,200 M⁻¹ cm⁻¹), 330 nm (ε = 38,000 M⁻¹ cm⁻¹), 261 nm (ε = 229,400 M⁻¹ cm⁻¹). Mass Spec. (EI, -ve mode): exact mass calculated for [C₂₈H₁₆B₂N₁₀O₄]²⁻: 289.0777; exact mass

found: 289.0778; difference: +0.3 ppm. Anal. Calcd. (%) for $C_{48}H_{36}B_2CO_2N_{10}O_4 \cdot CH_2Cl_2$: C, 56.52; H, 3.68; N, 13.45. Found: C, 55.64; H, 3.60; N, 13.50.

Reduced boron complex **5.16⁻**

In a nitrogen-filled glovebox, boron complex **5.13** (0.052 g, 0.15 mmol) was dissolved in dry CH_2Cl_2 (10 mL). In a separate flask, cobaltocene (0.28 g, 0.15 mmol) was dissolved in dry CH_2Cl_2 (5 mL). The cobaltocene solution was added dropwise to a stirred solution of **5.13**. This mixture was stirred for an additional 30 min



before it was filtered, and concentrated *in vacuo*. The dark purple/blue residue as dissolved in toluene, before pentane was added to this solution, and the mixture was left in the freezer overnight ($-35\text{ }^\circ\text{C}$). After this time, a dark purple microcrystalline powder had formed, which was collected as **5.16⁻**. Yield = 0.051 g, 58%. Melting point = $116\text{--}118\text{ }^\circ\text{C}$. ^1H NMR (400.1 MHz, CD_2Cl_2): δ 7.70–7.63 (m, 2H, aryl CH), 7.31–7.26 (m, 2H, aryl CH), 7.02–6.96 (m, 4H, aryl CH), 5.75 (s, 10H, $CoCp_2^+$ CH). $^{13}\text{C}\{^1\text{H}\}$ NMR (150.7 MHz, CD_2Cl_2): δ 157.8, 157.5, 145.9, 145.8, 134.4, 133.9, 131.2, 130.9, 120.7, 120.0, 114.7, 114.3, 114.3, 114.0, 85.2. ^{11}B NMR (128.3 MHz, $CDCl_3$): δ 4.5 (br s), 3.1 (d, $^1J_{BF} = 40$ Hz). ^{19}F NMR (376.1 MHz, $CDCl_3$): δ -136.4 (q, $^1J_{FB} = 28$ Hz), -147.4 (q, $^1J_{FB} = 40$ Hz). FT-IR (ATR): 3101 (m), 2961 (m), 2874 (w), 1601 (m), 1414 (m), 1315 (s), 1258 (m), 1147 (m), 1005 (m), 889 (m), 750 (s) cm^{-1} . UV-vis (CH_2Cl_2): λ_{max} 589 nm ($\epsilon = 18,000\text{ M}^{-1}\text{ cm}^{-1}$), 560 nm ($\epsilon = 17,000\text{ M}^{-1}\text{ cm}^{-1}$), 275 nm ($\epsilon = 2,500\text{ M}^{-1}\text{ cm}^{-1}$), 263 nm ($\epsilon = 20,700\text{ M}^{-1}\text{ cm}^{-1}$). Mass Spec. (EI, $-ve$ mode): exact mass calculated for $[C_{14}H_8B_2F_2N_5O_3]^-$ 354.0781; exact mass found: 354.0796; difference: +4.2 ppm.

5.5 References

- (1) Bosdet, M. J. D.; Piers, W. E. *Can. J. Chem.* **2009**, *87*, 8–29.
- (2) Ma, K.; Scheibitz, M.; Scholz, S.; Wagner, M. *J. Organomet. Chem.* **2002**, *652*, 11–19.
- (3) Brand, J.; Braunschweig, H.; Sen, S. S. *Acc. Chem. Res.* **2014**, *47*, 180–191.

- (4) Campbell, P. G.; Marwitz, A. J. V.; Liu, S.-Y. *Angew. Chem. Int. Ed.* **2012**, *51*, 6074–6092.
- (5) Campbell, P. G.; Zakharov, L. N.; Grant, D. J.; Dixon, D. A.; Liu, S.-Y. *J. Am. Chem. Soc.* **2010**, *132*, 3289–3291.
- (6) Wang, X.-Y.; Lin, H.-R.; Lei, T.; Yang, D.-C.; Zhuang, F.-D.; Wang, J.-Y.; Yuan, S.-C.; Pei, J. *Angew. Chem. Int. Ed.* **2013**, *52*, 3117–3120.
- (7) Ishibashi, J. S. A.; Marshall, J. L.; Mazière, A.; Lovinger, G. J.; Li, B.; Zakharov, L. N.; Dargelos, A.; Graciaa, A.; Chrostowska, A.; Liu, S.-Y. *J. Am. Chem. Soc.* **2014**, *136*, 15414–15421.
- (8) Braunschweig, H.; Ewing, W. C.; Geetharani, K.; Schäfer, M. *Angew. Chem. Int. Ed.* **2015**, *54*, 1662–1665.
- (9) Liew, S. K.; Holownia, A.; Tilley, A. J.; Carrera, E. I.; Seferos, D. S.; Yudin, A. K. *J. Org. Chem.* **2016**, *81*, 10444–10453.
- (10) Yang, D.-T.; Mellerup, S. K.; Peng, J.-B.; Wang, X.; Li, Q.-S.; Wang, S. *J. Am. Chem. Soc.* **2016**, *138*, 11513–11516.
- (11) Dilek, O.; Lei, Z.; Mukherjee, K.; Bane, S. *Chem. Commun.* **2015**, *51*, 16992–16995.
- (12) Braunschweig, H.; Herbst, T.; Rais, D.; Ghosh, S.; Kupfer, T.; Radacki, K.; Crawford, A. G.; Ward, R. M.; Marder, T. B.; Fernández, I.; Frenking, G. *J. Am. Chem. Soc.* **2009**, *131*, 8989–8999.
- (13) Pietsch, S.; Paul, U.; Cade, I. A.; Ingleson, M. J.; Radius, U.; Marder, T. B. *Chem. Eur. J.* **2015**, *21*, 9018–9021.
- (14) Baggett, A. W.; Guo, F.; Li, B.; Liu, S.-Y.; Jäkle, F. *Angew. Chem. Int. Ed.* **2015**, *54*, 11191–11195.
- (15) Noda, H.; Furutachi, M.; Asada, Y.; Shibasaki, M.; Kumagai, N. *Nat. Chem.* **2017**, DOI: 10.1038/nchem.2708.
- (16) Helten, H. *Chem. Eur. J.* **2016**, *22*, 12972–12982.
- (17) Grandl, M.; Rudolf, B.; Sun, Y.; Bechtel, D. F.; Pierik, A. J.; Pammer, F. *Organometallics* **2017**, DOI: 10.1021/acs.organomet.6b00916.
- (18) Chang, M.-C.; Otten, E. *Inorg. Chem.* **2015**, *54*, 8656–8664.

- (19) Pierce, G. A.; Aldridge, S.; Jones, C.; Gans-Eichler, T.; Stasch, A.; Coombs, N. D.; Willock, D. J. *Angew. Chem. Int. Ed.* **2007**, *46*, 2043–2046.
- (20) Lorbach, A.; Bolte, M.; Lerner, H.-W.; Wagner, M. *Chem. Commun.* **2010**, *46*, 3592–3594.
- (21) Arrowsmith, M.; Auerhammer, D.; Bertermann, R.; Braunschweig, H.; Bringmann, G.; Celik, M. A.; Dewhurst, R. D.; Finze, M.; Grüne, M.; Hailmann, M.; Hertle, T.; Krummenacher, I. *Angew. Chem. Int. Ed.* **2016**, *55*, 14464–14468.
- (22) Jaska, C. A.; Emslie, D. J. H.; Bosdet, M. J. D.; Piers, W. E.; Sorensen, T. S.; Parvez, M. *J. Am. Chem. Soc.* **2006**, *128*, 10885–10896.
- (23) Xie, X.; Adams, C. J.; Al-Ibadi, M. A. M.; McGrady, J. E.; Norman, N. C.; Russell, C. A. *Chem. Commun.* **2013**, *49*, 10364–10366.
- (24) Chen, J.; Lalancette, R. A.; Jäkle, F. *Chem. Commun.* **2013**, *49*, 4893–4895.
- (25) Gilroy, J. B.; Otieno, P. O.; Ferguson, M. J.; McDonald, R.; Hicks, R. G. *Inorg. Chem.* **2008**, *47*, 1279–1286.
- (26) M. J. Frisch, G. W. Trucks, H. B. Schlegel *et al.*, Gaussian 09, Revision E.01 (Gaussian, Inc., Wallingford CT, 2013).
- (27) Ernzerhof, M.; Scuseria, G. E. *J. Chem. Phys.* **1999**, *110*, 5029–5036.
- (28) Barbon, S. M.; Reinkeluers, P. A.; Price, J. T.; Staroverov, V. N.; Gilroy, J. B. *Chem. Eur. J.* **2014**, *20*, 11340–11344.
- (29) Gilroy, J. B.; Ferguson, M. J.; McDonald, R.; Patrick, B. O.; Hicks, R. G. *Chem. Commun.* **2007**, 126–128.
- (30) Chang, M.-C.; Chantzis, A.; Jacquemin, D.; Otten, E. *Dalton Trans.* **2016**, *45*, 9477–9484.
- (31) The contribution from cobaltocene is assumed to be negligible in the region of interest (>300 nm), as the molar absorptivities in this region are two orders of magnitude less than the complexes of interest (403 nm, $218 \text{ M}^{-1} \text{ cm}^{-1}$). See N. El Murr, *J. Organomet. Chem.*, **1976**, *112*, 189–199.
- (32) Quenching the reaction with ammonia did not afford the symmetric analog of **13**.
- (33) Fadeeva, V. P.; Tikhova, V. D.; Nikulicheva, O. N. *J. Anal. Chem.* **2008**, *63*, 1094–1106.
- (34) Liu, L.-L.; He, G.-Q.; Wang, Y.-H.; Hu, S.-Q. *RSC Adv.* **2015**, *5*, 101416–101426.

- (35) Bruker-Nonius, SAINT version 2013.8, 2013, Bruker-AXS, Madison, WI 53711, USA.
- (36) Bruker-Nonius, SADABS version 2012.1, 2012, Bruker-AXS, Madison, WI 53711, USA.
- (37) Bruker-Nonius, TWINABS version 2012.1, 2012, Bruker-AXS, Madison, WI 53711, USA.
- (38) Sheldrick, G. M. *Acta Cryst.* **2015**, *A71*, 3–8.
- (39) Spek, A. L. *Acta Cryst.* **2015**, *C71*, 9–19.
- (40) Sheldrick, G. M. *Acta Cryst.* **2015**, *C71*, 3–8.

Chapter 6

6 Conclusions and Future Work

6.1 Conclusions

The work included in this thesis describes the synthesis and characterization of a new class of boron complexes of formazan ligands, from structure-property relationships and unusual bonding modes to materials and applications. The straightforward synthesis of BF_2 complexes of formazan ligands from inexpensive starting materials was described. The tunability of the complexes was also probed and it was found that the presence of electron donating groups red-shifted absorption and emission maxima, as well as made the resulting complexes more difficult to reduce. The effect of substituent variation was found to be more drastic when the 1,5-*N*-aryl substituents were probed, than the 3-aryl substituents. It was also shown that the synthesis of asymmetrically substituted complexes, in the BF_2 complexes of triaryl formazanates, more than doubled the quantum yields of emission. The usefulness of a *p*-anisoole substituted BF_2 complex was demonstrated for cell imaging and electrochemiluminescence applications. These results will allow for the straightforward tuning of these complexes for future applications.

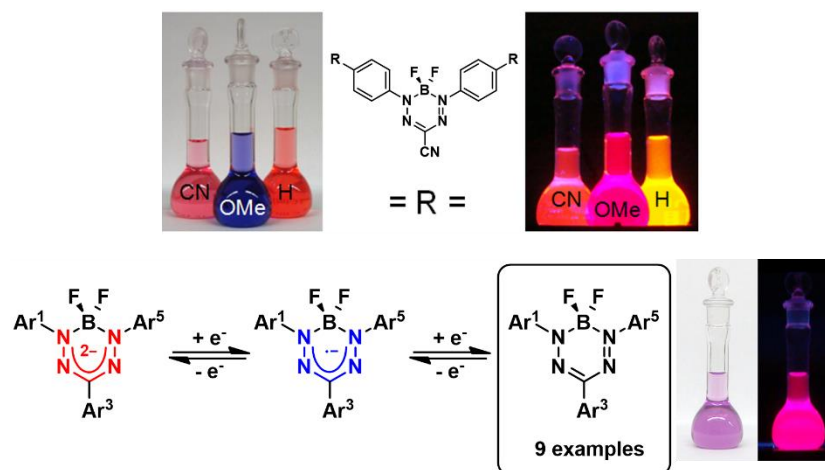


Figure 6.1. Substituent-driven optical and electronic properties of BF_2 complexes of formazanate ligands.

A second method used to affect the optical and electronic properties of these BF_2 complexes involved extending the π conjugation of the complexes, especially through the *N*-aryl substituents. It was shown that exchanging phenyl substituents for naphthyl substituents changed the properties of the resulting complexes. This change was more drastic for complexes when the R^3 substituents were cyano or nitro groups. In the case of triaryl formazanate complexes, there was a more significant change in properties when the *N*-aryl substituents were switched to naphthyl groups, versus the R^3 substituent. In all cases, the wavelength of maximum absorption and emission were red-shifted, and the quantum yield was increased. Dimers were also synthesized through a phenyl substituent in the R^3 position. In this case, it was found that *para*-bridged dimers showed some degree of communication between BF_2 formazanate backbones, with the same change in properties observed by extending the conjugation through naphthyl substituents. On the other hand, *meta*-bridged dimers, which are cross-conjugated, showed no communication, and exhibited very similar properties to the triphenyl-substituted BF_2 formazanate monomeric model complex. This work represents a stepping stone towards the development of π conjugated polymers with absorption and emission in the near-IR.

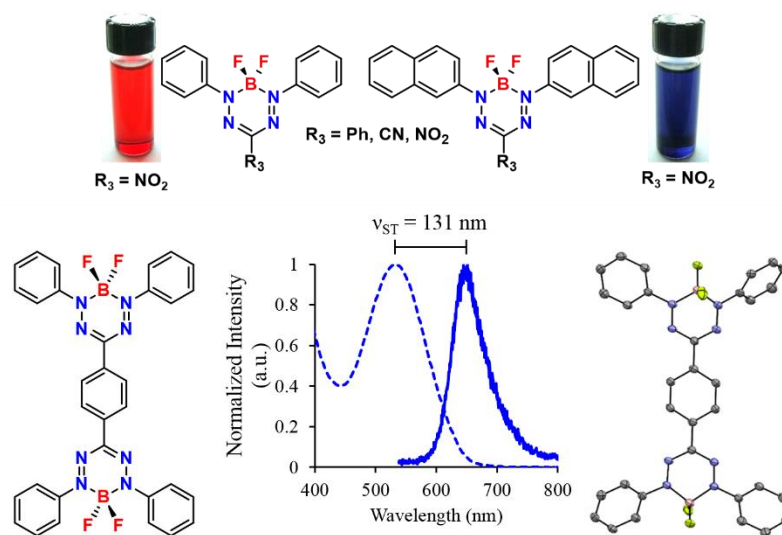


Figure 6.2. Extended conjugation through naphthyl substituents and benzene-bridged dimers, and the effect on the optical properties.

Appending alkyne substituents to BF_2 formazanate complexes allowed for the synthesis of new polymeric and molecular materials that would not be possible otherwise. We showed, using benzyl azide as a model azide, that copper-assisted alkyne-azide cycloaddition (CuAAC) was an efficient method for appending new functionalities onto BF_2 formazanate complexes. The formation of the triazole ring also red-shifted the absorption and emission maxima, and increased the emission quantum yields, as well as made the resulting complexes easier to reduce electrochemically. Appending one or two ferrocenes to 3-cyanoformazanate BF_2 complexes quenched their fluorescence. However, it was regenerated upon stoichiometric oxidation of the ferrocenes to ferrocenium. Water-soluble BF_2 complexes were also synthesized using CuAAC to attach tetraethylene glycol substituents, and the resulting complex was studied as a cell imaging agent. It was found that the dye stained both the cytoplasm and nucleus of the cells, but due to its low-energy emission, could be used for orthogonal imaging with DAPI, a blue dye which localizes in the nucleus. Finally, CuAAC was used to synthesize main-chain co-polymers of BF_2 formazanate complexes and 9,9-dihexylfluorene. Through the synthesis of a variety of model complexes, we showed that the conjugation did not extend through the triazole rings, however because the parent BF_2 complex has a small HOMO-LUMO gap, the resulting polymer had a low band gap (1.67 eV), and good film-forming properties. This work demonstrates a facile modification strategy for BF_2 formazanate complexes, which can be used to apply these complexes to a wide range of tasks.

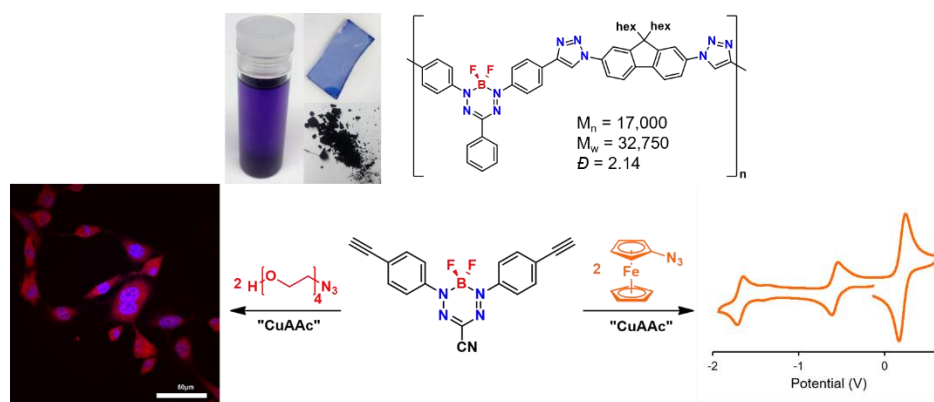


Figure 6.3. Copper-assisted alkyne-azide cycloaddition as a useful tool for the synthesis of polymeric and molecular materials.

Finally, a variety of unprecedented boron-nitrogen containing heterocycles were synthesized from the reaction of a single *o*-phenol substituted 3-cyanoformazan with excess $\text{BF}_3 \cdot \text{OEt}_2$ and NEt_3 . The 5 isolated complexes all contained at least one boron atom, and displayed interesting optical and electronic properties. The ratios between the five products could be controlled based on the reaction conditions employed, and these results were explained *via* density functional theory calculations. Two of these complexes were selected to undergo further reduction chemistry, and a stable anion, radical anion, and diradical dianion were isolated, and structurally characterized. This work will serve as a platform for the rational design of novel boron-nitrogen heterocycles with potential utility as light-harvesting and charge-transporting materials in the future.

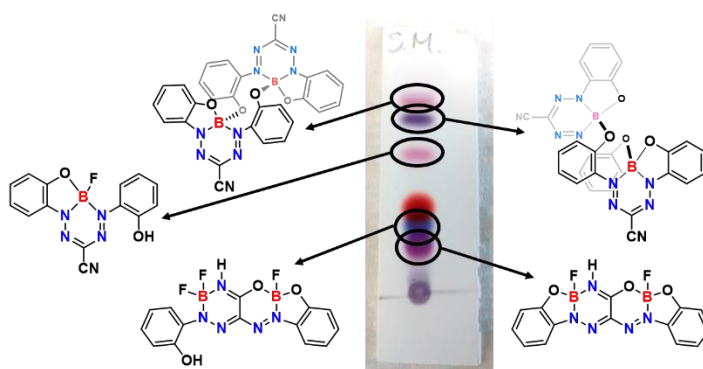


Figure 6.4. Synthesis of five new BN heterocycles from a single reaction.

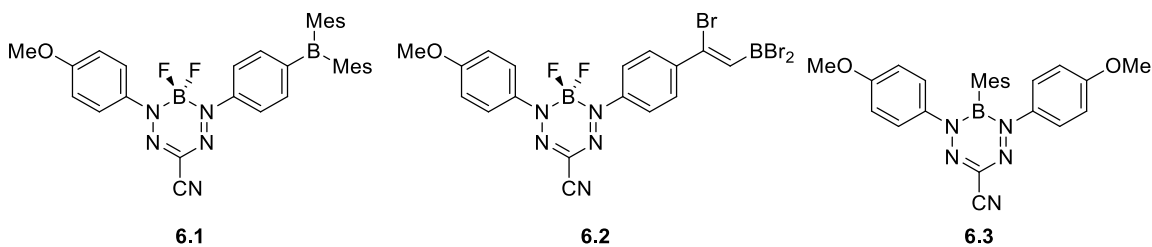
Overall, this work showed that BF_2 complexes of formazan ligands are an interesting and useful new class of materials. They are straightforward and inexpensive to synthesize, and the properties can be tuned through simple structural modification. With no extra synthetic effort, reactive functionalities such as alkynes and hydroxyl groups can be appended to these boron complexes, allowing for a simple starting material that can be reacted to form a variety of molecular and polymeric materials. To date, these complexes and materials have found application as cell imaging agents, redox sensors and electrochemiluminescent materials, but due to their unique optical and electronic properties, have the potential to impact many other fields of research.

6.2 Future Work

6.2.1 Molecular Materials: Three-Coordinate Boron Complexes

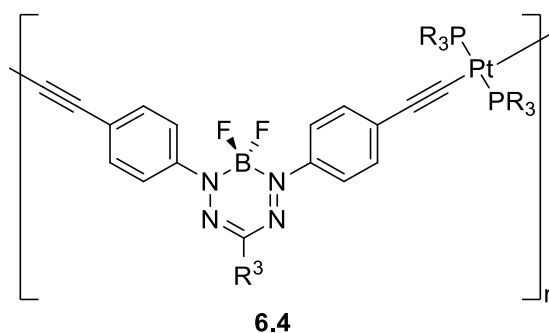
Three-coordinate boron complexes have been studied extensively over the last few decades, as the empty p orbital on boron, and the optical properties they possess make them attractive for a variety of applications.^[1] These three-coordinate boron complexes have been used for sensing applications,^[2-4] non-linear optical materials,^[5] OLEDs,^[6-7] and electroluminescent devices.^[8-9] Combining these properties with those of the BF₂ formazanate framework is attractive, and related complexes have exhibited red-shifted emission into the near-IR,^[10-11] multicolour emission,^[12-13] and excellent sensing ability.^[10-11,13-14]

There are many ways to append 3-coordinate boron species, including reaction with an aryl bromide. Bromo-substituted BF₂ formazanate complexes could be converted into **6.1** via reaction with silyldimesitylborane, as described by the Ito group.^[15] It has also been shown that BBr₃ will add over an alkyne substituent,^[16] and this reaction could be applied to alkyne-substituted BF₂ formazanates to form complexes such as **6.2**. Finally, a lithium-halogen exchange reaction can lead to the precursor to **6.3**, which would allow for 3-coordinate boron complexes to be appended to the four coordinate boron atom.^[17] In all of these cases, the same reactivity can be applied to a variety of different BF₂ formazanate complexes, such as asymmetric and symmetric derivatives, and complexes with various R³ substituents (*e.g.* CN, NO₂, Ar), though complexes with *p*-anisole *N*-aryl substituents, and R³ = CN are expected to have the most desirable optical properties. It is expected that the optical properties of these complexes would be very interesting, and the three-coordinate boron substituents would allow for use in sensing.



6.2.2 Polymeric Materials: BF₂ Formazanate Platinum Polyynes

The initial attempts to incorporate BF₂ formazanate complexes into polymers were intriguing, as even with a lack of extended π conjugation, the properties of the resulting material were promising. Another method to create BF₂ formazanate polymers, while likely maintaining extended conjugation, is incorporation into a platinum polyyn system (*e.g.* **6.4**). These polymers typically have red-shifted emission properties, are often phosphorescent,^[18] and have found application as light-emitting diodes,^[19-20] in photovoltaics,^[21-23] organic field effect transistors,^[24-25] and batteries,^[26] as well as non-linear optical materials,^[27-28] sensors,^[29-30] and patternable precursors to metal nanoparticles.^[31-32] These polymers can be synthesized with a range of BF₂ formazanate complexes by varying R³ (*e.g.* R³ = CN for improving fluorescence quantum yield, R³ = aryl for increased solubility), and are expected to have lower band gaps than the previously described BF₂ formazanate polymer synthesized *via* CuAAC chemistry, and will likely be promising light harvesting materials.



6.2.3 Device Fabrication

BF₂ complexes of formazanate ligands, and polymers based upon them, are well-suited for organic electronic applications, in large part, due to their inexpensive synthesis. By varying the substituents and tuning the properties of these complexes, the materials can be tailored for use as the functional component of a variety of electronic devices. For example, efficient electrochemiluminescence of BF₂ formazanate complexes has already been demonstrated. Appending water solubilizing groups could result in a water soluble complex with similar electrochemiluminescence properties, which could be incorporated into electrochemiluminescence devices. Similarly, polymers containing BF₂ formazanate

units have been shown to have low band gaps – even with limited π conjugation, and also exhibit good film-forming properties. For these reasons, they are excellent candidates for use as the active layer of lightweight and flexible organic photovoltaics. Their low-lying frontier orbitals are particularly well suited for inverted bulk heterojunction architectures (Figure 6.5).

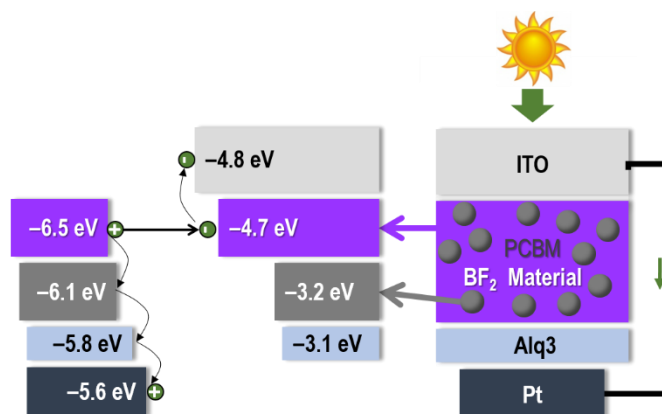


Figure 6.5. Proposed inverted bulk-heterojunction solar cell architecture comprised of an active layer containing BF_2 formazanate complexes.

6.3 References

- (1) Hudson, Z. M.; Wang, S. *Acc. Chem. Res.* **2009**, *42*, 1584–1596.
- (2) Hudnall, T. W.; Chiu, C.-W.; Gabbai, F. P. *Acc. Chem. Res.* **2009**, *42*, 388–397.
- (3) Wade, C. R.; Broomsgrove, A. E. J.; Aldridge, S.; Gabbai, F. P. *Chem. Rev.* **2010**, *110*, 3958–3984.
- (4) Liu, X. Y.; Bai, D. R.; Wang, S. *Angew. Chem. Int. Ed.* **2006**, *45*, 5475–5478.
- (5) Entwistle, C. D.; Marder, T. B. *Angew. Chem. Int. Ed.* **2002**, *41*, 2927–2931.
- (6) Wang, Z. B.; Helander, M. G.; Qiu, J.; Puzzo, D. P.; Greiner, M. T.; Hudson, Z. M.; Wang, S.; Liu, Z. W.; Lu, Z. H. *Nat. Photon.* **2011**, *5*, 753–757.
- (7) Jia, W. L.; Moran, M. J.; Yuan, Y.-Y.; Lu, Z. H.; Wang, S. *J. Mater. Chem.* **2005**, *15*, 3326–3333.
- (8) Doi, H.; Kinoshita, M.; Okumoto, K.; Shirota, Y. *Chem. Mater.* **2003**, *15*, 1080–1089.

- (9) Jia, W.-L.; Bai, D.-R.; McCormick, T.; Liu, Q.-D.; Motala, M.; Wang, R.-Y.; Seward, C.; Tao, Y.; Wang, S. *Chem. Eur. J.* **2004**, *10*, 994–1006.
- (10) Sarkar, S. K.; Mukherjee, S.; Thilagar, P. *Inorg. Chem.* **2014**, *53*, 2343–2345.
- (11) Swamy P, C. A.; Priyanka, R. N.; Mukherjee, S.; Thilagar, P. *Eur. J. Inorg. Chem.* **2015**, *2015*, 2338–2344.
- (12) Sarkar, S. K.; Thilagar, P. *Chem. Commun.* **2013**, *49*, 8558–8560.
- (13) Swamy P, C. A.; Mukherjee, S.; Thilagar, P. *Inorg. Chem.* **2014**, *53*, 4813–4823.
- (14) P, C. A. S.; Thilagar, P. *Inorg. Chem.* **2014**, *53*, 2776–2786.
- (15) Yamamoto, E.; Izumi, K.; Shishido, R.; Seki, T.; Tokodai, N.; Ito, H. *Chem. Eur. J.* **2016**, *22*, 17547–17551.
- (16) Lappert, M. F.; Prokai, B. *J. Organomet. Chem.* **1964**, *1*, 384–400.
- (17) Lu, J.-s.; Ko, S.-B.; Walters, N. R.; Wang, S. *Org. Lett.* **2012**, *14*, 5660–5663.
- (18) Ho, C.-L.; Yu, Z.-Q.; Wong, W.-Y. *Chem. Soc. Rev.* **2016**, *45*, 5264–5295.
- (19) Baldo, M. A.; O'Brien, D. F.; You, Y.; Shoustikov, A.; Sibley, S.; Thompson, M. E.; Forrest, S. R. *Nature* **1998**, *395*, 151–154.
- (20) Ho, C.-L.; Chui, C.-H.; Wong, W.-Y.; Aly, S. M.; Fortin, D.; Harvey, P. D.; Yao, B.; Xie, Z.; Wang, L. *Macromol. Chem. Phys.* **2009**, *210*, 1786–1798.
- (21) Mei, J.; Ogawa, K.; Kim, Y.-G.; Heston, N. C.; Arenas, D. J.; Nasrollahi, Z.; McCarley, T. D.; Tanner, D. B.; Reynolds, J. R.; Schanze, K. S. *ACS Appl. Mater. Interfaces* **2009**, *1*, 150–161.
- (22) Wong, W.-Y.; Wang, X.-Z.; He, Z.; Djurisić, A. B.; Yip, C.-T.; Cheung, K.-Y.; Wang, H.; Mak, C. S. K.; Chan, W.-K. *Nat. Mater.* **2007**, *6*, 521–527.
- (23) Liu, L.; Ho, C.-L.; Wong, W.-Y.; Cheung, K.-Y.; Fung, M.-K.; Lam, W.-T.; Djurišić, A. B.; Chan, W.-K. *Adv. Funct. Mater.* **2008**, *18*, 2824–2833.
- (24) Baek, N. S.; Hau, S. K.; Yip, H.-L.; Acton, O.; Chen, K.-S.; Jen, A. K. Y. *Chem. Mater.* **2008**, *20*, 5734–5736.
- (25) Yan, L.; Zhao, Y.; Wang, X.; Wang, X.-Z.; Wong, W.-Y.; Liu, Y.; Wu, W.; Xiao, Q.; Wang, G.; Zhou, X.; Zeng, W.; Li, C.; Wang, X.; Wu, H. *Macromol. Rapid Commun.* **2012**, *33*, 603–609.
- (26) Meng, Z.; Sato, K.; Sukegawa, T.; Oyaizu, K.; Ho, C.-L.; Xiang, J.; Feng, Y.-H.; Lo, Y. H.; Nishide, H.; Wong, W.-Y. *J. Organomet. Chem.* **2016**, *812*, 51–55.

- (27) Zhou, G.-J.; Wong, W.-Y.; Lin, Z.; Ye, C. *Angew. Chem. Int. Ed.* **2006**, *45*, 6189–6193.
- (28) Goudreault, T.; He, Z.; Guo, Y.; Ho, C.-L.; Zhan, H.; Wang, Q.; Ho, K. Y.-F.; Wong, K.-L.; Fortin, D.; Yao, B.; Xie, Z.; Wang, L.; Kwok, W.-M.; Harvey, P. D.; Wong, W.-Y. *Macromolecules* **2010**, *43*, 7936–7949.
- (29) Haskins-Glusac, K.; Pinto, M. R.; Tan, C.; Schanze, K. S. *J. Am. Chem. Soc.* **2004**, *126*, 14964–14971.
- (30) Liu, S.-J.; Chen, Y.; Xu, W.-J.; Zhao, Q.; Huang, W. *Macromol. Rapid Commun.* **2012**, *33*, 461–480.
- (31) Dong, Q.; Li, G.; Ho, C.-L.; Leung, C.-W.; Pong, P. W.-T.; Manners, I.; Wong, W.-Y. *Adv. Funct. Mater.* **2014**, *24*, 857–862.
- (32) Dong, Q.; Li, G.; Ho, C.-L.; Faisal, M.; Leung, C.-W.; Pong, P. W.-T.; Liu, K.; Tang, B. Z.; Manners, I.; Wong, W.-Y. *Adv. Mater.* **2012**, *24*, 1034–1040.

Appendices

Appendix A1 Permission to Reuse Copyrighted Material

Permission to Reproduce Figure 1.1a:

25/04/2017

RightsLink Printable License

**THE AMERICAN ASSOCIATION FOR THE ADVANCEMENT OF SCIENCE LICENSE
TERMS AND CONDITIONS**

Apr 25, 2017

This Agreement between Stephanie Barbon ("You") and The American Association for the Advancement of Science ("The American Association for the Advancement of Science") consists of your license details and the terms and conditions provided by The American Association for the Advancement of Science and Copyright Clearance Center.

License Number	4096101205895
License date	Apr 25, 2017
Licensed Content Publisher	The American Association for the Advancement of Science
Licensed Content Publication	Science
Licensed Content Title	Fluorescent Signaling in Parrots
Licensed Content Author	Kathryn E. Arnold,Ian P. F. Owens,N, Justin Marshall
Licensed Content Date	Jan 4, 2002
Licensed Content Volume	295
Licensed Content Issue	5552
Volume number	295
Issue number	5552
Type of Use	Thesis / Dissertation
Requestor type	Scientist/individual at a research institution
Format	Print and electronic
Portion	Figure
Number of figures/tables	1
Order reference number	
Title of your thesis / dissertation	Structural Modification, Polymerization and Applications of Boron Difluoride Formazanates
Expected completion date	Jun 2017
Estimated size(pages)	300
Requestor Location	Stephanie Barbon

Permission to Reproduce Figure 1.1b:

25/04/2017

RightsLink Printable License

**THE AMERICAN ASSOCIATION FOR THE ADVANCEMENT OF SCIENCE LICENSE
TERMS AND CONDITIONS**

Apr 25, 2017

This Agreement between Stephanie Barbon ("You") and The American Association for the Advancement of Science ("The American Association for the Advancement of Science") consists of your license details and the terms and conditions provided by The American Association for the Advancement of Science and Copyright Clearance Center.

License Number	4096101357939
License date	Apr 25, 2017
Licensed Content Publisher	The American Association for the Advancement of Science
Licensed Content Publication	Science
Licensed Content Title	Bioluminescence in the Ocean: Origins of Biological, Chemical, and Ecological Diversity
Licensed Content Author	E. A. Widder
Licensed Content Date	May 7, 2010
Licensed Content Volume	328
Licensed Content Issue	5979
Volume number	328
Issue number	5979
Type of Use	Thesis / Dissertation
Requestor type	Scientist/individual at a research institution
Format	Print and electronic
Portion	Figure
Number of figures/tables	1
Order reference number	
Title of your thesis / dissertation	Structural Modification, Polymerization and Applications of Boron Difluoride Formazanates
Expected completion date	Jun 2017
Estimated size(pages)	300
Requestor Location	Stephanie Barbon

Permission to Reproduce Figure 1.1c:

**E-JOURNAL**

ISSN: 1091-6490
Publication year(s): 1914 - present
Author/Editor: National Academy of Sciences (U.S.)
Publisher: NATIONAL ACADEMY OF SCIENCES
Rightsholder: NATIONAL ACADEMY OF SCIENCES / PROCEEDINGS

Language: English
Country of publication: United States of America

Academic**Photocopy or share content electronically****LICENSE COVERAGE****Annual Copyright License for Academic Institutions**

This permission type is covered. The Annual Copyright License authorizes the licensee's faculty, staff, students, and other authorized users to distribute print and electronic copies of copyrighted content within your institution through:

- Print or electronic coursepacks
- Classroom handouts
- Electronic reserves
- Institution Intranets
- Course/Learning Management systems (CMS/LMS)
- CD-ROM/DVD
- Other internal academic uses

The description above is provided for summary purposes only. Please refer to your institution's Annual Copyright License for the complete terms and conditions and scope of coverage of the license.

Covered by CCC Annual License - Academic

Permission to Reproduce Figure 1.1d:

Dear Ms. Barbon,

On behalf of the American Museum of Natural History, you are hereby granted nonexclusive world rights in all languages, and in any future editions, revisions, or translations to reproduce Figure 2 from the following paper in the introduction of your doctoral thesis:

Gruber, David F. and Sparks, John S. (2015). First observation of fluorescence in marine turtles. American Museum Novitates, 3845; New York : American Museum of Natural History.

We would appreciate if you could include the full citation for this content.

Best,
Mai

Mai Reitmeyer
 Sr. Research Services Librarian
 Department of Library Services
 American Museum of Natural History
 Central Park West @ 79th St.
 New York, NY 10024
 phone: (212) 313-7593
 fax: (212) 769-5009
<http://.../OWA/redir.aspx?C=3c45add588ad40c899a04a9cd4b779c8&URL=http%3a%2f%2flibrary.amnh.org>

<http://.../OWA/redir.aspx?C=3c45add588ad40c899a04a9cd4b779c8&URL=http%3a%2f%2flibrary.amnh.org>

Permission to Reproduce Figure 1.1e:

PLOS applies the [Creative Commons Attribution \(CC BY\) license](#) to articles and other works we publish. If you submit your paper for publication by PLOS, you agree to have the CC BY license applied to your work. Under this Open Access license, you as the author agree that anyone can reuse your article in whole or part for any purpose, for free, even for commercial purposes. Anyone may copy, distribute, or reuse the content as long as the author and original source are properly cited. This facilitates freedom in re-use and also ensures that PLOS content can be mined without barriers for the needs of research.

Permission to Reproduce Figure 1.3:

25/04/2017

RightsLink Printable License

JOHN WILEY AND SONS LICENSE TERMS AND CONDITIONS

Apr 25, 2017

This Agreement between Stephanie Barbon ("You") and John Wiley and Sons ("John Wiley and Sons") consists of your license details and the terms and conditions provided by John Wiley and Sons and Copyright Clearance Center.

License Number	4096110211830
License date	Apr 25, 2017
Licensed Content Publisher	John Wiley and Sons
Licensed Content Publication	Chemistry - A European Journal
Licensed Content Title	Conformationally Restricted Dipyrrromethene Boron Difluoride (BODIPY) Dyes: Highly Fluorescent, Multicolored Probes for Cellular Imaging
Licensed Content Author	Qingdong Zheng, Gaixia Xu, Paras N. Prasad
Licensed Content Date	May 21, 2008
Licensed Content Pages	8
Type of use	Dissertation/Thesis
Requestor type	University/Academic
Format	Print and electronic
Portion	Figure/table
Number of figures/tables	1
Original Wiley figure/table number(s)	Figure 7
Will you be translating?	No
Title of your thesis / dissertation	Structural Modification, Polymerization and Applications of Boron Difluoride Formazanates
Expected completion date	Jun 2017
Expected size (number of pages)	300
Requestor Location	Stephanie Barbon

Permission to Reproduce Figure 1.4:





Home Account Info Help 

Title: Spacer-free BODIPY fluorogens in antimicrobial peptides for direct imaging of fungal infection in human tissue

Author: Lorena Mendive-Tapia, Can Zhao, Ahsan R. Akram, Sara Preciado, Fernando Albericio et al.

Publication: Nature Communications

Publisher: Nature Publishing Group

Date: Mar 9, 2016

Copyright © 2016, Rights Managed by Nature Publishing Group

Logged in as:
Stephanie Barbon
Account #:
3001143867

LOGOUT

Creative Commons




The article for which you have requested permission has been distributed under a Creative Commons CC-BY license (please see the article itself for the license version number). You may reuse this material without obtaining permission from Nature Publishing Group, providing that the author and the original source of publication are fully acknowledged, as per the terms of the license.


For license terms, please see <http://creativecommons.org/>

CLOSE WINDOW

Permission to Reproduce Figure 1.5:

25/04/2017 RightsLink® by Copyright Clearance Center



[Home](#) [Account Info](#) [Help](#) 


Title: Ultralow-Power Near Infrared Lamp Light Operable Targeted Organic Nanoparticle Photodynamic Therapy

Author: Ling Huang, Zhanjun Li, Yang Zhao, et al

Publication: Journal of the American Chemical Society

Publisher: American Chemical Society

Date: Nov 1, 2016

Copyright © 2016, American Chemical Society

Logged in as: Stephanie Barbon [Logout](#)

PERMISSION/LICENSE IS GRANTED FOR YOUR ORDER AT NO CHARGE

This type of permission/license, instead of the standard Terms & Conditions, is sent to you because no fee is being charged for your order. Please note the following:

- Permission is granted for your request in both print and electronic formats, and translations.
- If figures and/or tables were requested, they may be adapted or used in part.
- Please print this page for your records and send a copy of it to your publisher/graduate school.
- Appropriate credit for the requested material should be given as follows: "Reprinted (adapted) with permission from (COMPLETE REFERENCE CITATION). Copyright (YEAR) American Chemical Society." Insert appropriate information in place of the capitalized words.
- One-time permission is granted only for the use specified in your request. No additional uses are granted (such as derivative works or other editions). For any other uses, please submit a new request.

If credit is given to another source for the material you requested, permission must be obtained from that source.

[BACK](#) [CLOSE WINDOW](#)

Copyright © 2017 Copyright Clearance Center, Inc. All Rights Reserved. [Privacy statement](#), [Terms and Conditions](#). Comments? We would like to hear from you. E-mail us at customer@copyright.com

Permission to Reproduce Figure 1.6:

25/04/2017

RightsLink Printable License

**NATURE PUBLISHING GROUP LICENSE
TERMS AND CONDITIONS**

Apr 25, 2017

This Agreement between Stephanie Barbon ("You") and Nature Publishing Group ("Nature Publishing Group") consists of your license details and the terms and conditions provided by Nature Publishing Group and Copyright Clearance Center.

License Number	4096110465121
License date	Apr 25, 2017
Licensed Content Publisher	Nature Publishing Group
Licensed Content Publication	Nature Communications
Licensed Content Title	Colour-tunable fluorescent multiblock micelles
Licensed Content Author	Zachary M. Hudson, David J. Lunn, Mitchell A. Winnik, Ian Manners
Licensed Content Date	Mar 5, 2014
Licensed Content Volume	5
Type of Use	reuse in a dissertation / thesis
Requestor type	academic/educational
Format	print and electronic
Portion	figures/tables/illustrations
Number of figures/tables/illustrations	1
High-res required	no
Figures	Figure 2
Author of this NPG article	no
Your reference number	
Title of your thesis / dissertation	Structural Modification, Polymerization and Applications of Boron Difluoride Formazanates
Expected completion date	Jun 2017
Estimated size (number of pages)	300
Requestor Location	Stephanie Barbon

Permission to Reproduce Figure 1.7:

26/04/2017

RightsLink Printable License

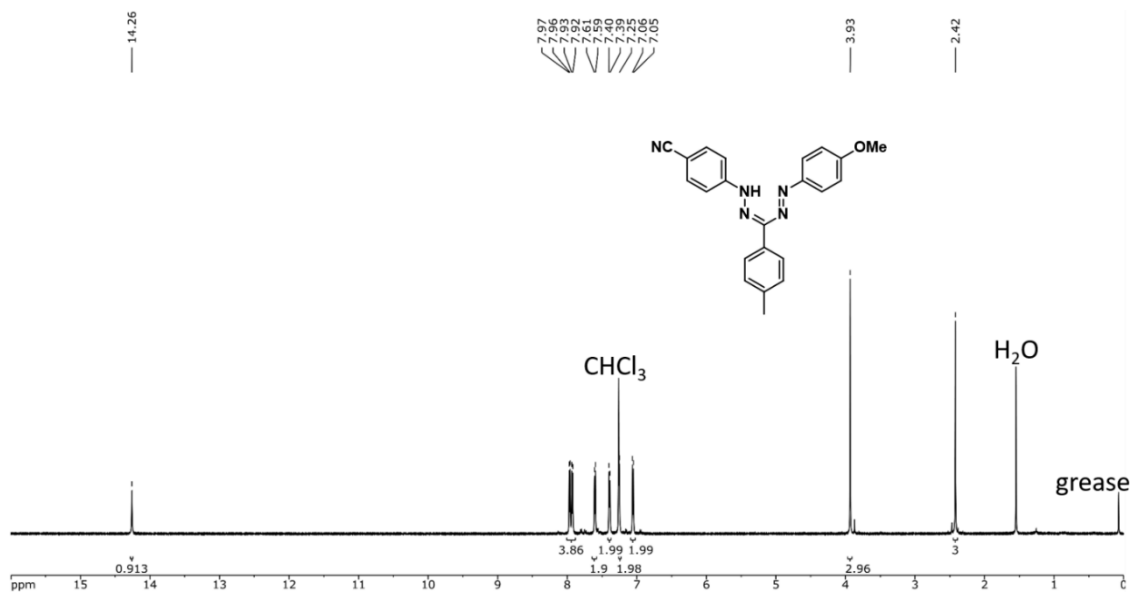
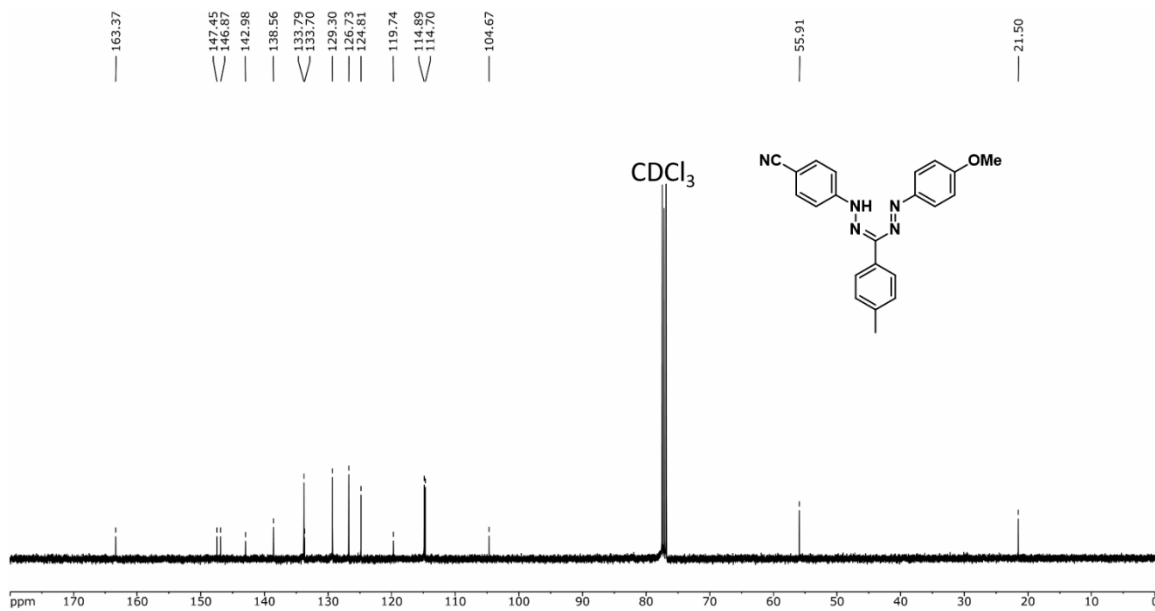
SPRINGER LICENSE TERMS AND CONDITIONS

Apr 26, 2017

This Agreement between Stephanie Barbon ("You") and Springer ("Springer") consists of your license details and the terms and conditions provided by Springer and Copyright Clearance Center.

License Number	4096500728593
License date	Apr 26, 2017
Licensed Content Publisher	Springer
Licensed Content Publication	Springer eBook
Licensed Content Title	Cell Sensitivity Assays: The MIT Assay
Licensed Content Author	Johan van Meerloo
Licensed Content Date	Jan 1, 2011
Type of Use	Thesis/Dissertation
Portion	Figures/tables/illustrations
Number of figures/tables/illustrations	1
Author of this Springer article	No
Order reference number	
Original figure numbers	Figure 1
Title of your thesis / dissertation	Structural Modification, Polymerization and Applications of Boron Difluoride Formazanates
Expected completion date	Jun 2017
Estimated size(pages)	300
Requestor Location	Stephanie Barbon

Appendix A2 Supporting Information for Chapter 2

Figure A2.1 ^1H NMR spectrum of 2.8g in CDCl_3 .Figure A2.2 $^{13}\text{C}\{^1\text{H}\}$ NMR spectrum of 2.8g in CDCl_3 .

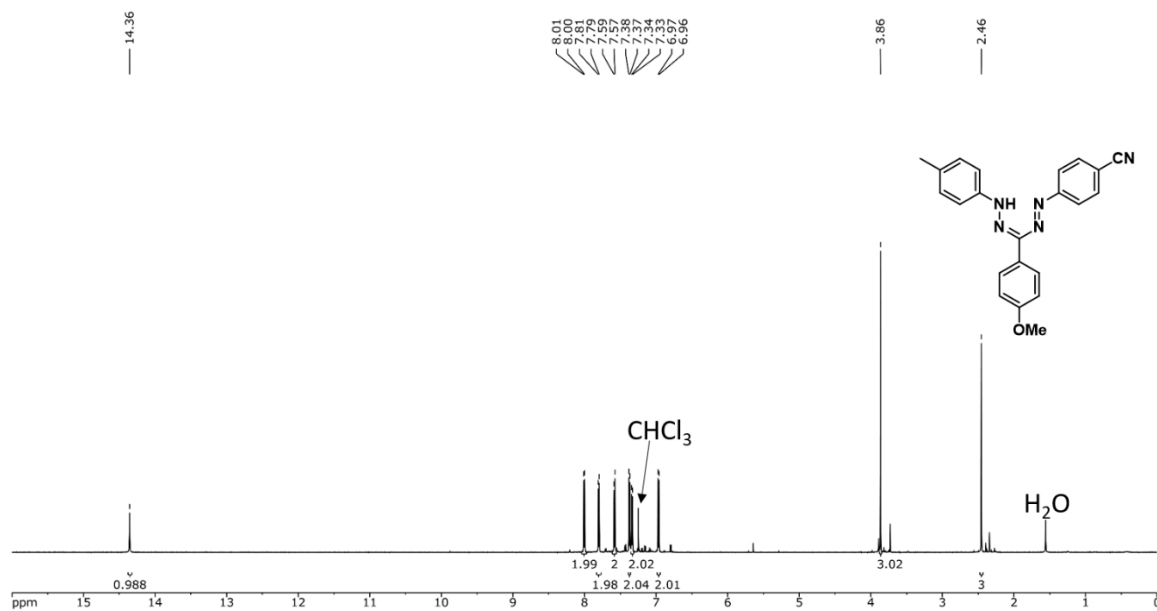


Figure A2.3 ^1H NMR spectrum of **2.8h** in CDCl_3 .

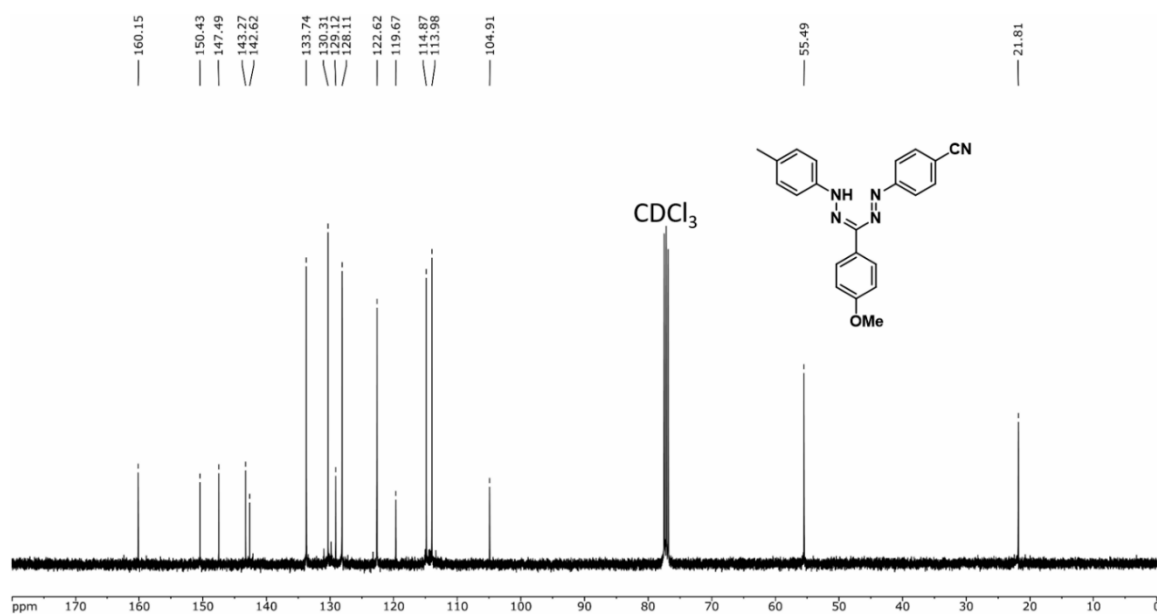


Figure A2.4 $^{13}\text{C}\{^1\text{H}\}$ NMR spectrum of **2.8h** in CDCl_3 .

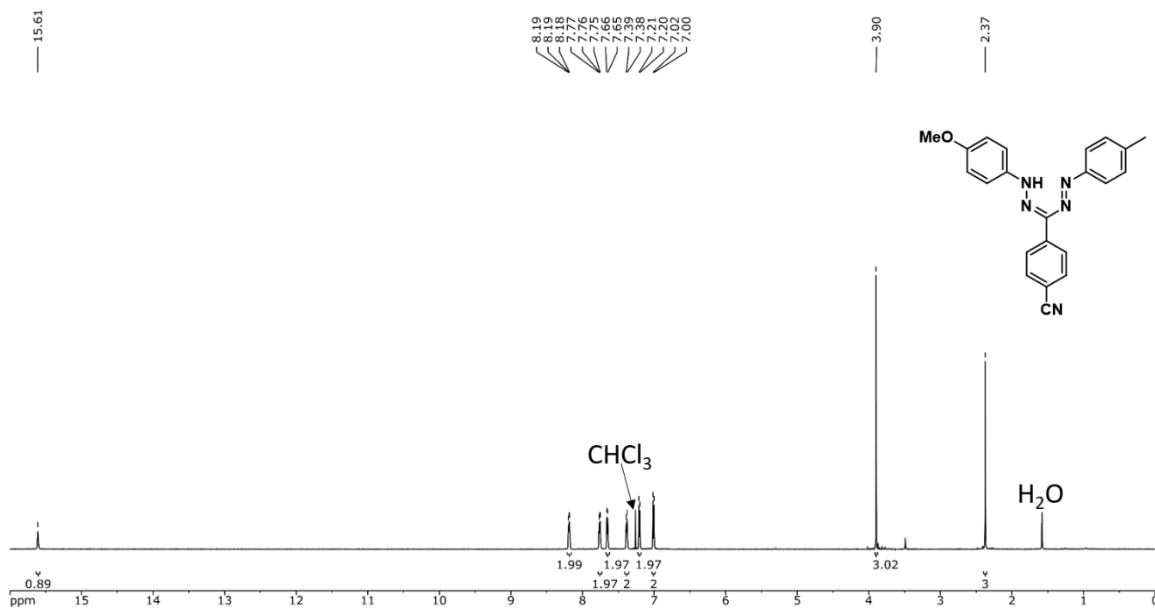


Figure A2.5 ^1H NMR spectrum of 2.8i in CDCl_3 .

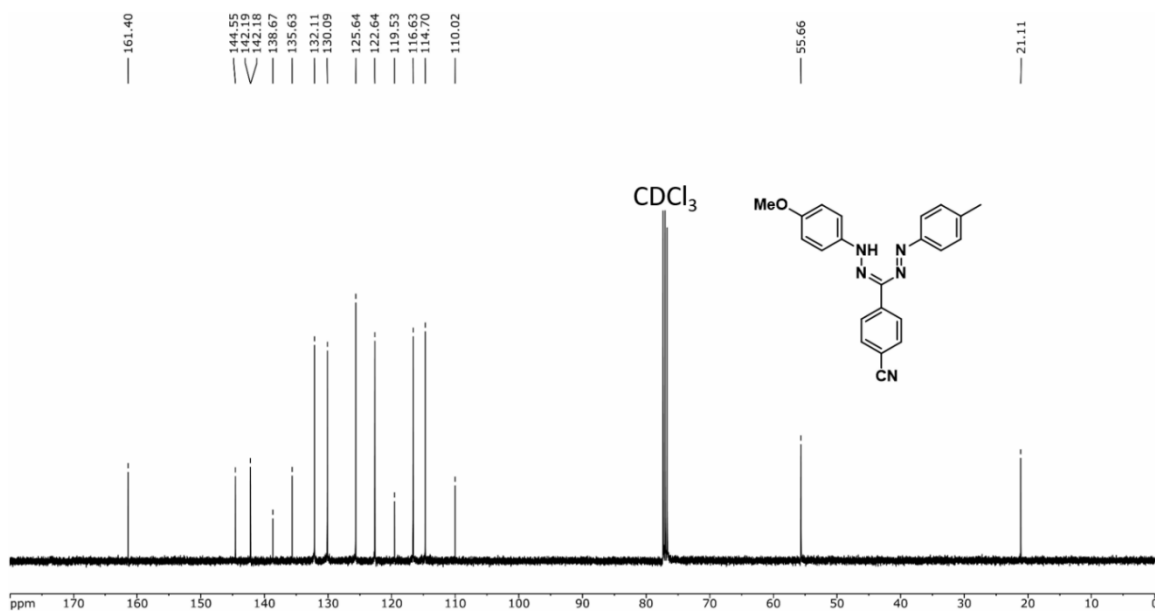


Figure A2.6 $^{13}\text{C}\{^1\text{H}\}$ NMR spectrum of 2.8i in CDCl_3 .

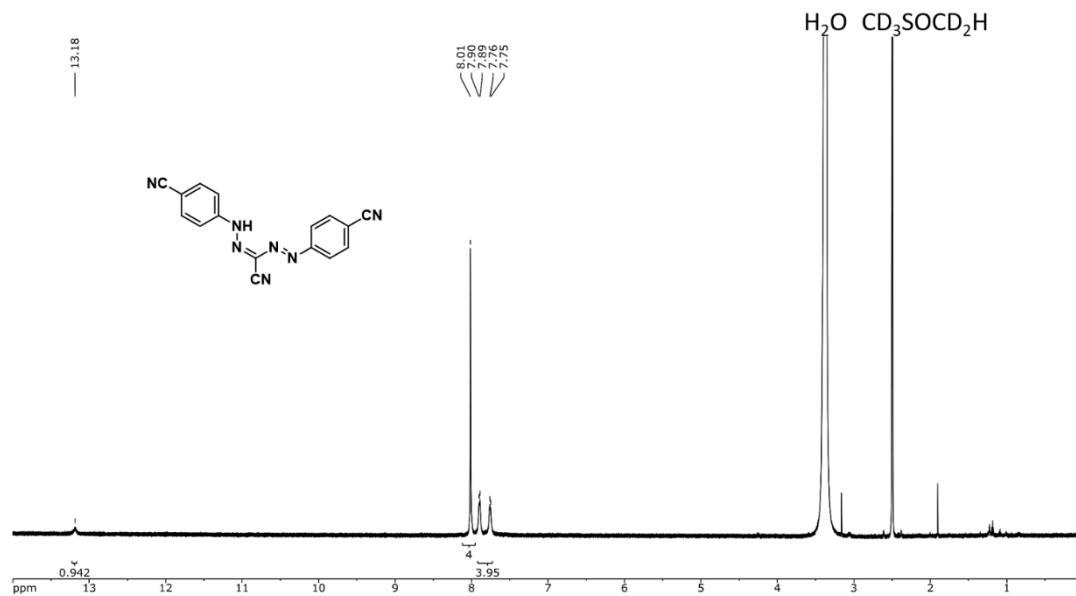


Figure A2.7 ^1H NMR spectrum of 2.8k in d_6 -DMSO.

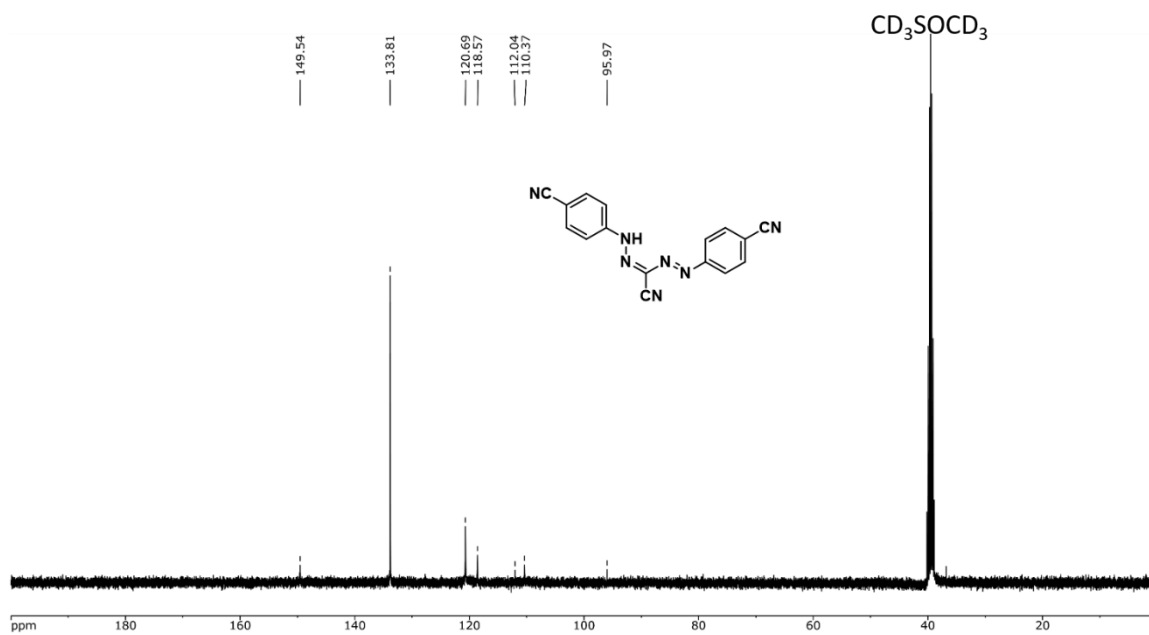


Figure A2.8 $^{13}\text{C}\{^1\text{H}\}$ NMR spectrum of 2.8k in d_6 -DMSO.

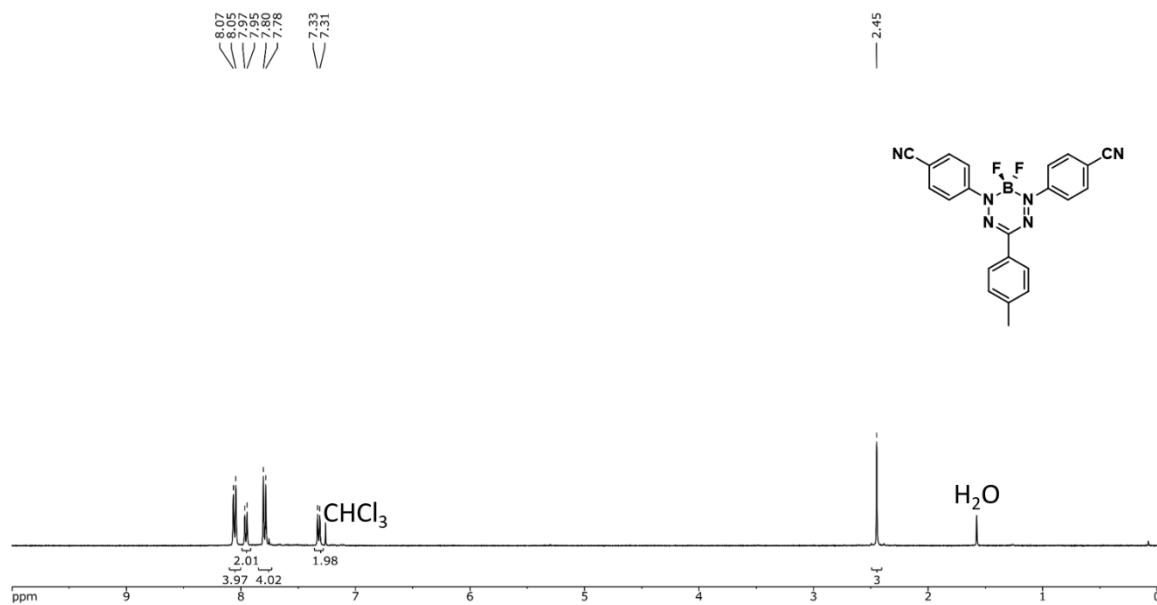


Figure A2.9 ^1H NMR spectrum of 2.13b in CDCl_3 .

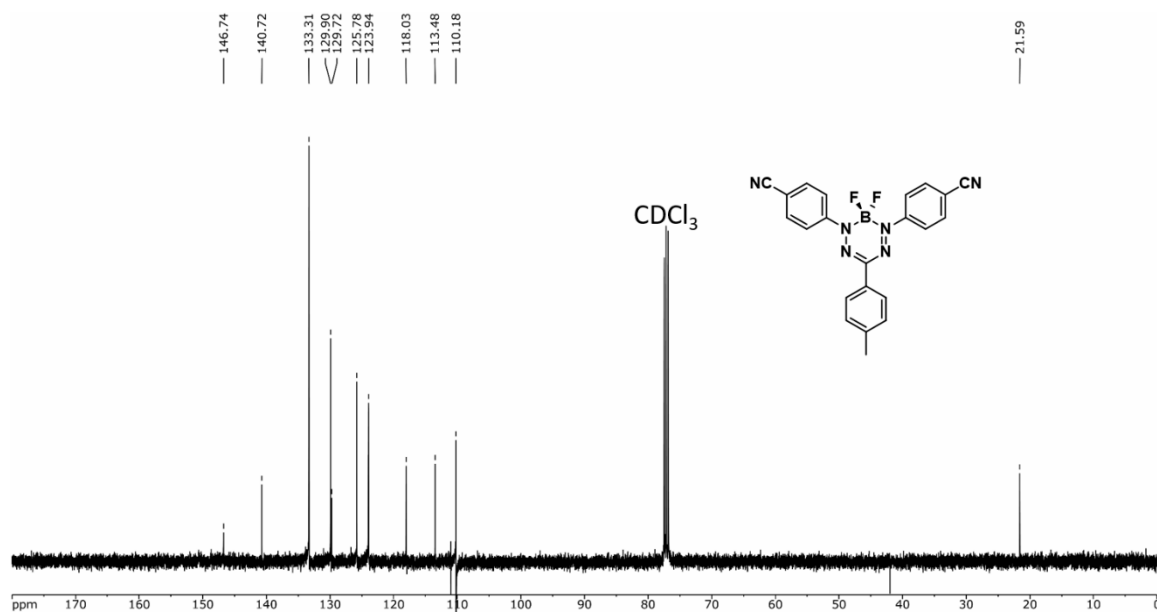
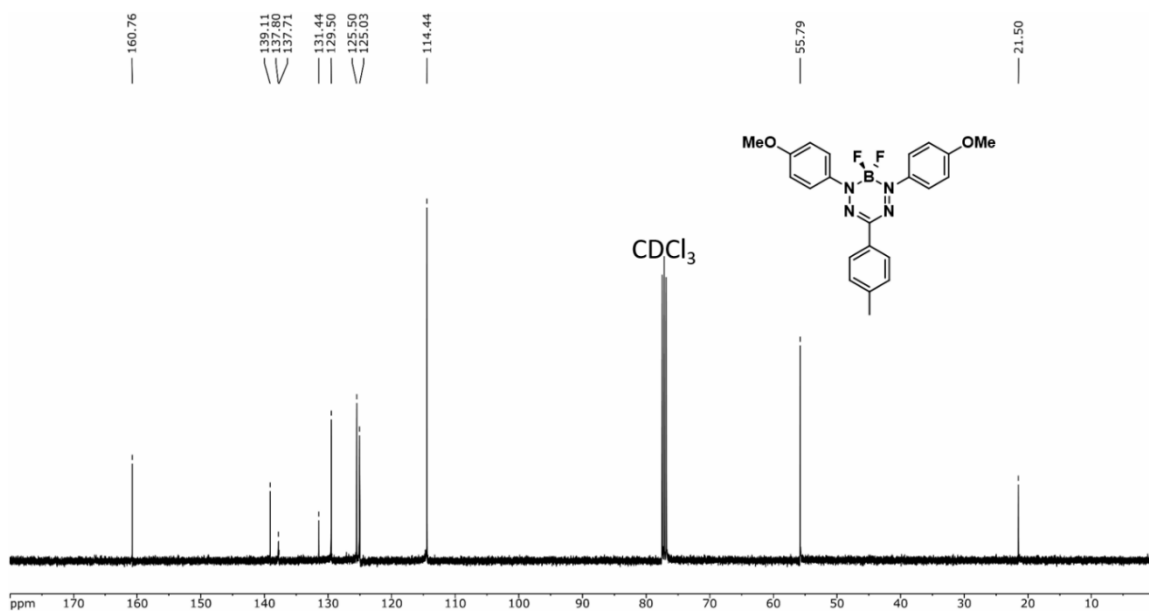
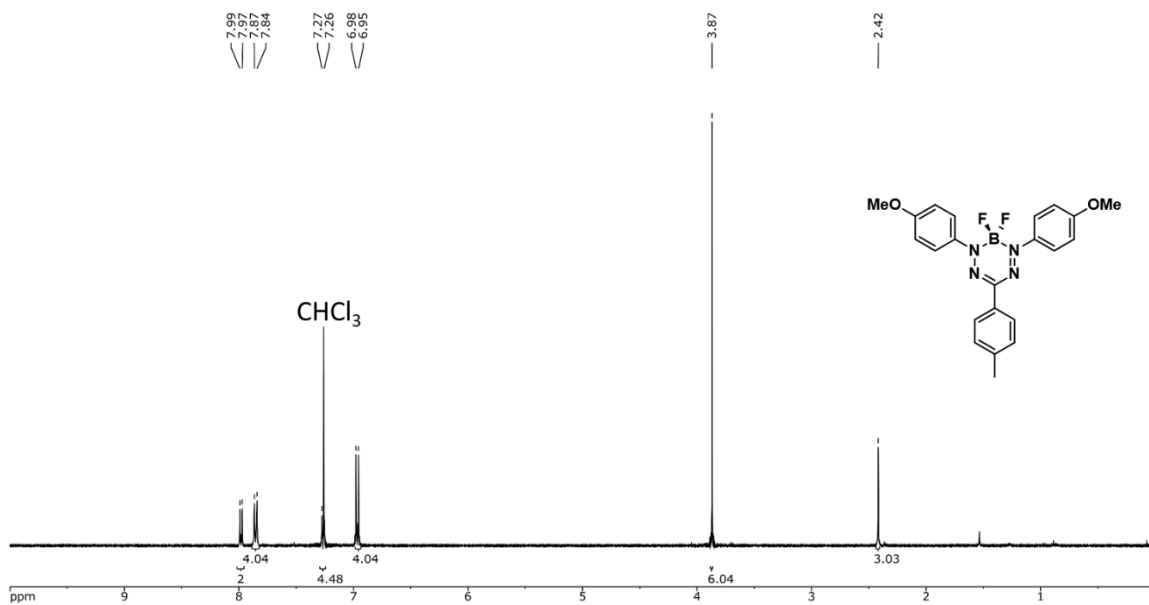


Figure A2.10 $^{13}\text{C}\{^1\text{H}\}$ NMR spectrum of 2.13b in CDCl_3 .



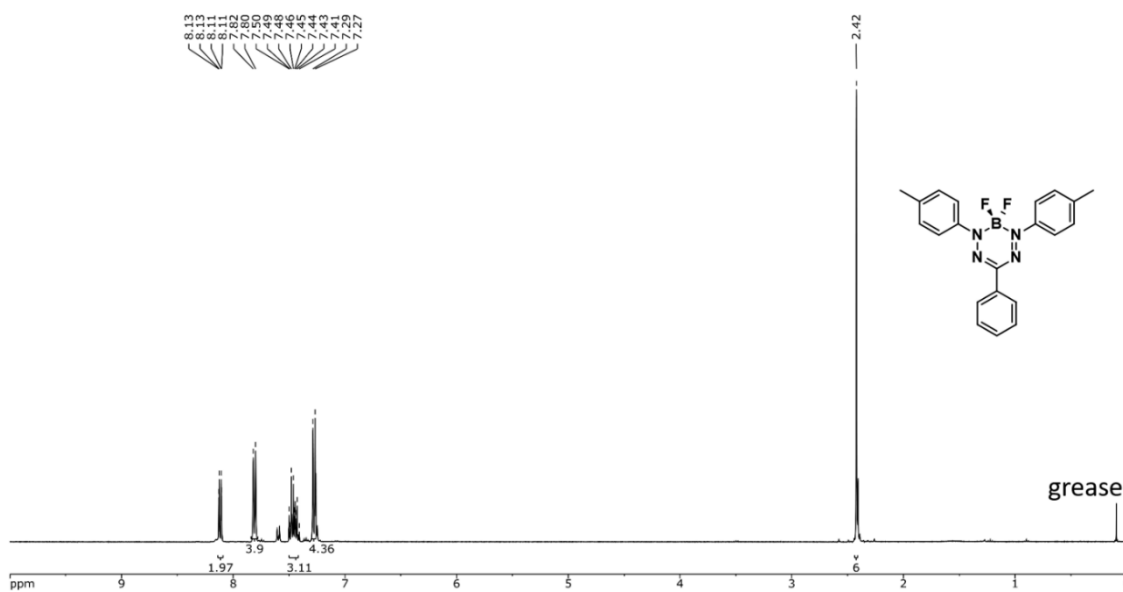


Figure A2.13 ^1H NMR spectrum of 2.13d in CDCl_3 .

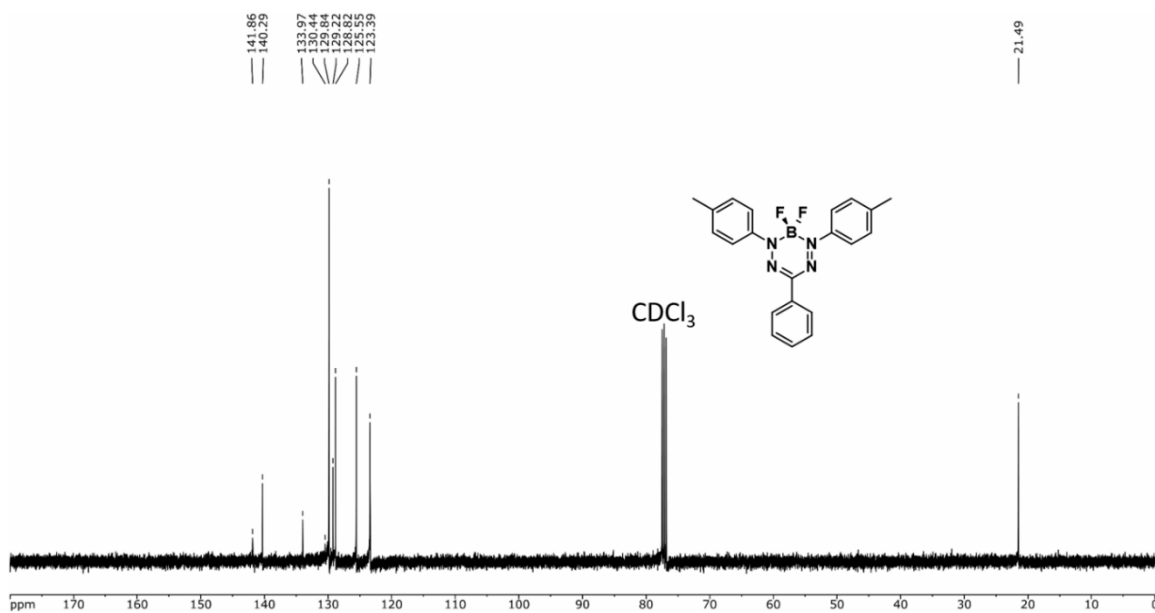


Figure A2.14 $^{13}\text{C}\{^1\text{H}\}$ NMR spectrum of 2.13d in CDCl_3 .

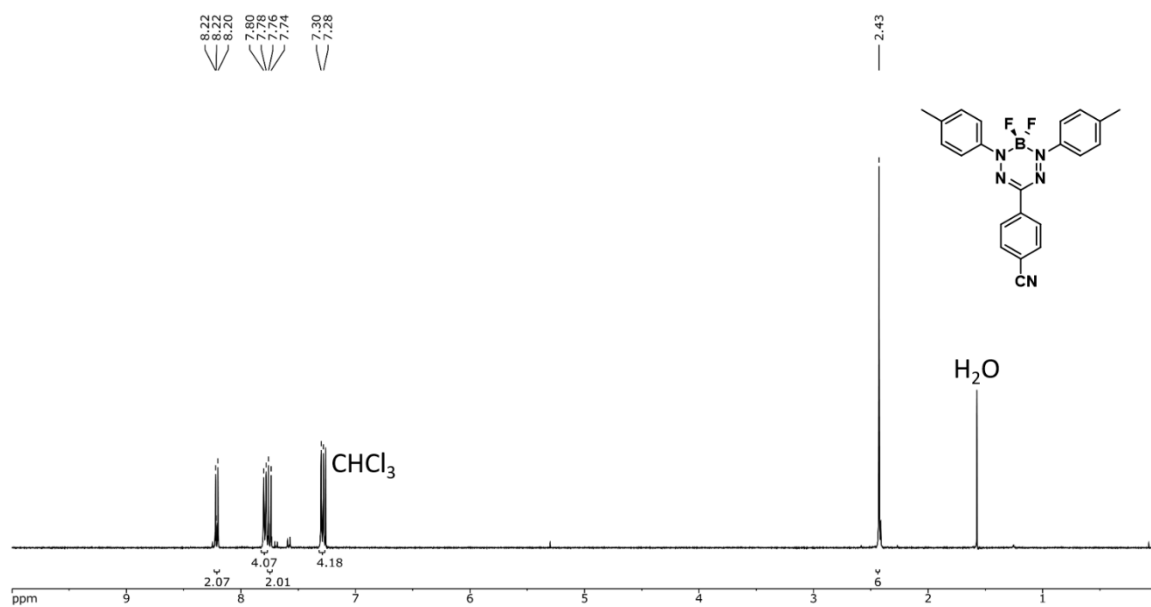


Figure A2.15 ^1H NMR spectrum of **2.13e** in CDCl_3 .

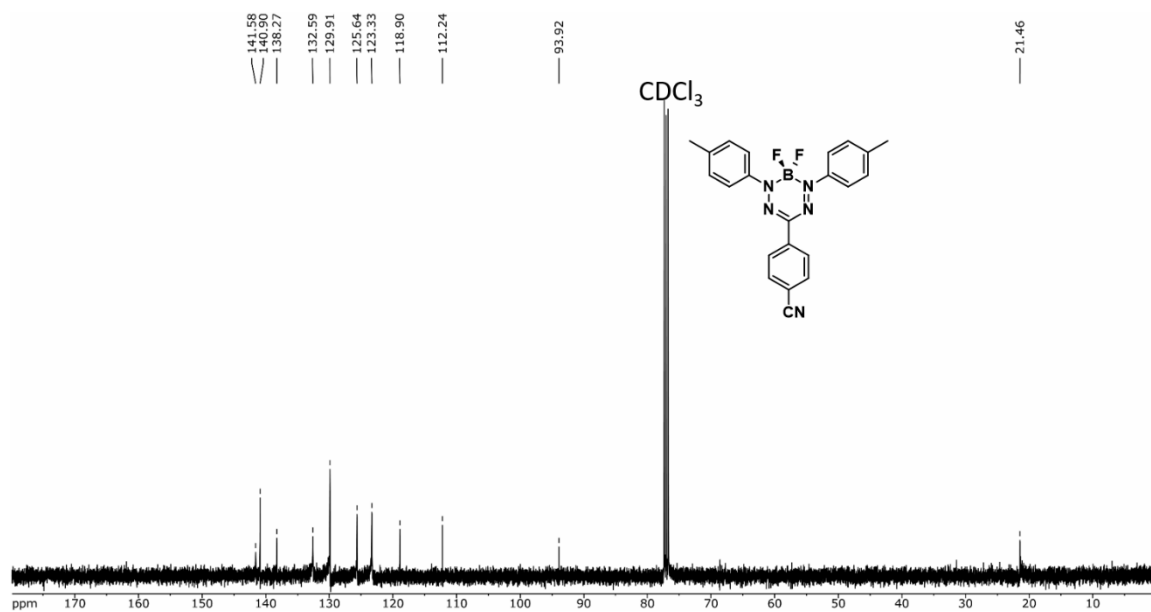


Figure A2.16 $^{13}\text{C}\{^1\text{H}\}$ NMR spectrum of **2.13e** in CDCl_3 .

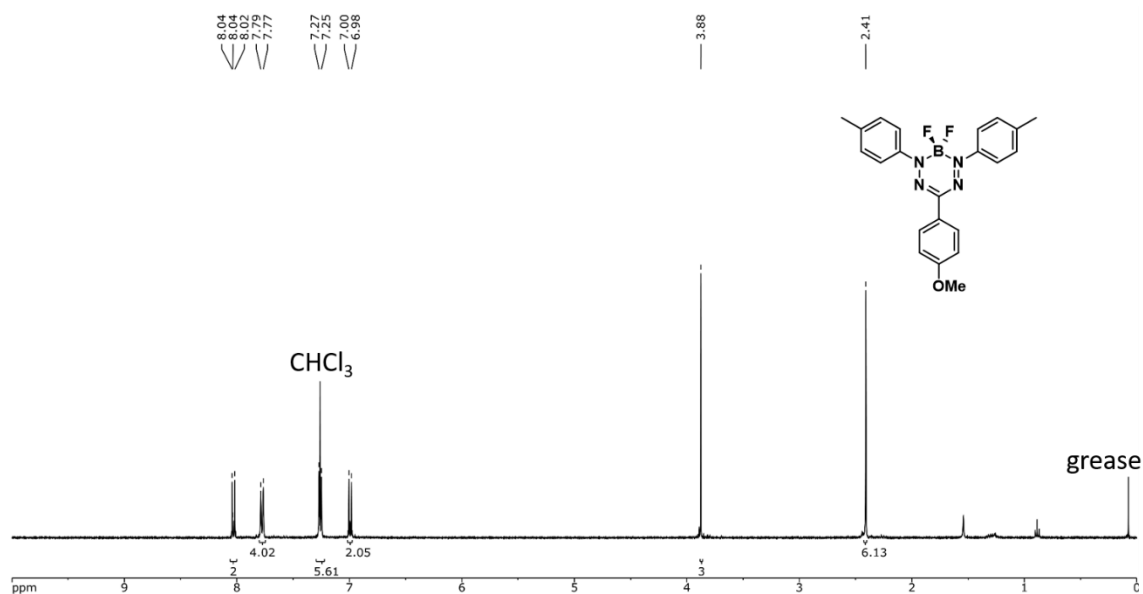


Figure A2.17 ^1H NMR spectrum of 2.13f in CDCl_3 .

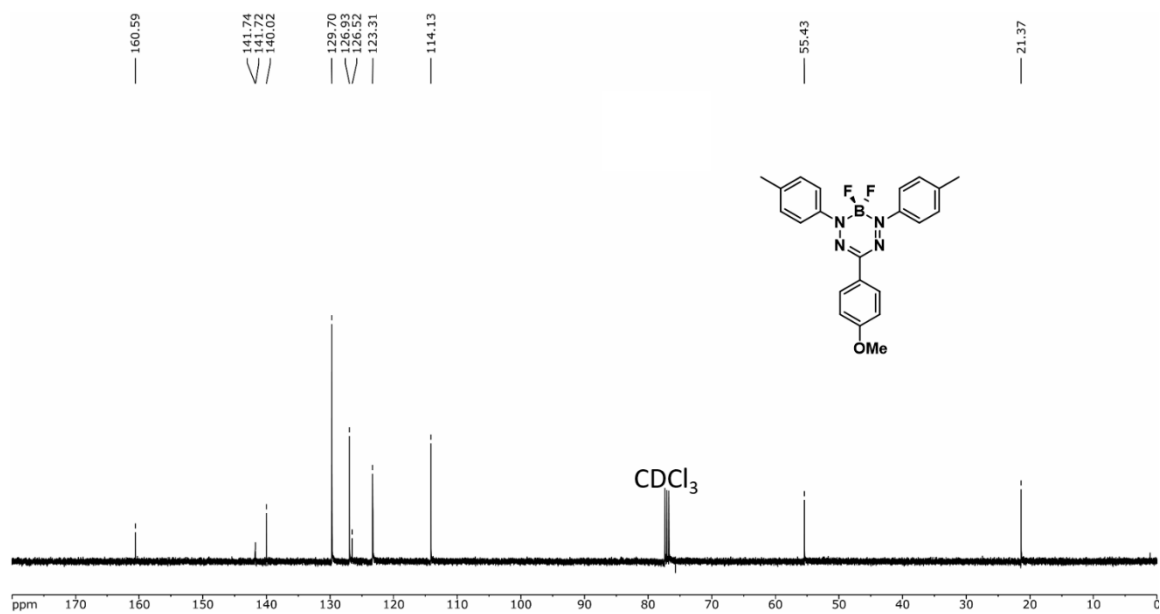


Figure A2.18 $^{13}\text{C}\{^1\text{H}\}$ NMR spectrum of 2.13f in CDCl_3 .

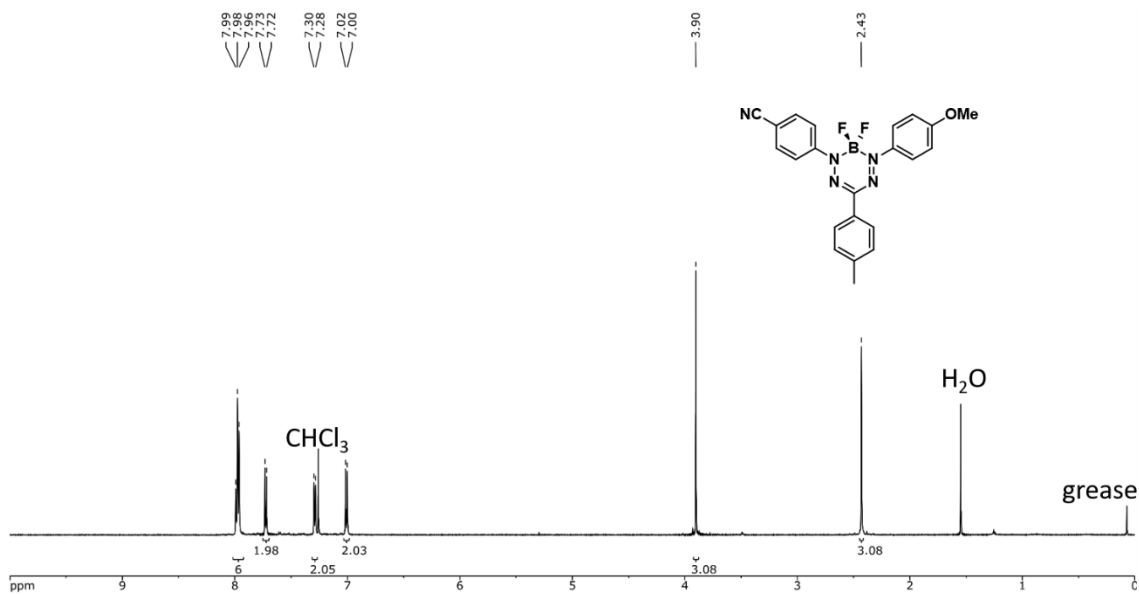


Figure A2.19 ^1H NMR spectrum of 2.13g in CDCl_3 .

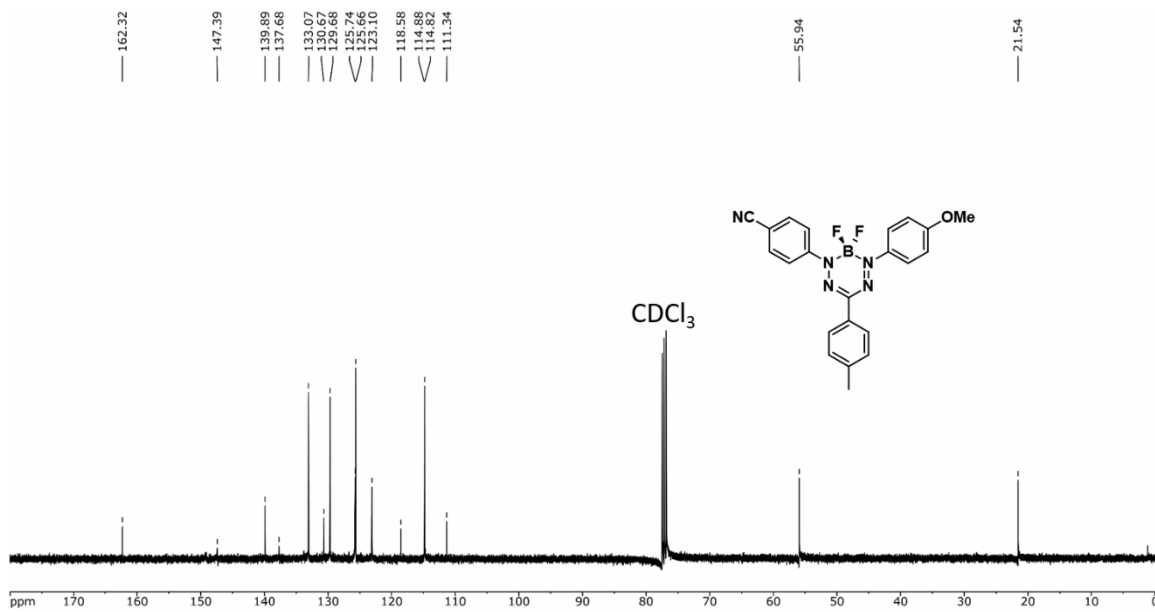


Figure A2.20 $^{13}\text{C}\{^1\text{H}\}$ NMR spectrum of 2.13g in CDCl_3 .

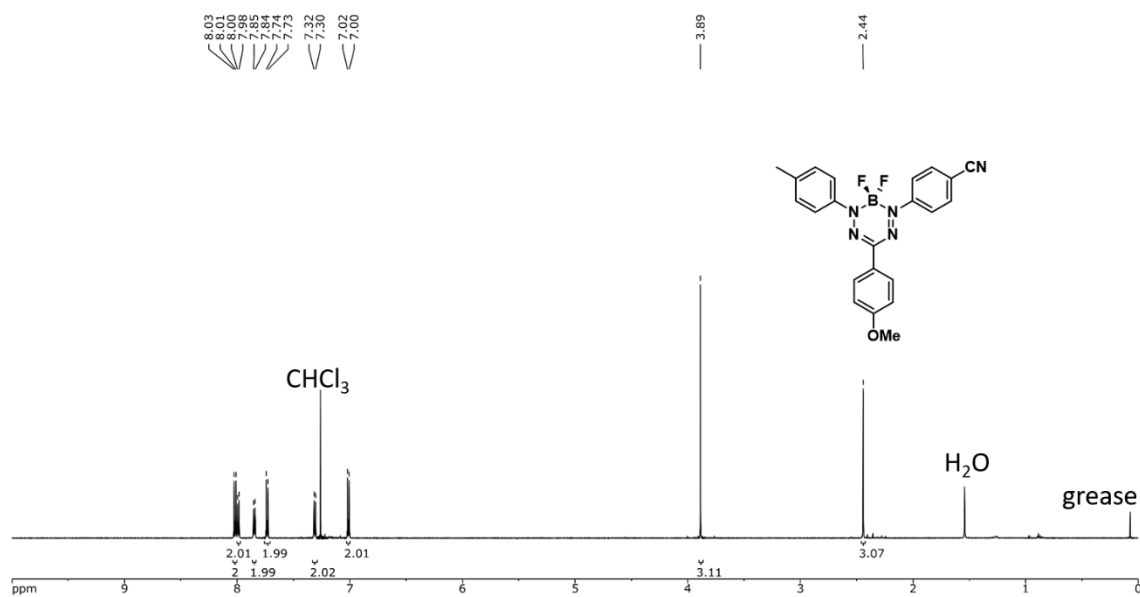


Figure A2.21 ^1H NMR spectrum of **2.13h** in CDCl_3 .

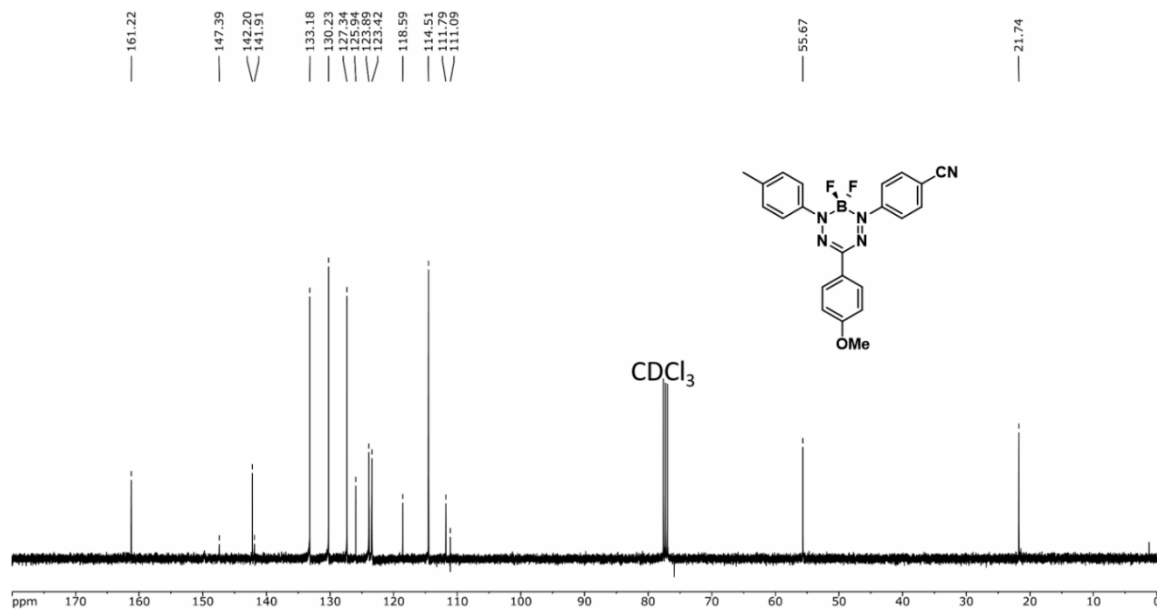


Figure A2.22 $^{13}\text{C}\{^1\text{H}\}$ NMR spectrum of **2.13h** in CDCl_3 .

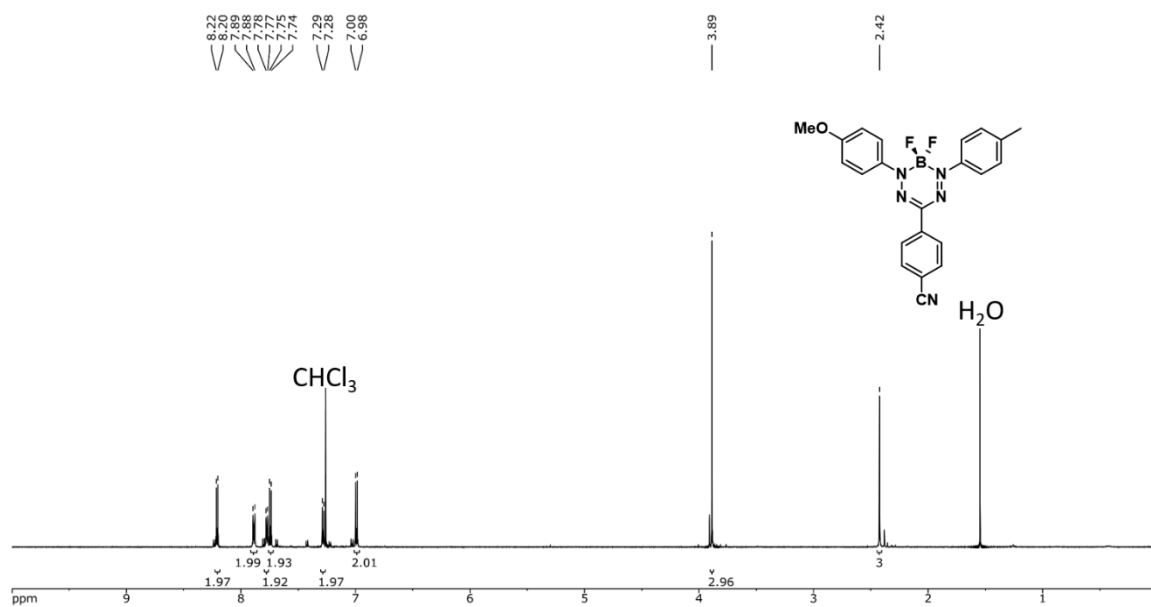


Figure A2.23 ^1H NMR spectrum of **2.13i** in CDCl_3 .

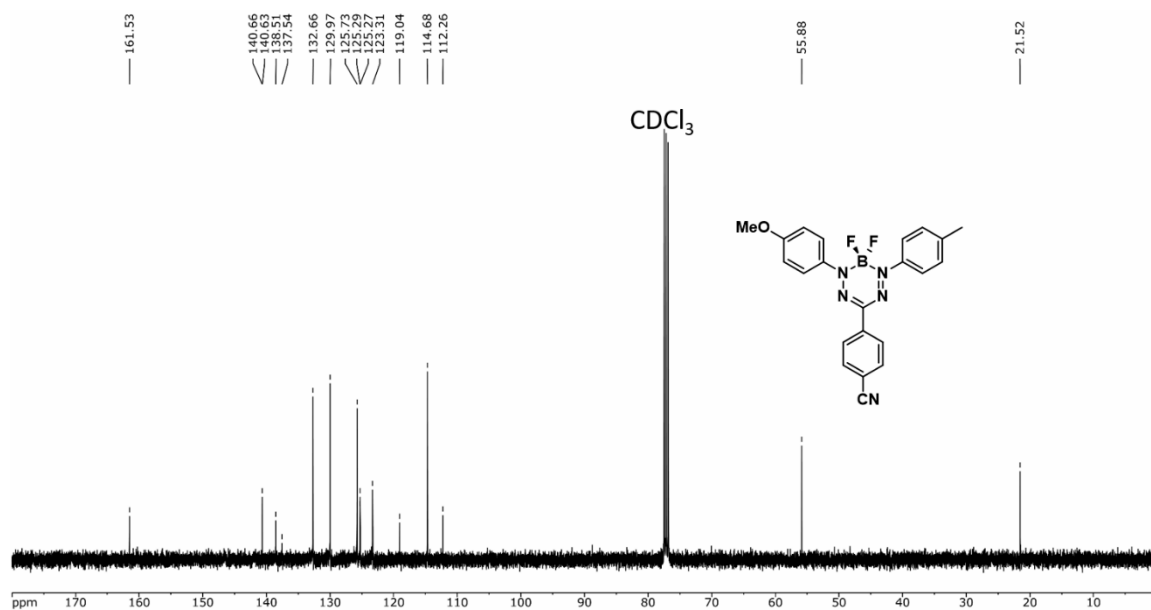


Figure A2.24 $^{13}\text{C}\{^1\text{H}\}$ NMR spectrum of **2.13i** in CDCl_3 .

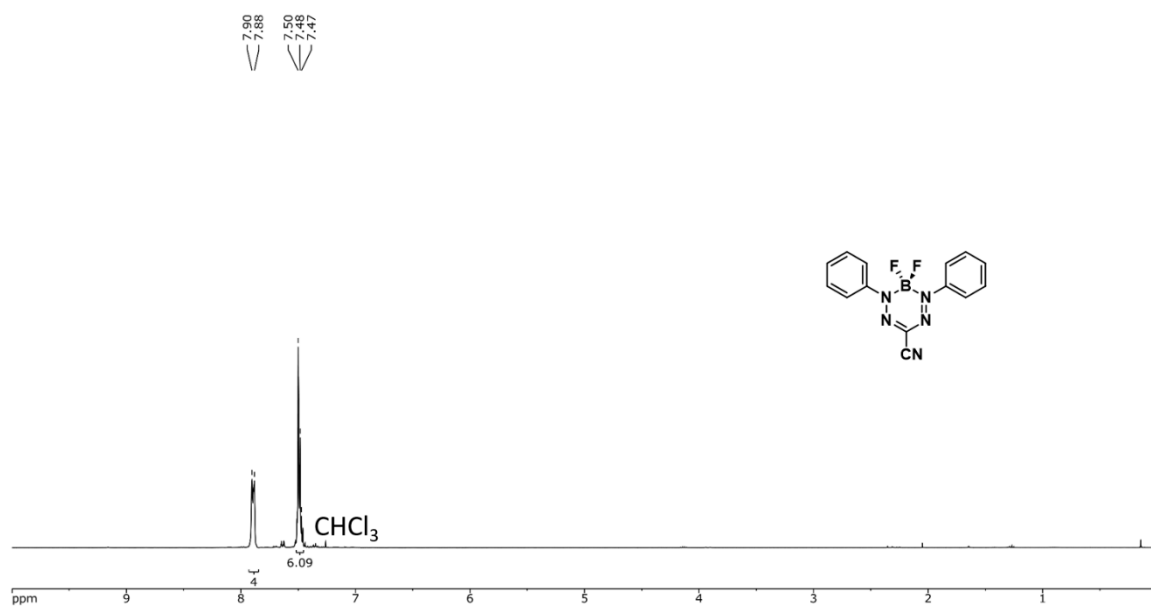


Figure A2.25 $^1\text{H NMR}$ spectrum of **2.13j** in CDCl_3 .

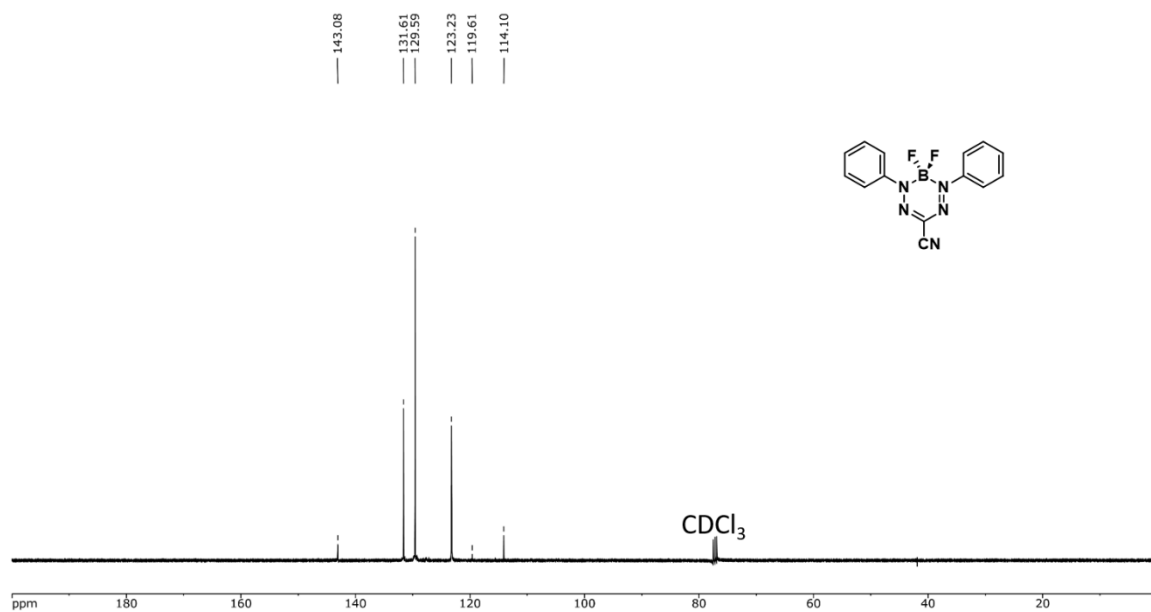


Figure A2.26 $^{13}\text{C}\{^1\text{H}\}$ NMR spectrum of **2.13j** in CDCl_3 .

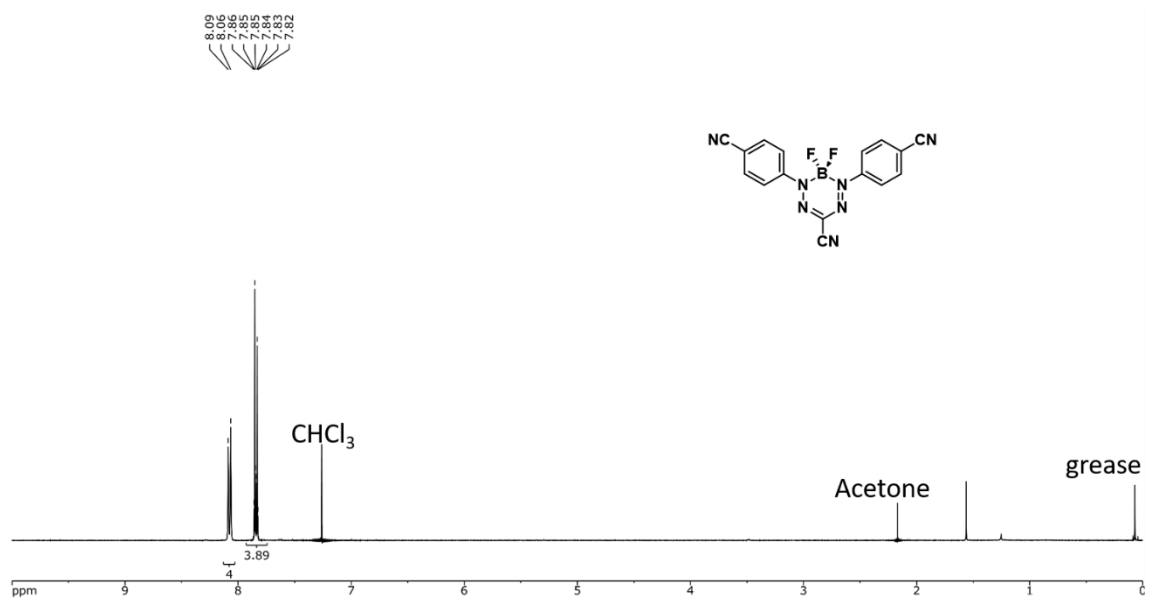


Figure A2.27 ^1H NMR spectrum of 2.13k in CDCl_3 .

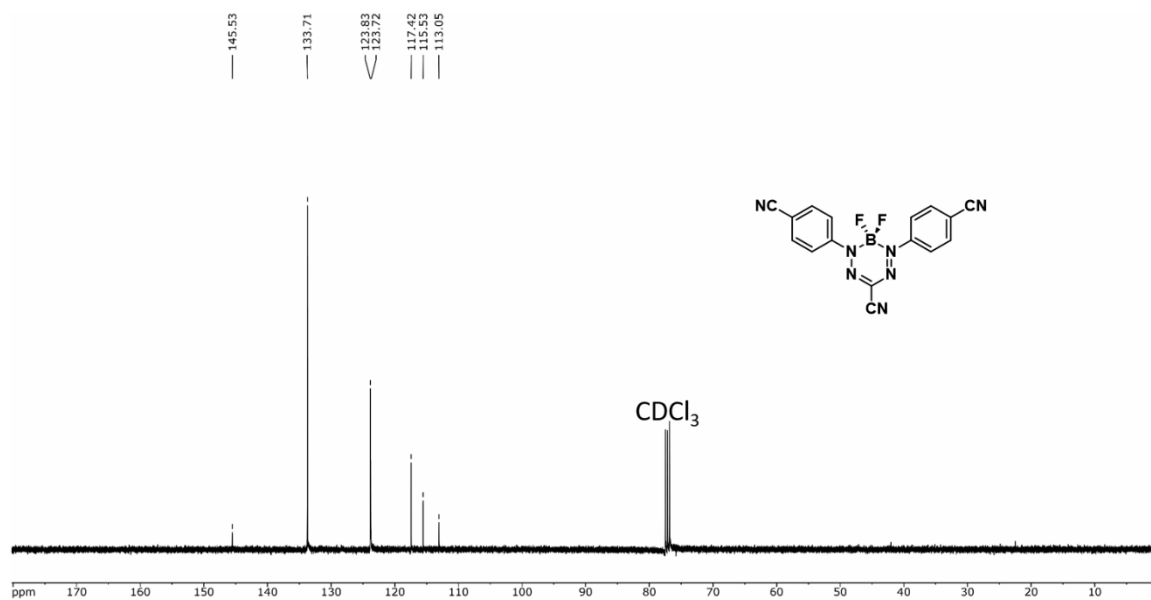


Figure A2.28 $^{13}\text{C}\{^1\text{H}\}$ NMR spectrum of 2.13k in CDCl_3 .

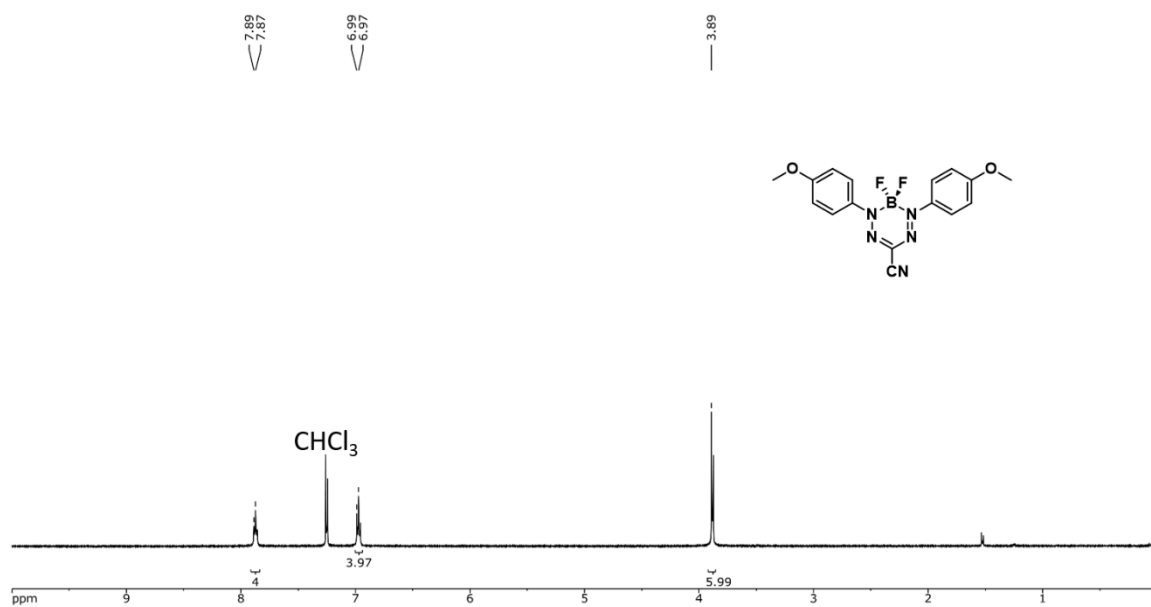


Figure A2.29 ^1H NMR spectrum of 2.131 in CDCl_3 .

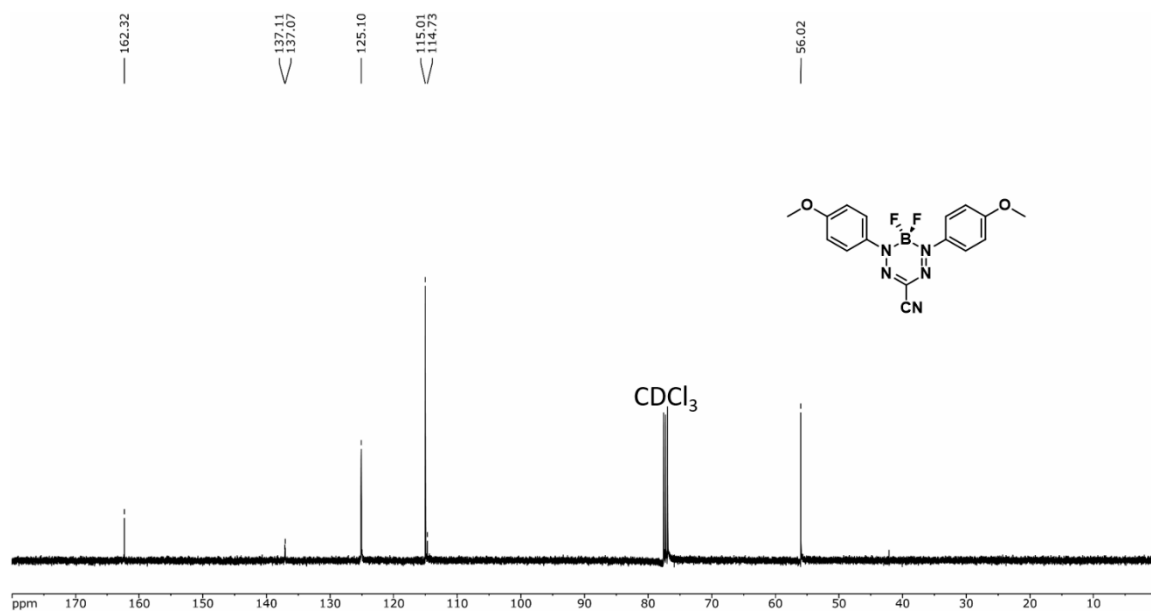


Figure A2.30 $^{13}\text{C}\{^1\text{H}\}$ NMR spectrum of 2.131 in CDCl_3 .

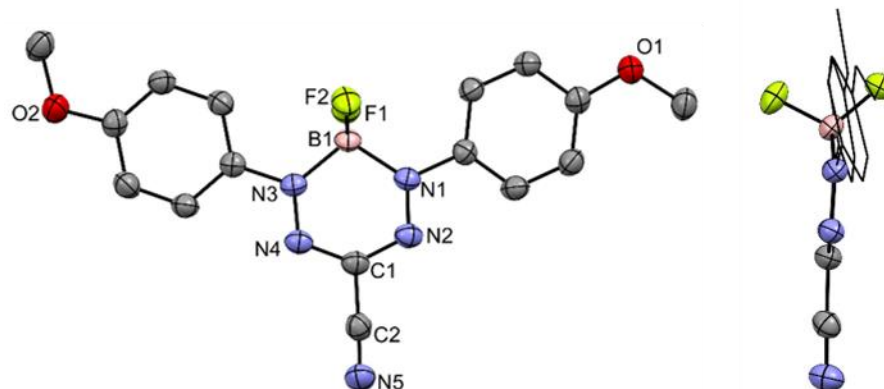


Figure A2.31 Solid-state structure of flat conformation of **2.13I**. Thermal ellipsoids are shown at 50% probability and hydrogen atoms have been removed for clarity.

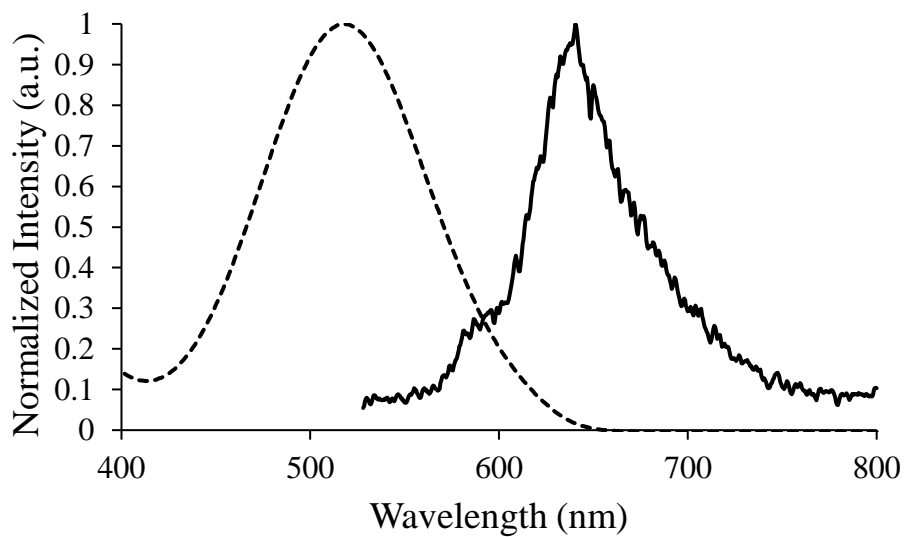


Figure A2.32 Normalized UV-vis absorption spectrum (dashed) and emission spectrum (solid) of **2.13a** in 10^{-5} M degassed toluene solution.

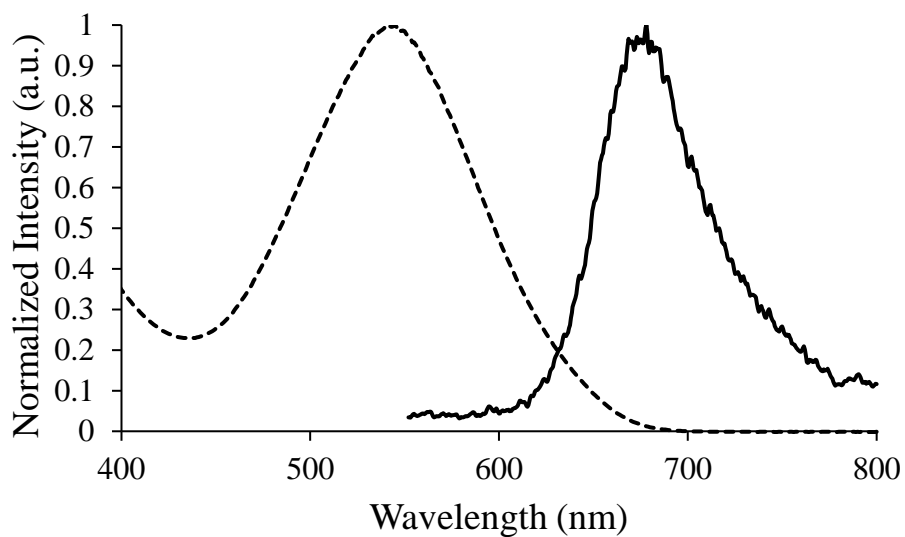


Figure A2.33 Normalized UV-vis absorption spectrum (dashed) and emission spectrum (solid) of **2.13b** in 10^{-5} M degassed toluene solution.

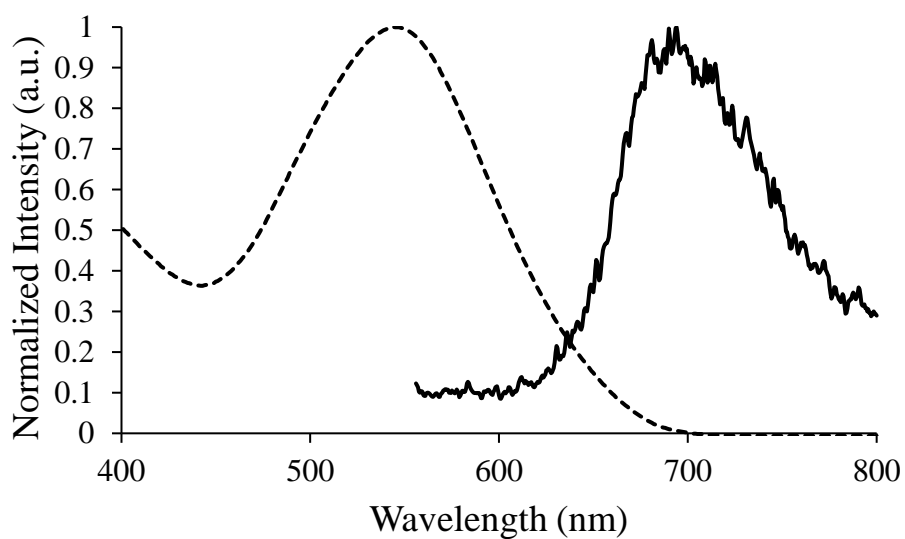


Figure A2.34 Normalized UV-vis absorption spectrum (dashed) and emission spectrum (solid) of **2.13c** in 10^{-5} M degassed toluene solution.

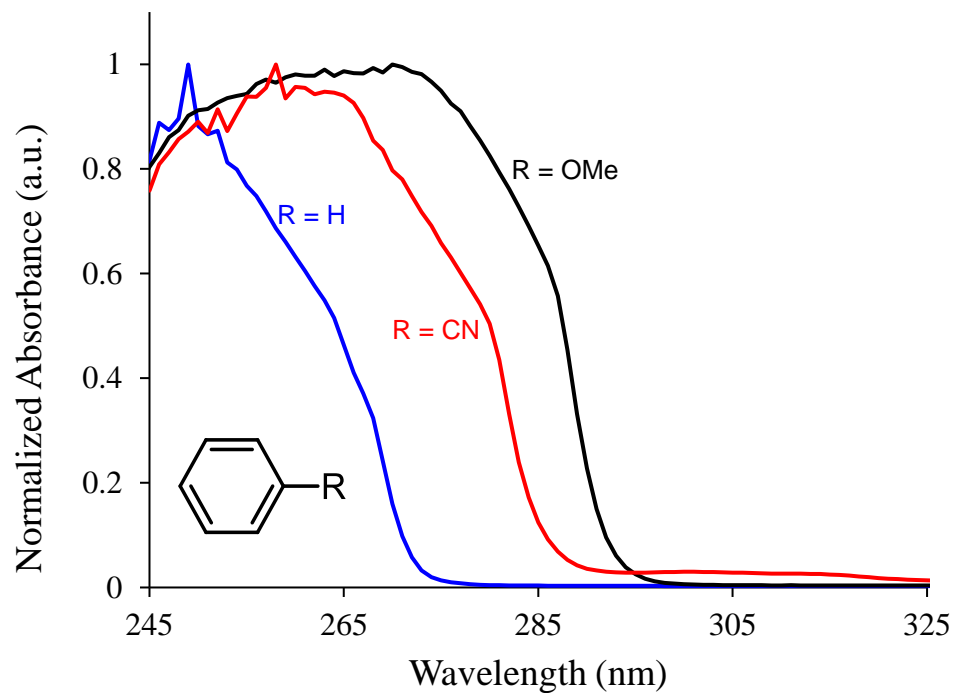


Figure A2.35 Normalized UV-vis absorption spectra of benzene, benzonitrile, and anisole in THF.

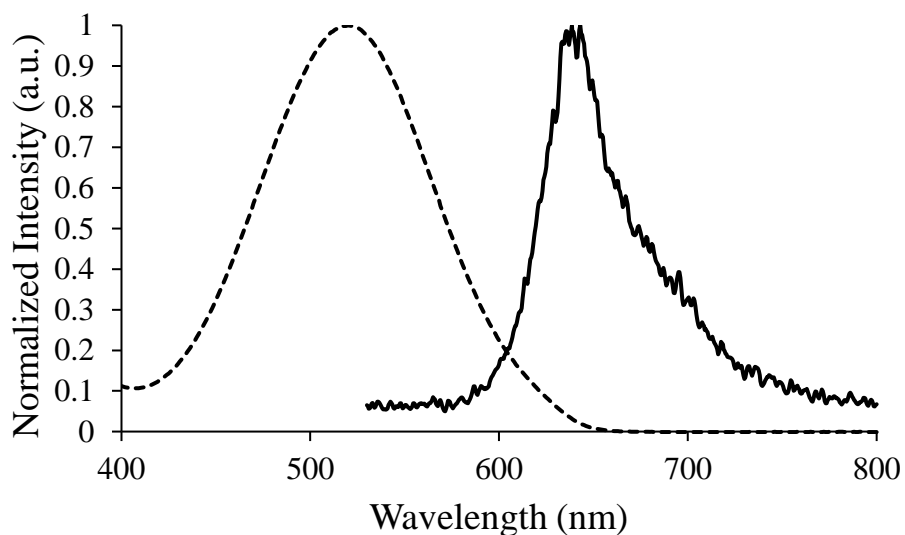


Figure A2.36 Normalized UV-vis absorption spectrum (dashed) and emission spectrum (solid) of **2.13d** in 10^{-5} M degassed toluene solution.

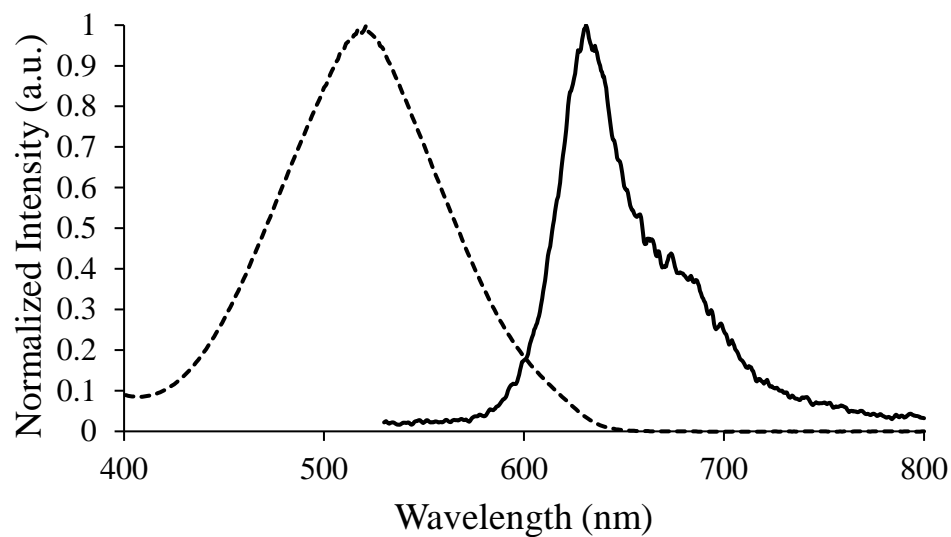


Figure A2.37 Normalized UV-vis absorption spectrum (dashed) and emission spectrum (solid) of **2.13e** in 10^{-5} M degassed toluene solution.

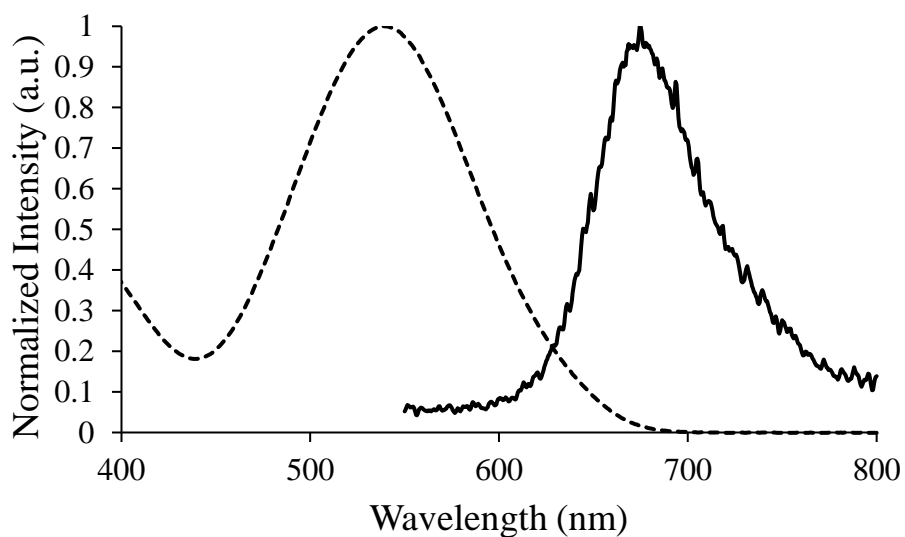


Figure A2.38 Normalized UV-vis absorption spectrum (dashed) and emission spectrum (solid) of **2.13f** in 10^{-5} M degassed toluene solution.

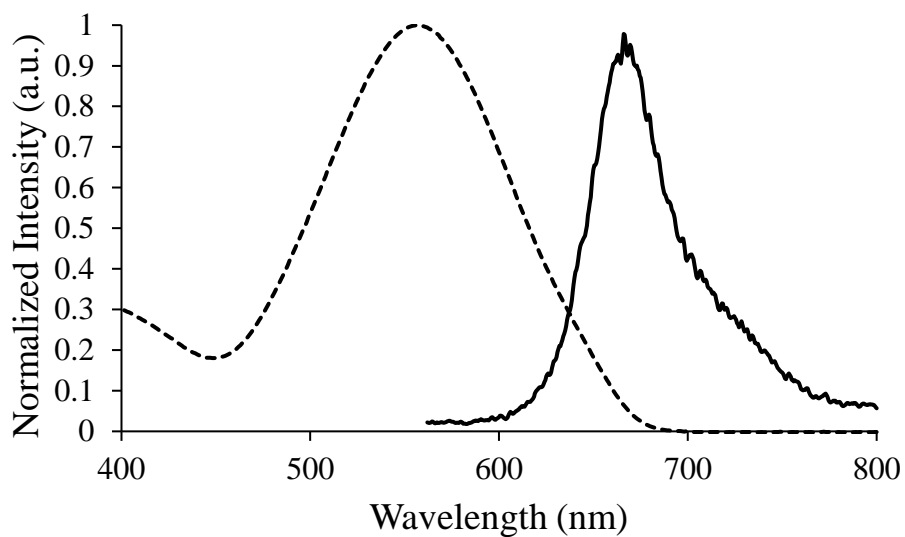


Figure A2.39 Normalized UV-vis absorption spectrum (dashed) and emission spectrum (solid) of **2.13g** in 10^{-5} M degassed toluene solution.

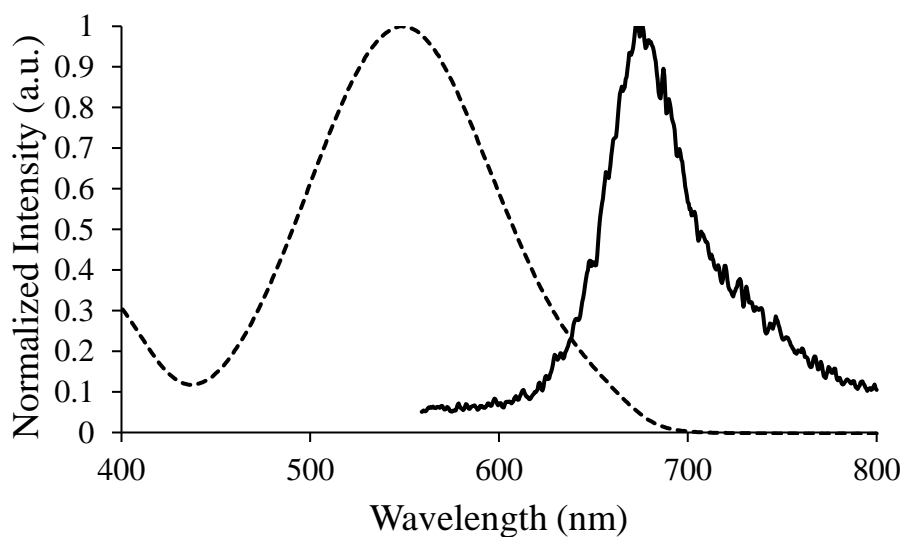


Figure A2.40 Normalized UV-vis absorption spectrum (dashed) and emission spectrum (solid) of **2.13h** in 10^{-5} M degassed toluene solution.

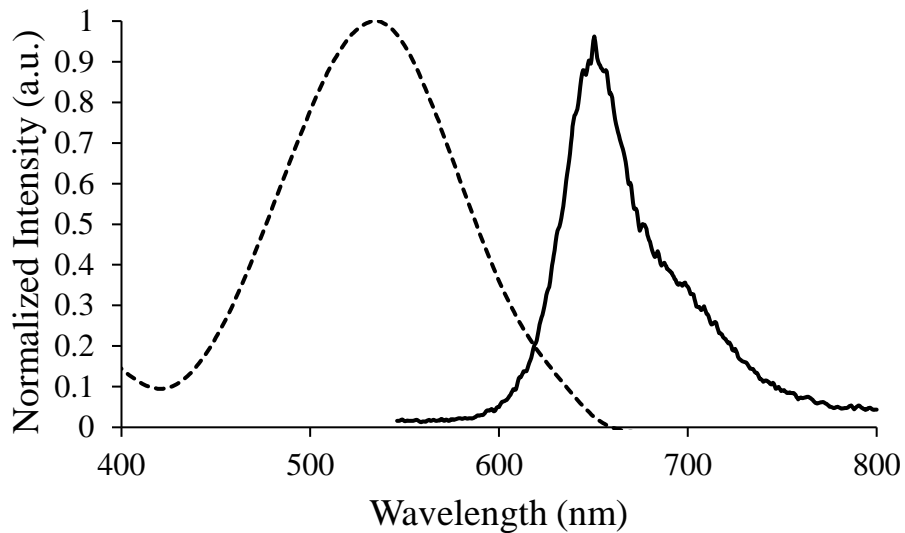


Figure A2.41 Normalized UV-vis absorption spectrum (dashed) and emission spectrum (solid) of **2.13i** in 10^{-5} M degassed toluene solution.

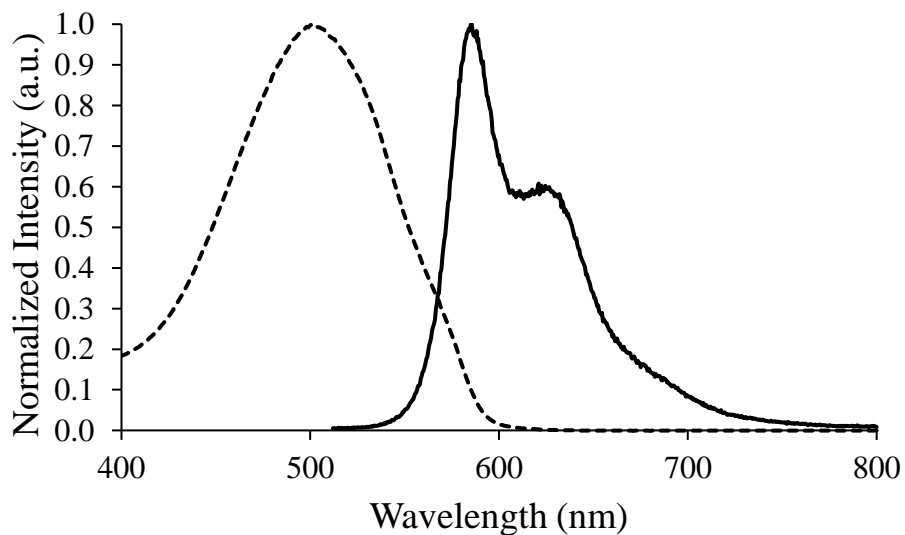


Figure A2.42 Normalized UV-vis absorption spectrum (dashed) and emission spectrum (solid) of **2.13j** in 10^{-5} M degassed toluene solution.

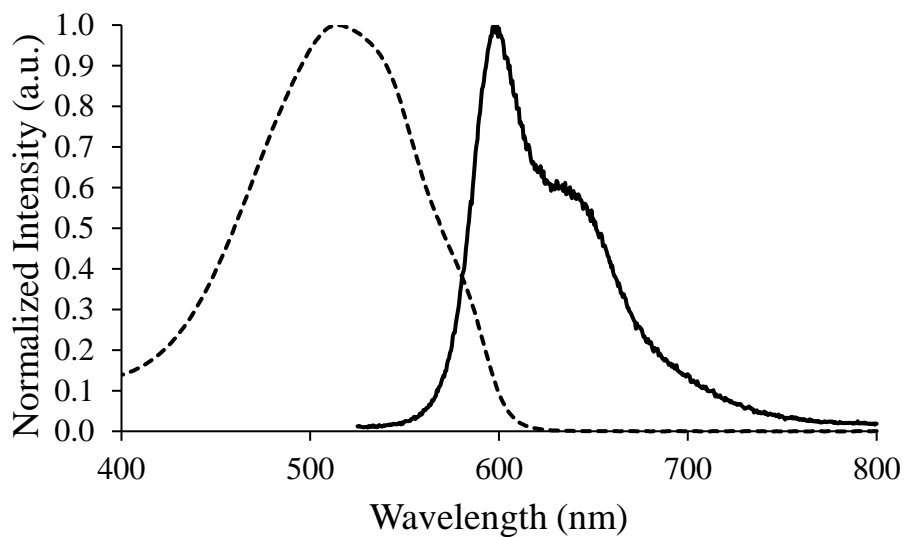


Figure A2.43 Normalized UV-vis absorption spectrum (dashed) and emission spectrum (solid) of **2.13k** in 10^{-5} M degassed toluene solution.

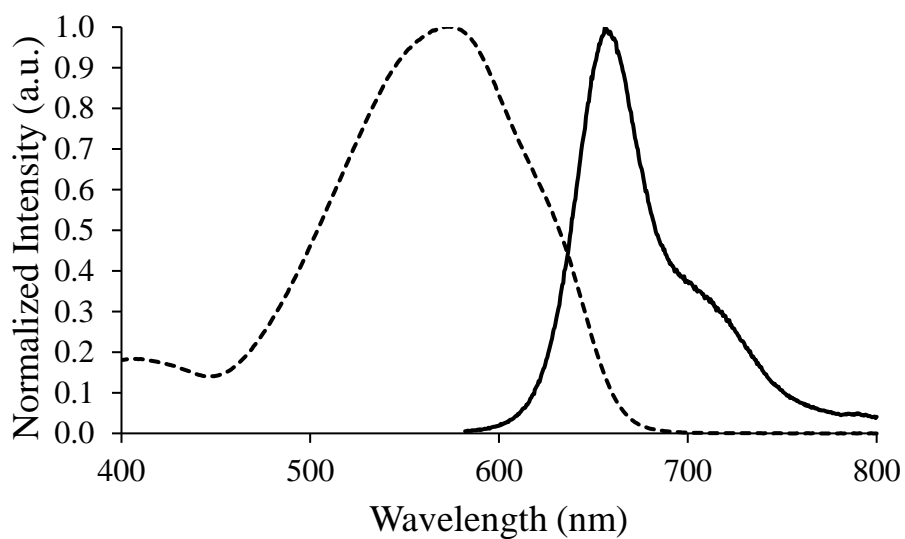


Figure A2.44 Normalized UV-vis absorption spectrum (dashed) and emission spectrum (solid) of **2.13l** in 10^{-5} M degassed toluene solution.

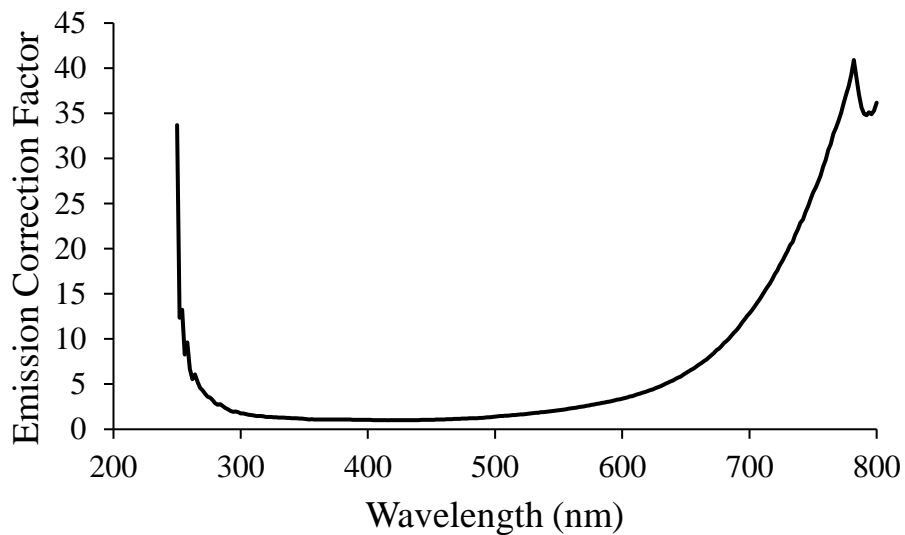


Figure A2.45 Wavelength-dependent emission correction provided by Photon Technology International.

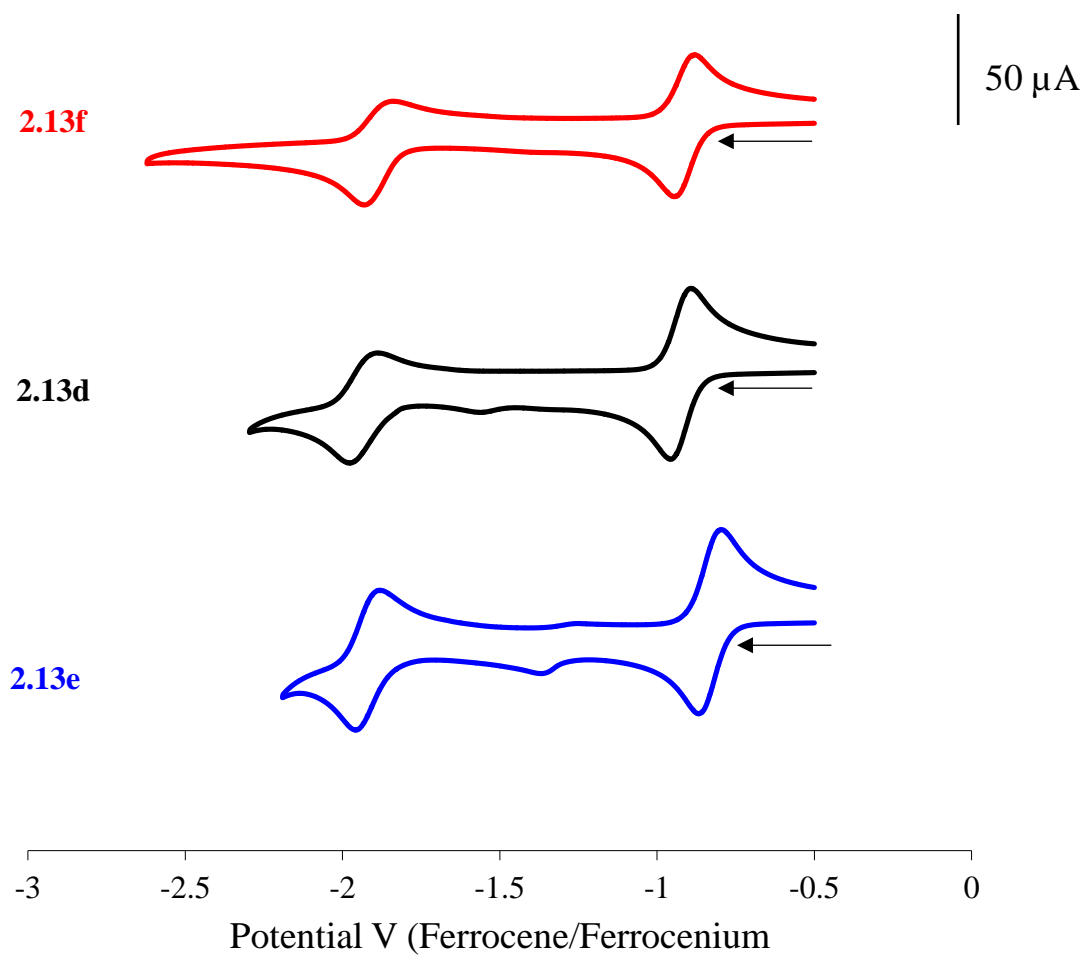


Figure A2.46 Cyclic voltammograms of **2.13d** (black), **2.13e** (blue) and **2.13f** (red) recorded at 250 mV s^{-1} in 1 mM acetonitrile solutions containing 0.1 M $[\text{nBu}_4\text{N}][\text{PF}_6]$ as supporting electrolyte.

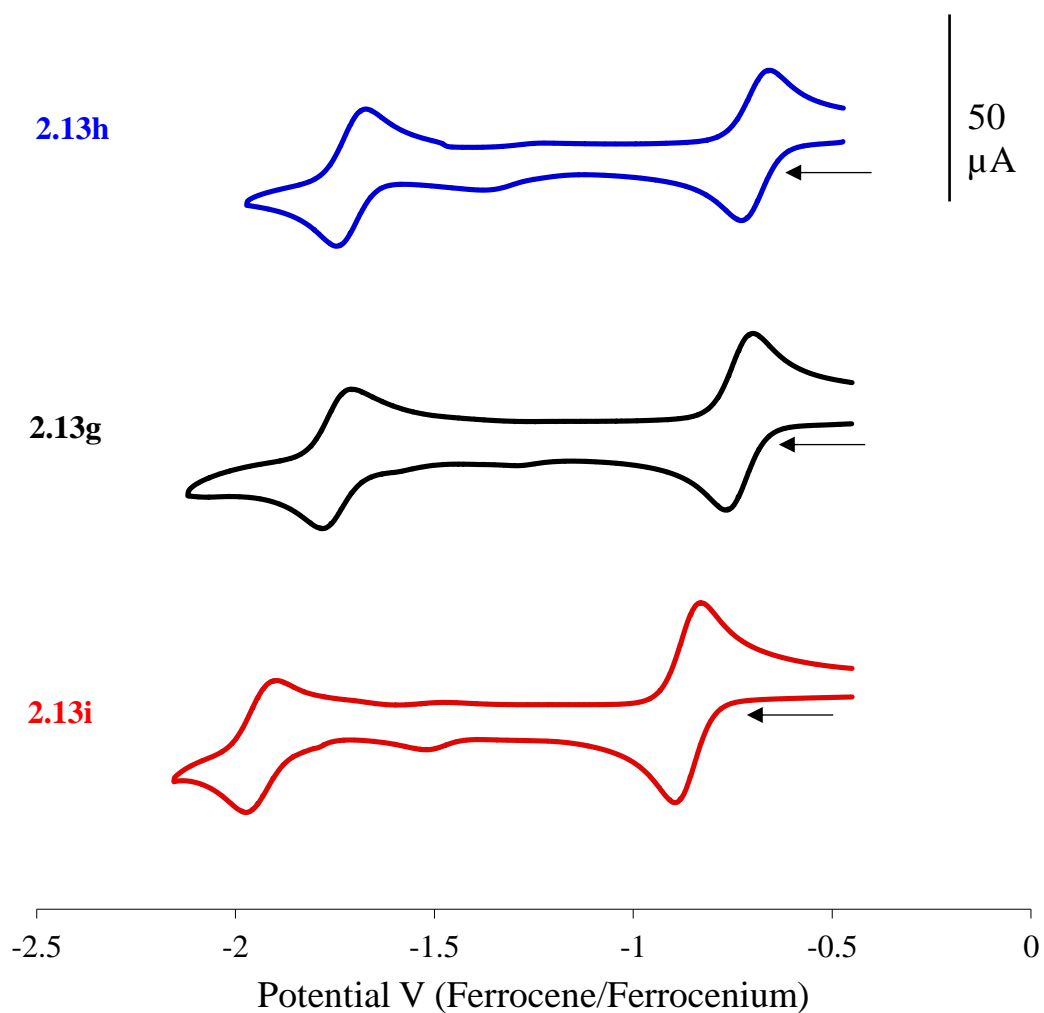


Figure A2.47 Cyclic voltammograms of **2.13g** (black), **2.13h** (blue) and **2.13i** (red) recorded at 250 mV s^{-1} in 1 mM acetonitrile solutions containing 0.1 M $[\text{nBu}_4\text{N}][\text{PF}_6]$ as supporting electrolyte.

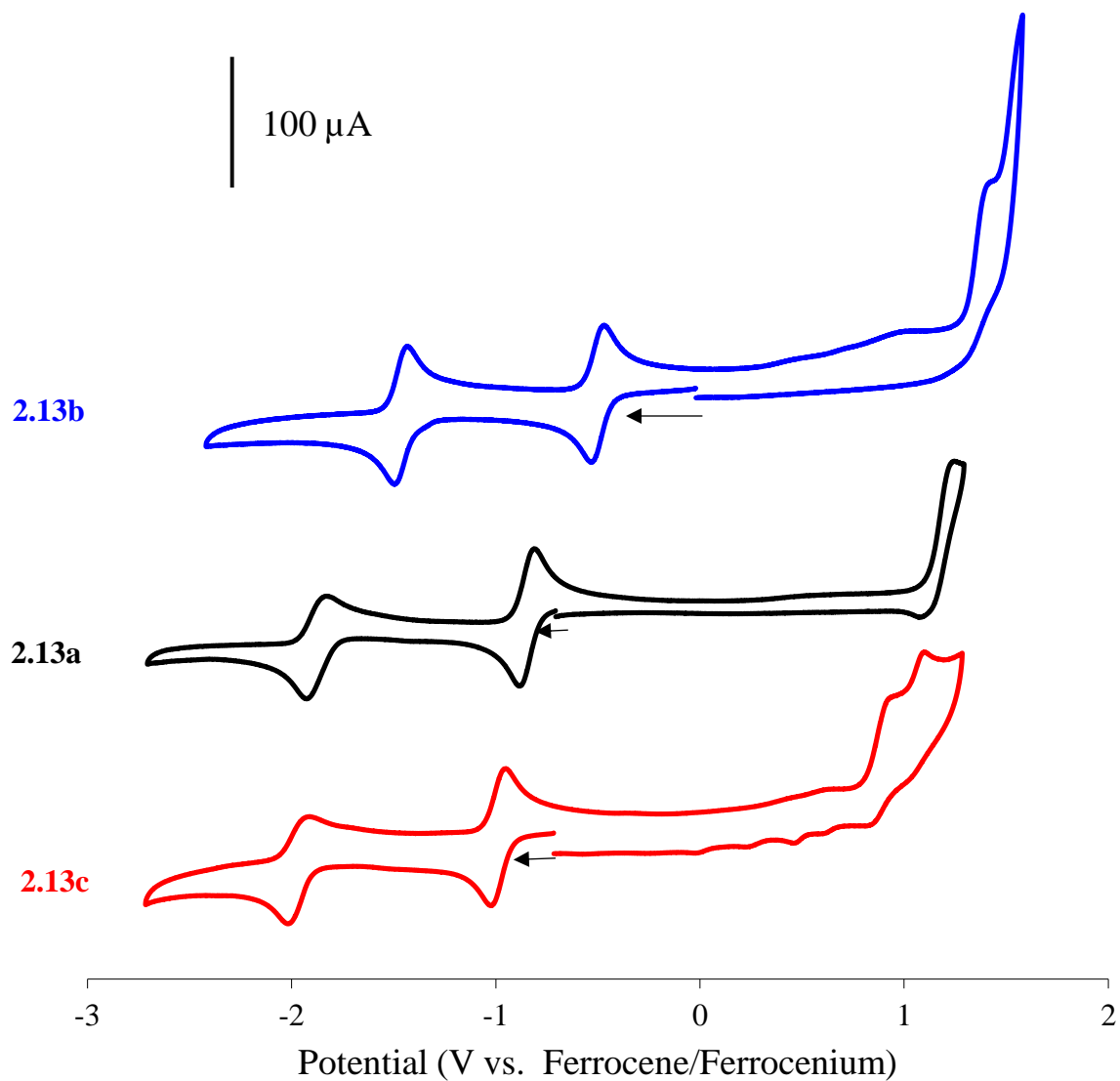


Figure A2.48 Cyclic voltammograms of **2.13a** (black), **2.13b** (blue) and **2.13c** (red) recorded at 250 mV s^{-1} in 1 mM acetonitrile solutions containing 0.1 M $[\text{nBu}_4\text{N}][\text{PF}_6]$ as supporting electrolyte.

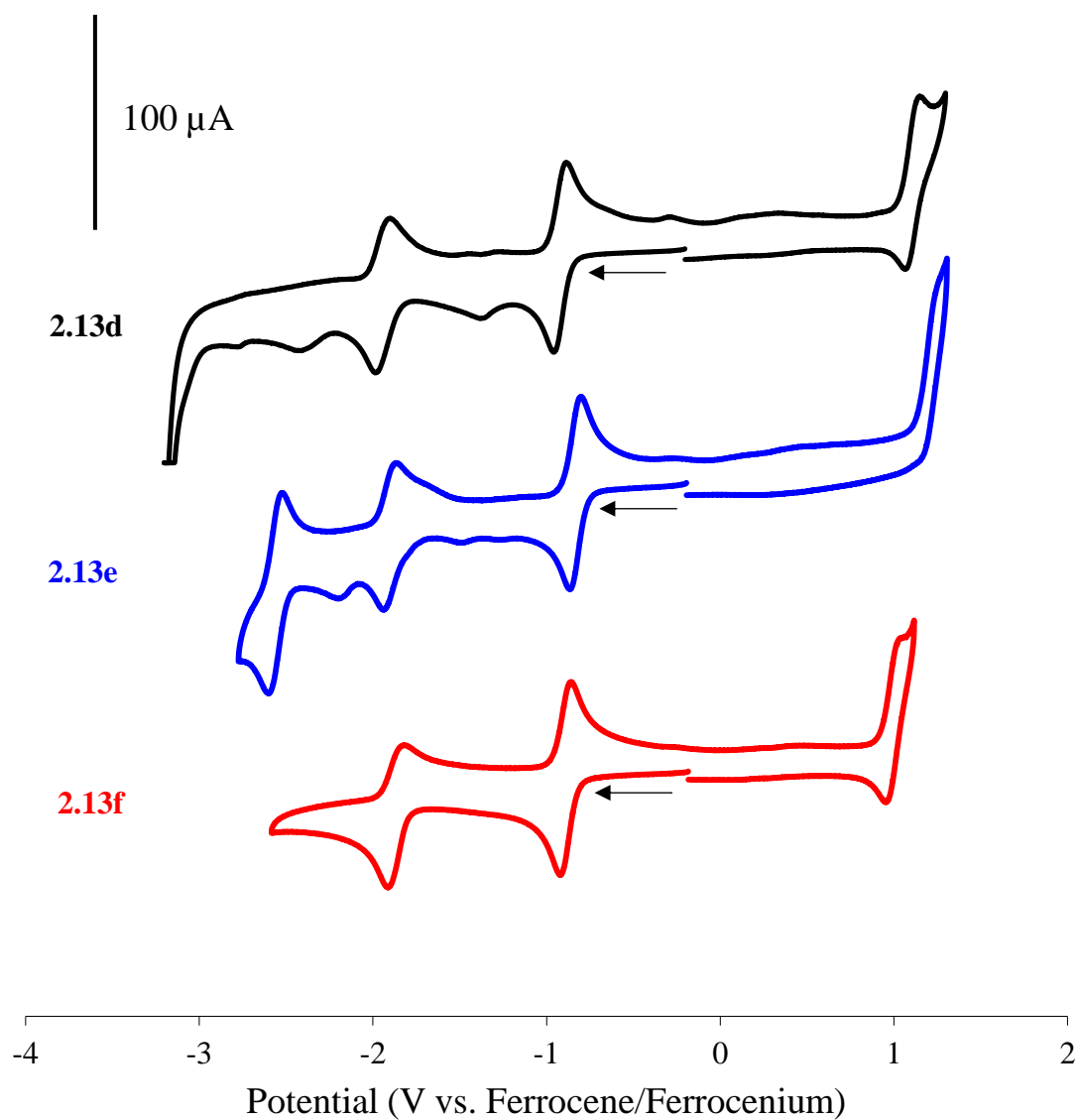


Figure A2.49 Cyclic voltammograms of **2.13d** (black), **2.13e** (blue) and **2.13f** (red) recorded at 250 mV s^{-1} in 1 mM acetonitrile solutions containing 0.1 M $[\text{nBu}_4\text{N}][\text{PF}_6]$ as supporting electrolyte.

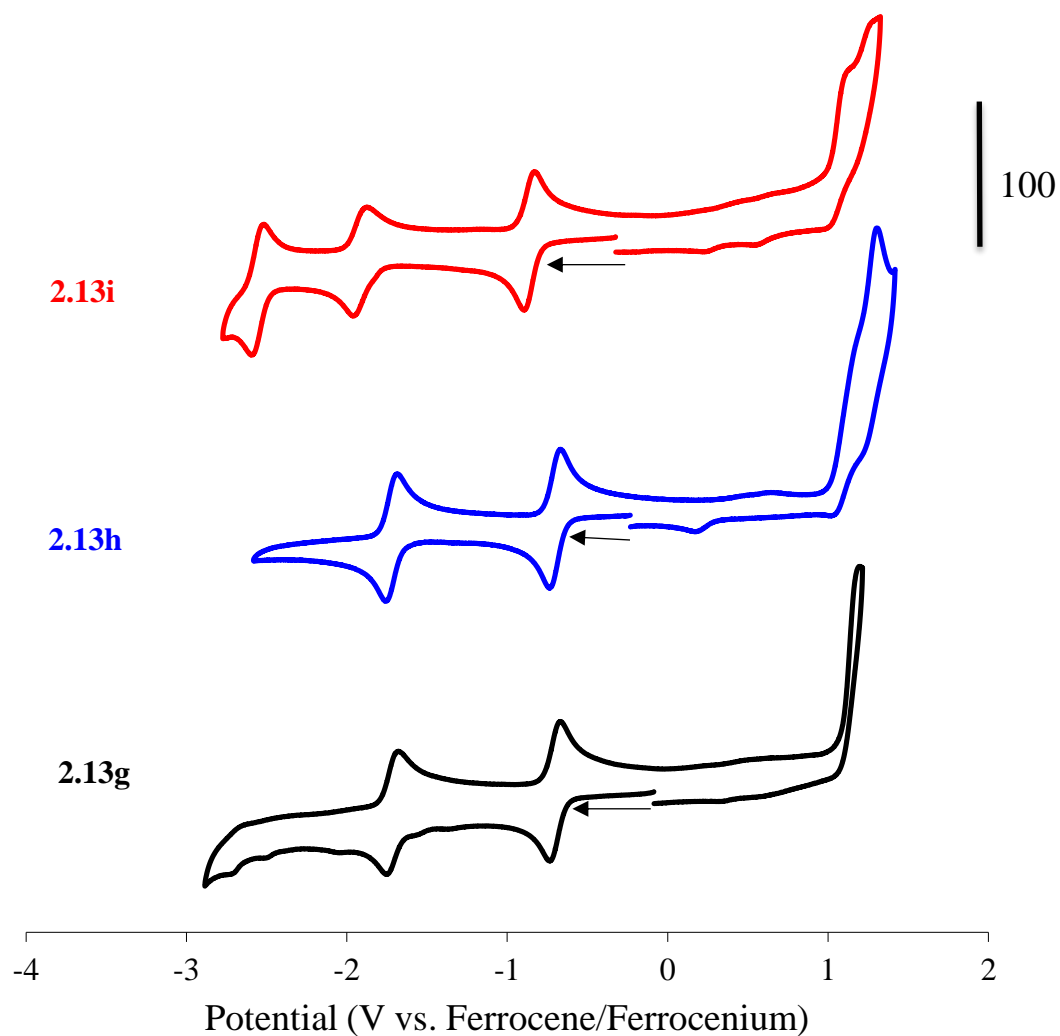


Figure A2.50 Cyclic voltammograms of **2.13g** (black), **2.13h** (blue) and **2.13i** (red) recorded at 250 mV s^{-1} in 1 mM acetonitrile solutions containing 0.1 M $[\text{nBu}_4\text{N}][\text{PF}_6]$ as supporting electrolyte.

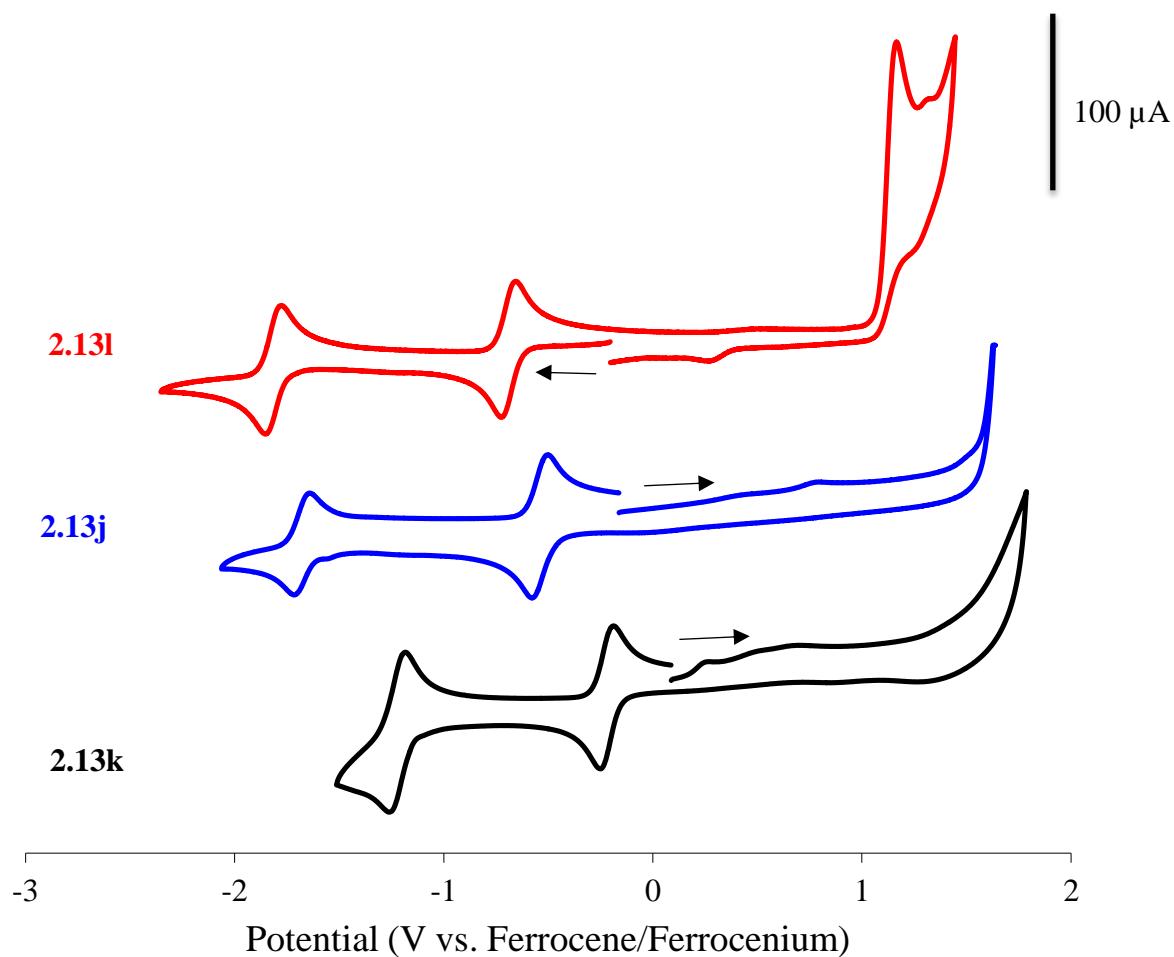


Figure A2.51 Cyclic voltammograms of **2.13j** (blue), **2.13k** (black) and **2.13l** (red) recorded at 100 mV s^{-1} in 1 mM acetonitrile solutions containing 0.1 M $[\text{nBu}_4\text{N}][\text{PF}_6]$ as supporting electrolyte.

Table A2.1 Total electronic energies of the optimized M06/6-311+G* structures of **2.13j–l**, calculated in vacuum and in toluene using the SCRF (PCM, Solvent=Toluene) Int(Grid=UltraFine) keywords.

Compound	E_e (vacuum), hartree		E_e (toluene), hartree	
	C_{2v}	C_s	C_{2v}	C_s
2.13j (R = H)	-1037.477334	-1037.479048	-1037.483066	-1037.485155
2.13k (R = CN)	-1221.893636	-1221.894770	-1221.904061	-1221.905495
2.13l (R = OMe)	-1266.464622	-1266.465720	-1266.472254	-1266.473716

Table A2.2 Lowest electronic excitations and HOMO/LUMO energies of BF₂ complexes **2.13j–l** in vacuum calculated at the M06/6-311+G* level of theory.

Compound	Lowest excitation energy ^a		ϵ_{HOMO} , eV	ϵ_{LUMO} , eV	HOMO–LUMO gap, eV
	eV	nm			
<i>C</i> _{2v} structures					
2.13j (R = H)	2.53	489	-6.97	-3.92	3.05
2.13k (R = CN)	2.46	505	-7.67	-4.70	2.97
2.13l (R = OMe)	2.29	541	-6.34	-3.60	2.74
<i>C</i> _s structures					
2.13j (R = H)	2.77	448	-7.12	-3.79	3.33
2.13k (R = CN)	2.65	468	-7.78	-4.58	3.20
2.13l (R = OMe)	2.46	504	-6.46	-3.50	2.96

^aComputed using time-dependent DFT. The first excited states of the *C*_{2v} and *C*_s structures have *B*₂ and *A*' symmetry, respectively.

Table A2.3 Lowest electronic excitations and HOMO/LUMO energies of the substituted BF₂ complexes in toluene solution calculated at the M06/6-311+G* level of theory using the SCRF method.

		Lowest excitation energy ^a		ϵ_{HOMO} , eV	ϵ_{LUMO} , eV	HOMO-LUMO gap, eV
		eV	nm			
<i>C</i> _{2v} structures	2.13j (R = H)	2.39	518	-6.94	-3.89	3.05
	2.13k (R = CN)	2.36	526	-7.49	-4.48	3.01
	2.13l (R = OMe)	2.12	58	-6.34	-3.63	2.71
<i>C</i> _s structures	2.13j (R = H)	2.65	468	-7.12	-3.76	3.36
	2.13k (R = CN)	2.57	483	-7.62	-4.36	3.26
	2.13l (R = OMe)	2.30	538	-6.47	-3.54	2.93

^aComputed using time-dependent DFT. The first excited states of the *C*_{2v} and *C*_s structures have *B*₂ and *A*' symmetry, respectively.

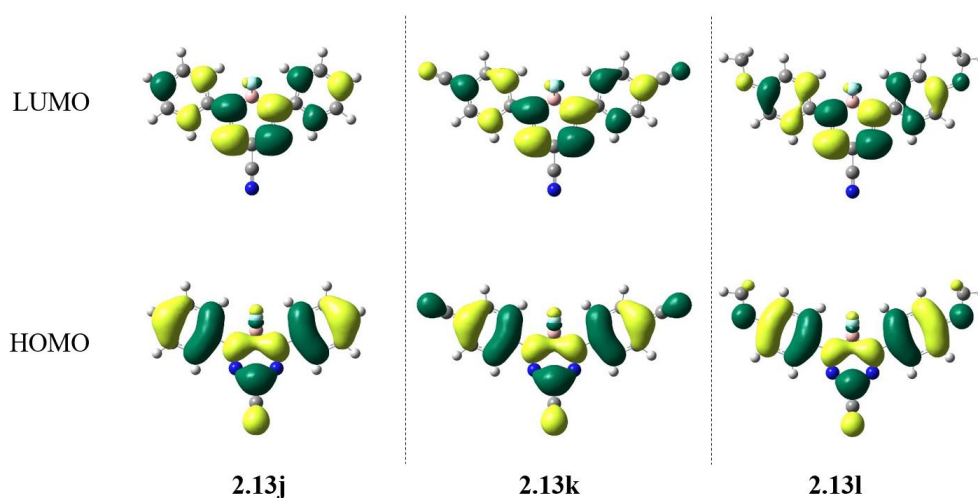
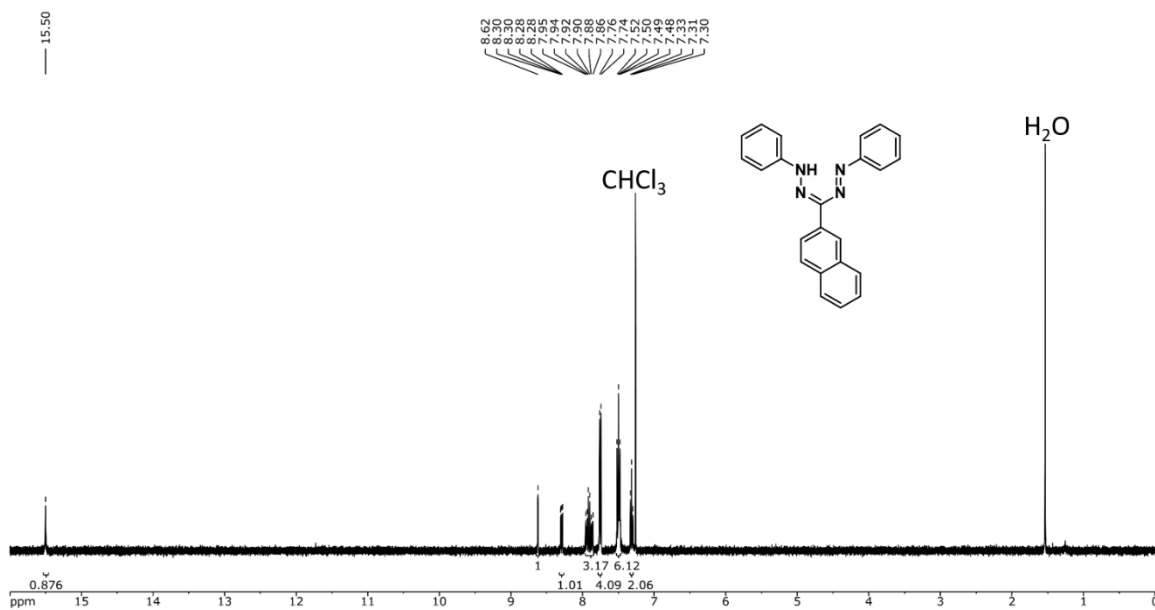
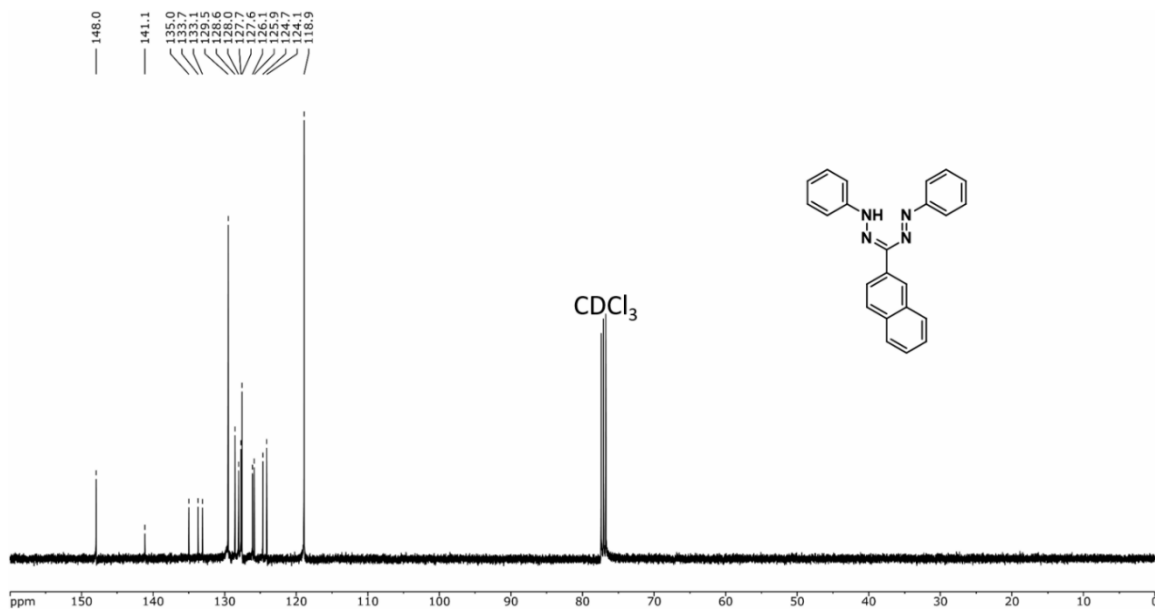


Figure A2.52 HOMOs and LUMOs for BF₂ complexes **2.13j**, **2.13k**, and **2.13l** calculated in toluene solution.

Appendix A3 Supporting Information for Chapter 3

Figure A3.1 ^1H NMR spectrum of **3.11b** in CDCl_3 .Figure A3.2 $^{13}\text{C}\{^1\text{H}\}$ NMR spectrum of **3.11b** in CDCl_3 .

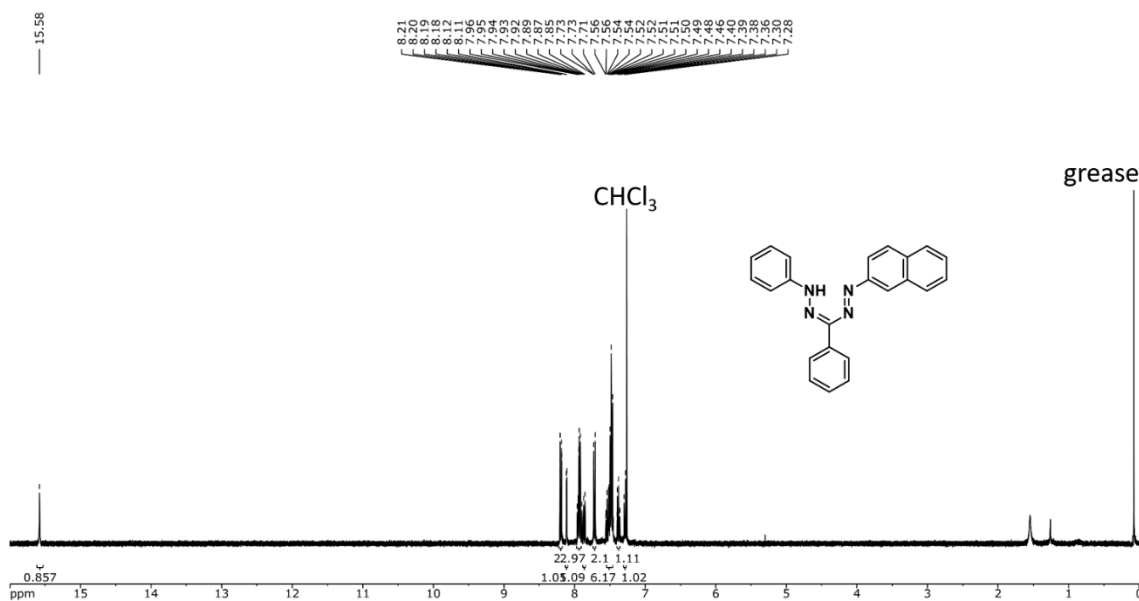


Figure A3.3 ^1H NMR spectrum of 3.11c in CDCl_3 .

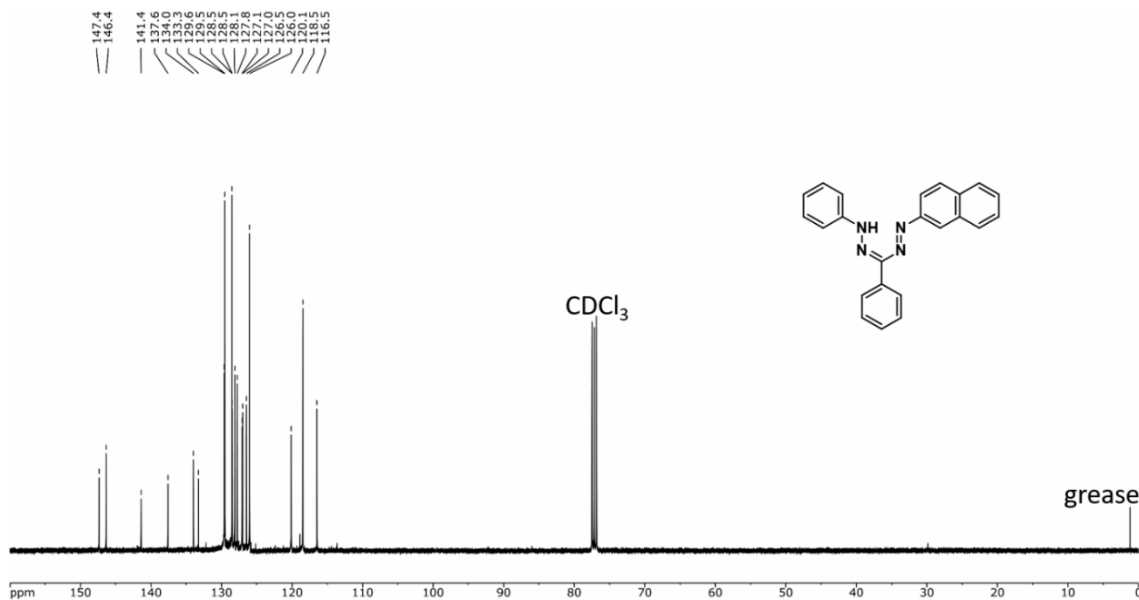


Figure A3.4 $^{13}\text{C}\{^1\text{H}\}$ NMR spectrum of 3.11c in CDCl_3 .

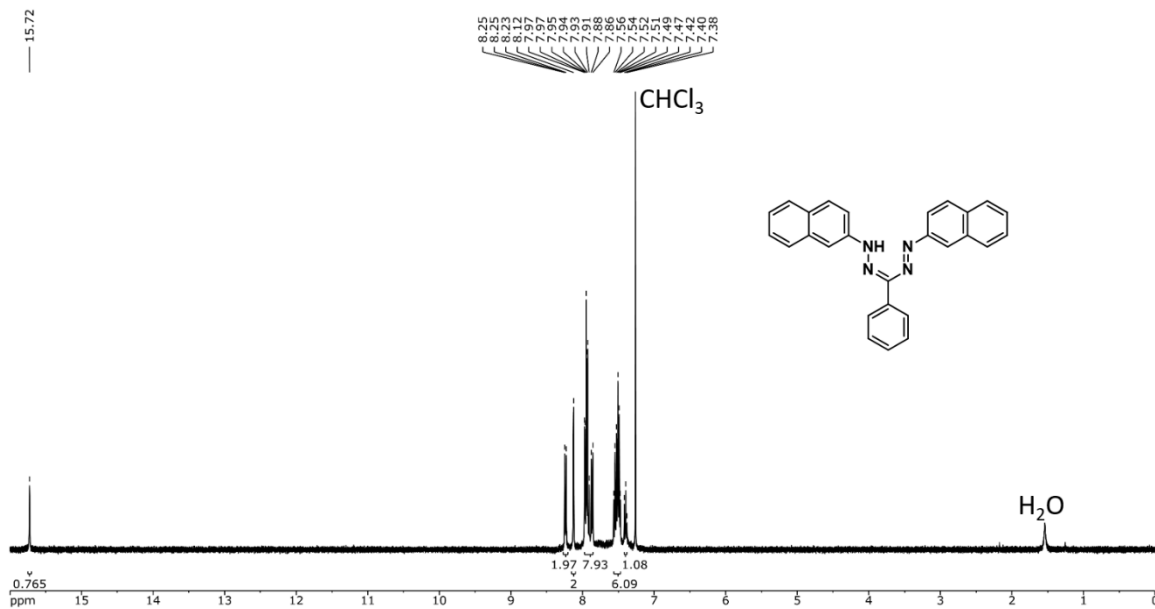


Figure A3.5 ^1H NMR spectrum of **3.11d** in CDCl_3 .

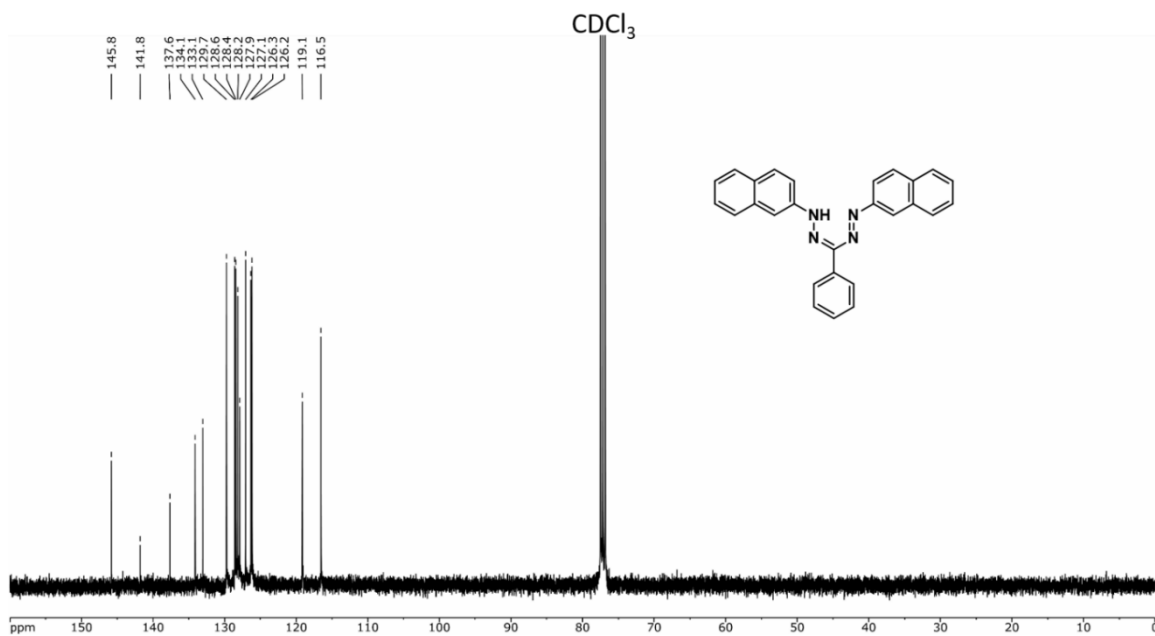


Figure A3.6 $^{13}\text{C}\{^1\text{H}\}$ NMR spectrum of **3.11d** in CDCl_3 .

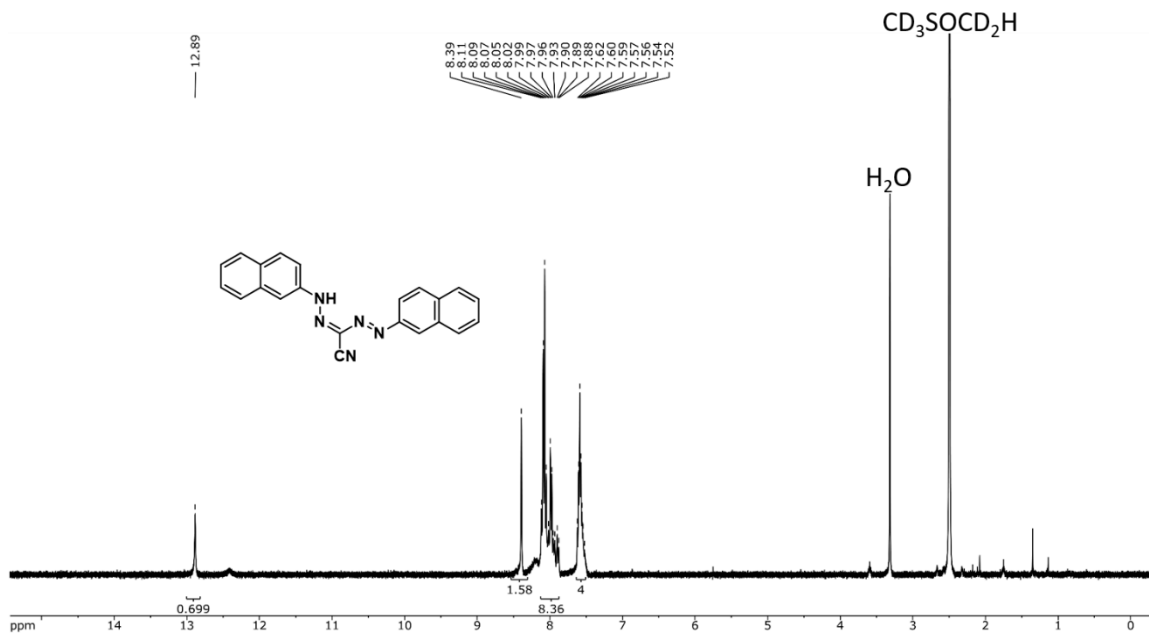


Figure A3.7 ^1H NMR spectrum of **3.11f** in $\text{DMSO-}d_6$.

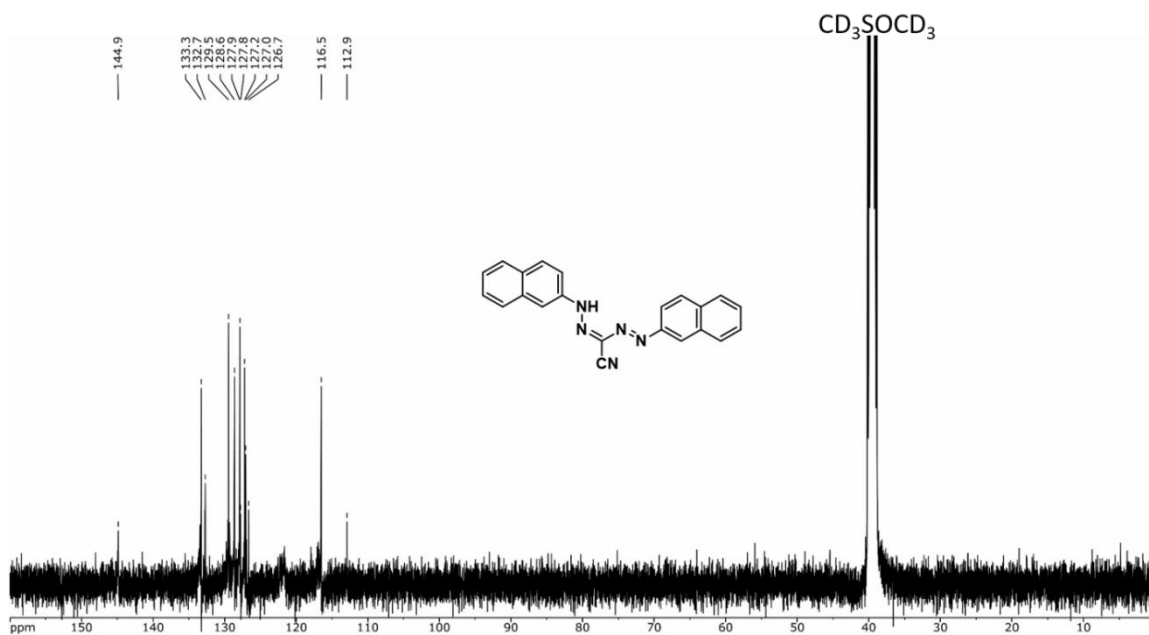


Figure A3.8 $^{13}\text{C}\{^1\text{H}\}$ NMR spectrum of **3.11f** in $\text{DMSO-}d_6$. This spectrum was measured for 10,000 scans on a 400 MHz spectrometer. The poor signal-to-noise ratio relates to the poor solubility of **3.11f**.

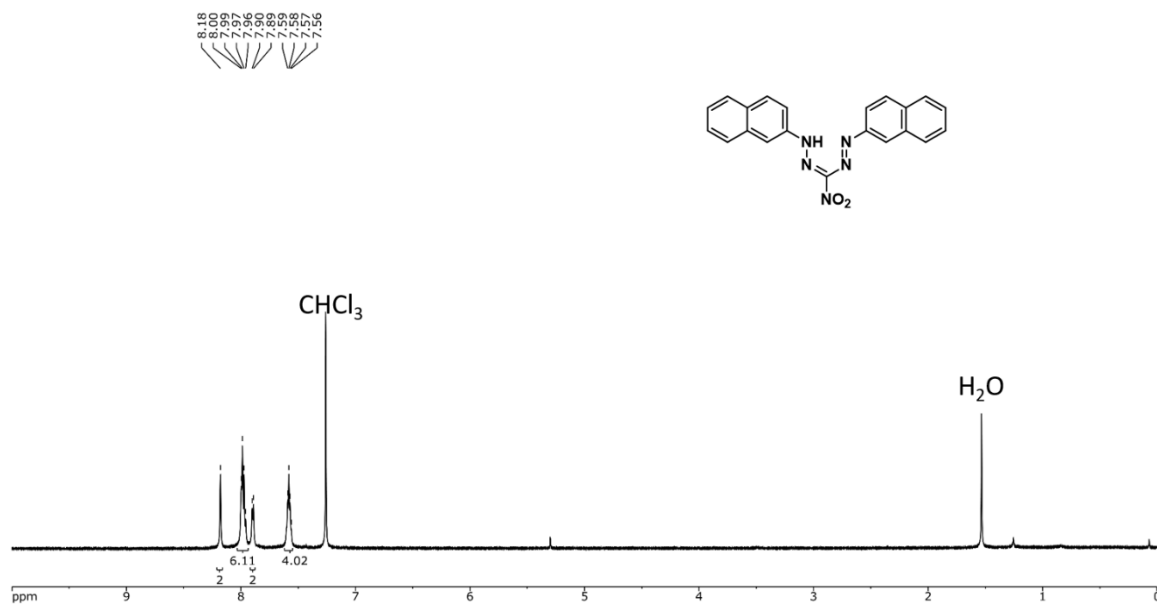


Figure A3.9 ^1H NMR spectrum of 3.11h in CDCl_3 .

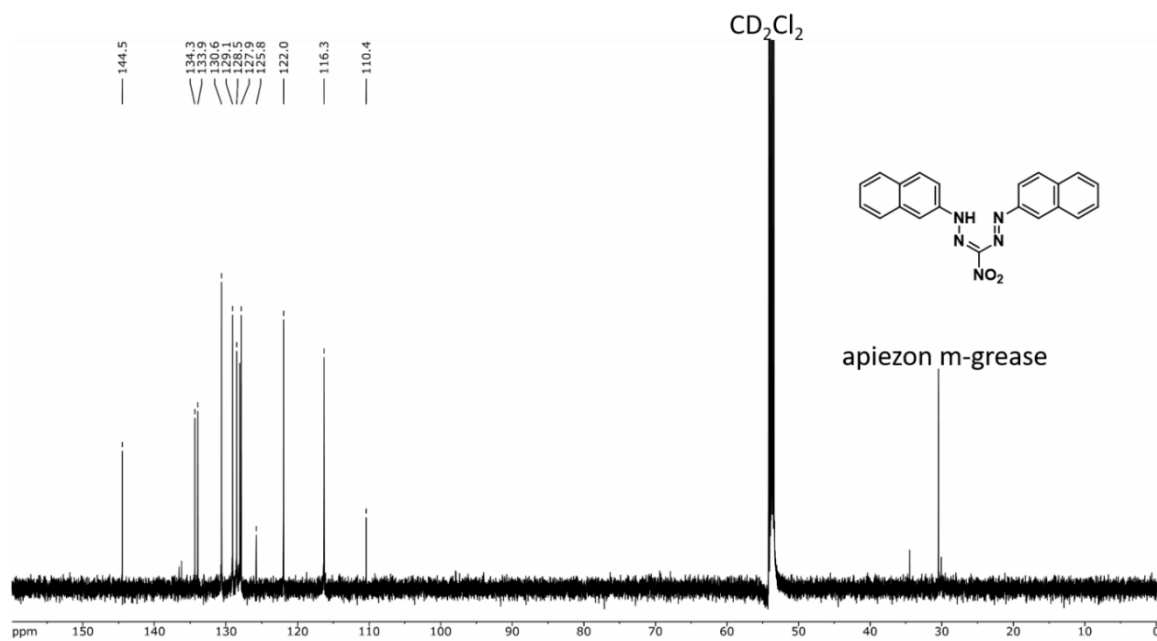


Figure A3.10 $^{13}\text{C}\{^1\text{H}\}$ NMR spectrum of 3.11h in CD_2Cl_2 .

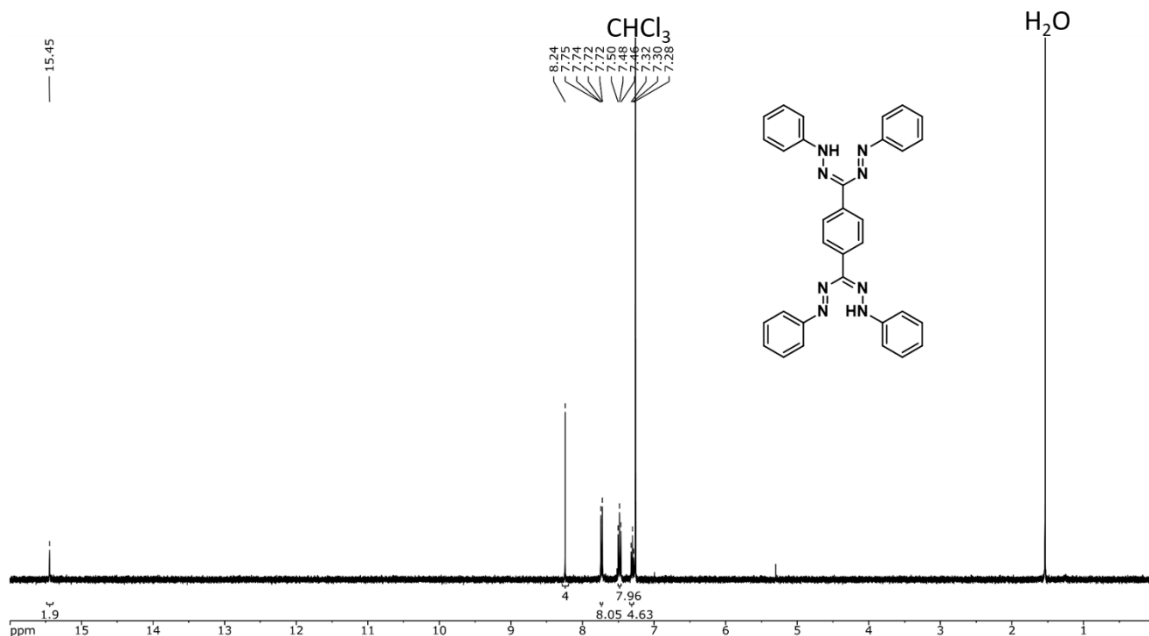


Figure A3.11 ^1H NMR spectrum of **3.11j** in CDCl_3 .

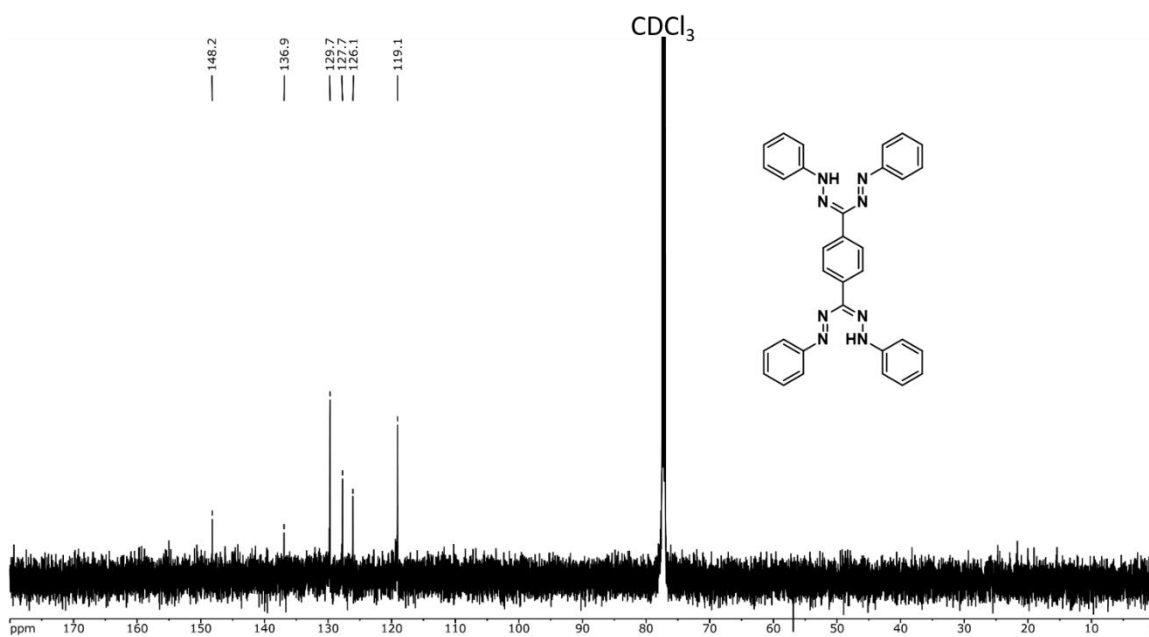


Figure A3.12 $^{13}\text{C}\{^1\text{H}\}$ NMR spectrum of **3.11j** in CDCl_3 . This spectrum was collected for 10,000 scans on a 600 MHz spectrometer. The poor signal-to-noise ratio relates to the poor solubility of **3.11j**.

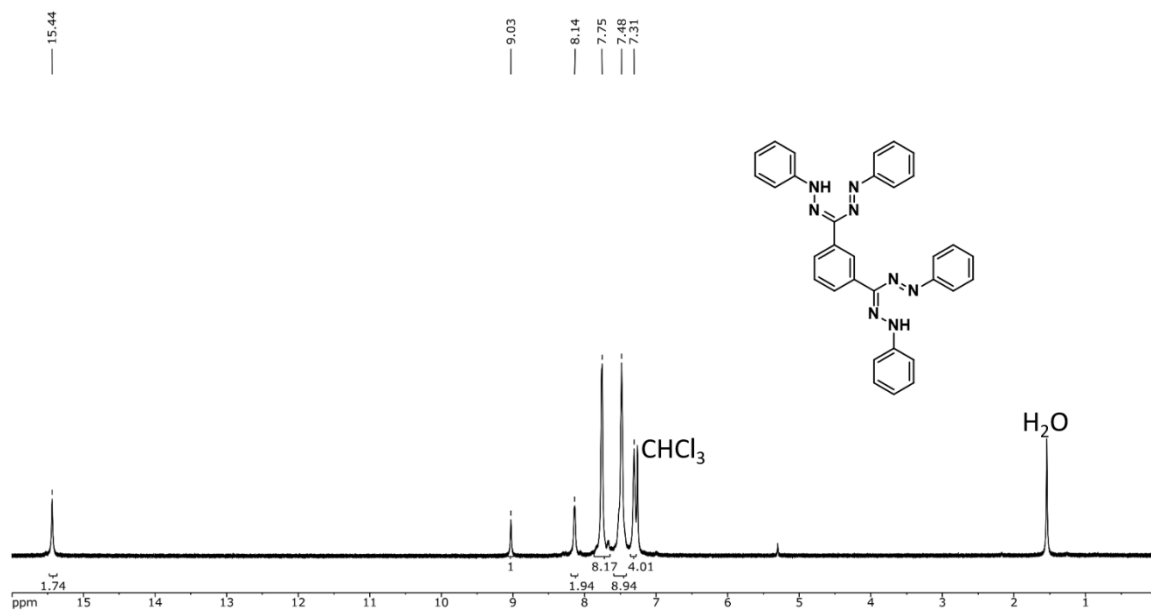


Figure A3.13 ^1H NMR spectrum of 3.11k in CDCl_3 .

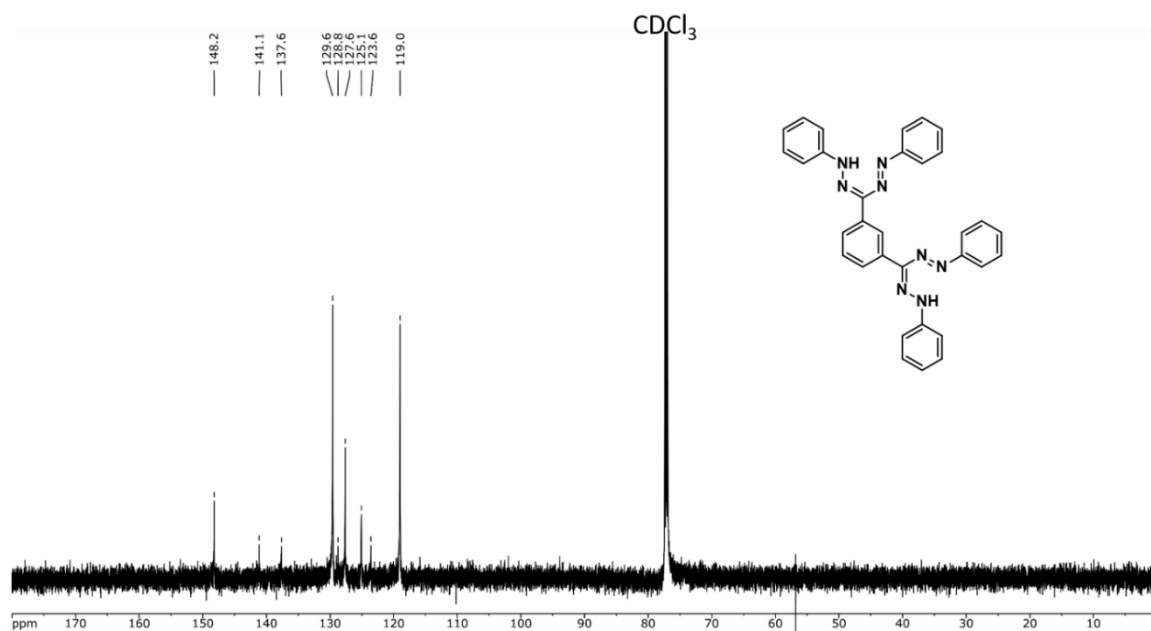


Figure A3.14 $^{13}\text{C}\{^1\text{H}\}$ NMR spectrum of 3.11k in CDCl_3 .

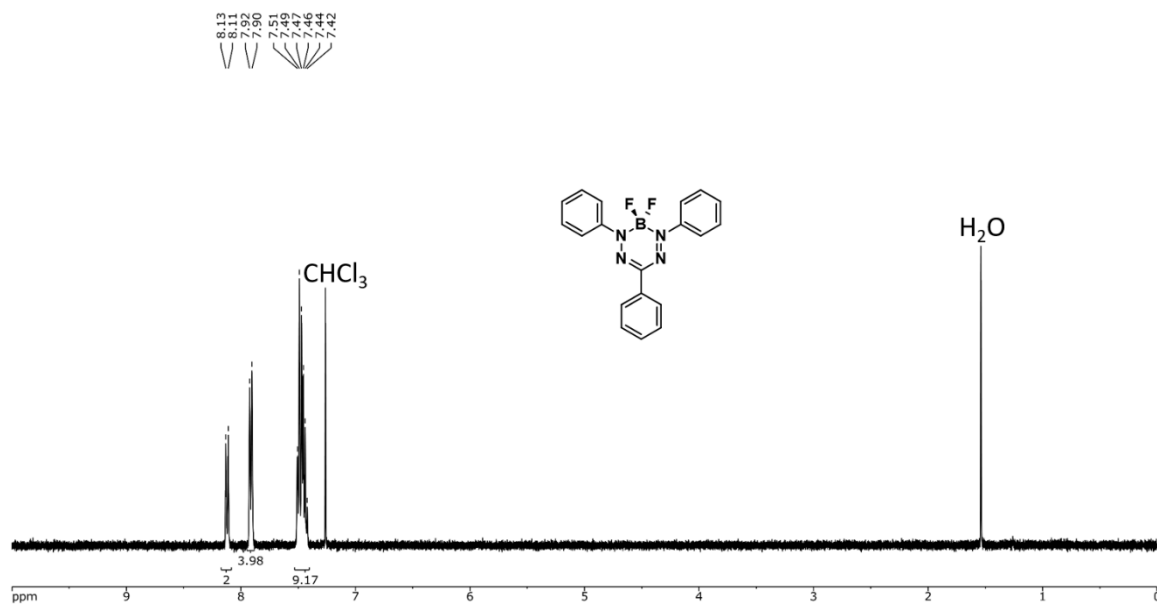


Figure A3.15 ^1H NMR spectrum of 3.10a in CDCl_3 .

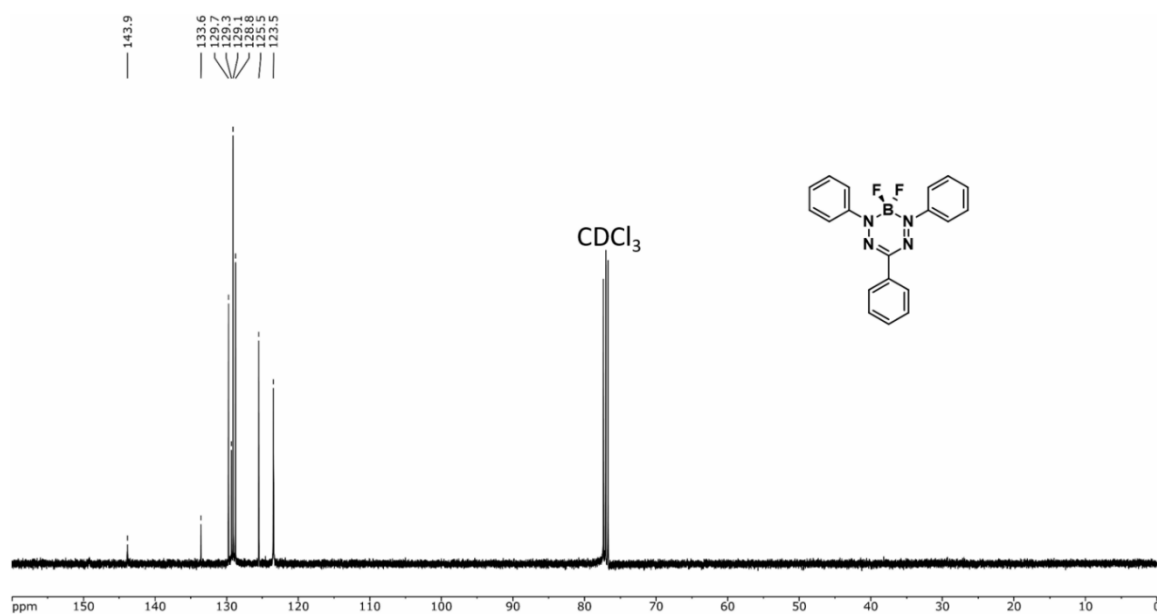


Figure A3.16 $^{13}\text{C}\{^1\text{H}\}$ NMR spectrum of 3.10a in CDCl_3 .

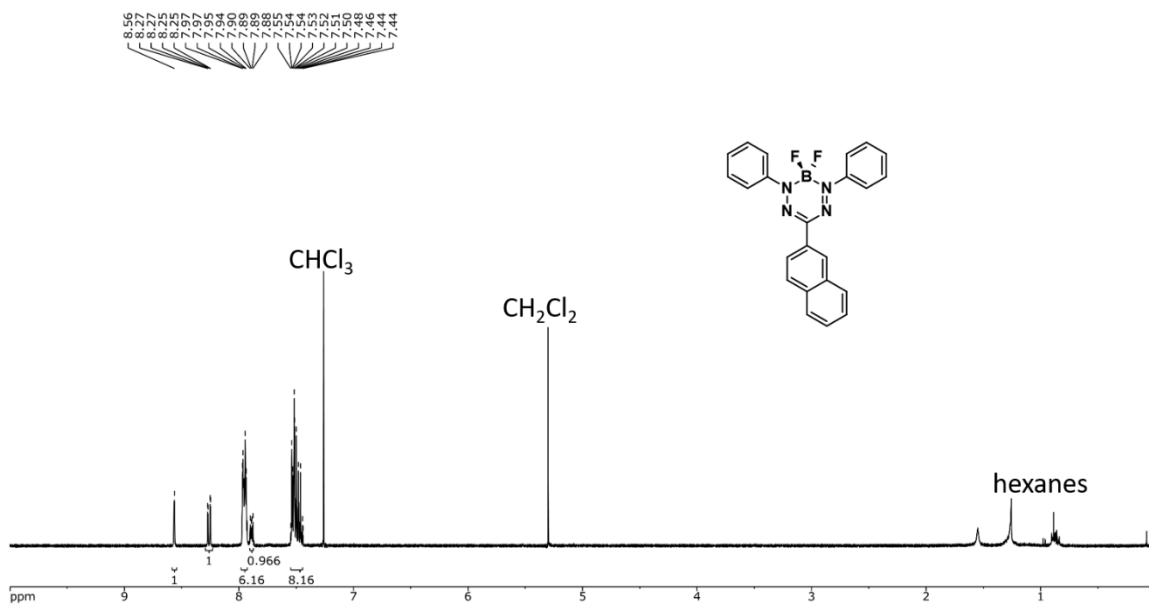


Figure A3.17 ^1H NMR spectrum of **3.10b** in CDCl_3 .

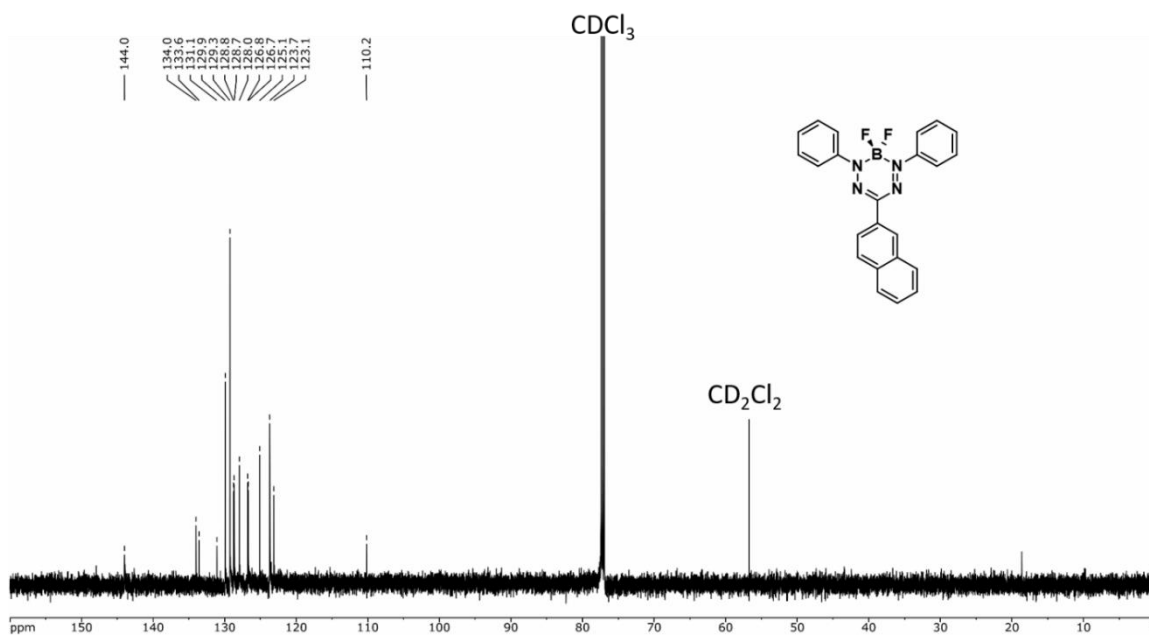


Figure A3.18 $^{13}\text{C}\{^1\text{H}\}$ NMR spectrum of **3.10b** in CDCl_3 .

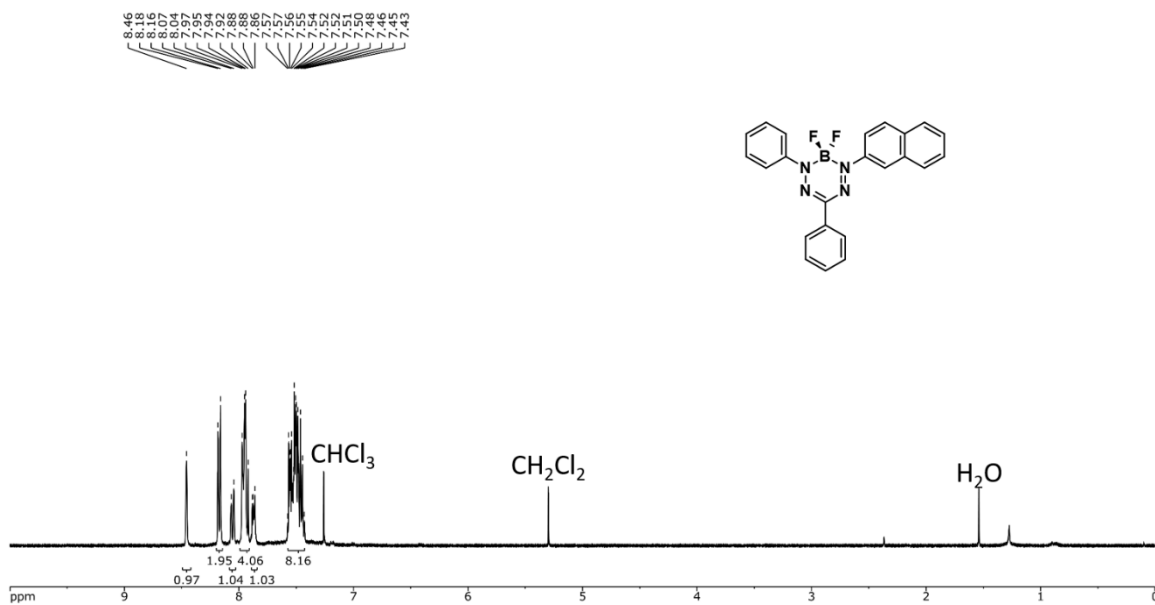


Figure A3.19 ^1H NMR spectrum of 3.10c in CDCl_3 .

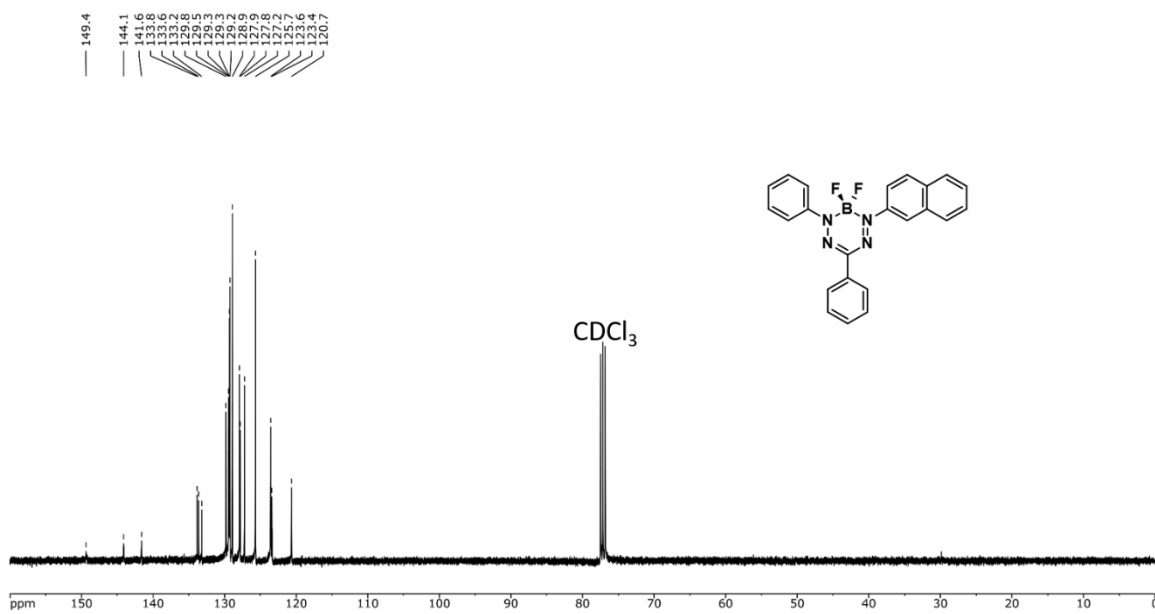


Figure A3.20 $^{13}\text{C}\{^1\text{H}\}$ NMR spectrum of 3.10c in CDCl_3 .

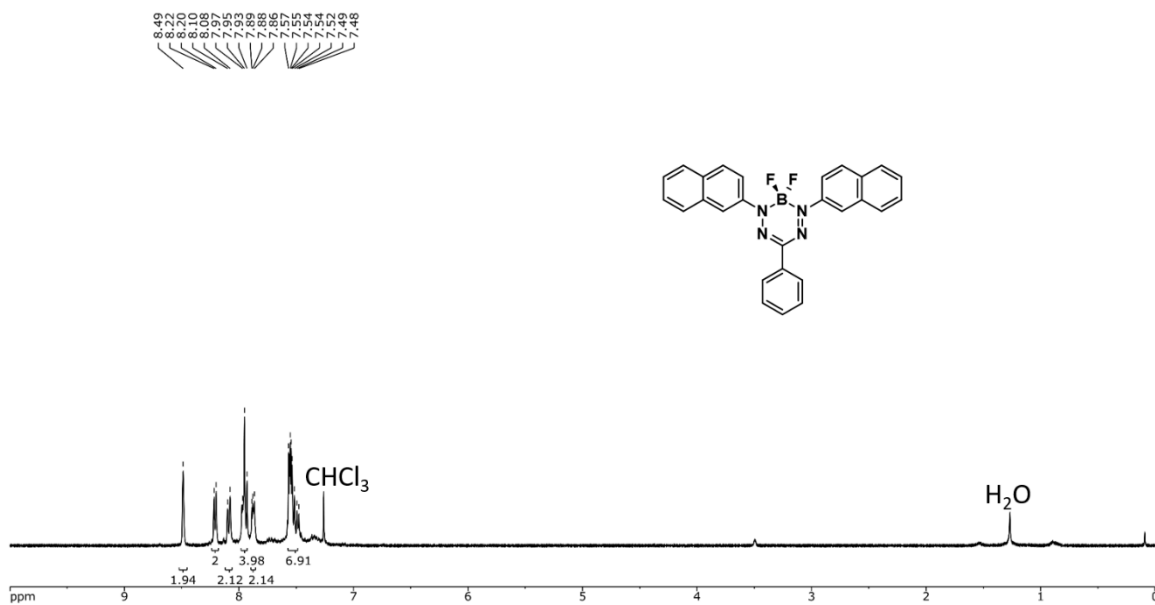


Figure A3.21 ^1H NMR spectrum of 3.10d in CDCl_3 .

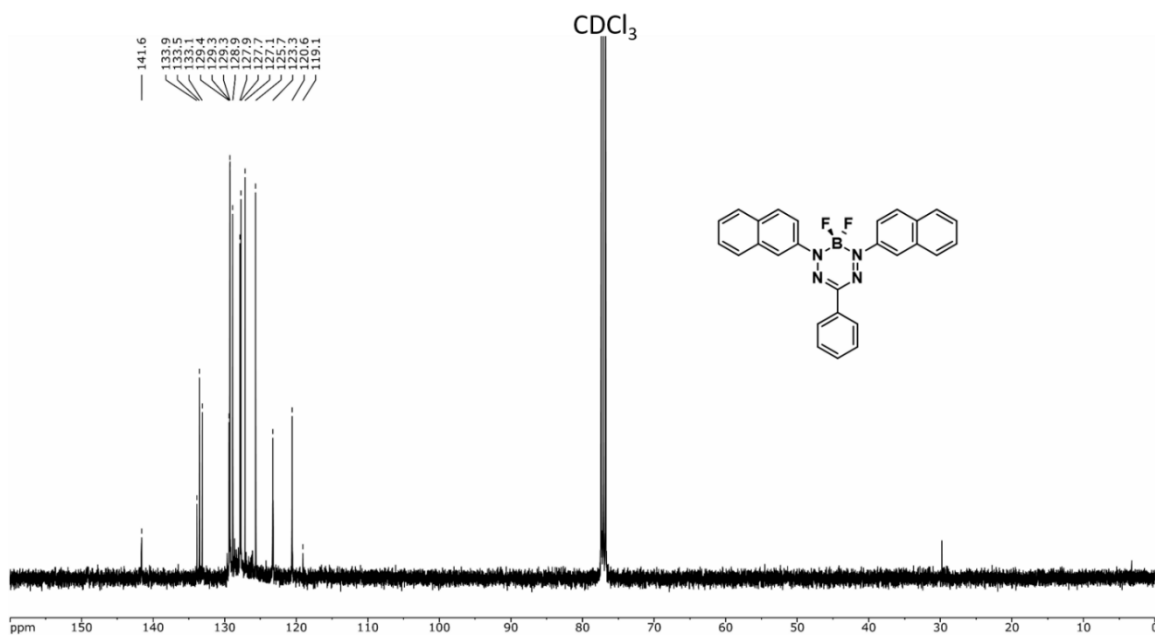


Figure A3.22 $^{13}\text{C}\{^1\text{H}\}$ NMR spectrum of 3.10d in CDCl_3 .

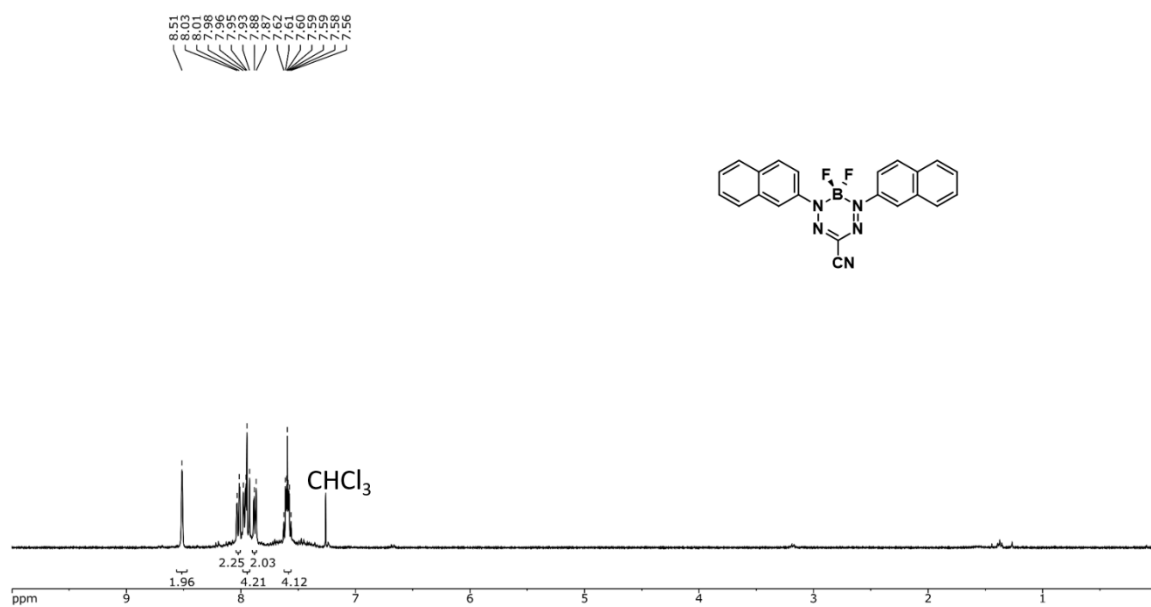


Figure A3.23 ^1H NMR spectrum of 3.10f in CDCl_3 .

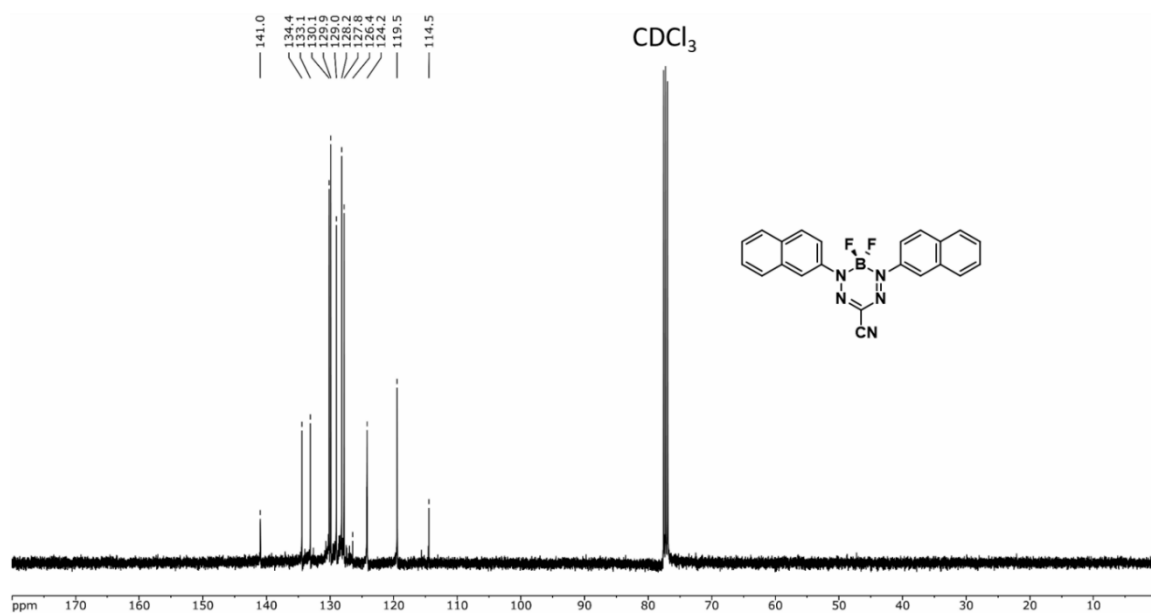
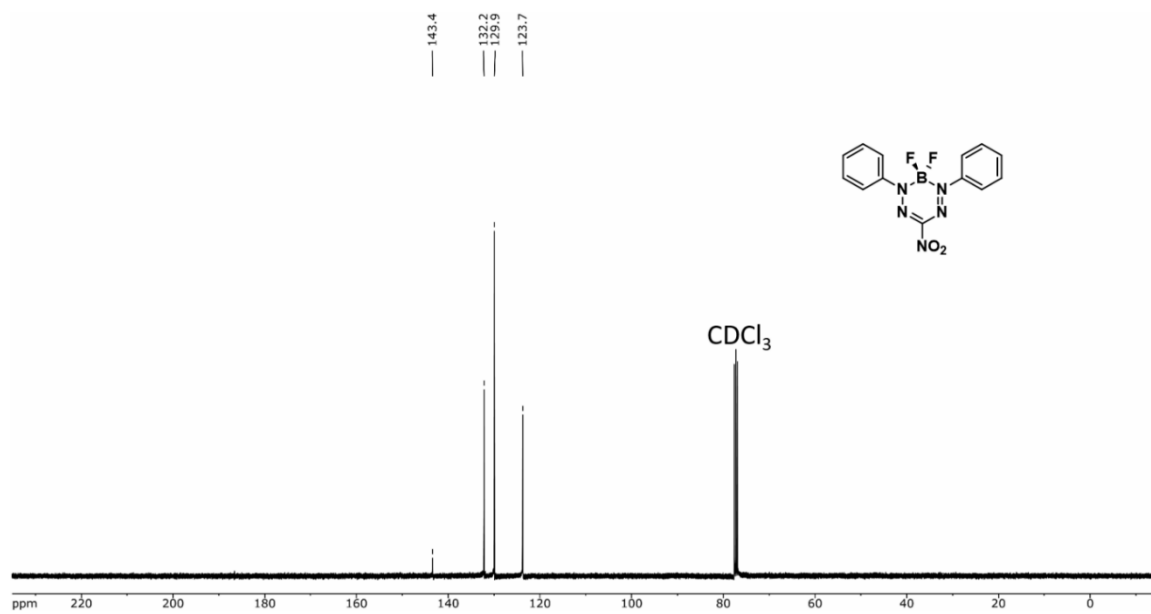
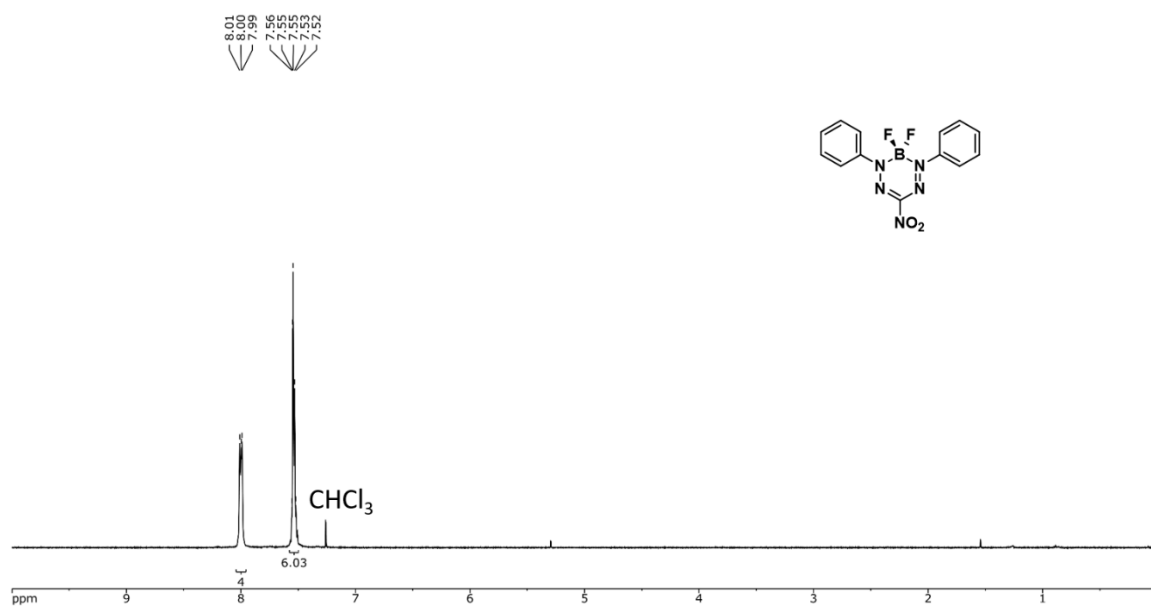


Figure A3.24 $^{13}\text{C}\{^1\text{H}\}$ NMR spectrum of 3.10f in CDCl_3 .



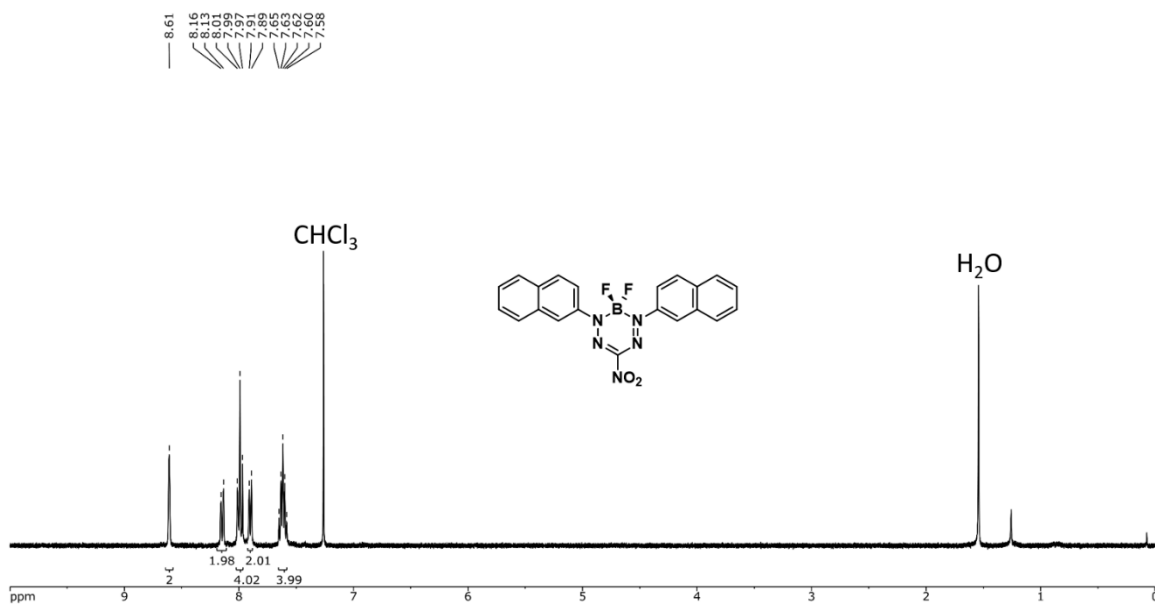


Figure A3.27 ^1H NMR spectrum of 3.10h in CDCl_3 .

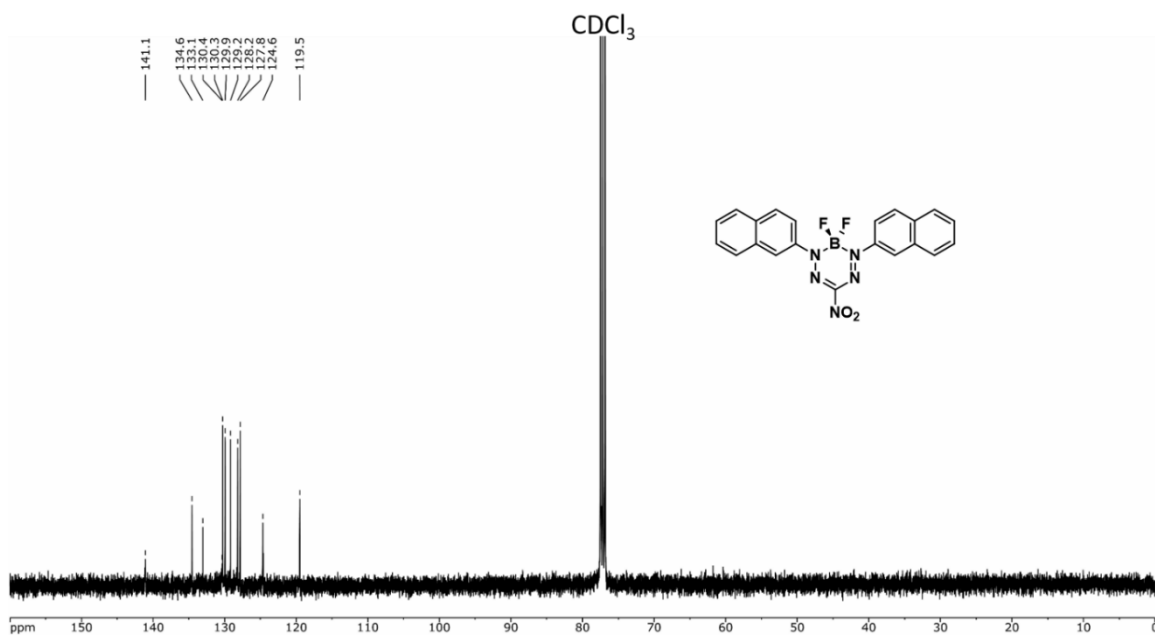


Figure A3.28 $^{13}\text{C}\{^1\text{H}\}$ NMR spectrum of 3.10h in CDCl_3 .

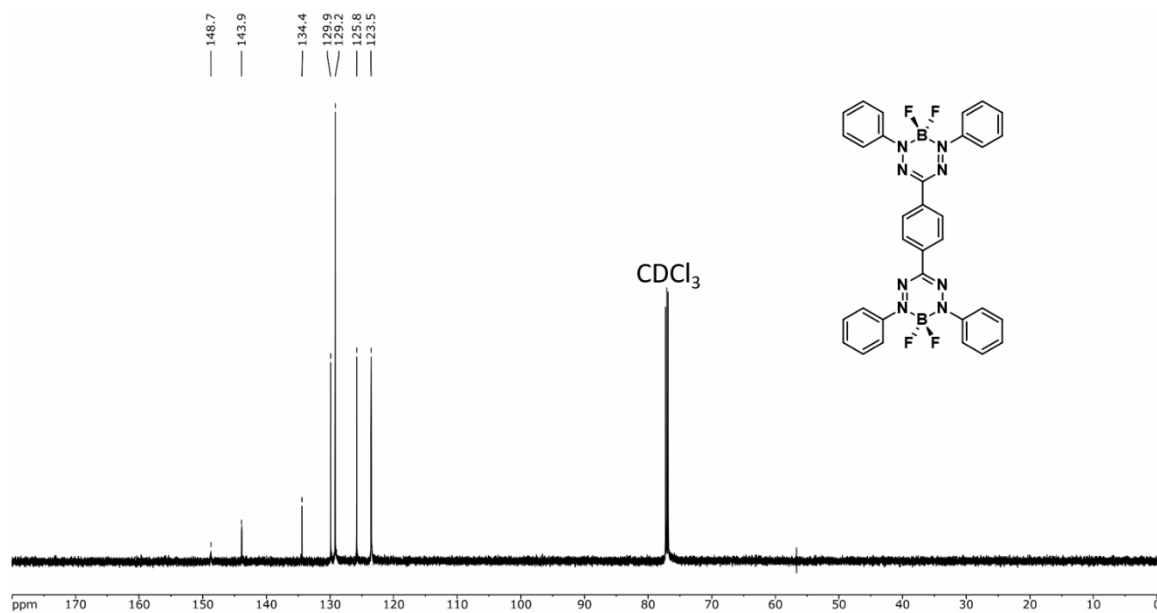


Figure A3.29 $^{13}\text{C}\{^1\text{H}\}$ NMR spectrum of 3.10j in CDCl_3 .

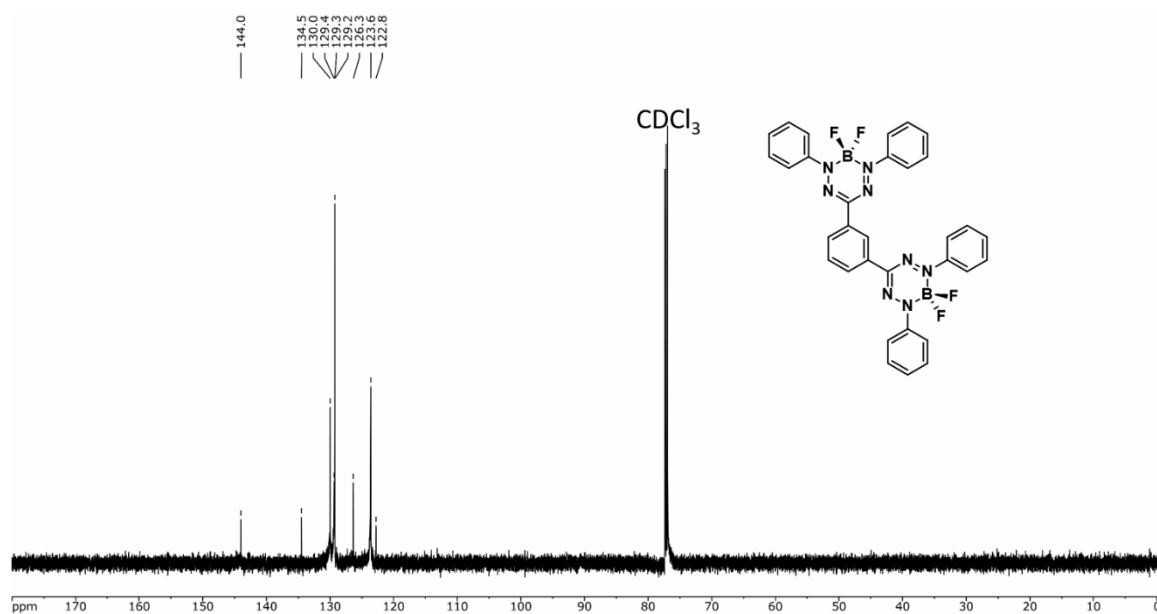


Figure A3.30 $^{13}\text{C}\{^1\text{H}\}$ NMR spectrum of 3.10k in CDCl_3 .

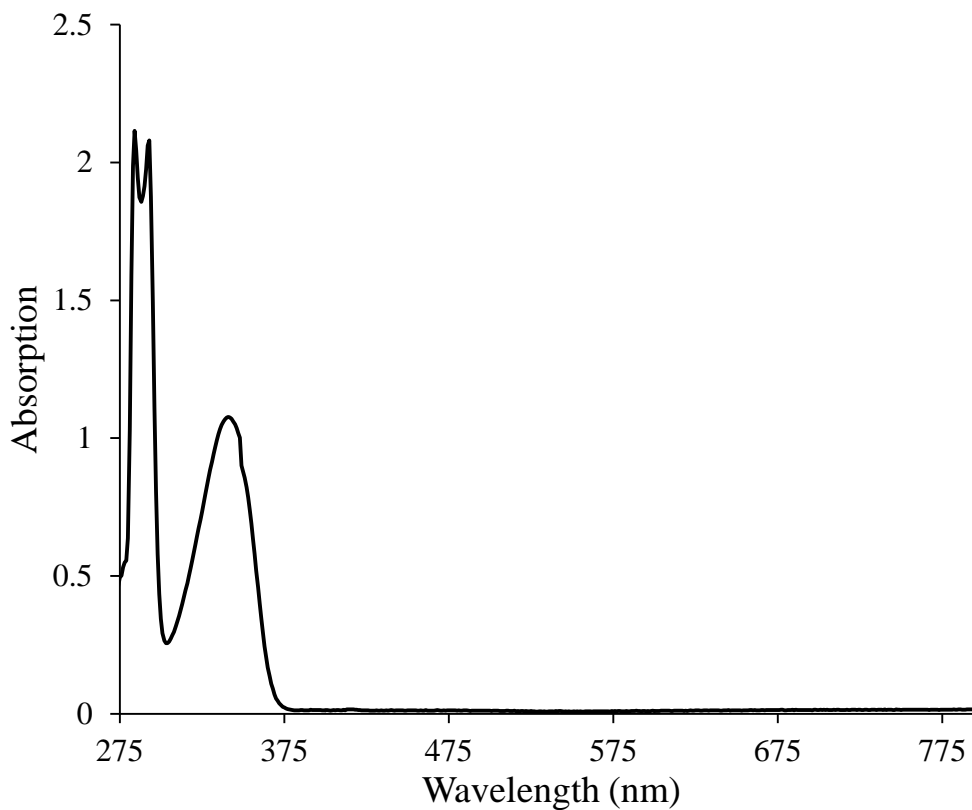


Figure A3.31 UV-vis absorption spectra of 2-naphthylamine in toluene.

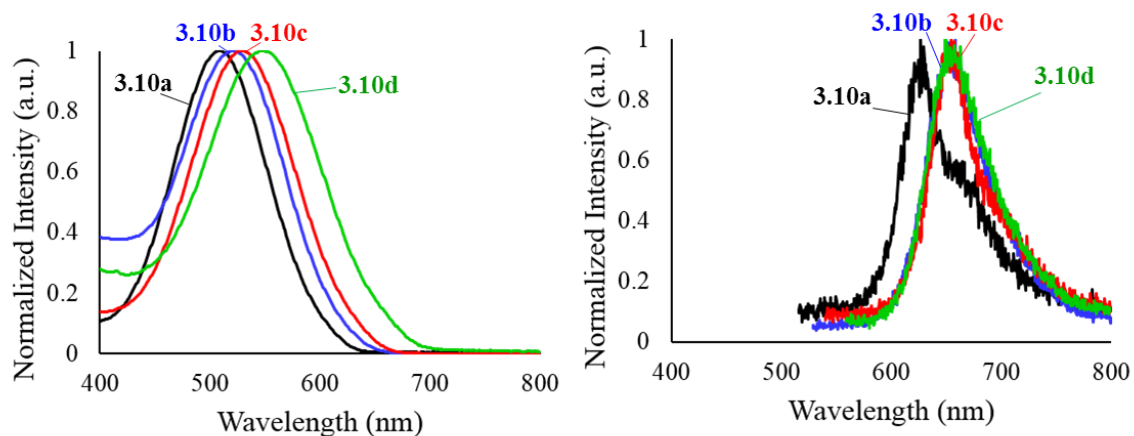


Figure A3.32 UV-vis absorption spectra (left) and emission spectra (right) of **3.10a** (black, $\text{Ar}^1 = \text{Ar}^5 = \text{R}^3 = \text{Ph}$), **3.10b** (blue, $\text{Ar}^1 = \text{Ar}^5 = \text{Ph}$, $\text{R}^3 = \text{Np}$), **3.10c** (red, $\text{Ar}^1 = \text{R}^3 = \text{Ph}$, $\text{Ar}^5 = \text{Np}$) and **3.10d** (green, $\text{Ar}^1 = \text{Ar}^5 = \text{Np}$, $\text{R}^3 = \text{Ph}$). All UV-vis absorption and emission spectra were recorded for 10^{-5} M degassed THF solutions.

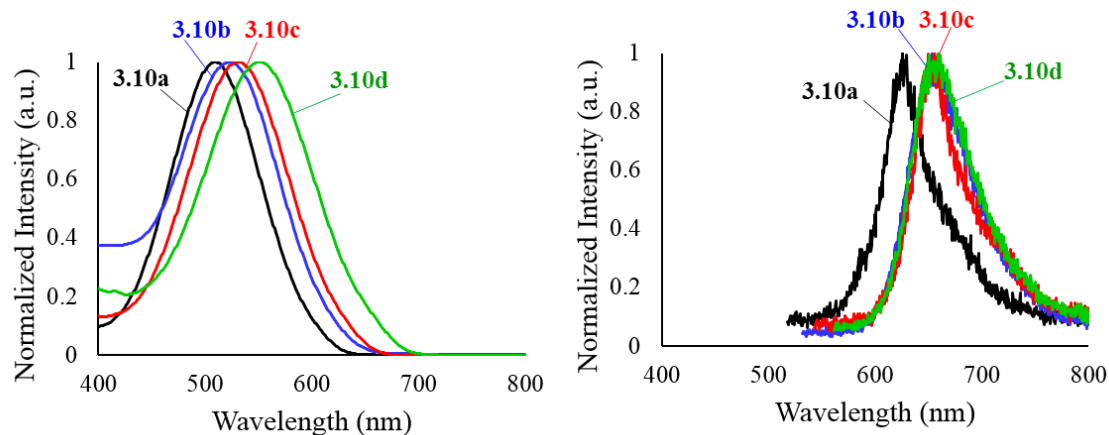


Figure A3.33 UV-vis absorption spectra (left) and emission spectra (right) of **3.10a** (black, Ar¹ = Ar⁵ = R³ = Ph), **3.10b** (blue, Ar¹ = Ar⁵ = Ph, R³ = Np), **3.10c** (red, Ar¹ = R³ = Ph, Ar⁵ = Np) and **3.10d** (green, Ar¹ = Ar⁵ = Np, R³ = Ph). All UV-vis absorption and emission spectra were recorded for 10⁻⁵ M degassed CH₂Cl₂ solutions.

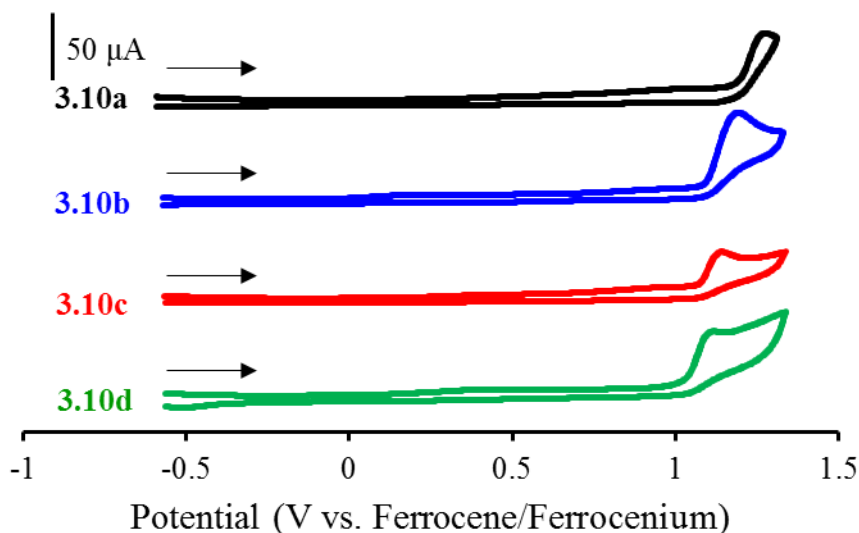


Figure A3.34 Cyclic voltammograms of **3.10a** (black, Ar¹ = Ar⁵ = R³ = phenyl), **3.10b** (blue, Ar¹ = Ar⁵ = phenyl, R³ = naphthyl), **3.10c** (red, Ar¹ = R³ = phenyl, Ar⁵ = naphthyl), and **3.10d** (green, Ar¹ = Ar⁵ = naphthyl, R³ = phenyl) recorded at 100 mV s⁻¹ in 1 mM CH₃CN solutions containing 0.1 M [nBu₄N][PF₆] as supporting electrolyte.

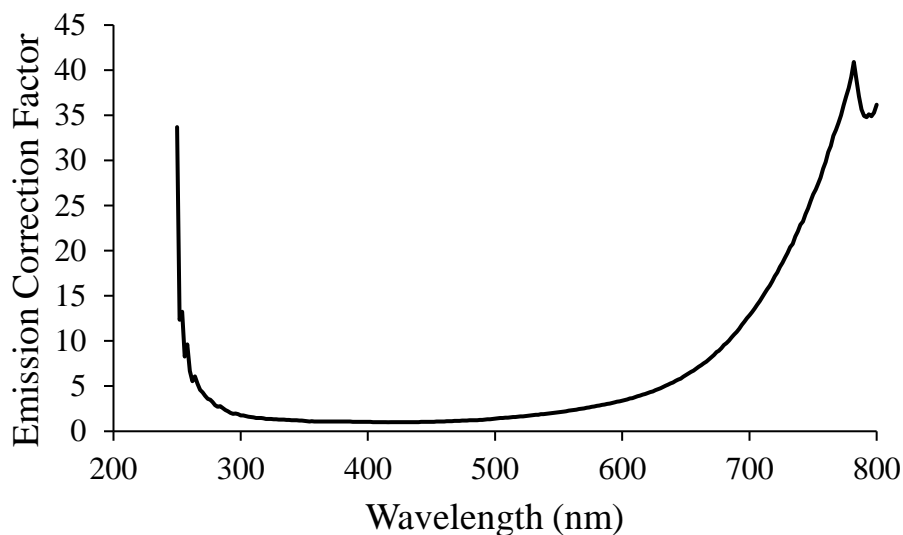


Figure A3.35 Wavelength-dependent emission correction provided by Photon Technology International.

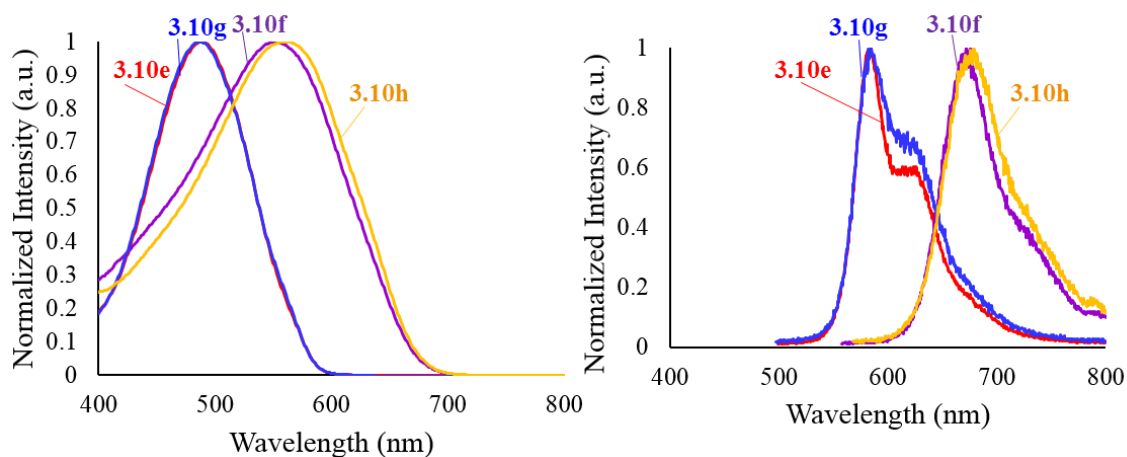


Figure A3.36 UV-vis absorption spectra (left) and emission spectra (right) of **3.10e** (red, Ar¹ = Ar⁵ = Ph, R³ = CN), **3.10f** (purple, Ar¹ = Ar⁵ = Np, R³ = CN), **3.10g** (blue, Ar¹ = Ar⁵ = Ph, R³ = NO₂) and **3.10h** (orange, Ar¹ = Ar⁵ = Np, R³ = NO₂). All UV-vis absorption and emission spectra were recorded for 10⁻⁵ M degassed THF solutions.

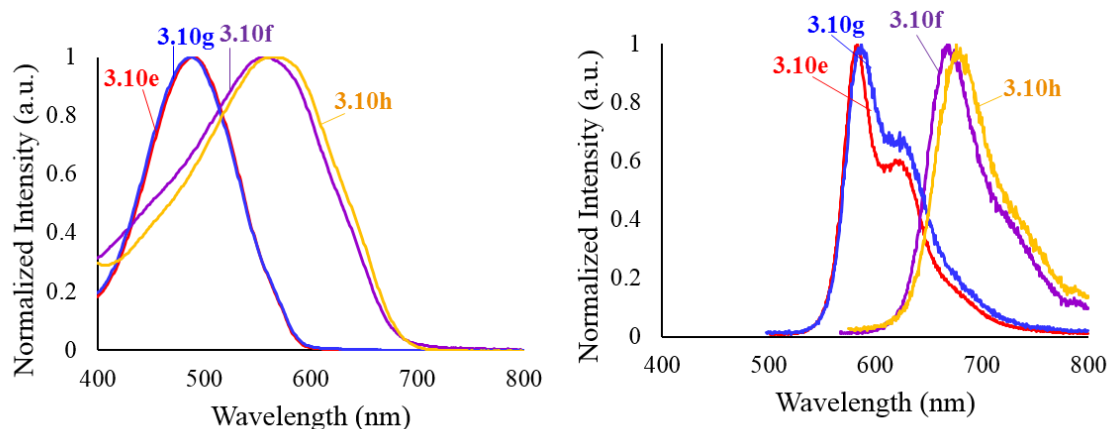


Figure A3.37 UV-vis absorption spectra (left) and emission spectra (right) of **3.10e** (red, Ar¹ = Ar⁵ = Ph, R³ = CN), **3.10f** (purple, Ar¹ = Ar⁵ = Np, R³ = CN), **3.10g** (blue, Ar¹ = Ar⁵ = Ph, R³ = NO₂) and **3.10h** (orange, Ar¹ = Ar⁵ = Np, R³ = NO₂). All UV-vis absorption and emission spectra were recorded for 10⁻⁵ M degassed CH₂Cl₂ solutions.

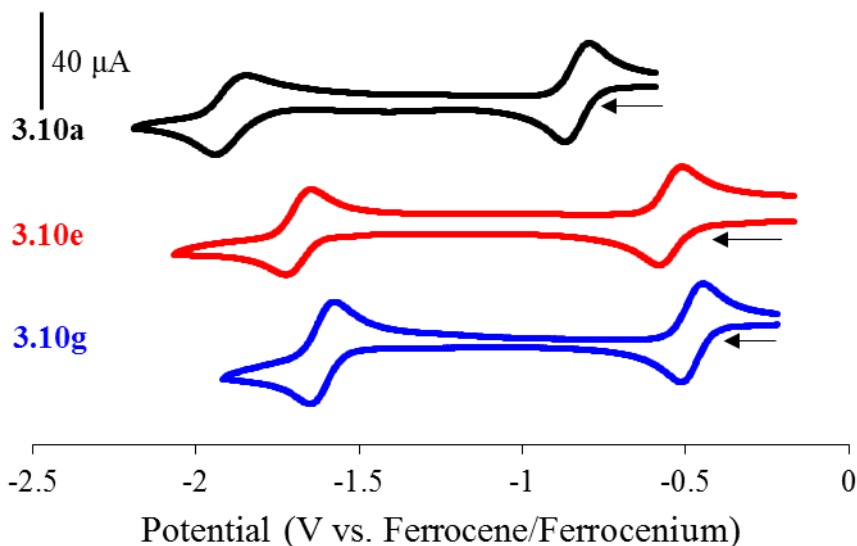


Figure A3.38 Cyclic voltammograms of **3.10a** (black, Ar¹ = Ar⁵ = R³ = phenyl), **3.10e** (red, Ar¹ = Ar⁵ = phenyl, R³ = cyano) and **3.10g** (blue, Ar¹ = Ar⁵ = phenyl, R³ = nitro) recorded at 100 mV s⁻¹ in 1 mM CH₃CN solutions containing 0.1 M [nBu₄N][PF₆] as supporting electrolyte.

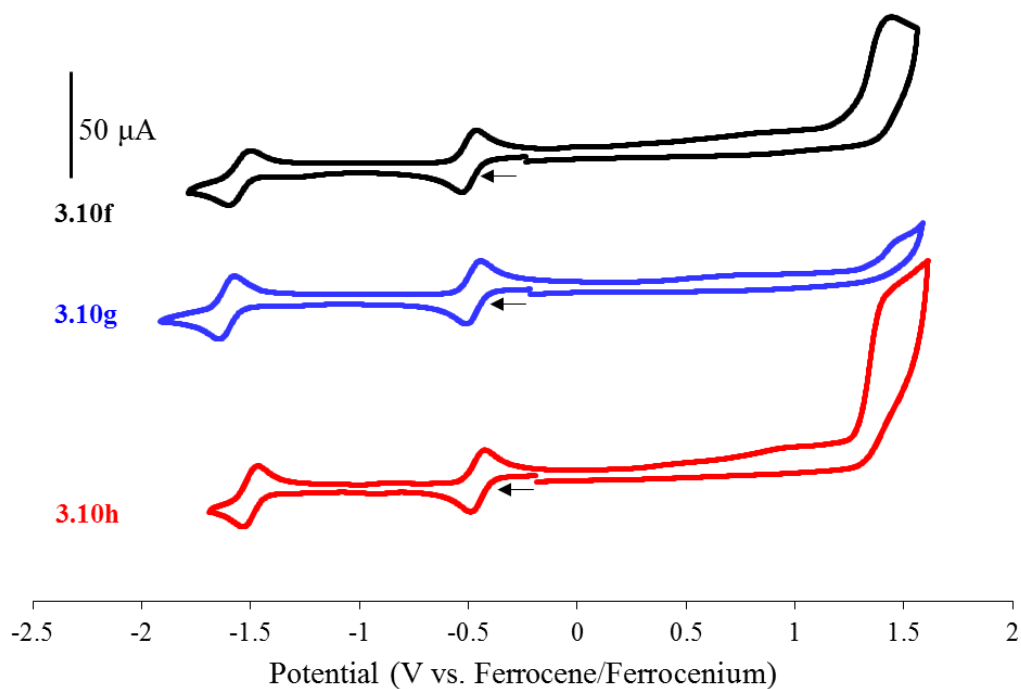


Figure A3.39 Cyclic voltammograms of **3.10f** (black, $\text{Ar}^1 = \text{Ar}^5 = \text{naphthyl}$, $\text{R}^3 = \text{cyano}$), **3.10g** (blue, $\text{Ar}^1 = \text{Ar}^5 = \text{phenyl}$, $\text{R}^3 = \text{nitro}$), and **3.10h** (red, $\text{Ar}^1 = \text{Ar}^5 = \text{naphthyl}$, $\text{R}^3 = \text{nitro}$) recorded at 100 mV s^{-1} in $1 \text{ mM CH}_3\text{CN}$ solutions containing $0.1 \text{ M } [n\text{Bu}_4\text{N}][\text{PF}_6]$ as supporting electrolyte.

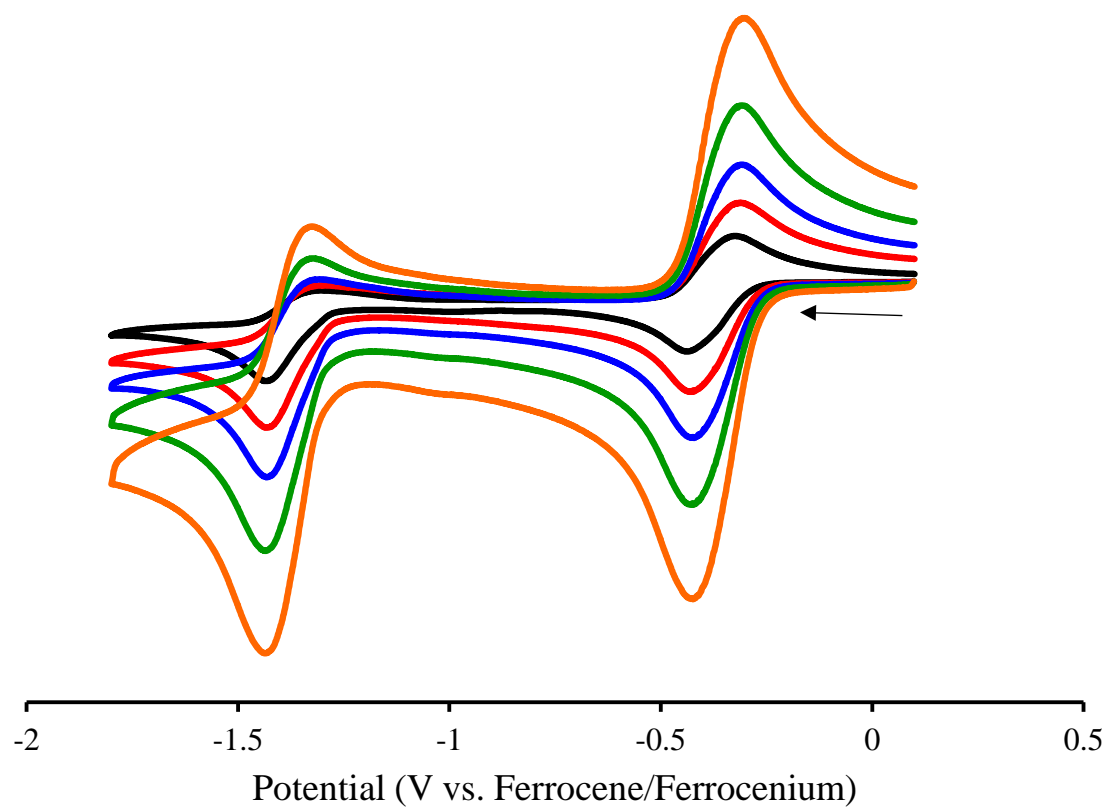


Figure A3.40 Scan rate dependence of **3.10j** in 1 mM CH₂Cl₂ solution containing 0.1 M [nBu₄N][PF₆] as supporting electrolyte run at 100 mV s⁻¹ (black), 250 mV s⁻¹ (red), 500 mV s⁻¹ (blue), 1000 mV s⁻¹ (green) and 2000 mV s⁻¹ (orange).

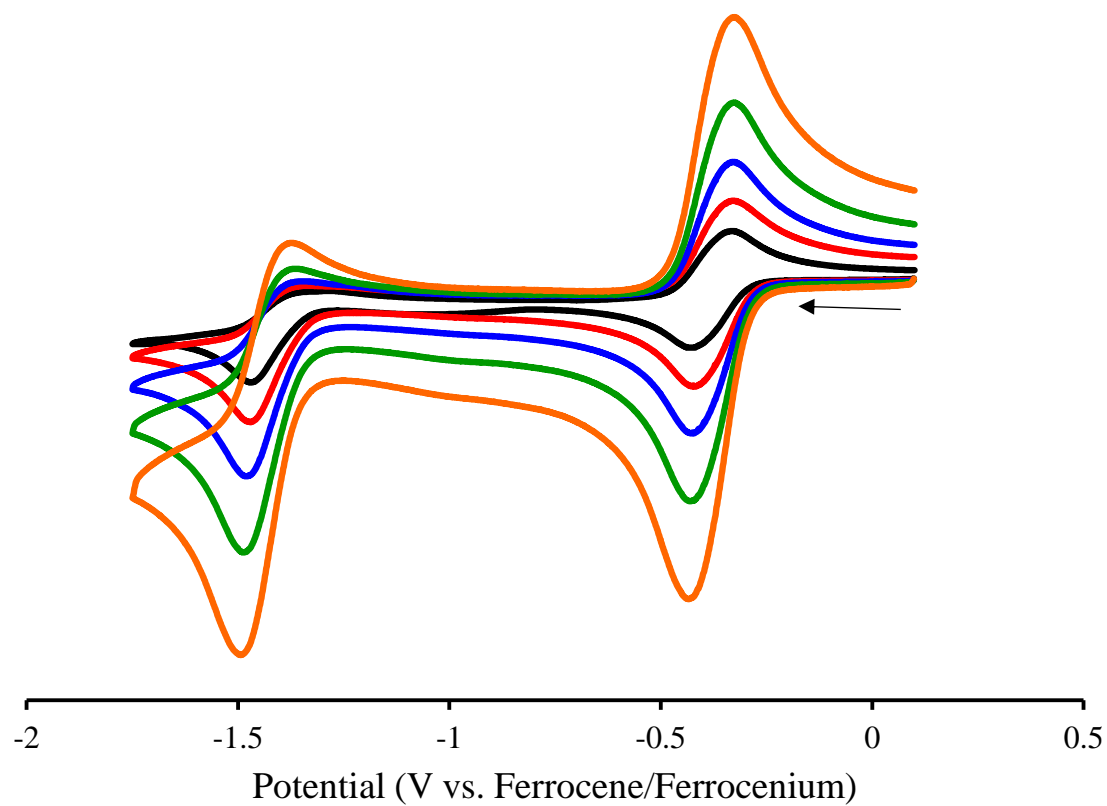


Figure A3.41 Scan rate dependence of **3.10k** in 1 mM CH_2Cl_2 solution containing 0.1 M $[\text{nBu}_4\text{N}][\text{PF}_6]$ as supporting electrolyte run at 100 mV s^{-1} (black), 250 mV s^{-1} (red), 500 mV s^{-1} (blue), 1000 mV s^{-1} (green) and 2000 mV s^{-1} (orange).

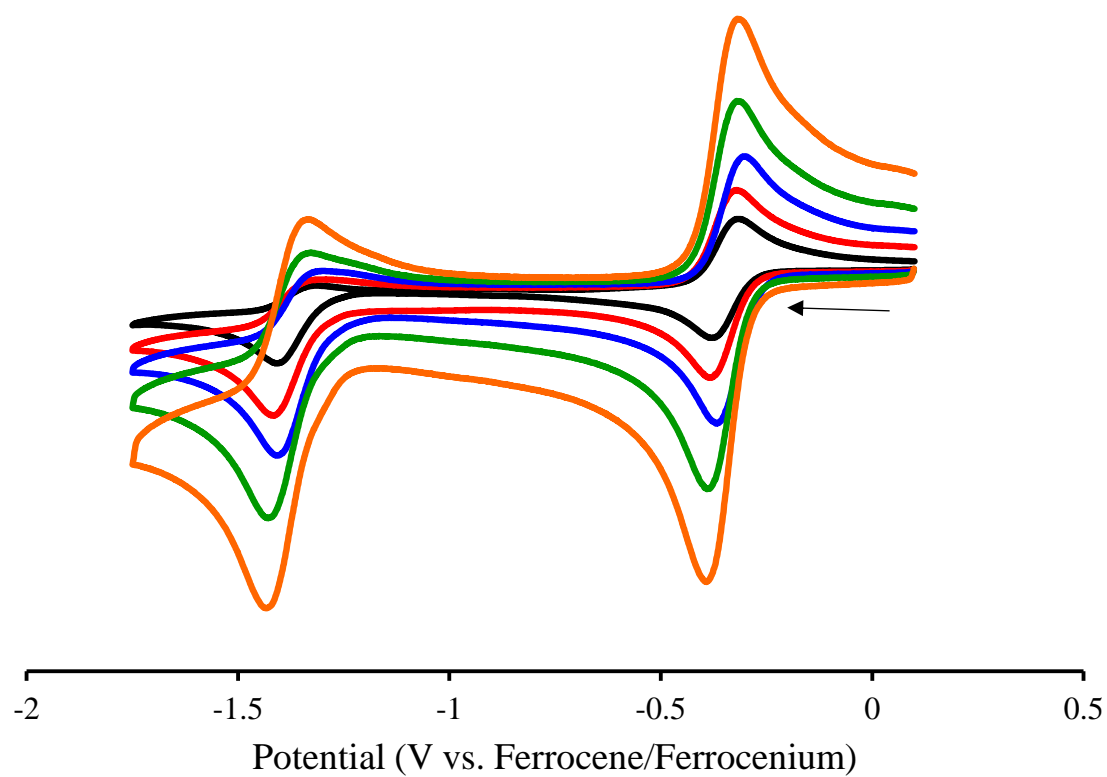


Figure A3.42 Scan rate dependence of **3.10a** in 1 mM CH₂Cl₂ solution containing 0.1 M [nBu₄N][PF₆] as supporting electrolyte run at 100 mV s⁻¹ (black), 250 mV s⁻¹ (red), 500 mV s⁻¹ (blue), 1000 mV s⁻¹ (green) and 2000 mV s⁻¹ (orange).

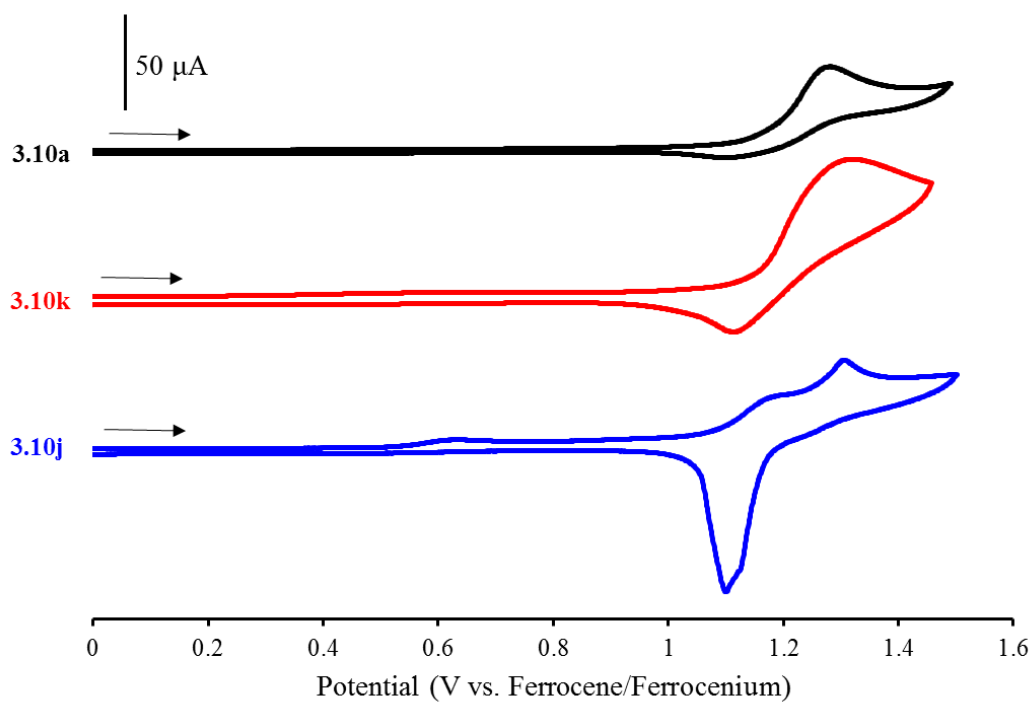


Figure A3.43 Cyclic voltammograms of **3.10j** (blue), **3.10k** (red) and **3.10a** (black) recorded at 100 mV s^{-1} in 1 mM CH_2Cl_2 solutions containing 0.1 M $[\text{nBu}_4\text{N}][\text{PF}_6]$ as supporting electrolyte.

Calculated M06/6-311+G* structures of 3.10a, 3.10e and 3.10g in vacuum. All coordinates are in Å.

M06/6-311+G* Int(Grid=UltraFine)

3.10a (R3 = Ph): Optimized M06/6-311+G* geometry (Cs), vacuum

```

0,1
C   -2.299578    0.585313    2.853536
C   -1.175665   -0.108575    2.411379
C   -0.668154   -1.174345    3.150842
C   -1.284588   -1.541730    4.333801
C   -2.404327   -0.851922    4.782527
C   -2.905976    0.209619    4.041017
N   -0.529006    0.292890    1.212974
B   -1.270421    0.958175    0.000000
F   -1.029154    2.312271    0.000000
N    0.745997    0.098380    1.175418
C    1.377226    0.181856    0.000000
C    2.849568    0.124243    0.000000
N    0.745997    0.098380   -1.175418
N   -0.529006    0.292890   -1.212974
C   -1.175665   -0.108575   -2.411379
C   -0.668154   -1.174345   -3.150842
C   -1.284588   -1.541730   -4.333801
C   -2.404327   -0.851922   -4.782527
C   -2.905976    0.209619   -4.041017
C   -2.299578    0.585313   -2.853536
F   -2.600368    0.644975    0.000000
H    0.204047   -1.707898   -2.784313
H   -0.892865   -2.378594   -4.907002
H   -2.888756   -1.144453   -5.711072
H   -3.777678    0.756474   -4.391756
H   -2.683402    1.422223   -2.278601
H    0.204047   -1.707898    2.784313
H   -0.892865   -2.378594    4.907002
H   -2.888756   -1.144453    5.711072
H   -3.777678    0.756474    4.391756
H   -2.683402    1.422223    2.278601
C    3.557768    0.101448   -1.201996
C    4.942106    0.038477   -1.199565
C    5.640459    0.003660    0.000000
C    4.942106    0.038477    1.199565
C    3.557768    0.101448    1.201996
H    3.013165    0.132890   -2.141827
H    5.480630    0.019967   -2.144471
H    6.727104   -0.043057    0.000000
H    5.480630    0.019967    2.144471
H    3.013165    0.132890    2.141827

```


M06/6-311+G* Int(Grid=UltraFine)

3.10e (R3 = CN): Optimized M06/6-311+G* geometry (Cs), vacuum

0,1

C	2.184147	0.281273	0.000000
N	1.592054	0.178650	1.193952
N	0.310659	0.227134	1.237759
B	-0.549547	0.698134	0.000000
F	-1.767671	0.086222	0.000000
N	0.310659	0.227134	-1.237759
N	1.592054	0.178650	-1.193952
F	-0.621312	2.069365	0.000000
C	-0.276053	-0.106306	-2.489581
C	3.614908	0.305524	0.000000
C	-0.276053	-0.106306	2.489581
N	4.766829	0.336450	0.000000
C	0.380141	-0.980914	-3.352634
C	-0.184198	-1.277993	-4.579801
C	-1.396999	-0.707861	-4.948618
C	-2.045561	0.162932	-4.083236
C	-1.493941	0.466078	-2.849707
H	1.325718	-1.421122	-3.050307
H	0.323173	-1.965514	-5.251801
H	-1.838958	-0.945645	-5.913137
H	-2.990577	0.616148	-4.371271
H	-1.995460	1.156584	-2.179414
C	0.380141	-0.980914	3.352634
C	-0.184198	-1.277993	4.579801
C	-1.396999	-0.707861	4.948618
C	-2.045561	0.162932	4.083236
C	-1.493941	0.466078	2.849707
H	1.325718	-1.421122	3.050307
H	0.323173	-1.965514	5.251801
H	-1.838958	-0.945645	5.913137
H	-2.990577	0.616148	4.371271
H	-1.995460	1.156584	2.179414

M06/6-311+G* Int(Grid=UltraFine)

3.10g (R3 = NO2): Optimized M06/6-311+G* geometry (Cs), vacuum

```

0,1
C   -1.728116    0.458177    2.847695
C   -0.508151   -0.115266    2.495884
C    0.152265   -0.974679    3.371506
C   -0.412065   -1.257196    4.601737
C   -1.628077   -0.687641    4.961672
C   -2.279483    0.169123    4.084700
N    0.078292    0.204595    1.240653
B   -0.775539    0.692758    0.000000
F   -0.819486    2.063567    0.000000
N    1.357319    0.123670    1.188209
C    1.925597    0.225301    0.000000
N    3.408092    0.213485    0.000000
N    1.357319    0.123670   -1.188209
N    0.078292    0.204595   -1.240653
C   -0.508151   -0.115266   -2.495884
C    0.152265   -0.974679   -3.371506
C   -0.412065   -1.257196   -4.601737
C   -1.628077   -0.687641   -4.961672
C   -2.279483    0.169123   -4.084700
C   -1.728116    0.458177   -2.847695
F   -2.002605    0.100989    0.000000
H    1.102650   -1.410422   -3.078049
H    0.098722   -1.931692   -5.284165
H   -2.069688   -0.914306   -5.929015
H   -3.226271    0.622642   -4.366210
H   -2.232219    1.138191   -2.168881
H    1.102650   -1.410422    3.078049
H    0.098722   -1.931692    5.284165
H   -2.069688   -0.914306    5.929015
H   -3.226271    0.622642    4.366210
H   -2.232219    1.138191    2.168881
O    3.954054    0.218392   -1.078741
O    3.954054    0.218392    1.078741

```

**Calculated M06/6-311+G* structures of 3.10a, 3.10e and 3.10g in toluene solution.
All coordinates are in Å.**

M06/6-311+G* Int(Grid=UltraFine) SCRF=(PCM,Solvent=Toluene)

3.10a (R3 = Ph): Optimized M06/6-311+G* geometry (Cs), toluene solution

```

0,1
C    -0.611350    -2.279560    2.867417
C     0.104011    -1.179417    2.400459
C     1.206309    -0.701602    3.105236
C     1.589108    -1.324593    4.280354
C     0.877827    -2.420599    4.754425
C    -0.220441    -2.892768    4.046850
N    -0.311587    -0.524373    1.210790
B    -0.985853    -1.253685    0.000000
F    -2.341242    -0.992310    0.000000
N    -0.106454     0.749541    1.174641
C    -0.189131     1.382462    0.000000
C    -0.123721     2.854518    0.000000
N    -0.106454     0.749541   -1.174641
N    -0.311587    -0.524373   -1.210790
C     0.104011    -1.179417   -2.400459
C     1.206309    -0.701602   -3.105236
C     1.589108    -1.324593   -4.280354
C     0.877827    -2.420599   -4.754425
C    -0.220441    -2.892768   -4.046850
C    -0.611350    -2.279560   -2.867417
F    -0.700175    -2.591220    0.000000
H     1.757648     0.150682   -2.718579
H     2.454186    -0.957127   -4.826777
H     1.182164    -2.909949   -5.676411
H    -0.783767    -3.745034   -4.418228
H    -1.478149    -2.638472   -2.320971
H     1.757648     0.150682    2.718579
H     2.454186    -0.957127    4.826777
H     1.182164    -2.909949    5.676411
H    -0.783767    -3.745034    4.418228
H    -1.478149    -2.638472    2.320971
C    -0.096846     3.562675   -1.202275
C    -0.025124     4.946992   -1.199985
C     0.014372     5.645258    0.000000
C    -0.025124     4.946992    1.199985
C    -0.096846     3.562675    1.202275
H    -0.131411     3.019430   -2.142747
H    -0.003057     5.485176   -2.144886
H     0.068311     6.731474    0.000000
H    -0.003057     5.485176    2.144886
H    -0.131411     3.019430    2.142747

```

M06/6-311+G* Int(Grid=UltraFine)SCRF=(PCM,Solvent=Toluene)

3.10e (R3 = CN): Optimized M06/6-311+G* geometry (Cs), toluene solution

```

0,1
C      2.186655      0.286978      0.000000
N      1.595515      0.184729      1.194429
N      0.314638      0.242583      1.236854
B     -0.535905      0.726978      0.000000
F     -1.767225      0.140288      0.000000
N      0.314638      0.242583     -1.236854
N      1.595515      0.184729     -1.194429
F     -0.584603      2.102405      0.000000
C     -0.278213     -0.104836     -2.482029
C      3.617127      0.302617      0.000000
C     -0.278213     -0.104836      2.482029
N      4.769362      0.327999      0.000000
C      0.352002     -1.025943     -3.315512
C     -0.216635     -1.338035     -4.537350
C     -1.407390     -0.736394     -4.928442
C     -2.030670      0.180259     -4.091368
C     -1.474626      0.498448     -2.863456
H      1.277777     -1.493989     -2.994080
H      0.268703     -2.062159     -5.186506
H     -1.852803     -0.985815     -5.888262
H     -2.957745      0.657477     -4.397742
H     -1.954943      1.225967     -2.216822
C      0.352002     -1.025943      3.315512
C     -0.216635     -1.338035      4.537350
C     -1.407390     -0.736394      4.928442
C     -2.030670      0.180259      4.091368
C     -1.474626      0.498448      2.863456
H      1.277777     -1.493989      2.994080
H      0.268703     -2.062159      5.186506
H     -1.852803     -0.985815      5.888262
H     -2.957745      0.657477      4.397742
H     -1.954943      1.225967      2.216822

```

M06/6-311+G* Int(Grid=UltraFine) SCRF=(PCM,Solvent=Toluene)

3.10g (R3 = NO2): Optimized M06/6-311+G* geometry (Cs), toluene solution

```

0,1
C   -1.702774    0.502704    2.861272
C   -0.512572   -0.114662    2.482338
C    0.107934   -1.040583    3.318257
C   -0.465476   -1.344361    4.539549
C   -1.650732   -0.729698    4.927865
C   -2.263486    0.192252    4.088952
N    0.085660    0.225908    1.238492
B   -0.750350    0.743507    0.000000
F   -0.743785    2.117743    0.000000
N    1.363411    0.127875    1.188524
C    1.932407    0.230393    0.000000
N    3.409584    0.207030    0.000000
N    1.363411    0.127875   -1.188524
N    0.085660    0.225908   -1.238492
C   -0.512572   -0.114662   -2.482338
C    0.107934   -1.040583   -3.318257
C   -0.465476   -1.344361   -4.539549
C   -1.650732   -0.729698   -4.927865
C   -2.263486    0.192252   -4.088952
C   -1.702774    0.502704   -2.861272
F   -2.000060    0.200581    0.000000
H    1.030993   -1.516047   -3.000226
H    0.012225   -2.071241   -5.191153
H   -2.099771   -0.972866   -5.887574
H   -3.185604    0.679852   -4.393724
H   -2.174852    1.234515   -2.213576
H    1.030993   -1.516047    3.000226
H    0.012225   -2.071241    5.191153
H   -2.099771   -0.972866    5.887574
H   -3.185604    0.679852    4.393724
H   -2.174852    1.234515    2.213576
O    3.961070    0.208547   -1.077611
O    3.961070    0.208547    1.077611

```

Appendix A4 Supporting Information for Chapter 4

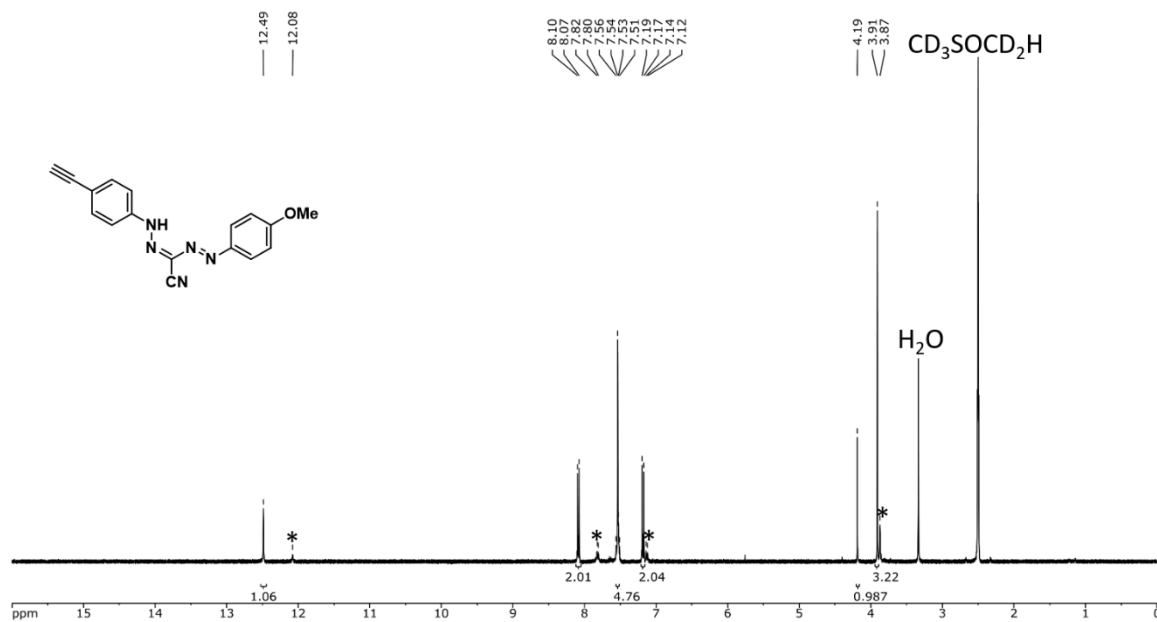


Figure A4.1 ^1H NMR spectrum of **4.8** in $\text{DMSO-}d_6$. Asterisks indicate signals from the minor isomer.

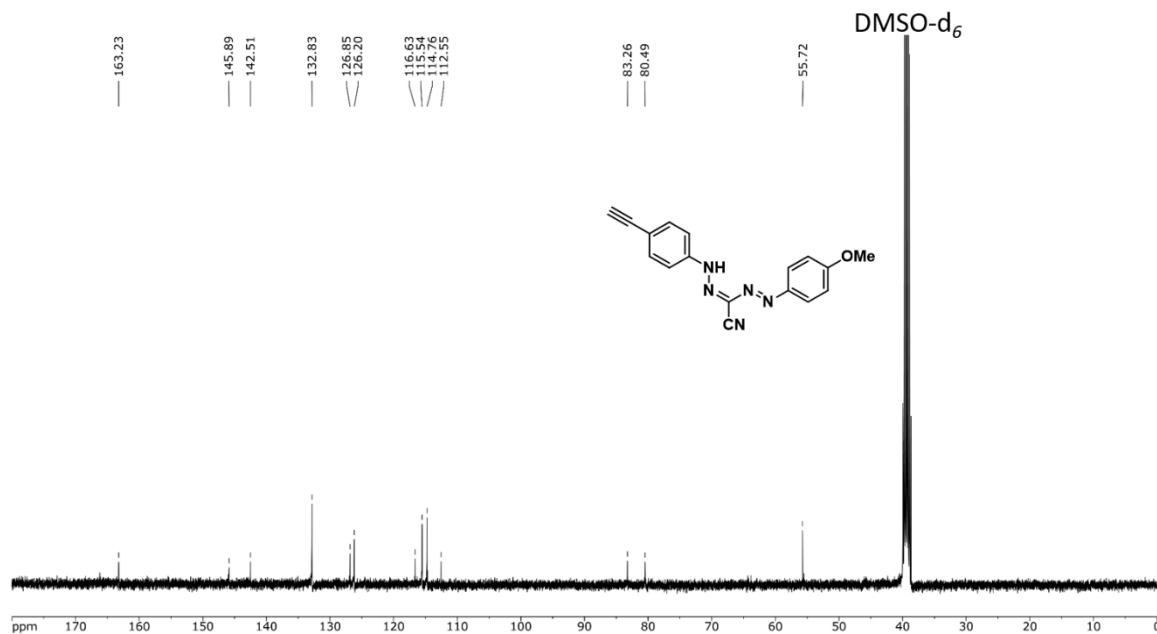


Figure A4.2 $^{13}\text{C}\{^1\text{H}\}$ NMR spectrum of **4.8** in $\text{DMSO-}d_6$.

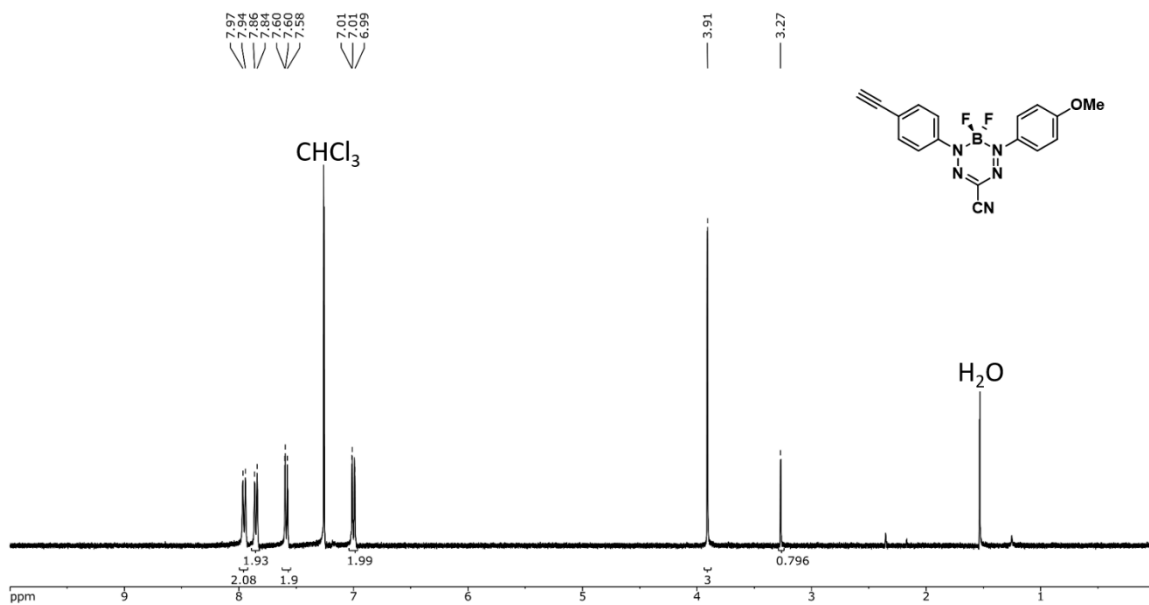


Figure A4.3 ^1H NMR spectrum of **4.9** in CDCl_3 .

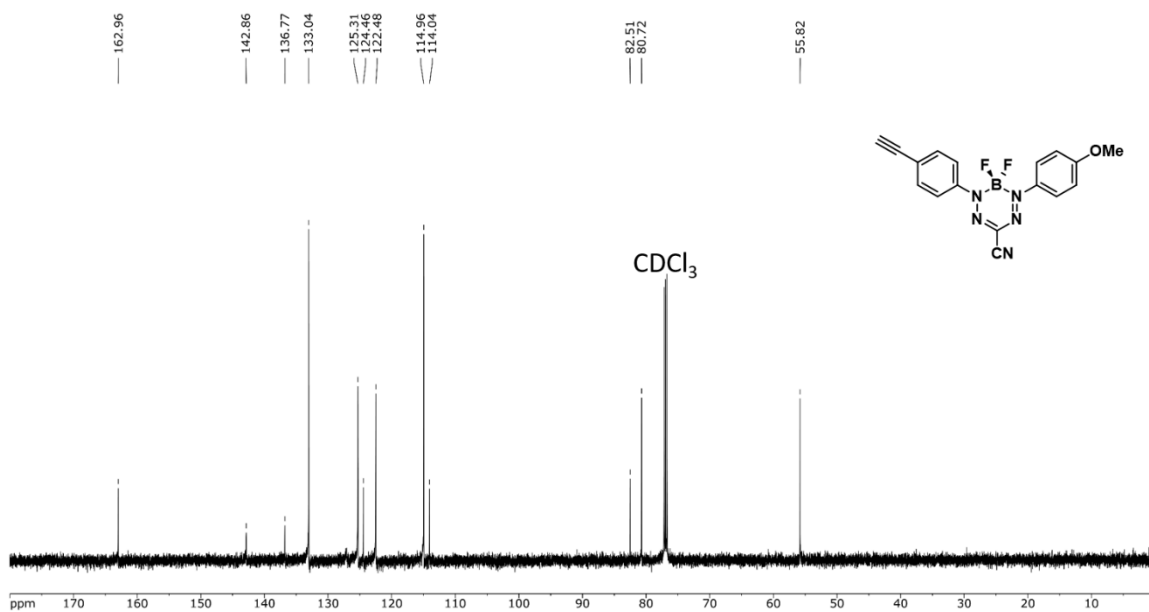


Figure A4.4 $^{13}\text{C}\{^1\text{H}\}$ NMR spectrum of **4.9** in CDCl_3 .

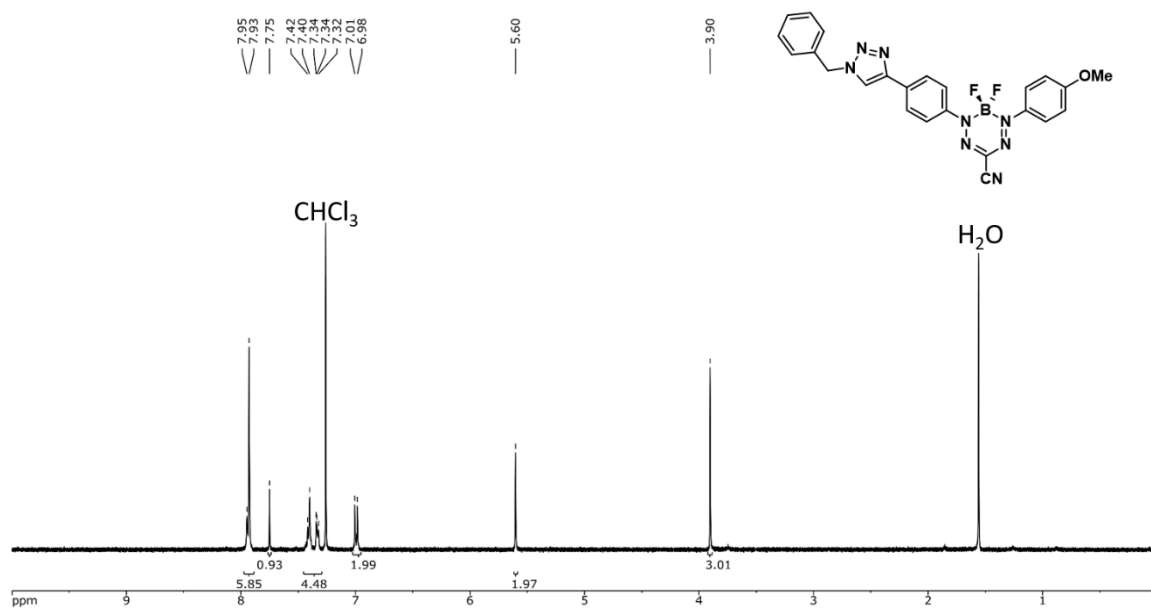


Figure A4.5 ^1H NMR spectrum of **4.10** in CDCl_3 .

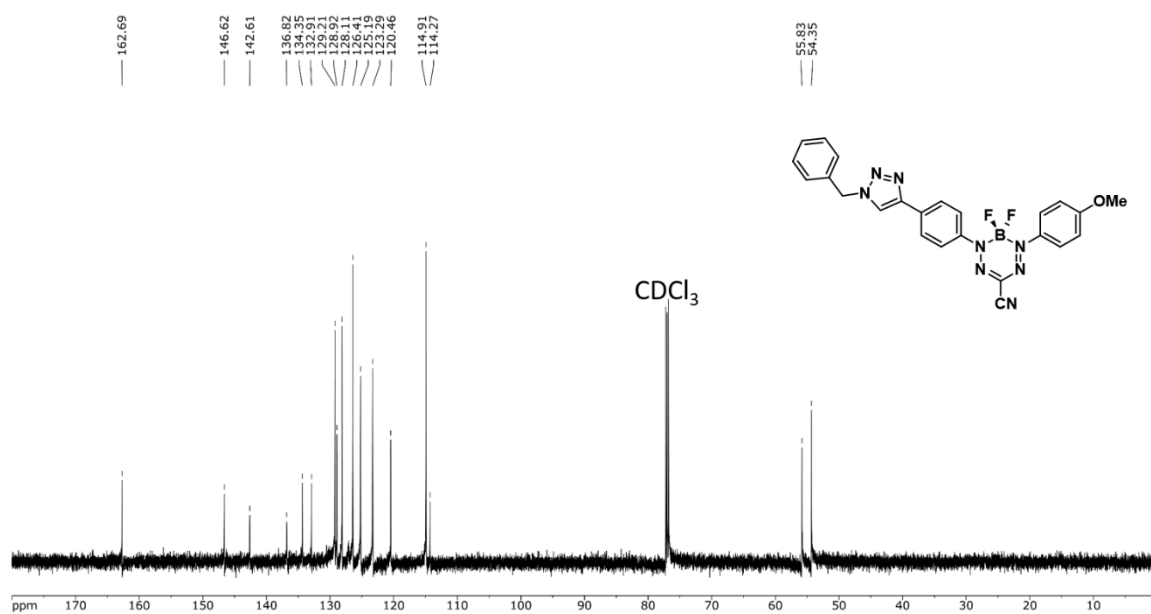


Figure A4.6 $^{13}\text{C}\{^1\text{H}\}$ NMR spectrum of **4.10** in CDCl_3 .

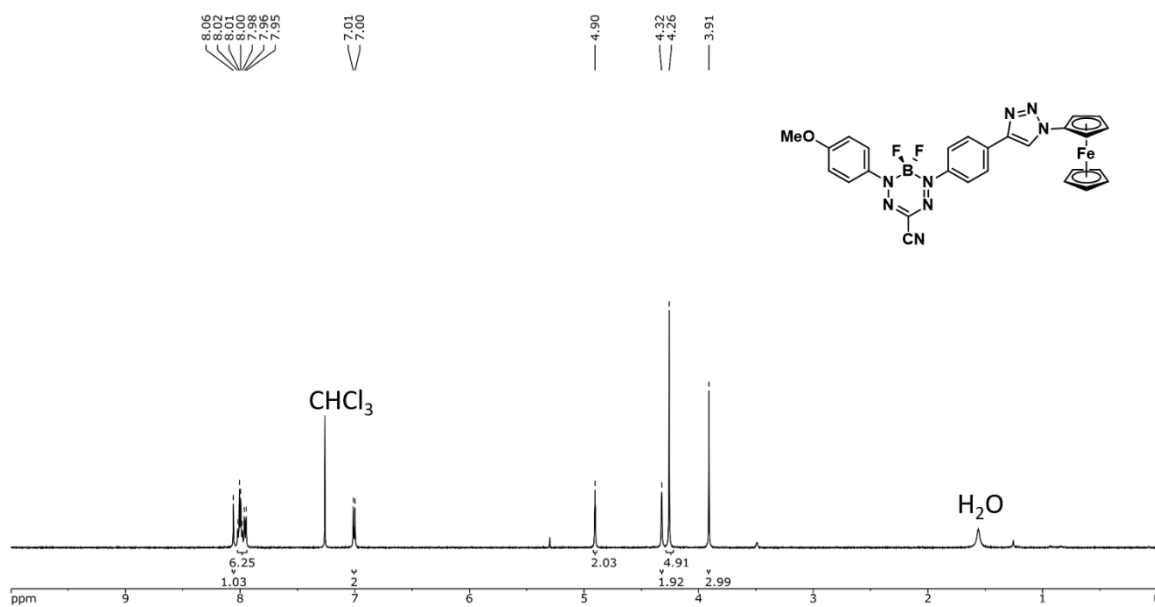


Figure A4.7 ^1H NMR spectrum of **4.11** in CDCl_3 .

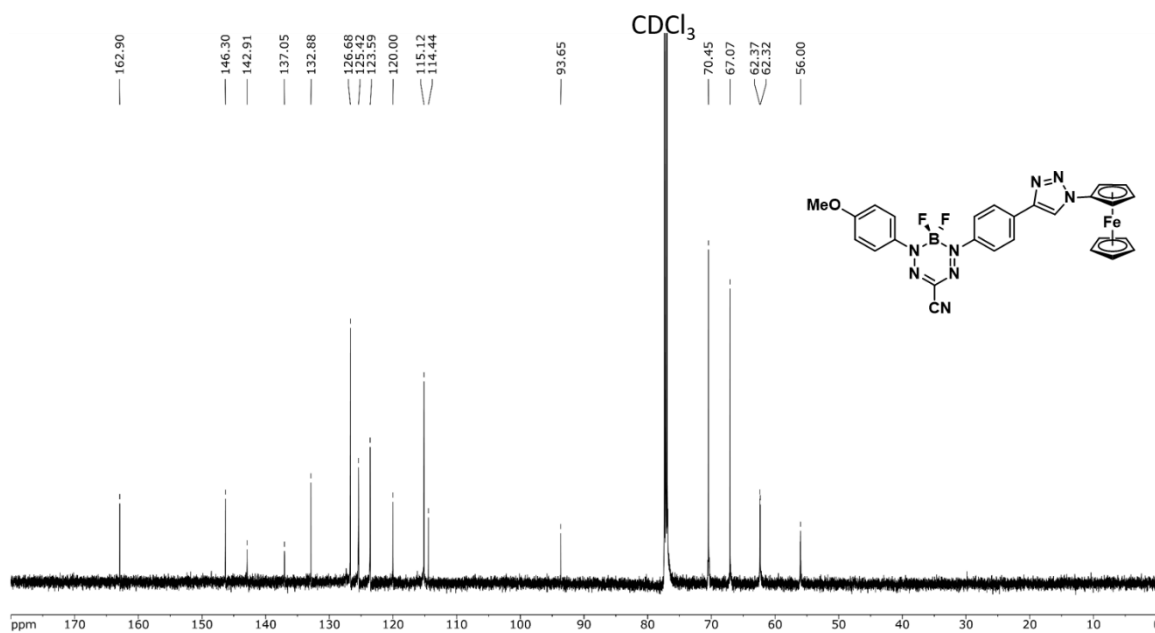


Figure A4.8 $^{13}\text{C}\{^1\text{H}\}$ NMR spectrum of **4.11** in CDCl_3 .

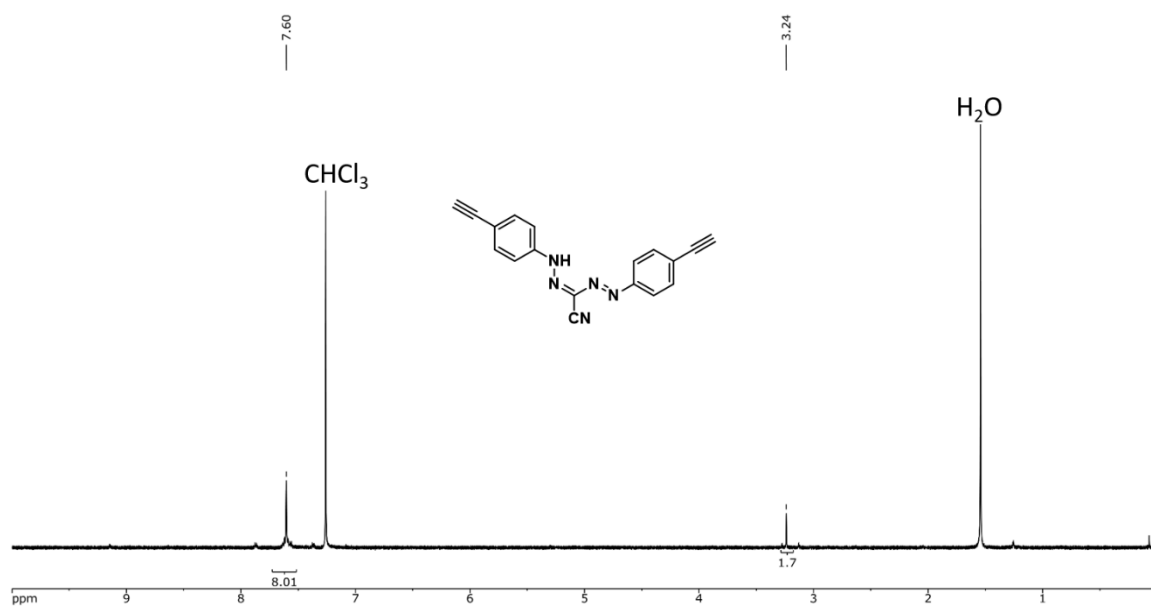


Figure A4.9 ^1H NMR spectrum of 4.12 in CDCl_3 .

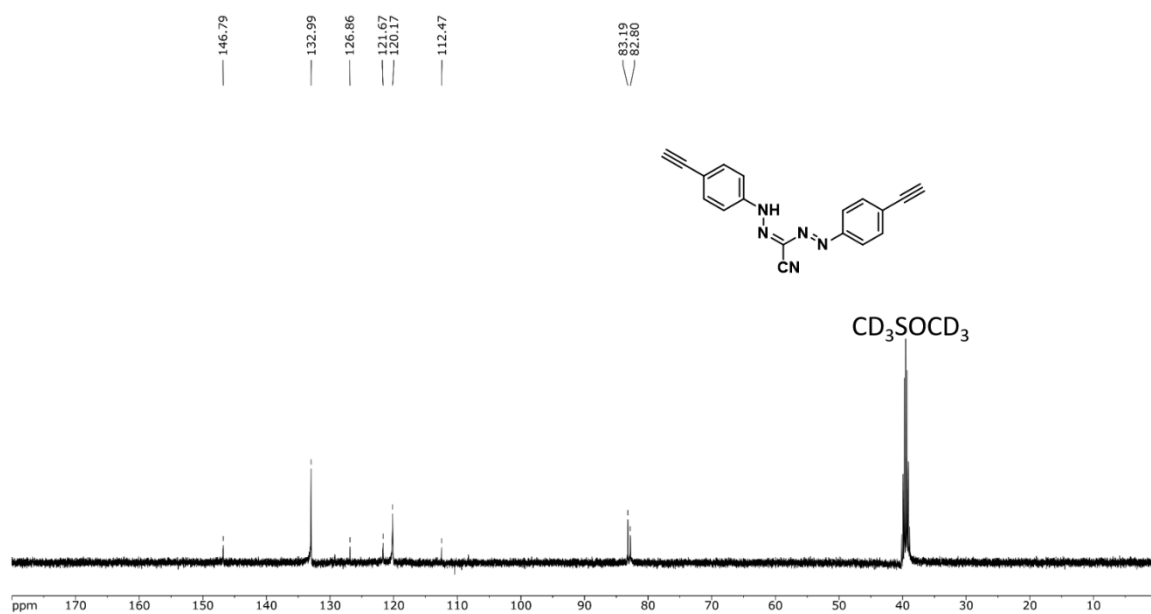
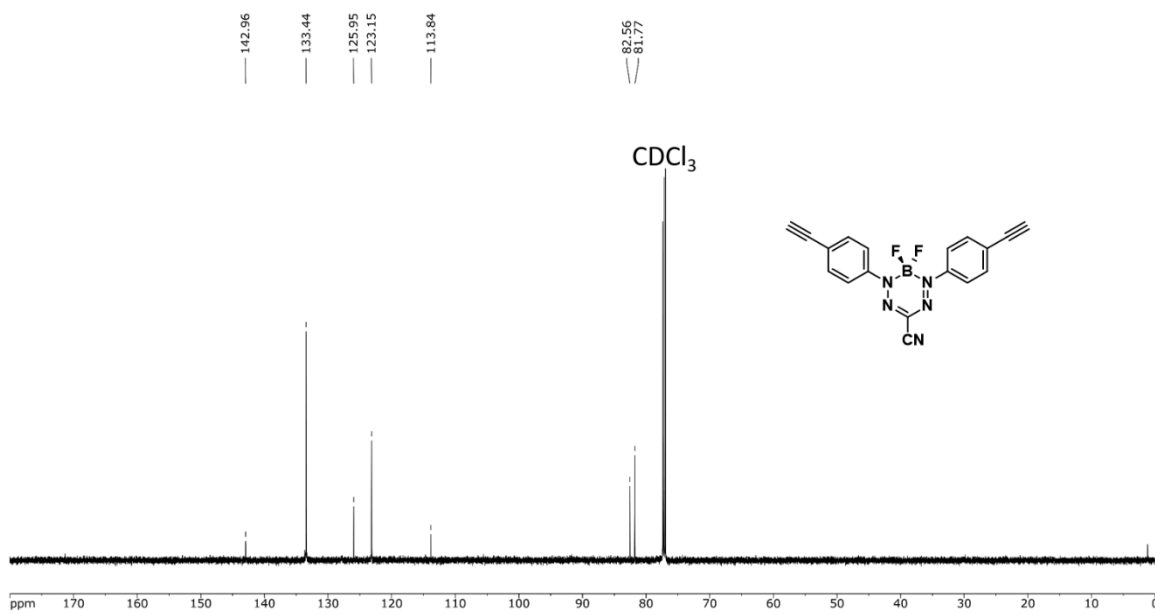
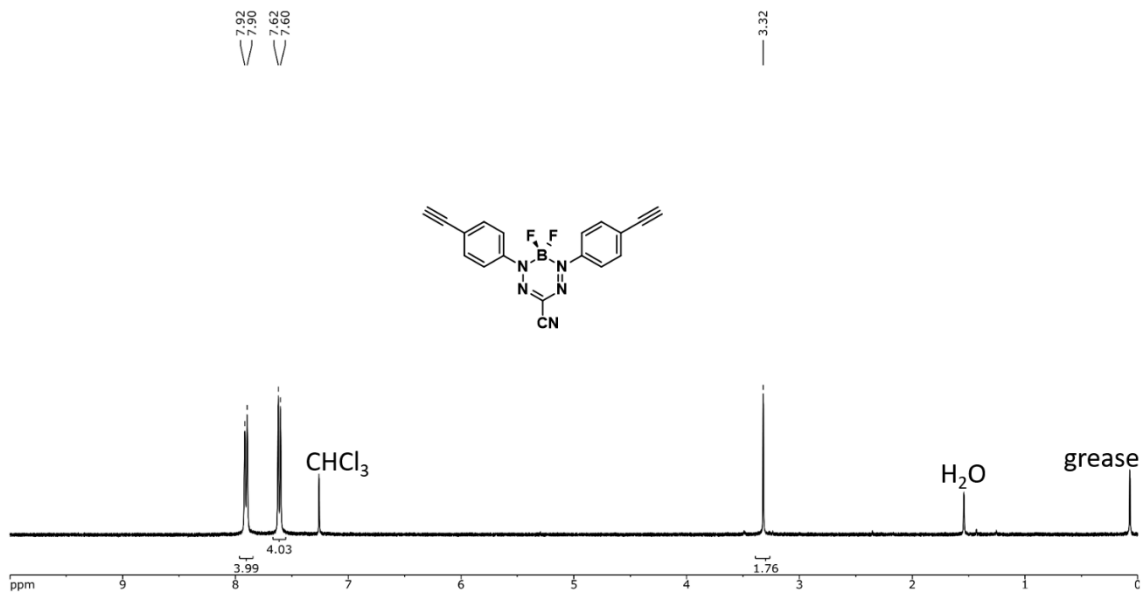
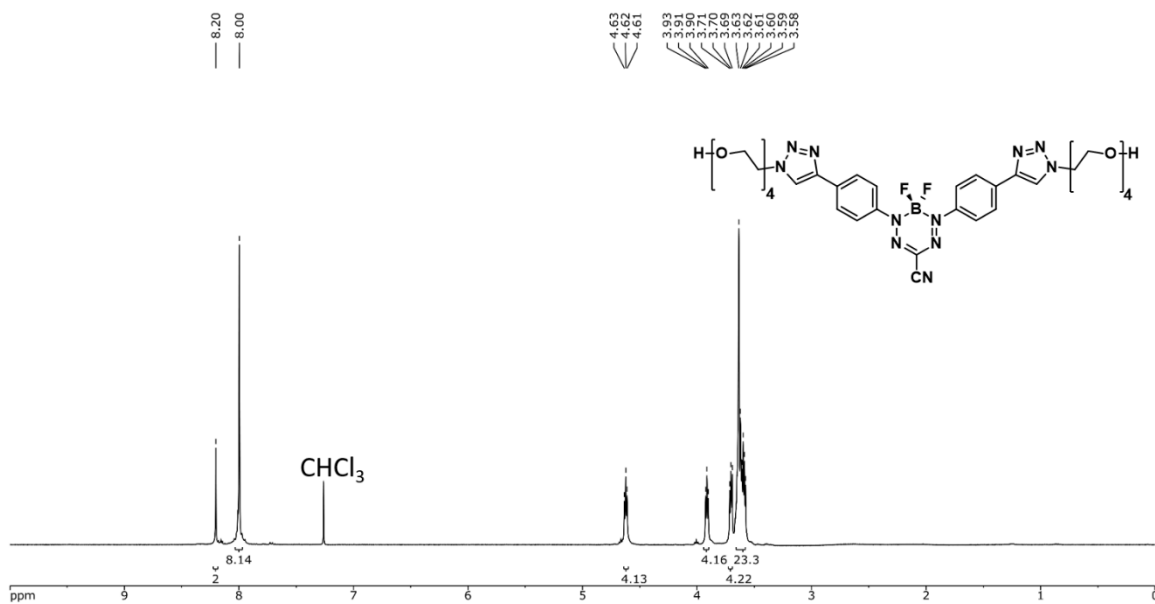
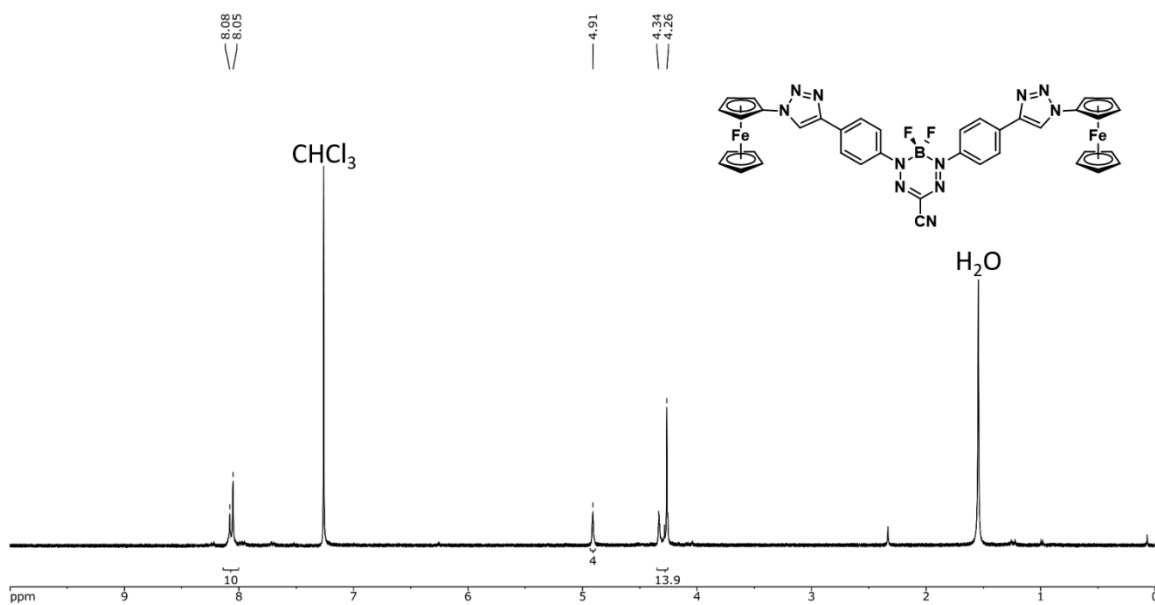


Figure A4.10 $^{13}\text{C}\{^1\text{H}\}$ NMR spectrum of 4.12 in $\text{DMSO-}d_6$.





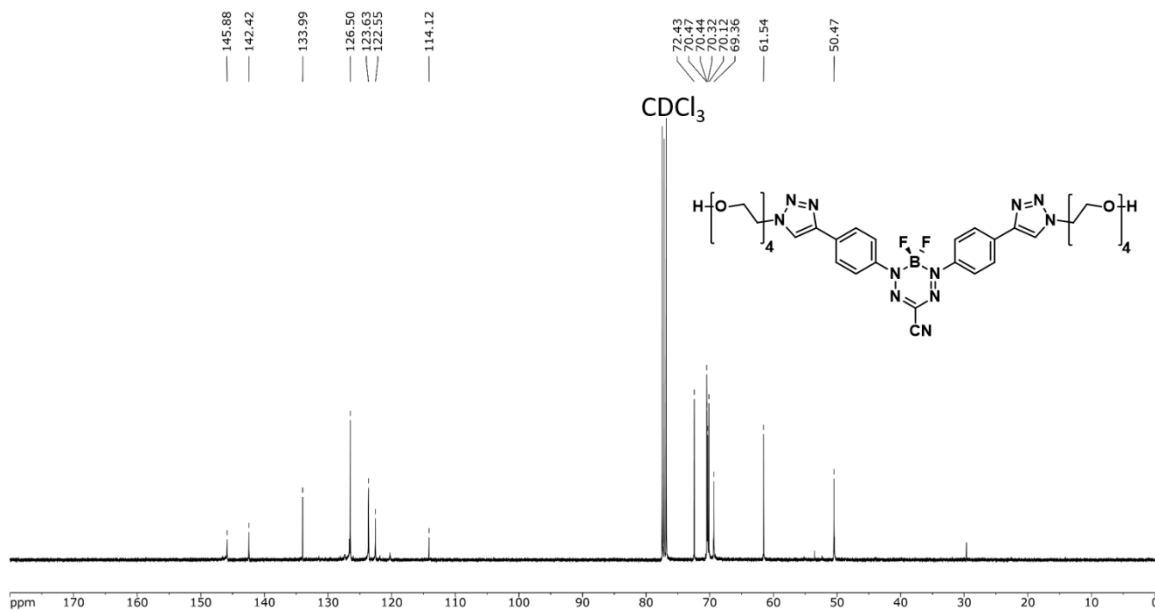


Figure A4.17 $^{13}\text{C}\{^1\text{H}\}$ NMR spectrum of **4.16** in CDCl_3 .

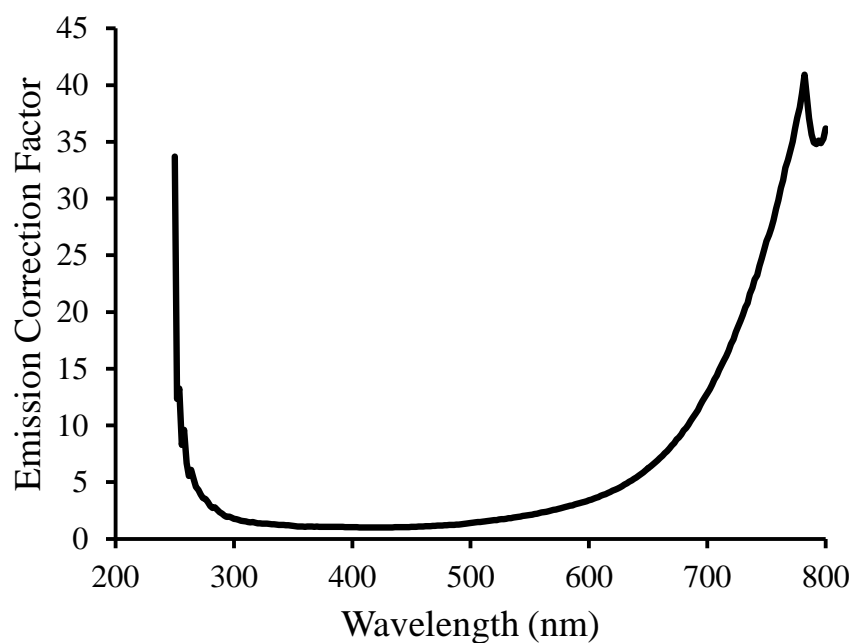


Figure A4.18 Wavelength-dependent emission correction provided by Photon Technology International.

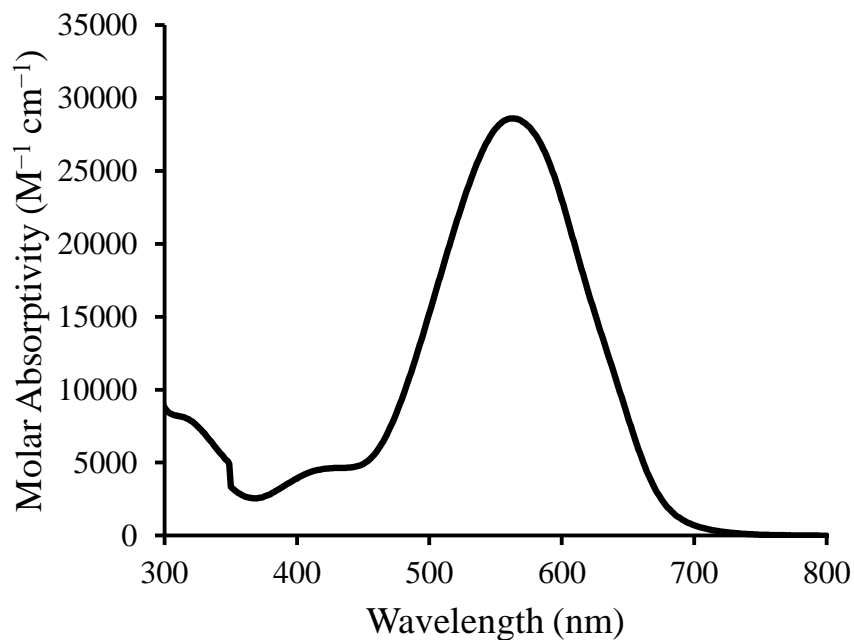


Figure A4.19 UV-vis absorption spectrum of **4.11** in CH₂Cl₂.

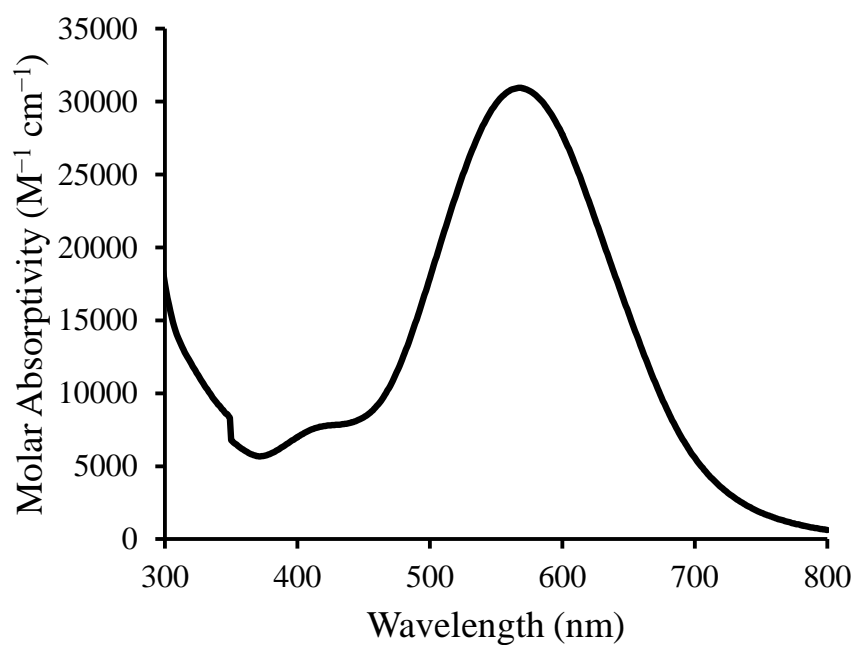


Figure A4.20 UV-vis absorption spectrum of **4.15** in CH₂Cl₂.

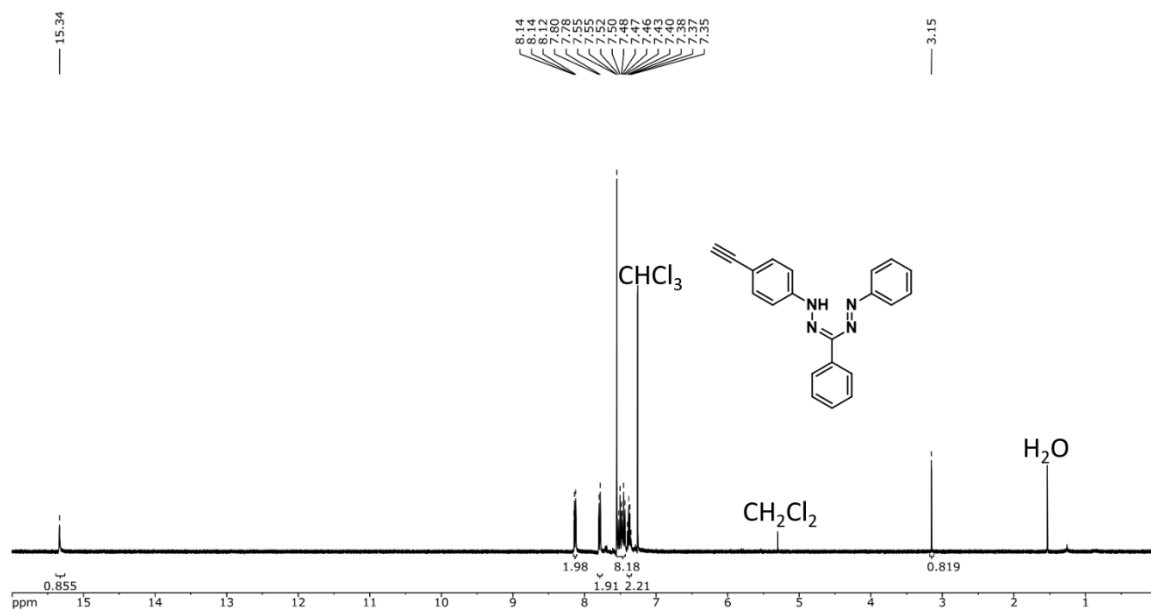


Figure A4.21 ^1H NMR spectrum of 1-*p*-ethynylphenyl-3,5-phenyl formazan in CDCl_3 .

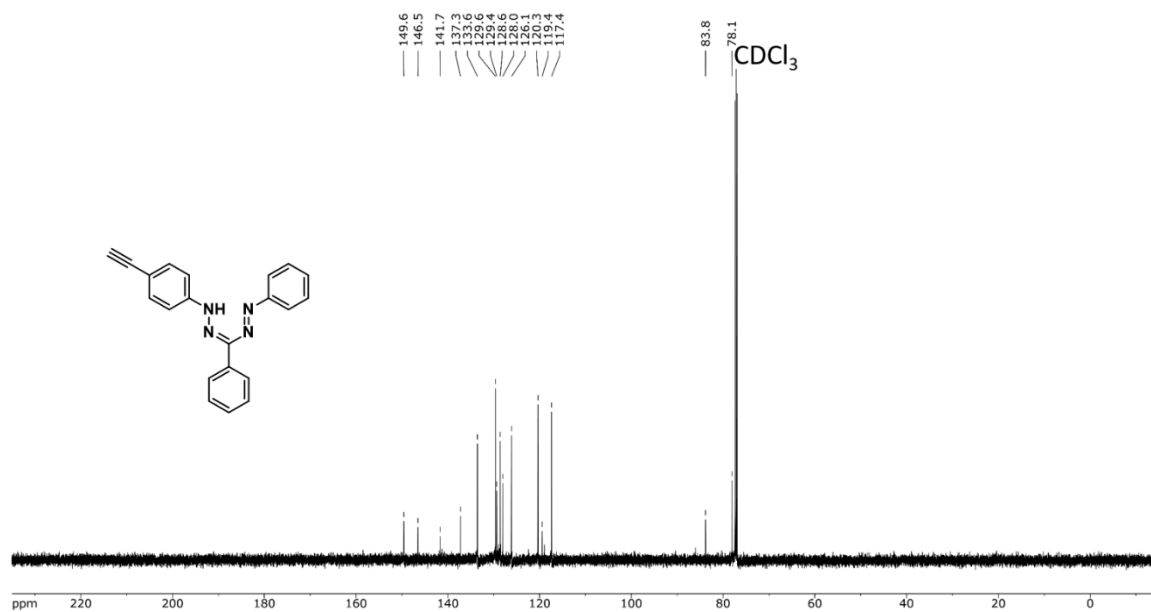
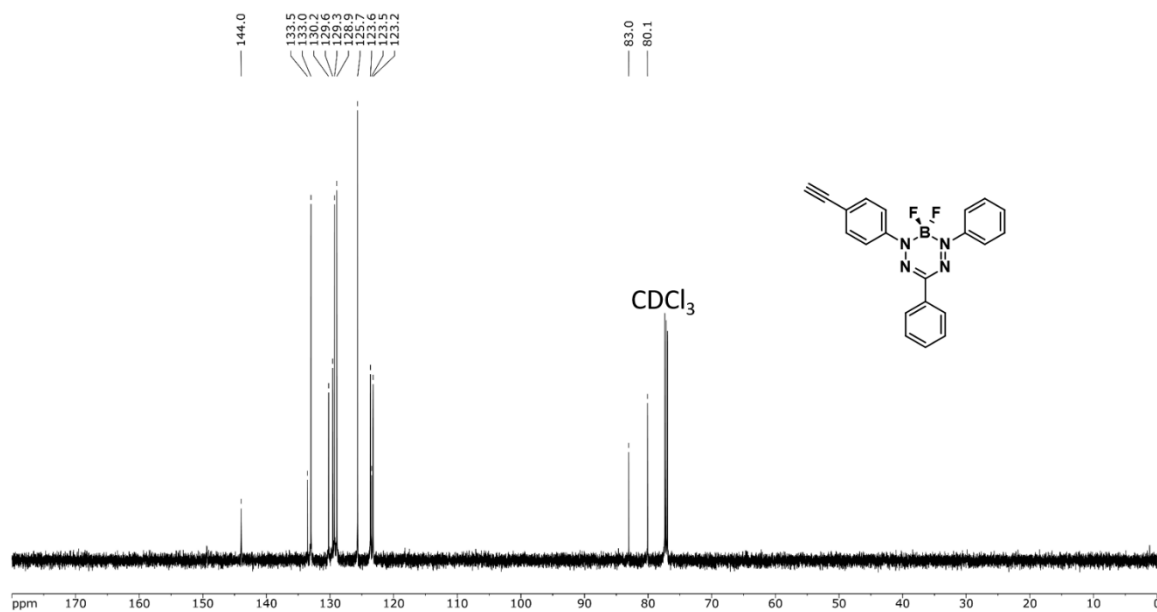
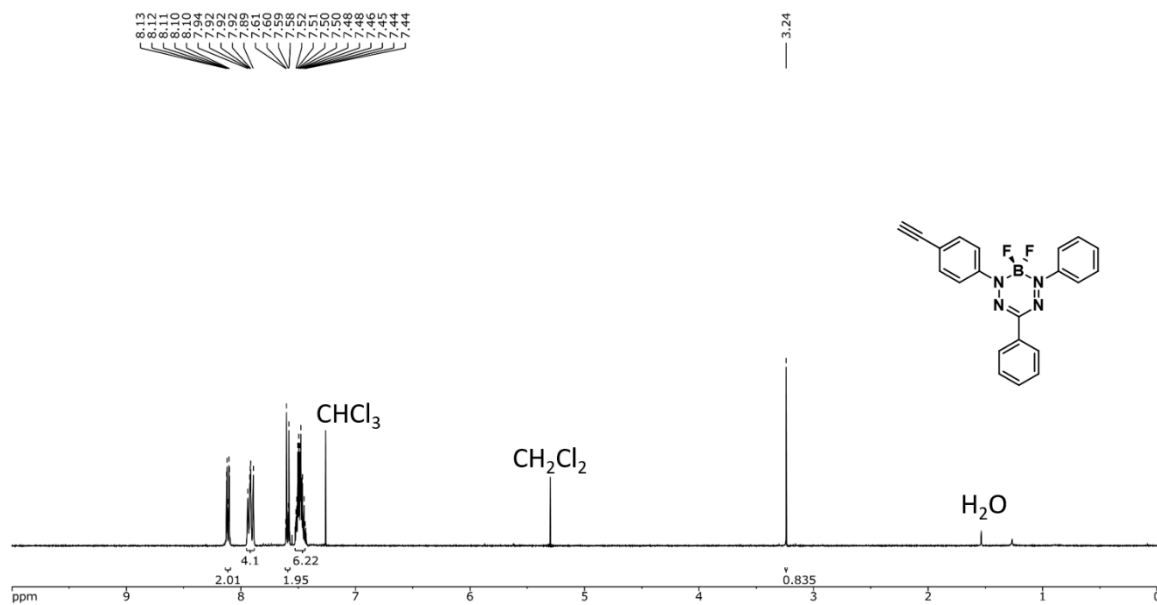


Figure A4.22 $^{13}\text{C}\{^1\text{H}\}$ NMR spectrum of 1-*p*-ethynylphenyl-3,5-phenyl formazan in CDCl_3 .



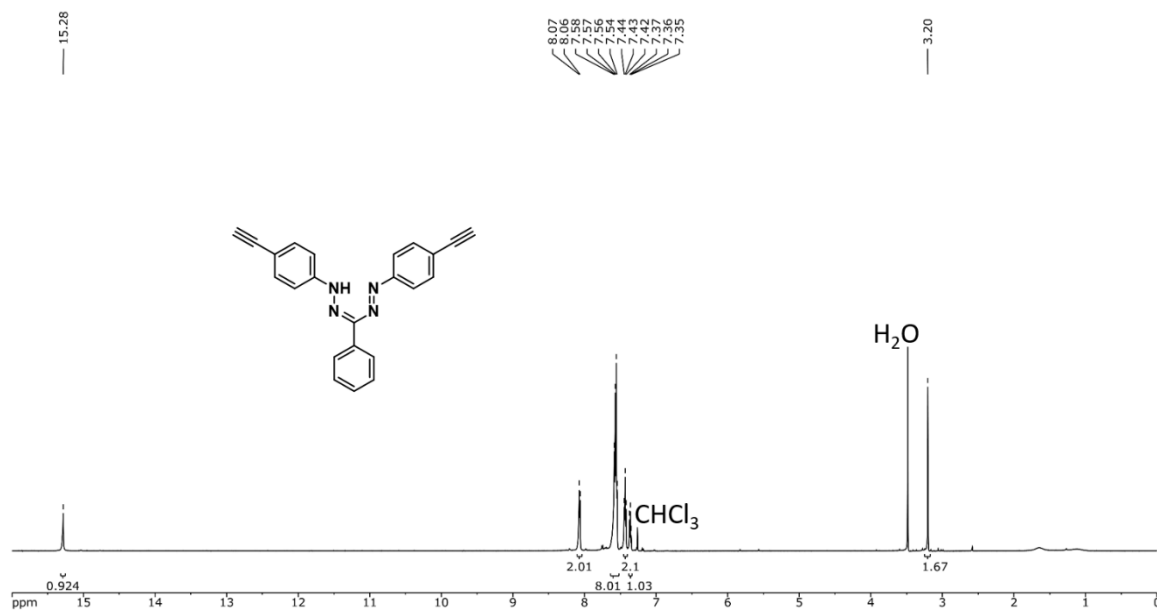


Figure A4.25 ^1H NMR spectrum of 1,5-*p*-ethynylphenyl-3-phenyl formazan in CDCl_3 .

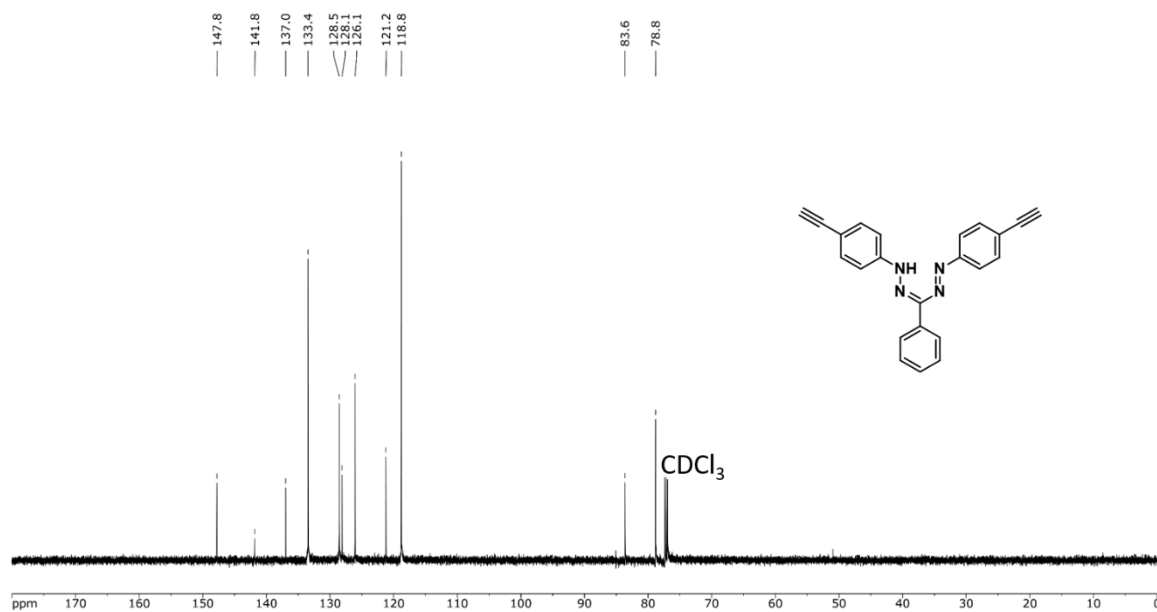


Figure A4.26 $^{13}\text{C}\{^1\text{H}\}$ NMR spectrum of 1,5-*p*-ethynylphenyl-3-phenyl formazan in CDCl_3 .

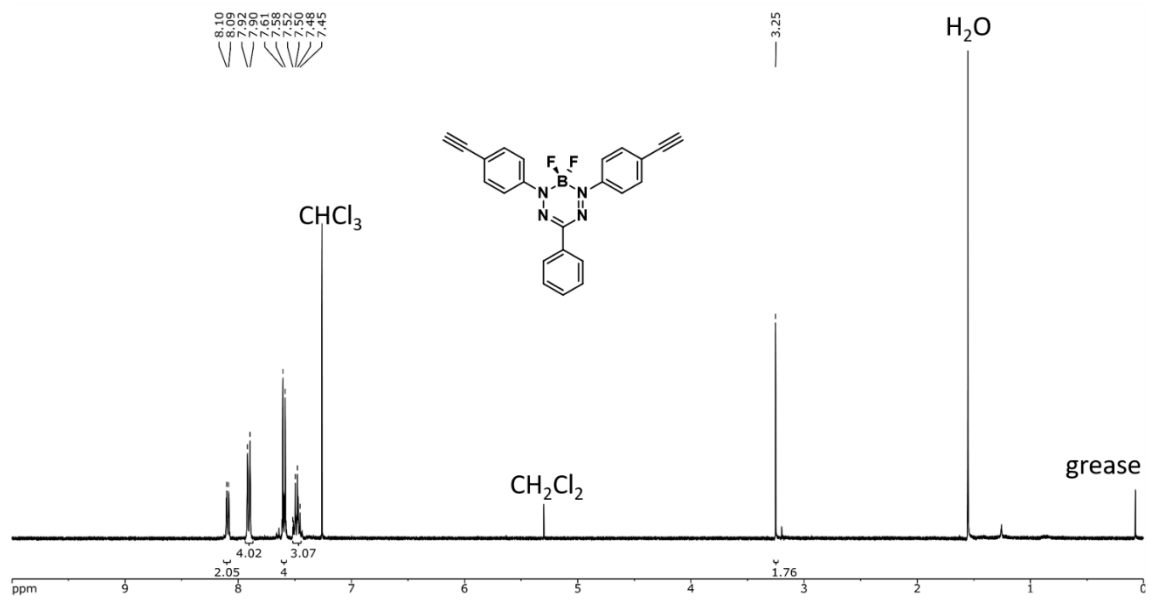


Figure A4.27 ^1H NMR spectrum of **4.18** in CDCl_3 .

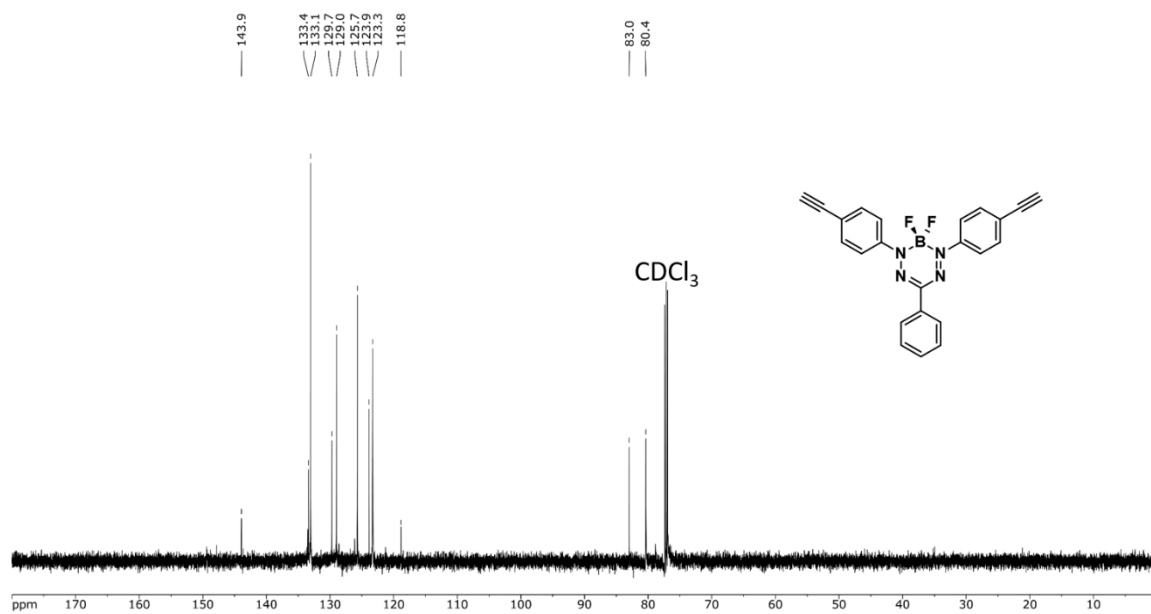


Figure A4.28 $^{13}\text{C}\{^1\text{H}\}$ NMR spectrum of **4.18** in CDCl_3 .

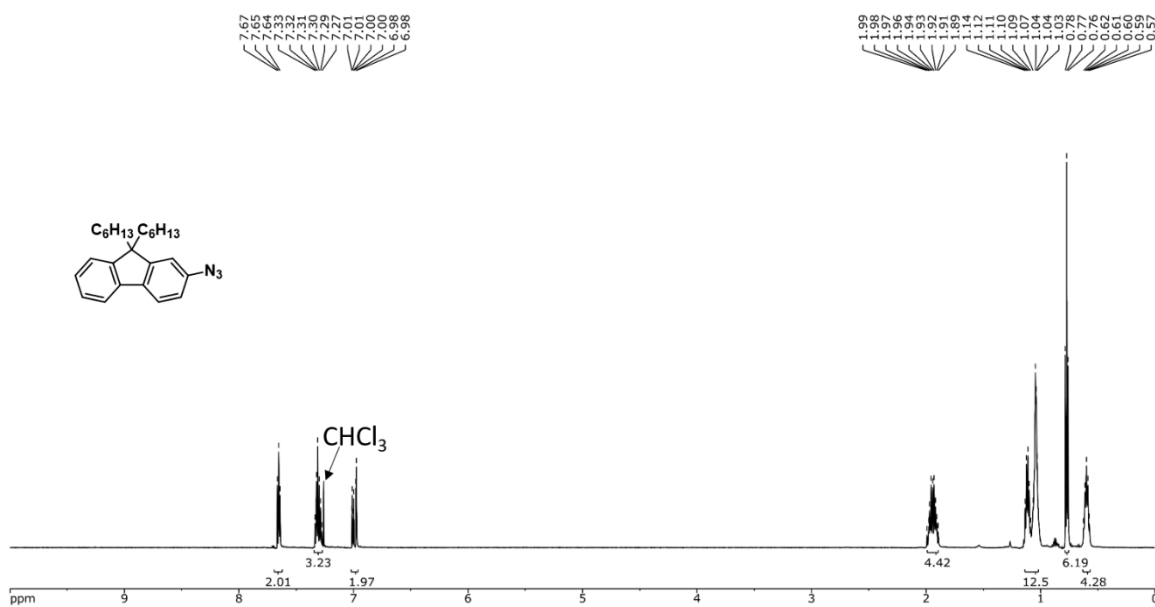


Figure A4.29 ^1H NMR spectrum of **4.19** in CDCl_3 .

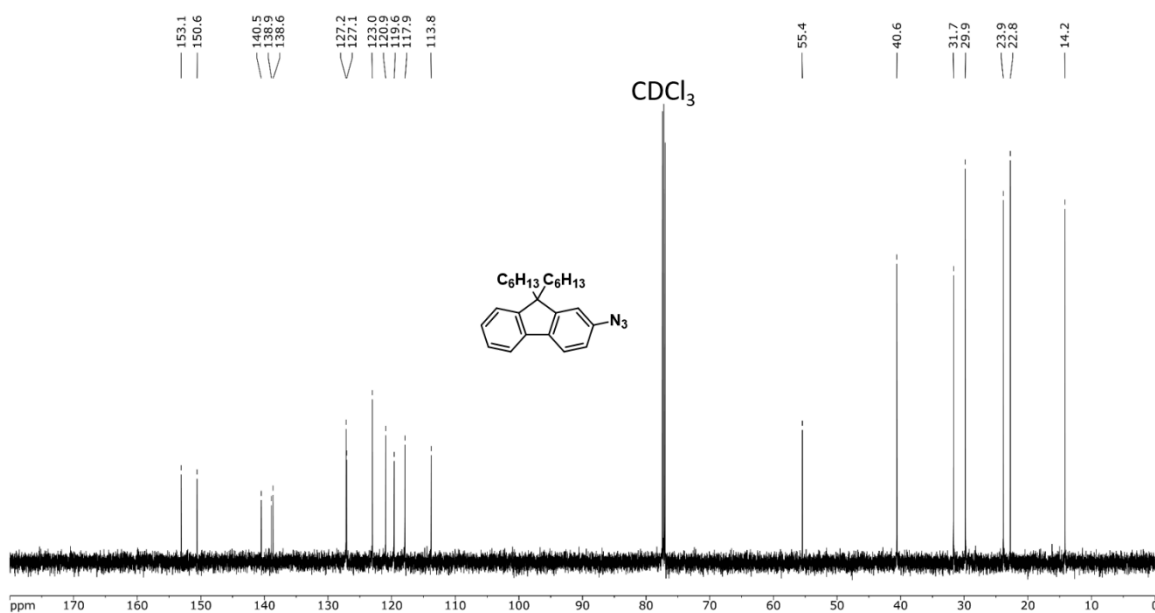


Figure A4.30 $^{13}\text{C}\{^1\text{H}\}$ NMR spectrum of **4.19** in CDCl_3 .

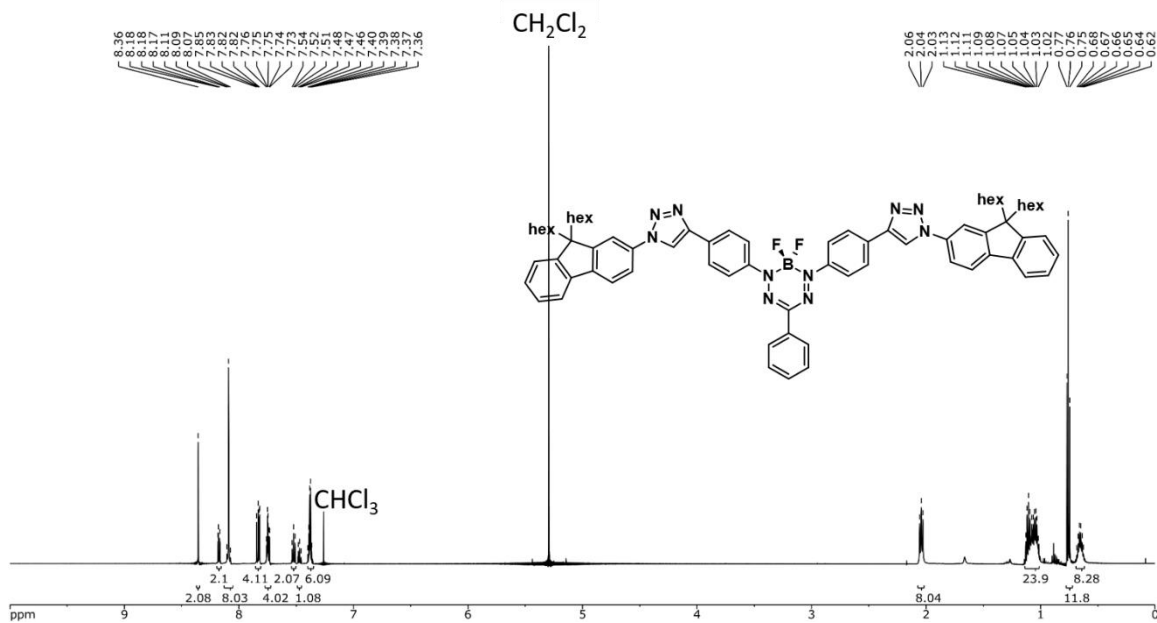


Figure A4.31 ^1H NMR spectrum of **4.24** in CDCl_3 .

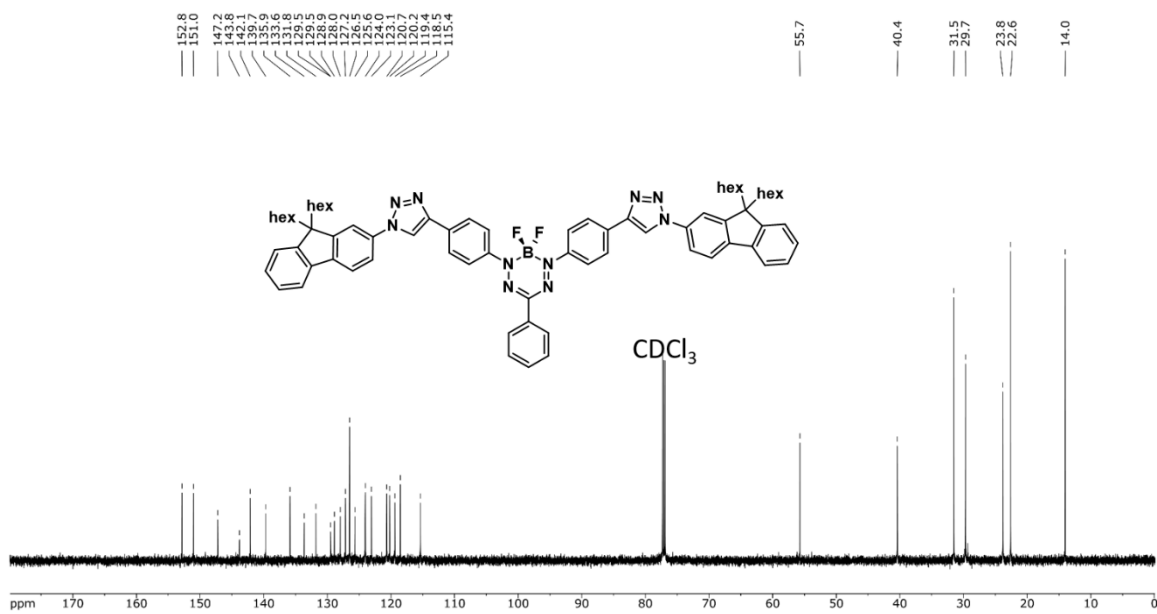


Figure A4.32 $^{13}\text{C}\{^1\text{H}\}$ NMR spectrum of **4.24** in CDCl_3 .

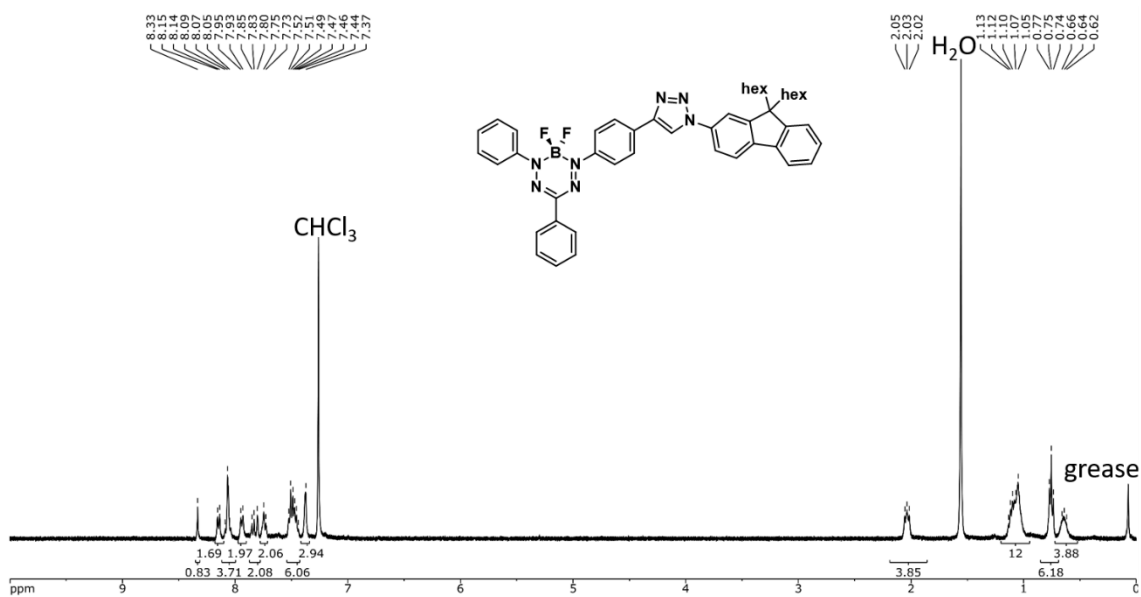


Figure A4.33 ^1H NMR spectrum of 4.25 in CDCl_3 .

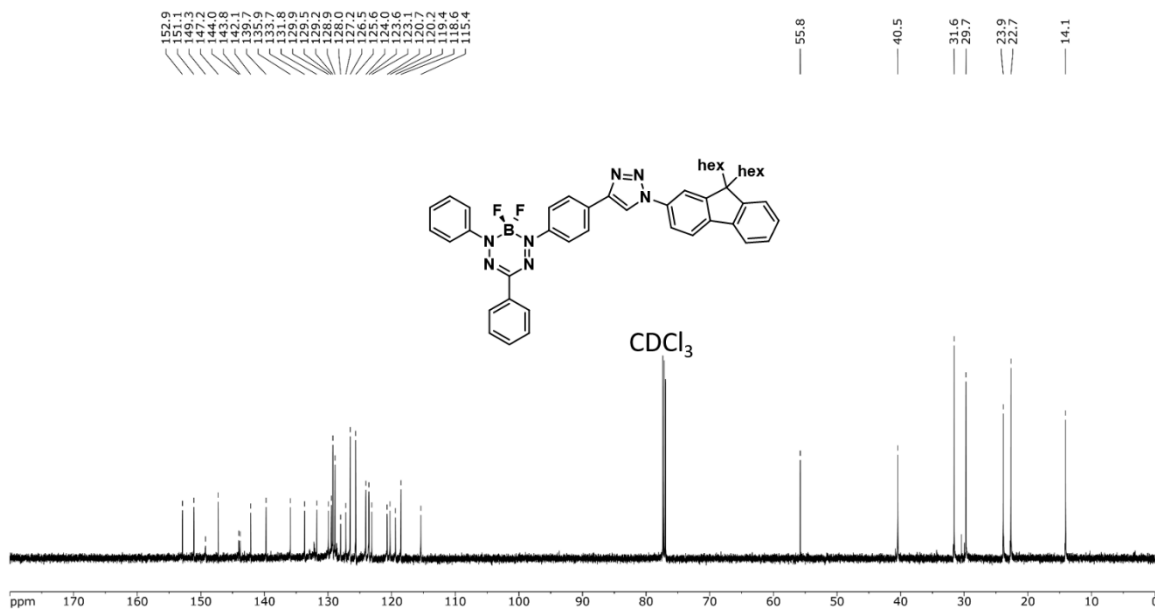


Figure A4.34 $^{13}\text{C}\{^1\text{H}\}$ NMR spectrum of 4.25 in CDCl_3 .

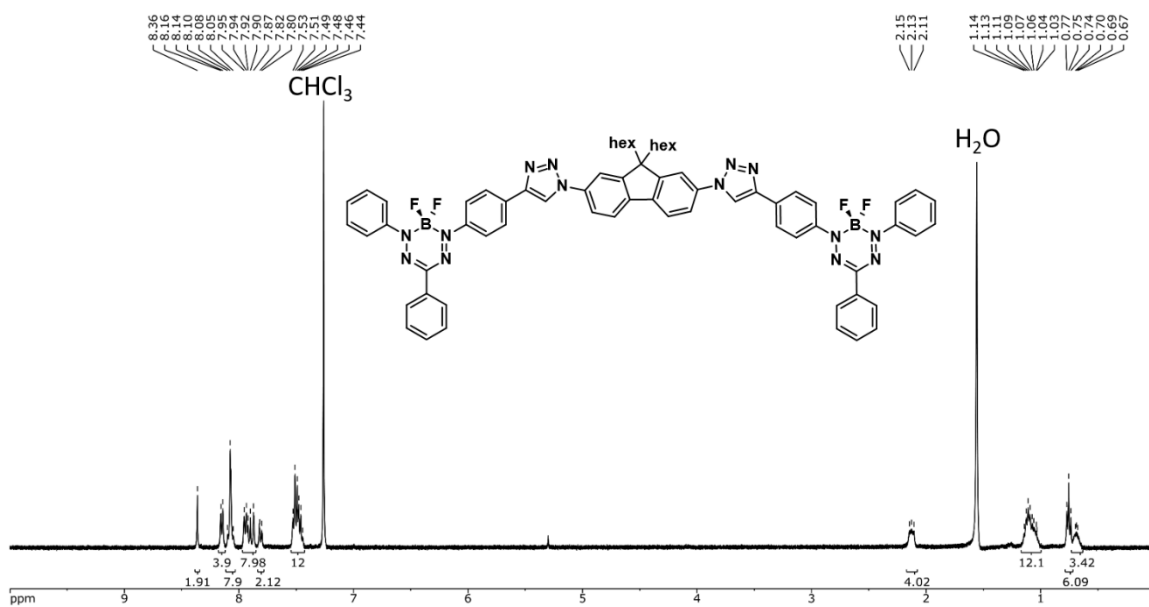


Figure A4.35 ^1H NMR spectrum of **4.26** in CDCl_3 .

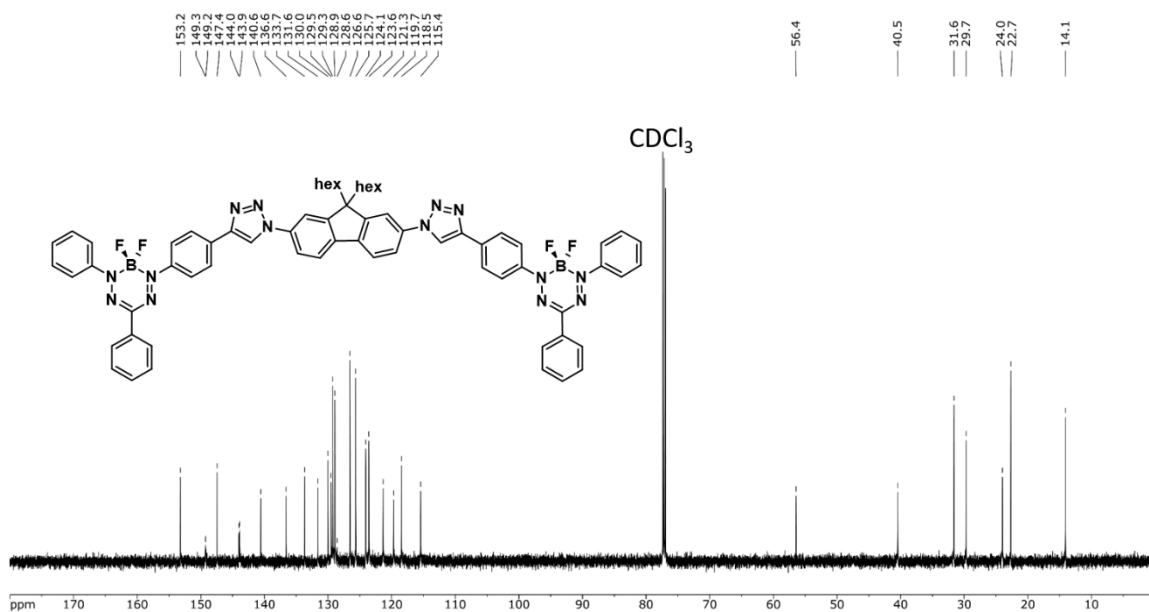


Figure A4.36 $^{13}\text{C}\{^1\text{H}\}$ NMR spectrum of **4.26** in CDCl_3 .

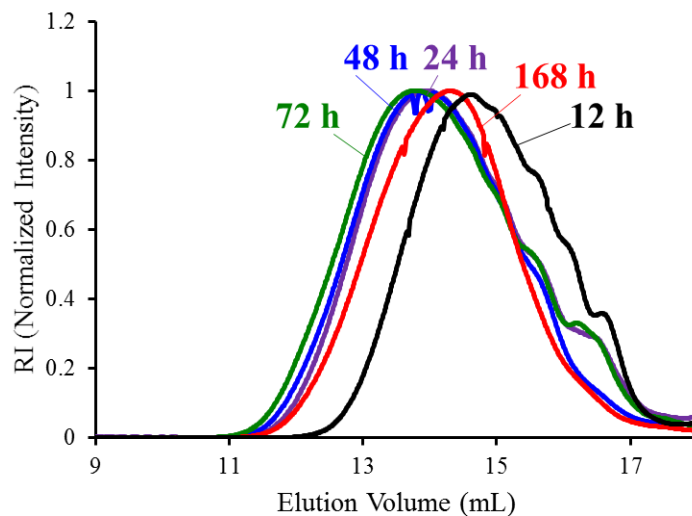


Figure A4.37 GPC traces for aliquots of polymer **4.21** taken at 12 h (black), 24 h (purple), 48 h (blue), 72 h (green) and 168 h (red).

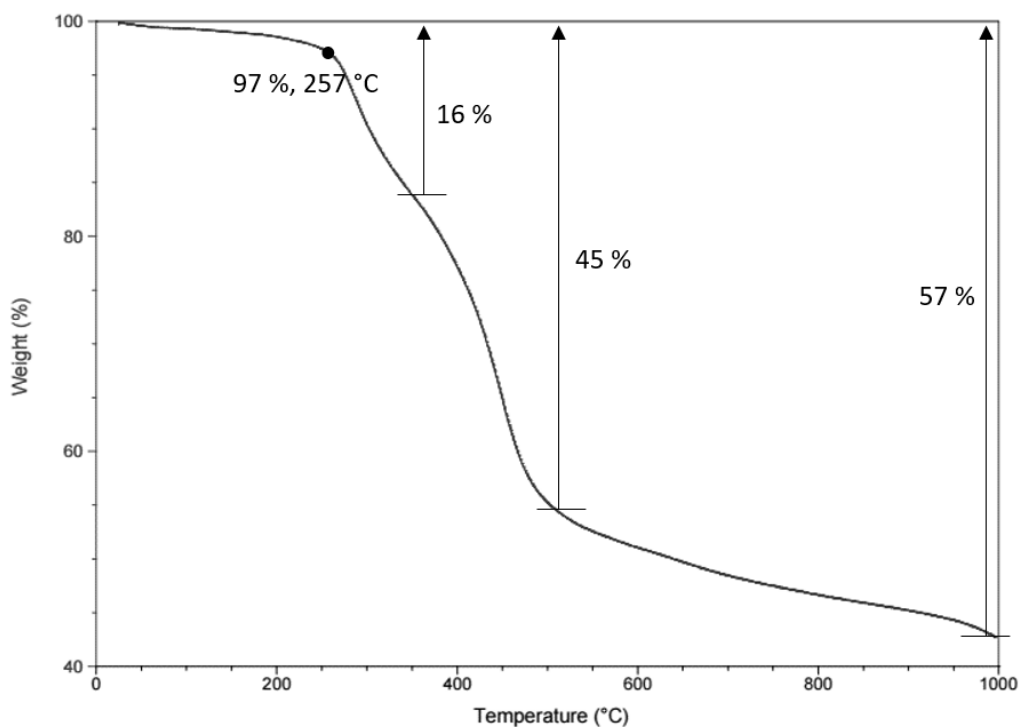


Figure A4.38 TGA trace for **4.21**.

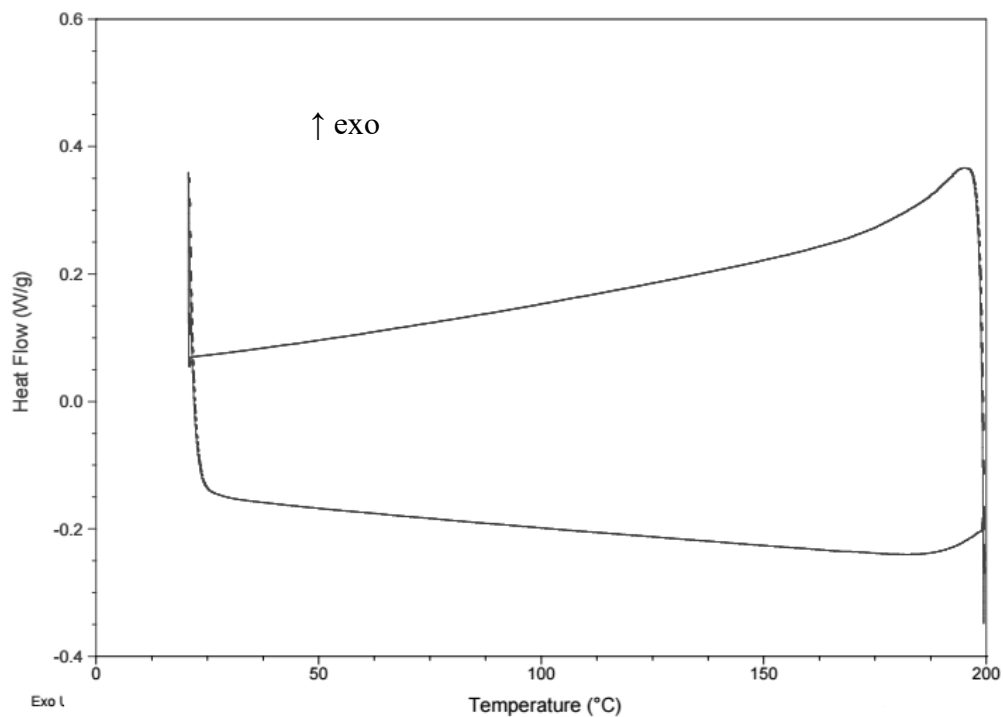


Figure A4.39 DSC thermogram collected for 4.21.

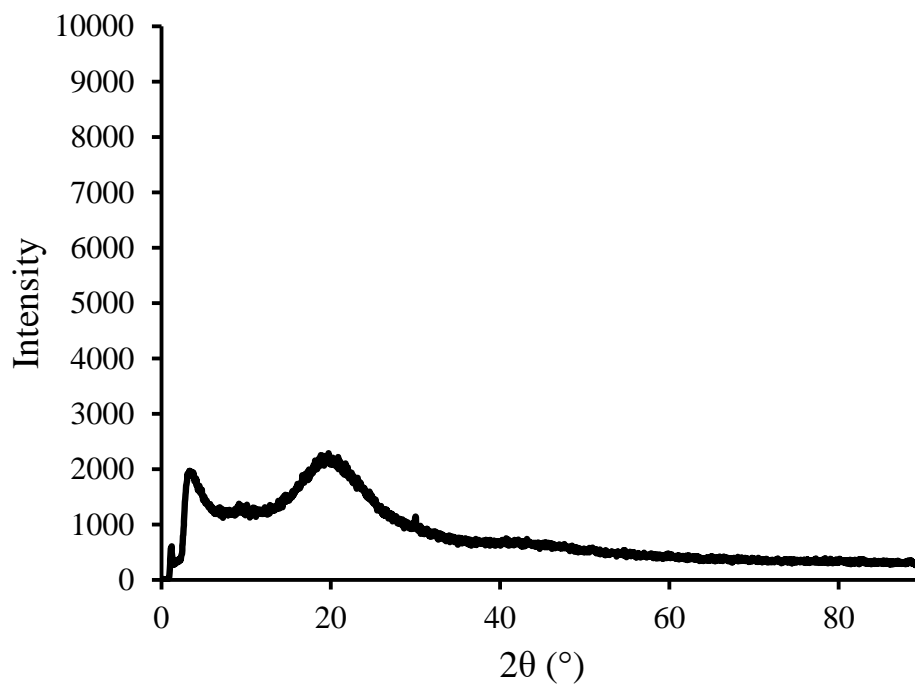


Figure A4.40 Powder X-ray diffractogram for 4.21 collected on a glass slide.

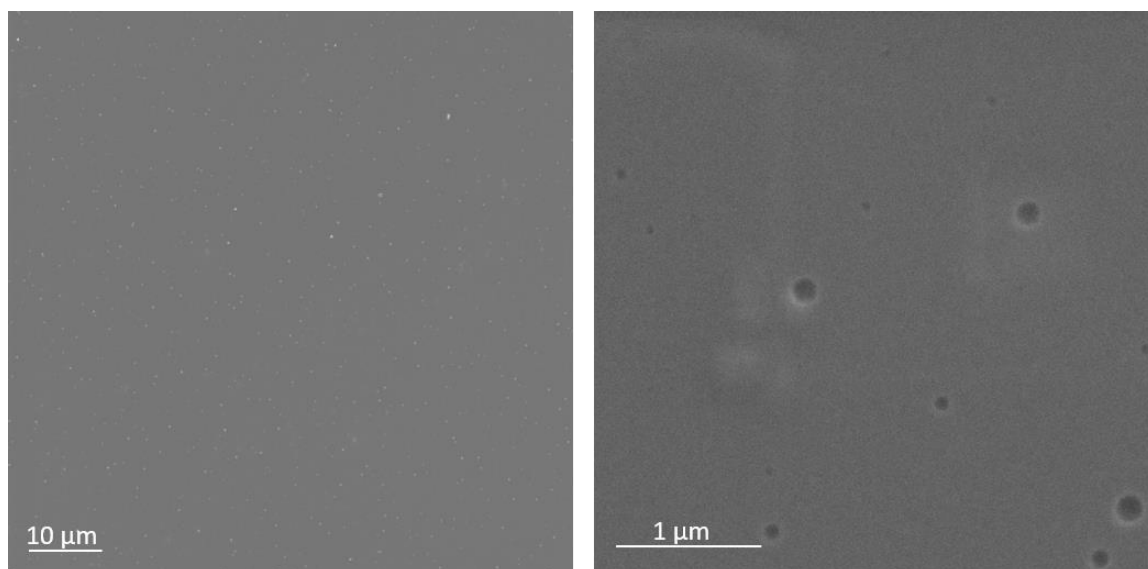


Figure A4.41 SEM images of a thin film of **4.21** prepared from a chlorobenzene solution on a silicon wafer.

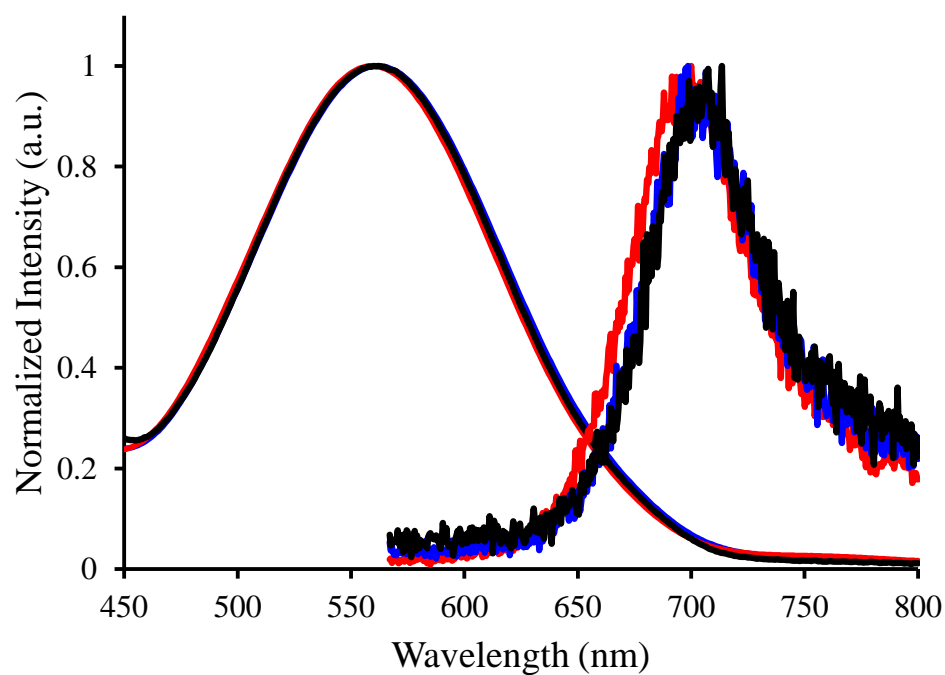


Figure A4.42 Normalized UV-vis absorption and emission spectra of **4.21** with number average molecular weight of $6,000 \text{ g mol}^{-1}$ (red), $10,000 \text{ g mol}^{-1}$ (blue) and $17,000 \text{ g mol}^{-1}$ (black) for 10^{-5} M DMF solution.

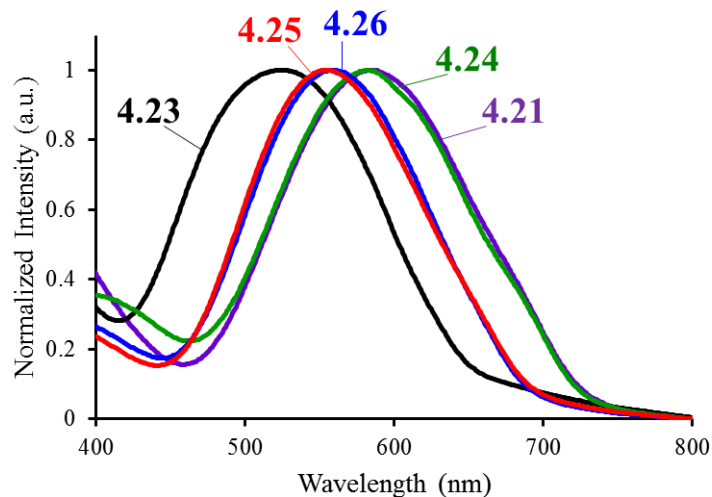


Figure A4.43 Normalized thin-film UV-vis absorption spectra of **4.21** (purple), **4.23** (black), **4.24** (green), **4.25** (red), and **4.26** (blue).

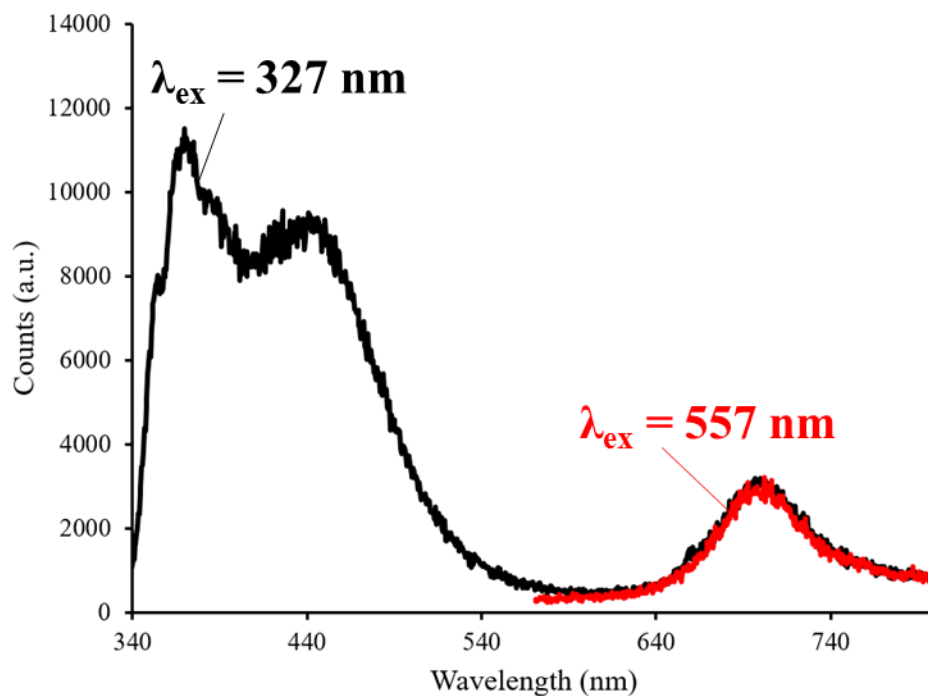


Figure A4.44 Emission spectra of **4.21** recorded at excitation wavelength of 327 nm (black) and 557 nm (red) for a 10^{-5} M degassed DMF solution.

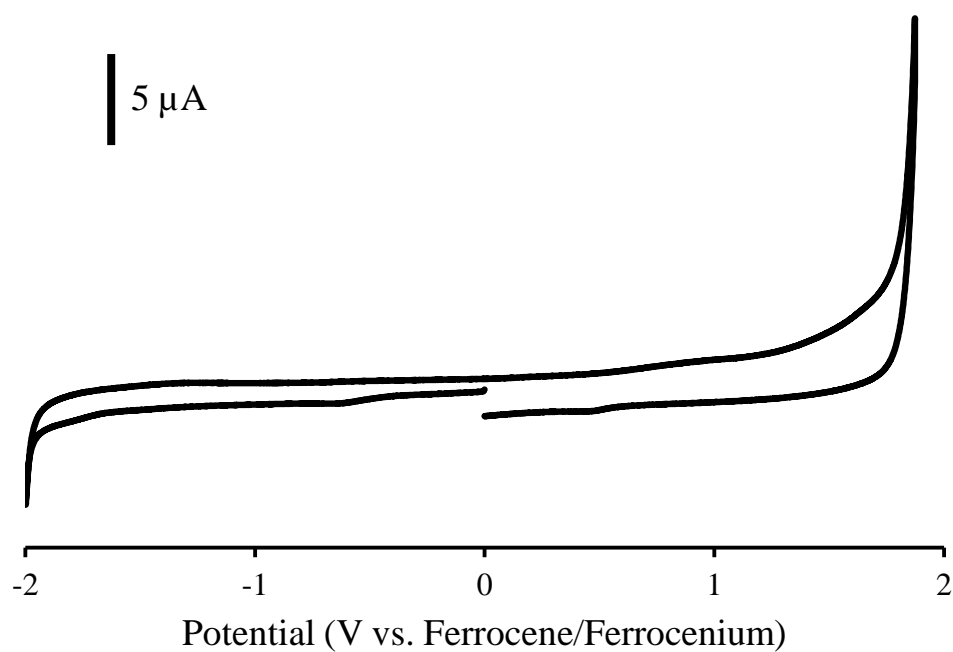


Figure A4.45 Cyclic voltammogram of **4.22** recorded at 100 mV s^{-1} in a 1 mM DMF solution containing 0.1 M $[\text{nBu}_4\text{N}][\text{PF}_6]$ as supporting electrolyte.

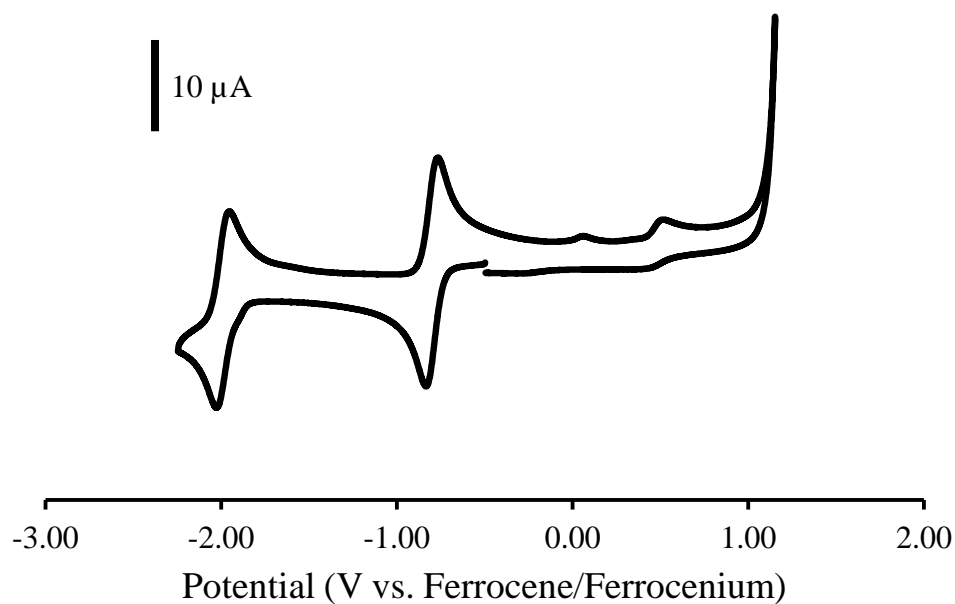


Figure A4.46 Cyclic voltammogram of **4.23** recorded at 100 mV s^{-1} in a 1 mM DMF solution containing 0.1 M $[\text{nBu}_4\text{N}][\text{PF}_6]$ as supporting electrolyte.

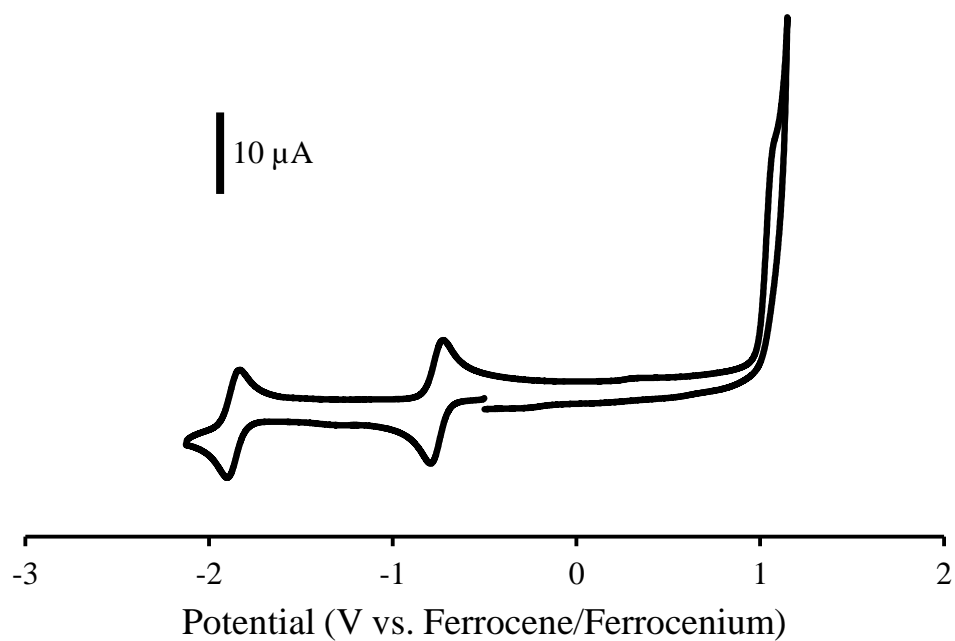


Figure A4.47 Cyclic voltammogram of **4.24** recorded at 100 mV s^{-1} in a 1 mM DMF solution containing 0.1 M $[n\text{Bu}_4\text{N}][\text{PF}_6]$ as supporting electrolyte.

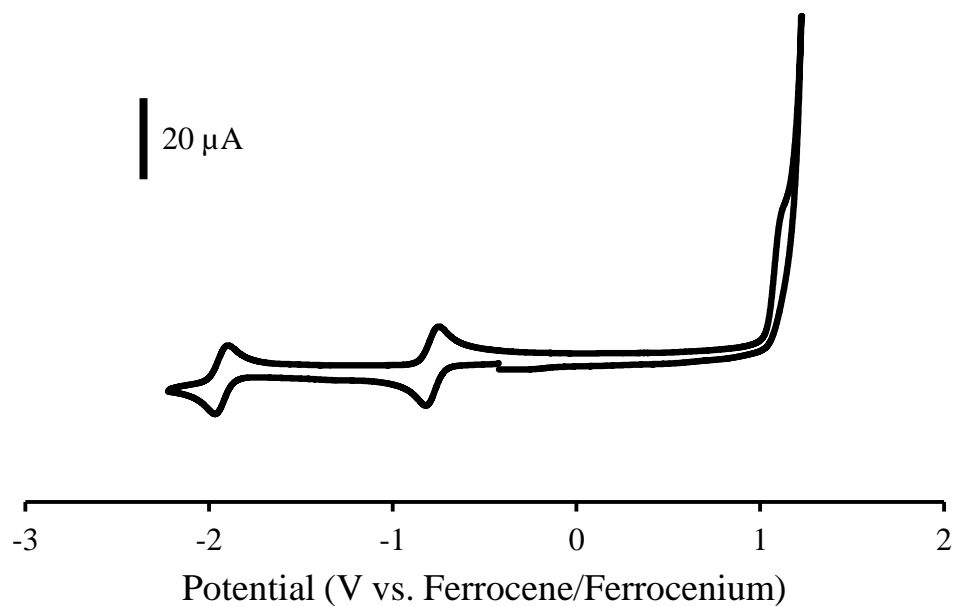


Figure A4.48 Cyclic voltammogram of **4.25** recorded at 100 mV s^{-1} in a 1 mM DMF solution containing 0.1 M $[n\text{Bu}_4\text{N}][\text{PF}_6]$ as supporting electrolyte.

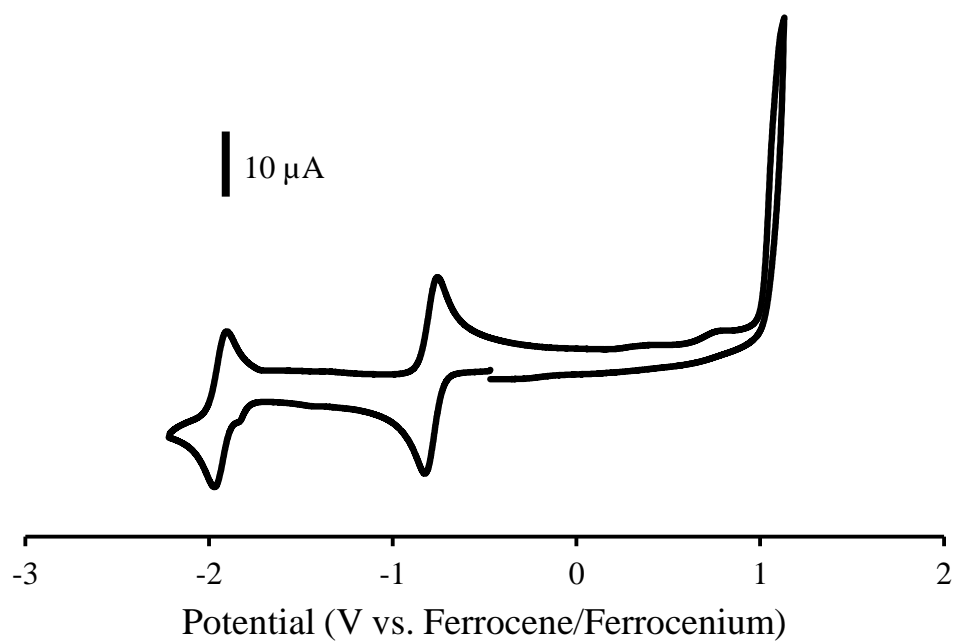


Figure A4.49 Cyclic voltammogram of **4.26** recorded at 100 mV s^{-1} in a 1 mM DMF solution containing 0.1 M $[\text{nBu}_4\text{N}][\text{PF}_6]$ as supporting electrolyte.

Appendix A5 Supporting Information for Chapter 5



Figure A5.1 Silica TLC plate showing the separation of the 6 components of the reaction mixture of formazan **5.7** with $\text{BF}_3 \cdot \text{OEt}_2$ and NEt_3 .

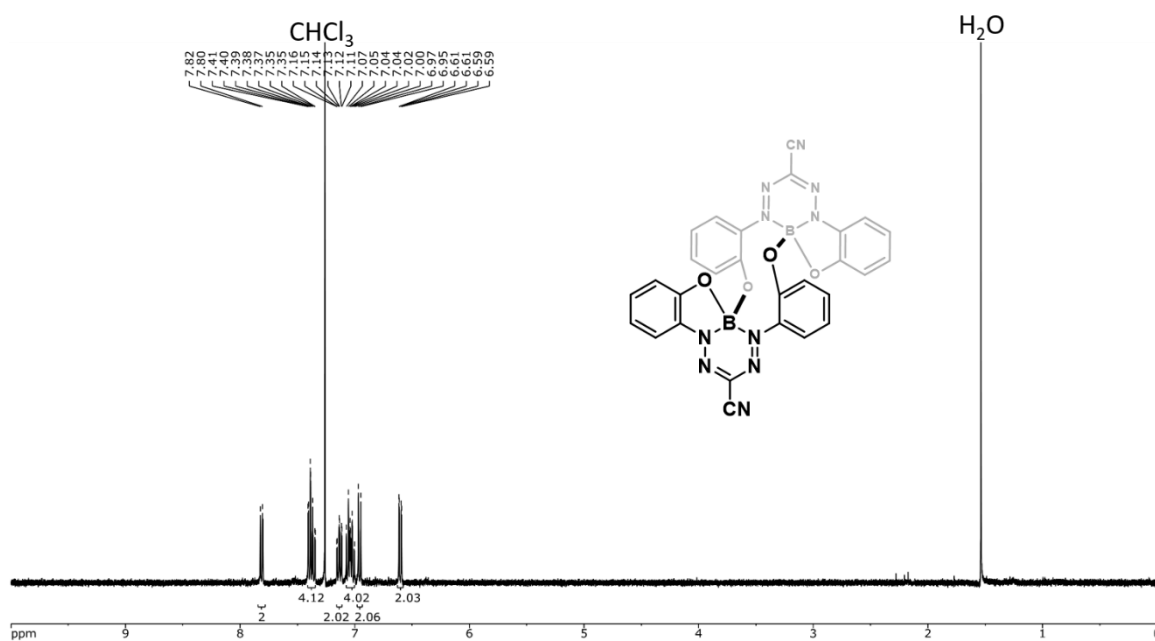


Figure A5.2 ^1H NMR spectrum of **5.9** in CDCl_3 .

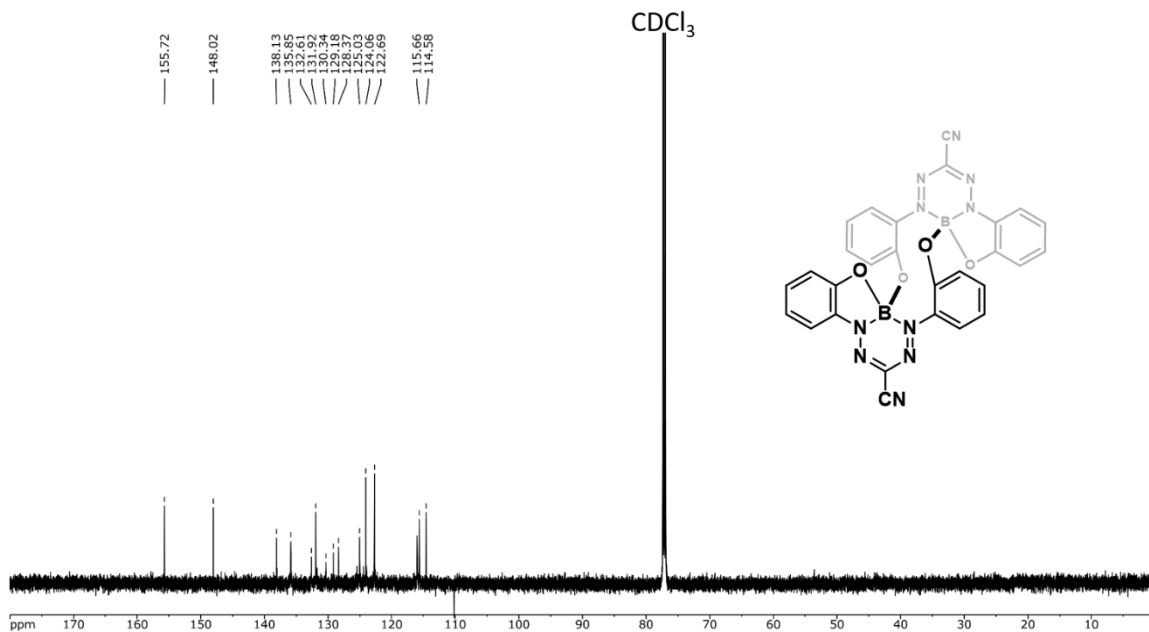


Figure A5.3 $^{13}\text{C}\{^1\text{H}\}$ NMR spectrum of 5.9 in CDCl_3 .

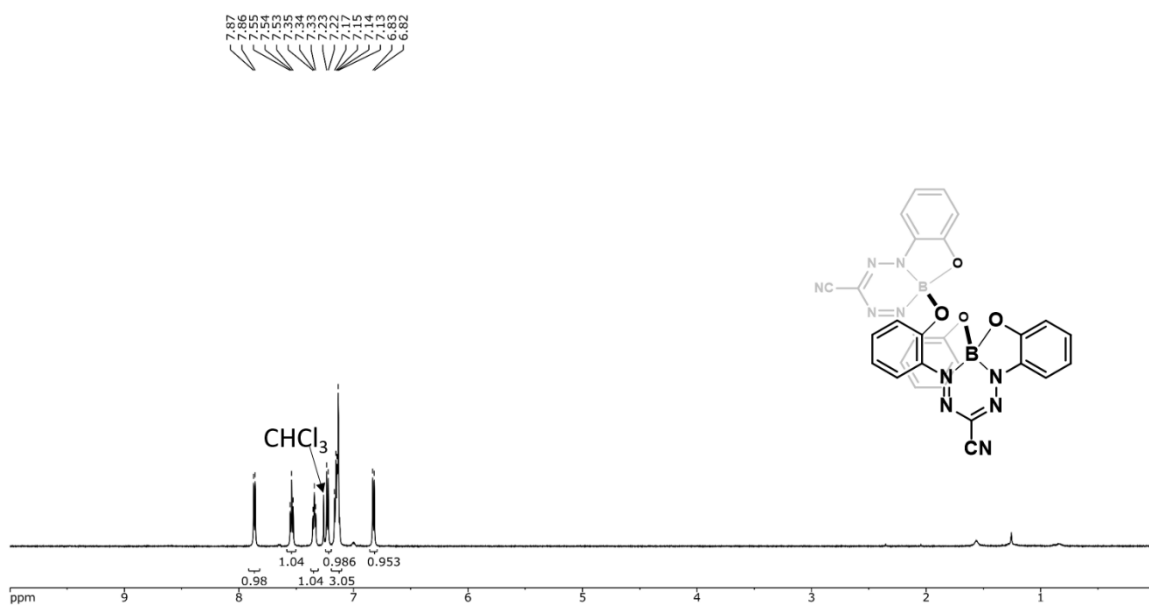


Figure A5.4 ^1H NMR spectrum of 5.10 in CDCl_3 .

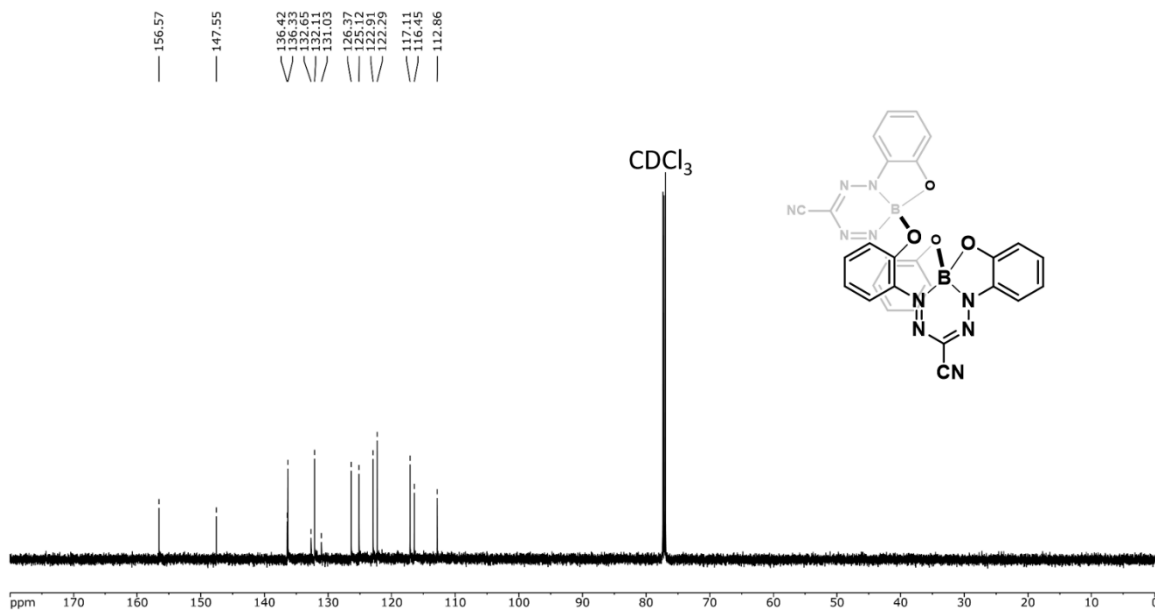


Figure A5.5 $^{13}\text{C}\{^1\text{H}\}$ NMR spectrum of **5.10** in CDCl_3 .

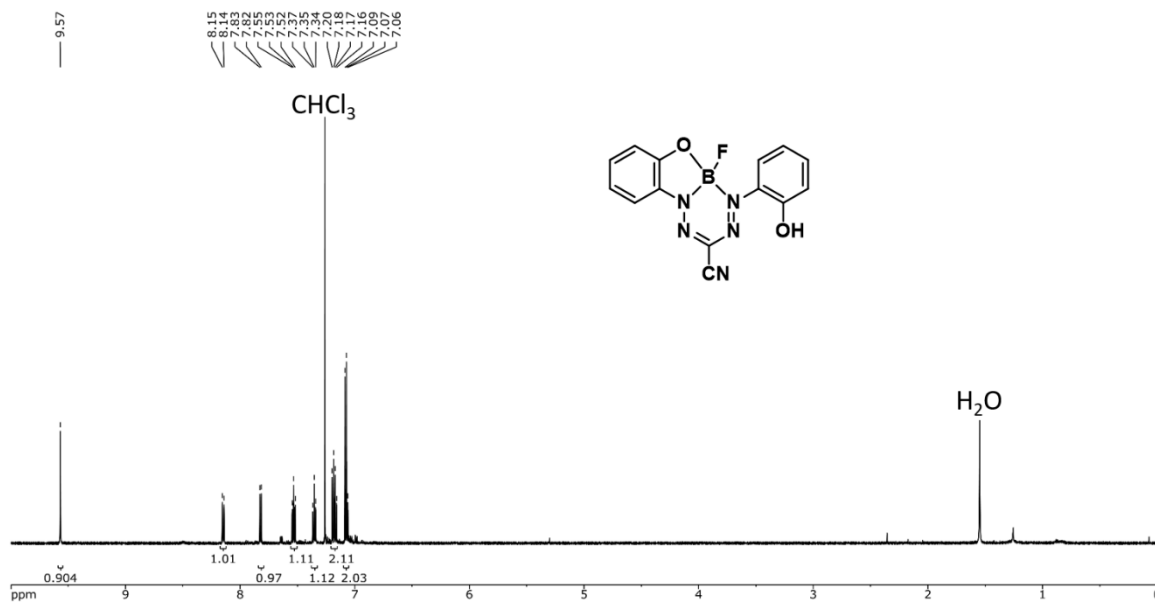


Figure A5.6 ^1H NMR spectrum of **5.11** in CDCl_3 .

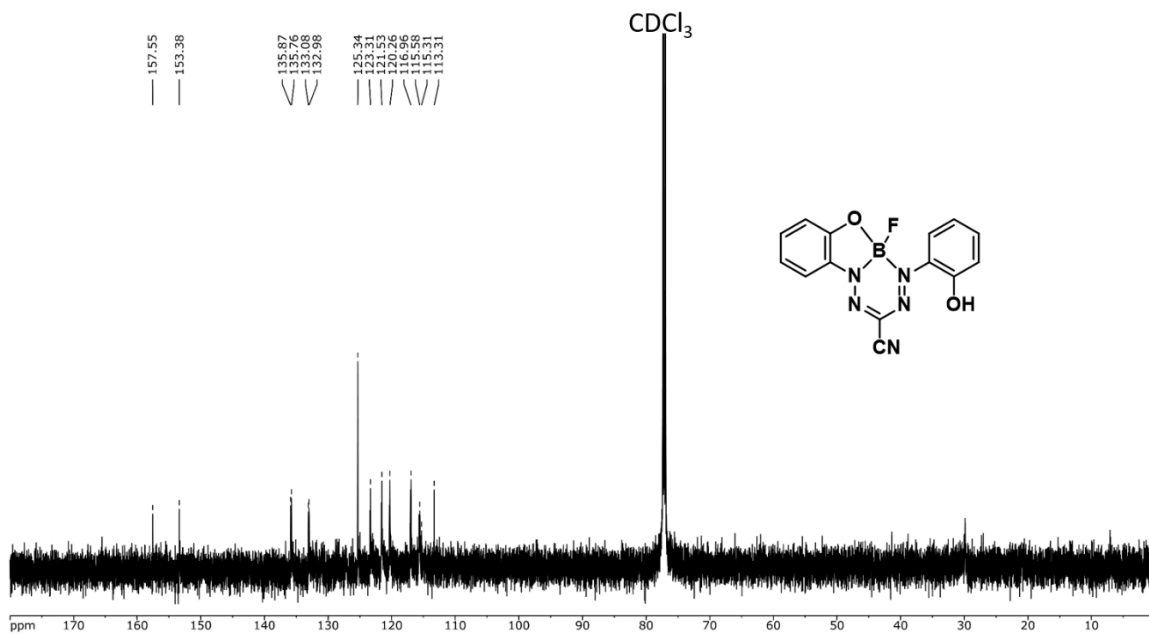


Figure A5.7 $^{13}\text{C}\{^1\text{H}\}$ NMR spectrum of **5.11** in CDCl_3 . This spectrum was rapidly collected for a saturated solution of compound **5.11**. Efforts to improve the S/N ratio were thwarted by the conversion of **5.11** to formazan **5.7** in solution.

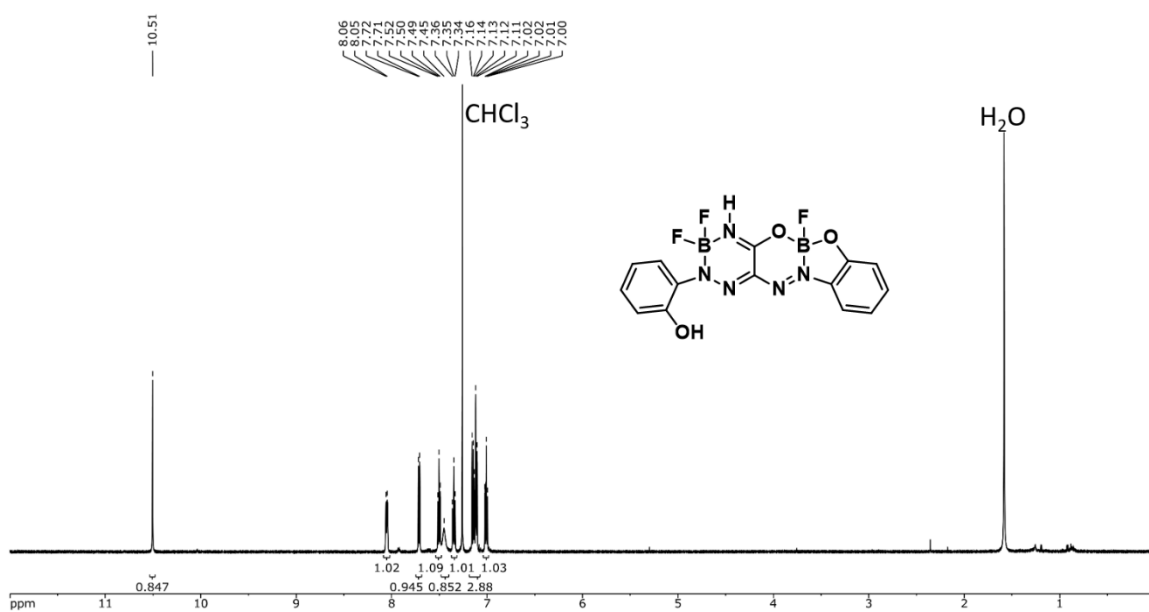


Figure A5.8 ^1H NMR spectrum of **5.12** in CDCl_3 .

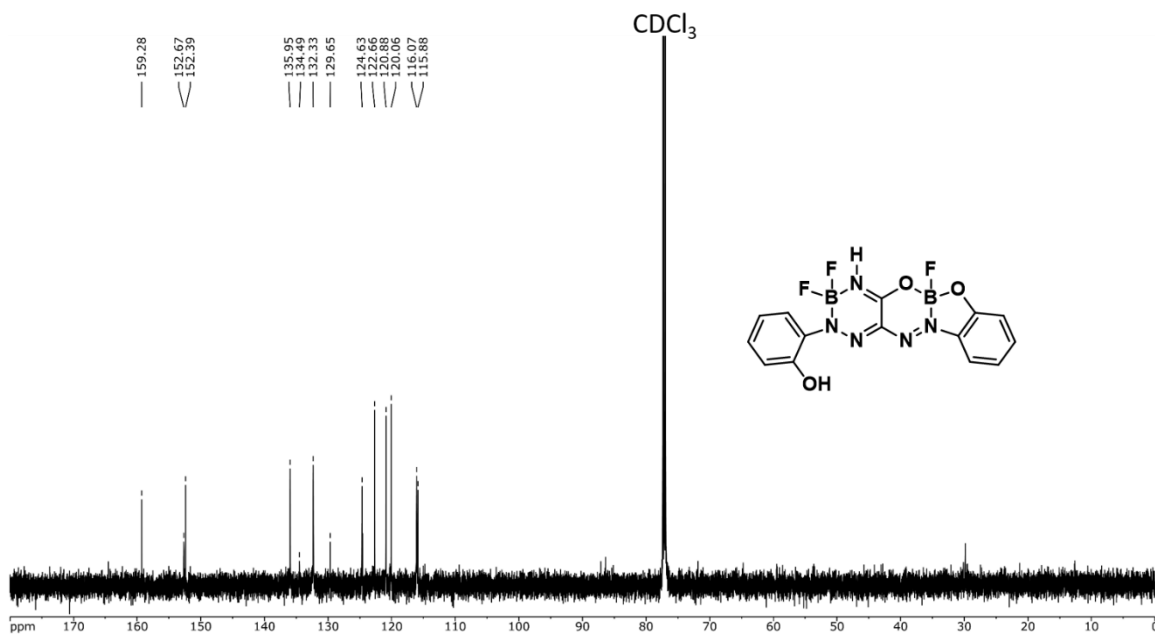


Figure A5.9 $^{13}\text{C}\{^1\text{H}\}$ NMR spectrum of 5.12 in CDCl_3 .

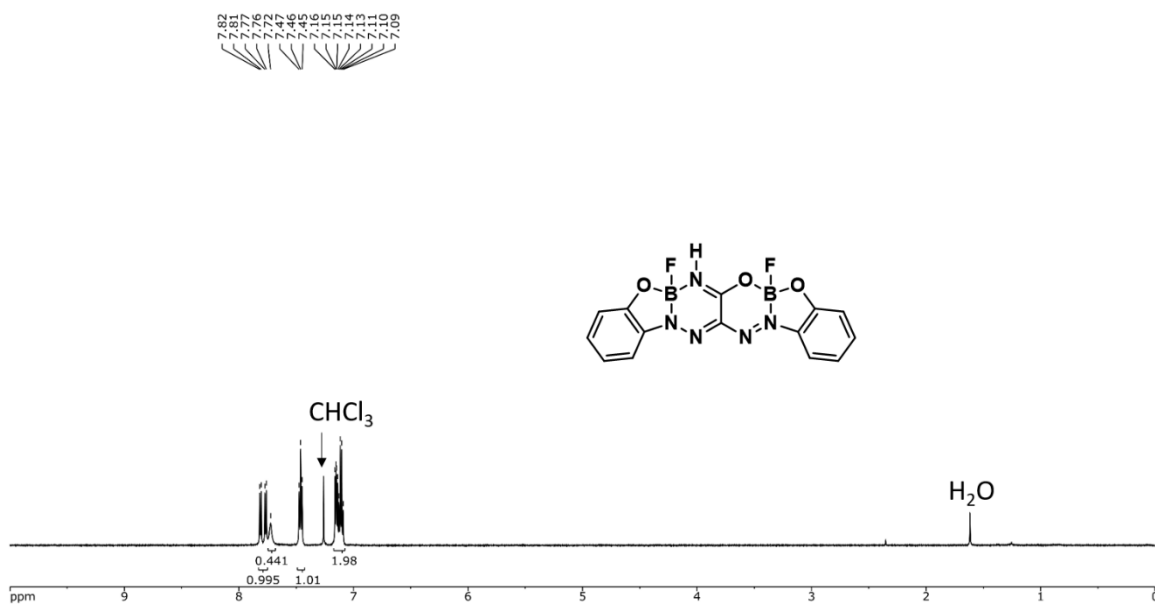


Figure A5.10 ^1H NMR spectrum of 5.13 in CDCl_3 .

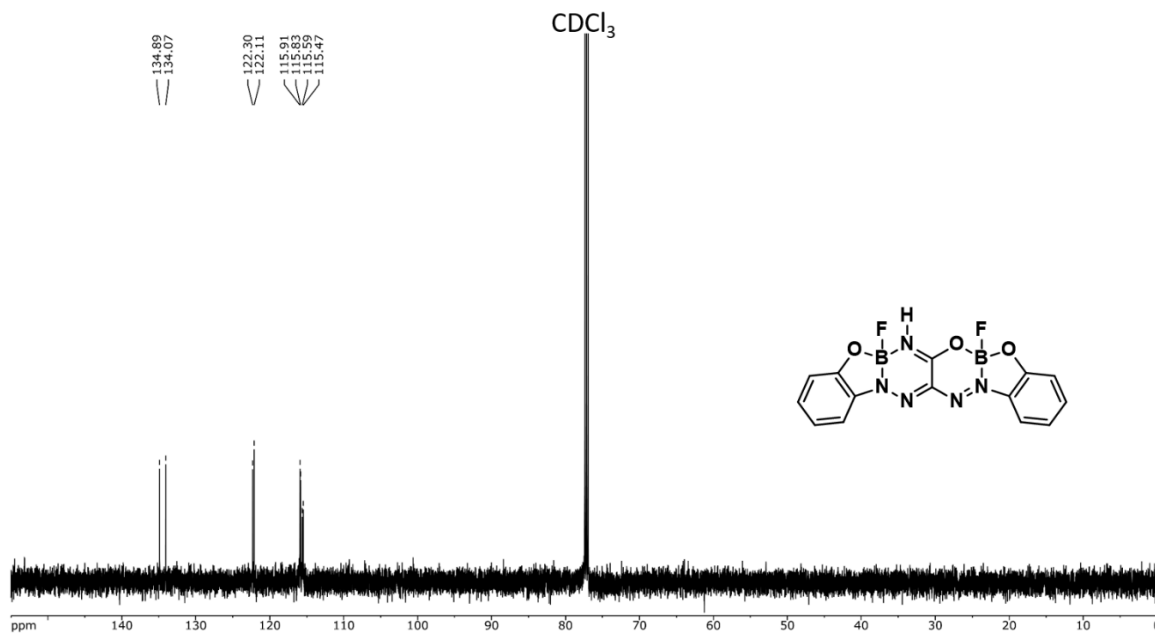


Figure A5.11 $^{13}\text{C}\{^1\text{H}\}$ NMR spectrum of **5.13** in CDCl_3 .

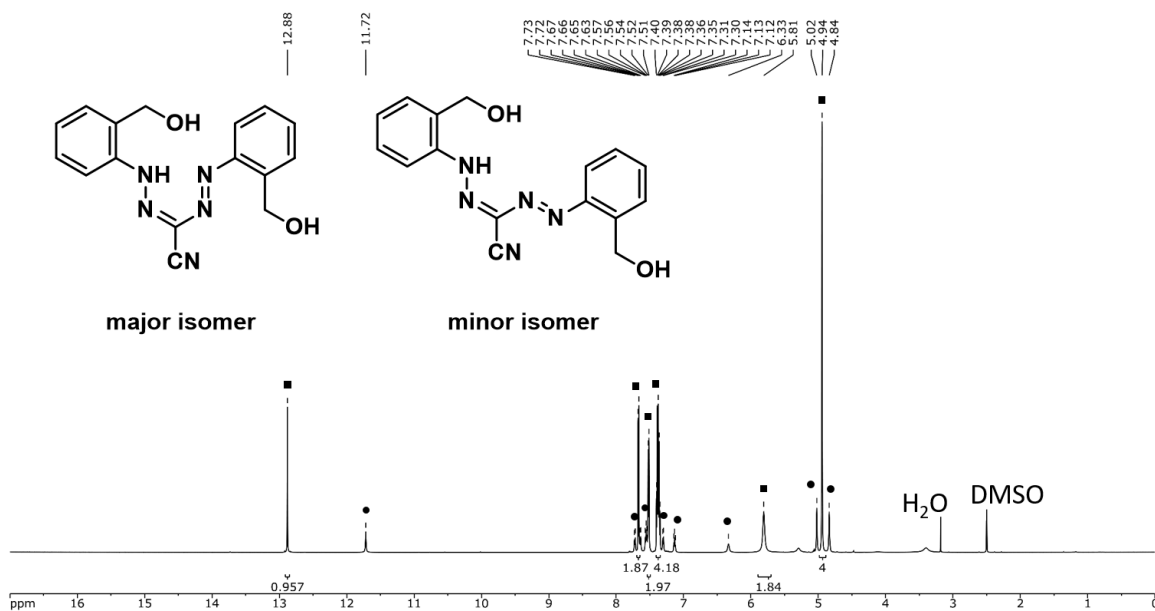


Figure A5.12 ^1H NMR spectrum of **5.14** in $\text{DMSO}-d_6$. Signals due to the major isomer have been marked with black squares, and those due to the minor isomer have been marked with black circles. Only signals from the major isomer have been integrated.

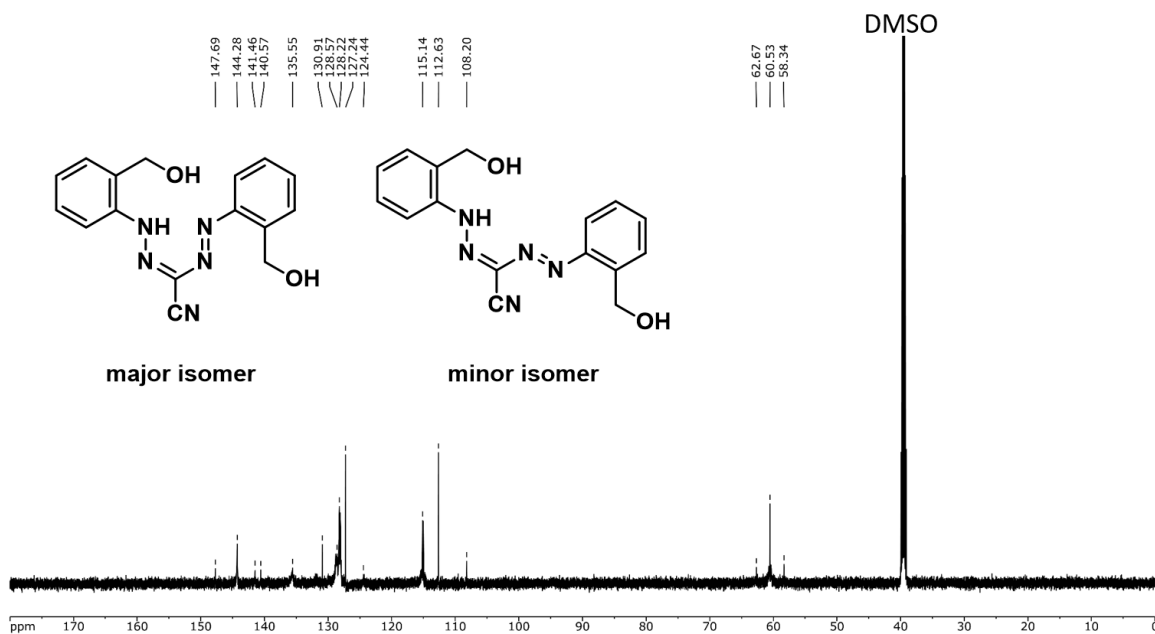


Figure A5.13 $^{13}\text{C}\{^1\text{H}\}$ NMR spectrum of **5.14** in $\text{DMSO-}d_6$. Formazan **5.14** was sparingly soluble in common NMR solvents. This spectrum was collected for a saturated solution over 10,000 scans on a 600 MHz NMR spectrometer.

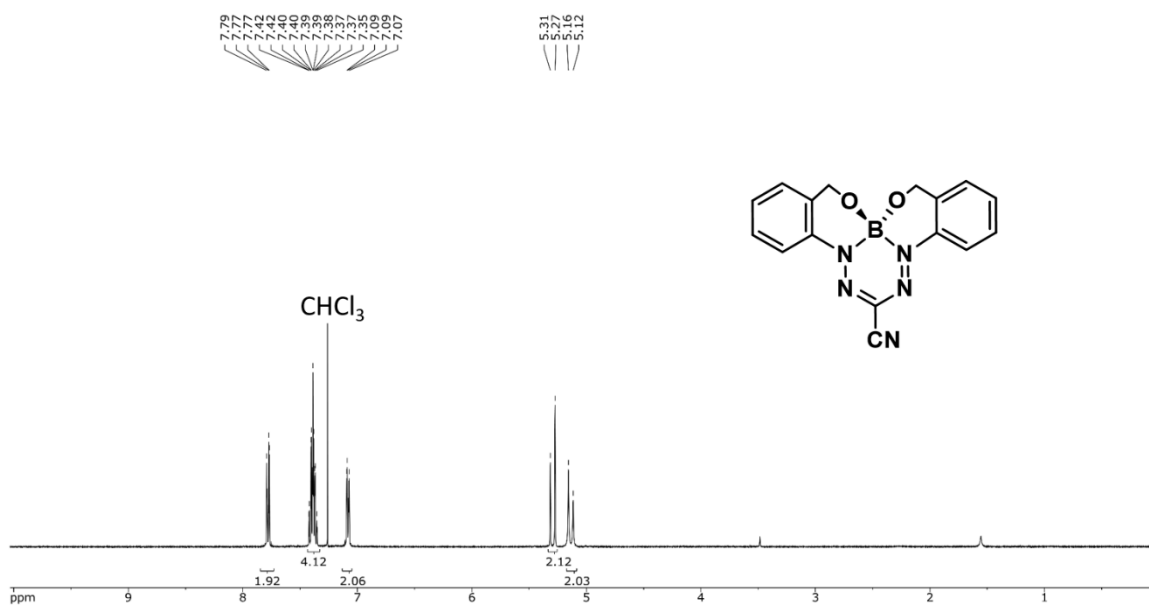


Figure A5.14 ^1H NMR spectrum of **5.15** in CDCl_3 .

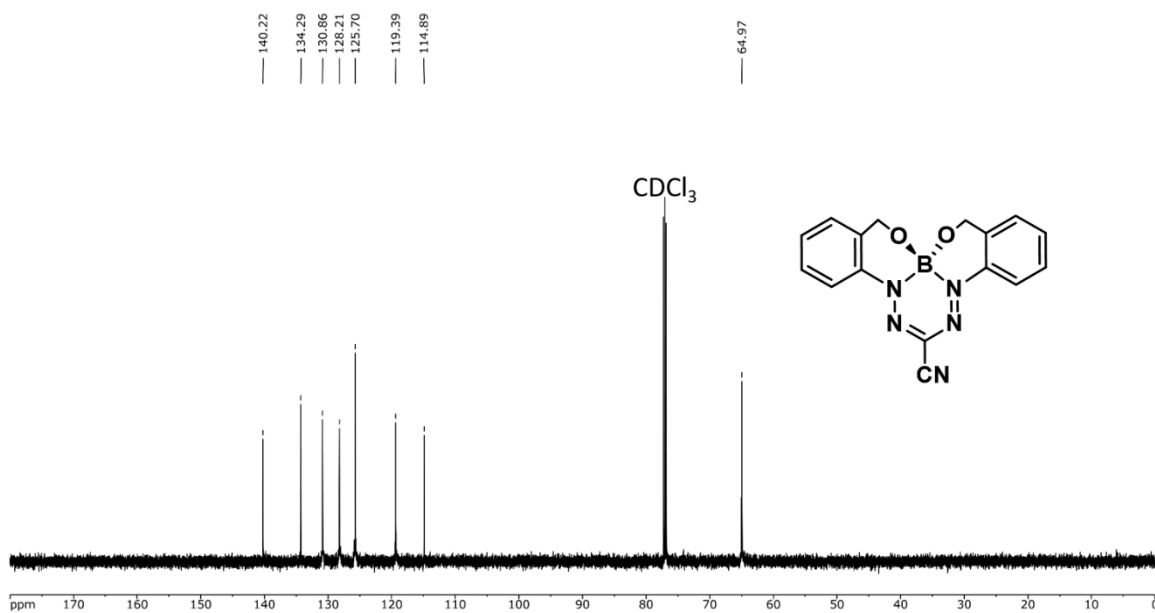


Figure A5.15 $^{13}\text{C}\{^1\text{H}\}$ NMR spectrum of **5.15** in CDCl_3 .

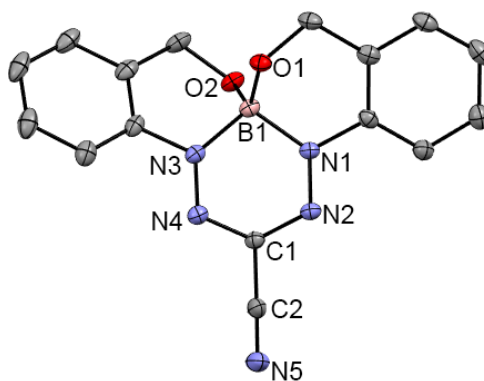


Figure A5.16 Solid-state structure of **5.15**. Thermal displacement ellipsoids are shown at the 50% probability level and hydrogen atoms have been removed for clarity.

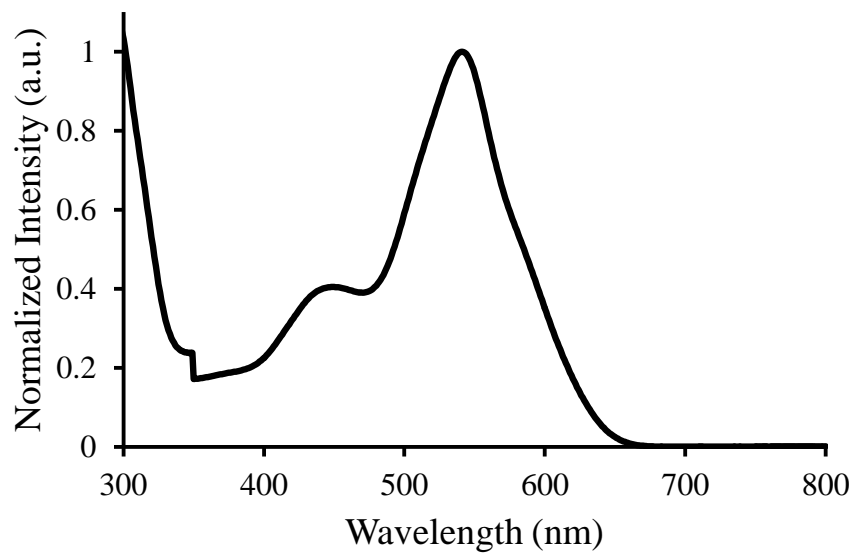


Figure A5.17 UV-vis absorption spectrum of complex **5.9** in Toluene.

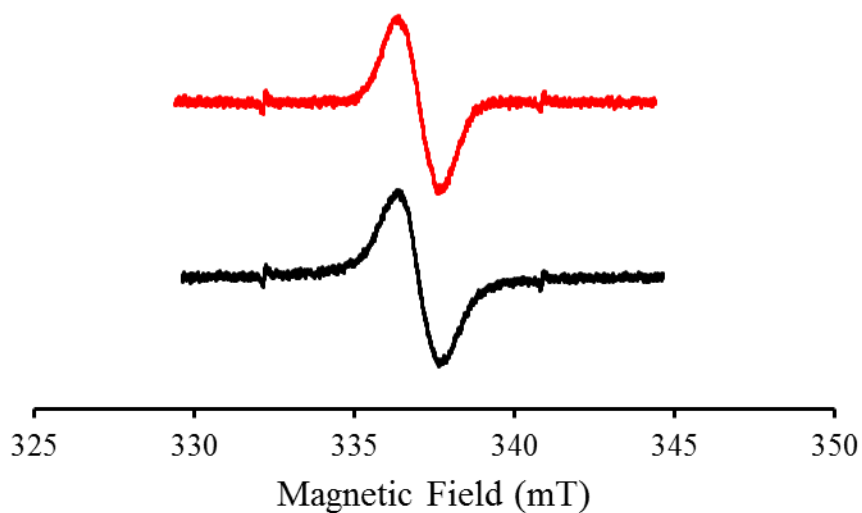


Figure A5.18 EPR spectra of $5.10^{\bullet-}$ (red) and $5.10^{\bullet 2-}$ (black) in CH_2Cl_2 .

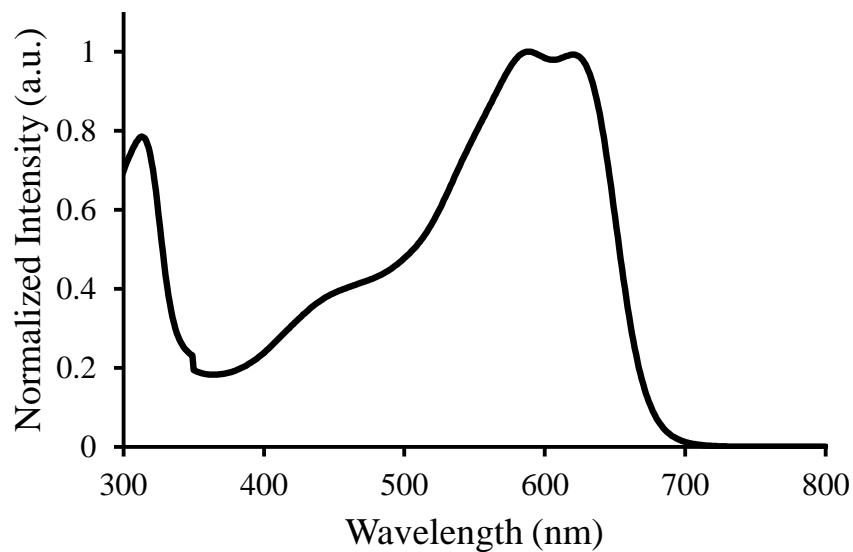


Figure A5.19 UV-vis absorption spectrum of complex **5.11** in toluene.

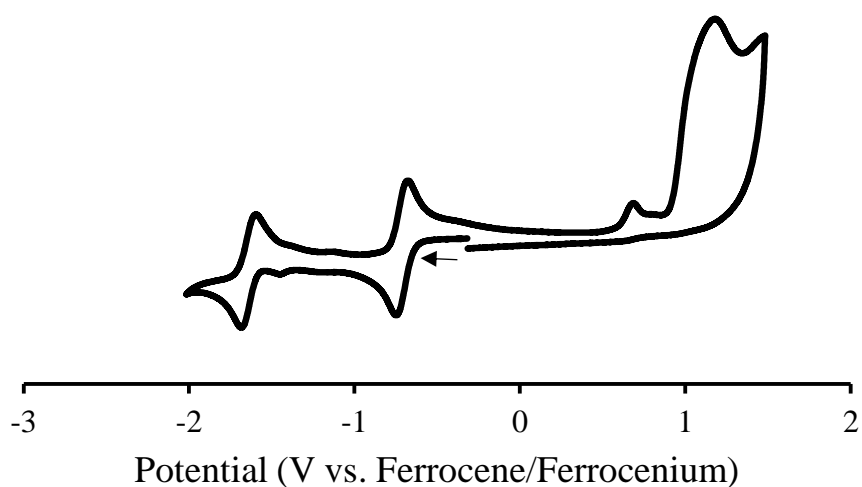


Figure A5.20 Cyclic voltammograms of complex **5.11** recorded at 100 mV s^{-1} in 1 mM CH_2Cl_2 solution containing 0.1 M $[\text{nBu}_4\text{N}][\text{PF}_6]$ as supporting electrolyte.

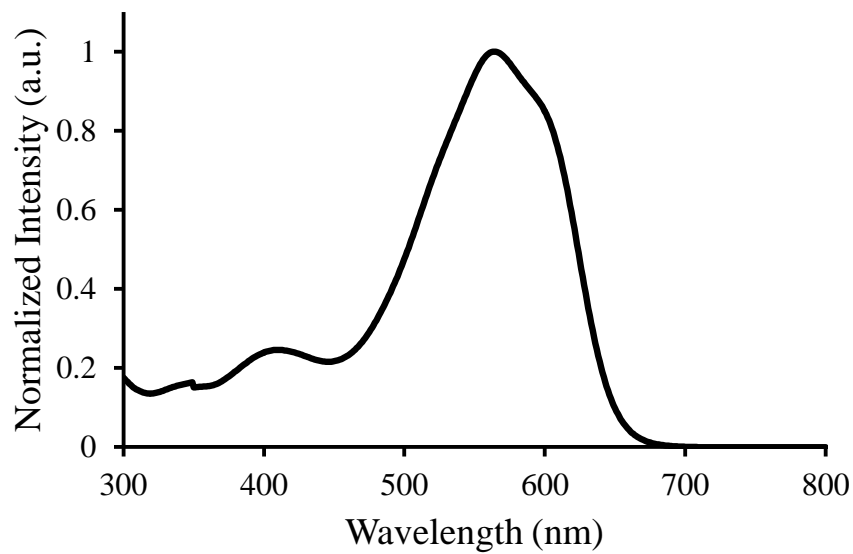


Figure A5.21 UV-vis absorption spectrum of complex **5.12** in toluene.

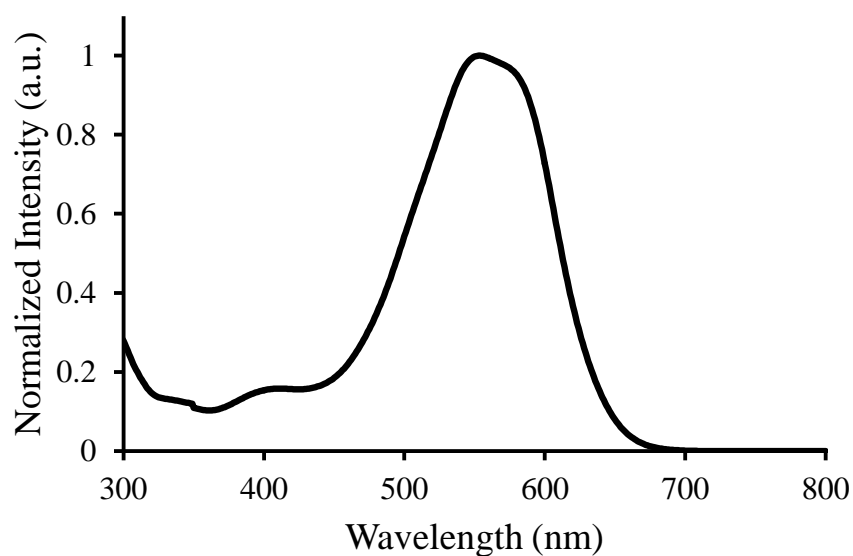


Figure A5.22 UV-vis absorption spectrum of complex **5.13** in toluene.

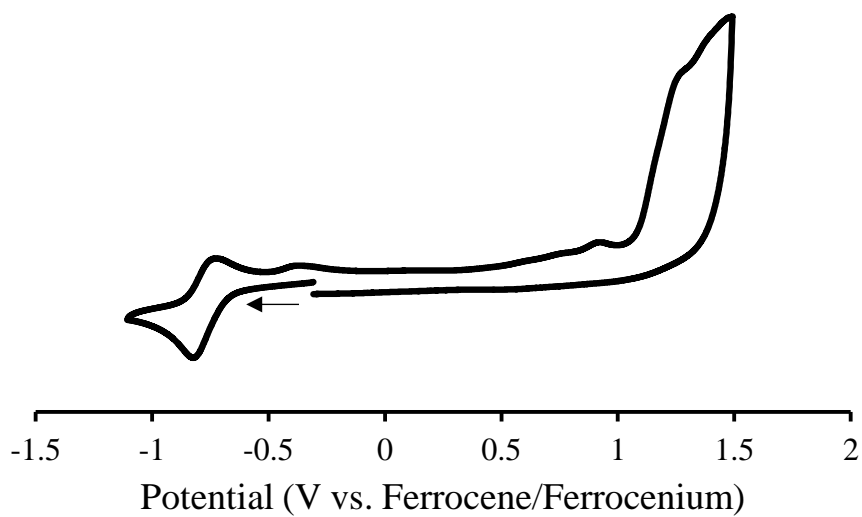


Figure A5.23 Cyclic voltammograms of complex **5.13** recorded at 100 mV s^{-1} in 1 mM CH_2Cl_2 solution containing 0.1 M $[\text{nBu}_4\text{N}][\text{PF}_6]$ as supporting electrolyte.

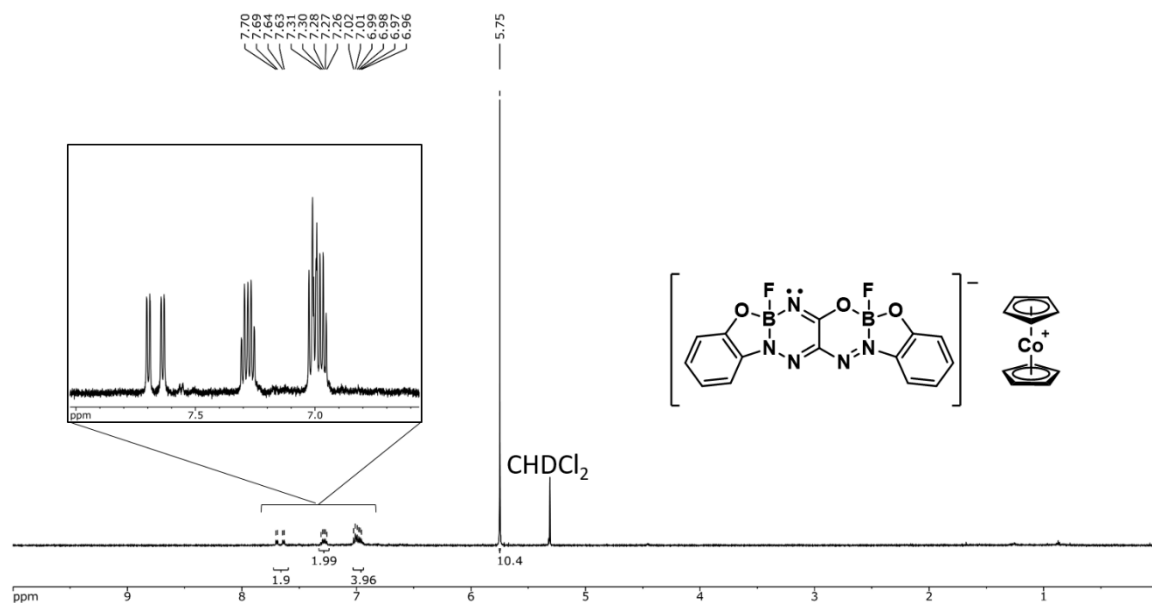


Figure A5.24 ^1H NMR spectrum of **5.16**⁻ in CD_2Cl_2 .

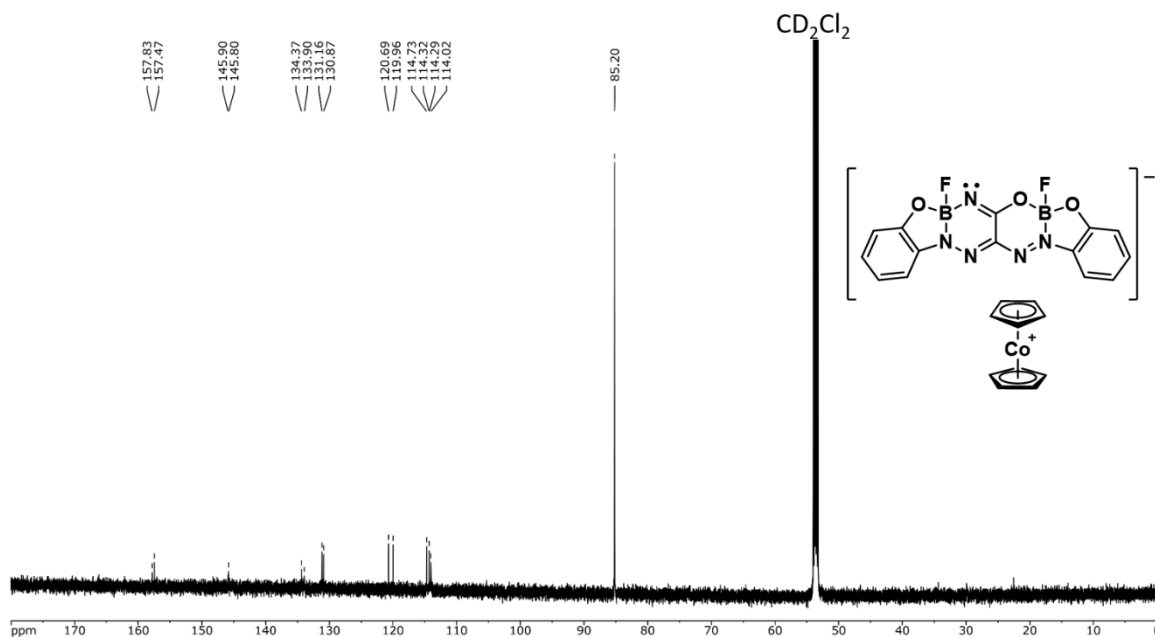


Figure A5.25 $^{13}\text{C}\{^1\text{H}\}$ NMR spectrum of **5.16⁻** in CD_2Cl_2 .

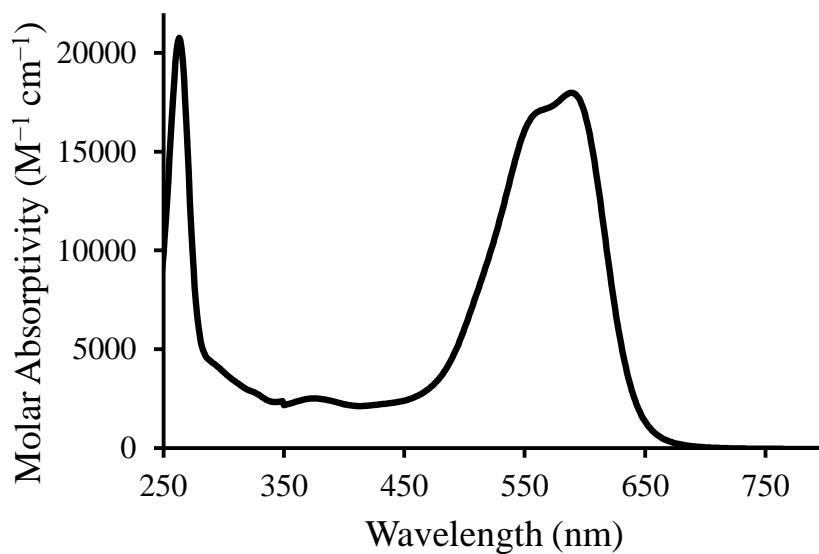


Figure A5.26 UV-vis absorption spectrum of complex **5.16⁻** in CH_2Cl_2 .

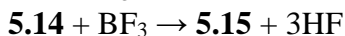
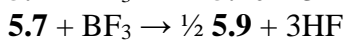
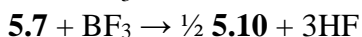
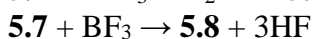
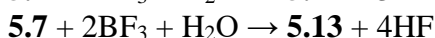
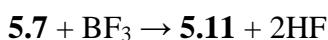
Table A5.1 Changes in the total electronic energy, enthalpy and Gibbs free energy for the reactions of **5.7** to form **5.8–5.13** and the reaction of **5.14** to form **5.15** in the gas phase and in a toluene solution calculated with the PBE1PBE density functional using the 6-311+G(d,p) basis set. All values are per mole of **7** or **14**.

Reaction	ΔE_e (kJ mol ⁻¹)	ΔH°_{353} (kJ mol ⁻¹)	ΔG°_{353} (kJ mol ⁻¹)
Gas phase			
5.7 → 5.8	180.7	161.2	91.2
5.7 → 5.9	100.7	85.7	47.1
5.7 → 5.10	105.9	90.7	53.4
5.7 → 5.11	35.8	26.9	2.1
5.7 → 5.12	-125.6	-124.4	-76.9
5.7 → 5.13	-49.7	-57.3	-54.0
5.14 → 5.15	90.5	70.9	-1.9
Toluene solution (polarized continuum model)			
5.7 → 5.8	164.8	145.3	75.7
5.7 → 5.9	87.4	72.4	34.1
5.7 → 5.10	91.7	76.6	39.9
5.7 → 5.11	27.4	18.3	-6.2
5.7 → 5.12	-133.4	-132.3	-84.2
5.7 → 5.13	-64.9	-72.6	-68.6
5.14 → 5.15	72.6	52.9	-19.4

Table A5.2 Frontier-orbital energies and first singlet-singlet electronic excitation energies (ΔE) of complexes **5.13** and **5.16⁻** in CH₂Cl₂ solution calculated with time-dependent density-functional theory at the PBE1PBE/6-311+G(d,p) level using the SCRFF method.

	Orbital energies (eV)		Oscillator strength	$\Delta E_{\text{calc'd}}$ (eV)	$\Delta E_{\text{calc'd}}$ (nm)	ΔE_{exp} (nm)
	HOMO	LUMO				
5.13	-6.49	-3.52	$f = 1.03$	2.44	508	577
5.16⁻	-5.66	-2.78	$f = 1.06$	2.40	516	589

Reaction stoichiometries used to compute ΔE_e , ΔH° , and ΔG° .



PBE1PBE 6-311+G(d,p) SCRF=(PCM,Solvent=Toluene)
 Temperature=353.15

Compound **5.7** / Optimized geometry

```

0,1
C    -1.338145    2.674505    0.000000
C     0.060995    2.592382    0.000000
C     0.827022    3.755473    0.000000
C     0.199532    4.991736    0.000000
C    -1.190403    5.071922    0.000000
C    -1.959715    3.913899    0.000000
N     0.607554    1.314706    0.000000
N     1.887252    1.109437    0.000000
C     2.315928   -0.135718    0.000000
C     3.741418   -0.280770    0.000000
N     4.889296   -0.403417    0.000000
O    -2.015987    1.492038    0.000000
N     1.639914   -1.330272    0.000000
N     0.369505   -1.287434    0.000000
C    -0.268958   -2.527007    0.000000
C     0.404712   -3.759547    0.000000
C    -0.300372   -4.943512    0.000000
C    -1.700308   -4.916026    0.000000
C    -2.382720   -3.714018    0.000000
C    -1.679345   -2.508578    0.000000
O    -2.398118   -1.374320    0.000000
H     0.000000    0.488219    0.000000
H     1.907020    3.669400    0.000000
H     0.797535    5.895805    0.000000
H    -1.682226    6.038164    0.000000
H    -3.044743    3.971027    0.000000
H    -2.964836    1.648221    0.000000
H    -3.466307   -3.678220    0.000000
H    -2.259920   -5.845584    0.000000
H     0.226808   -5.890820    0.000000
H     1.488066   -3.748244    0.000000
H    -1.821047   -0.599281    0.000000
  
```

PBE1PBE 6-311+G(d,p) SCRF=(PCM,Solvent=Toluene)
Temperature=353.15

Compound **5.8** / Optimized geometry

0,1

C	0.327682	2.046580	-1.230335
C	-0.591983	2.260988	-0.184316
C	-1.209127	3.480774	0.040633
C	-0.910848	4.509973	-0.840920
C	0.000000	4.310056	-1.885252
C	0.640276	3.091823	-2.087651
N	-0.559487	1.081419	0.564956
N	-0.544847	1.077341	1.849963
C	0.000000	0.000000	2.435296
C	0.000000	0.000000	3.864885
N	0.000000	0.000000	5.018247
O	0.862773	0.812684	-1.250301
B	0.000000	0.000000	-0.376825
O	-0.862773	-0.812684	-1.250301
C	-0.327682	-2.046580	-1.230335
C	0.591983	-2.260988	-0.184316
C	1.209127	-3.480774	0.040633
C	0.910848	-4.509973	-0.840920
C	0.000000	-4.310056	-1.885252
C	-0.640276	-3.091823	-2.087651
N	0.559487	-1.081419	0.564956
N	0.544847	-1.077341	1.849963
H	-1.355864	-2.949056	-2.888653
H	-0.215152	-5.132256	-2.559799
H	1.384174	-5.477305	-0.719292
H	1.893690	-3.613035	0.870418
H	-1.893690	3.613035	0.870418
H	-1.384174	5.477305	-0.719292
H	0.215152	5.132256	-2.559799
H	1.355864	2.949056	-2.888653

PBE1PBE 6-311+G(d,p) SCRF=(PCM,Solvent=Toluene)
Temperature=353.15

Compound **5.9** / Optimized geometry

0,1

B	1.627137	0.378695	0.072504
O	1.722202	-0.605396	1.138390
O	-0.929242	0.028181	1.110874
N	3.144283	0.677343	-0.190132
N	3.599868	1.671095	-0.851315
N	1.097367	1.808158	0.379998
N	1.558815	2.794668	-0.322321
N	3.339786	4.596541	-2.577468
C	2.676549	2.637870	-1.031152
C	3.046530	3.728337	-1.876812
C	3.904235	-0.262135	0.480285
C	3.000120	-0.989586	1.273159
C	3.467576	-1.986048	2.118057
H	2.780157	-2.549107	2.737915
C	4.835804	-2.230604	2.128814
H	5.223000	-3.012384	2.773810
C	5.731179	-1.499060	1.335293
H	6.790721	-1.723278	1.378794
C	5.275405	-0.490840	0.501800
H	5.946304	0.097945	-0.112865
C	0.114101	2.162238	1.332017
C	-0.918930	1.263014	1.645999
C	-1.892557	1.649503	2.563564
H	-2.677717	0.942664	2.808957
C	-1.851642	2.904902	3.152143
H	-2.617199	3.186116	3.867421
C	-0.827760	3.795247	2.836478
H	-0.785975	4.772316	3.304096
C	0.151542	3.421875	1.933536
H	0.962816	4.094570	1.681084
B	-1.627107	-0.378712	-0.072503
O	-1.722176	0.605358	-1.138409
O	0.929268	-0.028170	-1.110884
N	-3.144247	-0.677380	0.190127
N	-3.599817	-1.671130	0.851325
N	-1.097315	-1.808170	-0.379978
N	-1.558746	-2.794681	0.322351
N	-3.340351	-4.595963	2.577969
C	-2.676483	-2.637890	1.031177
C	-3.046443	-3.728361	1.876841
C	-3.904211	0.262070	-0.480319

C	-3.000099	0.989521	-1.273198
C	-3.467564	1.985956	-2.118123
H	-2.780148	2.549014	-2.737986
C	-4.835797	2.230488	-2.128901
H	-5.223000	3.012247	-2.773919
C	-5.731167	1.498944	-1.335375
H	-6.790712	1.723141	-1.378893
C	-5.275384	0.490750	-0.501856
H	-5.946279	-0.098035	0.112813
C	-0.114063	-2.162240	-1.332014
C	0.918946	-1.262999	-1.646020
C	1.892542	-1.649463	-2.563628
H	2.677680	-0.942607	-2.809045
C	1.851625	-2.904857	-3.152217
H	2.617160	-3.186051	-3.867527
C	0.827770	-3.795222	-2.836521
H	0.785984	-4.772288	-3.304146
C	-0.151507	-3.421872	-1.933543
H	-0.962764	-4.094580	-1.681070

PBE1PBE 6-311+G(d,p) SCRF=(PCM,Solvent=Toluene)
Temperature=353.15

Compound **5.10** / Optimized geometry

0,1			
B	-1.700471	0.509194	-0.107182
B	1.700472	0.509177	0.107217
N	-3.220933	0.246358	0.183959
N	-3.738638	-0.855451	0.570755
N	-1.312952	-0.829184	-0.795996
N	-1.836592	-1.943572	-0.377926
N	3.220923	0.246339	-0.183970
N	3.738618	-0.855465	-0.570794
N	1.312954	-0.829213	0.795993
N	1.836581	-1.943597	0.377897
N	-3.706508	-4.157069	1.395973
N	3.706311	-4.157078	-1.396170
O	-1.770810	1.690750	-0.944689
O	0.950576	0.792131	-1.082173
O	1.770835	1.690698	0.944773
O	-0.950598	0.792083	1.082231
C	-2.905957	-1.906988	0.414555
C	2.905935	-1.907003	-0.414598
C	-3.349152	-3.156814	0.946475
C	3.349126	-3.156820	-0.946541
C	-3.925915	1.376585	-0.187112

C	-3.009218	2.192802	-0.874748
C	-3.439291	3.385626	-1.440766
H	-2.744562	4.019428	-1.978713
C	-4.775905	3.729629	-1.282136
H	-5.130005	4.663939	-1.705087
C	-5.682752	2.908083	-0.596173
H	-6.717298	3.216603	-0.499999
C	-5.269285	1.706403	-0.046137
H	-5.950694	1.045553	0.476911
C	-0.464071	-0.946658	-1.921737
C	0.662502	-0.115204	-2.037872
C	1.460938	-0.219714	-3.174454
H	2.315594	0.441958	-3.263738
C	1.170606	-1.154704	-4.157406
H	1.805650	-1.224609	-5.034037
C	0.071517	-1.999899	-4.022080
H	-0.156458	-2.730989	-4.789169
C	-0.745854	-1.889923	-2.910945
H	-1.619711	-2.520746	-2.795251
C	3.925915	1.376559	0.187113
C	3.009239	2.192755	0.874800
C	3.439330	3.385567	1.440834
H	2.744620	4.019355	1.978819
C	4.775938	3.729575	1.282168
H	5.130046	4.663878	1.705131
C	5.682764	2.908049	0.596153
H	6.717306	3.216575	0.499953
C	5.269280	1.706383	0.046100
H	5.950674	1.045550	-0.476989
C	0.464084	-0.946704	1.921745
C	-0.662498	-0.115266	2.037904
C	-1.460921	-0.219804	3.174494
H	-2.315586	0.441854	3.263788
C	-1.170564	-1.154799	4.157433
H	-1.805598	-1.224728	5.034068
C	-0.071461	-1.999974	4.022086
H	0.156540	-2.731065	4.789164
C	0.745894	-1.889972	2.910940
H	1.619758	-2.520783	2.795234

PBE1PBE 6-311+G(d,p) SCRF=(PCM,Solvent=Toluene)
Temperature=353.15

Compound **5.11** / Optimized geometry

0,1

C	3.137551	-0.122566	-0.671405
C	2.016730	-0.550157	0.083456
C	1.991622	-1.856224	0.598267
C	3.024673	-2.733914	0.351399
C	4.111296	-2.320629	-0.423563
C	4.163946	-1.034388	-0.923588
N	0.919135	0.285088	0.344763
N	1.068154	1.559894	0.132999
C	0.010362	2.380472	0.146223
C	0.296764	3.773332	0.017687
N	0.531390	4.899111	-0.070755
O	3.274001	1.109968	-1.172111
N	-1.277329	2.014651	0.056429
N	-1.455260	0.766106	0.281011
B	-0.434690	-0.188805	0.950403
F	-0.383692	-0.007635	2.320339
O	-0.946691	-1.489976	0.563143
C	-2.186571	-1.324952	0.069419
C	-3.064051	-2.334857	-0.292145
C	-4.298161	-1.958970	-0.811425
C	-4.655052	-0.614833	-0.986207
C	-3.777088	0.400843	-0.644272
C	-2.552142	0.021371	-0.108384
H	1.146301	-2.174992	1.194231
H	-2.789345	-3.375206	-0.166151
H	-5.006136	-2.731867	-1.091123
H	-5.627944	-0.368805	-1.395566
H	-4.024131	1.447551	-0.777216
H	5.006100	-0.688804	-1.512383
H	4.926435	-3.006616	-0.627469
H	2.988985	-3.736377	0.760911
H	2.566033	1.666776	-0.792450

PBE1PBE 6-311+G(d,p) SCRF=(PCM,Solvent=Toluene)
 Temperature=353.15

Compound **5.12** / Optimized geometry

0,1

B	2.183982	-1.818880	-0.324651
B	-2.576550	-1.293297	0.467259
F	2.794967	-2.485348	0.723446
F	2.827831	-2.049986	-1.524950
F	-2.487766	-1.608838	1.807733
O	2.353382	2.674671	0.192720
H	1.568960	2.088756	0.232222
O	-3.910545	-1.414227	-0.070854
O	-1.522043	-2.021486	-0.265747
N	2.178547	-0.245079	-0.019915
N	1.104651	0.430554	0.159909
N	-2.279097	0.236072	0.259781
N	-1.128772	0.766826	0.199260
N	0.717416	-2.254473	-0.429989
H	0.526691	-3.222647	-0.666672
C	-0.111283	-0.125689	0.138254
C	-0.327416	-1.524143	-0.168996
C	3.391923	0.475786	0.020751
C	3.435242	1.892063	0.116319
C	4.677329	2.529749	0.124216
H	4.679379	3.611778	0.192972
C	5.851827	1.807817	0.053652
H	6.802831	2.329496	0.065680
C	5.814804	0.414770	-0.027109
H	6.731978	-0.160113	-0.075331
C	4.600524	-0.237330	-0.044065
H	4.577646	-1.315961	-0.101848
C	-3.494579	0.861251	0.040302
C	-4.427837	-0.174969	-0.160851
C	-5.745825	0.135536	-0.456307
H	-6.472309	-0.651806	-0.617670
C	-6.091767	1.480691	-0.537000
H	-7.119982	1.743770	-0.762057
C	-5.156514	2.504437	-0.339137
H	-5.470922	3.539110	-0.410808
C	-3.833794	2.205064	-0.052759
H	-3.088105	2.976891	0.098523

PBE1PBE 6-311+G(d,p) SCRF=(PCM,Solvent=Toluene)
Temperature=353.15

Compound **5.13** / Optimized geometry

0,1

B	2.385130	-1.336210	0.126747
B	-2.347129	-1.308270	0.106778
F	2.508466	-1.986910	1.348581
F	-2.352928	-1.985475	1.309615
O	3.623565	-1.384274	-0.634046
O	-3.599302	-1.391877	-0.609392
O	-1.148607	-1.700069	-0.658618
N	2.208091	0.206168	0.355151
N	1.127780	0.841489	0.551741
N	-2.214067	0.234732	0.352357
N	-1.133013	0.867997	0.540447
N	1.103261	-1.764396	-0.569938
H	1.015293	-2.637253	-1.078303
C	-0.008086	0.128070	0.398521
C	-0.027729	-1.174380	-0.262042
C	3.454729	0.784433	0.150357
C	4.249229	-0.206926	-0.454656
C	5.546942	0.093318	-0.840370
H	6.167056	-0.659773	-1.311917
C	6.014452	1.381220	-0.598637
H	7.030212	1.632223	-0.885780
C	5.215604	2.361386	0.002164
H	5.619790	3.352379	0.173479
C	3.912107	2.074585	0.379739
H	3.268659	2.816107	0.838917
C	-3.468428	0.791289	0.148994
C	-4.248116	-0.225130	-0.434961
C	-5.557299	0.040044	-0.804458
H	-6.166528	-0.732205	-1.258712
C	-6.049423	1.321033	-0.572860
H	-7.073914	1.546115	-0.850262
C	-5.265062	2.326746	0.004291
H	-5.689201	3.310653	0.167806
C	-3.950883	2.074028	0.368871
H	-3.319038	2.835147	0.811793

PBE1PBE 6-311+G(d,p) SCRF=(PCM,Solvent=Toluene)
Temperature=353.15

Compound **5.14** / Optimized geometry

0,1

C	3.387406	0.992871	0.977377
C	2.588139	0.231097	0.117467
C	3.091206	-0.955283	-0.441124
C	4.402363	-1.325808	-0.141871
C	5.192402	-0.573239	0.717147
C	4.676334	0.589142	1.282301
N	1.261979	0.629391	-0.181077
N	1.122066	1.883518	-0.154276
C	-0.150483	2.389086	-0.283820
C	-0.185718	3.817377	-0.401786
N	-0.207433	4.966778	-0.509229
C	2.285114	-1.840673	-1.347882
O	1.676476	-2.924912	-0.637495
N	-1.330873	1.820083	-0.209617
N	-1.478275	0.542473	-0.112405
C	-2.767927	0.009546	0.068976
C	-3.892720	0.825885	-0.050169
C	-5.155660	0.290980	0.148564
C	-5.306148	-1.055483	0.462844
C	-4.179908	-1.861462	0.573978
C	-2.899227	-1.351130	0.388049
C	-1.695694	-2.232986	0.548940
O	-0.882656	-2.108811	-0.599685
H	-0.681943	-0.095611	-0.223851
H	-3.762452	1.872184	-0.296536
H	-6.026270	0.930516	0.050233
H	-6.293993	-1.477480	0.611747
H	-4.290230	-2.915504	0.810420
H	4.814237	-2.218429	-0.606084
H	6.206373	-0.887933	0.939399
H	5.281043	1.183335	1.959196
H	2.972610	1.897797	1.405453
H	-0.030440	-2.555573	-0.450820
H	-1.136878	-1.933558	1.450310
H	-2.026412	-3.268108	0.697884
H	1.464525	-1.296882	-1.814370
H	2.928360	-2.241543	-2.139021
H	2.321798	-3.318660	-0.044242

PBE1PBE 6-311+G(d,p) SCRF=(PCM,Solvent=Toluene)
 Temperature=353.15

Compound **5.15** / Optimized geometry

0,1

B	0.000037	-0.336692	0.000062
O	-0.181540	-1.100147	-1.196879
O	0.181672	-1.099981	1.197097
N	-1.231434	0.611572	0.107399
N	-1.201660	1.886079	0.085106
N	1.231429	0.611652	-0.107383
N	1.201585	1.886156	-0.085105
N	-0.000445	5.057917	0.000089
C	-0.000057	2.476449	0.000007
C	-0.000096	3.903644	0.000020
C	-2.488008	-0.029378	0.069899
C	-2.530304	-1.299397	-0.517263
C	-3.758868	-1.954293	-0.556333
H	-3.818552	-2.936374	-1.016959
C	-4.902145	-1.364418	-0.036667
H	-5.848752	-1.892280	-0.081028
C	-4.838465	-0.093667	0.534985
H	-5.730997	0.367004	0.943615
C	-3.631396	0.578931	0.588698
H	-3.550921	1.563154	1.034857
C	-1.302381	-1.948128	-1.116114
H	-1.071132	-2.848764	-0.526580
H	-1.536217	-2.279958	-2.132411
C	2.488028	-0.029242	-0.069952
C	2.530426	-1.299194	0.517351
C	3.759002	-1.954068	0.556301
H	3.818774	-2.936109	1.017004
C	4.902199	-1.364225	0.036410
H	5.848815	-1.892075	0.080686
C	4.838420	-0.093533	-0.535357
H	5.730888	0.367111	-0.944161
C	3.631326	0.579031	-0.588976
H	3.550760	1.563200	-1.035240
C	1.302616	-1.947854	1.116519
H	1.071419	-2.848728	0.527334
H	1.536580	-2.279279	2.132925

PBE1PBE 6-311+G(d,p) SCRF=(PCM,Solvent=Dichloromethane)

Compound **5.13** / Optimized geometry in a CH₂Cl₂ solution, T = 298.15 K

0,1

B	2.384224	-1.334376	0.123754
B	-2.346392	-1.305692	0.103232
F	2.513945	-1.985812	1.351204
F	-2.361593	-1.989152	1.308473
O	3.624383	-1.384797	-0.633353
O	-3.598066	-1.390898	-0.613656
O	-1.149162	-1.703410	-0.655319
N	2.208447	0.205645	0.354730
N	1.127235	0.839656	0.551356
N	-2.214508	0.233497	0.353941
N	-1.132306	0.865285	0.541522
N	1.103279	-1.768768	-0.565686
H	1.019334	-2.639115	-1.080017
C	-0.007912	0.125836	0.398189
C	-0.026595	-1.177304	-0.261295
C	3.454770	0.785014	0.149926
C	4.250328	-0.205059	-0.455066
C	5.547542	0.094815	-0.841632
H	6.168751	-0.656500	-1.314748
C	6.014666	1.383454	-0.599949
H	7.029891	1.635142	-0.888026
C	5.215179	2.362894	0.001587
H	5.618611	3.354179	0.172683
C	3.911669	2.075595	0.379652
H	3.269685	2.817984	0.839388
C	-3.468720	0.791320	0.150464
C	-4.248635	-0.222041	-0.437511
C	-5.556659	0.043196	-0.808936
H	-6.166383	-0.726112	-1.267672
C	-6.049110	1.324216	-0.574335
H	-7.072786	1.550494	-0.853322
C	-5.265082	2.327565	0.007492
H	-5.688928	3.311170	0.173171
C	-3.951283	2.073666	0.373704
H	-3.321716	2.834410	0.820365

PBE1PBE 6-311+G(d,p) SCRF=(PCM,Solvent=Dichloromethane)

Compound **5.16⁻** / Optimized geometry in a CH₂Cl₂ solution, T = 298.15 K

0,1

B	2.323919	-1.342081	0.129995
B	-2.300714	-1.311908	0.036186
F	2.504349	-1.927498	1.412011
F	-2.339330	-2.013645	1.252958
O	3.619594	-1.410295	-0.597200
O	-3.593570	-1.390732	-0.649896
O	-1.151250	-1.685585	-0.739451
N	2.204764	0.214572	0.330991
N	1.121906	0.863949	0.500872
N	-2.202028	0.220056	0.329378
N	-1.115243	0.865147	0.504368
N	1.107758	-1.858968	-0.528442
C	0.000025	0.130903	0.347922
C	0.036065	-1.223452	-0.287823
C	3.454167	0.777511	0.126748
C	4.249485	-0.242533	-0.436158
C	5.560035	0.039315	-0.802772
H	6.182481	-0.731364	-1.243269
C	6.041017	1.328596	-0.588573
H	7.065292	1.559252	-0.863496
C	5.241937	2.333039	-0.031946
H	5.652143	3.325198	0.119565
C	3.926021	2.067182	0.326975
H	3.283365	2.830255	0.751570
C	-3.459925	0.775067	0.150865
C	-4.246082	-0.233981	-0.440112
C	-5.564092	0.031827	-0.778658
H	-6.177547	-0.734065	-1.239329
C	-6.064688	1.305979	-0.514324
H	-7.095468	1.528511	-0.770304
C	-5.275682	2.302245	0.067073
H	-5.699606	3.281891	0.257071
C	-3.950491	2.047316	0.403487
H	-3.316883	2.806048	0.848557

Curriculum Vitae

- Name:** Stephanie M. Barbon
- Post-secondary Education and Degrees:** University of Western Ontario
London, Ontario, Canada
2009-2013 B.Sc.
- The University of Western Ontario
London, Ontario, Canada
2013-2017 Ph.D.
- Honours and Awards:** Elings Fellowship Prize in Science
2017–2019
- Banting Postdoctoral Fellowship
2017–2019
- Natural Science and Engineering Research Council (NSERC)
Postdoctoral Fellowship
2017–2019
- Emerging Materials Chemistry Investigator
Canadian Chemistry Conference and Exhibition, 2017
- CSC Travel Award
2016
- Best Oral Presentation
Boron in the Americas XV Conference, 2016
- Robert and Ruth Lumsden Graduate Fellowship
2016
- Lipson-Baines Award in Chemistry
2016
- Outstanding Oral Presentation Award
Canadian Chemistry Conference and Exhibition, 2016
- Natural Science and Engineering Research Council (NSERC)
Canada Graduate Scholarship - Doctoral Level
2014-2017

Natural Science and Engineering Research Council (NSERC)
Canada Graduate Scholarship – Masters Level
2013-2014

Western Graduate Entrance Scholarship
2013

Runner-up Best Oral Presentation
Inorganic Discussion Weekend, 2013

Society for Chemical Industry (SCI) Merit Award
2013

Alumni Gold Medal Graduation Award
2013

Hypercube Scholar Prize Graduation Award
2013

Western Science Undergraduate Pre-thesis Award
2013

NSERC Undergraduate Student Research Award
The University of Western Ontario, 2012

Chemistry Alumni Scholarship
2012

UWO Incourse Scholarship Year IV
2012

NSERC Undergraduate Student Research Award
Memorial University, 2011

Chemistry Class of 1950 Scholarship
2011

William Wyatt Scholarship
2010

**Related Work
Experience**

Teaching Assistant – Chem 1024B, Chem 2271A
The University of Western Ontario
2013-2014

Publications:

Barbon, S. M.; Staroverov, V. N.; Gilroy, J. B. *Angew. Chem. Int. Ed.*, **2017**, DOI: 10.1002/anie.201704285.

Barbon, S. M.; Novoa, S.; Bender, D.; Groom, H.; Luyt, L. G.; Gilroy, J. B. *Org. Chem. Front.*, **2017**, *4*, 178–190.

Barbon, S. M.; Gilroy, J. B. *Polym. Chem.*, **2016**, *7*, 3589–3598.

Novoa, S.; Paquette, J. A.; Barbon, S. M.; Maar, R. R.; Gilroy, J. B. *J. Mater. Chem. C*, **2016**, *4*, 3987–3994.

Barbon, S. M.; Gobbo, P. G.; Luo, W.; Price, J. T.; Biesinger, M. C.; Workentin, M. S.; Gilroy, J. B. *Synlett*, **2016**, *26*, 304–308.

Maar, R. R.; Barbon, S. M.; Sharma, N.; Groom, H.; Luyt, L. G.; Gilroy, J. B. *Chem. Eur. J.*, **2015**, *21*, 15589–15599.

Rabiee Kenaree, A.; Cuthbert, T. J.; Barbon, S. M.; Boyle, P. D.; Gillies, E. R.; Ragogna, P. J.; Gilroy, J. B. *Organometallics*, **2015**, *34*, 4272–4280.

Barbon, S. M.; Price, J. T.; Yogarajah, U.; Gilroy, J. B. *RSC Adv.*, **2015**, *5*, 56316–56324.

Barbon, S. M.; Staroverov, V. N.; Gilroy, J. B. *J. Org. Chem.*, **2015**, *80*, 5226–5235.

Gobbo, P.; Romagnoli, T.; Barbon, S. M.; Price, J. T.; Keir, J. L. A.; Gilroy, J. B.; Workentin, M. S. *Chem. Commun.*, **2015**, *51*, 3766–3769.

Hesari, M.; Barbon, S. M.; Staroverov, V. N.; Ding, Z.; Gilroy, J. B. *Chem. Commun.*, **2015**, *51*, 3766–3769.

Barbon, S. M.; Price, J. T.; Reinkeluers, P. A.; Gilroy, J. B., *Inorg. Chem.*, **2014**, *53*, 10585–10593.

Barbon, S. M.; Reinkeluers, P. A.; Price, J. T.; Staroverov, V. N.; Gilroy, J. B. *Chem. Eur. J.*, **2014**, *20*, 11340–11344.

Barbon, S. M.; Staroverov, V. N.; Boyle, P. D.; Gilroy, J. B. *Dalton Trans.*, **2014**, *43*, 240–250.

Ikpo, N.; Barbon, S. M.; Drover, M. W.; Dawe, L. N.; Kerton, F. M. *Organometallics*, **2012**, *31*, 8145–8158.